frontiers | Research Topics

Changing biogeochemical and ecological dynamics in the south china sea in times of global change

Edited by
Shuwen Zhang, Fajin Chen, Tim Jennerjahn and Guangzhe Jin

Published in
Frontiers in Marine Science

ISSN 1664-8714
ISBN 978-2-83252-063-5
DOI 10.3389/978-2-83252-063-5

About Frontiers

Frontiers is more than just an open access publisher of scholarly articles: it is a pioneering approach to the world of academia, radically improving the way scholarly research is managed. The grand vision of Frontiers is a world where all people have an equal opportunity to seek, share and generate knowledge. Frontiers provides immediate and permanent online open access to all its publications, but this alone is not enough to realize our grand goals.

Frontiers journal series

The Frontiers journal series is a multi-tier and interdisciplinary set of open-access, online journals, promising a paradigm shift from the current review, selection and dissemination processes in academic publishing. All Frontiers journals are driven by researchers for researchers; therefore, they constitute a service to the scholarly community. At the same time, the *Frontiers journal series* operates on a revolutionary invention, the tiered publishing system, initially addressing specific communities of scholars, and gradually climbing up to broader public understanding, thus serving the interests of the lay society, too.

Dedication to quality

Each Frontiers article is a landmark of the highest quality, thanks to genuinely collaborative interactions between authors and review editors, who include some of the world's best academicians. Research must be certified by peers before entering a stream of knowledge that may eventually reach the public - and shape society; therefore, Frontiers only applies the most rigorous and unbiased reviews. Frontiers revolutionizes research publishing by freely delivering the most outstanding research, evaluated with no bias from both the academic and social point of view. By applying the most advanced information technologies, Frontiers is catapulting scholarly publishing into a new generation.

What are Frontiers Research Topics?

Frontiers Research Topics are very popular trademarks of the *Frontiers journals series*: they are collections of at least ten articles, all centered on a particular subject. With their unique mix of varied contributions from Original Research to Review Articles, Frontiers Research Topics unify the most influential researchers, the latest key findings and historical advances in a hot research area.

Find out more on how to host your own Frontiers Research Topic or contribute to one as an author by contacting the Frontiers editorial office: frontiersin.org/about/contact

Changing biogeochemical and ecological dynamics in the south china sea in times of global change

Topic editors

Shuwen Zhang — Shantou University, China

Fajin Chen — Guangdong Ocean University, China

Tim Jennerjahn — Leibniz Centre for Tropical Marine Research (LG), Germany

Guangzhe Jin — Guangdong Ocean University, China

Citation

Zhang, S., Chen, F., Jennerjahn, T., Jin, G., eds. (2023). *Changing biogeochemical and ecological dynamics in the south china sea in times of global change*. Lausanne: Frontiers Media SA. doi: 10.3389/978-2-83252-063-5

Table of contents

frontiers | Frontiers in Marine Science

TYPE Editorial
PUBLISHED 16 March 2023
DOI 10.3389/fmars.2023.1165859

OPEN ACCESS

EDITED AND REVIEWED BY
Eric 'Pieter Achterberg,
Helmholtz Association of German Research Centres (HZ), Germany

*CORRESPONDENCE
Shuwen Zhang
zhangsw@stu.edu.cn

SPECIALTY SECTION
This article was submitted to Marine Biogeochemistry, a section of the journal Frontiers in Marine Science

RECEIVED 14 February 2023
ACCEPTED 13 March 2023
PUBLISHED 16 March 2023

CITATION
Zhang S, Jennerjahn TC, Chen F and Jin G (2023) Editorial: Changing biogeochemical and ecological dynamics in the South China Sea in times of global change. *Front. Mar. Sci.* 10:1165859. doi: 10.3389/fmars.2023.1165859

Editorial: Changing biogeochemical and ecological dynamics in the South China Sea in times of global change

Shuwen Zhang[1]*, Tim C. Jennerjahn[2], Fajin Chen[3] and Guangzhe Jin[3]

[1]Institute of Marine Science, Shantou University, Shantou, China, [2]Department of Biogeochemistry and Geology, Leibniz Centre for Tropical Marine Research, Bremen, Germany, [3]College of Ocean and Meteorology, Guangdong Ocean University, Zhanjiang, China

KEYWORDS

seaweeds, climate change, evolutionary genetics, ecological responses, biodiversity conservation

Editorial on the Research Topic
Changing biogeochemical and ecological dynamics in the South China Sea in times of global change

1 Introduction

In general, ocean physical processes affect marine biogeochemical cycles and ecology. The South China Sea (SCS), the largest semi-enclosed tropical sea in the Pacific Ocean, has a variety of processes that are influenced by global change and human activities. The biogeochemistry and ecology of the SCS are controlled by a complex interplay of processes, many of which need to be better understood. Under the pressure of global change, interdisciplinary research efforts on the interaction of physical, biological, biogeochemical and sedimentological processes are required. Therefore, this Research Topic aims to facilitate discussions on the use of observational, experimental, and modeling approaches to clarify how physical dynamics at multiple temporal and spatial scales affect the biogeochemistry and ecology of the SCS in the context of global change. It is a collection of 14 original and novel articles in the following four areas of research.

2 The impact of multi-scale physical dynamics on the biogeochemistry and biology

The three papers in this section use observational data to better understand the coupled physical-biogeochemical processes in the SCS. Sun et al. investigated the important role of bacterial degradation of dimethylsulfoniopropionate (DMSP) on ecosystem productivity and global climate using the northern SCS as an example. This study showed that temperature and depth were the most important factors determining the taxonomic distribution of DMSP degradation genes in the Roseobacter group, as well as their abundance. It highlights the important role of the Roseobacter group in DMSP

degradation in tropical oceans. Wu et al. correlated the vertical distribution of chl-a being regulated by mesoscale eddies with mesoscale eddies in the SCS by observing the phytoplankton under a weak cold eddy and two warm eddies along the 18°N transect in the SCS. It is shown that the presence of phytoplankton and nutrients in cold eddies is accomplished by the motion associated with eddy-induced divergence. Li et al. investigated the different tolerance and resistance to upwelling among three species of mangroves through laboratory experiments. The study provides new insights into mangroves' response to upwelling.

3 The response of biogeochemical cycles and biology to increasing human activities

This section includes four papers, which come up with interesting implications for carbon research in the SCS, especially regarding China's "carbon neutral" policy. Ding et al. conducted laboratory incubation bioassay experiments and seagoing measurement campaigns in the spring and summer of 2015-2016 and 2019 to determine the primary production, terrestrial inputs from the Pearl River and the intrusion of the Kuroshio Current influencing the distribution and microbial degradation of dissolved organic carbon in the northern SCS. The dissolution of particles supplied by rivers around the SCS and the continental margin plays an important role in supplying additional Nd to the open SCS as deduced from surface water distribution and water column profiles by Wu et al. River discharge and anthropogenic inputs are also important external sources of dissolved organic matter (DOM) in low-salinity nearshore waters, i.e. estuaries and coasts in the Beibu Gulf as demonstrated by Zhu et al. In contrast, DOM in offshore waters is mainly generated by *in situ* biological activities. Chou et al. calculated the metabolic rate and carbon sink capacity of seagrass meadows from the dynamics of O2 and pCO2 in seagrass meadows in the Southeast Asian archipelago region, and found that seagrass meadows with high total primary production (GPP) do not necessarily have a high carbon sequestration potential.

4 The cycling of gases, nutrients and trace metals

Yu et al. used the distribution of dissolved silicate (DSi) and other environmental parameters to explore the role of marginal seas in deep-sea DSi regeneration in the western Pacific Ocean. They found that in oligotrophic marginal seas (such as the SCS), the DSi content in deep water was similar to that of the adjacent Pacific waters. However, in the nutrient-rich marginal seas (e.g., Bering Sea), the DSi content in the deep sea is significantly higher than in the adjacent deep Pacific. This is mainly due to deep-sea DSi regeneration in marginal sea basins, which is driven by high biogenic particle flux from highly productive surface waters. Liu et al. studied the active chlorophyll fluorescence at a high spatial and temporal resolution using fast repetition rate fluorometry (FRRf) throughout the outer continental shelf of the northern SCS, the basin of the northern SCS, the cyclonic eddy-influenced domain in the western SCS, and the southeastern SCS. They demonstrated that FRRf has become a powerful tool for assessing the physiological status of phytoplankton in the sea and can be linked to ocean dynamics at fine scales.

5 Reconstruction of the paleoenvironment by using sedimentary archives

The five papers in this section focus on the paleoenvironment in sedimentary archives, providing some new insights into the reconstruction of paleoceanography and paleoenvironment in the SCS. Liu et al. documented a Middle Miocene shallow-water contourite depositional system in the southwest SCS by interpreting seismic reflection data and calibrating results with the previous chronological framework. Showed by radiocarbon and optically stimulated luminescence (OSL) dating of cores from the Chaoshan delta along the SCS by Zhong et al., the Quaternary sedimentation of the Rongjiang Plain dates to at least the marine isotope stage (MIS)6 of the low sea level period during which fluvial processes mainly influenced the plain. Lin et al. were interested in establishing high-resolution chronologies on two cores from Zhuhai using quartz (OSL) and radiocarbon (14C) dating, and further reconstructing the Holocene sedimentary history of the Pearl River Delta. Yu et al. were able to reconstruct the low sea levels during the Last Glacial Maximum by examining and analyses of the deepest speleothems (-116 m) collected from the deepest known blue hole on a global scale, the Sansha Yongle Blue Hole, Xisha Islands in SCS, Li et al. investigated fossil assemblages and sedimentary microfacies on high-resolution samples from two adjacent sections of the South China Block on land using the divergent patterns of Permian–Triassic mass extinction (PTME) in different paleoenvironment water depths. They found that anoxic conditions were the likely major cause of the PTME in deep-sea environments.

6 Prospects and challenges

This Research Topic provides perspectives for current research on ocean dynamic processes closely related to the environmental and ecological characteristics of the SCS. However, there still needs to be more relevant research data. As a typical marginal sea system, the South China Sea receives a large number of materials of human origin through atmospheric deposition and riverine input, which faces an environmental and ecological challenge. On the other hand, the Dynamics of SCS are complex as it is connected to the Northwest Pacific Ocean through the Luzon Strait. The water exchange between the two basins greatly impacts the distribution, transportation, and circulation of materials within the South China Sea. The relevant studies on the coupling of biogeochemistry, i.e., the interdisciplinary study between multi-scale dynamical processes in the ocean, explaining the biogeochemical processes with more

detailed physical mechanisms, are still weak. Moreover, the related systemic studies about the ocean and the atmosphere in the SCS still need to be improved. For example, some dynamical processes in the ocean, although driven by the atmosphere, affect bioecology and finally affect the processes in marine geology, which still need further study. Future studies should continue to collect long-term observation data and establish a more detailed data support and research legacy for a more comprehensive and in-depth understanding of the ocean dynamics and related biological, chemical, and geological processes in the SCS region.

Author contributions

All authors listed have made a substantial, direct, and intellectual contribution to the work and approved it for publication.

Conflict of interest

The authors declare that the research was conducted in the absence of any commercial or financial relationships that could be construed as a potential conflict of interest.

Publisher's note

frontiers | Frontiers in Marine Science

ORIGINAL RESEARCH
published: 03 May 2022
doi: 10.3389/fmars.2022.895613

Abundance and Diversity of Dimethylsulfoniopropionate Degradation Genes of *Roseobacter* Group in the Northern South China Sea

Fulin Sun[1,2,3,4], *Youshao Wang*[1,2,3,4], *Zhaoyu Jiang*[5], *Cuici Sun*[1,2,3,4], *Yutu Wang*[1,2,3,4] *and Meilin Wu*[1,3,4*]

[1] State Key Laboratory of Tropical Oceanography, South China Sea Institute of Oceanology, Chinese Academy of Sciences, Guangzhou, China, [2] Daya Bay Marine Biology Research Station, Chinese Academy of Sciences, Shenzhen, China, [3] Southern Marine Science and Engineering Guangdong Laboratory (Guangzhou), Guangzhou, China, [4] Sanya Institute of Oceanology, South China Sea Institute of Oceanology, Sanya, China, [5] College of Life Sciences, Linyi University, Linyi, China

OPEN ACCESS

Edited by:
Fajin Chen,
Guangdong Ocean University, China

Reviewed by:
Peng Wu,
Chinese Academy of Fishery Sciences (CAFS), China
Yanpei Zhuang,
Jimei University, China
Yong Zhang,
Fujian Normal University, China

***Correspondence:**
Meilin Wu
mlwu@scsio.ac.cn

Specialty section:
This article was submitted to Marine Biogeochemistry, a section of the journal Frontiers in Marine Science

Received: 14 March 2022
Accepted: 01 April 2022
Published: 03 May 2022

Citation:
Sun F, Wang Y, Jiang Z, Sun C, Wang Y and Wu M (2022) Abundance and Diversity of Dimethylsulfoniopropionate Degradation Genes of Roseobacter Group in the Northern South China Sea. Front. Mar. Sci. 9:895613. doi: 10.3389/fmars.2022.895613

Bacterial degradation of dimethylsulfoniopropionate (DMSP) plays a significant role in ecosystem productivity and global climate. In this study, the abundance and diversity of *Roseobacter* group DMSP degradation genes were explored in spatial scale of the South China Sea (SCS). Quantitative PCR showed that a higher abundance of *dmdA* (DMSP demethylase) and *dddP* (DMSP lyase) genes was detected above 75 m than deep water, especially in surface water. A high ratio of *dmdA*/*dddP* existed in all sites and increased with water depth, indicating that demethylation was the main degradation pathway in the *Roseobacter* group. High-throughput sequencing analysis showed that distribution of *dmdA* gene had a significant layering structure in the northern SCS, and high taxonomic diversity of *dmdA* gene was observed in near-surface waters (25 and 50 m). *DmdA* gene in the *Roseobacter* group, such as *Leisingera*, *Nioella*, *Roseobacter*, *Roseovarius*, *Donghicola*, *Phaeobacter*, and *Tateyamaria*, had remarkable specificity due to the effect of different sites and water depths. Different ecological strategies of DMSP degradation may be used by members of the bacterial community harboring demethylation genes. In addition, many *dmdA* sequences were affiliated with unidentified bacteria, indicating that the SCS reserved high diversity of DMSP-degrading bacteria. Canonical correspondence analysis (CCA) suggested that temperature and depth were the most important factors to determine the taxonomic distribution of DMSP degradation genes in the *Roseobacter* group, as well as their abundance. This study highlighted the understanding of the role of *Roseobacter* group in DMSP degradation in the tropical ocean.

Keywords: *Roseobacter* group, dimethylsulfoniopropionate degradation genes, diversity, abundance, South China Sea

INTRODUCTION

Dimethylsulfoniopropionate (DMSP), an important sulfur compound, is mainly produced by marine phytoplankton in marine water (Howard et al., 2006; Michaud et al., 2007; Levine et al., 2012; Moran and Durham, 2019). Association with phytoplankton aggregates may provide many ecophysiological advantages to the marine *Roseobacter* group, including easy access to DMSP and other algal products (González et al., 1999; Amin et al., 2015). When released from phytoplankton, DMSP is mainly assimilated and degraded by members of bacteria *via* a demethylation or cleavage pathway (Malmstrom et al., 2004; Curson et al., 2011; Burkhardt et al., 2017; Raina et al., 2017). The demethylation pathway transforms the majority of DMSP to 3-methiolpropionate, which is then incorporated into the cell biomass (Kiene et al., 1999; Reisch C. R. et al., 2011). By contrast, the cleavage pathway converts DMSP to produce dimethylsulfide (DMS) through various DMSP lyases (Johnston et al., 2016). DMS represents the largest volatile sulfide in the ocean, and its oxidation production can form cloud nucleation and affect global climate (Andreae and Crutzen, 1997; Simó, 2001).

The *Roseobacter* group is affiliated with Alphaproteobacteria, and the majority is of marine origin, constituting a large proportion of the total bacterial community (Brinkhoff et al., 2008; Simon et al., 2017). Members of the *Roseobacter* group can establish symbiotic relationships with phytoplankton, partly through the exchange of DMSP (Liu et al., 2018; Nowinski et al., 2019; O'Brien et al., 2022). *Roseobacter* are often dominant with functional genes, which can encode the capabilities of oxidation sulfur compounds and methylated amines, and catabolism of various carbohydrates (Zhang et al., 2016). The *Roseobacter* group is considered to be a key participant in DMSP metabolism, and nearly 1/3 of DMSP assimilation process is performed through the *Roseobacter* group in the coastal area (Malmstrom et al., 2004). At least 80% of *Roseobacter* group cells contain *dmdA* in the Sargasso Sea (Howard et al., 2006; Howard et al., 2008). Of the seven *ddd* genes identified (*dddD*, *dddK*, *dddL*, *dddP*, *dddQ*, *dddY*, and *dddW*), *dddP* and *dddQ* genes are the most frequently detected in marine bacteria and mainly found in the *Roseobacter* group (Howard et al., 2008; Todd et al., 2009; Todd et al., 2011; Sun et al., 2016). To date, more and more the whole genomes of marine *Roseobacter* strains have been sequenced (Newton et al., 2010; Luo et al., 2012; Voget et al., 2015; Billerbeck et al., 2016; Bakenhus et al., 2018). According to the above studies, *dmdA* and *dddP* genes are the most important genes for DMSP degradation in the *Roseobacter* group.

The northern South China Sea (nSCS) is a marginal sea characterized by tropical and subtropical climates and representing typical oligotrophic characteristics with significant environmental gradients. High concentrations of DMSP and DMS are detected in surface water, especially between 20 and 75 m (Yang, 2000; Yang et al., 2008). Previous studies reported that the abundance of DMSP degradation genes had spatial variability in the seawater (Howard et al., 2011; Levine et al., 2012; Varaljay et al., 2012; Choi et al., 2015; Cui et al., 2015), indicating that DMSP degradation genes are strongly impacted by primary production, UV radiation, DMSP and DMS concentrations, and *Chl a* concentration. To date, DMSP degradation genes have been little reported in the SCS, and biogeography of DMSP degradation genes in spatial-vertical distribution of marine water needs further study. In this study, *dmdA* and *dddP* genes were targeted and collected from the surface to 200 m depth during a cruise across the SCS. The aims of this study were to describe the spatial–vertical distribution and abundance of *Roseobacter*-like DMSP degradation genes, and to explore the diversity shift of DMSP degradation genes related to water environment in the SCS.

MATERIALS AND METHODS

Sample Collection

The cruise was carried out in the South China Sea with the *Shiyan 3* from August to September 2011 (**Figure 1**). A conductivity-temperature-depth (CTD) system (SeaBird SBE-911 Plus, US) was deployed to acquire hydrographic parameters. Seawater samples were collected at different depths (0, 25, 50, 75, 100, 150, and 200 m) with CTD 12-L Niskin bottles (General Oceanics, Inc., Miami, FL). Once collected, the samples were immediately filtered using polycarbonate membranes (EMD Millipore, US) with a pore size of 0.22 μm. The filter was immediately placed in a 1.5-ml sterile centrifuge tube and stored in liquid nitrogen for further DNA extraction. Sample DNA were extracted using the DNA Extraction Kit (OMEGA, US) according to the protocol instructions. Nitrate (NO_3), phosphate (PO_4), silicate (SiO_3), and chlorophyll (*Chl* a) concentrations were measured according to the protocols of "the specialties for oceanography survey" (GB17378.4-2007, China).

Quantitative PCR of *dmdA* and *dddP* Genes Abundance in the *Roseobacter* Group

Two *dmdA* primers were used to amplify the different *Roseobacter* subclades (A/1 and A/2) (Varaljay et al., 2010) for the DMSP demethylase gene, and *dddP* primers targeting the *Roseobacter* group were used to detect the DMSP lyase genes (Levine et al., 2012). The reactions were performed in the iQ5 Real-Time PCR Detection System (Bio-Rad, US). Quantification was based on the increasing fluorescence intensity of the SYBR green dye during amplification. QPCR standards were made from PCR products amplified from environmental samples using the pMD19-T cloning kit (TaKaRa, Japan). The real-time PCR assay was performed in a 20-μL reaction volume with SYBR Premix Ex Taq II (TaKaRa, Japan). All qPCRs were run in triplicate for each sample. QPCR conditions were as follows: predenaturation at 95°C for 30 s, 35 cycles at 95°C for 5 s, and annealing at 60°C for 30 s. Tenfold serially diluted standard and no-template controls were run in triplicate for each reaction.

Illumina MiSeq Sequencing of *dmdA* Genes in the *Roseobacter* Group

The primer pairs, dmdA282F (5′-TGCTSTSAACGAYCCSGT-3′) and dmdA591R (5′-ACRTAGAYYTCRAAVCCBCCYT-3′) (Zeng et al., 2016), were used for *Roseobacter*-like *dmdA* gene amplification. PCR conditions were as follows: 94°C for 3 min, 35 cycles at 94°C for 1 min, 54°C for 30 s, extension at 72°C for 30 s,

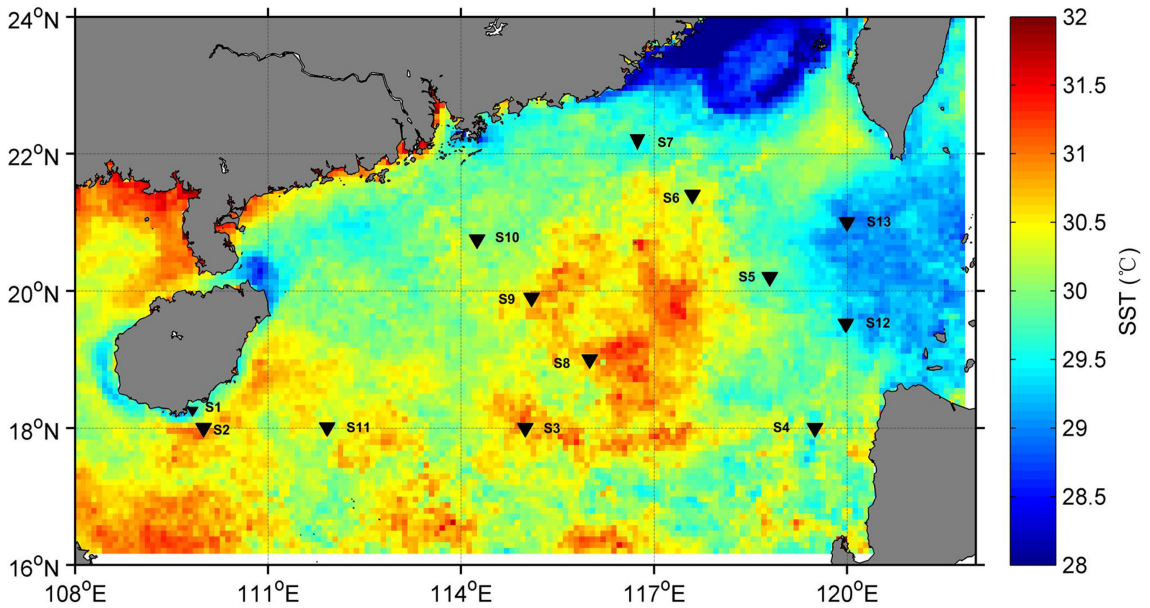

FIGURE 1 | Map of sampling stations in the South China Sea. Sea surface temperature (SST) during investigation time was shown in the base map that was obtained from NOAA.

and a final extension at 72°C for 10 min. The PCR comprised a 20-μL reaction volume containing 4 μL of 5× FastPfu Buffer, 2 μL of 2.5 mM dNTPs, 0.5 μL of FastPfu polymerase, 1.0 μL of primers (5 μM), and 10 ng of template DNA. A positive control and non-template control samples were run to validate PCR. PCR products were purified using the AxyPrep DNA Gel Extraction Kit (Axygen Biosciences, US), and quantified using QuantiFluor™-ST (Promega, US). An Illumina MiSeq platform (Illumina, US) was used for paired-end sequencing (2 × 300) according to the standard protocols.

For pair-ended reads obtained by Illumina sequencing, barcodes and primers were trimmed and then assembled using FLASH (V1.2.7). Reads that contained Ns were shorter than 50 bp or had primer mismatches which were also excluded. Sequences were compared with RDP reference database using VSEARCH (1.9.6) to detect chimeric sequences. Then sequences were grouped into OTUs (operational taxonomic units) using UPARSE (v7.0.1001), and pre-clustered at 97% sequence identity. The highest OTU frequencies were selected as representative OTU sequences. The taxonomy of each *dmd*A gene sequence was analyzed by RDP classifier algorithm against the NCBI non-redundant (nr) database using a confidence threshold of 70%.

RESULTS AND DISCUSSION

Characteristics of the Abundance of *dmdA* and *dddP* Gene in the South China Sea

Two subclades (A/1 and A/2) of *dmdA* genes and *dddP* genes were quantified using qPCR (**Figure 2**). The copy numbers of *dmdA* and *dddP* genes and their distribution in the northwestern SCS varied greatly among sampling sites and depths. This result was similar with the study in the Pacific Ocean (Cui et al., 2015), indicating that the abundance of DMSP degradation genes had great variability of abundance in the ocean. Overall, the abundance of *dmdA* and *dddP* genes located in the northwest SCS was higher than that located in the northeastern SCS. As seen from a spatial scale, sites (S1, S2, S3, S8, and S9) showed higher copy numbers of *dmdA* and *dddP* genes than other sites (S5, S6, S12, and S13). In these five stations, two sites (S1 and S2) are close to the shore, and the remaining three (S3, S8, S9) are in the middle of the survey area. Similar to previous studies in the SCS (Ling et al., 2012; Sun et al., 2015), bacterial community in the northwestern SCS had higher diversity than that in the northeastern SCS. The abundance difference is likely due to water temperature. As seen in **Figure 1**, the SST of the sites to the left of longitude 117°E is higher than that of the sites to the right. This result was similar to other reports that temperature is an important factor in determining the abundance of *dmdA* and *dddP* in surface water (Levine et al., 2012; Varaljay et al., 2012; Cui et al., 2015).

DmdA and *dddP* genes from the *Roseobacter* group were particularly enriched in surface waters with an order of magnitude difference in their abundance relative to deep waters (**Figure 2**), which indicated that the abundance of *dmdA* and *dddP* genes was strongly separated by water depth. Copy numbers of *dmdA* and *dddP* genes were higher above 75 m water than those below 100 m water, and the highest abundance of these genes was observed in the surface layer. Variation of gene abundance of *dmdA* and *dddP* may be closely related to the DMSP concentration in vertical depth. Previous studies reported that DMSP and DMS concentrations in SCS were markedly high

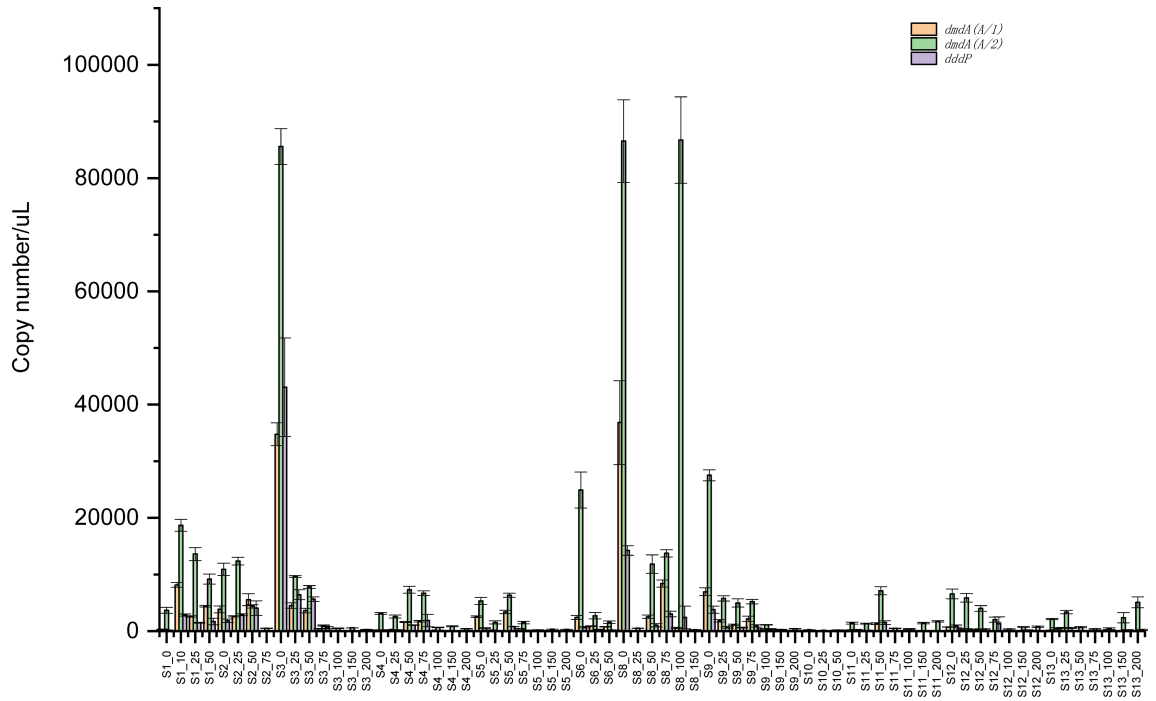

FIGURE 2 | Abundance of dmdA and dddP in the SCS from surface water to 200 m depth based on quantitative PCR.

in the surface seawater, and decreased gradually with increasing depth (Yang, 2000; Zhai et al., 2020). Other studies also reported that distribution patterns of *dmdA* and *dddP* were roughly consistent with the distribution characteristics of DMSP concentration, and were mainly influenced by the *Chl* a concentrations, depth, salinity, and temperature (Howard et al., 2011; Varaljay et al., 2012; Cui et al., 2015).

In addition, the copy numbers of the *dddP* gene were far lower than those of the *dmdA* gene at almost all sites and depths (**Figure 2**), even if only the *dmdA* A/2 clade was considered. The copy number ratios (*dmdA*/*dddP*) of these genes ranged from 2 to 156 times. The copy numbers of the *dmdA* A/2 gene were higher than those of the *dmdA* A/1 gene at almost all sites and depths, which suggested that subclade A2 was the main group of *Roseobacter* group in the demethylation pathway. The other study reported that two *Roseobacter* group *dmdA* gene subclades (A/1 and A/2) showed opposite depth distributions in the summer (Levine et al., 2012). Interestingly, high ratios of *dmdA*/*dddP* and *dmdA2*/*dmdA1* were mainly observed in deep waters (below 75 m), even if these three genes had relatively low abundance, indicating that demethylation is the main pathway of DMSP degradation in the water. Previous studies suggested that 80% of DMSP degradation is processed through the demethylation pathway, and only 20% is cleaved to DMS (Kiene et al., 1999). Marine bacteria keep the ability of DMSP demethylation to a suitable evolutionary pressure, which can explain the consistently stable and high *dmdA* gene frequencies in the ocean (Varaljay et al., 2012). In marine waters, nutrients and organic sulfur such as DMSP are important because cells need increased sulfur demand for growth, causing more sulfur to be incorporated into cell protein (Kiene et al., 1999).

Diversity Distribution of *dmdA* Gene in the *Roseobacter* Group

A total of 231,246 valid reads and 688 OTUs were obtained from the 19 samples through Illumina MiSeq sequencing analysis. Each of the samples contained 9155 to 17,955 reads, with OTUs ranging from 12 to 55. The coverage was more than 0.999, which suggested that sequencing data had favorable coverage for *dmdA* diversity. Diversity indices, including Shannon, Chao, Ace, and Simpson, are demonstrated in **Supplementary Table S1**. The result indicated that the *dmdA* gene had higher community diversity above 50 m than in deep waters (100 and 200 m).

The study revealed that the composition of the *dmdA* gene varied significantly among the sites and depths (ANOVA, $p < 0.01$). Overall, the *dmdA* gene was mainly affiliated with Alphaproteobacteria and Gammaproteobacteria (**Figure 3**). In most sites, the *dmdA* gene was dominated by Alphaproteobacteria, whereas a few of the samples (S2_0, S6_0, S6_50, and S9_25) were dominated by Gammaproteobacteria. In addition, low abundance of Acidithiobacillia-like *dmdA* gene was detected (1.37%). High abundance of *dmdA* (2.64%–87.95%), which had very low similarity with the amino acid identity of uncultured bacteria, was found in some samples. Moreover, 21.78% of all sequences had 73%–79% amino acid similarity with Gammaproteobacteria. This result provided further

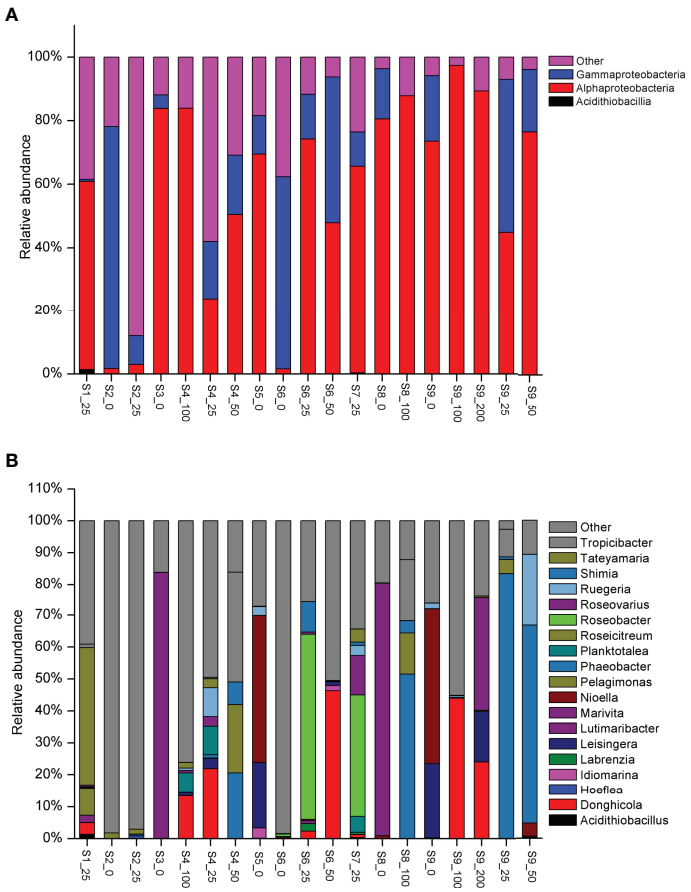

FIGURE 3 | Taxonomic distribution of samples through High-throughput sequencing analysis in class level **(A)** and genus level **(B)**.

evidence that ocean water contains a high diversity of *dmdA* genes, which has not yet been unearthed in the tropical ocean.

Overall, *dmdA* genes in the nSCS showed greater variation near surface water than in deep waters, which is related to the vertical structure of water (**Figure 3**). At the genus level, high abundance of *dmdA* genes below 100 m belonged to *Phaeobacter*, *Roseicitreum*, *Ruegeria*, *Tropicibacter*, and *Shimia*. The upwelling site (S1-25) was characterized by *Tateyamaria* (43.11%) and *Pelagimonas* (8.40%). These findings indicated that coastal upwelling had different *dmdA* taxonomy of the *Roseobacter* group with open water. S5_0 and S9_0 sites were dominated by *Leisingera* (>20%) and *Nioella* (>46%). S3_0 and S8_0 sites were characterized by highly abundant *Roseovarius* (>80%). Site S6_25 was mainly composed of *Roseobacter* (58%) and *Shimia* (9.56%). Site S7_25 was mainly composed of *Roseobacter* (38%), *Roseovarius* (12.32%), and *Planktotalea* (4.97%). The *dmdA* gene of *Donghicola* mainly dominated in the 25- and 50-m water layer. Moreover, *dmdA* genes of *Leisingera*, *Planktotalea*, *Roseovarius*, and *Ruegeria* were dominant in the 25- or 50-m water layer.

Principal component analysis (PCA) illustrated that the *dmdA* gene of the bacterial community had distinct differences among different sites and depths (**Figure 4**). The results indicated that the *dmdA* gene of the *Roseobacter* group in shallow water (0 m, 25 m, and 50 m) and deep layer (100 and 200 m) had clustered together separately. The *dmdA* gene of the deep water was separated by a large distance from the shallow layer. Overall, the results indicated the clearly distinct structure among sampling sites and depths (ANOVA, $p < 0.01$). Veen analysis showed that *dmdA* gene diversity had 14 and 11 common OTUs between the surface water and 25-m depth of the horizontal scale. Considering the vertical depths, no common OTU was found from the surface to 200 m water depths (**Figure 5**).

Environmental Factors Affected the Distribution of the *dmdA* Gene

The CCA analysis constructed a correlation between environmental factors and *dmdA* gene diversity (**Figure 6A**). The first ordination axis accounted for 32.1% of the cumulative percentage variance in the matrix, while the second axis accounted for 31.2%. *DmdA* gene in the upwelling (S1-25) was mainly positively related to *Chl* a and silicate concentration ($p<0.05$). *DmdA* gene below 100-m depth was negatively defined by water depth ($p<0.01$), while shallow water samples (0 m and 25 m) were strongly determined by water temperature ($p<0.01$). Other environmental factors, such as salinity, nitrate,

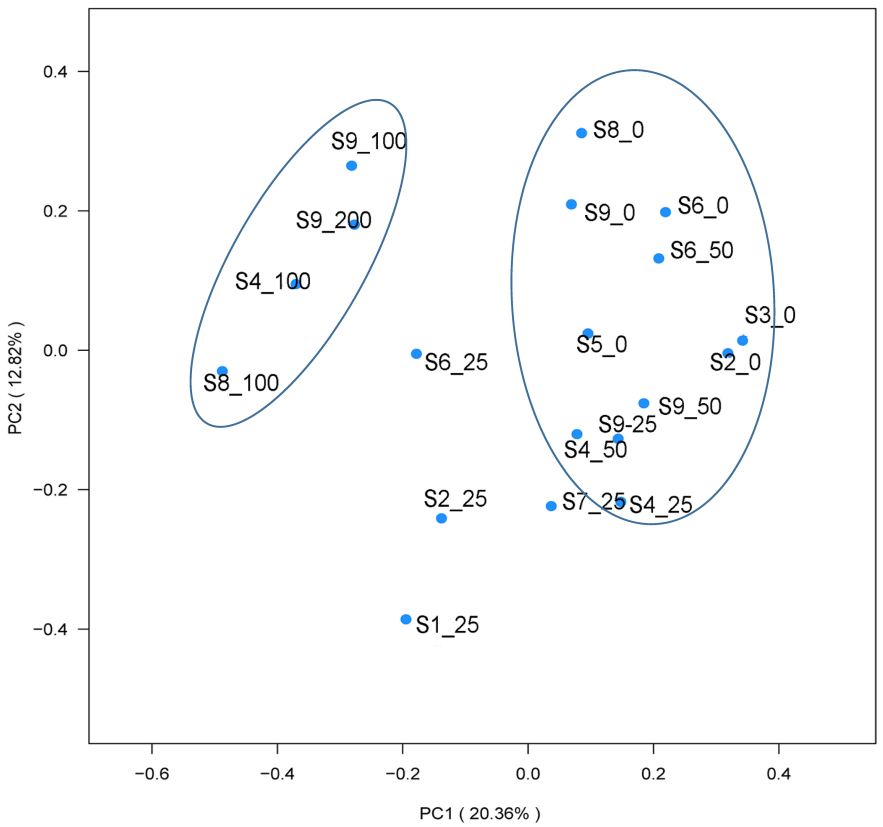

FIGURE 4 | Principal components analysis (PCA) based on phylogenetic UniFrac distance metrics.

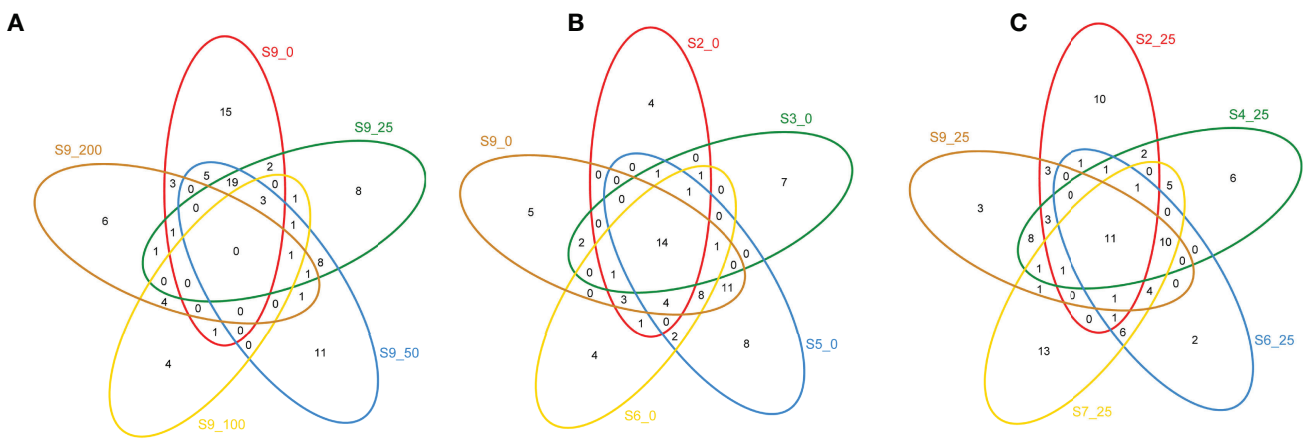

FIGURE 5 | Veen map analysis of *dmdA* gene diversity in spatial and vertical scale. **(A)** common OTUs in the vertical layers; **(B)** common OTUs in the surface water; **(C)** common OTUs in the 25-m water layers.

and phosphate, had no obvious effects on the diversity of *dmdA* genes.

In the CCA map (**Figure 6B**), cluster A, mainly composed by *Tateyamaria*, *Pelagimonas*, and *Marivita*, had significant correlation ($p < 0.05$) with *Chl* a and silicate concentration, which was influenced by the upwelling. High abundance OTUs of cluster B, which was afflicted with *Leisingera*, *Nioella*, *Roseovarius*, and *Roseobacter*, were mainly positively related to temperature. High abundance of OTUs (cluster C), which was afflicted with *Roseobacter*, *Shimia*, *Planktotalea*, and

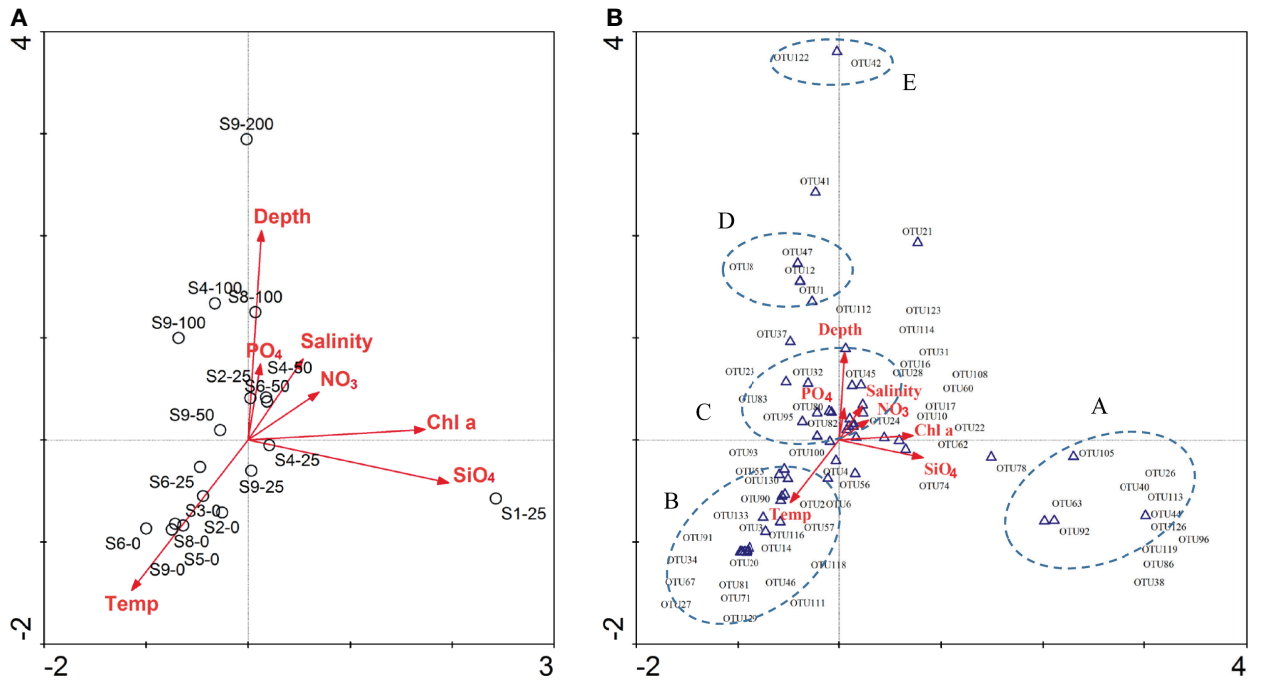

FIGURE 6 | Canonical correspondence analysis (CCA) of the relationship of *dmdA* gene diversity **(A)** and OTU level **(B)** in the *Roseobacter* group, with environmental factors. Areas surrounded by the blue dashed lines represented the dominant OTUs of different genera.

Donghicola, were mainly related to depth, phosphate, and salinity. Cluster D and E, mainly composed by *Phaeobacter*, *Roseicitreum*, *Ruegeria*, and *Tropicibacter*, were mainly positively related to depth, indicating that these *Roseobacter* OTUs were suitable to environment change with deep water. As described above, a high ratio of *dmdA*/*dddP* was found in deep water, which indicated that the *Roseobacter* group had more nutrition demand and greater degree of demethylation than DMSP cleavage. Different ecological strategies of DMSP degradation may be used by members of the bacterial community harboring demethylation and/or cleavage genes (Reisch C. et al., 2011). In previous studies, the *Roseobacter* group is the dominant microbial taxa in the offshore, upwelling, and mesoscale eddy of the South China Sea (Zhang et al., 2016; Sun et al., 2020; Sun et al., 2022), and diversity of DMSP degradation potential has obvious significance for sulfur material cycling and transformation.

CONCLUSION

This study showed that DMSP degradation genes varied significantly in spatial scale of the South China Sea. The current study found that temperature and water depth mainly induced variations in taxonomic affiliations of *Roseobacter* group DMSP degradation genes over space. These findings further implied that additional factors including light, salinity, and temperature, which are caused by an increase in depth, may play important roles in regulating the DMSP degradation genes. These factors play an important role in regulating the switch process between bacterial DMSP demethylation and DMSP cleavage. This study highlighted the understanding of the role of *Roseobacter* group in sulfur cycling and transformation conversion in the tropical ocean.

DATA AVAILABILITY STATEMENT

The datasets presented in this study can be found in online repositories. The names of the repository/repositories and accession number(s) can be found below: NCBI [accession: SRP133746].

AUTHOR CONTRIBUTIONS

All authors contributed to the article and approved the submitted version.

FUNDING

The present study was supported financially by Hainan Province Science and Technology Special Fund (ZDYF2021XDNY131), the Strategic Priority Research Program of the Chinese Academy of Sciences (XDA19060204), the Key Special Project for Introduced Talents Team of Southern Marine Science and Engineering Guangdong Laboratory (Guangzhou)

(GML2019ZD0303), the National Natural Science Foundation of China (31971480, 41406130 and 42073078), the National Key Research and Development Plan (2017FY100700), and the Project of Guangdong Science and Technology Department (2017A020216008).

SUPPLEMENTARY MATERIAL

The Supplementary Material for this article can be found online at: https://www.frontiersin.org/articles/10.3389/fmars.2022.895613/full#supplementary-material

REFERENCES

Amin, S. A., Hmelo, L. R., Van Tol, H. M., Durham, B. P., Carlson, L. T., Heal, K. R., et al. (2015). Interaction and Signalling Between a Cosmopolitan Phytoplankton and Associated Bacteria. *Nature* 522 (7554), 98–101. doi: 10.1038/nature14488

Andreae, M. O., and Crutzen, P. J. (1997). Atmospheric Aerosols - Biogeochemical Sources and Role in Atmospheric Chemistry. *Science* 276 (5315), 1052–1058. doi: 10.1126/science.276.5315.1052

Bakenhus, I., Voget, S., Poehlein, A., Brinkhoff, T., Daniel, R., and Simon, M. (2018). Genome Sequence of Planktotalea Frisia Type Strain (SH6-1T), a Representative of the Roseobacter Group Isolated From the North Sea During a Phytoplankton Bloom. *Stand. Genomic Sci.* 13 (1), 7. doi: 10.1186/s40793-018-0311-5

Billerbeck, S., Wemheuer, B., Voget, S., Poehlein, A., Giebel, H.-A., Brinkhoff, T., et al. (2016). Biogeography and Environmental Genomics of the Roseobacter-Affiliated Pelagic CHAB-I-5 Lineage. *Nat. Microbiol.* 1, 16063. doi: 10.1038/nmicrobiol.2016.63

Brinkhoff, T., Giebel, H. A., and Simon, M. (2008). Diversity, Ecology, and Genomics of the Roseobacter Clade: A Short Overview. *Arch. Microbiol.* 189 (6), 531–539. doi: 10.1007/s00203-008-0353-y

Burkhardt, I., Lauterbach, L., Brock, N. L., and Dickschat, J. S. (2017). Chemical Differentiation of Three DMSP Lyases From the Marine Roseobacter Group. *Org. Biomol. Chem.* 15 (20), 4432–4439. doi: 10.1039/C7OB00913E

Choi, D. H., Park, K.-T., An, S. M., Lee, K., Cho, J.-C., Lee, J.-H., et al. (2015). Pyrosequencing Revealed SAR116 Clade as Dominant dddP-Containing Bacteria in Oligotrophic NW Pacific Ocean. *PloS One* 10 (1), e0116271. doi: 10.1371/journal.pone.0116271

Cui, Y., Suzuki, S., Omori, Y., Wong, S.-K., Ijichi, M., Kaneko, R., et al. (2015). Abundance and Distribution of Dimethylsulfoniopropionate Degradation Genes and the Corresponding Bacterial Community Structure at Dimethyl Sulfide Hot Spots in the Tropical and Subtropical Pacific Ocean. *Appl. Environ. Microbiol.* 81 (12), 4184–4194. doi: 10.1128/aem.03873-14

Curson, A. R. J., Todd, J. D., Sullivan, M. J., and Johnston, A. W. B. (2011). Catabolism of Dimethylsulphoniopropionate: Microorganisms, Enzymes and Genes. *Nat. Rev. Microbiol.* 9, 849. doi: 10.1038/nrmicro2653

González, J. M., Kiene, R. P., and Moran, M. A. (1999). Transformation of Sulfur Compounds by an Abundant Lineage of Marine Bacteria in the α-Subclass of the ClassProteobacteria. *Appl. Environ. Microbiol.* 65 (9), 3810–3819. doi: 10.1128/AEM.65.9.3810-3819.1999

Howard, E. C., Henriksen, J. R., Buchan, A., Reisch, C. R., Bürgmann, H., Welsh, R., et al. (2006). Bacterial Taxa That Limit Sulfur Flux From the Ocean. *Science* 314 (5799), 649–652. doi: 10.1126/science.1130657

Howard, E. C., Sun, S., Biers, E. J., and Moran, M. A. (2008). Abundant and Diverse Bacteria Involved in DMSP Degradation in Marine Surface Waters. *Environ. Microbiol.* 10 (9), 2397–2410. doi: 10.1111/j.1462-2920.2008.01665.x

Howard, E. C., Sun, S., Reisch, C. R., del Valle, D. A., Bürgmann, H., Kiene, R. P., et al. (2011). Changes in Dimethylsulfoniopropionate Demethylase Gene Assemblages in Response to an Induced Phytoplankton Bloom. *Appl. Environ. Microbiol.* 77 (2), 524–531. doi: 10.1128/AEM.01457-10

Johnston, A. W. B., Green, R. T., and Todd, J. D. (2016). Enzymatic Breakage of Dimethylsulfoniopropionate—A Signature Molecule for Life at Sea. *Curr. Opin. Chem. Biol.* 31, 58–65. doi: 10.1016/j.cbpa.2016.01.011

Kiene, R. P., Linn, L. J., González, J., Moran, M. A., and Bruton, J. A. (1999). Dimethylsulfoniopropionate and Methanethiol Are Important Precursors of Methionine and Protein-Sulfur in Marine Bacterioplankton. *Appl. Environ. Microbiol.* 65 (10), 4549–4558. doi: 10.1128/AEM.65.10.4549-4558.1999

Levine, N. M., Varaljay, V. A., Toole, D. A., Dacey, J. W. H., Doney, S. C., and Moran, M. A. (2012). Environmental, Biochemical and Genetic Drivers of DMSP Degradation and DMS Production in the Sargasso Sea. *Environ. Microbiol.* 14 (5), 1210–1223. doi: 10.1111/j.1462-2920.2012.02700.x

Ling, J., Dong, J.-D., Wang, Y.-S., Zhang, Y.-Y., Deng, C., Lin, L., et al. (2012). Spatial Variation of Bacterial Community Structure of the Northern South China Sea in Relation to Water Chemistry. *Ecotoxicology* 21 (6), 1669–1679. doi: 10.1007/s10646-012-0941-0

Liu, J., Liu, J., Zhang, S.-H., Liang, J., Lin, H., Song, D., et al. (2018). Novel Insights Into Bacterial Dimethylsulfoniopropionate Catabolism in the East China Sea. *Front. Microbiol.* 9. doi: 10.3389/fmicb.2018.03206

Luo, H., Löytynoja, A., and Moran, M. A. (2012). Genome Content of Uncultivated Marine Roseobacters in the Surface Ocean. *Environ. Microbiol.* 14 (1), 41–51. doi: 10.1111/j.1462-2920.2011.02528.x

Malmstrom, R. R., Kiene, R. P., and Kirchman, D. L. (2004). Identification and Enumeration of Bacteria Assimilating Dimethylsulfoniopropionate (DMSP) in the North Atlantic and Gulf of Mexico. *Limnol. Oceanogr.* 49 (2), 597–606. doi: 10.4319/lo.2004.49.2.0597

Michaud, S., Levasseur, M., and Cantin, G. (2007). Seasonal Variations in Dimethylsulfoniopropionate and Dimethylsulfide Concentrations in Relation to the Plankton Community in the St. Lawrence Estuary. *Estuar. Coast Shelf Sci.* 71 (3-4), 741–750. doi: 10.1016/j.ecss.2006.09.020

Moran, M. A., and Durham, B. P. (2019). Sulfur Metabolites in the Pelagic Ocean. *Nat. Rev. Microbiol.* 17 (11), 665–678. doi: 10.1038/s41579-019-0250-1

Newton, R. J., Griffin, L. E., Bowles, K. M., Meile, C., Gifford, S., Givens, C. E., et al. (2010). Genome Characteristics of a Generalist Marine Bacterial Lineage. *ISME J.* 4 (6), 784–798. doi: 10.1038/ismej.2009.150

Nowinski, B., Motard-Côté, J., Landa, M., Preston, C. M., Scholin, C. A., Birch, J. M., et al. (2019). Microdiversity and Temporal Dynamics of Marine Bacterial Dimethylsulfoniopropionate Genes. *Environ. Microbiol.* 21 (5), 1687–1701. doi: 10.1111/1462-2920.14560

O'Brien, J., McParland, E. L., Bramucci, A. R., Siboni, N., Ostrowski, M., Kahlke, T., et al. (2022). Biogeographical and Seasonal Dynamics of the Marine Roseobacter Community and Ecological Links to DMSP-Producing Phytoplankton. *ISME Commun.* 2 (1), 16. doi: 10.1038/s43705-022-00099-3

Raina, J.-B., Clode, P. L., Cheong, S., Bougoure, J., Kilburn, M. R., Reeder, A., et al. (2017). Subcellular Tracking Reveals the Location of Dimethylsulfoniopropionate in Microalgae and Visualises its Uptake by Marine Bacteria. *eLife* 6, e23008. doi: 10.7554/eLife.23008

Reisch, C., Moran, M., and Whitman, W. (2011). Bacterial Catabolism of Dimethylsulfoniopropionate (DMSP). *Front. Microbiol.* 2 (172). doi: 10.3389/fmicb.2011.00172

Reisch, C. R., Stoudemayer, M. J., Varaljay, V. A., Amster, I. J., Moran, M. A., and Whitman, W. B. (2011). Novel Pathway for Assimilation of Dimethylsulphoniopropionate Widespread in Marine Bacteria. *Nature* 473, 208. doi: 10.1038/nature10078

Simó, R. (2001). Production of Atmospheric Sulfur by Oceanic Plankton: Biogeochemical, Ecological and Evolutionary Links. *Trends Ecol. Evol.* 16 (6), 287–294. doi: 10.1016/S0169-5347(01)02152-8

Simon, M., Scheuner, C., Meier-Kolthoff, J. P., Brinkhoff, T., Wagner-Döbler, I., Ulbrich, M., et al. (2017). Phylogenomics of Rhodobacteraceae Reveals Evolutionary Adaptation to Marine and Non-Marine Habitats. *ISME J.* 11 (6), 1483–1499. doi: 10.1038/ismej.2016.198

Sun, J., Todd, J. D., Thrash, J. C., Qian, Y., Qian, M. C., Temperton, B., et al. (2016). The Abundant Marine Bacterium Pelagibacter Simultaneously Catabolizes Dimethylsulfoniopropionate to the Gases Dimethyl Sulfide and Methanethiol. *Nat. Microbiol.* 1 (8), 16065. doi: 10.1038/nmicrobiol.2016.65

Sun, F.-L., Wang, Y.-S., Wu, M.-L., Jiang, Z.-Y., Sun, C.-C., and Cheng, H. (2015). Spatial and Vertical Distribution of Bacterial Community in the Northern South China Sea. *Ecotoxicology* 24 (7-8), 1478–1485. doi: 10.1007/s10646-015-1472-2

Sun, F., Wu, M., Wang, Y., Sun, C., and Xu, Z. (2020). Diversity and Potential Function of Bacterial Communities in Different Upwelling Systems. *Estuar. Coast Shelf Sci.* 237, 106698. doi: 10.1016/j.ecss.2020.106698

Sun, F., Xia, X., Simon, M., Wang, Y., Zhao, H., Sun, C., et al. (2022). Anticyclonic Eddy Driving Significant Changes in Prokaryotic and Eukaryotic Communities in the South China Sea. *Front. Mar. Sci.* 9. doi: 10.3389/fmars.2022.773548

Todd, J. D., Curson, A. R. J., Dupont, C. L., Nicholson, P., and Johnston, A. W. B. (2009). The dddP Gene, Encoding a Novel Enzyme That Converts Dimethylsulfoniopropionate Into Dimethyl Sulfide, Is Widespread in Ocean Metagenomes and Marine Bacteria and Also Occurs in Some Ascomycete Fungi. *Environ. Microbiol.* 11 (6), 1376–1385. doi: 10.1111/j.1462-2920.2009.01864.x

Todd, J. D., Curson, A. R., Kirkwood, M., Sullivan, M. J., Green, R. T., and Johnston, A. W. (2011). DddQ, a Novel, Cupin-Containing, Dimethylsulfoniopropionate Lyase in Marine Roseobacters and in Uncultured Marine Bacteria. *Environ. Microbiol.* 13 (2), 427–438. doi: 10.1111/j.1462-2920.2010.02348.x

Varaljay, V. A., Gifford, S. M., Wilson, S. T., Sharma, S., Karl, D. M., and Moran, M. A. (2012). Bacterial Dimethylsulfoniopropionate Degradation Genes in the Oligotrophic North Pacific Subtropical Gyre. *Appl. Environ. Microbiol.* 78 (8), 2775–2782. doi: 10.1128/AEM.07559-11

Varaljay, V. A., Howard, E. C., Sun, S., and Moran, M. A. (2010). Deep Sequencing of a Dimethylsulfoniopropionate-Degrading Gene (Dmda) by Using PCR Primer Pairs Designed on the Basis of Marine Metagenomic Data. *Appl. Environ. Microbiol.* 76 (2), 609–617. doi: 10.1128/AEM.01258-09

Voget, S., Billerbeck, S., Simon, M., and Daniel, R. (2015). Closed Genome Sequence of *Octadecabacter Temperatus* SB1, the First Mesophilic Species of the Genus *Octadecabacter*. *Genome Announcements* 3 (5), e01051–e01015. doi: 10.1128/genomeA.01051-15

Yang, G.-P. (2000). Spatial Distributions of Dimethylsulfide in the South China Sea. *Deep Sea Res. Pt I: Oceanogr. Res. Papers* 47 (2), 177–192. doi: 10.1016/S0967-0637(99)00058-8

Yang, G.-P., Jing, W.-W., Kang, Z.-Q., Zhang, H.-H., and Song, G.-S. (2008). Spatial Variations of Dimethylsulfide and Dimethylsulfoniopropionate in the Surface Microlayer and in the Subsurface Waters of the South China Sea During Springtime. *Mar. Environ. Res.* 65 (1), 85–97. doi: 10.1016/j.marenvres.2007.09.002

Zeng, Y.-X., Qiao, Z.-Y., Yu, Y., Li, H.-R., and Luo, W. (2016). Diversity of Bacterial Dimethylsulfoniopropionate Degradation Genes in Surface Seawater of Arctic Kongsfjorden. *Sci. Rep.* 6, 33031. doi: 10.1038/srep33031

Zhai, X., Song, Y.-C., Li, J.-L., Yang, J., Zhang, H.-H., and Yang, G.-P. (2020). Distribution Characteristics of Dimethylated Sulfur Compounds and Turnover of Dimethylsulfide in the Northern South China Sea During Summer. *J. Geophys. Res.: Biogeosci.* 125 (2), e2019JG005363. doi: 10.1029/2019JG005363

Zhang, Y., Sun, Y., Jiao, N., Stepanauskas, R., and Luo, H. (2016). Ecological Genomics of the Uncultivated Marine Roseobacter Lineage CHAB-I-5. *Appl. Environ. Microbiol.* 82 (7), 2100–2111. doi: 10.1128/aem.03678-15

Conflict of Interest: The authors declare that the research was conducted in the absence of any commercial or financial relationships that could be construed as a potential conflict of interest.

Publisher's Note: All claims expressed in this article are solely those of the authors and do not necessarily represent those of their affiliated organizations, or those of the publisher, the editors and the reviewers. Any product that may be evaluated in this article, or claim that may be made by its manufacturer, is not guaranteed or endorsed by the publisher.

frontiers | Frontiers in Marine Science

ORIGINAL RESEARCH
published: 10 June 2022
doi: 10.3389/fmars.2022.911492

Biotic Response to Rapid Environmental Changes During the Permian–Triassic Mass Extinction

Guoshan Li[1,2,3], Yongbiao Wang[3†], Sheng Li[3,4], Tan Wang[3], Wei Liao[5], Baozhu Deng[3] and Zhongping Lai[1]**

[1] Institute of Marine Sciences, Guangdong Provincial Key Laboratory of Marine Disaster Prediction and Prevention, Shantou University, Shantou, China, [2] Key Laboratory of Environment Change and Resources Use in Beibu Gulf (Nanning Normal University), Ministry of Education, Nanning, China, [3] School of Earth Sciences, China University of Geosciences (Wuhan), Wuhan, China, [4] No. 3 Institute of Geological and Mineral Resources Survey of Henan Geological Bureau, Zhengzhou, China, [5] Institute of Cultural Heritage, Shandong University, Qingdao, China

OPEN ACCESS

Edited by:
Fajin Chen,
Guangdong Ocean University, China

Reviewed by:
Zhicai Zhu,
Chinese Academy of Geological Sciences (CAGS), China
Hansheng Cao,
Guangdong Ocean University, China

***Correspondence:**
Guoshan Li
liguoshan@stu.edu.cn
Zhongping Lai
zhongping.lai@yahoo.com

†Deceased

Specialty section:
This article was submitted to Marine Biogeochemistry, a section of the journal Frontiers in Marine Science

Received: 02 April 2022
Accepted: 12 May 2022
Published: 10 June 2022

Citation:
Li G, Wang Y, Li S, Wang T, Liao W, Deng B and Lai Z (2022) Biotic Response to Rapid Environmental Changes During the Permian–Triassic Mass Extinction. Front. Mar. Sci. 9:911492. doi: 10.3389/fmars.2022.911492

The divergent patterns of Permian–Triassic mass extinction (PTME) have been extensively documented in varying water depth settings. We here investigated fossil assemblages and sedimentary microfacies on high-resolution samples from two adjacent sections of the South China Block: Chongyang from shallow-water platform and Chibi from deeper-water slop. At Chongyang, abundant benthos (over 80%), including rugose corals, fusulinids, calcareous algae, and large foraminifers, disappeared precipitously at the topmost of Changxing Formation grainstone, which suggested complete damage of the benthic ecosystem, confirming a sudden single-pulse extinction pattern. The end-Permian regression, marked by a karst surface, provided a plausible explanation for this extinction pattern. Whereas for the fauna in Chibi, the benthos was relatively abundant (20%–55%) with more trace fossils and lacking calcareous algae. Benthic abundance in Chibi reduced by two steps at the two claystone beds (Beds 10 and 18): bioclastic content dropped from an average of 50% in Beds 1–9 to 10% in Beds 11–17 and then to less than 5% in Beds 19–23, suggesting a two-pulse extinction. At the first pulse, large foraminifers were prominent victims in both shallow- and deeper-water settings. A plausible survival strategy for small-sized foraminifers was to migrate to deeper water to avoid extreme heat in shallow water. The early Triassic transgression prompted some small foraminifers to migrate back to original platforms and flourish briefly as disaster forms. At the Early Triassic mudstone with bottom-water settings in Chibi, the appearance of abundant small pyrite framboids (diameters of 4.74–5.96 μm), an indicator of intensified oxygen deficiency, was simultaneous with the two-step reduction of benthic diversity and abundance. Thus, anoxic conditions might be the main cause of the PTME at deeper-water settings. Our study is an example of the wider debate about biotic response to rapid environmental change for both the Permian–Triassic transition and modern days.

Keywords: Permian–Triassic mass extinction (PTME), sea-level changes, anoxic conditions, foraminiferal migration, South China Block (SCB)

1 INTRODUCTION

Mass extinctions were defined as the substantial increase in loss of taxon during a relatively short interval of geologic time, in other words, extinction rates significantly above background levels (Raup and Sepkoski, 1982; Sepkoski, 1986; Hallam and Wignall, 1997). They occurred five times in the past 600 million years (Myr) of Earth's history, known as the "Big Five," each resulting in the loss of 75%–96% of marine species biodiversity (Raup and Sepkoski, 1982; Erwin et al., 2002; Rong and Fang, 2004; Fan et al., 2020) and alteration of ecosystem structures (Aberhan and Kiessling, 2015). Current declines of biodiversity were about 1,000 times the background rate of extinction throughout geological time (Pimm et al., 2014), which may approach or exceed the magnitude of previous extinction events (Ceballos and Ehrlich, 2018). Thus, it has been suggested that Earth might be entering the sixth mass extinction (Ceballos et al., 2017; Cowie et al., 2022). While marine biodiversity decreases, the ocean system is experiencing great changes, including sea surface temperature rising (Seager et al., 2019), dissolved oxygen concentration declining (Breitburg et al., 2018), and seawater acidification (Ishida et al., 2021). The well-known Permian–Triassic mass extinction (PTME) might have been documented all these changes in modern oceans (Rong and Fang, 2004). The PTME was the severe biotic crisis of the "Big Five" (Erwin et al., 2002), resulting in the disappearance of over 80% skeletonized marine species in less than 0.03 Myr (Fan et al., 2020). Approximately >5 Myr after the crisis, the collapsed marine ecosystems did not fully recover until the beginning of the Middle Triassic (Algeo et al., 2011), indicating a significant transition in marine ecosystems from Paleozoic- to Mesozoic-type communities (Algeo et al., 2011; Song et al., 2018). Meanwhile, the terrestrial ecosystem changeover also took place nearby the Permian–Triassic boundary (PTB) (Benton and Newell, 2014; Yu et al., 2015; Zhu et al., 2020). The terrestrial ecological disturbance probably started 60,000–370,000 years before that in the ocean (Dal et al., 2022), however, the enhanced terrestrial input likely corresponding to the marine mass extinction (He et al., 2010; Benton and Newell, 2014). Nevertheless, discriminating the pattern and causes of the marine ecosystem collapse during the PTME can help us better understand the impact of rapid global warming on the ecosystems in both today and future crises.

Multiple studies on PTME have been conducted in various paleogeographical settings (e.g., Jin et al., 2000; Shen et al., 2011; Song et al., 2012; Liu et al., 2020; Li et al., 2021), but many aspects of the extinction, including its pattern and triggers, have long been disputed. Jin et al. (2000) proposed that the PTME occurred at the end-Permian as a single abrupt event based on 329 marine invertebrate species from the Meishan section in the South China Block (SCB). Yin et al. (2007) suggested a three-pulse pattern of PTME: a prelude extinction, main extinction, and the post-extinction event based on fossil records in various Permian–Triassic (P–Tr) boundary sections in the SCB. Conversely, Song et al. (2012) and Xie et al. (2005) suggested that the extinction crisis was divided into two episodic pulses from fossil records of various taxa in the Meishan section. A closer study of foraminiferal assemblage at the Liangfengya section revealed that foraminifers had two extinction pulses spanning the P–Tr boundary (Liu et al., 2020). Li et al. (2021) also found two extinction levels among benthic organisms at the Liangfengya section.

Numerous potential triggers for this crisis have been identified: rapid global warming (Sun et al., 2012), seawater anoxia/euxinia (Grice et al., 2005; Meyer et al., 2008; Hülse et al., 2021), sea-level changes (Hallam and Wignall, 1999; Ruban, 2020), and marine acidification (Payne et al., 2010; Clarkson et al., 2015). The most widely devastating mechanism was multiple environmental triggers that began with large igneous province eruptions, such as Siberian Traps (Black et al., 2012; Burgess et al., 2017; Joachimski et al., 2019; Kaiho et al., 2020), or Paleotethys ocean volcanism (Yin and Song, 2013).

However, the research on potential triggers of PTME could be affected indirectly by the uncertainty of the PTME process. Li et al. (2021) recently proposed that the two phases of PTME had different environmental triggers in the Liangfengya section. Their data confirmed that oxygen deficiency was key in the second pulse of PTME; however, the first pulse might have been triggered by other environmental factors such as high and oscillating temperatures (Sun et al., 2012) rather than an anoxia event (Isozaki, 1997; Grice et al., 2005).

Extinction patterns among benthos varied between shallow- and deep-water facies according to previous PTME investigations (e.g., Groves et al., 2005; Shen et al., 2006; Chen and Benton, 2012). To examine the intrinsic connection about various extinction patterns among environments of different water depths, we here investigated the lithologic succession and benthonic assemblages from Late Permian to Early Triassic in two adjoining sections. We further discussed the extinction patterns, possible environmental triggers, and survival mechanisms during the PTME. This investigation of biotic response to rapid environmental changes can help us better understand the extinction and survival process, including modern-day global environmental disasters.

2 Paleogeography and Sedimentary Background

During the Late Permian to the Early Triassic, the SCB was located near the paleoequator, in the eastern Paleotethys Ocean, where the shallow-water Yangtze Platform was separated by several deep-water siliciclastic basins (**Figure 1**). In the past two decades, attention was focused on the sedimentary successions in SCB. The huge exposures, length of the sections, and improved chronology provided a good opportunity to track environmental changes and restoration of benthic ecosystems during the P–Tr transition.

Abbreviations: BSE, backscattered electron; GSSP, Global Stratotype Section and Point; MEH, mass extinction horizon; MU, microbialite unit; OMZ, oxygen minimum zone; PTB, Permian–Triassic boundary; PTME, Permian–Triassic mass extinction; SCB, South China Block; SEM, scanning electron microscopy; SMF, standard microfacies.

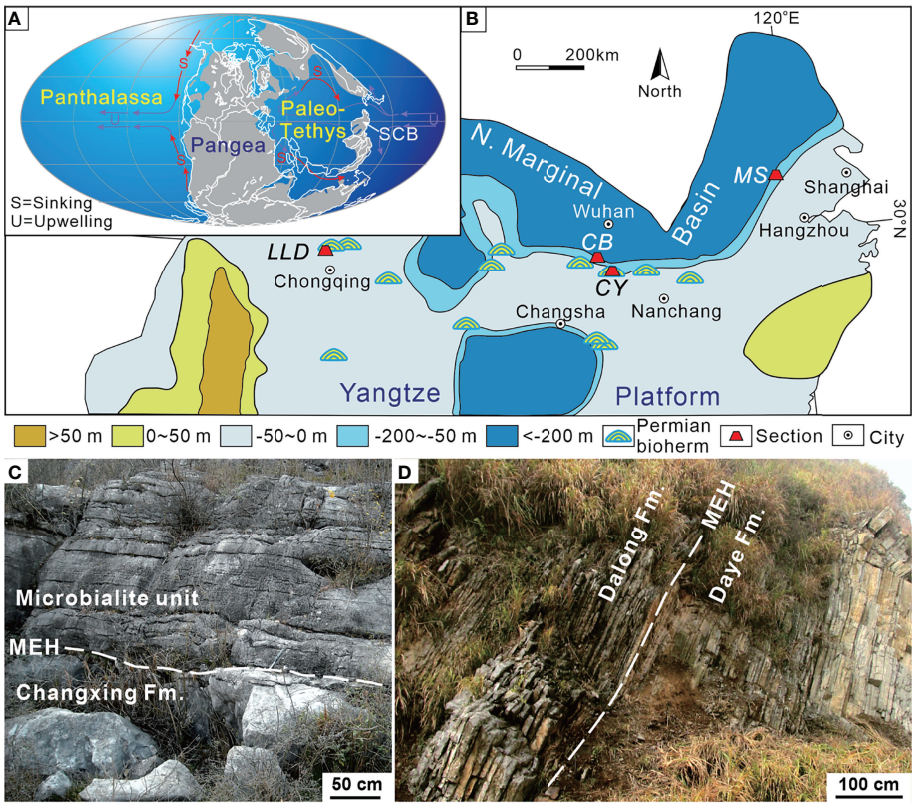

FIGURE 1 | Changhsingian paleogeographic map showing the location of the sections investigated. **(A)** Global map revised from Scotese (2001). **(B)** Base map of the South China Block revised from Wang and Jin (2000). **(C)** Field outcrop of the Chongyang section showing the lower part of the microbialite unit and Late Permian grainstone near the P–Tr boundary. **(D)** Field outcrop of the Chibi section in Xianning city showing the P–Tr transition sequence. MEH, mass extinction horizon; SCB, South China Block; *CB*, Chibi section; *CY*, Chongyang section; *LLD*, Laolongdong section; *MS*, Meishan section.

2.1 The Chongyang Section

The Chongyang section (114°20′16″E, 29°39′08″N), located at Dashi village of Chongyang County southeast of Hubei Province (**Figure 1B**), has been described by Wang et al. (2005). The P–Tr boundary successions are well exposed, making it easy to identify the mass extinction horizon (MEH) (**Figure 1C**). On the outcrop, the coral reef framestone and skeletal grainstone are visible in the lower part of the section (Yang et al., 2011), yielding foraminifera *Palaeofusulina sinensis*. The skeletal grainstone under the MEH is Late Permian in age on the basis of *Palaeofusulina*. The Late Permian grainstone contains more than 80% (relative to the sediments) fossils, including rugose corals, fusulinids, calcareous algae, foraminifers, crinoids, bryozoans, brachiopods, and several other metazoan fossils. On the top of the skeletal grainstone is now an undulating paleokarst surface, capped with weathering and erosion residual products (Wang et al., 2019). The paleokarst surface formed widely at the shallow platform of the SCB (Ezaki et al., 2003; Wu et al., 2010; Kershaw et al., 2012) due to its exposure by the end-Permian regression (Yin et al., 2014). The overlying microbialite unit (MU) is characterized by thrombolite and dendrolite, which differ distinctly from Late Permian skeletal grainstones. Yang et al. (2006) elucidated the composition and structure of microbialite ecosystems in the Chongyang section following the PTME. The MU lies on Permian skeletal grainstones and is overlain by thin-bedded micrites up to 8.5 m thick (**Figure 2**). The upper part of MU has several layers of molluskan grainstone. There is a regression hiatus between the Upper Permian Changxing Formation and the MU (Yin et al., 2014).

Despite the fact that conodont fossils such as *Hindeodus parvus*, *Hindeodus typicalis*, and *Hindeodus latidentatus* had been found in the middle MU (Yang et al., 2006), more comprehensive work from various sections indicated that conodont fossil *H. parvus* was actually preserved at the bottom of the MU (Jiang et al., 2014; Wang et al., 2016). Therefore, the P–Tr boundary in the Chogyang section was allocated to the bottom of the MU in this study, and the MU was assigned to the *H. parvus* Zone (Jiang et al., 2014; Wang et al., 2016).

2.2 The Chibi Section

The Chibi section (113°49′13″E, 29°42′01″N) is located at Fenghuang Mountain in southeast Hubei Province. This section is positioned in the transitional zone between the Yangtze Platform and the northern marginal deep siliceous

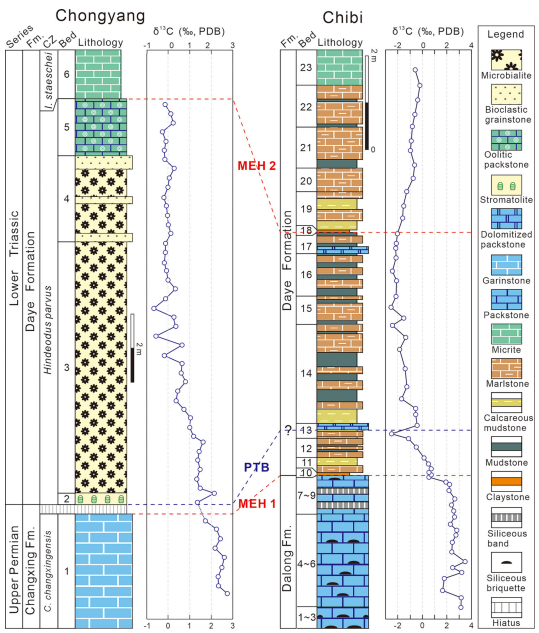

FIGURE 2 | Columnar sections of P–Tr successions of the Chongyang and Chibi sections. Conodont zonation of the Chongyang section from Yang et al. (2006) and Wang et al. (2019). The δ^{13}Ccarb of the Chongyang section from Wang et al. (2019). CZ, conodont zones; *C.*, *Clarkina*; *I.*, *Isarcicella*; MEH, mass extinction horizon; PTB, P–Tr boundary.

basin during the P–Tr transition (**Figure 1**; Feng et al., 1996). A deep siliciclastic deposition exists in the northern area to Chibi, such as Daye or Huangshi (Wang and Xia, 2003). The southern area consists of a shallow-water carbonate platform (Liu et al., 2010).

The particular paleogeographic setting resulted in the formation of a distinct sedimentary sequence within the P–Tr interval (**Figure 2**). The Upper Permian Dalong Formation (Beds 1–9) is characterized primarily by a sequence of thin- to medium-bedded bioclastic packstones interlayered with a small amount of siliceous thin beds. Packstones contain benthic fossils, such as foraminifers, calcareous algae, and echinoderms. The PTME occurred at the base of the first claystone (Bed 10), where a diversified benthic assemblage disappeared, which was dominated by small foraminifers and calcareous algae (Deng et al., 2015). Numerous siliceous beds had accumulated during the first MEH (MEH 1) in the Dalong Formation, indicating increased volcanism (Wang et al., 2019). The fine-grained lithologies of the overlying Daye Formation include micrites, marls, mudstones, and claystones, with sparse bivalves and ammonoids. Abundant small pyrite framboids in Beds 11–21 suggested a low oxygen level in bottom waters (Wignall and Hallam, 1996).

Although no identifiable conodont had been found to confirm the P–Tr boundary of the Chibi section, the Bed 25 "boundary clay" of the Meishan section, known as the Global Stratotype Section and Point (GSSP) for the P–Tr boundary (Yin et al., 2001), had been considered to be a reliable marker of P–Tr boundary (Peng and Tong, 1999). Bed 10 of the Chibi section can be compared to it based on the first appearance of the basal Triassic marker, the bivalve *Claraia wangi* (in Bed 17), *C. stachei* (in Bed 21), and the ammonoid *Hypophiceras* (in Bed 18) (**Figure 3**). Based on biostratigraphy, a large excursion of carbon isotope is a useful indicator of stratigraphic correlation (Song et al., 2012). The first negative shift was recorded at Bed 13 and a weaker positive shift is recorded at the lower part of Bed 14 of the Chibi section (**Figure 2**). Thus, the P–Tr boundary is located in the middle of Bed 13 (i.e., 94 cm above the first claystone of the Daye Formation base).

3 METHODS

3.1 Fossil Assemblage

Bioclastic was investigated under the microscope to examine the taxonomic composition of fossils. In each sample, calcareous algae, fusulinids, non-fusulinid foraminifers, bivalves, gastropods, ostracods, echinoderms, and microbes were classified according to guidelines of Flügel (2004). The changes of these fossil groups were recorded across the P–Tr boundary in the carbonate platform. A quantitative statistical method that was introduced by Payne et al. (2006) for bioclastic grains, i.e., a Figure of 500 points (or 300 points in some cases) was chosen to determine the contents of bioclastic grains, with an error of ±2.5% (Wen and Liu, 2009).

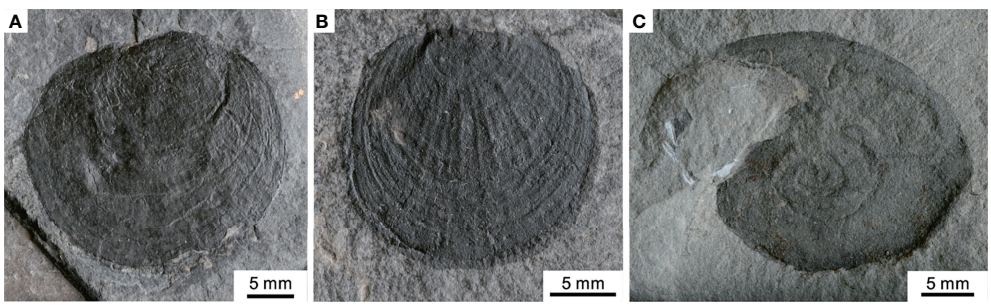

FIGURE 3 | The Early Triassic marker, bivalves and ammonoids of the Chibi section. **(A)** *Claraia wangi* from Bed 17. **(B)** *Claraia stachei* from Bed 21. **(C)** *Hypophiceras* sp. from Bed 18.

3.2 Microfacies Analysis

The analysis of carbonate microfacies was carried out according to standardized microfacies (SMF) and the depositional pattern (Flügel, 2004), focusing on fossil fragments and lithologic characters from both outcrops and thin sections. During the fieldwork, macrofossils, lithologic characters, and sedimentary structures were observed on outcrops. Small fossil fragments and other microlithologic characters in thin sections were examined under a polarizing microscope. The content of fossil fragments was calculated using the methodology by Payne et al. (2006).

3.3 Pyrite Framboid Analysis

Thirty vertically oriented samples with ca. 2 × 2 cm^2 in size across the P–Tr boundary in the Chibi section were selected to analyze size distributions of pyrite framboid for the study of redox conditions. Three samples from packstone of the Upper Permian Dalong Formation, 18 from the thin-bedded mudstone/marlstone of the P–Tr "transitional beds," and five from the Lower Triassic Daye Formation were investigated. Initially, each sample was polished for petrographic observation under a microscope. Pyrite framboids of each polished sample were measured *in situ* using an FEI Quanta 200 scanning electron microscope (SEM). A minimum of 120 pyrite framboids were measured for each sample wherever appropriate: this quantity was considered sufficient for the statistical analysis with an error less than 10% (Wilkin et al., 1996).

4 RESULTS

4.1 Fossil Assemblage and Microfacies of the End-Permian

The sedimentary sequence at the Chongyang section starts with gray thick-bedded bioclastic grainstones belonging to the Upper Permian Changxing Formation, yielding foraminifer *Palaeofusulina sinensis*. Thin-section data revealed that the Changxing Formation was mostly made up of skeletal grainstones cemented by sparite calcite, and that calcareous algae, fusulinids, non-fusulinida foraminifera, ostracods, gastropods, coral, bryozoan, and echinoderms were well-preserved fossil grains (**Figure 4A**). The biotic abundance was extremely high with an average of 66% (**Figure 4B**) and could come out >80% in some samples, implying a turbulent shallow-water platform environment. Furthermore, a number of fusulinids were identified in thin sections (**Figure 5**), indicating that the water depth was about 20–30 m (Yu, 1989). The foraminiferal assemblage was similar to those examined on shallow-water platforms elsewhere in the SCB, where *Reichelina*, *Cribrogenerina*, and *Palaeofusulina* were commonly abundant (Yang et al., 2011). The cement was largely composed of sparite and contained no micrite, indicating a high water-energy content. The presence of abundant algae and coral indicated that the seafloor was within the euphotic zone (**Figure 4A**). The diverse benthic community preserved in the Permian bioclastic grainstone of the Chongyang section indicates a well-oxygenated water column (Groves et al., 2005).

Microfacies type of Bed 1 was diagnosed in comparison with SMF, which was similar to SMF 18 (Flügel, 2004). According to the sedimentary model (Flügel, 2004), the Chongyang section was located in a typical shallow-marine carbonate platform environment with relatively high water-energy during the Late Permian Changhsingian.

The sedimentary sequence of the P–Tr interval at the Chibi section started with a dark gray thin-bedded bioclastic packstone with siliceous interbeds belonging to the Upper Permian Dalong Formation. The Dalong Formation was mainly composed of bioclastic packstone cemented by sparite calcite according to thin section (**Figure 6A**). Well-preserved fossils, such as calcareous algae, fusulinida, non-fusulinida foraminifera, and gastropods, had easily identified taxonomic traits and a weak orientation. The diversity was moderate, and the biotic abundance was relatively high, ranging from 20% to 55% (**Figure 6B**). These foraminifera fragments, such as *Reichelina*, *Earlandia*, and *Diplosphaerina*, have small particle sizes, ranging from 100 to 200 μm (**Figure 7**).

The Chibi section was dominated by benthos, in contrast to the typical deep-water silicalite basin characterized by planktonic radiolarian fossils (Meng et al., 2014). Those benthos were

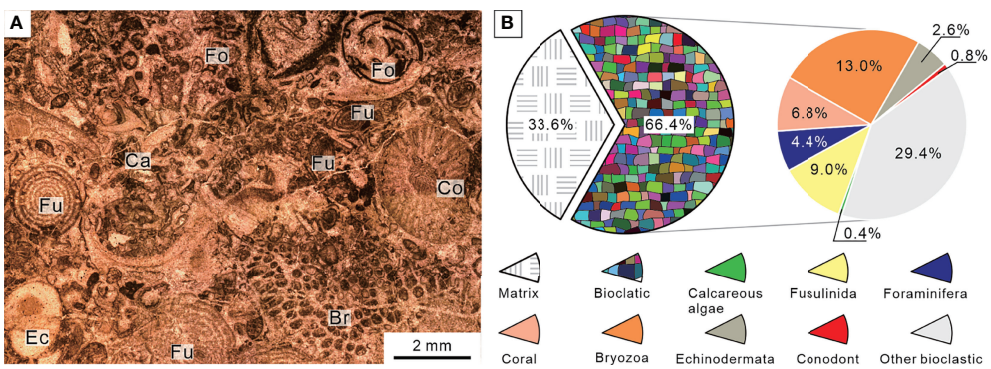

FIGURE 4 | Micropetrologic characters **(A)** and percentages of fossil assemblages **(B)** of bioclastic grainstones from Bed 1 in the Chongyang section before the PTME. Br, Bryozoa; Ca, Calcareous algae; Co, Coral; Ec, Echinodermata; Fo, Non-fusulinida foraminifera; Fu, Fusulinida.

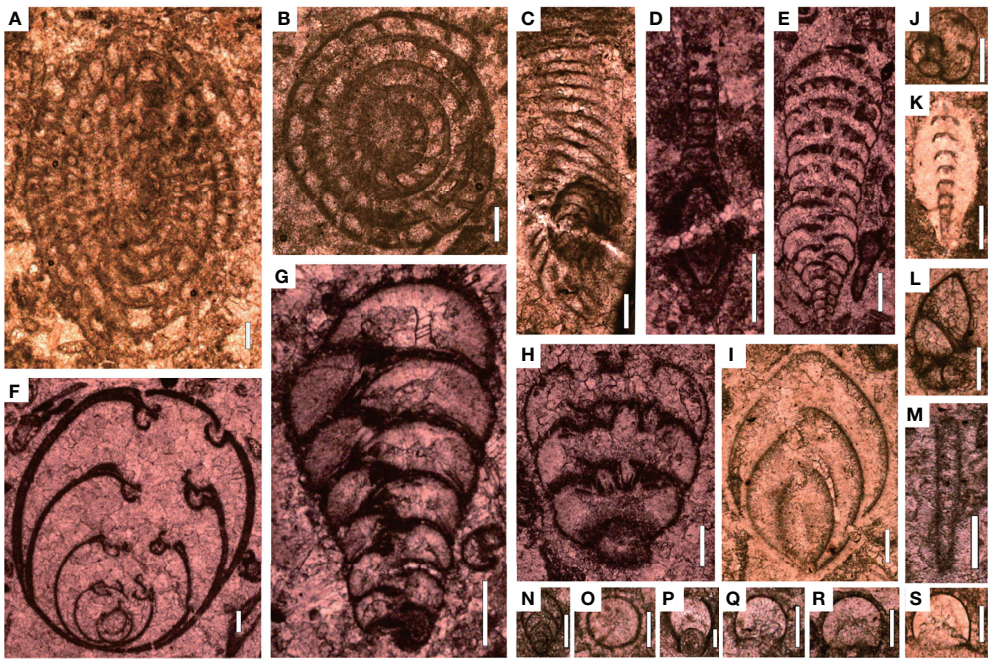

FIGURE 5 | Foraminifers from Bed 1 of the Chongyang section before the PTME. **(A)** Nankinella orientalis; **(B)** Sphaerulina crassispira; **(C)** Reichelina purlchra; **(D)** Reichelina media; **(E)** Climacannina spathulata; **(F)** Paraglobivalvulina piyasini; **(G)** Palaeotextularia longiseptata; **(H)** Cribrogenerina prosphaerica; **(I)** Ichthyofrondina palmata; **(J)** Poatendthyrasp.; **(K)** Pachyphloia ovata; **(L)** Globivalvulina sp.; **(M)** Earlandia sp.; **(N)** Frondina permica; **(O–S)** Diplosphaerna inaequalis. Scale bars in panels **(A–I)** are 200 μm in length and in panels **(J–S)** are 100 μm.

different from that of the Chongyang section, which is a typical shallow platform section in the Late Permian with a lower diversity. A few broken fragments of calcareous algae were found in thin sections (**Figure 6A**), which might have originated from the southern carbonate platform in shallower water (Deng et al., 2015). The cement was mainly composed of micrites and few sparites, indicating that water-energy was relatively low. Therefore, this microfacies resembles SMF 5 (Flügel, 2004). We inferred that the Chibi section was located at the bathyal outer slope between the shallow-water platform and the deep-water basin, slightly deeper than Meishan, during the end-Permian.

Multiple trace fossils were found in the bioclastic wackestone of Bed 6, about 2 m below the MEH 1 (**Figure 8**). The majority of these trace fossils were burrows several centimeters long. The abundance of burrows indicated that the seafloor was suitable for the life of benthic surface organisms and benthic endophytic burrowing organisms (Chen et al., 2015). The microfacies belong to SMF 9-BIOTRUB "burrowed bioclastic wackestone," which was found on the deep-water shelf (Flügel, 2004). Considering a

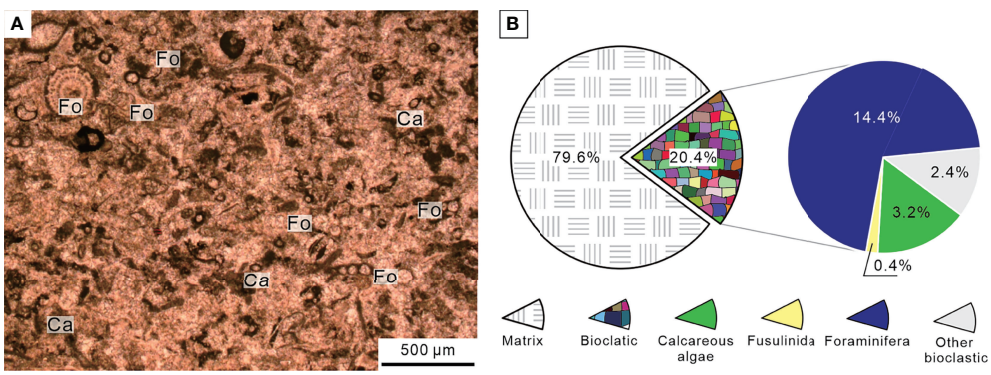

FIGURE 6 | Micropetrologic characters **(A)** and percentages of fossil assemblages **(B)** of bioclastic packstone from Bed 5 in the Chibi section before the PTME. Ca, Calcareous algae; Fo, Non-fusulinida foraminifera.

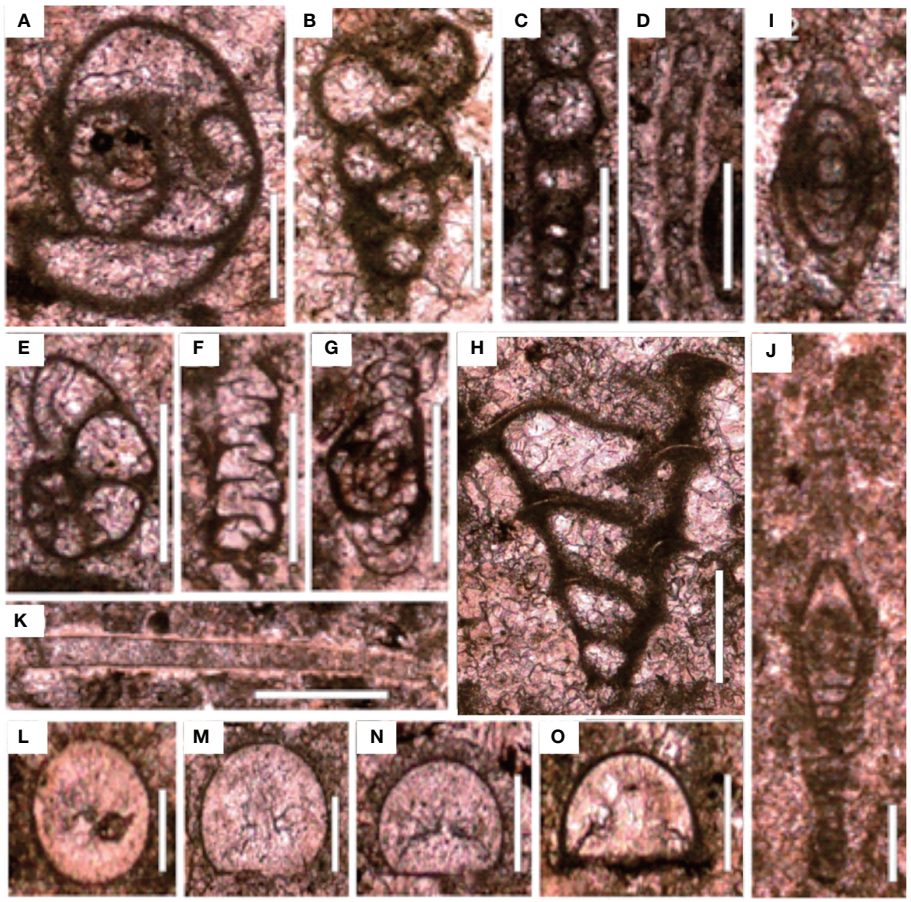

FIGURE 7 | Foraminifers from the Chibi section before the PTME. **(A)** Poatendothyra tenuis; **(B)** Dagmarita sp.; **(C)** Nodoinelloides neischajewi; **(D)** Rectocornuspira kalhori; **(E)** Globivalvulina sp.; **(F)** Ammovertella sp.; **(G)** Hemigordius sp.; **(H)** Dagmarita chanakchiensis; **(I)** Reichelina changhsingensis; **(J)** Reichelina matsushitai; **(K)** Earlandia sp.; **(L–O)** Diplosphaerina inarqualis. Scale bars in panels **(A–K)** are 100 μm in length and in panels **(L–O)** are 50 μm.

few broken algae fragments and fecal pellets, we proposed that the seafloor should be below the photic zone with a water depth of 100–200 m.

4.2 Fossil Assemblage and Microfacies During the Permian–Triassic Interval

Microbialites dominated the shallow platform of the SCB during the Early Triassic transgression directly after the end-Permian regression, representing a disaster biota due to the lack of skeletal organisms (Wang et al., 2005). The MU comprised a series of microbialite forms in the Chongyang section (Wang et al., 2019). Numerous metazoan fossils were found within the MU, including small foraminifera, microgastropods, and ostracods (Yang et al., 2011), all of which exhibited varying and had low diversity. One remarkable feature of microbialite is well-preserved calcified cyanobacteria (**Figure 9A**), reflecting an absence of metazoan predation. The microfacies was similar to that of SMF 21 (Flügel, 2004). The microfacies of Bed 2 belong to SMF 21-PORO, which was formed in very shallow supratidal environments, such as restricted or evaporitic lagoons. The microfacies of Beds 3 and 4 belong to SMF 21-PORO, which was formed mostly in shallow subtidal or intertidal environments.

Following the thrombolite disappearance, an oolitic packstone was deposited. These packstones consisted of poorly sorted ooids within the micrite matrix (**Figure 9B**). The rapid transition from thrombolite facies to an oolitic facies indicated a significant change in the marine environment. Majority of modern marine ooids are found in warm waters and wave/current churned settings (Diaz et al., 2015), such as the Great Bahama Bank (Harris et al., 2019), while poorly sorted ooids are in more tranquil environments (O'Reilly et al., 2017). The microfacies were similar to that of SMF 15 (Flügel, 2004). Modern stromatolites were reported mainly in Shark Bay and Bahamas in middle America, where the most prevalent water depths range from intertidal to 10 m (Chivas et al., 1990; Reid et al., 1995). We infer that this type of microfacies was formed in a relatively low water-energy environment along the platform margin and was the result of further deepening in the water depth during the Early Triassic transgression (Kershaw et al., 2012).

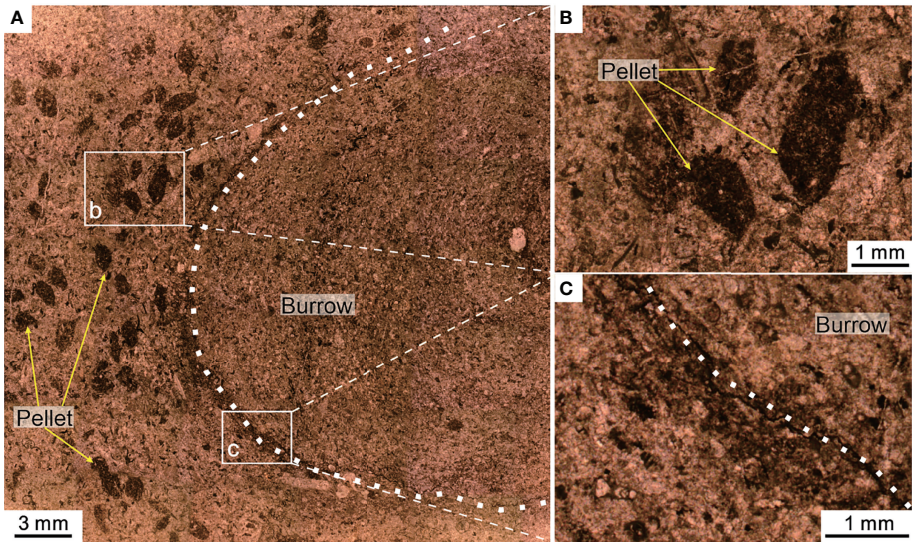

FIGURE 8 | Trace fossil (burrow) and fecal pellets from Bed 6 of the Chibi section before the PTME. **(A)** The cross-section of a burrow and the well-demarcated boundary (dotted line). Panels **(B, C)** are the magnified images from the two white boxes in panel **(A)**.

The lower part of Daye Formation (Beds 11–14) comprised dark thin-bedded fine-grained lithologies, including micrites, marls, mudstones, and claystones on outcrops. Bioclastic content was found to be very low, ca. 5%~10%, with a few small foraminifers, echinoderms, gastropods, and ostracods in thin sections (**Figure 10A**). Small pyrite framboids were relatively common. The microfacies was similar to SMF 8 (Flügel, 2004). This microfacies is common both in the deep open shelf and in shallow lagoons. The micritic matrix indicated a restricted low-energy environment. Thus, we inferred that the microfacies formed in tranquil subtidal facies. However, some echinoderm and small gastropod fragments occasionally have been found in Beds 15–17 (**Figure 10B**). Bioclastic content was higher than 25% and mainly composed of small gastropods and ostracods. This microfacies belonged to SMF 8 (Flügel, 2004). Accordingly, we inferred that this microfacies was formed in the deep shelf with a low water-energy, standing for the subtidal facies.

4.3 Fossil Assemblage and Microfacies of the Early Triassic

The topmost of the Chongyang section (Bed 6) comprised of gray medium- to thick-bedded micrites on outcrop. Rare fossil fragments were observed in thin sections under the microscope, but pyrite framboids were relatively common (**Figure 11A**). The microfacies was similar to that of SMF 9 (Flügel, 2004). For the micritic matrix and the lack of fossils, we inferred that this type of

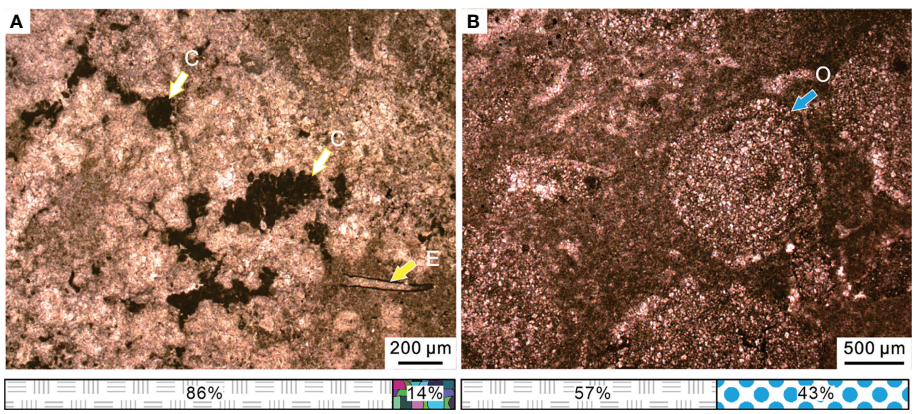

FIGURE 9 | **(A)** Spherical calcified cyanobacteria and small foraminifera *Earlandia* sp. of the microbialite from Bed 3 in the Chongyang section. **(B)** Micropetrologic characters of Bed 5 in the Chongyang section, including poorly sorted ooids within the micrite matrix. The legend is consistent with that of **Figure 4**. C, cyanobacteria; E, *Earlandia* sp.; O, ooids.

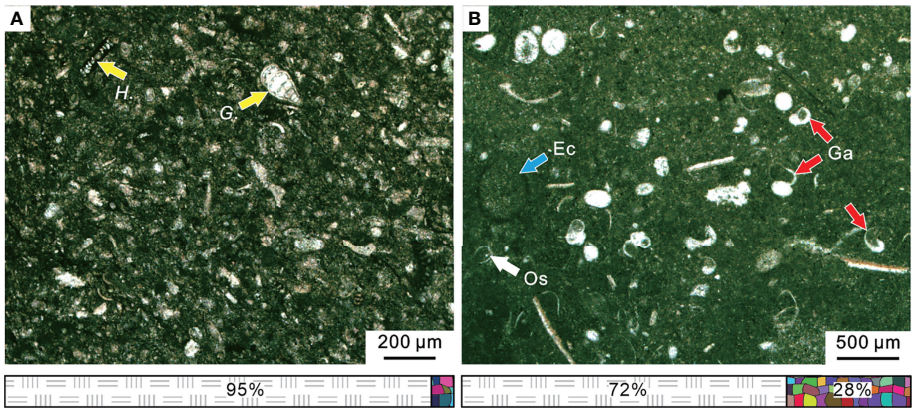

FIGURE 10 | Micropetrologic characters and fossil assemblages of micrites in the Chibi section during the PTME interval. **(A)** From Bed 11. **(B)** From Bed 15. The legend is consistent with that of **Figure 4**. Ec, Echinoderm; Ga, gastropod; Os, ostracod; *G.*, *Geinitzina*sp.; *H.*, *Hemigordius* spp. The legend is consistent with that of **Figure 4**.

microfacies was formed in restricted lagoons with a low water-energy.

Above the MEH 2, the Early Triassic stratigraphic succession of the Chibi section was mainly characterized by black mudstones with a gray-black marlstone interlayer that expanded with transgression and increased water depth. The abundance of bivalves found in field outcrop varied but showed low diversity. No benthic community was found in field outcrops or thin sections (**Figure 11B**). The microfacies was similar to SMF 9-L, which was located near the bottom of the slope or deep-water shelf (Flügel, 2004).

4.4 Pyrite Framboid Size Distributions in the Chibi Section

Out of the 26 samples, two samples from Dalong Formation had no pyrite framboids, while one (sample LFY -16) had a trace amount of pyrite framboids or authigenic crystals. However, backscattered electron (BSE) images revealed that 23 samples from the Daye Formation were generally rich in pyrite framboids (except sample LFY +379) (**Figure 12A**). A plot of mean diameter and standard deviation of pyrite framboid is shown in **Figure 12B** for the purpose of paleoredox interpretation. The parameters of size distribution are summarized in **Table 1**.

We collected 18 samples from the P–Tr transition beds (Beds 10–17) and measured 3,730 pyrite framboids (more than 200 framboids per sample) (**Table 1**). The majority of pyrite framboids were less than 10 μm. The mean diameters of the 18 samples varied from 4.08 ± 1.07 μm to 11.77 ± 4.90 μm, suggesting that the oxygen levels of bottom water fluctuated between upper dysoxia and anoxia during the P–Tr transition interval. We collected five samples from Beds 19–21 and measured 974 pyrite framboids (ca. 195 framboids per sample) (**Table 1**). These five samples had a mean diameter range of 4.74 ± 1.46 μm to 5.96 ± 1.67 μm, indicating that the bottom water at the Chibi site had a stable reduced oxygen environment (Bond and Wignall, 2010).

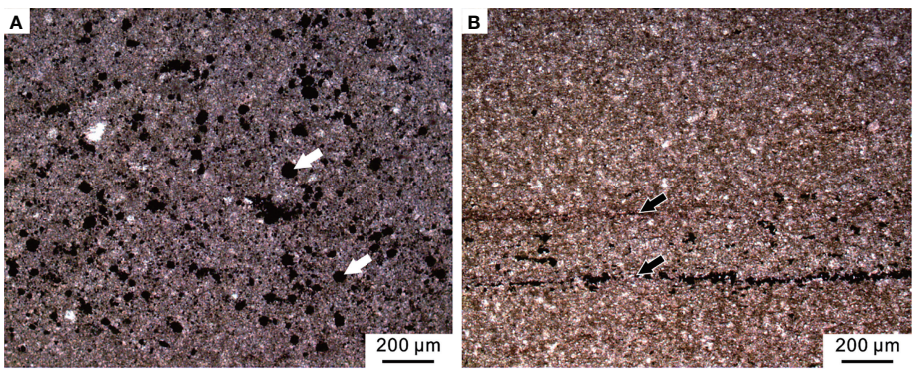

FIGURE 11 | Micropetrologic characters after the PTME. **(A)** Micrite from Bed 6 of the Chongyang section bearing abundant pyrite framboids (white arrows). **(B)** Mudstone from Bed 19 of the Chibi section, including organic laminas (black arrows).

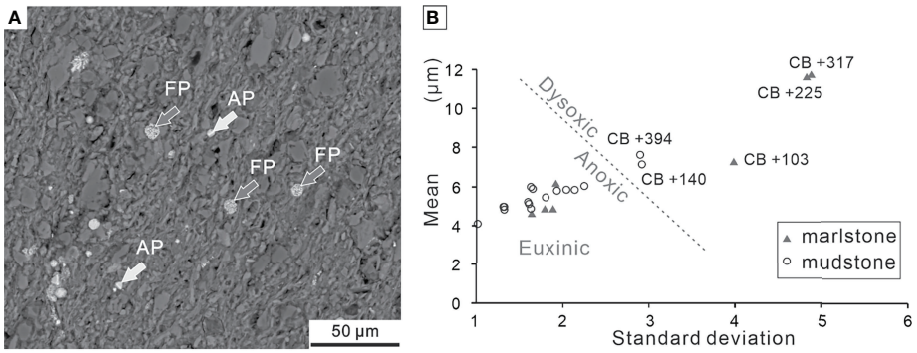

FIGURE 12 | **(A)** Overview of BSE images of framboidal pyrites and authigenic pyrites from Bed 19 of the Chibi section. **(B)** Cross-plot of mean diameter vs. standard deviation of pyrite framboids from the Chibi section. The boundary (dotted line) separating dysoxic and anoxic/euxinic fields is from Bond and Wignall (2010). FP, framboidal pyrites; AP, authigenic pyrites.

TABLE 1 | Pyrite sample parameters observed from the Chibi section.

Bed No.	Sample level (cm)	Lithology	Number of framboids measured	Minimum framboid diameter (μm)	Maximum framboid diameter (μm)	Mean framboid diameter (μm)	Standard deviation of framboid diameter	Median framboid diameter (μm)	Inferred redox conditions
21	+678	Mudstone	196	1.98	10.25	4.74	1.46	4.42	Anoxic
19	+606	Mudstone	178	2.23	12.14	5.84	2.03	5.39	Anoxic
	+574	Mudstone	201	2.07	12.18	5.96	1.67	5.86	Anoxic
	+548	Mudstone	208	2.29	9.38	4.94	1.36	4.71	Anoxic
	+525	Mudstone	191	2.66	11.02	5.91	1.70	5.60	Anoxic
17	+499	Mudstone	199	2.35	10.77	4.98	1.37	4.95	Anoxic
	+488	Mudstone	229	1.98	9.23	4.81	1.37	4.71	Anoxic
16	+468	Mudstone	185	2.11	10.34	5.20	1.64	4.87	Anoxic
	+453	Mudstone	183	2.03	13.56	6.03	2.30	5.56	Anoxic
	+394	Mudstone	177	2.44	15.73	7.66	2.94	7.21	Dysoxic
15	+379	Marlstone	63	2.24	11.06	6.17	1.97	6.10	Dysoxic
	+363	Mudstone	157	2.66	12.76	5.87	2.09	5.26	Anoxic
	+347	Mudstone	248	2.04	8.82	4.08	1.07	3.87	Anoxic
	+317	Marlstone	119	3.88	25.97	11.77	4.90	10.47	Dysoxic
14	+265	Mudstone	312	1.73	15.20	5.83	2.19	5.35	Anoxic
	+233	Mudstone	260	2.34	11.23	5.10	1.65	5.10	Anoxic
	+225	Marlstone	149	3.85	25.19	11.56	4.85	10.53	Dysoxic
	+185	Mudstone	262	2.29	11.29	5.43	1.85	5.09	Anoxic
	+140	Mudstone	281	1.82	16.35	7.16	2.96	6.47	Dysoxic
13	+103	Marlstone	266	2.41	22.32	7.30	4.01	6.15	Dysoxic
	+74	Marlstone	147	2.21	10.53	4.86	1.93	4.32	Anoxic
11	+35	Marlstone	254	1.76	11.87	4.86	1.83	4.53	Anoxic
	+12	Marlstone	239	1.76	10.87	4.62	1.68	4.19	Anoxic
9	-16	Limestone	8	5.10	10.25	#	#	#	Oxic
8	-34	Limestone	#	#	#	#	#	#	Oxic
	-53	Limestone	#	#	#	#	#	#	Oxic

Sample level "-53" means 53 cm below the first mass extinction horizon (MEH 1), and "+678" means 678 cm above the MEH 1. "#" means no data.

5 DISCUSSION

5.1 Single Abrupt Extinction Pulse in the Platform Setting

The PTME pattern has been debated for several decades (e.g., Stanley and Yang, 1994; Jin et al., 2000; Shen et al., 2011; Song et al., 2012; Dal et al., 2020). Investigations have revealed a complex process of the PTME. Among different benthos, on the one hand, the extinction patterns and magnitudes were varied: extinctions among foraminifers occurred as a one-pulse extinction pattern (Groves et al., 2005), whereas ostracods exhibited two extinction pulses (Forel, 2013; Wan et al., 2019). On the other hand, among different paleogeographic settings, sharply different patterns of the same faunas had also been observed, typified by foraminiferal extinction (Song et al., 2009; Zhang and Gu, 2015; Li et al., 2021).

The stratigraphic succession from the end-Permian to Early Triassic interval in the Chongyang section was very clear at the outcrop. The top of the Changxing Formation grainstones was coated by residual deposits enriched in ferric oxide, quartz, and

feldspar, which probably represented the weathering and erosion products following its exposure by the end-Permian regression (Wu et al., 2006). The overlying lower part of the Daye Formation was dominated by MU, indicating a dramatic change in the marine ecosystem from end-Permian to Early Triassic. The MEH was located topmost of the Changxing Formation grainstones.

The Upper Permian Changxing Formation in the Chongyang section was characterized by the deposition of reef framestone and grainstone enriched in diverse benthos, such as corals, calcareous algae, echinoderms, and foraminifers under the microscope (**Figure 13I**). However, most benthos such as rugose corals, fusulinida, calcareous algae, and large foraminifers disappeared in the topmost of the Changxing Formation grainstone. Small foraminifers, such as *Diplosphaerina inaequalis* and *Earlandia* sp., survived during this extinction pulse (**Figure 13H**) but eventually disappeared quickly (**Figure 13G**). The bioclastic abundance dropped to less than 15% (**Figure 9**), down from 66% or higher than this value in the Changxing Formation grainstones (**Figure 4**).

The pattern indicated a sudden extinction at the base of the MU in the Chongyang section. The abrupt extinction process had been documented in various shallow water settings of the Pangea (Groves et al., 2007; Angiolini et al., 2010). Foster et al. (2019) proposed that a shallow microbialite could provide a "refuge" for some marine invertebrates during mass extinction, where disaster forms could create a unique and ephemeral ecosystem. Significant disaster forms, such as ostracods, small gastropods, tubeworms, and brachiopods, bloomed ephemerally and formed a stratiform bioclastic grainstone in the MU of the Chongyang section (**Figure 14**). In summary, the Chongyang section from the shallow platform suffered an abrupt extinction pulse, resulting in a crashed ecosystem structure.

5.2 Two-Pulse Extinction in Slope Setting

However, compared to the Chongyang section, the benthos of the Chibi section, which was located on the outer slope, did not completely disappear after the first PTME pulse. The

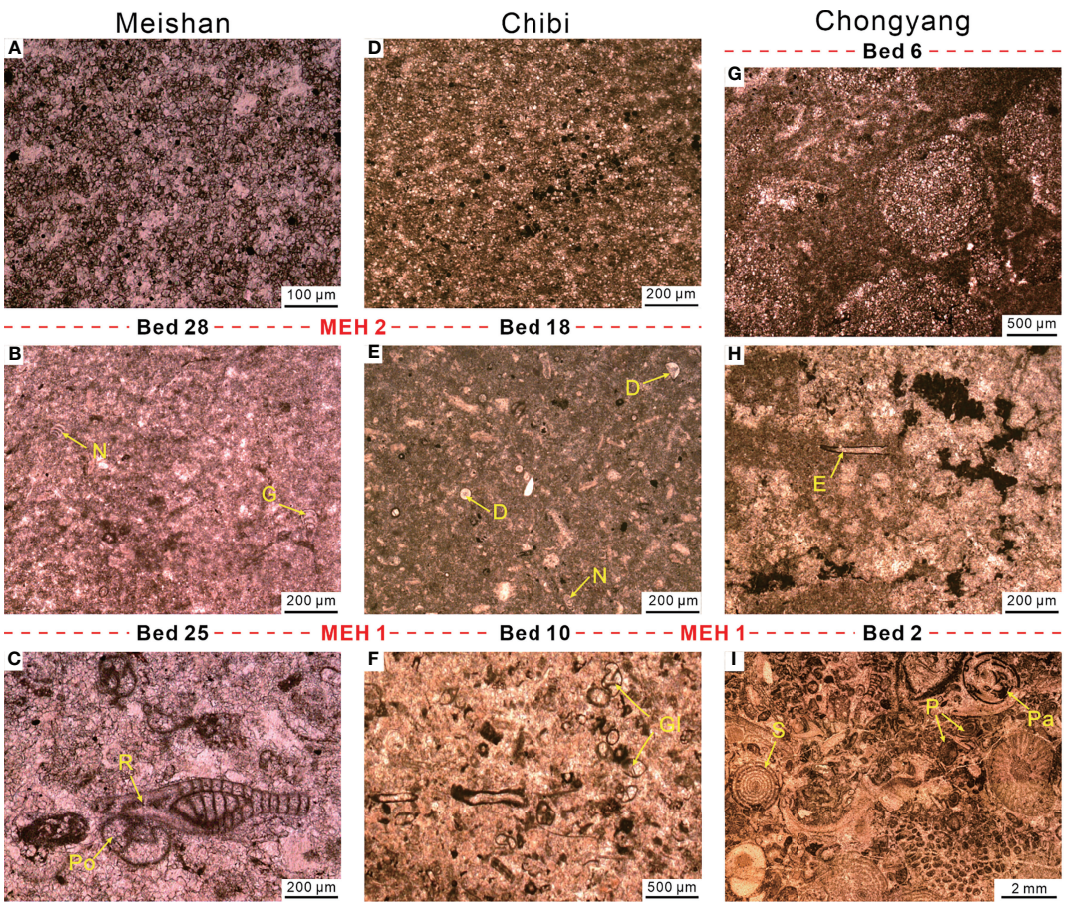

FIGURE 13 | Comparison of foraminifera features between Meishan **(A–C)**, Chibi **(D–F)**, and Chongyang **(G–I)** sections. **(A)** Micrite of Bed 29 with abundant pyrites but no fossil fragments. **(B)** Micrite of Bed 27a with few foraminifera. **(C)** Packstone of Bed 24, including abundant foraminifera and some algae fragments. **(D)** Marlstone of Bed 20 contains abundant pyrite. **(E)** Marlstone of Bed 13 contains few foraminifera. **(F)** Packstone of Bed 5 contains ca. 30% of algae and foraminifers. **(G)** Oolites of Bed 5. **(H)** Microbialite of Bed 3 containing few foraminifers and calcified cyanobacteria. **(I)** Grainstone of Bed 1, including over 80% bioclastic. D, *Diplosphaerina*; E, *Earlandia*; G, *Geinitzina*; Gl, *Globivalvulina*; N, *Nodosaria*; P, *Palaeofusulina*; Pa, *Paraglobivalvulina*; Po, *Poatendothyra*; R, *Reichelina*; S, *Sphaerulina*.

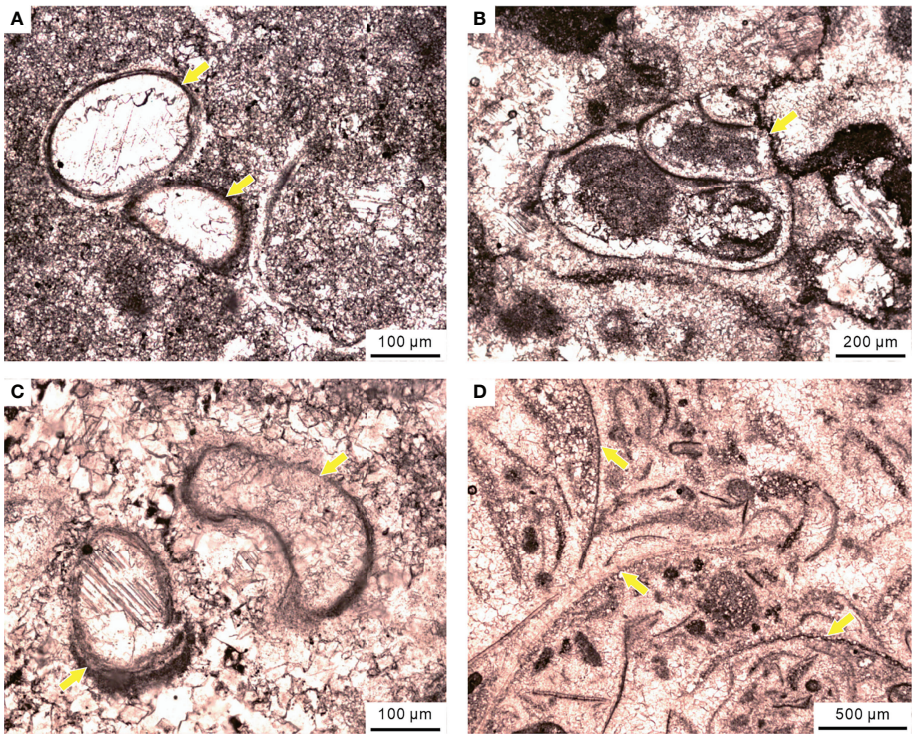

FIGURE 14 | Disaster forms in the MU of the Chongyang section during the PTME, including **(A)** ostracods, **(B)** small gastropods, **(C)** calcareous tubeworms, and **(D)** brachiopods.

foraminiferal diversity was substantially lower than that in Beds 1–9 before the first PTME pulse. Small foraminifers, such as *Earlandia*, *Geinitzina*, *Hemigoradius*, and *Nodosaria*, survived in the Chibi section (**Figures 10**, **13E**). The small foraminiferal assemblages from Beds 11–17 of the Chibi section were similar to those from P–Tr transition beds (Beds 25–27) of the Meishan section (**Figure 13B**; Song et al., 2009). It was worth noting that among the end-Permian foraminiferal assemblages, large-sized foraminifers disappeared in both Chongyang and Chibi sections after the first PTME pulse (**Figure 13**). Similarly, the large-sized foraminifers were also the most vulnerable victims of the first PTME pulse in the Liangfengya and Meishan sections (Song et al., 2007).

The bioclastic abundance dropped to less than 5% (**Figure 10A**), down from 20% or higher than this value in the Dalong Formation packstones (**Figure 6**). But the abundance of bioclastic from some samples of Beds 15–17 could reach or even exceeded the pre-extinction average, ca. 28% (**Figure 10B**). The second MEH (MEH 2) was located at the base of Bed 18, with disappearance of small-sized foraminifers *Diplosphaerina*, *Earlandia*, and *Nodosaria* (**Figure 13E**). The two-pulse extinction pattern of the Chibi section was similar to that in the Meishan section, i.e., the first pulse eliminated large-sized taxa with complex morphologies, and the second pulse chiefly affected the small ones (**Figure 13**). The two extinction pulses might be synchronous at the Chibi and Meishan sections, although this was less certain, for that we could not find well-preserved conodonts in the P–Tr boundary interval. Stratigraphic evidence (e.g., two claystone beds) and benthic assemblages suggested that the two extinction pulses in these two sections were synchronous.

5.3 Triggers of Migration and Extinction

5.3.1 Sea-Level and Sea Surface Temperature Changes

A correlation between global marine regressions and mass extinctions has been recognized since the last century, and sea-level fall was considered one of the prime causes of the events (Erwin, 1993; Gall et al., 1998). However, studies on numerous sections have called the generality of the regression–extinction relation into question (e.g., Hallam and Wignall, 1999; Baresel et al., 2017).

Seawater retreated from the Yangtze Platform at the end-Permian, reaching its lowest point in the *Clarkina meishanensis* and *Hindeodus changxingensis* zones (Yin et al., 2014), resulting in the absence of these two conodont zones and an ancient karst surface in most of the shallow-water platform. In shallow-water platforms of the SCB, Wu et al. (2010) pointed out that this hiatus was usually represented by concealed unconformity between the end-Permian limestone and the overlying MU, which coincided with *C. meishanensis* and *H. changxingensis* zones.

A sudden mass extinction pulse of benthos was recorded at the hiatus in the Chongyang section (**Figure 2**), and perhaps it was the hiatus of two conodont zones that had made the extinction seem more dramatic than it actually was. During the periods of drops in the sea level at the end-Permian (Yin et al., 2014), most of the shallow platform was exposed, and habitats of benthos were squeezed and fragmented. At the PTME interval, ca. 10°C rise of sea surface temperature (SST) was recorded in the tropics (Sun et al., 2012). Ocean warming has the potential to cause major shifts of planktonic distribution (Tarling et al., 2018). Overheating of surface waters during the PTB interval might result in extremely unsuitable habitats for shallow benthos. Climate modeling suggested that, in the tropics, water temperatures at 200-m depth were 10°C~12°C cooler than SST (Winguth et al., 2015).

In the context of global warming, the deep-ward migration of some shallow-water benthos was likely a more effective strategy than migration across the latitudes (Burrows et al., 2019). Thus, deeper waters might become a refuge for marine animals (Godbold et al., 2017). At the P–Tr transition, such extreme warming of SST could be a potentially potent driver for foraminifers to migrate to deeper and cooler waters. If an organism or population could not migrate, or when the rate of change exceeded its ability to do so, extinction was inevitable eventually. Mass extinctions might be related to shrunk habitats on shelves during severe regression (Newell, 1967; Fahrig, 2017). However, microfacies study revealed that the sea level of deeper-water sections was influenced slightly by the end-Permian major regression, so that foraminiferal diversity hotspot moved to the deeper-water slope (Liu et al., 2020).

The original exposed shallow platform was once again submerged by sea water and formed the MU succession during the Early Triassic transgression. The microfacies alterations of the MU reflected the early stages of the sea-level rise (Flügel, 2004). Some stratiform bioclastic grainstone layers were formed by small marine invertebrates in the MU of the Chongyang section. These invertebrates might have migrated from the original deeper-water slope during the sea-level rise and then bloomed in the shallow MU ephemerally as disaster forms (**Figure 14**).

Rapid high-amplitude regressive–transgressive couplets were frequent in the Earth's history (Miller et al., 2005), and most of them were not considered to be a probable cause of mass extinction (Hallam and Wignall, 1999). In short, sea-level change was a key driver of the migration between the platform and the slope but not the main trigger of mass extinction of marine benthos during the PTME interval.

5.3.2 Marine Euxinia/Anoxia

Widespread oceanic anoxia/euxinia (anoxic and sulfur-rich stratified ocean) shown by biomarkers (Grice et al., 2005), S-isotopic compositions (Riccardi et al., 2006), and pyrite framboid sizes (Wignall et al., 2005) has long been documented as a key trigger of the PTME (Isozaki, 1997; Grice et al., 2005; Meyer et al., 2008).

According to size distribution of pyrite framboids, Liao et al. (2010) indicated that the MU from the Laolongdong section grew in a lower dysoxic water column. The shallow-water anoxic event during the P–Tr transition has been considered to be the result of the expanding oxygen minimum zone (OMZ) (Algeo et al., 2010; Algeo and Twitchett, 2010). A recent study showed that the Northeast Pacific OMZ had expanded at a rate of 3.0 ± 0.7 m/year in the last 60 years and had lost 15% of its oxygen (Ross et al., 2020). Low oxygen levels could increase the dominance of benthos tolerant to anoxic conditions (Levin, 2003). For example, one foraminifer genus *Earlandia* flourished as the major "disaster form" in the MU after the first PTME pulse (**Figure 9A**) and probably migrated from the Chibi site during the Early Triassic transgression.

When compared to the Chongyang section, the decrease of algae abundance represented a decline in primary productivity, which might lead to the "dwarfism" of some consumers, e.g., foraminifera (Luo et al., 2006) and brachiopods (He et al., 2007). SEM was used to examine the samples from this stage, and no pyrite framboid was found in the two samples (**Table 1**), indicating that the water column contained a normal level of dissolved oxygen at that time (Bond and Wignall, 2010). This result was consistent with the paleomarine environment reflected by fossil assemblage and biogenic disturbance structure, in agreement with the "superanoxia" in the deep sea (Isozaki, 1997). In deep-water conditions, the dissolved oxygen level fluctuated, which could have induced reductions in the size of benthic foraminifers (Kaiho, 1998).

Another interesting feature was that those surviving foraminifers had a small size with simple morphology (**Figure 13**). For instance, *Nodosinelloides* had a mean volume value of ca. 6.2 log μm^3 in the end-Permian, which fell to 5.5 log μm^3 after the mass extinction (Song et al., 2011). The reduction in size and diversity of fauna with calcified skeletons have been linked to oxygen shortage in modern oceans (Byers, 1978; Levin, 2003). Laboratory experiments showed that the oxygen consumption rate increased significantly in foraminiferal specimens larger than 250 μm (Bradshaw, 1961). However, Luo et al. (2006) suggested that the size reduction of conodonts from the Meishan section was hardly related to anoxia. He et al. (2007) confirmed that there seemed to be no link between brachiopods shrinking and anoxic condition. Kaiho (1994) detected that benthic foraminifers were small-sized, thin-walled, and without sculpture if they inhabited in the lowered oxygen environment. Song et al. (2011) found that the anoxic event recorded in Bed 25 of the Meishan section coincided with the sharp reduction in foraminifer size. Therefore, Song et al. (2011) documented that small body sizes might have helped foraminifera to survive the mass extinction. The size distribution of pyrite framboids implied an anoxic bottom water in this study, while the foraminifera were smaller than pre-extinction foraminifer groups, particularly those extinction Permian groups (**Figure 13**). As a result, a relationship could be expected between anoxic conditions and the size reduction of the benthic foraminifers.

Wang et al. (2019) suggested that the increasing complexity in the benthic ecosystem might be related to hydrodynamic conditions of the Early Triassic transgression as revealed by texture and form of the MU. Our data showed another intriguing phenomenon that the metazoan assemblage in the MU of the

Chongyang section had good consistency with that in the Chibi section (**Figure 13**). This might shed light on transgression preceding the beginning of the Early Triassic, causing the metazoan to migrate from deep water to shallow platforms. A major increase in the δ^{13}C-depth gradient after the PTME suggested that deeper waters experienced more intense and prolonged oxygen restriction (Meyer et al., 2011).

Many layers of the MU contained calcified cyanobacteria (**Figure 9A**). Hypersalinity was one favorable chemical condition for the calcification of cyanobacteria (Pratt, 1984), which could inhibit ecological diversity of other organisms (Zhu et al., 1993). Most benthonic organisms tended to further reduce body size or diversity under high temperatures (Sun et al., 2012), anoxic water columns (Liao et al., 2010), and hypersalinity and intense evaporation (Zhu et al., 1993), whereas microbialite flourished in the shallow environment. This has led to a unique ecosystem dominated by "disaster forms" on shallow-water platforms of the SCB (**Figure 14**).

6 CONCLUSIONS

The PTME showed varied patterns among different paleogeographic sections. The shallow platform recorded one sudden extinction pulse at the topmost of the Changxing limestone, but the deeper-water slope suffered two pulses of marine extinction.

The end-Permian extensive regression caused the exposure of most shallow-marine platforms and then a sudden mass extinction. Sea level falls, extreme heat, and fragmented habitats led to the migration of some shallow-water benthos to deeper water at the same time.

During the Early Triassic transgression, some small foraminifers migrated from the slopes to the shallow platforms. A unique ecosystem has been rebuilt on shallow water platforms of the SCB due to high temperatures, strong evaporation, and hypersalinity after the first PTME pulse.

Pyrite framboid size distributions showed that oceanic anoxia was likely an important trigger contributing to the deeper-water benthic extinction. The abundant small pyrite framboids in the P–Tr transition beds suggested that the redox conditions of the bottom water changed immediately from oxic to anoxic after the MEH 1. Size distributions of these samples indicated that the bottom waters had a fluctuation between anoxic and upper dysoxic during the mass extinction. Pyrite framboid parameters indicated that oxygen deficiency in the bottom water was intensified and stable at anoxia after the second PTME pulse.

DATA AVAILABILITY STATEMENT

The original contributions presented in the study are included in the article/supplementary material. Further inquiries can be directed to the corresponding authors.

AUTHOR CONTRIBUTIONS

GL, YW, SL, TW, WL, and BD collected the samples and photographs in the field. GL, TW, and SL carried out the laboratory measurements and data analysis. YW supervised the data analysis. GL and ZL created the figures and wrote the article. All authors contributed to the ideas and final article.

ACKNOWLEDGMENTS

This study was jointly supported by the National Natural Science Foundation of China (Grant No. 41730320 and No. 41962003), Innovation and Entrepreneurship Project of Shantou (201112176541391), and STU Scientific Research Start-Up Foundation for Talents (NTF19003). Thanks are due to Dr. Rashid Pervez for polishing the language.

REFERENCES

Aberhan, M., and Kiessling, W. (2015). Persistent Ecological Shifts in Marine Molluscan Assemblages Across the End-Cretaceous Mass Extinction. *Proc. Natl. Acad. Sci. U.S.A.* 112, 7207–7212. doi: 10.1073/pnas.1422248112

Algeo, T. J., Chen, Z. Q., Fraiser, M. L., and Twitchett, R. J. (2011). Terrestrial–marine Teleconnections in the Collapse and Rebuilding of Early Triassic Marine Ecosystems. *Palaeogeogr. Palaeoclimatol. Palaeoecol.* 308, 1–11. doi: 10.1016/j.palaeo.2011.01.011

Algeo, T. J., Hinnov, L., Moser, J., Maynard, J. B., Elswick, E., Kuwahara, K., et al. (2010). Changes in Productivity and Redox Conditions in the Panthalassic Ocean During the Latest Permian. *Geology* 38 (2), 187–190. doi: 10.1130/G30483.1

Algeo, T. J., and Twitchett, R. J. (2010). Anomalous Early Triassic Sediment Fluxes Due to Elevated Weathering Rates and Their Biological Consequences. *Geology* 38 (11), 1023–1026. doi: 10.1130/G31203.1

Angiolini, L., Checconi, A., Gaetani, M., and Rettori, R. (2010). The Latest Permian Mass Extinction in the Alborz Mountains (North Iran). *Geol. J.* 45 (2–3), 216–229. doi: 10.1002/gj.1203

Baresel, B., Bucher, H., Bagherpour, B., Brosse, M., Guodun, K., and Schaltegger, U. (2017). Timing of Global Regression and Microbial Bloom Linked With the Permian-Triassic Boundary Mass Extinction: Implications for Driving Mechanisms. *Sci. Rep.* 7 (1), 1–8. doi: 10.1038/srep43630

Benton, M. J., and Newell, A. J. (2014). Impacts of Global Warming on Permo-Triassic Terrestrial Ecosystems. *Gondwana. Res.* 25, 1308–1337. doi: 10.1016/j.gr.2012.12.010

Black, B. A., Elkins-Tanton, L. T., Rowe, M. C., and Peate, I. U. (2012). Magnitude and Consequences of Volatile Release From the Siberian Traps. *Earth Planet. Sci. Lett.* 317-318, 363–373. doi: 10.1016/j.epsl.2011.12.001

Bond, D. P. G., and Wignall, P. B. (2010). Pyrite Framboid Study of Marine Permian–Triassic Boundary Sections: A Complex Anoxic Event and its Relationship to Contemporaneous Mass Extinction. *Geological. Soc. America Bull.* 122 (7-8), 1265–1279. doi: 10.1130/B30042.1

Bradshaw, J. S. (1961). Laboratory Experiments on the Ecology of Foraminifera. *Cushman. Found. Foram. Res. Contr.* 17, 87–106.

Breitburg, D., Levin, L. A., Oschlies, A., Grégoire, M., Chavez, F. P., Conley, D. J., et al. (2018). Declining Oxygen in the Global Ocean and Coastal Waters. *Science* 359 (6371), eaam7240. doi: 10.1126/science.aam7240

Burgess, S. D., Muirhead, J. D., and Bowring, S. A. (2017). Initial Pulse of Siberian Traps Sills as the Trigger of the End-Permian Mass Extinction. *Nat. Commun.* 8, 164–169. doi: 10.1038/s41467-017-00083-9

Burrows, M. T., Bates, A. E., Costello, M. J., Edwards, M., Edgar, G. J., Fox, C. J., et al. (2019). Ocean Community Warming Responses Explained by Thermal Affinities and Temperature Gradients. *Nat. Clim. Change* 9 (12), 959–963. doi: 10.1038/s41558-019-0631-5

Byers, C. W. (1978). Biofacies Patterns in Euxinic Basins: A General Model. *Special. Publ. – Soc. Economic. Paleontol. Mineral.* 25, 5–17. doi: 10.2110/pec.77.25.005

Ceballos, G., and Ehrlich, P. R. (2018). The Misunderstood Sixth Mass Extinction. *Science* 360 (6393), 1080–1081. doi: 10.1126/science.aau0191

Ceballos, G., Ehrlich, P. R., and Dirzo, R. (2017). Biological Annihilation *via* the Ongoing Sixth Mass Extinction Signaled by Vertebrate Population Losses and Declines. *Proc. Natl. Acad. Sci.* 114 (30), 6089–6096. doi: 10.1073/pnas.1704949114

Chen, Z. Q., and Benton, M. J. (2012). The Timing and Pattern of Biotic Recovery Following the End-Permian Mass Extinction. *Nat. Geosci.* 5 (6), 375–383. doi: 10.1038/ngeo1475

Chen, Z. Q., Yang, H., Luo, M., Benton, M. J., Kaiho, K., Zhao, L., et al. (2015). Complete Biotic and Sedimentary Records of the Permian–Triassic Transition From Meishan Section, South China: Ecologically Assessing Mass Extinction and its Aftermath. *Earth-Sci. Rev.* 149, 67–107. doi: 10.1016/j.earscirev.2014.10.005

Chivas, A. R., Torgersen, T., and Polach, H. A. (1990). Growth Rates and Holocene Development of Stromatolites From Shark Bay, Western Australia. *Aust. J. Earth Sci.* 37 (2), 113–121. doi: 10.1080/08120099008727913

Clarkson, M. O., Kasemann, S. A., Wood, R. A., Lenton, T. M., Daines, S. J., Richoz, S., et al. (2015). Ocean Acidification and the Permo-Triassic Mass Extinction. *Science* 348 (6231), 229–232. doi: 10.1126/science.aaa0193

Cowie, R. H., Bouchet, P., and Fontaine, B. (2022). The Sixth Mass Extinction: Fact, Fiction or Speculation? *Biol. Rev.* 97 (2), 640–663. doi: 10.1111/brv.12816

Dal, C. J., Song, H., Callegaro, S., Chu, D., Sun, Y., Hilton, J., et al. (2022). Environmental Crises at the Permian–Triassic Mass Extinction. *Nat. Rev. Earth Environ.* 3, 1–18. doi: 10.1038/s43017-021-00259-4

Deng, B., Yu, L., Wang, Y., Li, G., and Meng, Y. (2015). Evolution of Marine Conditionsand Sedimentation During the Permian-Triassic Transition in Chibi of Hubei Province (in Chinese With English Abstract). *Earth Sci. - J. China Univ. Geosci.* 40, 317–326. doi: 10.3799/dqkx.2015.024

Diaz, M. R., Swart, P. K., Eberli, G. P., Oehlert, A. M., Devlin, Q., Saeid, A., et al. (2015). Geochemical Evidence of Microbial Activity Within Ooids. *Sedimentology* 62, 2090–2112. doi: 10.1111/sed.12218

Erwin, D. H. (1993). *The Great Paleozoic Crisis: Life and Death in the Permian* (New York: ColumbiaUniv. Press), 327 pp.

Erwin, D. H., Bowring, S. A., and Yugan, J. (2002). End-Permian Mass Extinctions: A Review. *Special. Papers-Geological. Soc. America* 356, 363–383. doi: 10.1130/0-8137-2356-6.363

Ezaki, Y., Liu, J., and Adachi, N. (2003). Earliest Triassic Microbialite Micro-to Megastructures in the Huaying Area of Sichuan Province, South China: Implications for the Nature of Oceanic Conditions After the End-Permian Extinction. *Palaios* 18 (4-5), 388–402. doi: 10.1669/0883-1351(2003)018<0388:ETMMTM>2.0.CO;2

Fahrig, L. (2017). Ecological Responses to Habitat Fragmentation Per Se. *Annu. Rev. Ecol. Evol. Syst.* 48, 1–23. doi: 10.1146/annurev-ecolsys-110316-022612

Fan, J. X., Shen, S. Z., Erwin, D. H., Sadler, P. M., MacLeod, N., Cheng, Q. M., et al. (2020). A High-Resolution Summary of Cambrian to Early Triassic Marine Invertebrate Biodiversity. *Science* 367 (6475), 272–277. doi: 10.1126/science.aax4953

Feng, Z. Z., Yang, Y. Q., Jin, Z. K., He, Y. B., Wu, S. H., Xin, W. J., et al. (1996). Lithofacies Paleogeography of the Permian of South China. *Acta Sedimentol. Sin.* 14, 1–11. doi: 10.14027/j.cnki.cjxb.1996.02.001

Flügel, E. (2004). Microfacie of Carbonate Rocks: Analysis, Interpretation and Application, Berlin-Heidelberg. *Springer-Verlag*, 680–724. pp.

Forel, M.-B. (2013). The Permian–Triassic Mass Extinction: Ostracods (Crustacea) and Microbialites. *Compt. Rendus. Geosci.* 345 (4), 203–211. doi: 10.1016/j.crte.2013.03.003

Foster, W. J., Lehrmann, D. J., Yu, M., and Martindale, R. C. (2019). Facies Selectivity of Benthic Invertebrates in a Permian/Triassic Boundary Microbialite Succession: Implications for the "Microbialite Refuge" Hypothesis. *Geobiology* 17, 523–535. doi: 10.1111/gbi.12343

Gall, J. C., Grauvogel-Stamm, L., Nel, A., and Papier, F. (1998). The Permian Mass Extinction and the Triassic Recovery. *Comptes. Rendus. l'Academie. Des. Sci. Ser. IIA. Earth Planet. Sci.* 1 (326), 1–12.

Godbold, A., Schoepfer, S., Shen, S., and Henderson, C. M. (2017). Precarious Ephemeral Refugia During the Earliest Triassic. *Geology* 45 (7), 607–610. doi: 10.1130/G38793.1

Grice, K., Cao, C., Love, G. D., Bottcher, M. E., Twitchett, R. J., Grosjean, E., et al. (2005). Photic Zone Euxinia During the Permian–Triassic Superanoxic Event. *Science* 307, 706–709. doi: 10.1126/science.1104323

Groves, J., Altiner, D., and Rettori, R. (2005). Extinction, Survival, and Recovery of Lagenide Foraminifers in the Permian–Triassic Boundary Interval, Central Taurides, Turkey. *J. Paleontol.* 79, 1–39. doi: 10.1666/0022-3360(2005)79[1:ESAROL]2.0.CO;2

Groves, J. R., Payne, J. L., and Altiner, D. (2007). End-Permian Mass Extinction of Lagenide Foraminifers in the Southern Alps (Northern Italy). *J. Paleontol.* 81 (3), 415–434. doi: 10.1666/05123.1

Hallam, A., and Wignall, P. B. (1997). *Mass Extinctions and Their Aftermath* (UK: Oxford University Press).

Hallam, A., and Wignall, P. B. (1999). Mass Extinctions and Sea-Level Changes. *Earth-Sci. Rev.* 48 (4), 217–250. doi: 10.1016/S0012-8252(99)00055-0

Harris, P., Diaz, M. R., and Eberli, G. P. (2019). The Formation and Distribution of Modern Ooids on Great Bahama Bank. *Annu. Rev. Marine. ence.* 11 (1), 491–516. doi: 10.1146/annurev-marine-010318-095251

He, W., Shi, G. R., Feng, Q., Campi, M. J., Gu, S., and Bu, J. (2007). Brachiopod Miniaturization and its Possible Causes During the Permian-Triassic Crisis in Deep Water Environments, South China. *Palaeogeograp. Palaeoclimatol. Palaeoecol.* 252 (1-2), 145–163. doi: 10.1016/j.palaeo.2006.11.040

He, W. H., Twitchett, R. J., Zhang, Y., Shi, G. R., Feng, Q. L., Yu, J. X., et al. (2010). Controls on Body Size During the Late Permian Mass Extinction Event. *Geobiology* 8, 391–402. doi: 10.1111/j.1472-4669.2010.00248.x

Hülse, D., Lau, K. V., van de Velde, S. J., Arndt, S., Meyer, K. M., and Ridgwell, A. (2021). End-Permian Marine Extinction Due to Temperature-Driven Nutrient Recycling and Euxinia. *Nat. Geosci.* 14 (11), 862–867. doi: 10.1038/s41561-021-00829-7

Ishida, H., Isono, R. S., Kita, J., and Watanabe, Y. W. (2021). Long-Term Ocean Acidification Trends in Coastal Waters Around Japan. *Sci. Rep.* 11 (1), 1–7. doi: 10.1038/s41598-021-84657-0

Isozaki, Y. (1997). Permo-Triassic Boundary Superanoxia and Stratified Superocean: Records From Lost Deep Sea. *Science* 276, 235–238. doi: 10.1126/science.276.5310.235

Jiang, H., Lai, X., Sun, Y., Wignall, P. B., Liu, J., and Yan, C. (2014). Permian-Triassic Conodonts From Dajiang (Guizhou, South China) and Their Implication for the Age of Microbialite Deposition in the Aftermath of the End-Permian Mass Extinction. *J. Earth Sci.* 25, 413–430. doi: 10.1007/s12583-014-0444-4

Jin, Y. G., Wang, Y., Wang, W., Shang, Q. H., Cao, C. Q., and Erwin, D. H. (2000). Pattern of Marine Mass Extinction Near the Permian-Triassic Boundary in South China. *Science* 289, 432–436. doi: 10.1126/science.289.5478.432

Joachimski, M. M., Alekseev, A. S., Grigoryan, A., and Gatovsky, Y. A. (2019). Siberian Trap Volcanism, Global Warming and the Permian-Triassic Mass Extinction: New Insights From Armenian Permian-Triassic Sections. *GSA Bull.* 132, 427–443. doi: 10.1130/B35108.1

Kaiho, K. (1994). Benthic Foraminiferal Dissolved-Oxygen Index and Dissolved-Oxygen Levels in the Modern Ocean. *Geology* 22 (8), 719–722. doi: 10.1130/0091-7613(1994)022<0719:BFDOIA>2.3.CO;2

Kaiho, K. (1998). Global Climatic Forcing of Deep-Sea Benthic Foraminiferal Test Size During the Past 120 M.Y. *Geology* 26, 491–494. doi: 10.1130/0091-7613(1998)026<0491:GCFODS>2.3.CO;2

Kaiho, K., Aftabuzzaman, M., Jones, D. S., and Tian, L. (2020). Pulsed Volcanic Combustion Events Coincident With the End-Permian Terrestrial Disturbance and the Following Global Crisis. *Geology* 49, 289–293. doi: 10.1130/G48022.1

Kershaw, S., Crasquin, S., Li, Y., Collin, P., Forel, M., Mu, X., et al. (2012). Microbialites and Global Environmental Change Across the Permian–Triassic

Boundary: A Synthesis. *Geobiology* 10, 25–47. doi: 10.1111/j.1472-4669.2011.00302.x

Levin, L. A. (2003). "Oxygen Minimum Zone Bethos: Adaptation and Community Response to Hypoxia," in *Oceanography and Marine Biology. An Annual Review*, vol. 41 . Eds. R. N. Gibson and R. J. A. Atkinson, (Boca Raton: CRC Press) 1–45 pp.

Liao, W., Wang, Y., Kershaw, S., Weng, Z., and Hao, Y. (2010). Shallow-Marine Dysoxia Across the Permian–Triassic Boundary: Evidence From Pyrite Framboids in the Microbialite in South China. *Sediment. Geol.* 232 (1-2), 77–83. doi: 10.1016/j.sedgeo.2010.09.019

Li, G., Liao, W., Li, S., Wang, Y., and Lai, Z. (2021). Different Triggers for the Two Pulses of Mass Extinction Across the Permian and Triassic Boundary. *Sci. Rep.* 11, 6686. doi: 10.1038/s41598-021-86111-7

Liu, X., Song, H., Bond, D. P. G., Tong, J., and Benton, M. J. (2020). Migration Controls Extinction and Survival Patterns of Foraminifers During the Permian-Triassic Crisis in South China. *Earth-Sci. Rev.* 209, 103329. doi: 10.1016/j.earscirev.2020.103329

Liu, H., Wang, Y., Yuan, A., Yang, H., Song, H., and Zhang, S. (2010). Ostracod Fauna Across the Permian-Triassic Boundary at Chongyang, Hubei Province, and its Implication for the Process of the Mass Extinction. *Sci. China Earth Sci.* 53, 810–817. doi: 10.1007/s11430-010-0045-8

Luo, G., Lai, X., Jiang, H., and Zhang, K. (2006). Size Variation of the End Permian Conodont Neogondolella at Meishan Section, Changxing, Zhejiang and its Significance. *Sci. China Ser. D* 49, 337–347. doi: 10.1007/s11430-006-0337-1

Meng, Z., Wang, Y. B., Woods, A., Liao, W., and Li, G. S. (2014). Deep Shelf Biostrome of Late Permian in South China and its Implications for the Adaptability of Calcisponges to Water Depth. *Palaeogeogr. Palaeoclimatol. Palaeoecol.* 401, 132–141. doi: 10.1016/j.palaeo.2014.02.028

Meyer, K. M., Kump, L. R., and Ridgwell, A. (2008). Biogeochemical Controls on Photic-Zone Euxinia During the End-Permian Mass Extinction. *Geology* 36, 747–750. doi: 10.1130/G24618A.1

Meyer, K. M., Yu, M., Jost, A. B., Kelley, B. M., and Payne, J. L. (2011). ä13C Evidence that High Primary Productivity Delayed Recovery from End-Permian Massextinction. *Earth Planetary Science Letters* 302 (3-4), 378–384. doi: 10.1016/j.epsl.2010.12.033

Miller, K. G., Kominz, M. A., Browning, J. V., Wright, J. D., Mountain, G. S., Katz, M. E., et al. (2005). The Phanerozoic Record of Global Sea-Level Change. *Science* 310 (5752), 1293–1298.

Newell, N. D. (1967). Revolutions in the History of Life. *Geol. Soc Am. Spec. Pap.* 89, 63–91. doi: 10.1130/SPE89-p63

O'Reilly, S. S., Mariotti, G., Winter, A. R., Newman, S. A., Matys, E. D., McDermott, F., et al. (2017). Molecular Biosignatures Reveal Common Benthic Microbial Sources of Organic Matter in Ooids and Grapestones From Pigeon Cay, the Bahamas. *Geobiology* 15, 112–130. doi: 10.1111/gbi.12196

Payne, J. L., Lehrmann, D. J., Wei, J., and Knoll, A. H. (2006). The Pattern and Timing of Biotic Recovery From the End-Permian Extinction on the Great Bank of Guizhou, Guizhou Province, China. *Palaios* 21, 63–85. doi: 10.2110/palo.2005.p05-12p

Payne, J. L., Turchyn, A. V., Paytan, A., Depaolo, D. J., Lehrmann, D. J., Yu, M., et al. (2010). Calcium Isotope Constraints on the End-Permian Mass Extinction. *Proc. Natl. Acad. Sci. U. S. A.* 107 (19), 8543–8548. doi: 10.1073/pnas.0914065107

Peng, Y. Q., and Tong, J. N. (1999). Integrated Study on Permian-Triassic Boundary Bed Inyangtze Platform. *Earth Sci.* 24 (1), 39–48.

Pimm, S. L., Jenkins, C. N., Abell, R., Brooks, T. M., Gittleman, J. L., Joppa, L. N., et al. (2014). The Biodiversity of Species and Their Rates of Extinction, Distribution, and Protection. *Science* 344, 6187. doi: 10.1126/science.1246752

Pratt, B. R. (1984). Epiphyton and Renalcis-Diagenetic Microfossils From Calcification of Coccoid Blue-Green Algae. *J. Sediment. Petrol.* 54, 948–971.

Raup, D. M., and Sepkoski, J. J.Jr. (1982). Mass Extinctions in the Marine Fossil Record. *Science* 215, 1501–1503. doi: 10.1126/science.215.4539.1501

Reid, R. P., Macintyre, I. G., Browne, K. M., Steneck, R. S., and Miller, T. (1995). Modern Marine Stromatolites in the Exuma Cays, Bahamas: Uncommonly Common. *Facies* 33 (1), 1–17. doi: 10.1007/BF02537442

Riccardi, A. L., Arthur, M. A., and Kump, L. R. (2006). Sulfur Isotopic Evidence for Chemocline Upward Excursions During the End-Permian Mass Extinction. *Geochim. Cosmochim. Acta* 70 (23), 5740–5752. doi: 10.1016/j.gca.2006.08.005

Rong, J., and Fang, Z. (2004). *Mass Extinction and Recovery: Evicences From the Palaeozoic and Triassic of South China* (Hefei: University of Science and Technology of China Press).

Ross, T., Du Preez, C., and Ianson, D. (2020). Rapid Deep Ocean Deoxygenation and Acidification Threaten Life on Northeast Pacific Seamounts. *Global Change Biol.* 26 (11), 6424–6444. doi: 10.1111/gcb.15307

Ruban, D. A. (2020). Paleozoic–Mesozoic Eustatic Changes and Mass Extinctions: New Insights From Event Interpretation. *Life* 10 (11), 281. doi: 10.3390/life10110281

Scotese, C. R. (2001). *Atlas of Earth History* (Texas: University of Texas at Arlington, Department of Geology. PALEOMAP Project), 58 pp.

Seager, R., Cane, M., Henderson, N., Lee, D. E., Abernathey, R., and Zhang, H. (2019). Strengthening Tropical Pacific Zonal Sea Surface Temperature Gradient Consistent With Rising Greenhouse Gases. *Nat. Climate Change* 9 (7), 517–522. doi: 10.1038/s41558-019-0505-x

Sepkoski, J. J. (1986). "Phanerozoic Overview of Mass Extinction," in *Patterns and Processes in the History of Life. Dahlem Workshop Reports*, vol. vol 36 . Eds. D. M. Raup and D. Jablonski (Berlin, Heidelberg: Springer), 277–295. doi: 10.1007/978-3-642-70831-2_15

Shen, S. Z., Cao, C. Q., Henderson, C. M., Wang, X. D., Shi, G. R., Wang, Y., et al. (2006). End-Permian Mass Extinction Pattern in the Northern Peri-Gondwanan Region. *Palaeoworld* 15 (1), 3–30. doi: 10.1016/j.palwor.2006.03.005

Shen, S. Z., Crowley, J. L., Wang, Y., Bowring, S. A., Erwin, D. H., Sadler, P. M., et al. (2011). Calibrating the End-Permian Mass Extinction. *Science* 334, 1367–1372. doi: 10.1126/science.1213454

Song, H., Tong, J., and Chen, Z. Q. (2009). Two Episodes of Foraminiferal Extinction Near the Permian–Triassic Boundary at the Meishan Section, South China. *Aust. J. Earth Sci.* 56, 765–773. doi: 10.1080/08120090903002599

Song, H., Tong, J., and Chen, Z. Q. (2011). Evolutionary Dynamics of the Permian–Triassic Foraminifer Size: Evidence for Lilliput Effect in the End-Permian Mass Extinction and its Aftermath. *Palaeogeograp. Palaeoclimatol. Palaeoecol.* 308 (1-2), 98–110. doi: 10.1016/j.palaeo.2010.10.036

Song, H. J., Tong, J. N., Zhang, K. X., Wang, Q. X., and Chen, Z. Q. (2007). Foraminiferal Survivors From the Permian-Triassic Mass Extinction in the Meishan Section, South China. *Palaeoworld* 16, 105–119. doi: 10.1016/j.palwor.2007.05.016

Song, H., Wignall, P. B., and Dunhill, A. M. (2018). Decoupled Taxonomic and Ecological Recoveries From the Permo-Triassic Extinction. *Sci. Adv.* 4 (10), eaat5091. doi: 10.1126/sciadv.aat5091

Song, H., Wignall, P. B., Tong, J., and Yin, H. (2012). Two Pulses of Extinction During the Permian–Triassic Crisis. *Nat. Geosci.* 6, 52–56. doi: 10.1038/ngeo1649

Stanley, S., and Yang, X. (1994). A Double Mass Extinction at the End of the Paleozoic Era. *Science* 266 (5189), 1340–1344.

Sun, Y., Joachimski, M. M., Wignall, P. B., Yan, C., Chen, Y., Jiang, H., et al. (2012). Lethally Hot Temperatures During the Early Triassic Greenhouse. *Science* 338, 366–370. doi: 10.1126/science.1224126

Tarling, G. A., Ward, P., and Thorpe, S. E. (2018). Spatial Distributions of Southern Ocean Mesozooplankton Communities Have Been Resilient to Long-Term Surface Warming. *Global Change Biol.* 24 (1), 132–142. doi: 10.1111/gcb.13834

Wang, T., Burne, R. V., Yuan, A. H., Wang, Y. B., and Yi, Z. X. (2019). The Evolution of Microbialite Forms During the Early Triassic Transgression: A Case Study in Chongyang of Hubei Province, South China. *Palaeogeogr. Palaeoclimatol. Palaeoecol.* 519, 209–220. doi: 10.1016/j.palaeo.2018.01.043

Wang, Y., and Jin, Y. (2000). Permian Palaeogeographic Evolution of the Jiangnan Basin, South China. *Palaeogeogr. Palaeoclimatol. Palaeoecol.* 160, 35–44. doi: 10.1016/S0031-0182(00)00043-2

Wang, Y., Tong, J., Wang, J., and Zhou, X. (2005). Calcimicrobialite After End-Permian Mass Extinction in South China and its Pa-Laeoenvironmental Signifi-Cance. *Chin. Sci. Bull.* 50, 665–671. doi: 10.1360/982004-323

Wang, L., Wignall, P. B., Wang, Y., Jiang, H., Sun, Y., Li, G., et al. (2016). Depositional Conditions and Revised Age of the Permo-Triassic Microbialites at Gaohua Section, Cili County (Hunan Province, South China). *Palaeogeograp. Palaeoclimatol. Palaeoecol.* 443, 156–166. doi: 10.1016/j.palaeo.2015.11.032

Wang, G. Q., and Xia, W. C. (2003). The Changhsingian Conodont Zonation and Variation of Organic Carbon Isotope of Huangshi Ermen Section, Hubei Province. *Geoscience* 04, 378–386.

Wan, J., Yuan, A., Crasquin, S., Jiang, H., Yang, H., and Hu, X. (2019). High-Resolution Variation in Ostracod Assemblages From Microbialites Near the Permian-Triassic Boundary at Zuodeng, Guangxi Region, South China. *Palaeogeogr. Palaeoclimatol. Palaeoecol.* 535, 109349. doi: 10.1016/j.palaeo.2019.109349

Wen, J., and Liu, J. (2009). Quantitative Study of Bioclastic Grains in Carbonate Rocks: Theoretical Analysis and Application of Point-Counting Method. *J. Palaeogeogr.* 11, 581–592.

Wignall, P. B., and Hallam, A. (1996). Facies change and the end-Permian mass extinction in SE Sichuan, China. *Palaios* 587–596. doi: 10.2307/3515193

Wignall, P. B., Newton, R., and Brook field, M. E. (2005). Pyrite Framboid Evidence for Oxygenpoor Deposition During the Permian–Triassic Crisis in Kashmir. *Palaeogeogr. Palaeoclimatol. Palaeoecol.* 216, 183–188. doi: 10.1016/j.palaeo.2004.10.009

Wilkin, R. T., Barnes, H. L., and Brantley, S. L. (1996). The Size Distribution of Framboidal Pyrite in Modern Sediments: An Indicator of Redox Conditions. *Geochim. Cosmochim. Acta* 60, 3897–3912. doi: 10.1016/0016-7037(96)00209-8

Winguth, A. M., Shields, C. A., and Winguth, C. (2015). Transition Into a Hothouse World at the Permian–Triassic Boundary—a Model Study. *Palaeogeograp. Palaeoclimatol. Palaeoecol.* 440, 316–327. doi: 10.1016/j.palaeo.2015.09.008

Wu, Y. S., Jiang, H. X., and Fan, J. S. (2010). Evidence for Sea-Level Falls in the Permian-Triassic Transition in the Ziyun Area, South China. *Geological. J.* 45 (2–3), 170–185.

Wu, Y. S., Jiang, H. X., and Liao, T. P. (2006). Sea-Level Drops in the Permian-Triassic Boundary Section at Laolongdong, Chongqing, Sichuan Province. *Acta Petrologica. Sin.* 22 (9), 2405–2412.

Xie, S., Pancost, R. D., Yin, H., Wang, H., and Evershed, R. P. (2005). Two Episodes of Microbial Change Coupled With Permo/Triassic Faunal Mass Extinction. *Nature* 434 (7032), 494–497. doi: 10.1038/nature03396

Yang, H., Chen, Z. Q., Wang, Y., Tong, J., Song, H., and Chen, J. (2011). Composition and Structure of Microbialite Ecosystems Following the End-Permian Mass Extinction in South China. *Palaeogeogr. Palaeoclimatol. Palaeoecol.* 308, 111–128. doi: 10.1016/j.palaeo.2010.05.029

Yang, H., Zhang, S. X., Jiang, H. S., and Wang, Y. B. (2006). Age and General Characteristics of the Calimicrobialite Near the Permian-Triassic Boundary in Chongyang, Hubei Province. *J. China Univ. Geosci.* 17, 121–125. doi: 10.1016/S1002-0705(06)60016-2

Yin, H., Feng, Q., Lai, X., Baud, A., and Tong, J. (2007). The Protracted Permo-Triassic Crisis and Multi-Episode Extinction Around the Permian–Triassic Boundary. *Global Planet. Change* 55, 1–20. doi: 10.1016/j.gloplacha.2006.06.005

Yin, H., Jiang, H., Xia, W., Feng, Q., Zhang, N., and Shen, J. (2014). The End-Permian Regression in South China and its Implication on Mass Extinction. *Earth-Sci. Rev.* 137, 19–33. doi: 10.1016/j.earscirev.2013.06.003

Yin, H., and Song, H. (2013). Mass Extinction and Pangea Integration During the Paleozoic-Mesozoic Transition. *Sci. China Earth Sci.* 56, 1791–1803. doi: 10.1007/s11430-013-4624-3

Yin, H., Zhang, K., Tong, J., Yang, Z., and Wu, S. (2001). The Global Stratotype Section and Point (GSSP) of the Permian-Triassic Boundary. *Episodes* 24, 102–114. doi: 10.18814/epiiugs/2001/v24i2/004

Yu, S. Y. (1989). *Fossils Carbonates Microfacies* (Beijing: Geological Publishing House).

Yu, J. X., Broutin, J., Chen, Z. Q., Shi, X., Li, H., Chu, D. L., et al. (2015). Vegetation Changeover Across the Permian–Triassic Boundary in Southwest China Extinction, Survival, Recovery and Palaeoclimate: A Critical Review. *Earth Sci. Rev.* 149, 203–224. doi: 10.1016/j.earscirev.2015.04.005

Zhang, M., and Gu, S. (2015). Latest Permian Deep-Water Foraminifers From Daxiakou, Hubei, South China. *J. Paleontol.* 89 (3), 448–464. doi: 10.1017/jpa.2015.19

Zhu, Z., Kuang, H., Liu, Y., Benton, M. J., Newell, A. J., Xu, H., et al. (2020). Intensifying Aeolian Activity Following the End-Permian Mass Extinction: Evidence From the Late Permian–Early Triassic Terrestrial Sedimentary Record of the Ordos Basin, North China. *Sedimentology* 67 (5), 2691–2720. doi: 10.1111/sed.12716

Zhu, S., Liang, Y., and Du, R. (1993). *The Stromatolites of China* (Tianjin: Tianjin University Press), 191–196.

Conflict of Interest: The authors declare that the research was conducted in the absence of any commercial or financial relationships that could be construed as a potential conflict of interest.

Publisher's Note: All claims expressed in this article are solely those of the authors and do not necessarily represent those of their affiliated organizations, or those of the publisher, the editors and the reviewers. Any product that may be evaluated in this article, or claim that may be made by its manufacturer, is not guaranteed or endorsed by the publisher.

frontiers | Frontiers in Marine Science

ORIGINAL RESEARCH
published: 15 June 2022
doi: 10.3389/fmars.2022.925919

Role of Marginal Seas in Deep Ocean Regeneration of Dissolved Silica: A Case Study in the Marginal Seas of the Western Pacific

Xiaoqing Yu[1,2], *Yanpei Zhuang*[1,3*], *Xiaoxia Cai*[1] *and Di Qi*[1]

[1] Polar and Marine Research Institute, Jimei University, Xiamen, China, [2] Xiamen Municipal Southern Marine Testing Center, Xiamen, China, [3] Southern Marine Science and Engineering Guangdong Laboratory (Zhuhai), Zhuhai, China

Deep ocean regeneration of dissolved silica (DSi) is an essential part of the ocean silica cycle and is driven by a complex series of biogeochemical processes. Here we compare the distributions of DSi and other environmental parameters in several western Pacific marginal seas to explore the role of marginal seas in deep ocean DSi regeneration. Results show that in oligotrophic marginal seas (such as the South China Sea), the DSi content in deep waters is similar to that of the adjacent Pacific waters. However, in productive marginal seas (such as the Bering Sea), the DSi content in deep waters is markedly higher than that in adjacent Pacific waters at the same depths. This is mainly due to deep ocean DSi regeneration in the marginal sea basin, which is fueled by the high biogenic particle flux from the productive surface waters. On a global scale, deep ocean DSi regeneration is accelerated in productive marginal seas, causing marginal seas such as the Bering Sea to have the highest DSi concentrations of all global waters.

Keywords: marine Si cycle, deep waters, Bering Sea, South China Sea, marginal seas

OPEN ACCESS

Edited by:
Fajin Chen,
Guangdong Ocean University, China

Reviewed by:
Dongliang Lu,
Beibu Gulf University, China
Feng Ye,
Guangzhou Institute of Geochemistry, Chinese Academy of Sciences (CAS), China
Weifeng Yang,
Xiamen University, China

***Correspondence:**
Yanpei Zhuang
zhuangyp@jum.edu.cn

Specialty section:
This article was submitted to Marine Biogeochemistry, a section of the journal Frontiers in Marine Science

Received: *22 April 2022*
Accepted: *16 May 2022*
Published: *15 June 2022*

Citation:
Yu X, Zhuang Y, Cai X and Qi D (2022) Role of Marginal Seas in Deep Ocean Regeneration of Dissolved Silica: A Case Study in the Marginal Seas of the Western Pacific. Front. Mar. Sci. 9:925919. doi: 10.3389/fmars.2022.925919

INTRODUCTION

The present marine silica cycle appears to be near internal equilibrium, but has the dynamic interconversion of dissolved silica (DSi; also known as silicic acid) and biogenic silica (BSi; also known as opal) (Nelson et al., 1995; Ragueneau et al., 2006; Tréguer et al., 2021). BSi is produced mainly by pelagic siliceous organisms (mainly diatoms), which absorb DSi from the surface ocean to build their skeletons. They are then exported to the subsurface and deep waters under the action of the biological carbon pump (Moriceau et al., 2019). Benthic siliceous organisms (e.g., sponges) also contribute to oceanic BSi production (Maldonado et al., 2019). Global annual BSi production has recently been estimated at nearly 260 Tmol Si yr^{-1} (Tréguer et al., 2021). Approximately two-thirds of newly synthesized BSi are redissolved in the upper 2000 m of water column, and only ~5% is permanently buried in sediment (Tréguer and de la Rocha, 2013). The remaining BSi is redissolved to form DSi in deep waters and in surface sediment, and this contributes to deep ocean DSi regeneration in the ocean interior (Heinze et al., 2003). Large amounts of deep-water DSi reach the upper ocean by upwelling and vertical mixing in certain regions, such as the Southern and North Pacific oceans (Sarmiento et al., 2004).

Marginal seas lie between the continental margin and the open ocean, are separated from the open ocean by islands or archipelagos, and are influenced by both land and open ocean (Wang, 1999). Certain marginal seas may have high diatom productivity and thus high rates of BSi formation due to the input of nutrients and biogenic matter from coastal waters (e.g., the Bering Sea; Waga et al., 2022). Conversely, some marginal seas may be as oligotrophic as the open ocean, with phytoplankton biomass dominated by picophytoplankton rather than diatoms (e.g., the South China Sea; Li et al., 2022a). These differences are closely related to differences in the oceanic CO_2 flux (Dai et al., 2013), BSi export (Cao et al., 2020), and the biological carbon pump (Li et al., 2022b) in marginal seas. A mechanistic understanding of the role of marginal seas in deep ocean DSi regeneration is critical if we are to fully understand the functioning of the marine silica cycle.

The oceanic silica flux and budget, silica balance, and major redistribution pathways are well established for the global oceans and marginal seas (DeMaster, 1981; Nelson et al., 1995; Tréguer et al., 1995; Sarmiento et al., 2004; Wu and Liu, 2020; Ma et al., 2022). However, the role of marginal seas in deep ocean DSi regeneration has not yet been discussed in detail. Here, we use available data on nutrient distributions, salinity, apparent oxygen utilization (AOU), and nutrient tracers to explore differences in DSi distributions and their controlling factors in deep waters of the western Pacific marginal sea basins. We discuss the distinct role of marginal seas in deep ocean DSi regeneration using the South China Sea, Japan Sea, Okhotsk Sea, and Bering Sea as examples.

MATERIALS AND METHODS

Nutrient, dissolved oxygen, and hydrographic data were obtained from the World Ocean Database (WOD; https://www.ncei.noaa.gov/access/world-ocean-database/datawodgeo.html). The study area includes the North Atlantic, Southern, Indian, and North Pacific oceans, which are open ocean waters, and the Bering Sea, Okhotsk Sea, Japan Sea, and South China Sea, which are marginal seas (**Supplementary Table 1**). Although the data acquisition time in this study was from 1981 to 2016, the deep-water DSi data are still comparable, mainly because deep-water DSi does not change over long periods of time (at least hundreds of years) (Béthoux et al., 1998; Hendry et al., 2010). For spatial visualization and analysis of the nutrient and hydrographic data, we used Ocean Data View (ODV) version 4.4.1 (Schlitzer, 2018).

Nutrient tracer Si*, with a formula of $Si* = [DSi] - [NO_3^-]$ (Brzezinski et al., 2002; Sarmiento et al., 2004), is calculated to indicate an excess/deficit of silicate relative to nitrate. Another widely used nutrient tracer ($N* = ([NO_3^-]) - 16[PO_4^{3-}] + 2.90\ \mu mol/kg) \times 0.87$) is calculated to determine the net effect of nitrogen fixation and denitrification (Gruber and Sarmiento, 1997). AOU is calculated as the O_2 solubility in seawater minus the measured O_2 concentration (Garcia and Gordon, 1992).

RESULTS

DSi Distribution in Global Waters

We compared the DSi distributions of deep waters (>2000 m) of the North Atlantic, Southern, Indian, and North Pacific oceans as examples of the global ocean (**Figure 1**). The North Atlantic Ocean is the starting point of the global ocean conveyor belt (**Figure 1A**) and has the lowest deep-water DSi concentration (29.0 ± 12.1 μmol/kg) in the global ocean (**Figure 1B**). The average concentration of DSi in deep waters of the Southern Ocean is 111.0 ± 12.5 μmol/kg. The average deep-water DSi concentration in the Indian Ocean is 124.3 ± 4.5 μmol/kg, which is slightly higher than that in the Southern Ocean and nearly 95 μmol/kg higher than the average deep-water DSi concentration in the North Atlantic. The North Pacific is located at the end of the deep current in the global ocean conveyor belt (**Figure 1A**). The average deep-water concentration of DSi in the North Pacific is 157.7 ± 5.7 μmol/kg, which is nearly 129 and 34 μmol/kg higher than the average concentrations in the North Atlantic and Southern oceans, respectively. These results suggest that DSi accumulates during the transport of deep currents through the global ocean conveyor belt.

Deep-water DSi concentrations in the North Atlantic increase with increasing water depth (**Figure 1B**). The average DSi concentration at 2000-m water depth is 11.7 ± 0.8 μmol/kg, which increases to 22.2 ± 1.9 μmol/kg at 3000 m, and then to 43.9 ± 1.1 μmol/kg at 4000 m. Similarly, data from the Southern Ocean, another major region of deep-water formation, show an increase in DSi content with depth in deep waters. The average DSi concentration at a depth of 2000 m in the Southern Ocean is 86.3 ± 2.8 μmol/kg, and this increases to 124.0 ± 0.8 μmol/kg at a depth of 4000 m. In contrast, there are no increases in DSi content with depth in deep waters of the Indian and North Pacific oceans.

The regeneration of DSi (or dissolution of BSi) occurs concurrently with respiration of organic matter. Vertical profiles of nitrate concentrations typically show their highest values at depths of 500–1000 m (**Figure 1C**), coinciding with the depths at which rates of respiration are also at their highest (as indicated by AOU maxima, **Supplementary Figure S1A**) in the open oceans. Deep-water nitrate concentrations may decrease with increasing water depth owing to the removal of nitrogen during denitrification (as indicated by negative N* values, **Supplementary Figure S1B**). However, nitrate concentrations increase with depth in the deep-water layers (>2000 m) of the North Atlantic and Southern Ocean (**Figure 1C**). These results suggest high rates of organic matter remineralization and DSi regeneration in deep waters of the North Atlantic and Southern oceans, which may be associated with sinking biogenic particles during the formation of deep waters.

Deep-Water DSi Distribution in Marginal Seas

We compared deep-water DSi concentrations among the marginal seas of the western Pacific (the Bering Sea, Okhotsk Sea, Japan Sea, and South China Sea) and with the DSi

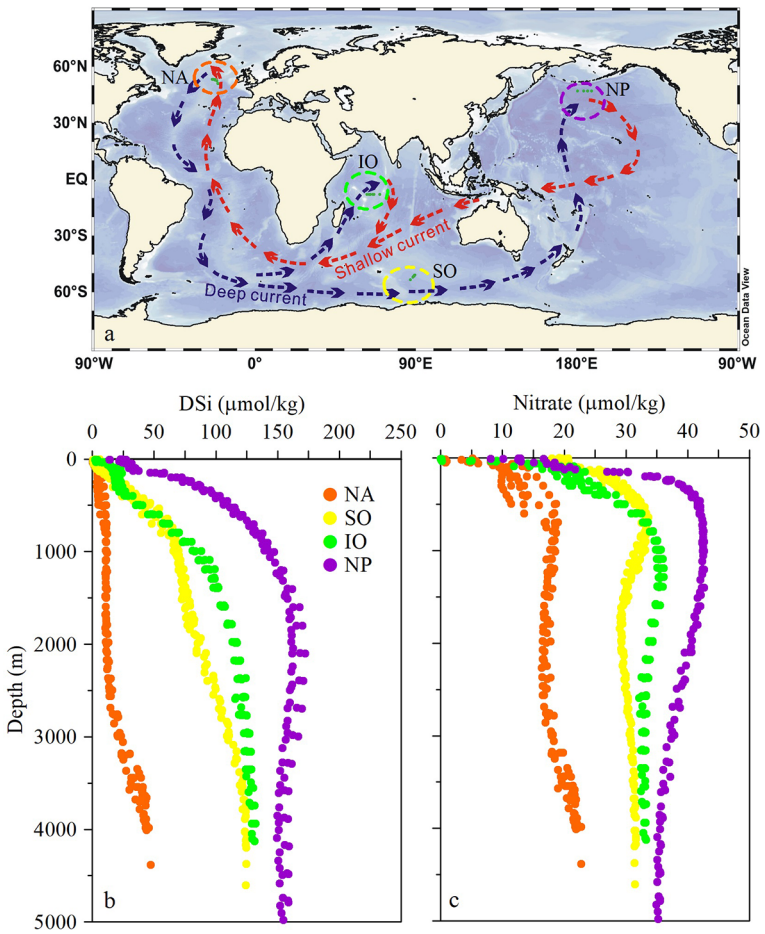

FIGURE 1 | Distribution of DSi and nitrate concentrations (μmol/kg) in the open oceans at different stages of the global ocean conveyor belt. **(A)** Schematic map of the global ocean conveyor belt (after Lozier, 2010); blue and red arrows indicate deep and shallow currents, respectively. Vertical distributions of **(B)** DSi and **(C)** nitrate concentrations in the study areas in the North Atlantic (NA), Southern (SO), Indian (IO), and North Pacific (NP) oceans.

concentrations of the adjacent Pacific waters for reference. There are three distinct patterns of deep-water DSi distribution in the marginal seas, with DSi concentrations either being higher, lower, or equal to the average of the adjacent Pacific waters (**Figure 2**). The average DSi concentration in deep waters of the Bering Sea is 212.6 ± 11.8 μmol/kg, which is ~50 μmol/kg higher than that in the adjacent deep Pacific Ocean (159.1 ± 6.5 μmol/kg). The deep-water DSi concentration in the Okhotsk Sea is slightly higher than that in the adjacent Pacific waters, with an average of 170.4 ± 2.6 μmol/kg. In contrast, the deep-water DSi concentration in the Japan Sea is far lower than that in the adjacent Pacific water, with an average value of only 80.1 ± 3.3 μmol/kg. The average DSi concentration in deep waters of the South China Sea is 151.4 ± 4.6 μmol/kg, which is close to the average DSi concentration of the adjacent Pacific waters (142.9 ± 2.0 μmol/kg).

The different patterns of deep-water DSi distribution in the marginal seas may be related to the effects of intrusion of deep currents from the Pacific Ocean on their deep waters. This is important because deep currents in the Pacific Ocean have accumulated large amounts of DSi along the global ocean conveyor belt. For example, the Japan Sea, which is only connected to the open ocean through a shallow waterway, does not receive large amounts of DSi-rich Pacific deep waters; therefore, the deep-water DSi reserve in the Japan Sea depends mainly on its internal silica cycle. This is supported by deep-water salinity distributions in the Japan Sea, which are markedly different from those in adjacent Pacific waters, whereas the other marginal seas show very similar salinity distributions to their adjacent Pacific waters (**Supplementary Figure S2**). In marginal seas where the main ocean current is derived directly from the open ocean, such as in the Bering Sea, the Okhotsk Sea, and the South China Sea, the deep-water DSi concentrations are equal to or higher than those of the inflowing Pacific Ocean waters.

The mean deep-water DSi concentration in the Bering Sea is 50 μmol/kg higher than that in the adjacent Pacific waters. This indicates that deep-water DSi distributions in the marginal seas are closely linked to deep DSi regeneration. We calculated deep-water DSi regeneration as the difference in DSi concentration between the seafloor and 2000-m depth in the water column

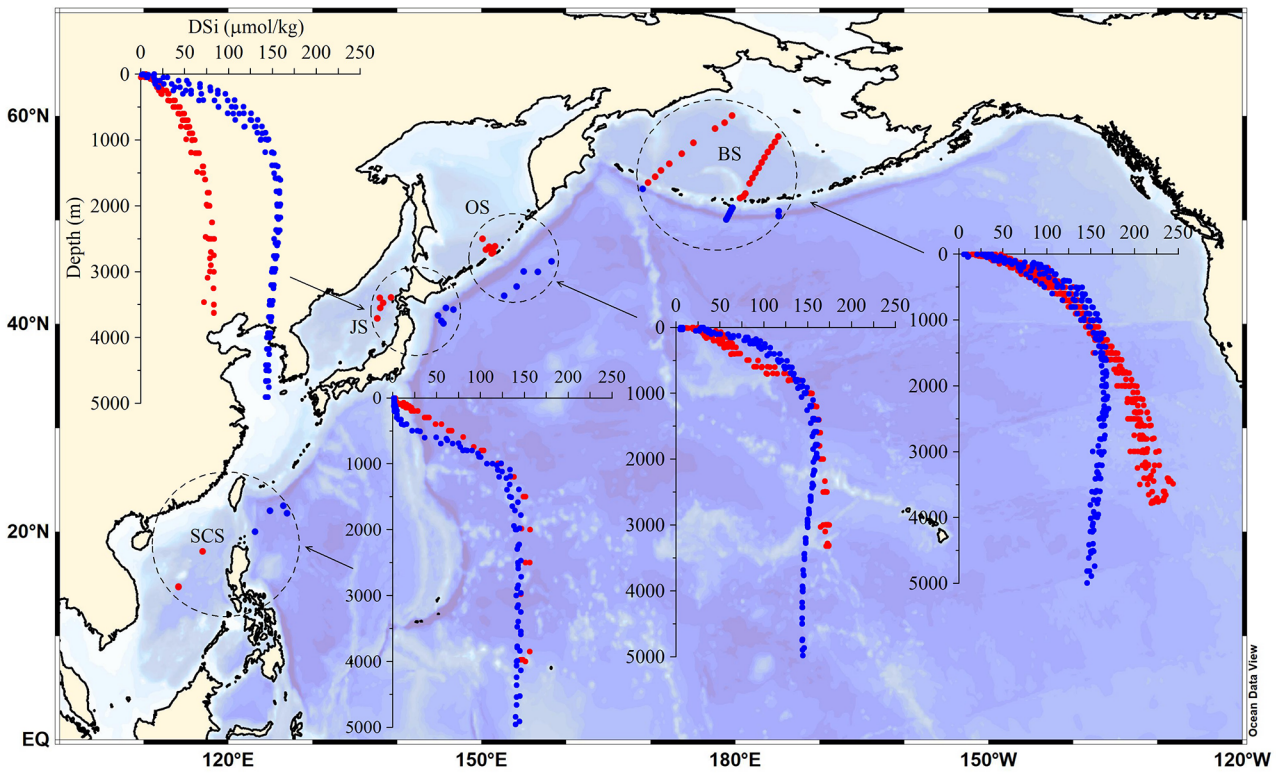

FIGURE 2 | Differences in deep-sea DSi concentration in different marginal seas (red dots) and their adjacent Pacific waters (blue dots). The marginal seas include the Bering Sea (BS), Okhotsk Sea (OS), Japan Sea (JS), and South China Sea (SCS).

($\Delta DSi_{(bottom-2000m)}$, μmol/kg). The $\Delta DSi_{(bottom-2000m)}$ value in the Bering Sea is 32.8 ± 4.0 μmol/kg (**Figure 3**), whereas the $\Delta DSi_{(bottom-2000m)}$ values in the Okhotsk Sea, Japan Sea, and South China Sea are 5.8 ± 2.6, 3.1 ± 2.5, and −0.5 ± 0.7 μmol/kg, respectively. $\Delta N_{(bottom-2000m)}$ is negative or close to 0 in the marginal seas, indicating nitrogen removal by denitrification. The Bering Sea show similar deep-water salinity distributions to the adjacent Pacific waters (**Supplementary Figure S2**), suggesting the influence of deep currents intrusion from the Pacific Ocean. However, no strong nitrate removal was observed in the deep North Pacific. These results indicate strong DSi regeneration in deep waters of the Bering Sea, accompanied by active nitrate removal.

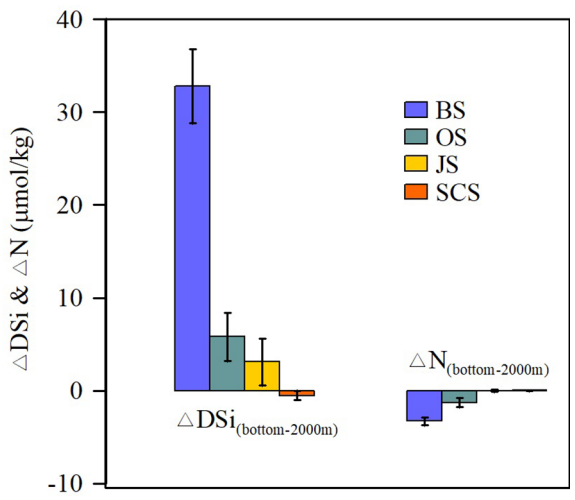

FIGURE 3 | $\Delta DSi_{(bottom-2000m)}$ (μmol/kg) and $\Delta N_{(bottom-2000m)}$ (μmol/kg) in the Bering Sea (BS), Okhotsk Sea (OS), Japan Sea (JS), and South China Sea (SCS).

Deep-Water DSi Distribution in the Bering Sea

As shown in **Figure 4**, the DSi distribution at shallow depths (<1000 m) in the Bering Sea is similar to that in the North Pacific. However, DSi concentrations in deep waters of the Bering Sea are markedly higher than those in the North Pacific, indicating high rates of DSi regeneration in the former (**Figure 4A**). DSi concentrations in the Bering Sea increase with water depth, and high silica concentrations (>225 μmol/kg) are observed in the near-bottom waters of the northern basin. DSi concentrations are as high as 241.4 μmol/kg, which means the deep waters of the Bering Sea have the highest reported DSi concentrations of the global ocean.

Microbial respiration of sinking biogenic detritus leads to the formation of AOU maxima (>300 μmol/kg) at depths between 300 and 1200 m in the North Pacific (**Figure 4B**). The layer

where AOU > 300 μmol/kg deepens to 1600 m in the Bering Sea (**Figure 4B**). As is the case with DSi, the deep-water concentrations of AOU in the Bering Sea are markedly higher than those in the North Pacific (**Figure 4B**), indicating high rates of organic matter remineralization in deep waters of the Bering Sea. However, nitrate concentrations in the deep waters of the Bering Sea are comparable to those in the Pacific Ocean (**Supplementary Figure S3A**); this may be due to nitrogen loss through intensive denitrification, as evidenced by the negative deep-water N* values in the Bering Sea (**Figure 4C**). Conversely, Si* values in the Bering Sea are extremely high, with an average Si* value of 174.8 ± 12.8 μmol/kg (**Supplementary Figure S3B**). These results suggest an active biogeochemical cycle and the rapid accumulation of DSi in deep waters of the Bering Sea.

DISCUSSION

The results indicate that deep-water (>2000 m) DSi reserves in the marginal seas of the western Pacific Ocean are first related to the extent to which they connect and exchange with the open ocean. When the main current of the marginal sea is derived from the open ocean (**Figures 5A, B**), such as in the Bering Sea, the Okhotsk Sea, and the South China Sea, the deep water receives a high DSi input from the open ocean, and the DSi concentrations are equal to or higher than those of the adjacent Pacific deep waters. The deep-water DSi concentration in the Bering Sea (average of 212.6 ± 11.8 μmol/kg) is ~50 μmol/kg higher than that in the adjacent deep Pacific Ocean. When there is limited connectivity between the marginal sea and the open ocean (e.g., the waterway is shallower than 100 m), deep waters in the marginal sea are not markedly affected by inputs from the adjacent ocean deep water and deep-water DSi concentrations are lower than those in the adjacent open ocean (**Figure 5C**), as observed for the Japan Sea. The deep-water DSi concentration in the Japan Sea (average of 80.1 ± 3.3 μmol/kg) is ~70 μmol/kg lower than that in the adjacent Pacific water. The deep-water DSi reserves of marginal seas are also strongly influenced by internal DSi regeneration. Higher rates of deep ocean DSi regeneration will lead to higher DSi concentrations in the deep waters of marginal seas than in the adjacent Pacific Ocean, as is the case in the Okhotsk Sea and the Bering Sea (**Figure 5B**).

The role of marginal seas in deep ocean DSi regeneration is tightly coupled with the formation of BSi *via* diatom production in the surface waters. The South China Sea, the largest marginal sea in the Pacific Ocean, has a very active biogeochemical cycle in

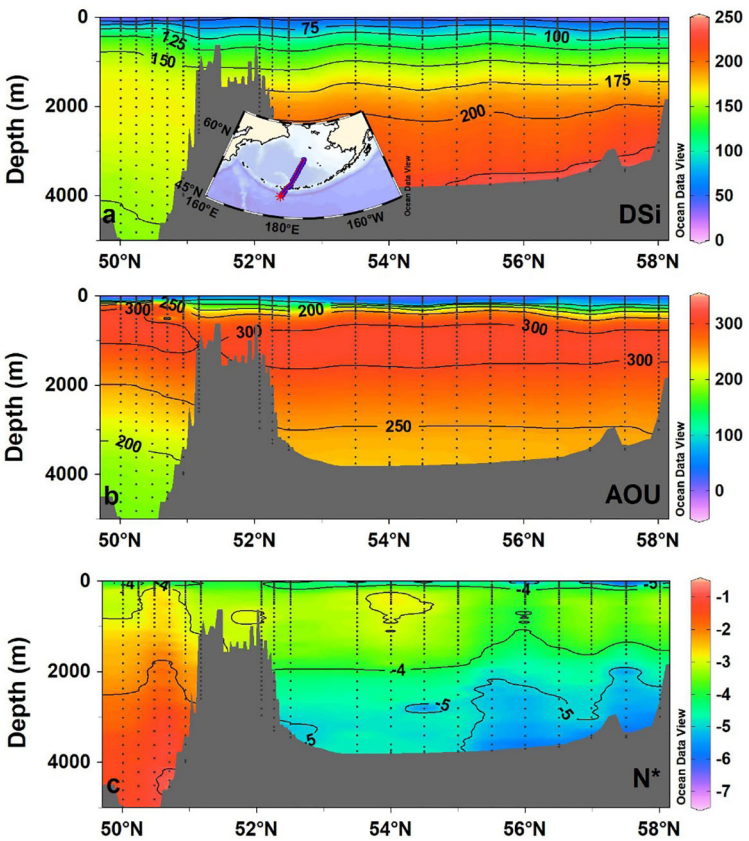

FIGURE 4 | Cross-sectional distribution of **(A)** DSi (μmol/kg), **(B)** apparent oxygen utilization (AOU; μmol/kg), and **(C)** N* (μmol/kg) in the North Pacific Ocean and Bering Sea. The nutrient tracer N* represents the net effect of nitrogen fixation and denitrification.

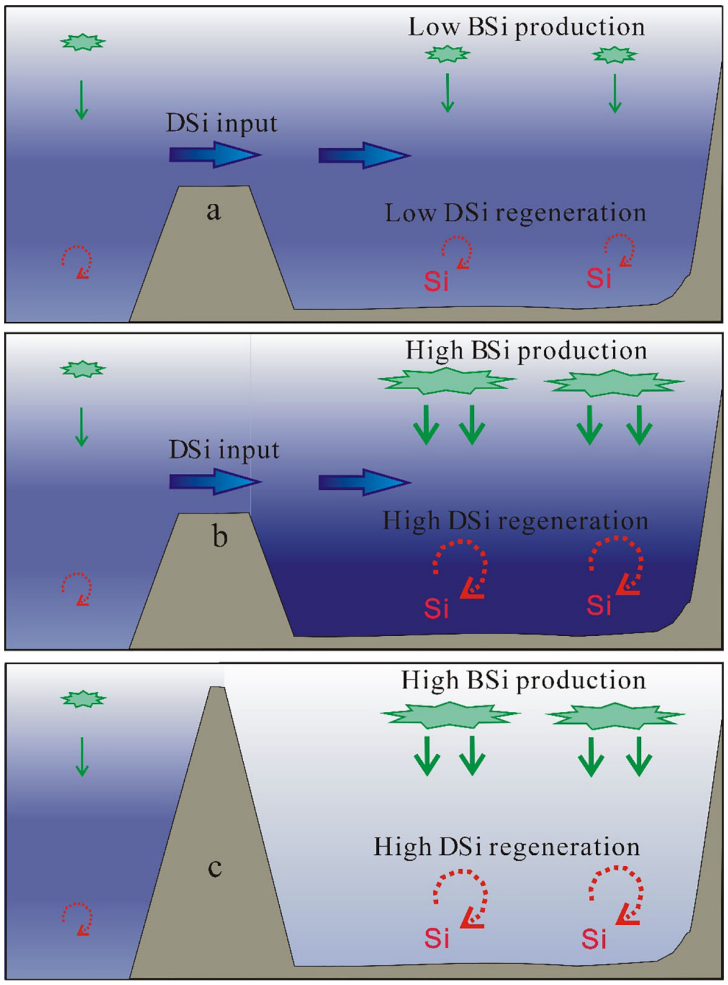

FIGURE 5 | Schematic diagrams showing the silica cycle in different marginal sea settings. **(A)** Oligotrophic marginal sea under the influence of open ocean inflow water; **(B)** productive marginal sea under the influence of open ocean inflow water; **(C)** marginal sea unaffected by open ocean inflow water. The background color indicates the concentration of DSi, with darker colors indicating higher concentrations.

its adjacent coastal waters (e.g., Cao et al., 2012; Lu et al., 2022). However, it is nutrient-poor in the mid-ocean, especially in anticyclonic eddies (Du et al., 2013; Zhuang et al., 2018; Sun et al., 2022), where persistent stratification limits the vertical influx of nutrients (Wong et al., 2007; Zhuang et al., 2021a). Here, the supply of nutrients to surface layers (and the subsequent increase in particles sinking to depth) depends on episodic events such as typhoons (Zhang et al., 2019; Chen et al., 2021). The monthly mean BSi flux in the central South China Sea ranges from 14.8 to 34.9 mg m^{-2} d^{-1}, with a high BSi flux during the northeastern monsoon period (Li et al., 2017). When the surface waters of marginal seas are oligotrophic, as in the South China Sea, the rates of formation and export of BSi are low (Yang et al., 2015), which leads to low rates of DSi regeneration of in deep waters (**Figure 5A**). It has been indicated that oligotrophic areas have low rates of BSi dissolution and benthic diffusion of DSi (Tréguer et al., 1995). Deep ocean DSi regeneration is more intense when the surface waters of marginal seas are productive (**Figure 5B**), such as in the Bering Sea and the Okhotsk Sea. The monthly mean BSi flux in the southern Bering Sea ranges from 48.4 to 805.0 mg m^{-2} d^{-1} (Akagi et al., 2011), which is an order of magnitude higher than that in the South China Sea (14.8 to 34.9 mg m^{-2} d^{-1}; Li et al., 2017). The strong particle flux through the water column in the productive marginal seas promotes the sinking of BSi to deep waters and sediment.

Other physical and biogeochemical factors also contribute to the high rates of deep ocean DSi regeneration in the Bering Sea. First, a summertime high-productivity zone, also known as the "green belt", exists along the shelf break of the Bering Sea and is maintained by upward influx of nutrients and iron from the subsurface (Springer et al., 1996; Tanaka et al., 2012). The phytoplankton community in the region is dominated by diatoms, which contribute to high biological production and thus high rates of BSi formation (Zhuang et al., 2020). Second, there are mechanisms that lead to the rapid sinking of biogenic particles in this area. For example, oceanic deep-water formation

in the Atlantic and Southern oceans leads to the rapid removal of additional particles from the surface by water mass subduction (Lohmann et al., 2006). Low surface temperatures in the subpolar Bering Sea favor BSi preservation, which results in reduced rates of respiration and silica dissolution in the upper ocean (Nelson et al., 1995; Iversen and Ploug, 2013). In contrast, high surface temperatures often promote the dissolution of BSi in the low-latitude oceans, such as the Japan Sea and the South China Sea. In addition, diatom-derived particles typically have lower decay rates (Cabrera-Brufau et al., 2021), which allows more biogenic particles to reach deep waters and sediment. AOU concentrations and $\Delta DSi_{(bottom-2000m)}$ values in deep waters of the Bering Sea (**Figure 3**) indicate concurrent organic matter remineralization and BSi dissolution as biogenic particles sink through deep waters. The amount of DSi regeneration varies throughout the global oceans, mostly because of differences in the rates of organic matter remineralization (Guidi et al., 2015). Hu et al. (2014) showed that the Bering Sea has an extremely high particle removal rate, which may be one of the main reasons for the high rates of DSi release in deep waters of the Bering Sea.

The Bering Sea experienced high rates of BSi export production, equal to those in the Southern and eastern equatorial Pacific oceans, but BSi concentrations in Bering Sea sediments are relatively low (Heinze et al., 2003). This strongly suggests that deep ocean DSi regeneration in the Bering Sea is accelerated relative to that in the open ocean. Earlier works have alluded to higher BSi recycling fluxes under low oxygen conditions (Berelson et al., 1987) and a decrease in BSi preservation under anoxic waters (Dale et al., 2021), suggesting a dependence of BSi preservation on oxygen levels. The deep waters of the Bering Sea have high rates of organic matter respiration and thus oxygen consumption, leading to low oxygen concentrations. These low oxygen conditions may also promote DSi regeneration. In addition, the high DSi concentrations (>225 μmol/kg) observed in the near-bottom waters of the Bering Sea basin (**Figure 4**) were most likely generated locally through dissolution of BSi in surface sediments. An average sedimentary denitrification rate of nearly 230 μmol N m^{-2} d^{-1} has been reported in the deep Bering Sea (>2000 m); this value is three times higher than the global average for the same depth (Lehmann et al., 2005). DSi is released into deep waters at the sediment–water interface, which increases the deep-water DSi reserves. Active benthic biogeochemical processes may also contribute to deep ocean DSi regeneration in the Bering Sea. The high regeneration rate of deep ocean DSi and upwelling water will eventually affect the regional nutrient budget and cycle (Zhuang et al., 2021b).

CONCLUSIONS

The role of marginal seas in deep ocean DSi regeneration is tightly coupled to the production and export of BSi in surface waters. In the nutrient-poor South China Sea, the deep-water DSi concentration is close to that of the adjacent Pacific waters, and deep ocean DSi regeneration is weak. Conversely, in the productive Bering Sea, deep-water DSi concentrations are much higher than those in the adjacent Pacific waters, and the capacity for deep DSi regeneration is strong; as a result, the Bering Sea has the highest reported deep-water DSi concentrations (>240 μmol/kg) in the global ocean. A combination of physical and biochemical factors, including low temperatures, diatom-dominance in the phytoplankton community, high particle export rate, and dissolution of opal in surface sediments, contribute to active DSi regeneration in deep waters of the Bering Sea.

Although marginal seas represent only a small fraction of the global ocean area, and the rapid accumulation of DSi in the deep waters of marginal seas may not seem globally significant, they may have important regional implications. Deep ocean DSi regeneration and organic matter respiration are accelerated in productive marginal seas, suggesting active deep ocean biogeochemical cycles in these regions and may support unexpectedly active ecosystem (e.g., bacteria) in the deep water and sediments. Besides, the upwelling water of the Bering Sea and its northward flow have important effects on the nutrient budget and ecosystem of the adjacent Arctic Ocean.

DATA AVAILABILITY STATEMENT

Publicly available datasets were analyzed in this study. This data can be found here: https://www.ncei.noaa.gov/access/world-ocean-database/datawodgeo.html.

AUTHOR CONTRIBUTIONS

Conceptualization, XY and YZ. methodology and software, XY and XC. Validation, XY and YZ. Data curation, XY and YZ. Writing—original draft preparation, XY. Writing—review and editing, YZ, XC, and DQ. Supervision and project administration, YZ. Funding acquisition, YZ and DQ. All authors have read and agreed to the published version of the manuscript.

FUNDING

This research was funded by National Key Research and Development Program of China (2019YFE0120900, and 2019YFE0114800), the Natural Science Foundation of Zhejiang Province (Y19D060024).

ACKNOWLEDGMENTS

We thank the World Ocean Database (https://www.ncei.noaa.gov/access/world-ocean-database/datawodgeo.html) for provision of the data.

SUPPLEMENTARY MATERIAL

The Supplementary Material for this article can be found online at: https://www.frontiersin.org/articles/10.3389/fmars.2022.925919/full#supplementary-material

REFERENCES

Akagi, T., Fu, F. F., Hongo, Y., and Takahashi, K. (2011). Composition of Rare Earth Elements in Settling Particles Collected in the Highly Productive North Pacific Ocean and Bering Sea: Implications for Siliceous-Matter Dissolution Kinetics and Formation of Two REE-Enriched Phases. *Geochim. Cosmochim. Ac.* 75 (17), 4857–4876. doi: 10.1016/j.gca.2011.06.001

Berelson, W. M., Hammond, D. E., and Johnson, K. S. (1987). Benthic Fluxes and the Cycling of Biogenic Silica and Carbon in Two Southern California Borderland Basins. *Geochim. Cosmochim. Ac.* 51 (6), 1345–1363. doi: 10.1016/0016-7037(87)90320-6

Béthoux, J. P., Morin, P., Chaumery, C., Connan, O., Gentili, B., and Ruiz-Pino, D. (1998). Nutrients in the Mediterranean Sea, Mass Balance and Statistical Analysis of Concentrations With Respect to Environmental Change. *Mar. Chem.* 63 (1–2), 155–169. doi: 10.1016/S0304-4203(98)00059-0

Brzezinski, M. A., Pride, C. J., Franck, V. M., Sigman, D. M., Sarmiento, J. L., Matsumoto, K., et al. (2002). A Switch From $Si(OH)_4$ to NO_3^- Depletion in the Glacial Southern Ocean. *Geophys. Res. Lett.* 29 (12), 1564. doi: 10.1029/2001GL014349

Cabrera-Brufau, M., Arin, L., Sala, M. M., Cermeño, P., and Marrasé, C. (2021). Diatom Dominance Enhances Resistance of Phytoplanktonic POM to Mesopelagic Microbial Decomposition. *Front. Mar. Sci.* 8. doi: 10.3389/fmars.2021.683354

Cao, Z., Frank, M., Dai, M., Grasse, P., and Ehlert, C. (2012). Silicon Isotope Constraints on Sources and Utilization of Silicic Acid in the Northern South China Sea. *Geochim. Cosmochim. Ac.* 97, 88–104. doi: 10.1016/j.gca.2012.08.039

Cao, Z., Wang, D., Zhang, Z., Zhou, K., Liu, X., Wang, L., et al. (2020). Seasonal Dynamics and Export of Biogenic Silica in the Upper Water Column of a Large Marginal Sea, the Northern South China Sea. *Prog. Oceanogr.* 188, 102421. doi: 10.1016/j.pocean.2020.102421

Chen, F., Huang, C., Lao, Q., Zhang, S., Chen, C., Zhou, X., et al. (2021). Typhoon Control of Precipitation Dual Isotopes in Southern China and its Palaeoenvironmental Implications. *J. Geophys. Res.* 126 (14), e2020JD034336. doi: 10.1029/2020JD034336

Dai, M., Cao, Z., Guo, X., Zhai, W., Liu, Z., Yin, Z., et al. (2013). Why are Some Marginal Seas Sources of Atmospheric CO_2? *Geophys. Res. Lett.* 40 (10), 2154–2158. doi: 10.1002/grl.50390

Dale, A. W., Paul, K. M., Clemens, D., Scholz, F., Schroller-Lomnitz, U., Wallmann, K., et al. (2021). Recycling and Burial of Biogenic Silica in an Open Margin Oxygen Minimum Zone. *Global Biogeochem. Cy.* 35 (2), e2020GB006583. doi: 10.1029/2020GB006583

DeMaster, D. J. (1981). The Supply and Accumulation of Silica in the Marine Environment. *Geochim. Cosmochim. Ac.* 45 (10), 1715–1732. doi: 10.1016/0016-7037(81)90006-5

Du, C., Liu, Z., Dai, M., Kao, S. J., Cao, Z., Zhang, Y., et al. (2013). Impact of the Kuroshio Intrusion on the Nutrient Inventory in the Upper Northern South China Sea: Insights From an Isopycnal Mixing Model. *Biogeosciences* 10 (10), 6419–6432. doi: 10.5194/bg-10-6419-2013

Garcia, H., and Gordon, L. I. (1992). Solubility of Oxygen at Different Temperature and Salinity. *Limnol. Oceanogr.* 37, 1307–1312. doi: 10.4319/lo.1992.37.6.1307

Gruber, N., and Sarmiento, J. L. (1997). Global Patterns of Marine Nitrogen Fixation and Denitrification. *Global Biogeochem. Cy.* 11 (2), 235–266. doi: 10.1029/97GB00077

Guidi, L., Legendre, L., Reygondeau, G., Uitz, J., Stemmann, L., and Henson, S. A. (2015). A New Look at Ocean Carbon Remineralization for Estimating Deepwater Sequestration. *Global Biogeochem. Cy.* 29 (7), 1044–1059. doi: 10.1002/2014GB005063

Heinze, C., Hupe, A., Maier-Reimer, E., Dittert, N. , and Ragueneau, O. (2003). Sensitivity of the Marine Biospheric Si Cycle for Biogeochemical Parameter Variations. *Global Biogeochem. Cy.* 17 (3), 1086. doi: 10.1029/2002GB001943

Hendry, K. R., Georg, R. B., Rickaby, R. E., Robinson, L. F., and Halliday, A. N. (2010). Deep Ocean Nutrients During the Last Glacial Maximum Deduced From Sponge Silicon Isotopic Compositions. *Earth Planet. Sci. Lett.* 292 (3–4), 290–300. doi: 10.1016/j.epsl.2010.02.005

Hu, W., Chen, M., Yang, W., Zhang, R., Qiu, Y., and Zheng, M. (2014). Enhanced Particle Scavenging in Deep Water of the Aleutian Basin Revealed by 210Po-210Pb Disequilibria. *J. Geophys. Res.* 119 (6), 3235–3248. doi: 10.1002/2014JC009819

Iversen, M. H., and Ploug, H. (2013). Temperature Effects on Carbon-Specific Respiration Rate and Sinking Velocity of Diatom Aggregates-Potential Implications for Deep Ocean Export Processes. *Biogeosciences* 10, 4073–4085. doi: 10.5194/bg-10-4073-2013

Lehmann, M. F., Sigman, D. M., McCorkle, D. C., Brunelle, B. G., Hoffmann, S., Kienast, M., et al. (2005). Origin of the Deep Bering Sea Nitrate Deficit: Constraints From the Nitrogen and Oxygen Isotopic Composition of Water Column Nitrate and Benthic Nitrate Fluxes. *Global Biogeochem. Cy.* 19, GB4005. doi: 10.1029/2005GB002508

Li, C., Chiang, K. P., Laws, E. A., Liu, X., Chen, J., Huang, Y., et al. (2022a). Quasi-Antiphase Diel Patterns of Abundance and Cell Size/Biomass of Picophytoplankton in the Oligotrophic Ocean. *Geophys. Res. Lett.*, 49, e2022GL097753. doi: 10.1029/2022GL097753

Li, H., Wiesner, M. G., Chen, J., Ling, Z., Zhang, J., and Ran, L. (2017). Long-Term Variation of Mesopelagic Biogenic Flux in the Central South China Sea: Impact of Monsoonal Seasonality and Mesoscale Eddy. *Deep-Sea. Res. Pt. I.* 126, 62–72. doi: 10.1016/j.dsr.2017.05.012

Li, H., Zhang, J., Xuan, J., Wu, Z., Ran, L., Wiesner, M. G., et al. (2022b). Asymmetric Response of the Biological Carbon Pump to the ENSO in the South China Sea. *Geophys. Res. Lett.* 49 (2), e2021GL095254. doi: 10.1029/2021GL095254

Lohmann, R., Jurado, E., Pilson, M. E., and Dachs, J. (2006). Oceanic Deep Water Formation as a Sink of Persistent Organic Pollutants. *Geophys. Res. Lett.* 33, L12607. doi: 10.1029/2006GL025953

Lozier, M. S. (2010). Deconstructing the Conveyor Belt. *Science* 328 (5985), 1507–1511. doi: doi 10.1126/science.118925

Lu, X., Zhou, X., Jin, G., Chen, F., Zhang, S., Li, Z., et al. (2022). Biological Impact of Typhoon Wipha in the Coastal Area of Western Guangdong: A Comparative Field Observation Perspective. *J. Geophys. Res.* 127 (2), e2021JG006589. doi: 10.1029/2021JG006589

Maldonado, M., López-Acosta, M., Sitjà, C., García-Puig, M., Galobart, C., Ercilla, G., et al. (2019). Sponge Skeletons as an Important Sink of Silicon in the Global Oceans. *Nat. Geosci.* 12 (10), 815–822. doi: 10.1038/s41561-019-0430-7

Ma, Y., Zhang, L., Liu, S., and Zhu, D. (2022). Silicon Balance in the South China Sea. *Biogeochemistry* 157, 327–353. doi: 10.1007/s10533-021-00879-4

Moriceau, B., Gehlen, M., Tréguer, P., Baines, S., Livage, J., and André, L. (2019). Biogeochemistry and Genomics of Silicification and Silicifiers. *Front. Mar. Sci.* 6. doi: 10.3389/fmars.2019.00057

Nelson, D. M., Tréguer, P., Brzezinski, M. A., Leynaert, A., and Quéguiner, B. (1995). Production and Dissolution of Biogenic Silica in the Ocean: Revised Global Estimates, Comparison With Regional Data and Relationship to Biogenic Sedimentation. *Global Biogeochem. Cy.* 9 (3), 359–372. doi: 10.1029/95GB01070

Ragueneau, O., Schultes, S., Bidle, K., Claquin, P., and Moriceau, B. (2006). Si and C Interactions in the World Ocean: Importance of Ecological Processes and Implications for the Role of Diatoms in the Biological Pump. *Global Biogeochem. Cy.* 20, GB4S02. doi: 10.1029/2006GB002688

Sarmiento, J. L., Gruber, N., Brzezinski, M. A., and Dunne, J. P. (2004). High-Latitude Controls of Thermocline Nutrients and Low Latitude Biological Productivity. *Nature* 427 (6969), 56–60.

Schlitzer, R. (2018). Ocean Data View. *odv.awi.de*. v.4.6.4., 2018.

Springer, A. M., McRoy, C. P., and Flint, M. V. (1996). The Bering Sea Green Belt: Shelf-Edge Processes and Ecosystem Production. *Fish. Oceanogr.* 5 (3–4), 205–223. doi: 10.1111/j.1365-2419.1996.tb00118.x

Sun, F., Xia, X., Simon, M., Wang, Y., Zhao, H., Sun, C., et al. (2022). Anticyclonic Eddy Driving Significant Changes in Prokaryotic and Eukaryotic Communities in the South China Sea. *Front. Mar. Sci.* 9. doi: 10.3389/fmars.2022.773548

Tanaka, T., Yasuda, I., Kuma, K., and Nishioka, J. (2012). Vertical Turbulent Iron Flux Sustains the Green Belt Along the Shelf Break in the Southeastern Bering Sea. *Geophys. Res. Lett.* 39, L08603. doi: 10.1029/2012GL051164

Tréguer, P. J., and de la Rocha, C. L. (2013). The World Ocean Silica Cycle. *Annu. Rev. Mar. Sci.* 5, 477–501. doi: 10.1146/annurev-marine-121211-172346

Tréguer, P., Nelson, D. M., Van Bennekom, A. J., DeMaster, D. J., Leynaert, A., and Quéguiner, B. (1995). The Silica Balance in the World Ocean: A Reestimate. *Science* 268 (5209), 375–379. doi: 10.1126/science.268.5209.375

Tréguer, P. J., Sutton, J. N., Brzezinski, M., Charette, M. A., Devries, T., Dutkiewicz, S., et al. (2021). Reviews and syntheses: The biogeochemical cycle of silicon in the modern ocean. *Biogeosciences*, 18 (4), 1269—1289.

Waga, H., Fujiwara, A., Hirawake, T., Suzuki, K., Yoshida, K., Abe, H., et al. (2022). Primary Productivity and Phytoplankton Community Structure in Surface Waters of the Western Subarctic Pacific and the Bering Sea During Summer With Reference to Bloom Stages. *Prog. Oceanogr.* 201, 102738. doi: 10.1016/j.pocean.2021.102738

Wang, P. (1999). Response of Western Pacific Marginal Seas to Glacial Cycles: Paleoceanographic and Sedimentological Features. *Mar. Geol.* 156 (1–4), 5–39. doi: 10.1016/S0025-3227(98)00172-8

Wong, G. T., Ku, T. L., Mulholland, M., Tseng, C. M., and Wang, D. P. (2007). The SouthEast Asian Time-Series Study (SEATS) and the Biogeochemistry of the South China Sea—an Overview. *Deep-Sea. Res. Pt. II.* 54 (14–15), 1434–1447. doi: 10.1016/j.dsr2.2007.05.012

Wu, B., and Liu, S. (2020). Dissolution Kinetics of Biogenic Silica and the Recalculated Silicon Balance of the East China Sea. *Sci. Total. Environ.* 743, 140552. doi: 10.1016/j.scitotenv.2020.140552

Yang, W., Chen, M., Zheng, M., He, Z., Zhang, X., Qiu, Y., et al. (2015). Influence of a Decaying Cyclonic Eddy on Biogenic Silica and Particulate Organic Carbon in the Tropical South China Sea Based on ^{234}Th-^{238}U Disequilibrium. *PloS One* 10 (8), e0136948. doi: 10.1371/journal.pone.0136948

Zhang, J., Li, H., Xuan, J., Wu, Z., Yang, Z., Wiesner, M. G., et al. (2019). Enhancement of Mesopelagic Sinking Particle Fluxes Due to Upwelling, Aerosol Deposition, and Monsoonal Influences in the Northwestern South China Sea. *J. Geophys. Res.* 124 (1), 99–112. doi: 10.1029/2018JC014704

Zhuang, Y., Jin, H., Cai, W. J., Li, H., Jin, M., Qi, D., et al. (2021a). Freshening Leads to a Three-Decade Trend of Declining Nutrients in the Western Arctic Ocean. *Environ. Res. Lett.* 16 (5), 054047. doi: 10.1088/1748-9326/abf58b

Zhuang, Y., Jin, H., Chen, J., Li, H., Ji, Z., Bai, Y., et al. (2018). Nutrient and Phytoplankton Dynamics Driven by the Beaufort Gyre in the Western Arctic Ocean During the Period 2008–2014. *Deep-Sea. Res. Pt. I.* 137, 30–37. doi: 10.1016/j.dsr.2018.05.002

Zhuang, Y., Jin, H., Chen, J., Ren, J., Zhang, Y., Lan, M., et al. (2020). Phytoplankton Community Structure at Subsurface Chlorophyll Maxima on the Western Arctic Shelf: Patterns, Causes, and Ecological Importance. *J. Geophys. Res.* 125 (6), e2019JG005570. doi: 10.1029/2019JG005570

Zhuang, Y., Jin, H., Zhang, Y., Li, H., Zhang, T., Li, Y., et al. (2021b). Incursion of Alaska Coastal Water as a Mechanism Promoting Small Phytoplankton in the Western Arctic Ocean. *Prog. Oceanogr.* 197, 102639. doi: 10.1016/j.pocean.2021.102639

Conflict of Interest: The authors declare that the research was conducted in the absence of any commercial or financial relationships that could be construed as a potential conflict of interest.

Publisher's Note: All claims expressed in this article are solely those of the authors and do not necessarily represent those of their affiliated organizations, or those of the publisher, the editors and the reviewers. Any product that may be evaluated in this article, or claim that may be made by its manufacturer, is not guaranteed or endorsed by the publisher.

frontiers | Frontiers in Marine Science

TYPE Original Research
PUBLISHED 22 July 2022
DOI 10.3389/fmars.2022.946231

OPEN ACCESS

EDITED BY:
Guangzhe Jin,
Guangdong Ocean University, China

REVIEWED BY:
Xu Dong,
Ministry of Natural Resources, China
Shiguo Wu,
Institute of Deep-Sea Science and Engineering (CAS), China

*CORRESPONDENCE:
Zhenyu Lei
44231234@qq.com
Ming Su
suming3@mail.sysu.edu.cn

SPECIALTY SECTION:
This article was submitted to Marine Biogeochemistry, a section of the journal Frontiers in Marine Science

RECEIVED: 17 May 2022
ACCEPTED: 24 June 2022
PUBLISHED: 22 July 2022

CITATION:
Liu S, Liang Z, Zhang B, Su H, Lei Z and Su M (2022) Carbonate contourite drifts in the southwest South China Sea: Sedimentary, paleoceanographic and economic implications. Front. Mar. Sci. 9:946231. 10.3389/fmars.2022.946231

Carbonate contourite drifts in the southwest South China Sea: Sedimentary, paleoceanographic and economic implications

Shan Liu[1,2], Zijun Liang[1], Boda Zhang[1], Haixia Su[1], Zhenyu Lei[3*] and Ming Su[1,2,4*]

[1]School of Marine Science, Sun Yat-sen University, Zhuhai, China, [2]Southern Marine Science and Engineering Guangdong Laboratory (Zhuhai), Zhuhai, China, [3]Guangzhou Marine Geology Survey, China Geological Survey, Ministry of Natural Resources, Guangzhou, China, [4]Guangdong Provincial Key Laboratory of Marine Resources and Coastal Engineering, Guangzhou, China

Contourite drifts are significant sedimentary features and provide clues for the reconstruction of paleoceanography and paleoenvironment. Although they have been increasingly identified in the world's ocean, shallow-water contourite drifts (< 300 m depth) remain poorly understood and the examples are rare. This study documents a Middle Miocene shallow-water contourite depositional system in the southwest South China Sea by interpreting seismic reflection data and calibrating results with the previous chronological framework. The depositional system consisted of six mounded drifts and six moats. The contourite features were generated in seismic unit III (16-10.5 Ma) and distributed adjacent to carbonate reefs. They were formed on the proto-continental shelf (50-200 m depth) and shaped by the wind-driven currents. Changes in the sedimentary stacking patterns suggest three evolutionary stages of the contourite features. Stage I represents the growth of the Middle Miocene contourite depositional system between 16 and 10.5 Ma. Stage II marks the termination of carbonate drifts and the burial of the Late Miocene sedimentation during 10.5-5.3 Ma. Stage III started with the development of modern deep-water sedimentary systems since 5.3 Ma. The contourite features are compared with the examples on other South China Sea margins. Significant changes in the paleoceanography occurred at 10.5 Ma and 6.5-5.3 Ma when the dominated bottom currents shifted from the monsoonal wind-driven currents to the North Pacific waters, and then the modern circulation system. The Middle Miocene mounded drifts were likely sourced by the coarse-grained carbonate sands. Fluid flow escaped from the coarse-grained contourite layers and natural gas leakage occurs on the seafloor. Shallow-water carbonate contourite drifts can be served as a good gas reservoir and have great economic potential.

KEYWORDS

contourite depositional system, sedimentary process, bottom current, carbonate reef, southwest South China Sea

1 Introduction

Bottom currents are vital oceanographic processes of redistributing sediments (Hanebuth et al., 2015; de Castro et al., 2021; Rodrigues et al., 2022), shaping seafloor morphology (Howe et al., 2006; Hernández-Molina et al., 2017; Yin et al., 2022), influencing marine ecosystems (Loeb et al., 2010; Cimino et al., 2020), and transporting pollutants (Martin et al., 2017; Kane and Clare, 2019). The persistent bottom currents that are commonly driven by winds, thermohaline circulation, eddies, and tides can create alongslope sedimentary features on the continental margin through geological timescales (Hernández-Molina et al., 2008; Rebesco et al., 2014). The combination of the depositional (i.e., contourite drifts) and erosional features (i.e., moats, contourite channels), known as the contourite depositional system, provides clues for the reconstruction of palaeoceanographic and paleoenvironmental conditions (Llave et al., 2007; García et al., 2016; de Weger et al., 2020; Kirby et al., 2021).

Since the 1960s (Heezen and Hollister, 1964; Heezen et al., 1966), contourite depositional systems have been increasingly observed in the deep basins (García et al., 2016; Pérez et al., 2019; Ng et al., 2021), on the continental slops (Roque et al., 2012; Hernández-Molina et al., 2016; Yin et al., 2019), in the shallow marine (Pepe et al., 2018; Mulder et al., 2019), and in lakes (Ceramicola et al., 2001; Wagner et al., 2012). However, identified shallow-water contourite drifts are not as much as deep-water ones (Thran et al., 2018). Shallow-water contourite drifts are those influenced by contour-parallel flows at a water depth shallower than 300 m (Verdicchio and Trincardi, 2008). Some of the well-studied examples are the Maldives (Lüdmann et al., 2013; Betzler et al., 2018) and the Bahamas (Chabaud et al., 2016; Mulder et al., 2019) archipelagos. The contourite depositional systems were formed adjacent to carbonate reefs, platforms, or atolls and situated in the pathway of major surface currents (Lüdmann et al., 2013; Betzler et al., 2014). This type of drifts, defined as carbonate contourite drifts, commonly consisted of coarse-grained carbonated sediments and has an economic significance for hydrocarbon exploration (Viana, 2008; Eberli and Betzler, 2019).

In the tropical Pacific Ocean, the Middle Miocene was an important period for the shallow-water carbonate drifts because of widely distributed carbonate platforms and enhanced surface currents (Lüdmann et al., 2013; Betzler et al., 2018; Mathew et al., 2020). The proto-continental shelf in the South China Sea was under the comparable paleoceanographic and paleoenvironmental conditions and served as a preferable region for the development of carbonates during the Middle Miocene (Wu et al., 2016; Yan et al., 2020; Makhankova et al., 2021; Yang et al., 2021). The formation of the carbonate contourite drifts would be theoretically significant as the case of the Maldives (Lüdmann et al., 2013; Betzler et al., 2014). However, studies on the shallow-water carbonate drifts in the South China Sea are rare. The sedimentary, paleoceanographic, and economic implications of the carbonate contourite drifts remain poorly investigated.

This study focuses on the continental margin in the southwest South China Sea, which offers a key area to study carbonate contourite drifts and contributes to a better understanding of South China Sea paleoceanography. The objectives of this work are: 1) to identify the Middle Miocene contourite depositional system; 2) to determine the contourite evolutionary stages; 3) to discuss paleoceanographic changes in the South China Sea; and 4) to demonstrate the economic importance of shallow-water carbonate drifts.

2 Regional setting

2.1 Geological setting

The South China Sea is a marginal sea located in the NW Pacific Ocean. Seafloor spreading and tectonic opening of the South China Sea initiated during the Cenozoic at ~33-30 Ma (Sibuet et al., 2016). In the southwest South China Sea, sedimentary basins were subsequently formed and further separated by the NW-SE orientated Tinjar fault (**Figure 1A**) (Morley, 2002; Barckhausen and Roeser, 2004). The basins were widened because of the widespread extensional tectonics during the Middle and Late Eocene (Hall, 2002; Hutchison, 2004). The direction of the seafloor spreading significantly changed during the Early Miocene in the South China Sea (~23-16 Ma) (Chang et al., 2022). Regional collision consequently uplifted the sedimentary basins (Hutchison, 2004; Cullen, 2010). The southwest South China Sea went into a regional quiescence stage and rapid subsidence occurred from the Middle Miocene (~10.5 Ma) onward (Hutchison, 2004; Madon et al., 2013; Zhang et al., 2020).

2.2 Physiographic domains

The southwest South China Sea consists of several physiographic domains (Liu et al., 2021). The Sunda continental shelf extends from 0 to 260 m water depth (**Figure 1B**). Modern carbonate reefs are widely observed on the shelf (Mathew et al., 2020). The continental slope extends to the Nanwei Bank (also known as the Rifleman Bank) and the Wan'an Plateau from 260 to 2360 m water depth (**Figure 1B**). Eight seamounts are shown. They are the Daoming, Yangxin, Zhuzhen, Zhuliang, Changjun, Nanan, Beikang, and Andu seamounts from the west to the east, respectively (**Figure 1B**). Modern sedimentary systems on the continental slope contain mass-transport deposits (MTDs), contourite drifts, turbidites, and pockmarks (He et al., 2018; Zhang et al., 2020; Liu et al., 2021; Huang et al., 2022).

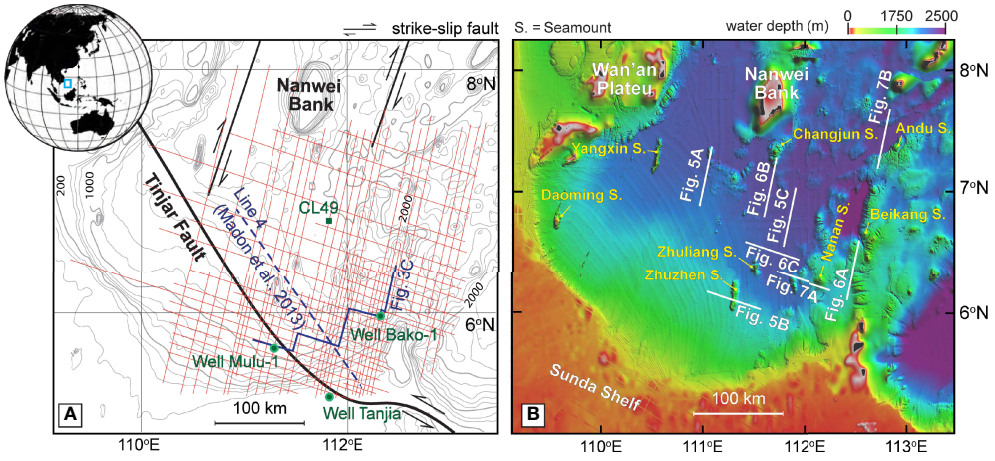

FIGURE 1
(A) Region map of the study area with the location of the strike-slip faults (Huang et al., 2022), seismic reflection data, borehole wells (Luo et al., 2020; Makhankova et al., 2021) and piston core CL49 (Huang et al., 2022). Contour lines every 200 m; and **(B)** Bathymetry map indicating physiographic domains (Liu et al., 2021) and seismic lines used in this study.

2.3 Present-day oceanography

The modern oceanic circulation in the South China Sea consists of the Surface (SW), Intermediate (IW), Deep (DW), and Bottom (BW) waters from the surface to the sea bottom (Tian et al., 2006). The SW that appears from 0 and 300 m water depth has a seasonal variation and is under the influence of monsoon winds (**Figure 2A**) (Qu et al., 2009). The IW is sourced from the North Pacific Intermediate Water (NPIW) (Tian et al., 2006). The water mass circulates in an anticyclonic pattern and entered the southern SCS between a water depth of 300 and 750 m (**Figures 2B, C**). The DW that originated from the North Pacific

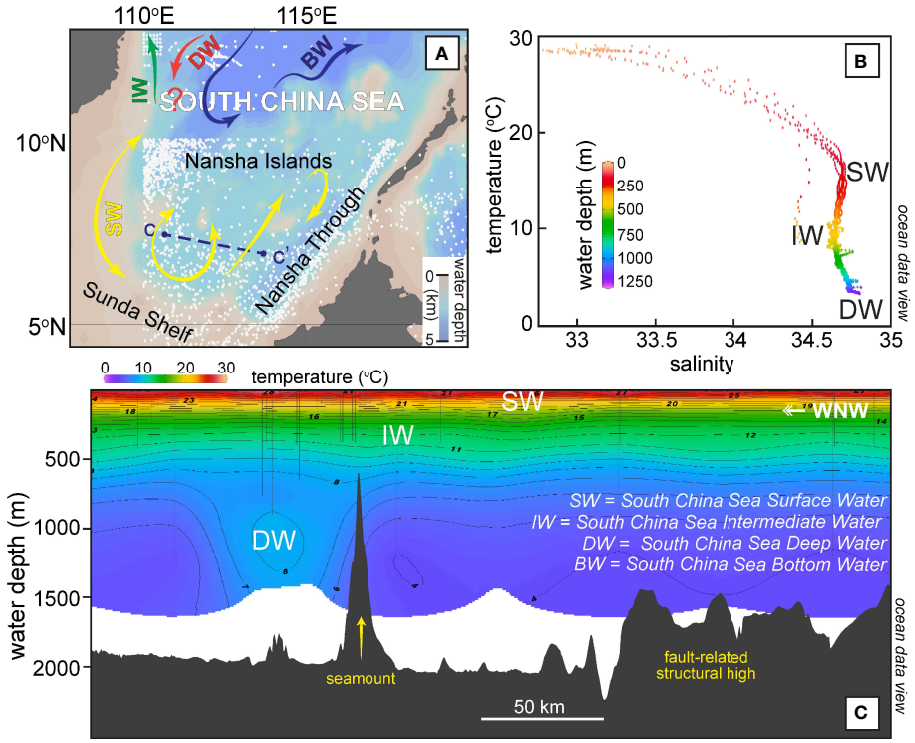

FIGURE 2
(A) Oceanic circulation in the southwest South China Sea (Tian et al., 2006; Liu et al., 2021) and location of CTD stations; **(B)** Potential temperature versus salinity diagram from the water masses in the study area (World Ocean Database, 2013); and **(C)** Oceanographic cross-section of the study area. The water column color ranges indicate temperature. The location of this profile is shown in **(A)**.

Deep Water (NPDW) is observed below a water depth of 1500 m around the Luzon Strait (Qu et al., 2006). The DW is characterized by a cyclonic circulation pattern and the core is 200-300 m shallower in the southern South China Sea (**Figure 2C**) (Liu et al., 2021). The BW is a deep-water overflow transported through the Luzon Strait into the SCS (Zhou et al., 2017). It moves below a water depth of 2000 m in a cyclonic flowing pattern (**Figure 1**) (Tian et al., 2006).

3 Data and methods

3.1 Bathymetry, seismic, and oceanographic data

The datasets used for this study contain high-resolution multibeam bathymetry, multichannel seismic reflection profiles, and oceanographic observation (**Figures 1, 2**). Bathymetric and seismic datasets were obtained during the R/V Tanbao cruise in 1996, 2009, and 2013 *via* the Guangzhou Marine Geological Survey. A SeaBEAM 2112 system was used for acquiring multibeam bathymetry. The system operated at a center frequency of 12 kHz with a swath width of 120 degrees. The multichannel seismic data were acquired by using a Seal 408 streamer recording system. The seismic source was a 32-bolt airgun array with a total volume of 5080 in^3. The dominant frequency ranged from 40 to 60 Hz. The seismic reflection data were further processed by applying a bandpass filter, amplitude recovery, velocity analysis, and pre-stack time migration. Vertical CTD profiles were extracted from the World Ocean Database (2013) (**Figure 2**) (Boyer et al., 2013). The temperature cross-section (**Figure 2C**) was made utilizing the Ocean Data View (ODV) software.

3.2 Seismic interpretation methods

The seismic reflection profiles are interpreted using the Petrel software. The vertical scale is expressed by two-way travel time (TWT). The seismic stratigraphic division for major depositional units is based on the identification of regional discontinuities (T_3 T_2, and T_1) (Catuneanu et al., 2009). T_3 is marked as a regional erosional discontinuity, while T_2 and T_1 are identified by the vertical variation of acoustic facies (**Figure 3A**). These discontinuities are matched with the seismic stratigraphic documented by Luo et al. (2020) through connected seismic profiles (**Figure 3C**). The correlation between seismic data and drill core data (Well Mulu-1

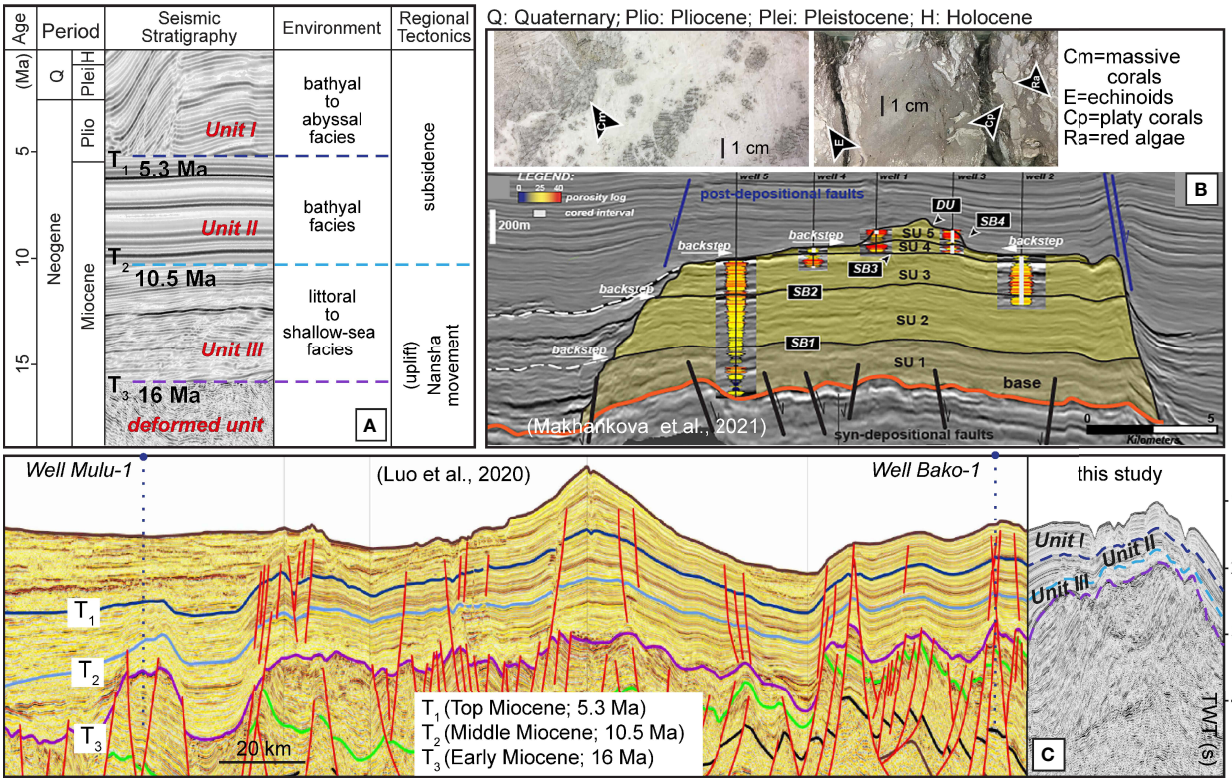

FIGURE 3
(A) Seismic stratigraphic framework, environmental changes, and regional tectonics (Lei et al., 2019; Luo et al., 2020) of the study area; **(B)** Lithology and the seismic profile of the Middle Miocene carbonate reef on the Sunda Shelf; and **(C)** Seismic correlation of the stratigraphic framework in the southwest South China Sea.

and Bako-1) indicate possible chronostratigraphic constraint of the study area (**Figure 3**).

The interpretation of contourite drifts is based on the mounded geometry, continuous oblique to subparallel reflections, and onlap reflection terminations, while moats are characterized by U-shaped erosional features (Faugères et al., 1999; Faugères and Stow, 2008; Rebesco et al., 2014). Carbonate reefs are characterized by the mounded geometry, disrupted to chaotic reflections, and bi-directional downlap reflection terminations (**Figure 4**) (Burgess et al., 2013; Hendry et al., 2021).

4 Results and interpretation

4.1 Seismic stratigraphic analysis

Three major seismic units (UIII-UI from old to young), separated by main discontinuities (T_3 T_2, and T_1), are identified below the present seafloor in the seismic profiles (**Figure 3A**). UIII is characterized by moderate to high amplitude and semi-continuous chaotic-subparallel reflections. The unit is separated from the base unit by discontinuity T_3 (**Figure 5**). Mounded features with onlap and downlap terminations are identified on the continental slope and at the seamount flanks (**Figures 5, 6**). Some mounded features are only observed at the lower part of UIII (**Figures 5C, 6C**). The unit has a maximum sedimentary thickness of 1 s TWT at the lower continental shelf, but the thickness decreases seawards (**Figure 3C**).

UII is bounded by discontinuity T_2 at its base. The unit consists of high amplitude and continuous subparallel reflections (**Figures 5, 6**). The sedimentary thickness is relatively constant at about 0.2 s TWT. UI is bounded by discontinuity T_1 at the base and by the seafloor at its top. The unit is internally characterized by moderate-high amplitude and continuous oblique-subparallel reflections. Several fault-controlled contourite drifts were previously identified in the upper part of this unit (**Figure 10**) (Liu et al., 2021). The thickness of this unit reaches the maximum value (1.2 s TWT) at the depositional section of MTDs (**Figure 10**) (He et al., 2018).

4.2 Buried carbonate reefs

Mounded features were widely observed atop discontinuity T_3 in the study area (Wu et al., 2016; Yan et al., 2020). Their internal seismic features are moderate to high amplitude and disrupted to chaotic reflections, while the external shape is characterized by the mounded geometry (**Figure 6**). The boundary of these mounded features exhibits high amplitude reflectors. Bi-directional downlap terminations are shown (**Figure 4**). Although volcanism was active during the early Miocene in the study area (Yan et al., 2008), these features are not likely the volcanogenic mounds. Volcanogenic mounds are generally characterized by pull-up features and volcanic intrusion (or direct connection with sills) in seismic profiles (Magee et al., 2013), which do not match with the observation in the study area (**Figures 5**, **6**). Besides, evidence from drilling demonstrates that these mounded features possibly contained skeletal grainstone and coral framestone with massive corals (**Figure 3B**) (Makhankova et al., 2021). Drillings from the adjacent regions, such as the Dangerous Ground, also show the presence of mounded carbonate reefs (Steuer et al., 2014; Banerjee and Ahmed Salim, 2021; Li et al., 2022). Thus, these mounded features are most likely the carbonate reefs.

Buried carbonate reefs were previously observed on the Sunda Shelf (Mathew et al., 2020) and the continental slope (Yan et al., 2020) (**Figures 3B**, **7**). In addition to these identified ones, three carbonate reefs (A, B, and C) are recognized in UIII in this study (**Figure 7**). U-shaped erosional features and mounded depositional features are observed on one side of the carbonate reefs A, B, and C (**Figure 6**). Carbonate reef A was 0.7 s TWT high, and the width reached 8 km. Carbonate reef B was 0.6 s TWT high and 7 km wide. The height and width of carbonate reef

feature	example	termination	amplitude	reflection	shape	distribution	unit
mounded drifts 1-3	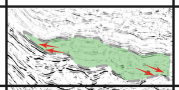	onlap downlap	low to moderate	oblique to subparallel	mounded	seamount, structural high	UIII
mounded drifts 4-6	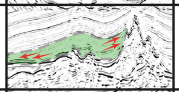	onlap downlap	moderate	oblique to subparallel	mounded	carbonate reef	UIII
moat	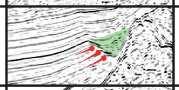	truncation	—	—	U-shaped	mounded drift	UIII
carbonate reef	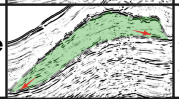	bi-directional downlap	moderate to high	disrupted to chaotic	convex to mounded	widely distributed	UIII

FIGURE 4
Seismic expression, distribution, geometry, and examples of contourite features and carbonate reefs in seismic unit III.

C were 0.3 s TWT and 6 km. The top of carbonate reefs A and B reached T_2, while carbonate reef C only grew to the middle part of UIII (Figure 6).

4.3 A buried contourite depositional system

4.3.1 Mounded drifts

Six mounded drifts (MD 1-6) are identified in UIII (Figs. 5 and 6). MD-3 and -6 only show at the lower part of UIII (Figs. 5C and 6C). MD -1, -2, and -3 are characterized by moderated amplitude and oblique to subparallel reflections (Figure 4). Low-angle onlap and downlap terminations are observed onto T_3 (Figures 4, 5). MD-1 was 0.4 s TWT thick and 21 km wide and extended along a structural high between 2.8 and 3.4 s TWT (Figure 5A). MD-2 was distributed along the southern flank of the Zhuzhen Seamount between 2.9 and 4.0 s TWT (Figures 5B, 7). The thickness was 0.3 s TWT and the width reached 17 km. MD-3 was relatively thin and only generated at the lower part of UIII between 3.3 and 4.2 s TWT (Figure 5C). The drift was 0.15 s TWT thick and 16 km wide.

MD -4, -5, and -6 are associated with carbonate reefs A, B, and C in UIII, respectively (Figure 6). These drifts exhibit moderate amplitude and oblique to subparallel reflections (Figure 6). High-angle onlap terminations are recognized onto carbonate reefs, while low-angle downlap terminations are shown towards T3 (Figs. 4 and 6). MD-4 was 0.4 s TWT thick and 9 km wide. The drift extended along the southern flank of carbonate reef A between 2.1 and 2.7 s TWT (Figs. 6A and 8). MD-5 was distributed along the southern flank of carbonate reef B between 2.6 and 3.6 s TWT (Figs. 6B and 8). The thickness was 0.4 s TWT and the width reached 11 km. MD-6 was located along the western flank of carbonate reef C between 2.5 and 2.9 s TWT (Figs. 6C and 8). The drift was generated at the lower part of UIII with a thickness of 0.3 TWT and a width of 11 km.

4.3.2 Moats

Six moats (Mo 1-6) were associated with the mounded drifts in UIII (Figs. 5, 6, and 8). The distribution was parallel to the seamount, structural high, and carbonate reefs (Figure 7). They were W-E and NNE-SSW orientated and exhibited truncations and U-shaped geometry (Figure 4). The incision was around 50 ms TWT and the width ranged from 0.7 to 4 km (Figures 5, 6).

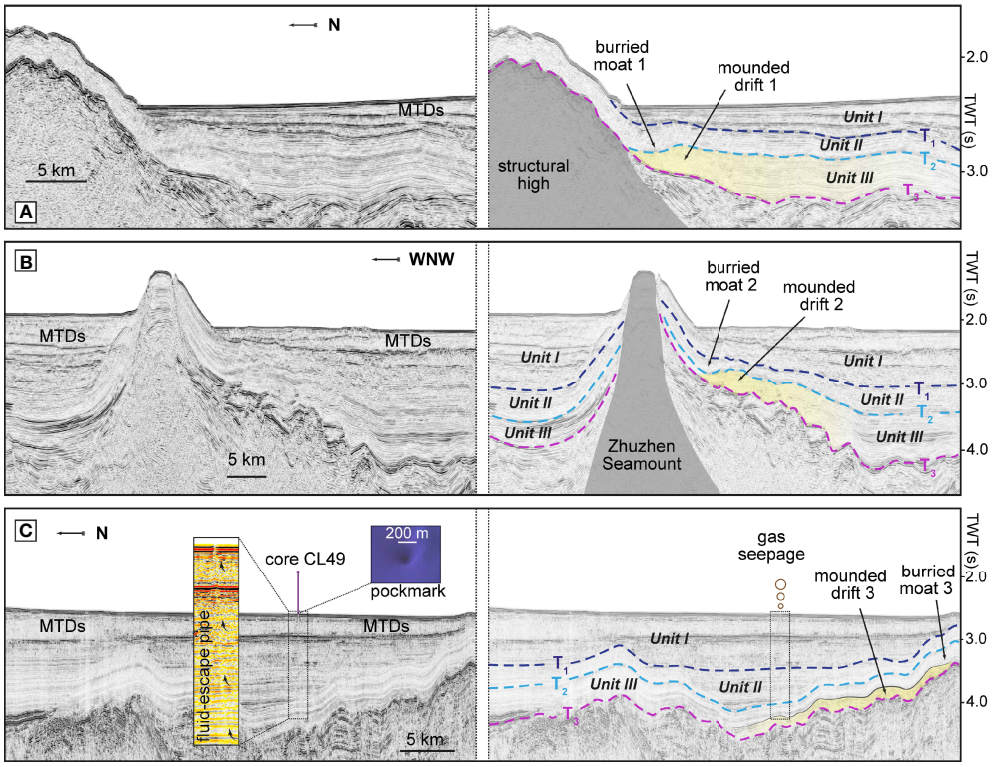

FIGURE 5
Seismic profiles and their interpretation, showing mounded drifts 1-3 and associated moats in seismic unit III. The location of these seismic lines is displayed in Figure 1B. Discontinuities T_3 (16 Ma; purple dotted line), T_2 (10.5 Ma; light blue dotted line) and T_1 (5.3 Ma; dark blue dotted line) are indicated. A fluid-escape pipe and its expression at the seafloor are shown in **(C)**.

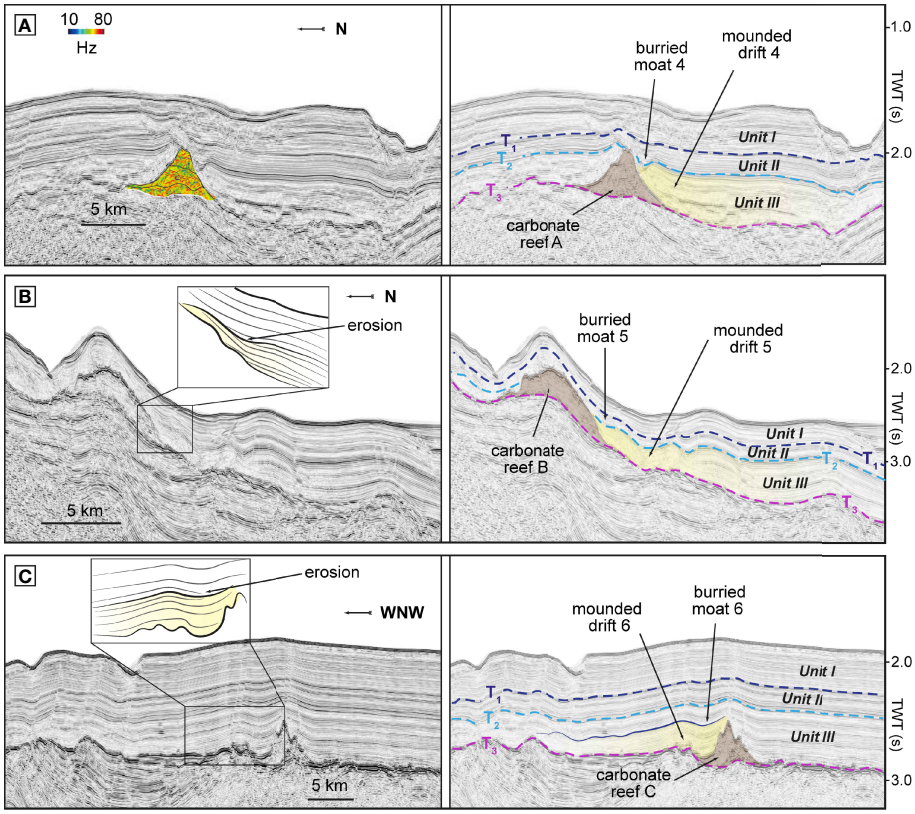

FIGURE 6
Seismic profiles and their interpretation, showing carbonate mounded drifts 1-3, associated moats, and carbonate reefs **(A–C)** in seismic unit III. The location of these seismic lines is displayed in **Figure 1B**. Discontinuities T_3 (16 Ma; purple dotted line), T_2 (10.5 Ma; light blue dotted line), and T_1 (5.3 Ma; dark blue dotted line) are indicated. Instantaneous frequency profile of carbonate reef A is indicated in **(A)**.

4.4 A fluid-escape pipe

A fluid-escape pipe, previously identified by Huang et al. (2022), extends from UIII to the seafloor. The root of the pipe is located at the lower part of MD-3 (**Figure 5C**). This fluid-escape pipe shows pulled-up reflections. The seafloor expression of the pipe is a pockmark with a diameter of 210 m (**Figure 5C**). A piston core CL49 acquired at this location indicated the formation of gas seepage conduits at the seafloor (Huang et al., 2022).

5 Discussion

5.1 Chronological framework

Discontinuities T_3, T_2, and T_1 of this study are correlated with previous chronostratigraphic interpretations of the southwest South China Sea (**Figure 3C**) (Madon et al., 2013; Luo et al., 2020; Huang et al., 2022). The correlation between seismic data and drill core data (Well Mulu-1 and Bako-1) shows that T_3 corresponds to the Middle Miocene unconformity (MMU; 16 Ma). T_2 marks a transition of depositional styles from shallow water to deep marine, related to Wanan tectonic movement at 10.5 Ma, while T_1 is correlated to Guangya tectonic movement at 5.3 Ma (Luo et al., 2020). Thus, UIII has a Middle Miocene age (16-10.5 Ma), UII a Late Miocene age (10.5-5.3 Ma), and UI a Pliocene-Quaternary age (<5.3 Ma) based on the chronostratigraphic constraints.

5.2 Evolutionary stages of the contourite features

The major changes in the sedimentary stacking pattern and the outlined chronology of UIII, UII, and UI indicate three evolutionary stages of the contourite features: I) carbonate drift stage; II) burial stage; and III) modern stage (**Figure 8**). The carbonate drift stage reflects the growth of the Middle Miocene contourite depositional system between 16 and 10.5 Ma. The burial stage marks the terminated growth of carbonate drifts which are buried by the Late Miocene sedimentation during 10.5-5.3 Ma. The modern stage started with the development of Quaternary deep-water sedimentary systems since 5.3 Ma. These modern sedimentary systems are some of the major morphological features on the present-day seafloor in the study area.

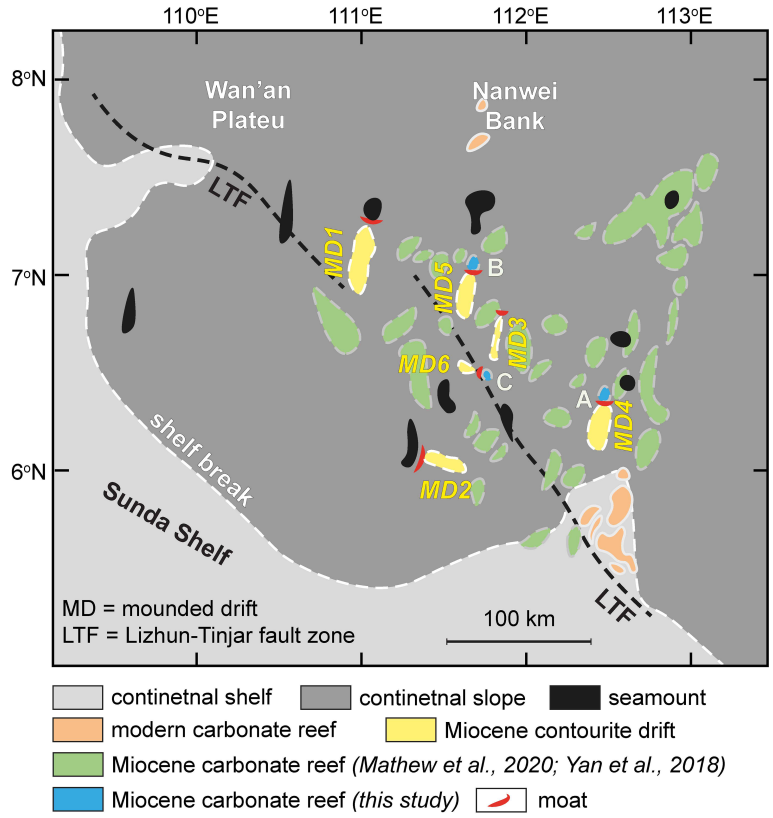

FIGURE 7
Distribution and location of the Middle Miocene contourite depositional system and carbonate reefs **(A–C)**. The location of previously identified Middle Miocene carbonated reefs is adapted from Mathew et al. (2020) and Yan et al. (2018).

5.2.1 Carbonate drift stage (16-10.5 Ma)

The carbonate drift stage (UIII) began with the growth of the Middle Miocene contourite drifts in the study area at 16 Ma (**Figure 8A**), coeval to the initial build-up of carbonate reefs on the Sunda Shelf in the southern South China Sea after ~18-15.5 Ma (Vahrenkamp et al., 2004; Mathew et al., 2020; Makhankova et al., 2021). Corals and foraminifera that constructed carbonate reefs on the proto-Sunda shelf indicated a shallow lagoon (<20 m depth) paleoenvironment during the Middle Miocene (**Figure 3B**) (Makhankova et al., 2021). The present-day continental slope south of the Nanwei Bank was used to be the outer continental shelf (50-200 m depth) during this period (**Figure 9A**) (Collins et al., 2018). Thus, the Middle Miocene contourite depositional system in UIII was generated in a shallow-marine setting.

Shallow-water contourite deposits can be shaped by bottom currents driven by four forces: 1) thermohaline circulation (Vandorpe et al., 2011); 2) wind-induced circulation (Nishida et al., 2022); 3) tidal flow (Lüdmann et al., 2013); and 4) processes at the water-mass interface (Verdicchio and Trincardi, 2008). For the reasons explained below, the Middle Miocene contourite depositional system in the study area was likely related to the wind-induced circulation.

The ocean circulation of the North Pacific enhanced and started to resemble the modern pattern after ~14 Ma (Nathan and Leckie, 2009; Kender et al., 2018). Surface waters had the possibility to intrude into the South China Sea because of its open connection with the Pacific (**Figure 9A**). However, the N-S thermocline gradient in the South China Sea only occurred after 11.5-10.6 Ma (Li et al., 2005; Jian et al., 2006). Contourite drifts in UIII were unlikely linked to the thermohaline circulation or processes at the water-mass interface because of the absence of stratified waters in the South China Sea during the Middle Miocene.

Sedimentary records on the Sunda Shelf showed a significant influence of tidal currents on the sediment deposition during the Middle Miocene (Koša, 2015; Amir Hassan et al., 2017). The related tidal currents were able to transport fine-grained sand and silt but were too weak to generate erosional features on the seafloor (Collins et al., 2017; Collins et al., 2018). Thus, tidal-induced circulation could hardly create moats in UIII and was not involved in the formation of the Middle Miocene contourite depositional system in the study area.

The Middle Miocene was also a significant period for the onset of the modern-like East Asian monsoon system (Betzler et al., 2016). The intensification of the East Asian monsoon at ~15-10 Ma greatly enhanced the seasonal wind-driven currents

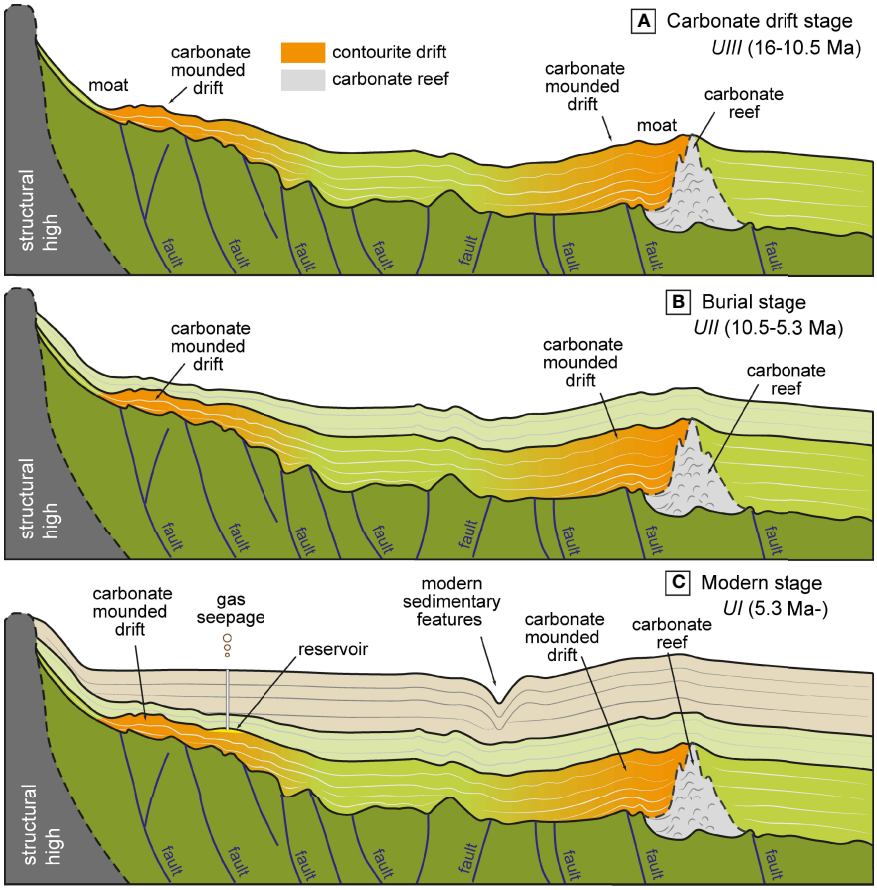

FIGURE 8
Sketch of evolutionary stages of the contourite features in the southwest South China Sea: **(A)** Carbonate drift stage (16-10.5 Ma); **(B)** Burial stage (10.5-5.3 Ma); and **(C)** Modern Stage (5.3 Ma to present day).

at the sea surface (Farnsworth et al., 2019; Holbourn et al., 2021; Ting et al., 2021). Siliciclastic materials were transported to the ocean, forming carbonate reefs and contourite drifts e.g., in the Maldives and on the proto-Sunda Shelf (Lüdmann et al., 2013; Betzler et al., 2016; Betzler et al., 2018). The W-E and NNE-SSW orientated moats in UIII in the study area indicate possible directions of wind-driven currents (**Figure 10**), which are comparable with the observation on the proto-Sunda Shelf (Ting et al., 2021). The reconstructed Middle Miocene wind-driven currents, resembled the modern pattern (Mathew et al., 2020; Ting et al., 2021), was namely flowed towards the north-northeast and the east during summer and winter monsoon in the study area (**Figure 9A**). Thus, wind-driven currents were responsible for the formation of the Middle Miocene contourite depositional system in UIII.

Notice that MD-3 and -6 only show at the lower part of UIII (**Figures 5C** and **6C**). They were at a close distance and located at the Lizhun-Tinjar fault zone (**Figure 7**). The development of MD -3 and -6 was most likely hindered due to regional tectonic activities. Reactivation of the Lizhun-Tinjar fault zone uplifted the paleo-seafloor and formed structural highs during the Middle Miocene (Liu et al., 2004). The resulted topographic barriers could profoundly change the pathway of oceanic currents (Gordon et al., 2003) and, in turn, control the development of contourite drifts.

5.2.2 Burial stage (10.5-5.3 Ma)

The burial stage (UII) of the contourite depositional system occurred between 10.5-5.3 Ma (**Figure 8B**). The contourite features became inactive and were buried by younger deposits after discontinuity T_2 (**Figures 5**, **6**). This prominent change in sedimentary stacking pattern was linked to variations in tectonics, paleoenvironment, and paleoceanography during the Late Miocene. Unlike the Middle Miocene tectonic uplift induced by the collision between the Nansha Islands (Dangerous Grounds) and the Borneo (Hutchison, 2004; Cullen, 2010; Ding et al., 2013), large-scale tectonics terminated at 10.5 Ma and rapid subsidence occurred in the southern South China Sea (Morley, 2016) (**Figure 3A**). The present-day continental slope

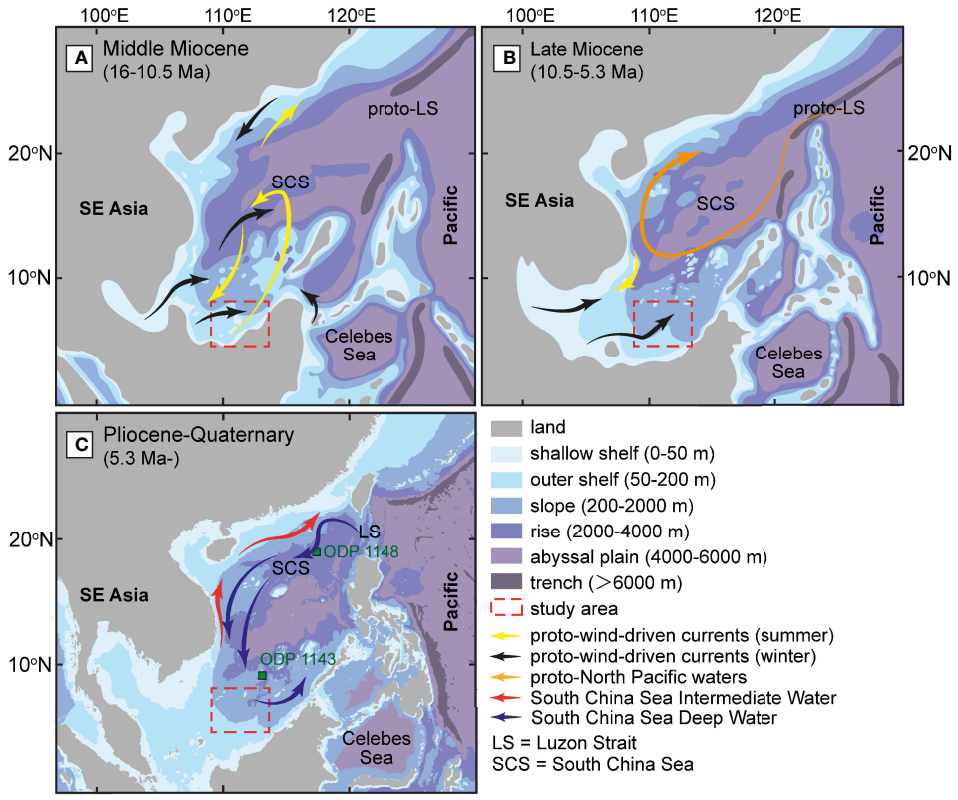

FIGURE 9
Dominated ocean circulation in the South China Sea. Effective bottom currents were associated with (A) monsoonal wind-driven currents (the Middle Miocene); (B) the North Pacific Tropical Water (the Late Miocene); and (C) the South China Sea Intermediate and Deep waters (the present day). Paleogeographic maps are modified from Collins et al. (2018).

of the southwest South China Sea consequently transferred from shallow-marine to bathyal environments (Ding et al., 2013; Yan et al., 2020) (**Figure 9B**). Terrigenous clastic input greatly increased and most of the previously constructed carbonates reefs were drowned (Wu et al., 2016; Makhankova et al., 2021; Ting et al., 2021).

Wind-driven currents no longer influenced the deep seafloor in the study area, but stratified water masses persistently occupied the intermediate and deep layers of the southern South China Sea after 9.6 Ma (Li et al., 2005; Jian et al., 2006). Although the proto-North Pacific waters (NPW) influenced the South China Sea in an anticyclonic pattern during this time interval (Yin et al., 2021), the water mass flowed at the surface layer and could not create contourite features at the deeper site in the southwest South China Sea (**Figure 9B**).

5.2.3 Modern stage (<5.3 Ma)

The modern stage (UI) started with the generation of the present-day contourite drifts (**Figure 10**) (Liu et al., 2021). The modern-like ocean circulation was initiated after the establishment of the modern morphology of the Luzon Strait (**Figure 9C**) (Tian et al., 2017). The DW enters the study area with a significant intensification in the velocity and generates numbers of contourite drifts and moats on the present-day seafloor (Liu et al., 2021).

5.3 Paleoceanographic implications

The evolution of the contourite depositional systems in the southwest South China Sea is compared with the contourite examples on other South China Sea margins (**Figure 11**). Changes in the South China Sea paleoceanography significantly influenced the sedimentary records along the water-mass pathways (**Figure 11**). The dominated bottom currents on sedimentary processes shifted from the monsoonal wind-driven currents to the NPW at 10.5 Ma and then the modern-like circulation system at 6.5-5.3 Ma (**Figure 9**).

The middle Miocene South China Sea was widely influenced by the monsoonal wind-driven currents (**Figure 9A**). The enhanced East Asian monsoon promoted surface currents (Farnsworth et al., 2019; Holbourn et al., 2021; Ting et al., 2021), which strongly shaped the morphology of the proto-continental shelves in the northern (Tian et al., 2015), the northwest (Zhuo

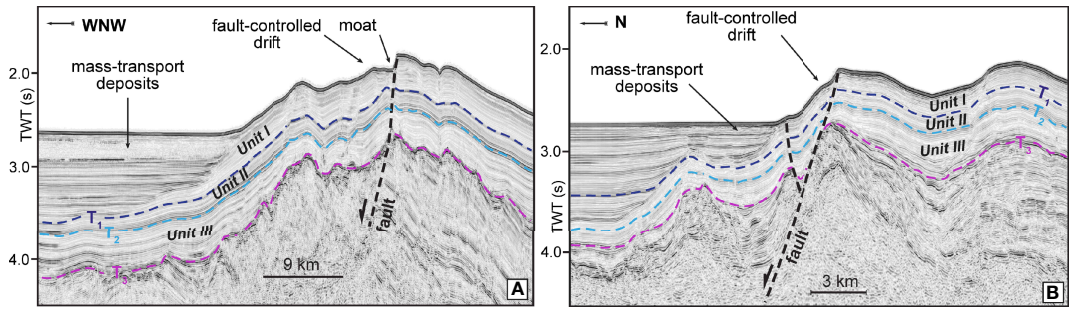

FIGURE 10
Seismic profiles and their interpretation, showing present-day fault-controlled contourite drifts (Liu et al., 2021) and mass-transport deposits (He et al., 2018) in the seismic unit I. The location of these seismic lines is displayed in **Figure 1B**. Discontinuities T_3 (16 Ma; purple dotted line), T_2 (10.5 Ma; light blue dotted line), and T_1 (5.3 Ma; dark blue dotted line) are indicated.

et al., 2014), and the southwest South China Sea. The related wind-driven currents created mounded contourite features in the Xisha region (Tian et al., 2015), the Zhongjian basin (Yang et al., 2021) and the study area (**Figure 11**). The development of these contourite features terminated at 10.5 Ma.

After 10.6 Ma, the latitudinal thermocline gradient firstly appeared in the South China Sea (Jian et al., 2006), coinciding with the intrusion of the proto-NPW (Yin et al., 2021). The monsoonal wind-driven currents only created contourite features on the proto-Sunda Shelf in the southwest South China Sea (Mathew et al., 2020), while the proto-NPW profoundly influenced the western (Yin et al., 2021) and northwest (Palamenghi et al., 2015), and northern margins (Wang et al., 2022) in the South China Sea during the Late Miocene (**Figure 9B**). The external shape of these contourite drifts varied from mounded (Palamenghi et al., 2015; Yin et al., 2021) to sheeted geometry (Wang et al., 2022) towards the distal site of the proto-NPW pathway. The proto-NPW would gradually lose the energy towards the northern South China Sea as the sheeted drifts are shaped by weak bottom currents (Faugères et al., 1999; Hernández-Molina et al., 2008; Rebesco et al., 2014).

Benthic foraminiferal $\delta^{18}O$ and $\delta^{13}C$ of ODP Sites 1143 and 1148 have indicated significant changes in the South China Sea paleoceanography at 6.5 Ma (**Figure 11**) (Li et al., 2006; Tian et al., 2017), coeval with the initial isolation of the South China Sea (Chen et al., 2015; Tian et al., 2017; Huang et al., 2018). The sandwich-like (inflow-outflow-inflow) water mass exchange was initiated through the Luzon Strait (Chen et al., 2015; Yin et al., 2021). The present-day anticyclonic IW (Tian et al., 2006) and cyclonic DW (Qu et al., 2006) were consequently formed in the South China Sea (**Figure 9C**), generating contourite depositional systems along IW and DW pathways from the latest Miocene onwards (**Figure 11**) (Palamenghi et al., 2015; Chen et al., 2016; Wang et al., 2018; Chen et al., 2019; Chen et al., 2021; Liu et al., 2021; Yin et al., 2021).

5.4 Economic implications

Shallow-water contourite drifts in UIII are served as a good gas reservoir in the study area. The fluid-escape pipe that is

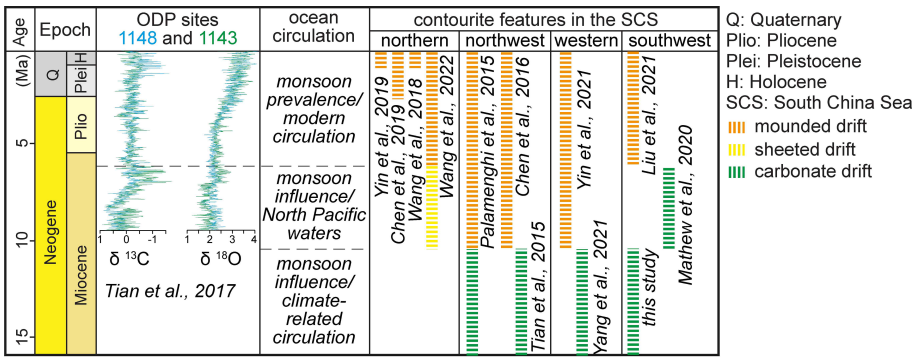

FIGURE 11
The formation time and distribution of contourite features in the South China Sea since the Middle Miocene. Dominated oceanic circulation and paleoceanography are indicated. The location of ODP sites 1148 and 1143 is shown in **Figure 9C**.

deeply rooted at the mounded drift 3 extended to the seafloor and formed a pockmark (**Figure 5C**). The core CL49 acquired at the pockmark shows intense methane leakage from the fluid-escape pipe (**Table 1**), indicating sufficient hydrocarbon fluid sources in the deep part of seismic units (Huang et al., 2022). Previous studies demonstrated that the deformed seismic unit below T_3 (in **Figure 5**) was the Eocene to Late Miocene source rocks (Zhang et al., 2017). They contained mixed Type II/III kerogen and potentially supplied 1.4855×10^{12} m^3 natural gas in the study area (Zhang et al., 2017; Lei et al., 2019; Tang et al., 2021). Therefore, natural gas was likely migrated upwards from the deformed unit *via* previously documented faults (**Figure 3C**) (e.g., Lei et al., 2019; Luo et al., 2020) and then reserved in buried contourite drifts in UIII.

The true lithology of these shallow-water contourite drifts in UIII is unknown because of the limited dataset. However, they were most likely coarse-grained and poorly sorted. Shallow-water contourite drifts in UIII were generated in adjacent or associated with carbonate reefs in the study area (**Figure 7**). Such contourite deposits are directly sourced from the adjacent reefs and composed of coarse-grained carbonate sands (Lüdmann et al., 2013; Chabaud et al., 2016; Eberli and Betzler, 2019). Coarse-grained carbonate drifts are potential hydrocarbon reservoirs because of their high porosity, high permeability, and effective lateral and vertical transmissibility of fluids (Viana, 2008). Similar examples were observed in the eastern Gulf of Cádiz (León et al., 2014), the western Alborán Sea (Somoza et al., 2012; León et al., 2014), and the mid-Norwegian margin (Hustoft et al., 2010; Plaza-Faverola et al., 2010), where fluid flow escaped from the coarse-grained contourite layers and caused natural gas leakage. Similarities between these contourite examples indicate the great economic potential of the Middle Miocene carbonate contourite drifts in the southwest South China Sea.

TABLE 1 Hydrocarbon components and carbon isotope values of the methane in core CL49 (Huang et al., 2022).

Interval(mbsf)	Methane (ppm)	Propane (ppm)	C_1/C_{2+} ratio
0.5–0.6	23.9	0.45	23.7
1.1-1.2	23.0	0.38	60.5
1.7-1.8	24.2	0.41	59.0
2.3-2.4	22.4	0.36	62.2
2.9-3.0	22.9	0.52	11.3
3.5-3.6	21.7	0.34	63.8
4.1-4.2	21.6	0.52	17.9
4.7-4.8	22.8	0.41	25.9
5.3-5.4	19.1	0.23	83.0
5.9-6.0	22.6	–	–
6.5-6.6	1298	–	–
7.1-7.2	1249	–	–

6 Conclusion

This study demonstrates the previously undocumented occurrence of carbonate contourite drifts in the southwest South China Sea. Analysis of seismic reflection data and previously established chronology allows the identification of the Middle Miocene contourite depositional system. The distribution, characteristics, and evolution of the contourite features have significant sedimentary, paleoceanographic, and economic implications:

- Three evolutionary phases are identified for the contourite drifts' construction: I) a carbonate drift stage (16-10.5 Ma) where six carbonate contourite drifts were built by the monsoonal wind-driven currents; II) a burial stage (10.5-5.3 Ma) where contourite features became inactive and were buried by younger deposits; and III) a modern stage from the 5.3 Ma till the present-day, characterized by the modern contourite features associated with the South China Sea Deep Water;
- The dominated bottom currents in the South China Sea shifted from the monsoonal wind-driven currents to the North Pacific waters at 10.5 Ma and then the modern circulation system at 6.5-5.3 Ma. The paleoceanographic changes significantly influenced the sedimentary records along the water-mass pathways in the South China Sea.
- Shallow-water carbonate contourite drifts are good gas reservoirs. They were generated in adjacent or associated with carbonate reefs during the Middle Miocene. The drifts were possibly composed of coarse-grained carbonate sands. Fluid flow escaped from the coarse-grained contourite layers and caused intense methane leakage on the seafloor.

Data availability statement

The oceanographic data of this study are available in the World Ocean Database (2013)(https://www.nodc.noaa.gov/OC5/WOD13). Seismic profiles and bathymetric data acquired by the China Geological Survey are not publicly available due to privacy or ethical restrictions. Requests to access these datasets should be directed to ZLe, 44231234@qq.com.

Author contributions

SL wrote the manuscript and interpreted all the datasets. MS, Zli, and BZ interpreted the bathymetry data and seismic profiles. ZLe was involved in the acquisition and processing of the seismic profiles. HS took part in the geomorphological interpretation. All authors contributed to the article and approved the submitted version.

Funding

This study was supported by the China Postdoctoral Science Foundation (NO. 2020TQ0369 and NO. 2021M703668). This study was carried out within the framework of the Geological Investigation Programs (No. DD20160155) of the China Geological Survey. The study was also supported by Southern Marine Science and Engineering Guangdong Laboratory (Zhuhai) (No. SML2021SP307).

Acknowledgments

The authors wish to thank all crews and scientific researchers participated in the R/V Tanbao cruise in 1996, 2009, and 2013 during the acquisition of bathymetric and seismic datasets. The authors also thanks Dr. Haiteng Zhuo and Dr. Qin Yongpeng for their valuable suggestions, which have greatly improved this manuscript.

Conflict of interest

The authors declare that the research was conducted in the absence of any commercial or financial relationships that could be construed as a potential conflict of interest.

Publisher's note

All claims expressed in this article are solely those of the authors and do not necessarily represent those of their affiliated organizations, or those of the publisher, the editors and the reviewers. Any product that may be evaluated in this article, or claim that may be made by its manufacturer, is not guaranteed or endorsed by the publisher.

References

Amir Hassan, M. H., Johnson, H. D., Allison, P. A. and Abdullah, W. H. (2017). *Sedimentology and stratigraphic architecture of a Miocene retrogradational, tide-dominated delta system: Balingian province, offshore Sarawak, Malaysia* Vol. 444 (London: Geological Society), 215. Special Publications. doi: 10.1144/SP444.12

Banerjee, A. and Ahmed Salim, A. M. (2021). Stratigraphic evolution of deep-water dangerous grounds in the south China Sea, NW sabah platform region, Malaysia. *J. Petroleum Sci. Eng.* 201, 108434. doi: 10.1016/j.petrol.2021.108434

Barckhausen, U. and Roeser, H. A. (2004). "Seafloor spreading anomalies in the south China Sea revisited," in *Continent-ocean interactions within East Asian marginal seas*, eds. P. Clift, W. Kuhnt, P. Wang, and D. Hayes (Washington DC, USA: American Geophysical Union), 121–125.

Betzler, C., Eberli, G. P., Kroon, D., Wright, J. D., Swart, P. K., Nath, B. N., et al. (2016). The abrupt onset of the modern south Asian monsoon winds. *Sci. Rep.* 6 (1), 29838. doi: 10.1038/srep29838

Betzler, C., Eberli, G. P., Lüdmann, T., Reolid, J., Kroon, D., Reijmer, J. J. G., et al. (2018). Refinement of Miocene sea level and monsoon events from the sedimentary archive of the Maldives (Indian ocean). *Prog. Earth Planetary Sci.* 5 (1), 5. doi: 10.1186/s40645-018-0165-x

Betzler, C., Lindhorst, S., Eberli, G. P., Lüdmann, T., Möbius, J., Ludwig, J., et al. (2014). Periplatform drift: The combined result of contour current and off-bank transport along carbonate platforms. *Geology* 42 (10), 871–874. doi: 10.1130/g35900.1

Boyer, T. P., Antonov, J. I., Baranova, O. K., Garcia, H. E., Johnson, D. R., Mishonov, A. V., et al. (2013). *World ocean database 2013*. doi: 10.7289/V5NZ85MT

Burgess, P. M., Winefield, P., Minzoni, M. and Elders, C. (2013). *Methods for identification of isolated carbonate buildups from seismic reflection data.* Am Assoc Pet Geol Bul. (AAPG Bulletin), 97 1071–1098. doi: 10.1306/12051212011

Catuneanu, O., Abreu, V., Bhattacharya, J. P., Blum, M. D., Dalrymple, R. W., Eriksson, P. G., et al. (2009). Towards the standardization of sequence stratigraphy. *Earth-Science Rev.* 92 (1), 1–33. doi: 10.1016/j.earscirev.2008.10.003

Ceramicola, S., Rebesco, M., De Batist, M. and Khlystov, O. (2001). Seismic evidence of small-scale lacustrine drifts in lake baikal (Russia). *Mar. Geophysical Res.* 22 (5), 445–464. doi: 10.1023/a:1016351700435

Chabaud, L., Ducassou, E., Tournadour, E., Mulder, T., Reijmer, J. J. G., Conesa, G., et al. (2016). Sedimentary processes determining the modern carbonate periplatform drift of little bahama bank. *Mar. Geology* 378, 213–229. doi: 10.1016/j.margeo.2015.11.006

Chang, S.-P., Pubellier, M., Delescluse, M., Qiu, Y., Nirrengarten, M., Mohn, G., et al. (2022). Crustal architecture and evolution of the southwestern south China Sea: Implications to continental breakup. *Mar. Petroleum Geology* 136, 105450. doi: 10.1016/j.marpetgeo.2021.105450

Chen, W.-H., Huang, C.-Y., Lin, Y.-J., Zhao, Q., Yan, Y., Chen, D., et al. (2015). Depleted deep south China Sea δ13C paleoceanographic events in response to tectonic evolution in Taiwan–Luzon strait since middle Miocene. *Deep Sea Res. Part II: Topical Stud. Oceanography* 122, 195–225. doi: 10.1016/j.dsr2.2015.02.005

Chen, H., Xie, X., Zhang, W., Shu, Y., Wang, D., Vandorpe, T., et al. (2016). Deep-water sedimentary systems and their relationship with bottom currents at the intersection of xisha trough and Northwest Sub-basin, south China Sea. *Mar. Geology* 378, 101–113. doi: 10.1016/j.margeo.2015.11.002

Chen, H., Zhang, W., Xie, X., Gao, Y., Liu, S., Ren, J., et al. (2021). Linking oceanographic processes to contourite features: Numerical modelling of currents influencing a contourite depositional system on the northern south China Sea margin. *Mar. Geology* 444, 106714. doi: 10.1016/j.margeo.2021.106714

Chen, H., Zhang, W., Xie, X. and Ren, J. (2019). Sediment dynamics driven by contour currents and mesoscale eddies along continental slope: A case study of the northern south China Sea. *Mar. Geology* 409, 48–66. doi: 10.1016/j.margeo.2018.12.012

Cimino, M. A., Santora, J. A., Schroeder, I., Sydeman, W., Jacox, M. G., Hazen, E. L., et al. (2020). Essential krill species habitat resolved by seasonal upwelling and ocean circulation models within the large marine ecosystem of the California current system. *Ecography* 43 (10), 1536–1549. doi: 10.1111/ecog.05204

Collins, D. S., Avdis, A., Allison, P. A., Johnson, H. D., Hill, J. and Piggott, M. D. (2018). Controls on tidal sedimentation and preservation: Insights from numerical tidal modelling in the late oligocene–Miocene south China Sea, southeast Asia. *Sedimentology* 65 (7), 2468–2505. doi: 10.1111/sed.12474

Collins, D. S., Avdis, A., Allison, P. A., Johnson, H. D., Hill, J., Piggott, M. D., et al. (2017). Tidal dynamics and mangrove carbon sequestration during the oligo–Miocene in the south China Sea. *Nat. Commun.* 8 (1), 15698. doi: 10.1038/ncomms15698

Cullen, A. B. (2010). Transverse segmentation of the baram-balabac basin, NW Borneo: refining the model of borneos tectonic evolution. *Petroleum Geosci.* 16 (1), 3. doi: 10.1144/1354-079309-828

de Castro, S., Hernández-Molina, F. J., de Weger, W., Jiménez-Espejo, F. J., Rodríguez-Tovar, F. J., Mena, A., et al. (2021). Contourite characterization and its discrimination from other deep-water deposits in the gulf of cadiz contourite depositional system. *Sedimentology* 68 (3), 987–1027. doi: 10.1111/sed.12813

de Weger, W., Hernández-Molina, F. J., Flecker, R., Sierro, F. J., Chiarella, D., Krijgsman, W., et al. (2020). Late Miocene contourite channel system reveals intermittent overflow behavior. *Geology* 48 (12), 1194–1199. doi: 10.1130/G47944.1

Ding, W., Franke, D., Li, J. and Steuer, S. (2013). Seismic stratigraphy and tectonic structure from a composite multi-channel seismic profile across the entire dangerous grounds, south China Sea. *Tectonophysics* 582, 162–176. doi: 10.1016/j.tecto.2012.09.026

Eberli, G. P. and Betzler, C. (2019). Characteristics of modern carbonate contourite drifts. *Sedimentology* 66 (4), 1163–1191. doi: 10.1111/sed.12584

Farnsworth, A., Lunt Daniel, J., Robinson Stuart, A., Valdes Paul, J., Roberts William, H. G., Clift Peter, D., et al. (2019). *Past East Asian monsoon evolution controlled by paleogeography, not CO2* (eaax1697: Science Advances 5(10). doi: 10.1126/sciadv.aax1697

Faugères, J. C. and Stow, D. A. V. (2008). "Chapter 14 contourite drifts: Nature, evolution and controls," in *Developments in sedimentology*, vol. 257-288 . Eds. Rebesco, M. and Camerlenghi, A. (Amsterdam, NL: Elsevier).

Faugères, J.-C., Stow, D. A. V., Imbert, P. and Viana, A. (1999). Seismic features diagnostic of contourite drifts. *Mar. Geology* 162 (1), 1–38. doi: 10.1016/S0025-3227(99)00068-7

García, M., Lobo, F. J., Maldonado, A., Hernández-Molina, F. J., Bohoyo, F. and Pérez, L. F. (2016). High-resolution seismic stratigraphy and morphology of the scan basin contourite fan, southern Scotia Sea, Antarctica. *Mar. Geology* 378, 361–373. doi: 10.1016/j.margeo.2016.01.011

Gordon, A. L., Giulivi, C. F. and Ilahude, A. G. (2003). Deep topographic barriers within the Indonesian seas. *Deep Sea Res. Part II: Topical Stud. Oceanography* 50 (12), 2205–2228. doi: 10.1016/S0967-0645(03)00053-5

Hall, R. (2002). Cenozoic Geological and plate tectonic evolution of SE Asia and the SW pacific: computer-based reconstructions, model and animations. *J. Asian Earth Sci.* 20 (4), 353–431. doi: 10.1016/S1367-9120(01)00069-4

Hanebuth, T. J. J., Zhang, W., Hofmann, A. L., Lowemark, L. A. and Schwenk, T. (2015). Oceanic density fronts steering bottom-current induced sedimentation deduced from a 50 ka contourite-drift record and numerical modeling (off NW Spain). *Quaternary Sci. Rev.* 112, 207–225. doi: 10.1016/j.quascirev.2015.01.027

Heezen, B. C. and Hollister, C. (1964). Deep-sea current evidence from abyssal sediments. *Mar. Geology* 1 (2), 141–174. doi: 10.1016/0025-3227(64)90012-X

Heezen, B. C., Hollister, C. D. and Ruddiman, W. F. (1966). Shaping of the continental rise by deep geostrophic contour currents. *Science* 152(3721), 502. doi: 10.1126/science.152.3721.502

He, Y., Kuang, Z. and Xu, M. (2018) Seismic reflection characteristics and triggering mechanism of mass transport deposits of Quaternary in Beikang Basin, Geological Science and Technology Information. 37 (4), 258–268. doi: 10.19509/j.cnki.dzkq.2018.0435.

Hendry, J., Burgess, P., Hunt, D., Janson, X. and Zampetti, V. (2021). *Seismic characterization of carbonate platforms and reservoirs: an introduction and review* Vol. 509 (London: Geological Society), 1. Special Publications. doi: 10.1144/SP509-2021-51

Hernández-Molina, F. J., Campbell, S., Badalini, G., Thompson, P., Walker, R., Soto, M., et al. (2017). Large Bedforms on contourite terraces: Sedimentary and conceptual implications. *Geology* 46 (1), 27–30. doi: 10.1130/G39655.1

Hernández-Molina, F. J., Llave, E. and Stow, D. A. V. (2008). Chapter 19 Continental Slope Contourites," in *Developments Sedimentology*, eds. M. Rebesco and A. Camerlenghi. (Amsterdam, NL: Elsevier), 379–408. doi: 10.1016/S0070-4571(08)10019-X

Hernández-Molina, F. J., Sierro, F. J., Llave, E., Roque, C., Stow, D. A. V., Williams, T., et al. (2016). Evolution of the gulf of cadiz margin and southwest Portugal contourite depositional system: Tectonic, sedimentary and paleoceanographic implications from IODP expedition 339. *Mar. Geology* 377, 7–39. doi: 10.1016/j.margeo.2015.09.013

Holbourn, A., Kuhnt, W., Clemens, S. C. and Heslop, D. (2021). A ~12 myr Miocene record of East Asian monsoon variability from the south China Sea. *Paleoceanography Paleoclimatology* 36 (7), e2021PA004267. doi: 10.1029/2021PA004267

Howe, J. A., Stoker, M. S., Masson, D. G., Pudsey, C. J., Morris, P., Larter, R. D., et al. (2006). Seabed morphology and the bottom-current pathways around rosemary bank seamount, northern rockall trough, north Atlantic. *Mar. Petroleum Geology* 23 (2), 165–181. doi: 10.1016/j.marpetgeo.2005.08.003

Huang, C.-Y., Chen, W.-H., Wang, M.-H., Lin, C.-T., Yang, S., Li, X., et al. (2018). Juxtaposed sequence stratigraphy, temporal-spatial variations of sedimentation and development of modern-forming forearc lichi mélange in north Luzon trough forearc basin onshore and offshore eastern Taiwan: An overview. *Earth-Science Rev.* 182, 102–140. doi: 10.1016/j.earscirev.2018.01.015

Huang, W., Meng, M., Zhang, W., Shang, J., Liang, J., Wan, Z., et al. (2022). Geological, geophysical, and geochemical characteristics of deep-routed fluid seepage and its indication of gas hydrate occurrence in the beikang basin, southern south China Sea. *Mar. Petroleum Geology* 139, 105610. doi: 10.1016/j.marpetgeo.2022.105610

Hustoft, S., Bünz, S. and Mienert, J. (2010). Three-dimensional seismic analysis of the morphology and spatial distribution of chimneys beneath the nyegga pockmark field, offshore mid-Norway. *Basin Res.* 22 (4), 465–480. doi: 10.1111/j.1365-2117.2010.00486.x

Hutchison, C. S. (2004). Marginal basin evolution: the southern south China Sea. *Mar. Petroleum Geology* 21 (9), 1129–1148. doi: 10.1016/j.marpetgeo.2004.07.002

Jian, Z., Yu, Y., Li, B., Wang, J., Zhang, X. and Zhou, Z. (2006). Phased evolution of the south–north hydrographic gradient in the south China Sea since the middle Miocene. *Palaeogeography Palaeoclimatology Palaeoecol.* 230 (3), 251–263. doi: 10.1016/j.palaeo.2005.07.018

Kane, I. A. and Clare, M. A. (2019). Dispersion, accumulation, and the ultimate fate of microplastics in deep-marine environments: A review and future directions. *Front. Earth Sci.* 7 (80). doi: 10.3389/feart.2019.00080

Kender, S., Bogus, K. A., Cobb, T. D. and Thomas, D. J. (2018). Neodymium evidence for increased circumpolar deep water flow to the north pacific during the middle Miocene climate transition. *Paleoceanography Paleoclimatology* 33 (7), 672–682. doi: 10.1029/2017PA003309

Kirby, A., Hernández-Molina, F. J., Rodriguez, P. and Conti, B. (2021). Sedimentary stacking pattern of plastered drifts: An example from the Cenozoic on the Uruguayan continental slope. *Mar. Geology* 440, 106567. doi: 10.1016/j.margeo.2021.106567

Koša, E. (2015). Sea-Level changes, shoreline journeys, and the seismic stratigraphy of central luconia, Miocene-present, offshore Sarawak, NW Borneo. *Mar. Petroleum Geology* 59, 35–55. doi: 10.1016/j.marpetgeo.2014.07.005

Lei, Z.-y., Zhang, L., Su, M. and Qian, X. (2019). Types, characteristics and implication for hydrocarbon exploration of the middle Miocene deep-water sediments in beikang basin, southern south China Sea. *China Geology* 2 (1), 85–93. doi: 10.31035/cg2018094

León, R., Somoza, L., Medialdea, T., González, F. J., Gimenez-Moreno, C. J. and Pérez-López, R. (2014). Pockmarks on either side of the strait of Gibraltar: formation from overpressured shallow contourite gas reservoirs and internal wave action during the last glacial sea-level lowstand? *Geo-Marine Lett.* 34 (2), 131–151. doi: 10.1007/s00367-014-0358-2

Li, B., Jian, Z., Li, Q., Tian, J. and Wang, P. (2005). Paleoceanography of the south China Sea since the middle Miocene: evidence from planktonic foraminifera. *Mar. Micropaleontology* 54 (1), 49–62. doi: 10.1016/j.marmicro.2004.09.003

Liu, S., Hernández-Molina, F. J., Lei, Z., Duarte, D., Chen, H., Wang, C., et al. (2021). Fault-controlled contourite drifts in the southern south China Sea: Tectonic, oceanographic, and conceptual implications. *Mar. Geology* 433, 106420. doi: 10.1016/j.margeo.2021.106420

Liu, H.-l., Yan, P., Zhang, B.-y., Sun, Y., Zhang, Y.-x., Shu, L.-s., et al. (2004). Role of the wan-Na fault system in the western nansha islands (Southern south China Sea). *J. Asian Earth Sci.* 23 (2), 221–233. doi: 10.1016/S1367-9120(03)00121-4

Li, Q., Wang, P., Zhao, Q., Shao, L., Zhong, G., Tian, J., et al. (2006). A 33 ma lithostratigraphic record of tectonic and paleoceanographic evolution of the south China Sea. *Mar. Geology* 230 (3), 217–235. doi: 10.1016/j.margeo.2006.05.006

Li, G., Xu, W., Luo, Y., Liu, J., Zhao, J., Feng, Y., et al. (2022). *Strontium isotope stratigraphy and LA-ICP-MS U-Pb carbonate age constraints on the Cenozoic tectonic evolution of the southern south China Sea* (Geol Soc Am Bull). doi: 10.1130/b36365.1

Llave, E., Hernández-Molina, F. J., Stow, D. A. V., Fernández-Puga, M. C., García, M., Vázquez, J. T., et al. (2007). Reconstructions of the Mediterranean outflow water during the quaternary based on the study of changes in buried mounded drift stacking pattern in the gulf of cadiz. *Mar. Geophysical Res.* 28 (4), 379–394. doi: 10.1007/s11001-007-9040-7

Loeb, V., Hofmann, E. E., Klinck, J. M. and Holm-Hansen, O. (2010). Hydrographic control of the marine ecosystem in the south Shetland-elephant island and bransfield strait region. *Deep Sea Res. Part II: Topical Stud. Oceanography* 57 (7), 519–542. doi: 10.1016/j.dsr2.2009.10.004

Lüdmann, T., Kalvelage, C., Betzler, C., Fürstenau, J. and Hübscher, C. (2013). The Maldives, a giant isolated carbonate platform dominated by bottom currents. *Mar. Petroleum Geology* 43, 326–340. doi: 10.1016/j.marpetgeo.2013.01.004

Luo, S., Wang, X., Zhang, L., Lei, Z. and Shuai, Q. (2020). Study of high-quality sandstone in early Miocene sequence of beikang-zengmu basin, the southern south China Sea. *Mar. Geology Quaternary Geology* 40 (2), 111–123. doi: 10.16562/j.cnki.0256-1492.2018122601

Madon, M., Kim, C. L. and Wong, R. (2013). The structure and stratigraphy of deepwater Sarawak, Malaysia: Implications for tectonic evolution. *J. Asian Earth Sci.* 76, 312–333. doi: 10.1016/j.jseaes.2013.04.040

Magee, C., Hunt-Stewart, E. and Jackson, C. A. L. (2013). Volcano growth mechanisms and the role of sub-volcanic intrusions: Insights from 2D seismic reflection data. *Earth Planetary Sci. Lett.* 373, 41–53. doi: 10.1016/j.epsl.2013.04.041

Makhankova, A., Sautter, B., Mathew, M., Menier, D. and Poppelreiter, M. (2021). Seismic stratigraphy and sedimentology of a Miocene carbonate platform in luconia, south China Sea. *Geological J.* 56 (1), 1–17. doi: 10.1002/gj.3942

Martin, J., Lusher, A., Thompson, R. C. and Morley, A. (2017). The deposition and accumulation of microplastics in marine sediments and bottom water from the Irish continental shelf. *Sci. Rep.* 7 (1), 10772. doi: 10.1038/s41598-017-11079-2

Mathew, M., Makhankova, A., Menier, D., Sautter, B., Betzler, C. and Pierson, B. (2020). The emergence of Miocene reefs in south China Sea and its resilient adaptability under varying eustatic, climatic and oceanographic conditions. *Sci. Rep.* 10 (1), 7141. doi: 10.1038/s41598-020-64119-9

Morley, C. K. (2002). A tectonic model for the tertiary evolution of strike–slip faults and rift basins in SE Asia. *Tectonophysics* 347 (4), 189–215. doi: 10.1016/S0040-1951(02)00061-6

Morley, C. K. (2016). Major unconformities/termination of extension events and associated surfaces in the south China seas: Review and implications for tectonic development. *J. Asian Earth Sci.* 120, 62–86. doi: 10.1016/j.jseaes.2016.01.013

Mulder, T., Ducassou, E., Hanquiez, V., Principaud, M., Fauquembergue, K., Tournadour, E., et al. (2019). Contour current imprints and contourite drifts in the Bahamian archipelago. *Sedimentology* 66 (4), 1192–1221. doi: 10.1111/sed.12587

Nathan, S. A. and Leckie, R. M. (2009). Early history of the Western pacific warm pool during the middle to late Miocene (~13.2–5.8 ma): Role of sea-level change and implications for equatorial circulation. *Palaeogeography Palaeoclimatology Palaeoecol.* 274 (3), 140–159. doi: 10.1016/j.palaeo.2009.01.007

Ng, Z. L., Hernández-Molina, F. J., Duarte, D., Roque, C., Sierro, F. J., Llave, E., et al. (2021). Late Miocene contourite depositional system of the gulf of cádiz: The sedimentary signature of the paleo-Mediterranean outflow water. *Mar. Geology* 442, 106605. doi: 10.1016/j.margeo.2021.106605

Nishida, N., Itaki, T., Amano, A., Katayama, H., Sato, T., Stow, D., et al. (2022). Anatomy and dynamics of a mixed contourite sand sheet, Ryukyu island arc, northwestern pacific ocean. *Mar. Geology* 444, 106707. doi: 10.1016/j.margeo.2021.106707

Palamenghi, L., Keil, H. and Spiess, V. (2015). Sequence stratigraphic framework of a mixed turbidite-contourite depositional system along the NW slope of the south China Sea. *Geo-Marine Lett.* 35 (1), 1–21. doi: 10.1007/s00367-014-0385-z

Pepe, F., Di Donato, V., Insinga, D., Molisso, F., Faraci, C., Sacchi, M., et al. (2018). Seismic stratigraphy of upper quaternary shallow-water contourite drifts in the gulf of taranto (Ionian Sea, southern Italy). *Mar. Geology* 397, 79–92. doi: 10.1016/j.margeo.2017.12.004

Pérez, L. F., Hernández-Molina, F. J., Lodolo, E., Bohoyo, F., Galindo-Zaldívar, J. and Maldonado, A. (2019). Oceanographic and climatic consequences of the tectonic evolution of the southern scotia sea basins, Antarctica. *Earth-Science Rev.* 198, 102922. doi: 10.1016/j.earscirev.2019.102922

Plaza-Faverola, A., Bünz, S. and Mienert, J. (2010). Fluid distributions inferred from p-wave velocity and reflection seismic amplitude anomalies beneath the nyegga pockmark field of the mid-Norwegian margin. *Mar. Petroleum Geology* 27 (1), 46–60. doi: 10.1016/j.marpetgeo.2009.07.007

Qu, T., Girton, J. B. and Whitehead, J. A. (2006). Deepwater overflow through Luzon strait. *J. Geophysical Research: Oceans* 111, C01002. doi: 10.1029/2005JC003139

Qu, T., Song, Y. T. and Yamagata, T. (2009). An introduction to the south China Sea throughflow: Its dynamics, variability, and application for climate. *Dynamics Atmospheres Oceans* 47 (1), 3–14. doi: 10.1016/j.dynatmoce.2008.05.001

Rebesco, M., Hernández-Molina, F. J., Van Rooij, D. and Wåhlin, A. (2014). Contourites and associated sediments controlled by deep-water circulation processes: State-of-the-art and future considerations. *Mar. Geology* 352, 111–154. doi: 10.1016/j.margeo.2014.03.011

Rodrigues, S., Hernández-Molina, F. J., Hillenbrand, C. D., Lucchi, R. G., Rodríguez-Tovar, F. J., Rebesco, M., et al. (2022). Recognizing key sedimentary facies and their distribution in mixed turbidite–contourite depositional systems: The case of the pacific margin of the Antarctic peninsula. *Sedimentology*. 69,1953–1991. doi: 10.1111/sed.12978

Roque, C., Duarte, H., Terrinha, P., Valadares, V., Noiva, J., Cachão, M., et al. (2012). Pliocene and quaternary depositional model of the Algarve margin contourite drifts (Gulf of cadiz, SW iberia): Seismic architecture, tectonic control and paleoceanographic insights. *Mar. Geology* 303–306, 42–62. doi: 10.1016/j.margeo.2011.11.001

Sibuet, J.-C., Yeh, Y.-C. and Lee, C.-S. (2016). Geodynamics of the south China Sea. *Tectonophysics* 692, 98–119. doi: 10.1016/j.tecto.2016.02.022

Somoza, L., Medialdea, T., León, R., Ercilla, G., Vázquez, J. T., Farran, M.l., et al. (2012). Structure of mud volcano systems and pockmarks in the region of the ceuta contourite depositional system (Western alborán Sea). *Mar. Geology* 332–334, 4–26. doi: 10.1016/j.margeo.2012.06.002

Steuer, S., Franke, D., Meresse, F., Savva, D., Pubellier, M. and Auxietre, J.-L. (2014). Oligocene–Miocene carbonates and their role for constraining the rifting and collision history of the dangerous grounds, south China Sea. *Mar. Petroleum Geology* 58, 644–657. doi: 10.1016/j.marpetgeo.2013.12.010

Tang, W., Zhao, Z., Song, S., Wang, Y., Xie, X. and Liu, S. (2021).). differences in the tectonic evolution of basins in the central-southern south China Sea and their hydrocarbon accumulation conditions. *Acta Geologica Sin. - English Edition* 95 (1), 30–40. doi: 10.1111/1755-6724.14638

Thran, A. C., Dutkiewicz, A., Spence, P. and Müller, R. D. (2018). Controls on the global distribution of contourite drifts: Insights from an eddy-resolving ocean model. *Earth Planetary Sci. Lett.* 489, 228–240. doi: 10.1016/j.epsl.2018.02.044

Tian, J., Ma, X., Zhou, J. and Wang, W. (2017). Subsidence of the northern south China Sea and formation of the bashi strait in the latest Miocene: Paleoceanographic evidences from 9-myr high resolution benthic foraminiferal δ18O and δ13C records. *Palaeogeography Palaeoclimatology Palaeoecol.* 466, 382–391. doi: 10.1016/j.palaeo.2016.11.041

Tian, J., Wu, S., Lv, F., Wang, D., Wang, B., Zhang, X., et al. (2015). Middle Miocene mound-shaped sediment packages on the slope of the xisha carbonate platforms, south China Sea: Combined result of gravity flow and bottom current. *Deep Sea Res. Part II: Topical Stud. Oceanography* 122, 172–184. doi: 10.1016/j.dsr2.2015.06.016

Tian, J., Yang, Q., Liang, X., Xie, L., Hu, D., Wang, F., et al. (2006). *Observation of Luzon strait transport* (Geophysical Research Letters 33 (19). doi: 10.1029/2006GL026272

Ting, K. K., Tan, Y. E., Chiew, E., Lee, E. L., Azudin, A. N. and Ishak, N. A. (2021). *Assessing controls on isolated carbonate platform development in central luconia, NW Borneo, from a regional 3D seismic facies and geomorphology investigation* Vol. 509 (London: Geological Society), 29. Special Publications. doi: 10.1144/SP509-2019-89

Vahrenkamp, V. C., David, F., Duijndam, P., Newall, M. and Crevello, P. (2004). "Growth architecture, faulting, and karstification of a middle Miocene carbonate platform, luconia province, offshore Sarawak, malaysia", in *Seismic imaging of carbonate reservoirs and systems*. Eds. Eberli, G. P., Masaferro, J. L. and Sarg, J. F. R. (American Association of Petroleum Geologists).

Vandorpe, T. P., Van Rooij, D., Stow, D. A. V. and Henriet, J.-P. (2011). Pliocene to recent shallow-water contourite deposits on the shelf and shelf edge off south-western mallorca, Spain. *Geo-Marine Lett.* 31 (5), 391–403. doi: 10.1007/s00367-011-0248-9

Verdicchio, G. and Trincardi, F. (2008). "Chapter 20 shallow-water contourites," in *Developments in sedimentology*. Eds. Rebesco, M. and Camerlenghi, A. (Amsterdam, NL: Elsevier), 409–433.

Viana, A. R. (2008). "Chapter 23 economic relevance of contourites," in *Developments in sedimentology*. Eds. Rebesco, M. and Camerlenghi, A. (Amsterdam, NL: Elsevier), 491–510.

Wagner, B., Aufgebauer, A., Vogel, H., Zanchetta, G., Sulpizio, R. and Damaschke, M. (2012). Late pleistocene and Holocene contourite drift in lake prespa (Albania/F.Y.R. @ of Macedonia/Greece). *Quaternary Int.* 274, 112–121. doi: 10.1016/j.quaint.2012.02.016

Wang, X., Cai, F., Sun, Z., Li, Q., Li, A., Sun, Y., et al. (2022). *Late Miocene–quaternary seismic stratigraphic responses to tectonic and climatic changes at the northeastern margin of the south China Sea* (Geol Soc Am Bull.). doi: 10.1130/B36224.1

Wang, X., Zhuo, H., Wang, Y., Mao, P., He, M., Chen, W., et al. (2018). Controls of contour currents on intra-canyon mixed sedimentary processes: Insights from the pearl river canyon, northern south China Sea. *Mar. Geology* 406, 193–213. doi: 10.1016/j.margeo.2018.09.016

World Ocean Database. (2013). Available at: https://www.nodc.noaa.gov/OC5/WOD13 [Accessed April 17, 2022].

Wu, S., Zhang, X., Yang, Z., Wu, T., Gao, J. and Wang, D. (2016). Spatial and temporal evolution of Cenozoic carbonate platforms on the continental margins of the south China Sea: Response to opening of the ocean basin. *Interpretation* 4 (3), SP1–SP19. doi: 10.1190/INT-2015-0162.1

Yang, Z., Li, X., Huang, L., Wang, L., Wu, S. and Zhang, X. (2021). Development of the Miocene guangle carbonate platform in the south China Sea: Architecture and controlling factors. *Acta Geologica Sin. - English Edition* 95 (1), 177–191. doi: 10.1111/1755-6724.14639

Yan, Q., Shi, X., Wang, K., Bu, W. and Xiao, L. (2008). *Major element, trace element and Sr, Nd and Pb isotope studies of Cenozoic basalts from the south China Sea*, Sci. China D Earth. (4),51. 550–566. doi: 10.1007/s11430-008-0026-3

Yan, W., Zhang, G., Xia, B., Zhang, L., Yang, Z., Lei, Z., et al. (2020). Seismic characteristics and development patterns of Miocene carbonate platform in the beikang basin, southern south China Sea. *Acta Geologica Sin. - English Edition* 94 (5), 1651–1661. doi: 10.1111/1755-6724.14399

Yan, W., Zhang, G., Zhang, L., Xia, B., Yang, Z., Lei, Z., et al. (2018). Seismic responses and distribution characteristics of the Miocene carbonate platforms in the beikang basin of southern south China Sea. *Mar. Geology Quaternary Geology* 38 (6), 118–126. doi: 10.16562/j.cnki.0256-1492.2018.06.012

Yin, S., Hernández-Molina, F. J., Lin, L., Chen, J., Ding, W. and Li, J. (2021). Isolation of the south China Sea from the north pacific subtropical gyre since the latest Miocene due to formation of the Luzon strait. *Sci. Rep.* 11 (1), 1562. doi: 10.1038/s41598-020-79941-4

Yin, S., Hernández-Molina, F. J., Miramontes, E., Shen, Z., Yang, C., Gao, J., et al. (2022). Sequential bedform development in mixed turbidite–contourite systems: An example from the cosmonaut Sea, East Antarctica. *Geomorphology* 410, 108287. doi: 10.1016/j.geomorph.2022.108287

Yin, S., Hernández-Molina, F. J., Zhang, W., Li, J., Wang, L., Ding, W., et al. (2019). The influence of oceanographic processes on contourite features: A multidisciplinary study of the northern south China Sea. *Mar. Geology* 415, 105967. doi: 10.1016/j.margeo.2019.105967

Zhang, H., Shao, L., Zhang, G., Cui, Y., Zhao, Z. and Hou, Y. (2020). The response of Cenozoic sedimentary evolution coupled with the formation of the south China Sea. *Geological J.* 55 (10), 6989–7010. doi: 10.1002/gj.3856

Zhang, G., Tang, W., Xie, X., Zhao, Z. and Zhao, Z. (2017). Petroleum geological characteristics of two basin belts in southern continental margin in south China Sea. *Petroleum Explor. Dev.* 44 (6), 899–910. doi: 10.1016/S1876-3804(17)30102-7

Zhou, C., Zhao, W., Tian, J., Zhao, X., Zhu, Y., Yang, Q., et al. (2017). Deep Western boundary current in the south China Sea. *Sci. Rep.* 7 (1), 9303. doi: 10.1038/s41598-017-09436-2

Zhuo, H., Wang, Y., Shi, H., Zhu, M., He, M., Chen, W., et al. (2014). Seismic geomorphology, architecture and genesis of Miocene shelf sand ridges in the pearl river mouth basin, northern south China Sea. *Mar. Petroleum Geology* 54, 106–122. doi: 10.1016/j.marpetgeo.2014.03.002

frontiers | Frontiers in Marine Science

TYPE Original Research
PUBLISHED 28 July 2022
DOI 10.3389/fmars.2022.948665

OPEN ACCESS

EDITED BY
Guangzhe Jin,
Guangdong Ocean University, China

REVIEWED BY
Yiguo Hong,
Guangzhou University, China
Peng Wu,
South China Sea Fisheries Research Institute, Chinese Academy of Fishery Sciences (CAFS), China

*CORRESPONDENCE
Mei-Lin Wu
mlwu@scsio.ac.cn
You-Shao Wang
yswang@scsio.ac.cn
Yu-Tu Wang
ytwang@scsio.ac.cn
Fu-Lin Sun
flsun@scsio.ac.cn

SPECIALTY SECTION
This article was submitted to Marine Biogeochemistry, a section of the journal Frontiers in Marine Science

RECEIVED 20 May 2022
ACCEPTED 04 July 2022
PUBLISHED 28 July 2022

CITATION
Wu M-L, Wang Y-S, Wang Y-T, Sun F-L, Li X, Gu F-F and Xiang J-C (2022) Vertical patterns of chlorophyll *a* in the euphotic layer are related to mesoscale eddies in the South China Sea. *Front. Mar. Sci.* 9:948665. doi: 10.3389/fmars.2022.948665

Vertical patterns of chlorophyll *a* in the euphotic layer are related to mesoscale eddies in the South China Sea

Mei-Lin Wu[1,2,3,4]*, You-Shao Wang[1,2,3,4]*, Yu-Tu Wang[1,2,3,4]*, Fu-Lin Sun[1,2,3,4]*, Xiaomei Li[1,2,3,4,5], Fang-Fang Gu[6] and Jing-Chang Xiang[7]

[1]State Key Laboratory of Tropical Oceanography, South China Sea Institute of Oceanology, Chinese Academy of Sciences, Guangzhou, China, [2]Southern Marine Science and Engineering Guangdong Laboratory (Guangzhou), Guangzhou, China, [3]Innovation Academy of South China Sea Ecology and Environmental Engineering, Chinese Academy of Sciences, Guangzhou, China, [4]Daya Bay Marine Biology Research Station, Chinese Academy of Sciences, Shenzhen, China, [5]College of Earth and Planetary Science, University of Chinese Academy of Sciences, Beijing, China, [6]Guangzhou Chemical Reagent Factory, Guangzhou, China, [7]Guangdong Zhihuan Innovative Environmental Technology Co. Ltd, Guangzhou, China

Phytoplankton closely connects with the hydrodynamics and biogeochemical environment of the ocean. While research focusing on both the physiochemical factors and hydrodynamics regulating phytoplankton has already been conducted, the coupling mechanism between mesoscale eddies and the vertical distribution of phyto
plankton in the South China Sea (SCS) is still not well understood. Here, phytoplankton was studied under one weak-cold and two warm eddies along the 18°N transect in the SCS. The results show that the vertical distribution of chlorophyll (chl-*a*) presented a similar pattern at all four sampling stations. The mixed layer is less than 50 m. It is the same as the meridional salinity gradients that may be distinguished above a depth of 60 m. The subsurface chlorophyll maximum at the edge of a warm (WI) and cold eddy (CI) at E413 and E411 was shallower than that at the edge of a warm eddy (WII) at E407 and E409, indicating that temperature and salinity may be the important driving factors. On the whole, mesoscale eddies had a significant influence on the vertical pattern of chl-*a* in the SCS during the study period.

KEYWORDS

South China Sea, phytoplankton, subsurface chlorophyll maximum, cold eddy, warm eddy

Introduction

Phytoplankton is considered the most important marine primary producer at the bottom of the food web. They produce about half of the oxygen in the atmosphere, by photosynthesis, which is equal to the amount of oxygen produced by all land plants per year. During the period 1998–2018, global marine primary production ranged from 38.8 to 42.1 Gt C/year (Kulk et al., 2020). It is estimated that diatoms account for 45% of marine primary productivity (Mann, 1999). Phytoplankton has an important influence on marine biogeochemical cycles. Generally, phytoplankton is affected by the environment of the water column, including its physical dynamics, chemical elements, and biological activities. In coastal ecosystems, phytoplankton succession is governed largely by upwelling events, indicating the importance of mesoscale variability for the functioning of the ecosystem in the southern Benguela upwelling system (Burger et al., 2020). In the southeast Gulf of Mexico, upwelling can enhance phytoplankton growth and change its composition, resulting in phytoplankton blooms (Medina-Gomez et al., 2019).

In the open sea, short-term changes in phytoplankton communities are affected by hydrodynamics such as mesoscale eddies. Biochemical elements in cold eddies are brought to shallower waters, while in warm eddies, they are sent to deeper waters. For example, chlorophyll concentrations in cold eddies are higher than in warm eddies (depth > 70 m) in the western part of the North Pacific (Chang et al., 2017). The maximum chlorophyll *a* (chl-*a*) layer in an eddy center rises to form a dome structure, although the total chl-*a* biomass does not increase significantly (Wang et al., 2016). Cold and warm eddies have different influences on phytoplankton and nutrients. The cyclonic eddy characterized by enhanced nutrients and chlorophyll is mostly restricted to the subsurface waters (Jyothibabu et al., 2015). In the western South China Sea (SCS), total chl-*a* increases significantly in warm eddies but does not change much at cold eddies (Zhong and Huang, 2013; Xu et al., 2022). Nonetheless, in the southwestern Canada Basin, the warm core eddy with high ammonium shelf water can provide ammonium for the euphotic zone of the Basin and maintain a 30% higher biomass of picophytoplankton (<2 μm) than the surrounding waters (Nishino et al., 2011). In the SCS, both upwelling and cold eddies are characterized by high nutrient levels and chlorophyll levels, and low levels of dissolved oxygen, while warm eddies are just the opposite (Ning et al., 2004). High dissolved oxygen (DO) content is moved from the upper layer to the lower layer by warm eddies in the SCS (Liu et al., 2012). However, very few studies attempt to examine the influence of cold and warm eddies on the vertical distribution of phytoplankton maxima.

A cold core eddy is formed intermittently throughout the year due to the Kuroshio intrusion, which may have an important impact on the biogeochemical cycle in the SCS (Chen et al., 2007; Sun et al., 2022). The cold eddy significantly increases the primary productivity at the 25-m layer, which is mainly affected by the nutrients in the western part of the SCS (Leng et al., 2016). The phytoplankton features influenced by the different eddies are significantly different (Huang et al., 2010). Lin et al. (2014) used satellite data to discover that in the SCS, phytoplankton size classes change from picoplankton to micro- and nanoplankton driven by cold eddies, but the contribution of picoplankton to chlorophyll remained almost unchanged. Mesoscale eddies did not significantly influence the dominance of the dominant groups in the western SCS (Zhong and Huang, 2013).

The SCS is a large, semienclosed marginal sea with several straits that are connected to the Pacific and Indian oceans, and is characterized by complex hydrodynamics and biogeochemistry. In the northern SCS, phytoplankton in the summer is mainly driven by upwelling and river plume processes (Xu et al., 2018). Similarly, phytoplankton relatively responds to the hydrodynamics of the SCS. In the present study, the vertical distribution of phytoplankton caused by the combined action between the warm and cold eddies is explained. In particular, we explored whether the physical environment, including a thermocline, is advantageous to the formation and maintenance of chl-*a* at its maximum in the euphotic layer.

Materials and methods

Sampling and sample analysis

The research cruise was conducted from 15 September to 04 October 2004. During the cruise, temperatures and salinities were obtained with a SeaBird model SBE9/11. Discrete water samples (surface, 25, 50, 75, 100, 150, and 200 m) were collected with GO-FLO bottles mounted on a rosette sampling assembly (Whatman Company: General Oceanic). Seawater was filtered through a GF/F filter (Whatman, 25 mm), and the filter paper was wrapped in aluminum foil and stored at −20°C pending analysis. Chl-*a* content was measured by fluorescence with a Turner Design 10 fluorometer. The sampling stations of this study, located at 18°N, were collected during the cruise from 23 to 25 September 2004 (Figure 1).

Data from remote sensing

Sea-level anomaly data (SLA) obtained from the TOPEX/Poseidon and JASON altimeters (http://www.aviso.oceanobs.com/) were used to estimate surface circulations. The SLA data were used to estimate thermocline displacement. In an ideal two-layer system, the depth of the upper layer **(A)** is *D*,

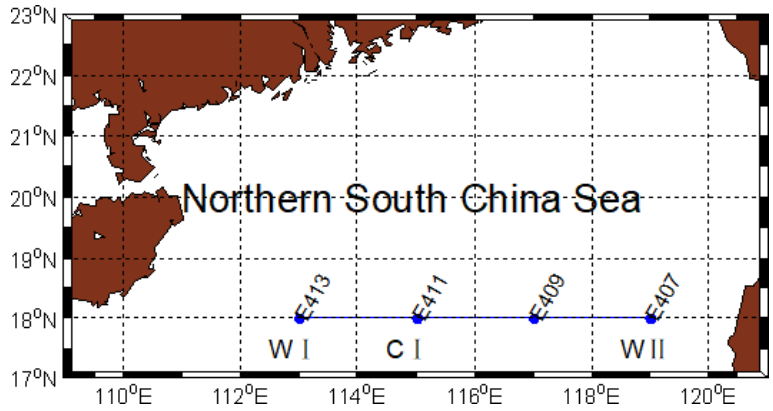

FIGURE 1
Sampling stations in the northern South China Sea during the research cruise, 2004.

with density ρ_1 and temperature T_1 , while a motionless lower layer (B) has density $\rho_2=\rho_1+\Delta\rho$ and temperature T_2 . $\Delta\rho$ and Δh are the density differences between A and B and the SLA, respectively (Rebert et al., 1985). The thermocline displacement (ΔD) was calculated with Eq. (1).

$$\Delta D = \frac{\Delta h \rho_1}{\Delta \rho} \quad (1)$$

Mixed layer and depth of the thermocline top

Mixed layer depth (MLD) is the depth characterized by the density gradient, and this gradient was $\sigma\theta = 0.1$ unit m^{-1} (Tseng et al., 2005). The top thermocline depth (TTD) was defined as the depth above which the temperature is greater than the surface temperature (the latter measured at 10 m depth) minus 0.2°C.

Results

Physical background

Temperature and salinity

Both the salinity and temperature profiles of the transect at 18°N, from the surface to 200 m depth, are shown in Figure 2. The surface salinity indicated that there was a high temperature (~29.5°C) and low salinity (~33.4) at the transect stations (E405 and E407), which was in good agreement with the positive SLA field. Above 50 m, there was low salinity and a high-temperature tongue from about 114.5°E towards the east. The TTD along the transect from westward to eastward (from E413 to E407) deepened. The characteristic of a warm core eddy is that there is a deep thermocline in the center and the depth of the thermocline around the eddy fringe is very shallow.

The isotherms show how the warm surface seawater (above 28°C) moved eastward, generating a meridional temperature gradient. Meridional salinity gradients may be distinguished above a depth of 60 m (Figure 2). The maximum salinity (s = 34.6) in tropical waters reached ~120 m. It is the intermediate water circulation from the west to the east in SCS.

Mixed layer and euphotic layer depth

MLD is less than 50 m in the upper layer in E411 and E413 (Figure 3). That is to say, MLD is the same water layer in E411 and E413, and the water layer at less than 50 m depth has the same temperature and salinity. On the other hand, chemical and biological parameters may show a small difference.

Sea surface height anomaly

The SLA showed that there were two warm eddies and a weak cold eddy in the sampling transect before and during the study period. The sampling stations located at the warm eddy edge or inside it (E413 located in c; and E407 and E409 located in WII) have high values of SLA, while E11 located in the cold eddy (CI) has low values of SLA (Figure 4). The mesoscale eddy changed over time. Interestingly, the WI was distinct from 28 August to 22 September and then disappeared. In contrast, the cold eddy (CI) became gradually stronger before and during the sampling period.

Biological activities

The vertical distribution of chl-*a* at the sampling stations is shown in Figure 5. The subsurface chlorophyll maximum, with values between 0.1 and 0.3 mg m^{-3}, varied from 50 to 150 m (Figure 5). In addition, the chl-*a* maximum (0.3 mg m^{-3}) at E407 was 50% higher than in the water of the cold eddy at E413 (0.2 mg m^{-3}) above the euphotic zone (about 80 m).

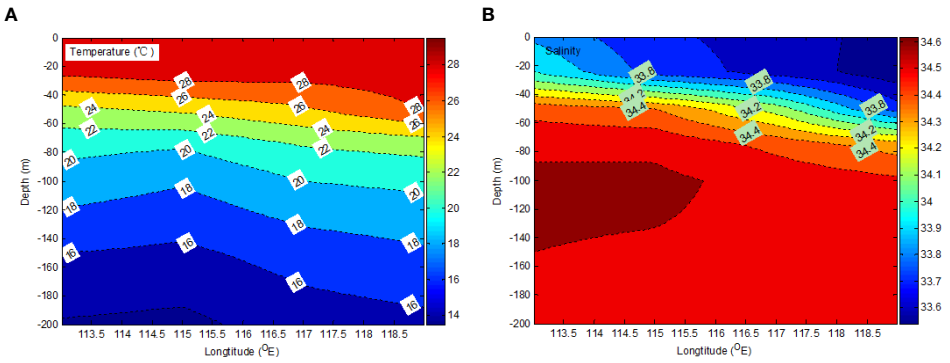

FIGURE 2
Vertical distributions of temperature **(A)** and salinity **(B)** at different depths.

Discussion

Chl-*a* content ranged from 0.10 to 0.30 mg m^{-3} in the SCS. The chlorophyll maximum was 0.30 mg m^{-3} in the top 75 m of E407 and 0.20 mg m^{-3} in the top 25 m of E413. Chl-*a* content varied from 0.01 to 1.95 mg m^{-3} in the SCS (Ning et al., 2004). The subsurface chlorophyll maximum, with values between 0.10 and 0.60 mg m^{-3}, ranged from 50 to 100 m in the SCS. Integrated phytoplankton biomass (chl-*a*) at four stations was similar in the euphotic layer. These observations are similar to those in a previous study (Ning et al., 2004). However, there are differences between the edges of cold and warm eddies. The chl-*a* maximum (~0.20 mg m^{-3}) at the base of the surface mixed layer (25 m) was found at the edge of the warm (WI) and cold eddy (CI) at E413, while chl-*a* maxima (~0.30 mg m^{-3}) at the warm eddy edge were observed at E407 and E409, and deepened to 75 m depth in that area (Figure 5). The chl-*a* maximum (0.24 ± 0.60 mg m^{-3}) at 75 m was found in the water of a warm eddy in the western SCS (Zhong and Huang, 2013). The averaged water column-integrated concentration of total chlorophyll inside the eddy was similar to that outside the eddy, and an enhancement of phytoplankton biomass and an increase in the range of the depth of the chl-*a* maximum (DCM) layer were detected within the eddy (Dai et al., 2020). The subsurface chlorophyll maxima layers contained approximately 50% of the chl-*a* standing stock in the water column, and the contribution increased to >70% for

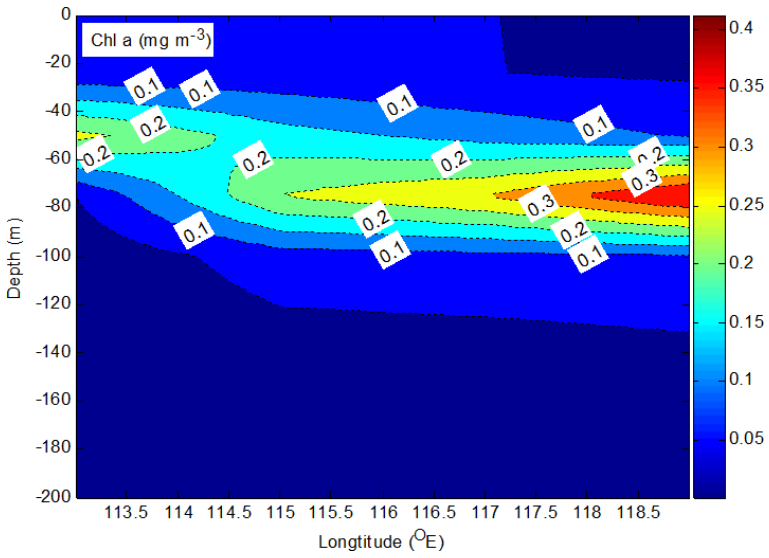

FIGURE 3
Mixed layer depth at the sampling stations.

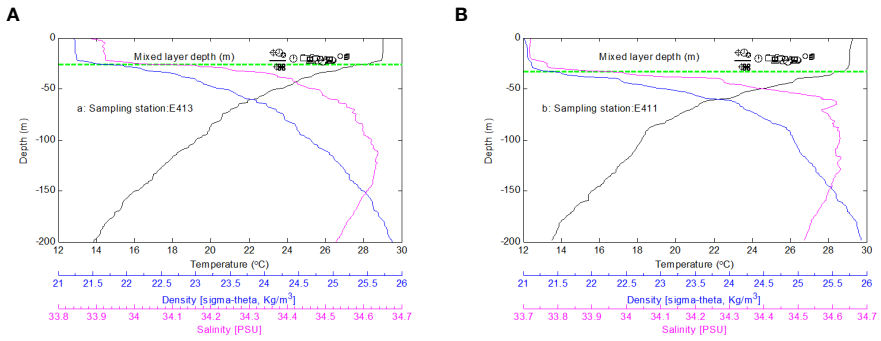

FIGURE 4
The 8-day mean SLA from AVISO. **(A)** Before the sampling period, from 28/08/2004 to 29/09/2004; **(B)** during the sampling period, 23/09/2004 to 25/09/2004.

high-biomass areas, suggesting the biological importance of the summer subsurface chlorophyll maxima in the shelf ecosystem (Zhuang et al., 2020).

What made the difference? The explanation may be physical processes. From the SLA figures, the cold eddy began to form for several days at the stations (E411 and E413). The isotherm at the depth range of 60 to 200 m at E411 was shallower than at E413 and other stations (Figure 5), by about 10 m, and a warm eddy may have played a role in determining this scenario. The research stations (E407 and E409) were located at the edge of the warm eddy shown in Figure 3. Thus, the alternating patches of cold and warm eddies along 18°N can be further verified. The

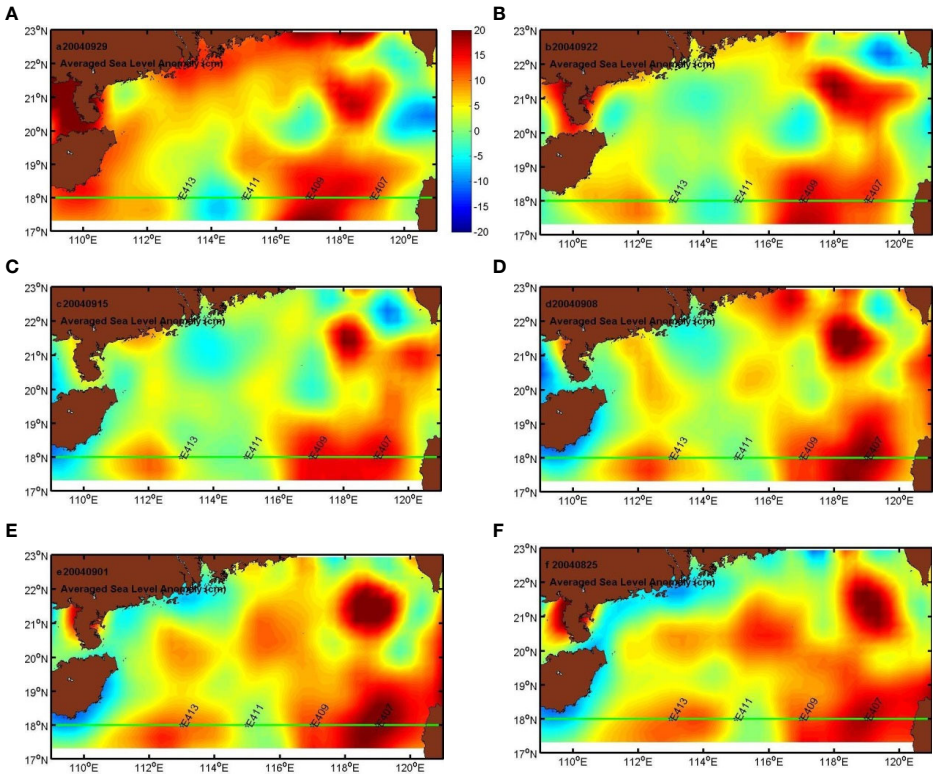

FIGURE 5
8-day mean SLA from AVISO **(A–F)** Before and after the sampling time: from 28/8/2004 to 29/9/2004; **(B)** the sampling time: 23-25/9/2004.

altimetry data were used to estimate thermocline displacement. Figure 3 indicates that the surface depression (Δh = −3 cm) occurred before the period of sampling (23/09/2004). If necessary, $\Delta\rho$ = 2.3 kg m^{-3} was used in Eq. (1); ΔD was 20.5 m. Therefore, the thermocline displacement is similar to the observed displacement at E407. Compared with E413, the displacement inferred that the subsurface chlorophyll maximum at E407 may deepen by about 20 m in the upper layer. According to the above chl-*a* profile, the downward movement caused by WII resulted in phytoplankton moving from the mixed layer to the deep layer (Figure 5).

This interesting phenomenon was found in the East Sea (Kim et al., 2012), the SCS, and the Indian Ocean where the subsurface chlorophyll maximum was below the euphotic zone (Thompson et al., 2007; Huang et al., 2010). Because there was a significant difference between the warm (WII) and cold (CI) eddies above the euphotic zone, phytoplankton might grow under different physical conditions. Nutrients (nitrate and phosphate) are depleted within the euphotic zone in the SCS (Wong et al., 2007). Under this scenario, nutrients may be the limiting factor for phytoplankton in the mixed layer. Warm eddies could determine the distribution of nutrients in the euphotic layer and regulate phytoplankton patterns in the coastal, shelf, and open ocean ecosystem (Kim et al., 2012).

The uplift or downward movement of environmental factors was accompanied by the cold or warm eddies, respectively. From the SLA figures, there was about a 1-month time lag from 22 August to 23 September. There were two warm eddies (E413, E407, and E409) and embryonic forms of a cold eddy (E411) at the sampling stations before the sampling period. As time went by, the E413 site was situated at the edge of the warm and cold eddies (WI and CI), while E411 was sited at the edge of the cold and warm eddies (CI and WII) during the sampling period. Interestingly, the observed chl-*a* maximum layer at E413 (50 m) was less than that at E407 and E409 (75 m), while it was also found at E411 (75 m), where the cold eddy (CI) gradually strengthened before and during the sampling period (Figure 5).

Conclusion

In this study, we provide field evidence for the vertical distribution of chl-*a* being regulated by mesoscale eddies, including the cold and warm eddies in the euphotic layer of the SCS. Inside a warm eddy, the maximum depth of chl-*a* is deeper than it is on the edge of such an eddy—the point of interaction between the gradually vanishing warm eddy and slowly boosting cold eddy. The occurrence of mesoscale eddies, confirmed by the SLA satellite data and *in situ* measured temperature and salinity, induced the vertical pattern of chl-*a*.

Interpretation of these findings concludes that the mesoscale eddies have an important influence on the chemical parameters and biological activities of the open sea. The water convergency induced by a warm eddy causes downwards transport while the water convergency induced by a cold eddy induces upwards transport; therefore, the presence of phytoplankton and nutrients in cold eddies is accomplished by the motion associated with eddy-induced divergence (convergence). It is the complicated interaction among different mesoscale eddies in the open sea that creates the resulting biogeochemistry.

Data availability statement

The original contributions presented in the study are included in the article/supplementary material. Further inquiries can be directed to the corresponding author/s.

Author contributions

All authors contributed to the article and approved the submitted version.

Funding

The research was supported by the National Natural Science Foundation of China (No. 31971480), the Key Special Project for Introduced Talents Team of Southern Marine Science and Engineering Guangdong Laboratory (Guangzhou) (Nos. GML2019ZD0303 and GML2019ZD0404), the Strategic Priority Research Program of the Chinese Academy of Sciences (No. XDA19060204), Hainan Province Science and Technology Special Fund (ZDYF2021XDNY131), and members of the scientific research team of the RV Shiyan 3 for help at sea.

Acknowledgments

The research was supported by the National Natural Science Foundation of China (No. 31971480), Key Special Project for Introduced Talents Team of Southern Marine Science and Engineering Guangdong Laboratory (Guangzhou) (Nos. GML2019ZD0303 and GML2019ZD0404), the Strategic Priority Research Program of the Chinese Academy of Sciences (No. XDA19060204), Hainan Province Science and Technology Special Fund (ZDYF2021XDNY131) and members of the scientific research team of the RV Shiyan 3 for help at sea.

Conflict of interest

Author J-CX was employed by Guangdong Zhihuan Innovative Environmental Technology Co. Ltd.

The remaining authors declare that the research was conducted in the absence of any commercial or financial relationships that could be construed as a potential conflict of interest.

Publisher's note

References

Burger, J. M., Moloney, C. L., Walker, D. R., Parrott, R. G., and Fawcett, S. E. (2020). Drivers of short-term variability in phytoplankton production in an embayment of the southern benguela upwelling system. *J. Mar. Syst.* 208, 1–16. doi: 10.1016/j.jmarsys.2020.103341

Chang, Y. L., Miyazawa, Y., Oey, L. Y., Kodaira, T., and Huang, S. (2017). The formation processes of phytoplankton growth and decline in mesoscale eddies in the western north pacific ocean. *J. Geophysical Rese-Oceans* 122 (5), 4444–4455. doi: 10.1002/2017JC012722

Chen, Y. L. L., Chen, H. Y., Lin, I. I., Lee, M. A., and Chang, J. (2007). Effects of cold eddy on phytoplankton production and assemblages in Luzon strait bordering the south China Sea. *J. Oceanography* 63 (4), 671–683. doi: 10.1007/s10872-007-0059-9

Dai, S., Zhao, Y. F., Liu, H. J., Hu, Z. Y., Zheng, S., Zhu, M. L., et al. (2020). The effects of a warm-core eddy on chlorophyll a distribution and phytoplankton community structure in the northern south China Sea in spring 2017. *J. Mar. Syst.* 210, 1–12. doi: 10.1016/j.jmarsys.2020.103396

Huang, B. Q., Hu, J., Xu, H. Z., Cao, Z. R., and Wang, D. X. (2010). Phytoplankton community at warm eddies in the northern south China Sea in winter 2003/2004. *Deep-Sea Res. Part Ii-Topical Stud. Oceanography* 57 (19-20), 1792–1798. doi: 10.1016/j.dsr2.2010.04.005

Jyothibabu, R., Vinayachandran, P. N., Madhu, N. V., Robin, R. S., Karnan, C., Jagadeesan, L., et al. (2015). Phytoplankton size structure in the southern bay of Bengal modified by the summer monsoon current and associated eddies: Implications on the vertical biogenic flux. *J. Mar. Syst.* 143, 98–119. doi: 10.1016/j.jmarsys.2014.10.018

Kim, D., Yang, E. J., Kim, K. H., Shin, C. W., Park, J., Yoo, S., et al. (2012). Impact of an anticyclonic eddy on the summer nutrient and chlorophyll a distributions in the ulleung basin, East Sea (Japan Sea). *ICES J. Mar. Sci.* 69 (1), 23–29. doi: 10.1093/icesjms/fsr178

Kulk, G., Platt, T., Dingle, J., Jackson, T., Jonsson, B. F., Bouman, H. A., et al. (2020). Primary production, an index of climate change in the ocean: Satellite-based estimates over two decades. *Remote Sens.* 12 (5), 1–26. doi: 10.3390/rs12050826

Leng, X., Yang, Y., Sun, J., Zhang, G., Xu, W., Feng, Y., et al. (2016). Mesoscale physical processes on the effects of distribution of nutrients and chlorophyll ain the western south China Sea in summer. *Acta Oceanol Sin.* 38 (4), 66–75. doi: 10.3969/j.issn.0253-4193.2016.04.006

Lin, J., Cao, W., Wang, G., and Hu, S. (2014). Satellite-observed variability of phytoplankton size classes associated with a cold eddy in the south China Sea. *Mar. pollut. Bull.* 83 (1), 190–197. doi: 10.1016/j.marpolbul.2014.03.052

Liu, C., Zhuang, W., Xia, H., and Du, Y. (2012). Mesoscale observation in the northeast south China Sea during winter 2009-2010. *Acta Oceanol Sin.* 34 (1), 8–16. doi: 10.1007/s11783-011-0280-z

Mann, D. G. (1999). The species concept in diatoms. *Phycologia* 38 (6), 437–495. doi: 10.2216/i0031-8884-38-6-437.1

Medina-Gomez, I., Trujillo, A. A., Marino-Tapia, I., Cruz, G., Herrera-Silveira, J., and Enriquez, C. (2019). Phytoplankton responses under a joint upwelling event and an algal bloom scenario in the southeast gulf of Mexico. *Continental Shelf Res.* 184, 30–43. doi: 10.1016/j.csr.2019.07.006

Ning, X., Chai, F., Xue, H., Cai, Y., Liu, C., and Shi, J. (2004). Physical-biological oceanographic coupling influencing phytoplankton and primary production in the south China Sea. *J. Geophys. Res.* 109, C10005. doi: 10.1029/2004JC002365

Nishino, S., Itoh, M., Kawaguchi, Y., Kikuchi, T., and Aoyama, M. (2011). Impact of an unusually large warm-core eddy on distributions of nutrients and phytoplankton in the southwestern Canada basin during late summer/early fall 2010. *Geophysical Res. Lett.* 38, 1–6. doi: 10.1029/2011GL047885

Rebert, J. P., Donguy, J.-R., Eldin, G., and Wyrtki, K. (1985). Relations between sea level, thermocline depth, heat content, and dynamic height in the tropical pacific ocean. *J. Geophysical Res: Oceans (1978–2012)* 90 (C6), 11719–11725. doi: 10.1029/JC090iC06p11719

Sun, F., Xia, X., Simon, M., Wang, Y., Zhao, H., Sun, C., et al. (2022). Anticyclonic eddy driving significant changes in prokaryotic and eukaryotic communities in the south China Sea. *Front. Mar. Sci.* 9. doi: 10.3389/fmars.2022.773548

Thompson, P. A., Pesant, S., and Waite, A. M. (2007). Contrasting the vertical differences in the phytoplankton biology of a dipole pair of eddies in the south-eastern Indian ocean. *Deep Sea Res. Part II: Topical Stud. Oceanography* 54 (8), 1003–1028. doi: 10.1016/j.dsr2.2006.12.009

Tseng, C. -M., Wong, G. T., Lin, I. -I., Wu, C. -R., and Liu, K. -K. (2005). A unique seasonal pattern in phytoplankton biomass in low-latitude waters in the South China Sea. *Geophys. Res. Lett.* 32 (8), L08608. doi: 10.1029/2004GL022111

Wang, L., Huang, B., Chiang, K. P., Liu, X., Chen, B., Xie, Y., et al. (2016). Physical-biological coupling in the Western south China Sea: The response of phytoplankton community to a mesoscale cyclonic eddy. *PloS One* 11 (4), 1–18. doi: 10.1371/journal.pone.0153735

Wong, G. T., Tseng, C. M., Wen, L. S., and Chung, S. W. (2007). Nutrient dynamics and n-anomaly at the SEATS station. *Deep Sea Res. Part II: Topical Stud. Oceanography* 54 (14), 1528–1545. doi: 10.1016/j.dsr2.2007.05.011

Xu, Z., Li, S., Hu, J., Wang, S., Wang, B., Guo, M., et al. (2018). Summer phytoplankton responses to upwelling and river plume in northern south China Sea. *J. Trop. Oceanography* 37 (6), 92–103. doi: 10.11978/2018001

Xu, W., Wang, G., Cheng, X., Jiang, L., Zhou, W., and Cao, W. (2022). Characteristics of subsurface chlorophyll maxima during the boreal summer in the south China Sea with respect to environmental properties. *Sci. Total Environ.* 820, 1–11. doi: 10.1016/j.scitotenv.2022.153243

Zhong, C. X., Xiao, W. P., and Huang, B. Q. (2013). The response of phytoplankton to mesoscale eddies in Western south China Sea. *Advance Mar. Sci.* 31 (2), 213–220.

Zhuang, Y. P., Jin, H. Y., Chen, J. F., Ren, J., Zhang, Y., Lan, M. S., et al. (2020). Phytoplankton community structure at subsurface chlorophyll maxima on the Western Arctic shelf: Patterns, causes, and ecological importance. *J. Geophysical Res-Biogeosci* 125 (6), 1–15. doi: 10.1029/2019JG005570

frontiers | Frontiers in Marine Science

TYPE Original Research
PUBLISHED 16 August 2022
DOI 10.3389/fmars.2022.989055

OPEN ACCESS

EDITED BY
Fajin Chen,
Guangdong Ocean University, China

REVIEWED BY
Peng Zhao,
Hainan University, China
Wenzhe Xu,
Tianjin University of Science and Technology, China
Senthilnathan Lakshmanan,
Amet University, India

*CORRESPONDENCE
Meilin Wu
mlwu@scsio.ac.cn

SPECIALTY SECTION
This article was submitted to Marine Biogeochemistry, a section of the journal Frontiers in Marine Science

RECEIVED 08 July 2022
ACCEPTED 25 July 2022
PUBLISHED 16 August 2022

CITATION
Li X, Wang Y, Zhang Y, Xiang J, Yang Z, Gu F and Wu M (2022) Evaluating the physiological and biochemical responses of different mangrove species to upwelling. *Front. Mar. Sci.* 9:989055. doi: 10.3389/fmars.2022.989055

Evaluating the physiological and biochemical responses of different mangrove species to upwelling

Xiaomei Li[1,2,3,4], Yutu Wang[1,2,3,5], Yuhang Zhang[1,2,3,4], Jingchang Xiang[6], Zhihao Yang[7], Fangfang Gu[8] and Meilin Wu[1,2,3,5]*

[1]State Key Laboratory of Tropical Oceanography, South China Sea Institute of Oceanology, Chinese Academy of Sciences, Guangzhou, China, [2]Southern Marine Science and Engineering Guangdong Laboratory, Guangzhou, China, [3]Innovation Academy of South China Sea Ecology and Environmental Engineering, Chinese Academy of Sciences, Guangzhou, China, [4]College of Earth and Planetary Science, University of Chinese Academy of Sciences, Beijing, China, [5]Daya Bay Marine Biology Research Station, Chinese Academy of Sciences, Shenzhen, China, [6]Guangdong Zhihuan Innovative Environmental Technology Co. Ltd., Guangzhou, China, [7]Guangdong Marine Development Planning Research Center, Guangzhou, China, [8]Guangzhou Chemical Reagent Factory, Guangzhou, China

Mangroves are unique forest communities with an abundance of species, high productivity and high ecological, social and economic value. Evaluation of the stress resistance of mangrove plants has mainly focused on the effects of high salinity, heavy metals and flooding, with fewer studies evaluating resistance to upwelling stress. Mangrove species of *Avicennia marina*, *Aegiceras corniculatum* and *Kandelia obovata* were submitted to three temperature upwelling (5, 10 and 15°C) and several physiological and biochemical parameters were measured at six time points (0, 6, 12, 24, 72 and 168 h). The data demonstrated: a certain amount of damage occurred to mangrove plants in the face of prolonged upwelling; different mangrove plants have different response strategies to upwelling; mangrove plants are not sensitive to different upwelling temperatures; the resistance of mangrove plants to upwelling stress was in the following order: A. *marina*< K. *obovata*< A. *corniculatum*. Markers of damage such as relative electrical conductivity (REC), malondialdehyde (MDA) and reactive oxygen species (ROS) among all mangrove species were significantly higher with prolonged upwelling stress. The contents of photosynthetic pigments in all three mangrove species also increased. Superoxide dismutase activity (SOD) was maintained at a high level in both control and treatment groupss. By contrary, the change of peroxidase activity (POD) of *A. marina* and *K. obovata* was larger than that of *A. corniculatum*. Catalase activity (CAT) in *A. marina* and *K. obovata* significantly increased under upwelling at both 5 and 10°C while there was no obvious variation of CAT in *A. corniculatum*. Soluble protein and Soluble sugar contents showed no clear variation but stayed at fairly high levels. However, proline content in *A. corniculatum* significantly increased under long-term upwelling stress while this was not the case in the other two species. High correlation could be observed between *A. marina* and MDA, O_2- and POD in PCA while A.

corniculatum showed association with proline and soluble sugar. In conclusion, the ability of *A. corniculatum* to tolerate upwelling stress might be due mainly to increases in the activities of SOD and the inducing of proline biosynthesis, while, *A marina* and *K. obovata* tolerated upwelling stress by adjusting activity levels of SOD, POD and CAT. Segregation in both principal component analysis (PCA) and hierarchical cluster analysis (HCA) further indicated different tolerances and resistances to upwelling between the three species. Our study provides new insights into the stress response of mangroves to upwelling.

KEYWORDS

upwelling, mangrove, photosynthetic pigments, membrane permeability, reactive oxygen species, osmoregulatory system, antioxidant enzyme

1 Introduction

Mangroves are trees or large shrubs, including ferns and a single species of palm, which normally grow in or adjacent to the intertidal zone and which have developed special adaptations for this environment (Mark Spalding, 2010). Known as "the Earth's Tropical Coast Guard", mangroves play several ecological roles including providing habitats for wildlife, stabilizing sediment, protecting shorelines and sequestering carbon (Walters et al, 2008; Simpson et al, 2019). Distributed in regions of warm temperatures, mangroves are susceptible to temperature variation. Studies of mangrove resistance to low temperatures have been widely reported (Peereman et al, 2021; Lu et al, 2021). The development of mangroves in Qinzhou Bay over the past 3000 years showed that low air temperature causes mangrove degradation by impacting their diversity, productivity and area (Zhang et al, 2021). It was also reported that cold event resulted in decreases in seedling growth rates and net ecosystem CO_2 uptake in mangroves (Song et al., 2020). However, most studies of mangrove stressors have focused on low air temperatures induced by extreme climate events; studies on low water temperatures induced by ocean currents are rare. As a coastal ecosystem, mangroves are substantially affected by changing ocean currents such as upwelling activity (Ximenes et al, 2021). Upwelling is an oceanic process which transports cold and saline water to the surface (Wang et al, 2015). Exposure to water at low temperatures can harm the formation of mangrove propagules (Rachel Collin, 2016). Through harming the development of mangrove propagules, upwelling affected the distribution of mangrove plants (Ximenes et al., 2018). Low-temperature seawater caused by upwelling poses a threat to mangrove plants. In our previous study, *Kandelia obovata* (a mangrove plant) showed oxidative damage under upwelling stress with higher contents of hydrogen peroxide (H_2O_2) and malondialdehyde (MDA) (Li et al, 2022). Previous studies have also reported that low temperatures could impair water and nutrient intake, stimulate reactive oxygen species (ROS) production and disturb normal photosynthesis and metabolism (Ensminger et al, 2006; Viswanathan et al, 2007; Wang et al, 2019).

Plants mediate the adverse effects of temperature downshifts through stress tolerance defense mechanisms. The primary mechanisms involved in low temperature stress are related to the activation of ROS scavenger systems, alterations in protein and sugar synthesis, proline accumulations and photosynthesis changes (Theochairs et al, 2012). Under chilling, olives exhibited increased catalase (CAT), superoxide dismutase (SOD) and peroxidase (POD) activity to protect and stabilize cell membranes and structures, adapting to the environment (Petruccelli et al., 2022). The accumulation of osmoregulatory substances (e.g., soluble sugar, soluble protein, and proline) significantly increased cytosol concentration and prevented excessive protoplasmic dehydration, which enhanced cold tolerance (Jiang et al., 2022). Moreover, increasing chlorophyll contents to produce more carbon-based defensive chemicals could alleviate low temperature stress (Agathokleous et al, 2020).

Avicennia marina, *Aegiceras corniculatum* and *Kandelia obovata* are dominant mangrove species in South China, and it has been reported that these three species show different resistances to low temperature (Lin, 1997; Geng et al, 2021). The leaves of *Avicennia marina* suffered more serious damages than *Aegiceras corniculatum* and *Kandelia obovata* under 2008 chilling event in southern China (Chen et al, 2017). Besides, the distribution of mangroves on tidal zone reflects their adaptation to environmental changes (Ariel E. Lugo, 1974). Thus, low-tide zone mangroves (A. *marina* and A. *corniculatum*) and middle-

tide zone mangrove (K. *obovata*) were chosen. In the present study, we investigated the physiological and biochemical characteristics of these three mangrove species to upwelling stress. This research focused on investigating the response mechanism of different mangrove species to upwelling, aiding understanding about the stress resistance of mangroves under upwelling, and providing a theoretical basis for mangrove protection. In detail, the objectives of the study were to:

(1) investigate indexes of injury including the membrane damage indicator (relative electrical conductivity and malonaldehyde content) and ROS production (superoxide anion radical and hydrogen peroxide) of three mangrove species under upwelling stresses of 5, 10 and 15°C at time points of 0, 6, 12, 24, 72 and 168 h of exposure.

(2) investigate indexes of protection including photosynthetic pigments (chlorophyll a, chlorophyll b, and carotenoid), antioxidant enzyme activities (superoxide dismutase, peroxidase, and catalase) and osmotic regulation substances (proline, soluble sugar and soluble protein) of three mangrove species during upwelling at water temperatures of 5, 10 and 15°C at time points of 0, 6, 12, 24, 72 and 168 h.

(3) employ principal component analysis (PCA) and hierarchical cluster analysis (HCA) to compare different responses to upwelling stress among different mangrove species.

2 Materials and methods

2.1 Plant materials and treatments

Healthy propagules of *A. marina*, *A. corniculatum* and *K. obovata* were collected form the nursey of Qi'ao Island Mangrove Nature Reserve in Guangdong. Seedlings were planted in clean sand and fertilized with 1/2 Hoagland's solution. Three months later, the seedlings were subjected to upwelling stress. The upwelling stress conditions were as follow: water temperature (5, 10 and 15°C), measured at multiple time points (0, 6, 12, 24, 72 and 168 h), in each case at the same air temperature (25°C) and water salinity (20 psu), 20,000 light densities regularly, and 70% humidity. Among that, 0h is the blank control of the experiment. The experimental conditions were set based on the actual situation in upwelling zone and appropriate modifications were made in order to obtain significant changes in indoor simulation (Jianyu Hu, 2016; Burchard et al, 2017). Fresh leaves were collected for determination of physiological and biochemical indexes and each index had three repetitions.

2.2 Determination method

2.2.1 Determination of pigments

Chlorophyll a (Chl *a*), chlorophyll b (Chl *b*) and carotenoid (*Caro*) contents were detected by spectrophotometry (UV-1780, SHIMADZU, Japan). Leaf samples (0.2 g) were cut into 2-mm pieces and transferred to tubes with 20 ml solution of 95% ethanol for 24 h until the tissue faded. The content of photosynthetic pigments was determined at wavelengths of 665, 649 and 470 nm (Li et al, 2021).

$$\text{Chl } a = 13.95 \times A_{665} - 6.88 \times A_{649}$$

$$\text{Chl } b = 24.96 \times A_{649} - 2.79 \times A_{665}$$

$$Caro = \frac{1000 \times A_{470} - 2.05 \times \text{Chl } a - 114.8 \times \text{Chl } b}{245}$$

2.2.2 Relative electrical conductivity

REC was measured using an electrical conductivity meter (DDB-303A, INESA, China), following (Zhang L. X. et al, 2021) with a slight modification. Leaf samples were washed with distilled water and then placed in tubes with 10 ml of distilled water. After 3 hours kept at room temperature, the initial electrical conductivity (R1) was measured. Then the samples were boiled for 20 min at 100°C. After cooling, the electrical conductivity was measured again (R2). REC was calculated as the percentage ratio of R1/R2.

2.2.3 Determination of superoxide anion radical

The content of O_2- was measured using the hydroxylamine oxidation method with an assay kit (for plants) purchased from YaJi Biological Institute (Shanghai, China). The content was calculated from the reaction of O_2- with hydroxylamine solution under acidic conditions (Yang et al, 2020).

2.2.4 Determination of soluble protein, soluble sugar and proline

The SP content of the mangrove leaves was determined in accordance with the spectrophotometry method of (M.Bradford, 1976) using bovine serum albumin as the calibration standard. SS content was measured using anthrone colorimetry (Feng et al, 2019). The concentration of proline was determined according to ninhydrin colorimetry (Khoma et al, 2021).

2.2.5 Extraction and assay of lipid peroxidation, hydrogen peroxide and antioxidant enzymes

Fresh leaf samples (roughly 1.0 g) were ground into powder in liquid nitrogen and then homogenized with 0.1 mol/L Tris hydrochloride buffer (PH 7.8). Subsequently, the homogenate was subjected to centrifugation at 3500 rpm at 4°C for 20 min,

and then the supernatant was cryopreserved for determination. The level of lipid peroxidation in mangrove leaves was expressed as malondialdehyde (MDA) content, according to the thiobarbituric acid (TBA) method (Md. Jahirul Islam, 2020).

The hydrogen peroxide (H_2O_2) content was determined using the absorption of titanium peroxide complex at 405nm. (Wang et al, 2020). Superoxide dismutase (SOD) activity was measured at 560 nm with the nitro blue tetrazolium (NBT) photoreduction method (Wu et al, 2020). Peroxidase (POD) activity was estimated based on the absorbance of guaiacol oxidation at 470 nm while catalase (CAT) activity was measured as the decrease rate in the absorbance of H_2O_2 (Li et al, 2013).

2.3 Statistical analyses

One-way analysis of variance (ANOVA) and *post hoc* multiple mean comparisons (Tukey's test) were carried out to determine the significance of differences in each parameter, using SPSS (version 23). Data were presented as mean ± standard deviation (SD). P<0.05 was interpreted as indicating a significant difference between the control and treatment groupss. The responses of three mangrove plants to upwelling stress were profiled through hierarchical cluster analysis (HCA) and principal component analysis (PCA). PCA was conducted in Origin (version 2021) and HCA was performed in R (3.4.4).

3. Results

3.1 Effect of upwelling stress on the content of chlorophylls and carotenoids

As demonstrated in Figure 1, pigment increases were observed in all three mangrove species under upwelling stress. The contents of chl *a*, chl *b* and *caro* in leaves of *A. marina* and *A. corniculatum* slightly decreased at first and then increased.

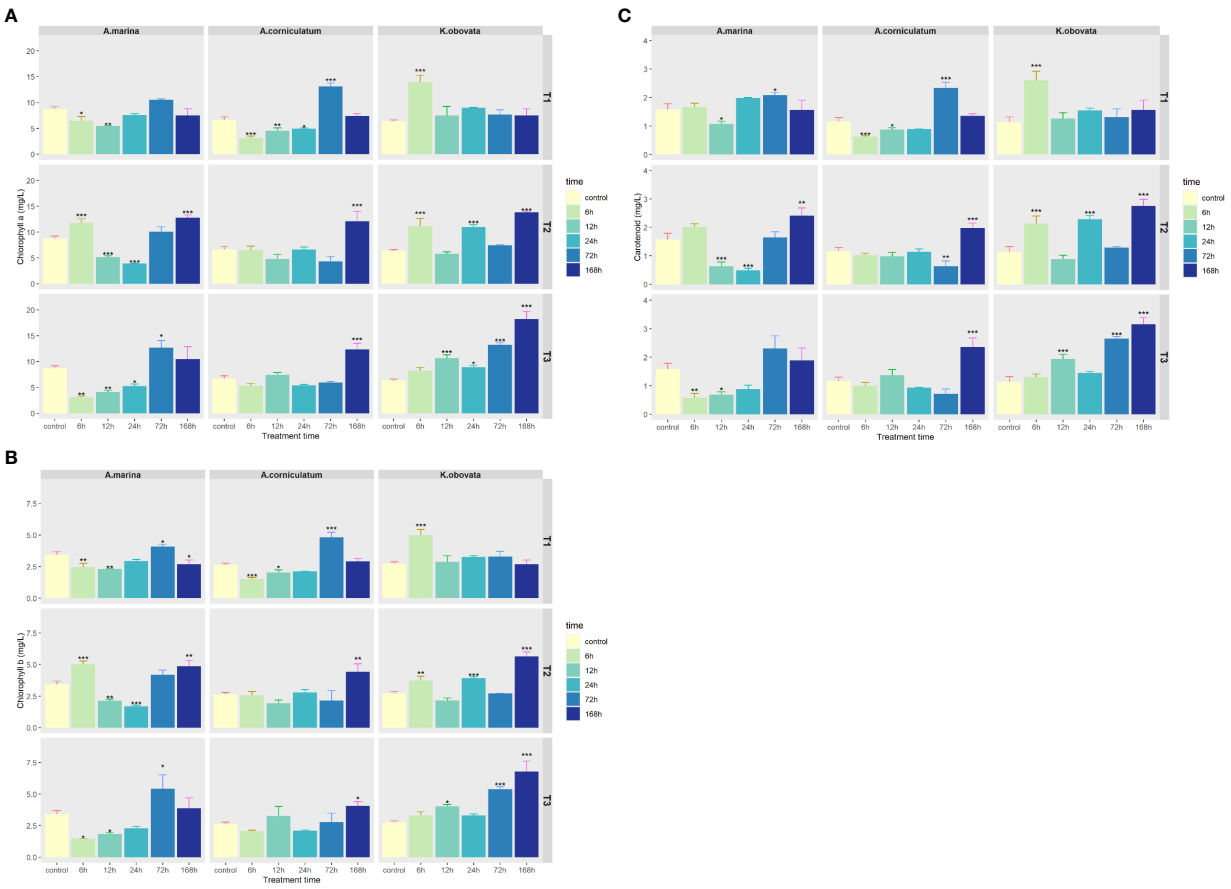

FIGURE 1
The changes of **(A)** Chlorophyll a, **(B)** Chlorophyll b and **(C)** Carotenoid contents under different upwelling stresses. * indicates that there are significant differences between control and treatment groups (p<0.05(*), p<0.01(**), p<0.001(***)). "T1" means 5°C upwelling stress, "T2" means 10°C upwelling stress and "T3" means 15°C upwelling stress.

The contents of pigments in *A. marina* changed significantly under short term upwelling stress (6–24 h) ($p<0.05$). For *A. corniculatum*, chlorophyll and carotenoid contents changed significantly in a short period of time under 5°C upwelling while under 10 and 15°C they changed significantly in the later period (after 72h) ($p<0.05$). At 5°C, the pigment contents of *K. obovata* significantly increased during 6 h of exposure ($p<0.05$) while there was no significant difference in pigment contents during later time periods. By contrast, under 10 and 15°C upwellings, in *K. obovata* the pigment contents fluctuated.

3.2 Effect of upwelling stress on membrane systems

As shown in Figure 2A, RECs of *A. marina* first decreased and then increased over treatment time. RECs of *A. corniculatum* and *K. obovata* increased with increasing treatment time.

As shown in Figure 2B, the MDA contents in mangrove species were in the following decreasing order: *A. marina* (21.43–86.75 nmol/g), *K. obovata* (3.40–18.18 nmol/g), *A. corniculatum* (1.33–7.54 nmol/g). The MDA content of *A. marina* significantly increased under upwelling ($p<0.05$). Moreover, the MDA of *A. marina* in upwellings at 5 and 10°C reached a peak at 6–24 h of treatment, while at 15°C, the peak showed at 168 h. Accumulation of MDA in *A. corniculatum* occurred with a prolonged period of stress, while MDA decreased over time in *K. obovata*.

3.3 Effect of upwelling stress on the production of ROS

Changes of ROS in three mangrove plants under upwelling treatments are shown in Figure 3. The amount of O_2- in each plant was in the following descending order: *A. marina* (2439.04–4810.27 μm/g), *K. obovata* (74.78–784.06 μm/g), *A. corniculatum* (38.79–674.09 μm/g) (Figure 3A). Compared to the control, O_2- content significantly increased under upwelling in *A. marina* ($p<0.05$). The content of O_2- in *K. obovata* decreased at first and then increased. The O_2- content of *A. corniculatum* only significantly increased at 6 h under 5°C upwelling stress ($p<0.05$), while under 10 and 15°C there was no apparent change.

Responses of H_2O_2 content to upwelling are shown in Figure 3B. H_2O_2 contents in *A. marina* under 5°C upwelling significantly increased, while under 10 and 15°C, they were significantly lower than the control ($p<0.05$). H_2O_2 content of *A. corniculatum* significantly decreased in the later period of the 5°C-upwelling treatment and significantly increased in the later period of the 10°C and 15°C upwelling periods ($p<0.05$). The H_2O_2 content of K. *obovata* first reduced and then generally rose under the 5 and 10°C upwellings. Under the 15°C upwelling, the H_2O_2 content of *K. obovata* ultimately decreased, and was lower than that observed in the control.

3.4 Effect of upwelling stress on the activity of antioxidant enzymes

The activities of some antioxidant enzymes (CAT, POD, SOD) during upwelling were investigated and are shown in Figure 4. The SOD activity of three mangrove species is basically the same (Figure 4A). There is no significant change in SOD under 5°C upwelling for *A. marina*. Under 10 and 15°C upwelling, the SOD of *A. marina* first decreased, and then significantly increased after 72 h ($p<0.05$). Exposed to upwelling, the activity of SOD in *A. corniculatum* and *K. obovata* declined slightly. Changes of POD were most obvious in *A. marina*, followed by *K. obovata* and *A. corniculatum* (Figure 4B). The POD of *A. marina* significantly increased with duration of upwelling ($p<0.05$). The POD of *A. corniculatum* significantly rosed for 6 and 72 h under a 5°C upwelling while showing a declining trend under 10 and 15°C upwellings ($p<0.05$). The POD of *K. obovata* first decreased and then significantly increased for 168 h under a 5°C upwelling ($p<0.05$). Under 10 and 15°C treatments, changes of POD showed a trend of increasing first and then decreasing.

Under 5 and 10°C upwellings, the activities of CAT in the three mangrove plants changed more than at 15°C (Figure 4C). The CAT of *A. marina* and *A. corniculatum* reached its peak mainly at 24 and 72 h while *K. obovata* showed a different trend. Under 5°C, the maximum CAT of *K. obovata* appeared at 6 h and then declined. In K. *obovata*, at 10°C CAT reached a peak at 12 and 168 h.

3.5 Effect of upwelling stress on the content of osmotic adjusting substances

The variation in levels of proline contents in *A. marina* and *K. obovata* was different to that of *A. corniculatum* (Figure 5A). Changes of proline content in *A. marina* and *K. obovata* were comparatively small, ranging from 16.84 to 121.71μg/g and 21.53 to 174.00 μg/g, respectively. Interestingly, 72 and 168 h upwelling stress induced a tremendous increase in the proline content of *A. corniculatum* ($p<0.05$).

SS contents in *A. marina* showed an increase over treatment time (Figure 5B). The SS contents in *A. corniculatum* first increased and then decreased under stress. There were no significant differences in *K. obovata* in a 5°C upwelling. The minimum SS of *K. obovata* occurred after 24 h at 10°C, and after 72 h at 15°C. Under upwelling stress, SP contents in three

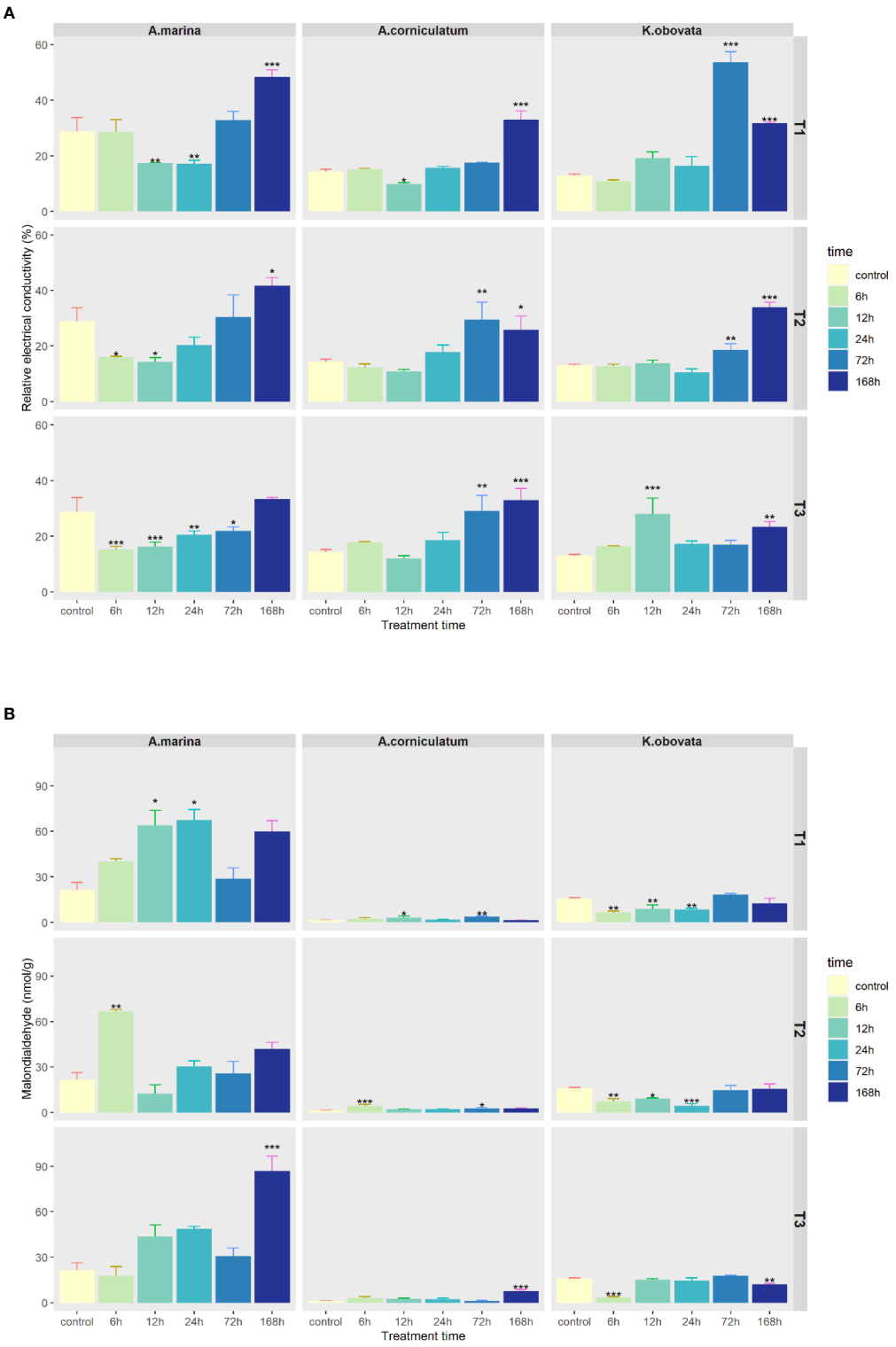

FIGURE 2
Changes of **(A)** Relative electrical conductivity and **(B)** Malondialdehyde content under upwelling stress. * indicates that there are significant differences between control and treatment groups ($p<0.05$(*), $p<0.01$(**), $p<0.001$(***)). "T1" means 5°C upwelling stress, "T2" means 10°C upwelling stress and "T3" means 15°C upwelling stress.

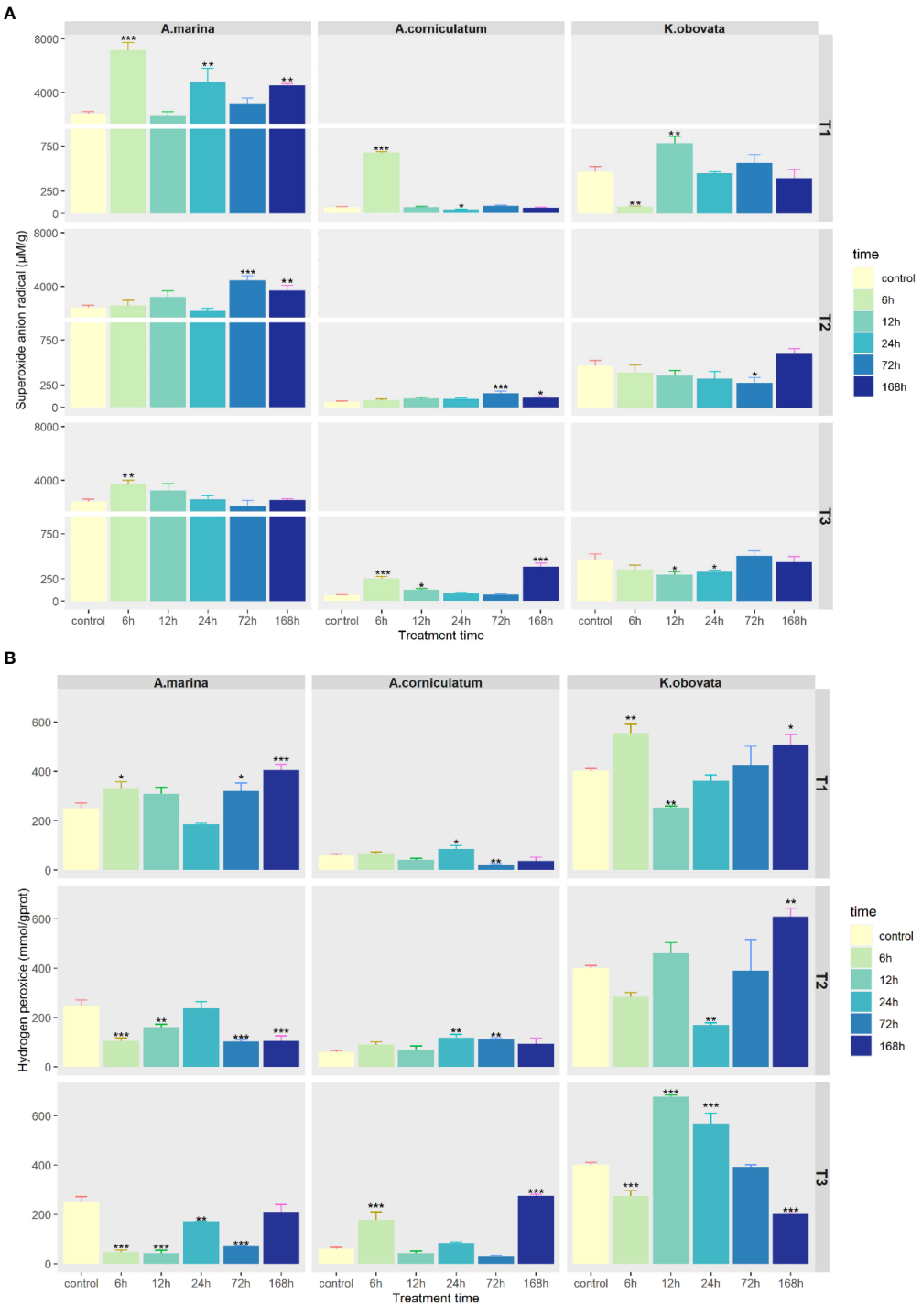

FIGURE 3
Changes of **(A)** Superoxide anion radical and **(B)** Hydrogen peroxide contents under upwelling stress. * indicates that there are significant differences between control and treatment groups [p<0.05(*), p<0.01(**), p<0.001(***)]. "T1" means 5°C upwelling stress, "T2" means 10°C upwelling stress and "T3" means 15°C upwelling stress.

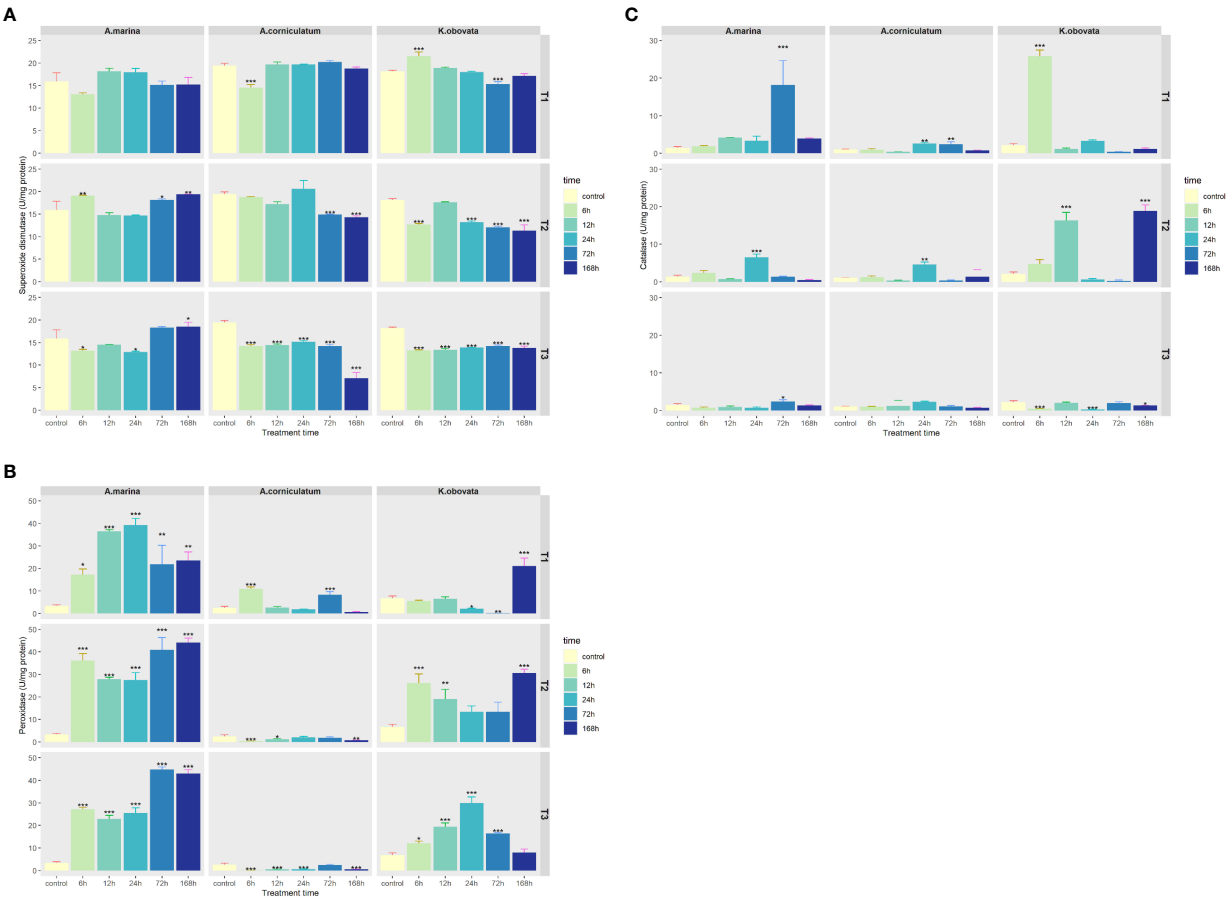

FIGURE 4
Changes of **(A)** Superoxide dismutase, **(B)** Peroxidase and **(C)** Catalase activities under upwelling stress. * indicates that there are significant differences between control and treatment groups ($p<0.05$(*), $p<0.01$(**), $p<0.001$(***)). "T1" means 5°C upwelling stress, "T2" means 10°C upwelling stress and "T3" means 15°C upwelling stress.

mangrove plants were essentially consistent (Figure 5C). At 5°C, the SP contents of the three mangrove plants stabilized at about the same level except after 6 h of stress. At 10 and 15°C, the SP contents of the three mangrove plants significantly increased for 12–72 h ($p<0.05$).

3.6 Principal component analysis

The biplots of PC1 and PC2 based on the analysis of physiological and biochemical traits in three mangrove species under different temperature upwellings were shown in Figures 6 and 7. The first two principal components explained 49.4% of the total variance. The percentage variance and eigenvalues for the first component (PC1) and the second principal component (PC2) were presented in Table 1. PC1 explained 28.6% of the variation. Pigments (chl *a*, chl *b* and *caro*), H_2O_2, REC, MDA and CAT showed a high positive association in PC1 while SOD showed a negative association (loading coefficient >0.2214, Table 1). PC2 explained 20.8% of the variation. While there was a high positive correlation between MDA, O_2- and POD parameters with PC2, proline and SS were negatively correlated with PC2 (loading coefficient >0.2022, Table 1). In addition, a correlation was observed in *A. marina* between O_2-, MDA and POD. Proline and SS were associated with *A. corniculatum*. Furthermore, a clear distinction between mangrove species under upwelling stress was observed. However, different upwelling temperatures did create an obvious separation in the biplot (Figure 7).

3.7 Hierarchical clustering analysis

Physiological and biochemical parameters were subjected to hierarchical cluster analysis using a Euclidean distance matrix *via* Ward's method of agglomeration (Figure 8). Based on the

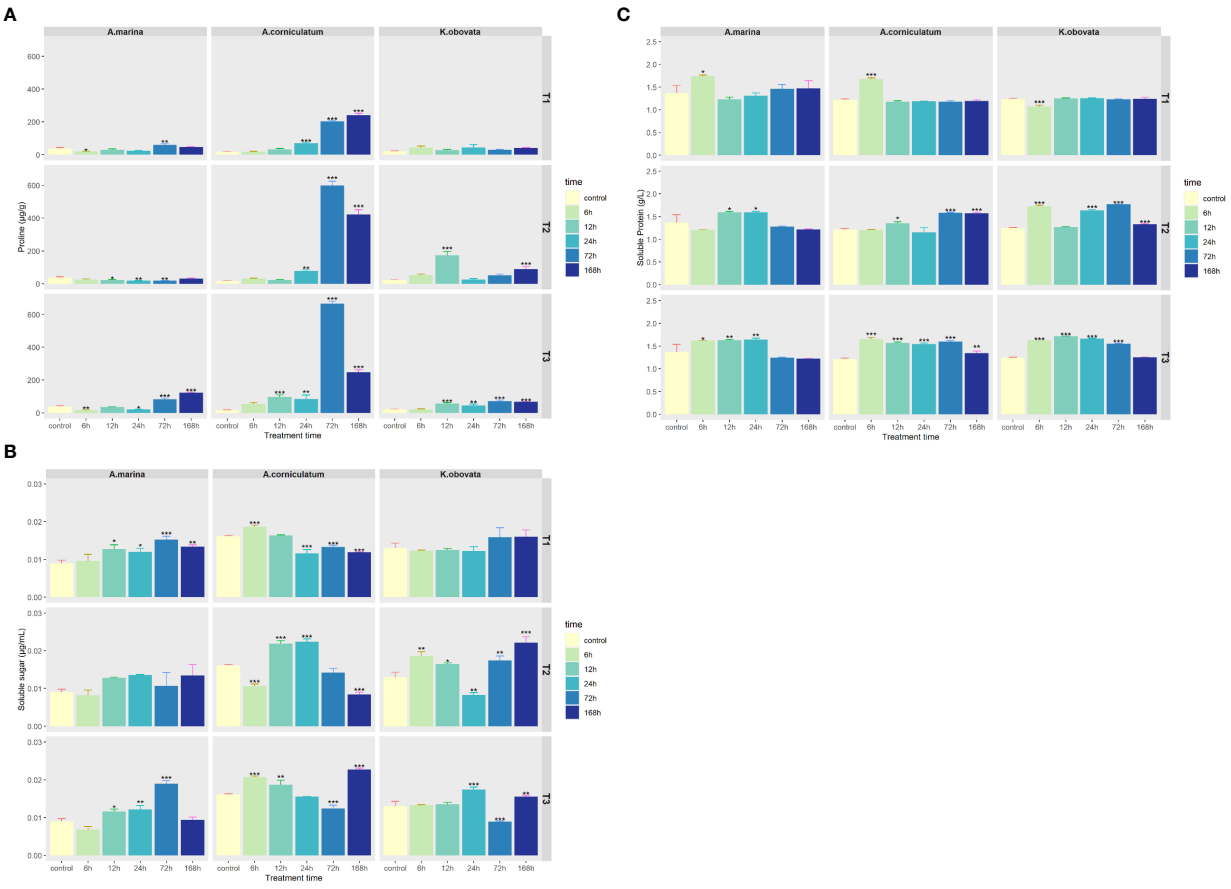

FIGURE 5
Changes of **(A)** proline, **(B)** Soluble sugar and **(C)** Soluble protein contents under upwelling stress. * indicates that there are significant differences between control and treatment groups [p<0.05(*), p<0.01(**), p<0.001(***)]. "T1" means 5℃ upwelling stress, "T2" means 10℃ upwelling stress and "T3" means 15℃ upwelling stress.

dendrogram result, three major clusters were observed which were consistent with PCA. Each cluster was basically composed of one mangrove species. Accordingly, leaf samples of *A. marina* under different upwelling treatments were placed in cluster 1, samples of *A. corniculatum* were placed in cluster 2, and samples of *K. obovata*, and two of *A. corniculatum*, were placed in cluster 3.

4. Discussion

As a result of global climate change, upwelling activity becomes more frequent. Air-water temperature differences caused by upwellings may affect the development, growth and distribution of mangroves. Thus, *A. marina*, *A. corniculatum* and *K. obovata* were selected for a comprehensive investigation into the regulatory mechanisms underlying upwelling stress.

4.1 Damages of mangrove plans under upwelling stress

Low temperature dysregulates active oxygen metabolism in plants, which leads to oxidative stress, cell membrane lipid peroxidation, protein denaturation and nucleotide damage (Jingjing Yu, 2020). Accumulations of O_2- and H_2O_2 in three mangrove species were observed under 5℃ upwelling stress (Figure 3). The O_2- content of *A. marina* was much higher than that of *A. corniculatum* and K. *obovata*, indicating that A. *marina* was more sensitive to upwelling stress. Moreover, in A. *marina* the lower the temperature, the higher the ROS contents. Similar results were reported in silage corn under chilling stress (Jiaxu Wu, 2022). However, there was no such trend in *A. corniculatum* and *K. obovata*, indicating that they were less sensitive to upwelling temperature.

REC and MDA are usually selected as indicators of increased membrane leakage and decreased membrane fluidity. Membrane

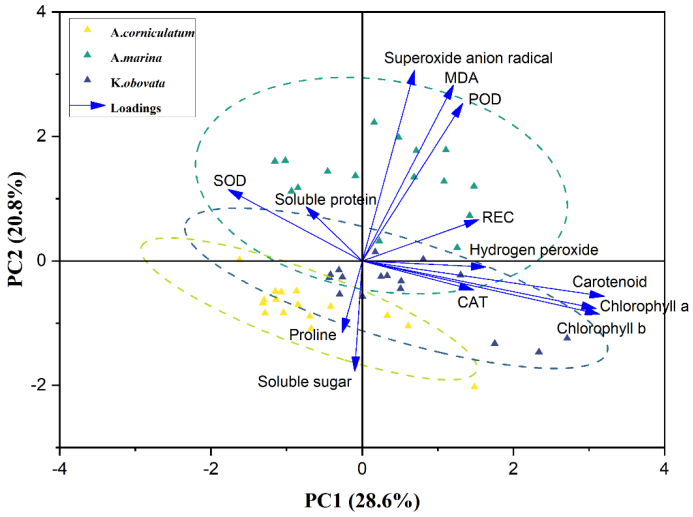

FIGURE 6
Biplot for the first two principal components was analyzed using the principal component analysis (PCA) for 13 traits among 3 mangrove species possessing different treatment. Yellow, green and gray triangles are representing three different mangrove plants. Arrows represented traits while its length is based on the contribution of each trait to separate the accessions. Relative electrical conductivity (REC), malondialdehyde (MDA), superoxide dismutase (SOD), peroxidase (POD) and catalase (CAT).

systems are particularly sensitive to low temperature and ROS-induced oxidation of membrane lipid is a reflection of stress-induced damage at the cellular level (Zheng et al, 2021). In the present study, REC increased in the three mangrove species under upwelling stress (Figure 2A), indicating that upwelling stress induced membrane injury. MDA content in *A. marina* significantly increased while it remained stable in *A. corniculatum* and *K. obovata* (Figure 2B). Moreover, the MDA of *A. marina* was much higher than that of *A. corniculatum* and *K. obovata*, which could be explained by the accumulation of O_2-.

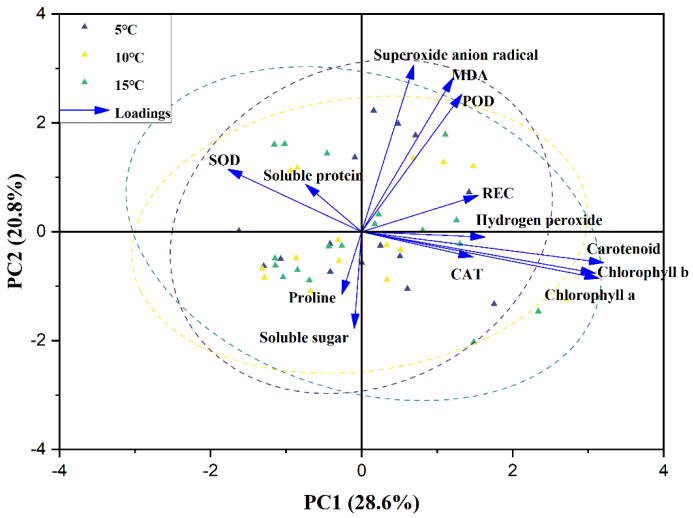

FIGURE 7
Biplot for the first two principal components was analyzed using the principal component analysis (PCA) for 13 traits among 54 samples under 3 different upwelling temperature. Yellow, green and gray triangles are representing three different upwelling temperature. Arrows represented traits while its length is based on the contribution of each trait to separate the accessions. Relative electrical conductivity (REC), malondialdehyde (MDA), superoxide dismutase (SOD), peroxidase (POD) and catalase (CAT).

TABLE 1 Variable loading, percentage variation and eigenvalue derived from PCA for the measured characteristics in three mangrove species under all upwelling treatments.

Variable	PC1	PC2
REC	**0.2314**	0.1167
MDA	0.1815	**0.4944**
Chlorophyll a	**0.4714**	-0.1499
Chlorophyll b	**0.4645**	-0.1337
Carotenoid	**0.4805**	-0.0997
Hydrogen peroxide	**0.2455**	-0.0171
Superoxide anion radical	0.1039	**0.5367**
Soluble protein	-0.1114	0.1523
Soluble sugar	-0.0147	**-0.3102**
Proline	-0.0395	**-0.2022**
SOD	**-0.2658**	0.2011
POD	0.1995	**0.4427**
CAT	**0.2214**	-0.0816
Variance (%)	28.6102	20.7689
Eigenvalue	3.7193	2.6999

PC1, the first principal component; PC2, the second principal component; Relative electrical conductivity (REC); malondialdehyde (MDA); superoxide dismutase (SOD); peroxidase (POD) and catalase (CAT). The bold values represent that the absolute value < 0.2214 in the Colum of PC1 and the absolute value <0.2022 in the Colum of PC2.

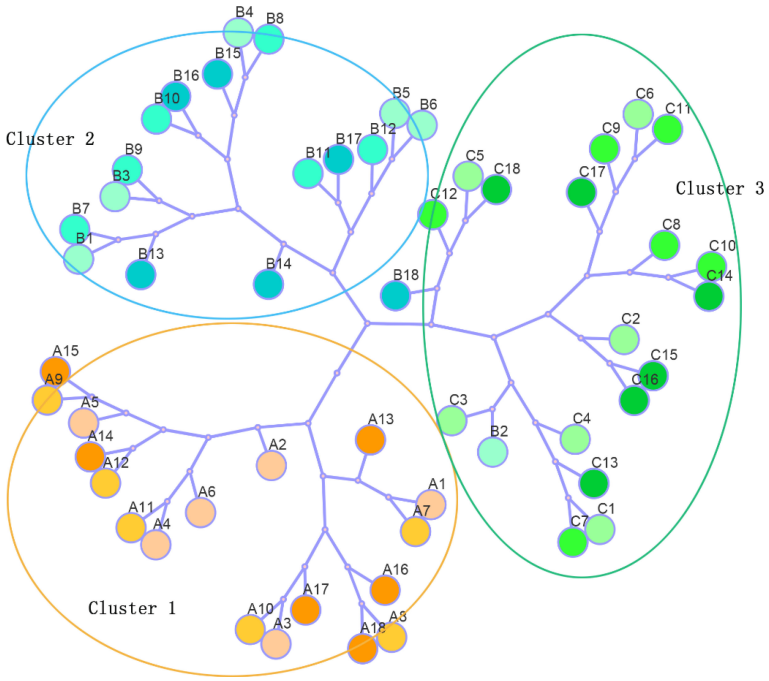

FIGURE 8
Dendrogram was exhibited by cluster analysis of A. *marina*, A. *corniculatum* and K. *obovata* under different upwelling treatment based on the Euclidean distance using physiological and biochemical traits. A represented A. *marina* (yellow circles), B represented A. *corniculatum* (blue circles), C represented K. *obovata* (green circles). Numbers 1-18 represented 5°C upwelling stress-0h, 6h, 12h, 24h,72h and 168h; 10°Cupwelling stress-0h, 6h, 12h, 24h, 72h and 168h; 15°C upwelling stress-0h, 6h, 12h, 24h, 72h and 168h.

4.2 Adjustment mechanism of mangrove plants under upwelling stress

Photosynthetic systems are sensitive to temperature variation, and reduced chlorophyll content usually occurs in plants at low temperatures because chlorophyll biosynthetic enzymes are affected and so biosynthesis progresses slowly (Matej Vosnjak, 2021). In our study, reductions in pigment contents could be observed in *A. marina* and *A. corniculatum* under short-term upwelling stress (6–24 h) which indicates that short-term upwelling caused a degree of damage to mangroves (Figure 1). With increased stress time, pigment contents increased and by significantly more than that of the control group ($p<0.05$), which could be attributed to the protection of protective pigments and other antioxidants in the leaves. Plants are also able to construct a defense system that actively increases their chlorophyll contents and prevents decreases in photosynthesis and energy production (Zhang et al, 2019). In our study, mangroves showed a certain tolerance to long-term upwelling stress because this stress induced increases in pigment contents (Agathokleous et al, 2020). Photosynthesis results in a large increase in the production of ROS (Foyer, 2018). The three mangrove species maintained relatively stable and high chlorophyll contents under long-term upwelling stress, which might be another reason for the high ROS production.

Plants have evolved an efficient enzyme antioxidant mechanism to prevent the oxidative damages caused by ROS (Popov et al, 2020). Among the enzymatic systems, SOD is able to rapidly eliminate O_2- and convert it into H_2O_2, and the generated H_2O_2 is then converted to water and dioxygen by POD and CAT (Honglin Huang, 2019). Stable and high levels of SOD activity were observed in the three mangrove species when exposed to an upwelling stress (Figure 4A) and this might indicate the essential involvement of SOD in scavenging ROS. Compared to the other mangrove plants, POD activity of *A. marina* also showed strong activity (Figure 4B). However, the ROS contents of *A. marina* remained high indicating that the plants' ROS scavenging machinery was not able to defend against oxidative injury. The same results occurred in *K. obovata* with its accumulation of ROS and rather high levels of SOD and POD activity. Under upwelling stress, CAT activity was low in all three mangrove plants (Figure 4C) indicating their "weak affinity" to H_2O_2; this result was also observed in barley under conditions of drought and low temperatures (Zhanassova et al., 2021). Changes in SOD, POD and CAT activity and ROS accumulation in response to upwelling were different in the three mangrove species, indicating that different mangrove plants use different enzyme response mechanisms under these circumstances.

Increases in osmosis-regulating substances (including proline, soluble sugar and soluble protein) can effectively promote the ability of osmotic regulation, enzyme and protein stabilization, ROS detoxification, and the integrity of protective membranes (M. L. Cai, 2020). Proline contents of *A. marina* and *K. obovata* showed no obvious variation under upwelling stress, and proline content of *A. corniculatum* significantly increased under long-term stress (Figure 5A). This showed that long-term upwelling stimulated proline production in *A. corniculatum* to alleviate stress, and proline played an important role in ROS scavenging. Both SS and SP contents among three mangrove species showed slight changes under upwelling stress (Figure 5B, Figure 5C). These results showed that osmotic adjustment substances might not function as the main defense against the stresses of upwelling.

4.3 Species effect and temperature effect under upwelling stress

PCA was performed to detect the relationships among parameters, temperature and mangrove species, during upwelling stress (Figures 6, 7). Pigment contents, ROS, REC, MDA, CAT and POD were observed in the same quadrant, and ANOVA results showed an increasing trend under upwelling stress suggesting some homogeneity in the regulatory mechanism of these traits in the face of upwelling stress for three mangrove species (Behrooz Sarabi, 2022). Previous studies showed that plants respond differently to different temperatures under chilling stress (Ok et al, 2020; Wang et al, 2021). In our research, none of the mangrove species exhibited markedly different responses to variations in upwelling water temperatures, indicating that mangroves are not sensitive to temperature variations in upwelling stress compared to low air or water temperatures.

However, PCA results revealed substantial differences in the dynamics of the responses by *A. marina*, *A. corniculatum* and *K. obovata* to upwelling stress, and these results were further characterized by the results of HCA (Figure 8). Both the PCA and HCA results showed the well separation of different mangrove species during upwelling, which revealed that different mangrove species show distinct sensitivities and tolerances to upwelling stress. The sensitivity of mangrove species to upwelling was preliminarily characterized as A. *corniculatum*< K. *obovata*< A. *marina* which was consistent with their sensitivity to low air temperature (Chen et al, 2017). The aggregation of species and indicators could well explain the tolerance of different species to upwelling. Correlations between *A. marina* and MDA, O_2- and POD in PCA revealed that *A. marina* might be the most intolerant species to upwelling stress with its high activities of SOD and POD but high accumulation of MDA and ROS. *A. corniculatum* did not show damage during short-term upwelling and proline played a major role in alleviating stress during long-term upwelling. According to the PCA and ANOVA results, *K. obovata* alleviated and adapted to upwelling stress by adjusting antioxidant enzyme activity.

5 Conclusion

The changes of *A. marina*, *A. corniculatum* and *K. obovata* under three upwelling temperatures over different exposure durations were comprehensively analyzed. The results showed that upwelling stress causes varying degrees of damage to mangrove plants, and species separation in response was observed, although there was no distinct difference in response of each species to upwelling temperature. Upwelling stress triggered accumulation in ROS resulting in increases of REC and MDA. In accordance with REC, MDA and ROS accumulation, the amount of resistance to upwelling was preliminarily characterized as *A. marina*< *K. obovata*< *A. corniculatum*, and PCA and HCA results strongly supported this conclusion. Upwelling stress also induced increases in plant pigments to synthesize more energy in order to resist adversity. Further, the response mechanisms of each mangrove species to upwelling were different. *A. marina* rapidly activated antioxidant enzyme systems though not enough to scavenge the over-produced ROS. Increased osmotic adjustment substances might be an effective means for *A. corniculatum* to resist long-term upwelling stress. As for *K. obovata*, an antioxidant enzyme system played an important role in resisting upwelling stress. These findings may provide a theoretical basis for further analysis of the physiological and biochemical mechanism of stress tolerance of mangrove plants.

Data availability statement

The original contributions presented in the study are included in the Article/supplementary material, further inquiries can be directed to the corresponding author.

Author contributions

MW and XL contributed to conception and design of the study. XL organized the database, performed the statistical analysis and wrote the first draft of the manuscript. YW, YZ, ZY, JX and FG contributed to review and edit the manuscript. All authors contributed to the article and approved the submitted version.

Funding

This research was supported by the National Natural Science Foundation of China (NO. 31971480), Key Special Project for Introduced Talents Team of Southern Marine Science and Engineering Guangdong Laboratory (Guangzhou) (Nos. 241GML2019ZD0303 and GML2019ZD0303) and the Strategic Priority Research Program of the Chinese Academy of Sciences (No. XDA19060204).

Conflict of interest

Author JX is employed by Guangdong Zhihuan Innovative Environmental Technology Co. Ltd, China. Author FG is employed by Guangzhou Chemical Reagent Factory, China.

The remaining authors declare that the research was conducted in the absence of any commercial or financial relationships that could be construed as a potential conflict of interest.

Publisher's note

References

Agathokleous, E., Feng, Z., and Penuelas, J. (2020). Chlorophyll hormesis: Are chlorophylls major components of stress biology in higher plants? *Sci. Total. Environ.* 726, 138637. doi: 10.1016/j.scitotenv.2020.138637

Ariel E. Lugo, S. C. S. (1974). The ecology of mangroves. *Annu. Rev. Ecol. Evolution. Systematics.* 5, 39–64. doi: 10.1146/annurev.es.05.110174.000351

Behrooz Sarabi, J. G. (2022). Evaluating the physiological and biochemical responses of melon plants to NaCl salinity stress using supervised and unsupervised statistical analysis. *Plant Stress* 4, 100067. doi: 10.1016/j.stress.2022.100067

Bradford, M. M. (1976). A rapid and sensitive method for the quantitation of microgram quantities of protein utilizing the principle of protein-dye binding.Anal.Biochem. *Analytical. Biochem.* 72 (1-2), 248–254. doi: 10.1006/abio.1976.9999

Burchard, H., Basdurak, N. B., Gräwe, U., Knoll, M., Mohrholz, V., and Müller, S. (2017). Salinity inversions in the thermocline under upwelling favorable winds. *Geophysical. Res. Lett.* 44 (3), 1422–1428. doi: 10.1002/2016gl072101

Cai, M. L., Zhang, Q. L., Zheng, X. T., Zhai, J. J., and Peng, C. L. (2020). Comparison of leaves and stems of paederia scandens (Lour.) merr. in tolerance to low temperature. *Photosynthetica* 58 (3), 846–852. doi: 10.32615/ps.2020.034

Chen, L., Wang, W., Li, Q. Q., Zhang, Y., Yang, S., Osland, M. J., et al. (2017). Mangrove species responses to winter air temperature extremes in China. *Ecosphere* 8 (6), e01865. doi: 10.1002/ecs2.1865

Chinnusamy, V., Zhu, J., and Zhu, J. (2007). Cold stress regulation of gene expression in plants. *Trends Plant Sci.* 12 (10), 444–451. doi: 10.1016/j.tplants.2007.07.002

Ensminger, I., Busch, F., and Huner, N. P. A. (2006). Photostasis and cold acclimation sensing low temperature through photosynthesis. *Physiologia. Plantarum.* 126, 28–44. doi: 10.1111/j.1399-3054.2005.00627.x

Feng, J., Dong, P., Li, R-M., Li, C-L., Xie, X-B., and Shi, Q-S. (2019). Effects of wood fiber properties on mold resistance of wood polypropylene composites. *International Biodeterioration & Biodegradation* 140, 152–159. doi: 10.1016/j.ibiod.2019.04.005

Foyer, C. H. (2018). Reactive oxygen species, oxidative signaling and the regulation of photosynthesis. *Environ. Exp. Bot.* 154, 134–142. doi: 10.1016/j.envexpbot.2018.05.003

Geng, Q., Wang, Z., Tao, J., Kimura, M. K., Liu, H., Hogetsu, T., et al. (2021). Ocean currents drove genetic structure of seven dominant mangrove species along the coastlines of southern China. *Front. Genet.* 12, 615911. doi: 10.3389/fgene.2021.615911

Huang, H., Ullah, F., Zhou, D., Yi, M., and Zhao, Yu (2019). Mechanisms of ROS regulation of plant development and stress responses. *Front. Plant Sci.* 10. doi: 10.3389/fpls.2019.00800

Islam, GMd. J., Kim, J. W., Begum, M. K., Sohel, Md. A. T., and Lim, Y.S. (2020). Physiological and biochemical changes in sugar beet seedlings to confer stress adaptability under drought condition. *Plants (Basel).* 9 (11), 1511. doi: 10.3390/plants9111511

Jiang, G., Hassan, M. A., Muhammad, N., Arshad, M., Chen, X., Xu, Y., et al. (2022). Comparative physiology and transcriptome analysis of young spikes in response to late spring coldness in wheat (*Triticum aestivum l.*). *Front. Plant Sci.* 13. doi: 10.3389/fpls.2022.811884

Jianyu Hu, X. W. (2016). Progress on upwelling studies in the China seas. *Rev. Geophysics.* 54 (3), 653–673. doi: 10.1002/2015rg000505

Jingjing Yu, D. S., Yang, D., Dong, T., Tang, Z., Li, H., Han, Y., et al. (2020). Chilling and heat stress-induced physiological changes and MicroRNA-related mechanism in sweetpotato (*Ipomoea batatas* l.). *Front. Plant Sci.* 11. doi: 10.3389/fpls.2020.00687

Khoma, Y. A., Nesterenko, O. G., Kutsokon, N. K., Khudolieieva, L. V., Shevchenko, V. V., and Rashydov, N. M. (2021). Proline content in the leaves of poplar and willow under water deficit. *Regul. Mech. Biosyst.* 12 (3), 519–522. doi: 10.15421/022171

Lei Wang, J. Z., and Liu, C. (2021). Arash arabmarkade). antioxidant activity of potato seedlings at different storage temperatures. *Int. J. Chem. Eng.*, 1–11. doi: 10.1155/2021/5573644

Lin, P. (1997). *Mangrove ecosystem in China* (Beijing: Science press).

Li, M., Wang, Z., Chen, L. Q., Wang, J. J., Li, H. Y., Han, Y. H., et al. (2021). The relationship between the photosynthetic pigments, carotenoids and yield of broomcorn millet (Panicum miliaceum; poaceae). *Appl. Ecol. Environ. Res.* 19 (1), 191–203. doi: 10.15666/aeer/1901_191203

Li, X-M., Wang, Y-S., Dong, J-D., and Wu, M-L. (2022). Physiological and biochemical response of kandelia obovata to upwelling stress. *Water* 14 (6), 899. doi: 10.3390/w14060899

Li, H.X., Xiao, Y., Cao, L.L., Yan, Xu, Li, C., Shi, H.-Y., et al. (2013). Cerebroside c increases tolerance to chilling injury and alters lipid composition in wheat roots. *PloS One* 8 (9), e73380. doi: 10.1371/journal.pone.0073380

Lu, W.X., Zhang, B.H., Zhang, Y.Y., and Yang, S.C. (2021). Differentiation of cold tolerance in an artificial population of a mangrove species, *Kandelia obovata*, is associated with geographic origins. *Front. Plant Sci.* 12, 695746. doi: 10.3389/fpls.2021.695746

Mark Spalding, M. K. (2010). "Lorna collin," in *World atlas of mangroves* (London, UK: Routledge).

Ok, J., Kim, S. H., Ma, K.B., Kim, D., Jeong, H. S., and Shin, H. (2020) Seaonal fluctuation of freezing tolerance and soluble sugar content in three sweet persimmon cultivars *Hortic. Sci. technol* 39 (3), 305–313. doi: 10.7235/HORT.20210027

Peereman, J., Hogan, J. A., and Lin, T.-C. (2021). Cold wave-induced reductions in NDII and ChlRE for North-Western pacific mangroves varies with latitude and climate history. *Remote Sens.* 13 (14), 2732. doi: 10.3390/rs13142732

Petruccelli, R., Bartolini, G., Ganino, T., Zelasco, S., Lombardo, L., Perri, E., et al. (2022). Cold stress, freezing adaptation, varietal susceptibility of *Olea europaea l.*: A review. *Plants (Basel).* 11 (10), 1367. doi: 10.3390/plants11101367

Popov, V. N., and Naraikina, N. V. (2020). Change of antioxidant enzyme activity during low-temperature hardening of *Nicotiana tabacum* l. and *Secale cereale* l. *Russian J. Plant Physiol.* 67 (5), 898–905. doi: 10.1134/s1021443720050118

Rachel Collin, I. O. (2016). Influence of seasonal environmental variation on the reproduction of four tropical marine gastropods. *Mar. Ecol. Prog. Ser.* 555, 125–139. doi: 10.3354/meps11815

Simpson, L. T., Stein, C. M., Osborne, T. Z., and Feller, I. C. (2019). Mangroves dramatically increase carbon storage after 3 years of encroachment. *Hydrobiologia* 834 (1), 13–26. doi: 10.1007/s10750-019-3905-z

Song, W., Feng, J., Krauss, K. W., Zhao, Y., Wang, Z., and Lin, G. (2020). Non-freezing cold event stresses can cause significant damage to mangrove seedlings: assessing the role of warming and nitrogen enrichment in a mesocosm study. *Environ. Res. Commun.* 2 (3). doi: 10.1088/2515-7620/ab7a77

Theochairs, A., Clément, C., and Barka, E. A. (2012). Physiological and molecular changes in plants grown at low temperatures. *Planta* 235 (6), 1091–1105. doi: 10.1007/s00425-012-1641-y

Vosnjak, M., Šircelj, H., Hudina, M., and Usenik, V. (2021). Response of chloroplast pigments, sugars and phenolics of sweet cherry leaves to chilling. *Sci. Rep.* 11 (1), 7210. doi: 10.1038/s41598-021-86732-y

Walters, B. B., Ronnback, Patrik , Kovacs, J. M., Crona, B., Hussain, S. A., Badola, R., et al. (2008). Ethnobiology, socio-economics and management of mangrove forests: A review. *Aquat. Bot.* 89 (2), 220–236. doi: 10.1016/j.aquabot.2008.02.009

Wang, D., Gouhier, T. C., Menge, B. A., and Ganguly, A. R. (2015)7539. Intensification and spatial homogenization of coastal upwelling under climate change. *Nature* 518, 390–394. doi: 10.1038/nature14235

Wang, L., Zhang, J.L., Liu, C., and Arabmarkadeh, A.. (2021). Antioxidant Activity of Potato Seedlings at Different Storage Temperatures. *Int. J. Chem. Engineering*, 1–11. doi: 10.1155/2021/5573644

Wang, R.R., Huang, J., Liang, A.C., Wang, Y., Mur, Alejandro Jose Mur, Wang, M., et al. (2020). Zinc and copper enhance cucumber tolerance to fusaric acid by mediating its distribution and toxicity and modifying the antioxidant system. *Int. J. Mol. Sci.* 21 (9). doi: 10.3390/ijms21093370

Wang, Z., Yu, D., Zheng, C., Wang, Y., Cai, Lu, Guo, J., et al. (2019). Ecophysiological analysis of mangrove seedlings *Kandelia obovata* exposed to natural low temperature at near 30°N. *J. Mar. Sci. Eng.* 7 (9), 292. doi: 10.3390/jmse7090292

Wu, L.L., Deng, Z., Cao, L.F., and Meng, Li (2020). Effect of plant density on yield and quality of perilla sprouts. *Sci. Rep.* 10 (1), 9937. doi: 10.1038/s41598-020-67106-2

Wu, J., Nadeem, M., Galagedara, L., Thomas, R., and Cheema, M. (2022). Effects of chilling stress on morphological, physiological, and biochemical attributes of silage corn genotypes during seedling establishment. *Plants (Basel).* 11 (9), 1217. doi: 10.3390/plants11091217

Ximenes, A. C., Ponsoni, L., Lira, C. F., Dahdouh-Guebas, F., and Koedam, N. (2021). Seasonal atmospheric and oceanographic factors influencing poleward mangrove expansion in the southeastern American coast. *Estuarine. Coast. Shelf. Sci.* 262, 107607. doi: 10.1016/j.ecss.2021.107607

Ximenes, A. C., Ponsoni, L., Lira, C. F., Koedam, N., and Dahdouh-Guebas, F. (2018). Does Sea surface temperature contribute to determining range limits and expansion of mangroves in Eastern south America (Brazil)? *Remote Sens.* 10 (11), 1787. doi: 10.3390/rs10111787

Yang, J., Cao, Y., and Zhang, N. (2020). Spectrophotometric method for superoxide anion radical detection in a visible light (400-780 nm) system. *Spectrochim. Acta A. Mol. Biomol. Spectrosc.* 239, 118556. doi: 10.1016/j.saa.2020.118556

Zhanassova, K., Kurmanbayeva, A., Gadilgereyeva, B., Yermukhambetova, R., Iksat, N., Amanbayeva, U., et al. (2021). ROS status and antioxidant enzyme activities in response to combined temperature and drought stresses in barley. *Acta Physiologiae. Plantarum.* 43 (8), 114. doi: 10.1007/s11738-021-03281-7

Zhang, L. X., Chang, Q. S., Hou, X. G., Chen, S. D., Zhang, Q. M., Wang, J. Z., et al. (2021). Biochemical and photosystem characteristics of wild-type and chl b-deficient mutant in tree peony (*Paeonia suffruticosa*). *Photosynthetica* 59 (2), 256–265. doi: 10.32615/ps.2021.019

Zhang, F.H., Lu, K., Gu, Y., Zhang, L., Li, W.Y., and Li, Ze (2019). Effects of low-temperature stress and brassinolide application on the photosynthesis and leaf structure of tung tree seedlings. *Front. Plant Sci.* 10. doi: 10.3389/fpls.2019.01767

Zhang, Y., Meng, X., Xia, P., and Li, Z. (2021). Response of mangrove development to air temperature variation over the past 3000 years in qinzhou bay, tropical China. *Front. Earth Sci.* 9. doi: 10.3389/feart.2021.678189

Zheng, Y. L., Yang, Y. Q., Wang, M., Hu, S. J., Wu, J. R., and Yu, Z. X. (2021). Differences in lipid homeostasis and membrane lipid unsaturation confer differential tolerance to low temperatures in two *Cycas species*. *BMC Plant Biol.* 21 (1), 377. doi: 10.1186/s12870-021-03158-4

frontiers | Frontiers in Marine Science

TYPE Original Research
PUBLISHED 16 August 2022
DOI 10.3389/fmars.2022.973694

OPEN ACCESS

EDITED BY
Fajin Chen,
Guangdong Ocean University, China

REVIEWED BY
Guisheng Song,
Tianjin University, China
Liyang Yang,
Fuzhou University, China
Chao Wang,
Guangdong Ocean University, China

*CORRESPONDENCE
Xuchen Wang
xuchenwang@ouc.edu.cn

SPECIALTY SECTION
This article was submitted to Marine Biogeochemistry, a section of the journal Frontiers in Marine Science

RECEIVED 20 June 2022
ACCEPTED 25 July 2022
PUBLISHED 16 August 2022

CITATION
Ding L, Shan S, Luo C and Wang X (2022) Distribution and microbial degradation of dissolved organic carbon in the northern South China Sea.
Front. Mar. Sci. 9:973694.
doi: 10.3389/fmars.2022.973694

Distribution and microbial degradation of dissolved organic carbon in the northern South China Sea

Ling Ding[1,2], Sen Shan[3], Chunle Luo[1] and Xuchen Wang[1]*

[1]Frontiers Science Center for Deep Ocean Multispheres and Earth System, and Key Laboratory of Marine Chemistry Theory and Technology, Ocean University of China, Qingdao, China, [2]School of Naval Architecture and Port Engineering, Shandong Jiaotong University, Weihai, China, [3]North China Sea Administration, Ministry of Natural Resources, Qingdao, China

Dissolved organic carbon (DOC) is the largest reduced carbon pool in the ocean, and it plays significant roles not only in the ocean carbon cycle but also in the control of many biogeochemical processes in the ocean. We present the concentrations and distribution of DOC in the northern South China Sea (SCS) and western North Pacific (NP) in the spring and summer seasons of 2015-2016 and 2019. Laboratory incubation bioassay experiments were also conducted to determine the microbiological respiration of DOC. In the SCS, the concentrations of DOC varied within a range of 38-95 μM, and the large spatial variations in DOC in the upper 100 m depth were influenced by a combination of factors, including primary production, terrestrial inputs from the Pearl River and the intrusion of the Kuroshio Current. The mesopelagic DOC distribution in the northern SCS basin was largely influenced by the physical mixing of upwelled deep water; however, biological processes were estimated to account for 6-20% of the modulation in DOC concentrations. Compared with the deep DOC levels in open ocean areas, a slightly excessive DOC concentration (~ 3-4 μM) was observed in the deep water of the SCS basin. Approximately 10-20% of the DOC was consumed by mesopelagic and/or deep water bacteria in the incubation bioassay experiments, and labile DOC was preferentially respired, resulting in decreased $\delta^{13}C$ and $\Delta^{14}C$ values of DOC.

KEYWORDS

carbon cycle, biogeochemistry, dissolved organic carbon, microbial degradation, South China Sea

Introduction

Dissolved organic carbon (DOC) is the largest exchangeable organic carbon pool (~ 662 Pg) in the ocean, equal in size to atmospheric inorganic carbon (Hansell et al., 2009). DOC plays important roles not only in the oceanic carbon cycle but also in supporting and controlling the microbial communities in the ocean (Hansell and

Carlson, 2001; Azam and Worden, 2004; Fenchel, 2008; Benner and Amon, 2015). Minor changes in the DOC pool could thus have a considerable impact on both the carbon cycle and biogeochemical processes in the marine system (Carlson et al., 2010; Nelson and Carlson, 2012; Benner and Amon, 2015; Druffel et al., 2016). The ultimate source of oceanic DOC is thought to be derived from *in situ* primary production that is directly linked to oceanic CO_2 systems (Carlson et al., 1998; Carlson and Hansell, 2015). The removal of DOC *via* microbial uptake is the dominant biological consumption mechanism in the ocean (Hansell et al., 2009; Carlson and Hansell, 2015). As a result, a delicate balance exists between the production and degradation of DOC in the oceanic water column, and the concentrations and distribution of DOC in the deep ocean have been found to be quite consistent (Hansell et al., 2009; Carlson and Hansell, 2015; Druffel et al., 2016; Druffel et al., 2021).

The most dynamic changes in DOC distributions are found in the euphotic zone of the ocean. High DOC concentrations (70-90 μM) have been widely observed in surface water (≤ 100 m) and are related to primary production. Labile DOC (LDOC) is mainly produced from extracellular release by phytoplankton, zooplankton excretion, solubilization and remineralization of particulate organic carbon (POC) (Hansell, 2013; Carlson and Hansell, 2015). After release, the majority of LDOC is rapidly consumed and turned over within hours to days, supporting heterotrophic microbial production and resulting in remains of inorganic constituents (such as CO_2 and nutrients) being suspended within the euphotic zone in the ocean (Carlson and Ducklow, 1996; Cherrier et al., 1996; Hansell, 2013; Carlson and Hansell, 2015). The magnitude of DOC accumulation and export in the euphotic zones of different oceanic regions is therefore ultimately derived from the uncoupling of DOC production and consumption processes. In highly productive regions with high nutrient supplies from upwelling, such as the Peru coast and California Current, high primary production results in high DOC generation and consumption rates (Kirchman et al., 1991; Zweifel et al., 1993; Ducklow, 1999). In contrast, in open ocean sites with low available nutrients, low primary production results in low DOC concentrations and low consumption rates (Carlson and Ducklow, 1996; Carlson et al., 1996; Ducklow, 1999).

It has been estimated that ~17% of new production globally could escape rapid microbial degradation and accumulate in the surface layer of the ocean as semilabile DOC (Hansell and Carlson, 1998). If this portion of the DOC pool is exported into the ocean interior, the majority of exported DOC could become available to microbes and be remineralized within the mesopelagic zone (Hansell et al., 2002; Carlson et al., 2004; Carlson et al., 2010). Instead, a significant fraction of DOC (~ 38 μM), termed refractory DOC resisting to microbial degradation, is present throughout the water column in the ocean. This refractory DOC, characterized by old ^{14}C ages (4,000-6,000 years), likely survives multiple ocean mixing cycles in the ocean (Druffel et al., 1992; Druffel et al., 2019). In fact, DOC in the ocean is a complex mixture comprising thousands of individual molecules, including carbohydrates, proteins, lipids and black carbon (Ziolkowski and Druffel, 2010; Riedel and Dittmar, 2014; Repeta, 2015). Researchers have observed that high molecular weight (HMW) components of DOC were more bioavailable and that carbohydrate-like and protein-like materials comprised younger DOC fractions, whereas low molecular weight (LMW) components and lipids in the oceanic DOC pool were more recalcitrant and were thousands of years old (Guo et al., 1996; Loh et al., 2004; Repeta and Aluwihare, 2006; Benner and Amon, 2015).

Numerous seawater incubation and field studies (spanning days to months) have been conducted to quantify the fate of accumulated DOC and further elucidate the mechanisms controlling the microbial degradation of DOC in the ocean (Carlson et al., 2004; Nelson and Carlson, 2012; Shen and Benner, 2020). Based on these studies, the molecular size and chemical composition of DOC, which are likely linked to its variable radiocarbon age (via $\Delta^{14}C$), appeared to be the primary controls on its bioavailability and degradation in the ocean (Walker et al., 2011; Walker et al., 2016; Shen and Benner, 2020). In addition to quantifying the removal of oceanic DOC, these experiments were also used as platforms to assess the transformation of DOC composition as well as the concomitant shifts in microbial community structures (Carlson et al., 2004; Liu et al., 2020; Varela et al., 2020). While these bioassay experiments focused on the microbial degradation of DOC and provided potential linkages between DOC utilization and microbial lineages, the variation in the $\Delta^{14}C$-DOC values (or radiocarbon ages) during DOC degradation is still enigmatic and only supposed, lacking direct evidence of simultaneous carbon isotope measurements of DOC (both $\delta^{13}C$-DOC and $\Delta^{14}C$-DOC).

The South China Sea (SCS) is one of the largest semienclosed marginal seas in the North Pacific Ocean, covering an area of approximately 3.5×10^6 km^2. A few studies have reported that the surface distribution and seasonal dynamics of DOC in the SCS are largely modulated by water circulation and physical mixing processes (Hung et al., 2007; Pan and Wong, 2015; Meng et al., 2017; Zhang et al., 2020). The carbon isotope (^{13}C and ^{14}C) measurements of DOC further suggested that the dynamics of the DOC pool were mainly controlled by diffusive mixing and intensified vertical motion, rapid water exchange through the Luzon Strait and good water mixing in the SCS basin (Ding et al., 2020). However, Wu et al. (2017) and Ma et al. (2022) observed a significant dependence of DOC on biological production using measured and model results. Despite these studies on the dynamics of DOC in the SCS, the nature of its microbial degradation has not been well studied, and knowledge of the

variations in DOC concentrations and the Δ^{14}C-DOC values concomitant with DOC removal is still limited.

In this paper, we present the results of our field investigation of the concentrations and distribution of DOC in the northern SCS and the western North Pacific (NP). This field investigation was combined with laboratory incubation bioassay experiments characterizing the concentration and carbon isotopic (^{13}C and ^{14}C) signatures to evaluate the biological and hydrodynamic controls on the distribution of DOC in the northern SCS and to identify changes in DOC concentration and isotopic values associated with DOC degradation at the Southeast Asian Time-series Study (SEATS) site in the SCS.

Methods

Study areas

The SCS has an average water depth of 1,350 m and a maximum water depth of ~ 5,000 m in the northeast region (Chen et al., 2001). It is connected to the open ocean only through the Luzon Strait, with a maximal sill depth of approximately 2,200 m, and to the East China Sea (ECS) through the shallow Taiwan Strait (~ 50 m) (Figure 1). The northern SCS has an extensive shelf and is influenced by the input of the Pearl River, which is the second largest river in China and ranks 17th in the world in terms of annual water discharge (Dai et al., 2014). The surface circulation in the SCS is driven by a seasonal monsoon influence, which is characterized by a cyclonic circulation gyre in the entire deep basin during the northeast monsoon prevailing in winter and a strong anticyclonic gyre mainly in the south and a weakened cyclonic gyre in the north during the southwest monsoon that prevailing in summer (Liu et al., 2002; Qu et al., 2006; Wang and Li, 2009). These basin-wide surface circulation gyres effectively isolate the interior SCS from the influence of land runoff. Moreover, the Kuroshio intrusion through the Luzon Strait located at the northeastern rim also has an important impact on the circulation in the northern SCS, which is stronger in winter and weaker in summer (Nan et al., 2015; Jiang et al., 2020). Under the influence of seasonal atmospheric and oceanic forcing, the oceanic biogeochemistry in the SCS varies in space and time.

Sample collection and processes

Water samples for DOC concentration analysis were collected from two stations (S4 and S5) in the northern SCS during a summer cruise in July 2015 onboard R/V *Shiyan 3*, from 11 stations (A1, 2A1, A3, A6, A8, A10, K4, G2, F1, Y1 and SEATS) covering the northern shelf-slope-basin regions of the SCS during a spring-summer cruise in May-June 2016 onboard R/V *Dongfanghong-2* and from six stations (C06, C09, C16, C20, C26 and C28) nearby the Luzon Strait during a summer cruise in July August 2019 onboard R/V *Haida* (Figure 1). Among these

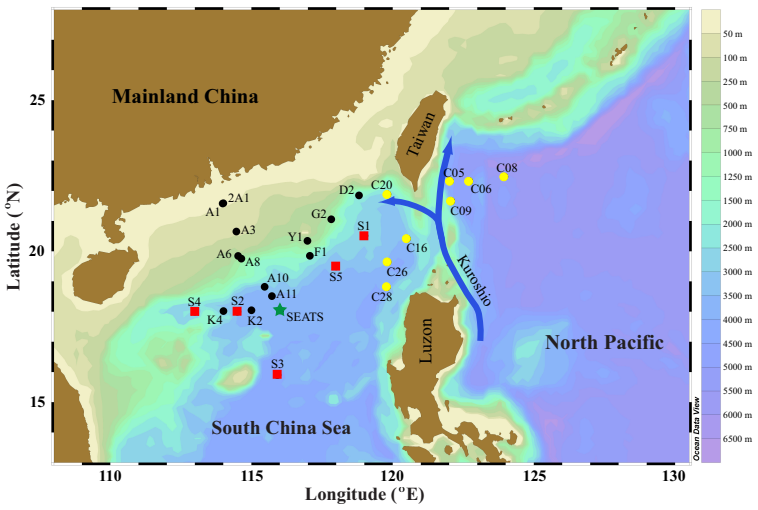

FIGURE 1
Map showing the study region and the locations of sampling stations in the northern SCS and western NP during three cruises in 2015 (red squares), 2016 (black circles) and 2019 (yellow circles), as described in the text. Seawater samples used for the incubation bioassay experiments were collected at the SEATS site (green star) during the cruise in May-June 2016. The blue arrows are the Kuroshio Current and its branching path into the SCS. Sampling stations in the SCS and western NP, from which published data were used for data validation in this paper, are also shown: S1, S2 and S3 (red squares) from the same cruise in 2015; D2, A11 and K2 (black circles) from the same cruise in 2016; and C05 and C08 (yellow circles) from the same cruise in 2019 (Ding et al., 2020). This map was created with Ocean Data View (ODV) (Schlitzer, 2017).

sampling stations, SEATS (18.3 °N and 115.5 °E) is the Southeast Asian time-series study site established in 1999, at which primary production and the carbon cycle have been extensively studied in recent decades. Water samples from these stations were collected using 5 L or 12 L Niskin bottles deployed on a rosette with a calibrated conductivity-temperature-depth (CTD) recorder that recorded the depth profiles of temperature and salinity. The CTD was calibrated at the National Center of Ocean Standards and Metrology in China (NCOSM) before the cruises and were within the calibration term of validity. In addition, large volumes of seawater (4-13 L) from the surface layer (5 m) and at 700 m and 1,500 m depths were collected at the SEATS site during the cruise in May-June 2016 for incubation bioassay experiments as described below.

After collection, water samples for DOC concentration analysis were transferred directly into a 1 L precombusted (550°C for 4 h) glass bottle that was first rinsed three times with seawater. The water was filtered immediately through Whatman GF/F filters (~ 0.7 μm, precombusted at 550°C for 4 h) on board. The filtered seawater was then acidified with super high purity 85% H_3PO_4 to pH ≤ 2 and preserved frozen at -20°C for analysis in the laboratory.

DOC incubation experiments

Previous studies have demonstrated that the surface water DOC that was originally resistant to degradation could be available to the mesopelagic microbial assemblage in the open ocean (Carlson et al., 2004; Nelson and Carlson, 2012; Shen and Benner, 2020). To test this in the SCS, we conducted incubation experiments by mixing filtered and unfiltered seawater from different depth at the SEATS site to evaluate the removal of DOC and simultaneous changes in the isotopic composition of bulk DOC. The designation of the experiments was based on Carlson et al. (2004). Briefly, surface seawater (5 m) was filtered with 0.22 μm Millipore polycarbonate filtrate (rinsed with the same seawater) to remove bacteria and then mixed separately with unfiltered mesopelagic (700 m) or deep (1500 m) seawater at a ratio of 2:1 (volume/volume). The mixed seawater in each experiment was well shaken and incubated with O_2 in the dark at room temperature (~26°C) for 180 days. Both incubations were conducted in duplicates. Samples for DOC concentration analysis were taken at various incubation time intervals (25-40 days) throughout the experiments by draining seawater directly from the incubation carboys into precombusted glass vials to prevent potential contamination. In addition, seawater samples for Δ^{14}C-DOC and δ^{13}C-DOC measurements were collected at the beginning and end of the experiments.

DOC concentration and isotope measurements

The DOC concentrations were analyzed by the high-temperature catalytic oxidation method (Sharp et al., 1995) using a Shimadzu TOC-L analyzer equipped with an ASI-V autosampler. The concentrations of DOC were calibrated using a six-point calibration curve generated from DOC standards prepared using potassium hydrogen phthalate and UV-oxidized Milli-Q high purity water. The instrumental blank and standard validations for DOC were checked against reference samples of low-carbon water and deep seawater that were provided by Dr. Hansell's Laboratory at the University of Miami, USA. Blank subtraction was carried out using Milli-Q water that was analyzed before each sample. The average blank associated with DOC measurements was ≤ 4 μM, and the analytic precision on triplicate injections was ± 3%. All DOC samples were analyzed in duplicate, and the standard deviations of the replicate measurements ranged from ± 0.1 to 4.0 μM.

For Δ^{14}C-DOC measurements, seawater samples were UV-oxidized and extracted as gaseous CO_2 using a previously described modified method (Xue et al., 2015). Briefly, following the UV-oxidation of DOC, the generated CO_2 was purged and collected with ultrahigh purity helium gas through the vacuum line cryogenically and flame-sealed inside a 6 mm OD quartz tube. The oxidization efficiency that was tested using a DOC standard solution (oxalic acid) was ~ 95% (Xue et al., 2015). Both the δ^{13}C and Δ^{14}C were measured at the National Ocean Sciences Accelerator Mass Spectrometry (NOSAMS) facility at the Woods Hole Oceanography Institution (WHOI). The gaseous CO_2 was split into a small fraction for δ^{13}C measurement using a VG isotope ratio mass spectrometer, and the rest was graphitized for Δ^{14}C analysis using accelerator mass spectrometry. Radiocarbon results were reported as modern fraction (McNichol et al., 1994), and δ^{13}C values were reported in ‰ relative to the Vienna Pee Dee Belemnite (VPDB) standard. The analytic precision for δ^{13}C is <0.2‰, and the error of Δ^{14}C measurement is ±5‰, as determined from the standard.

Results

Hydrographic characteristics

The hydrographic data (temperature and salinity) are listed in Supplementary Table S1, and the vertical profiles are plotted in Figure 2. The characteristics of the water are further described in the *T-S* diagram (Figure 3A). The water temperature was higher at the surface (5 m: 26.8-30.8°C), decreased with depth down to approximately 1,500 m (2.7° C), and then remained constant at depths below 1,500 m at

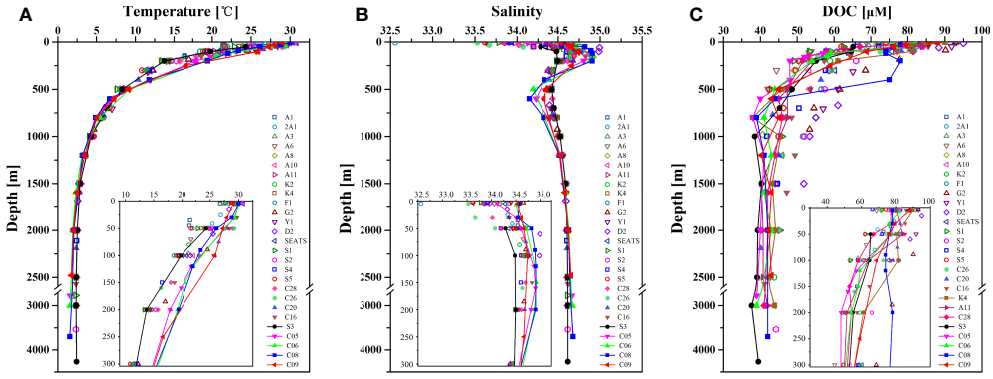

FIGURE 2
Depth profiles of **(A)** water temperature, **(B)** salinity, and **(C)** DOC concentrations measured at the 27 stations in the northern SCS and western NP during three cruises in 2015, 2016 and 2019 in this study and a previous report, as described in Figure 1. The depth below 2,500 m is on a different scale, and the inset figures show profiles in the upper 300 m depth. Note that the hydrographic data and DOC concentrations for eight stations (S1, S2, S3, D2, A11, K2, C05 and C08) were collected on the same cruises and have been previously published (Ding et al., 2020). These data are cited for comparison with the 19 stations in this study.

density levels of σ_0 ≥27.6 kg/m^3 at all stations (Figures 2A, 3A). The salinity ranged from 32.56 to 34.99 and exhibited a profile trend that was opposite to that of temperature (Figure 2B), i.e., lower at the surface (5 m: 32.56-34.65), increasing rapidly with depth to a maximum at a water depth of approximately 60-200 m (at a density range of 23.1-25.2 σ_0) and decreasing again to a minimum at a water depth of approximately 500-600 m (σ_0 ~26.8 kg/m^3). Importantly, the salinity maximum and minimum values were significantly weakened in the northern SCS compared to those in the western NP (i.e., stations C05, C06 and C08). The salinity remained relatively homogeneous below 1,500 m (at σ_0 ≥27.6 kg/m^3) for all stations (Figures 2B, 3A). The abnormally lower surface salinity (S=32.56) at station 2A1, which was sampled after heavy rainfall, should be noted. In contrast, as shown in the *T-S* diagram (Figure 3A), a less curved inverse "*S*" shape of the *T-S* property was observed in the northern SCS (i.e., stations S3, A10 and C26).

Concentrations and distribution of DOC

At the 27 stations sampled on the three cruises in this study and in a previous study (Ding et al., 2020), the concentrations of DOC varied within a range of 38-95 μM for the spring and summer seasons of 2015-2016 and 2019 in the northern SCS and western NP (Figure 2C and Table S1). High DOC concentrations (66-95 μM) were measured in the upper 20 m of the water column (σ_0 < 22.3; Figures 2C, 3B), especially at the 2A1 shelf station and at stations (D2, Y1, G2 and F1) (91-95 μM) near southwestern Taiwan and the western Luzon Strait region. The DOC concentrations decreased rapidly down to a depth of approximately 800 m and then remained relatively low and constant in a range of 38-45 μM below a 2,000 m depth at a density σ_0 > 27.6 across all stations (Figures 2C, 3B). The average DOC concentrations below a 1,500 depth at most stations (except S4 and D2) were similar within analytic error, ranging from 39 ± 1 μM (S3) to 44 ± 3 μM (C16), compared well to the concentrations in the deep western NP (39-43 μM, average 41 ± 2 μM). As plotted in Figures 2C, 3B, the DOC concentrations showed large spatial variations above the 100 m water depth (at σ_0 ≤ 24.9) among the stations, with visibly higher values (78-95 μM) at stations (D2, Y1, G2, F1, C16 and C20) near southwestern Taiwan and the western Luzon Strait than at stations S1, A6, A8 and C28 (53-77 μM).

Degradation of DOC at SEATS

In the laboratory incubation experiments, when the surface water (5 m) in which bacteria were removed was mixed with the water from 700 m and 1500 m depths in which bacteria were present, we observed DOC concentration changes (Table 1 and Figure 4). The measured initial DOC concentrations in the mixed water (71 ± 1 μM and 68 ± 2 μM) were consistent with the calculated DOC concentrations (72 μM and 69 μM) of a simulated mixed water column by diluting surface water DOC (84 μM) with 33% lower DOC water (47 μM) from 700 m, and 33% lower DOC water (41 μM) from 1,500 m, respectively. This indicates that the addition of mesopelagic or deep bacterial inoculum resulted in no notable differences between the *in situ* concentrations and initial DOC concentrations in the incubation (Table 1), and no inadvertent contamination of labile DOC was

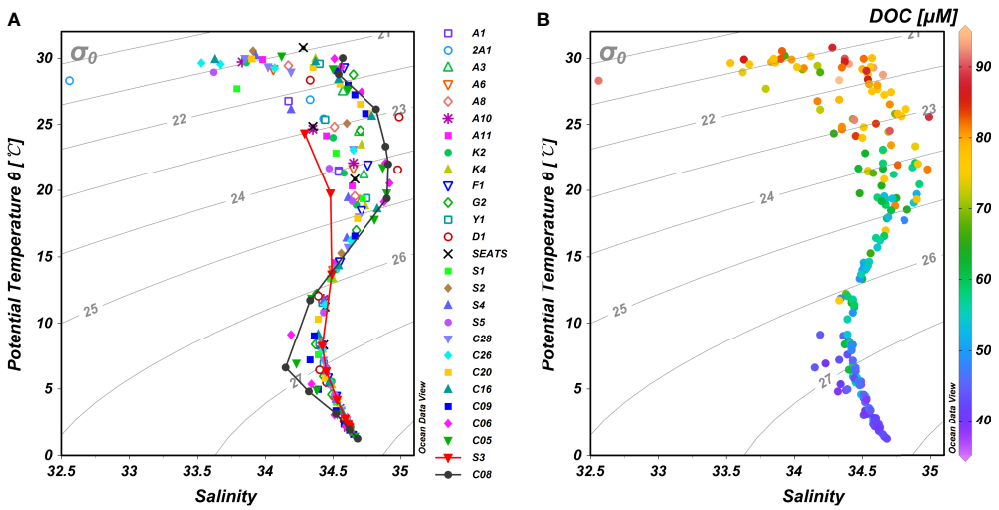

FIGURE 3
Plots of **(A)** potential temperature versus salinity (*T-S*) alone and **(B)** superimposed by observed DOC concentrations at stations in the northern SCS and western NP measured during three cruises (2015, 2016 and 2019). The σ_0 isolines (gray) are included in the figures. The colored symbols in panel **(A)** correspond to CTD data, and solid lines (red and black) designate the representative T-S properties of the SCS and Kuroshio Current at stations S3 and C08, respectively (Ding et al., 2020). All figures were generated using ODV (Schlitzer, 2017).

added during the experimental preparation as suggested previously (Carlson et al., 2004; Li et al., 2021). The DOC concentrations increased to their highest values (76 μM and 73 μM) from the initial concentrations after 25 days and then subsequently decreased with incubation time from 25-180 days (Figure 4). At the end of the incubation (180 days), the initial DOC concentration decreased from 71 μM to 62 μM (Expt. SM521) and from 68 μM to 61 μM (Expt. SD521), and approximately 13% and 10% of the DOC was respired, respectively (Table 1).

The isotopic values measured for DOC at the beginning of and after the incubation experiments also showed noticeable changes. In Expt. SM521 and Expt. SD521, the $\delta^{13}C$ values of DOC decreased from their initial values of -22.3‰ and -22.4‰ to -22.8‰ and -23.1‰, respectively, by the end of the incubation experiments. For the $\Delta^{14}C$ values of DOC, significant decreases of -25‰ and -76‰ were observed in Expt. SM521 and Expt. SD521, respectively, by the end of the incubation experiments (Table 1).

Discussion

Processes that control the concentration and profiles of DOC in the SCS

As the SCS is the largest marginal sea in the western NP, the distribution and dynamics of its DOC could be influenced by many factors, such as primary production, terrestrial inputs from the Pearl River, water exchange with the Kuroshio Current and hydrodynamic mixing of different water masses (Dai et al., 2009; Wu et al., 2015; Meng et al., 2017; Ding et al., 2020; Zhang et al., 2020; Ma et al., 2022). The large variations in the measured DOC concentrations (53-95 μM) above the 100 m water depth were consistent with the results of previous studies (55-97 μM) conducted in the SCS (Pan and Wong, 2015; Wu et al., 2015; Zhang et al., 2020). The surface DOC concentration was notably up to ca. 91 μM at station 2A1, which was sampled after a heavy rain event in early summer near the Pearl River Estuary. Low

TABLE 1 Concentration of DOC and its isotopic values measured at the beginning (Day 0) and end (Day 180) of the two laboratory incubation experiments using seawater collected from the SEATS site.

Experiment ID	Treatment	DOC (μM)		$\delta^{13}C$-DOC (‰)		$\Delta^{14}C$-DOC (‰)	
		Day 0	Day 180	Day 0	Day 180	Day 0	Day 180
SM521	5 m filtrate mixed with unfiltered 700 m seawater	71 ± 1	62 ± 1	-22.3	-22.8	-304	-329
SD521	5 m filtrate mixed with unfiltered 1,500 m seawater	68 ± 2	61 ± 1	-22.4	-23.1	-315	-391

For the two incubation experiments, approximately 6 L of filtered (0.2 μm, to remove bacteria) surface seawater was mixed with 3 L of unfiltered seawater from a 700 m depth (SM521), and 6 L of filtered (0.2 μm) surface seawater was mixed with 3 L of unfiltered seawater from a 1,500 m depth (SD521) within 1 h of seawater collection and filtration.

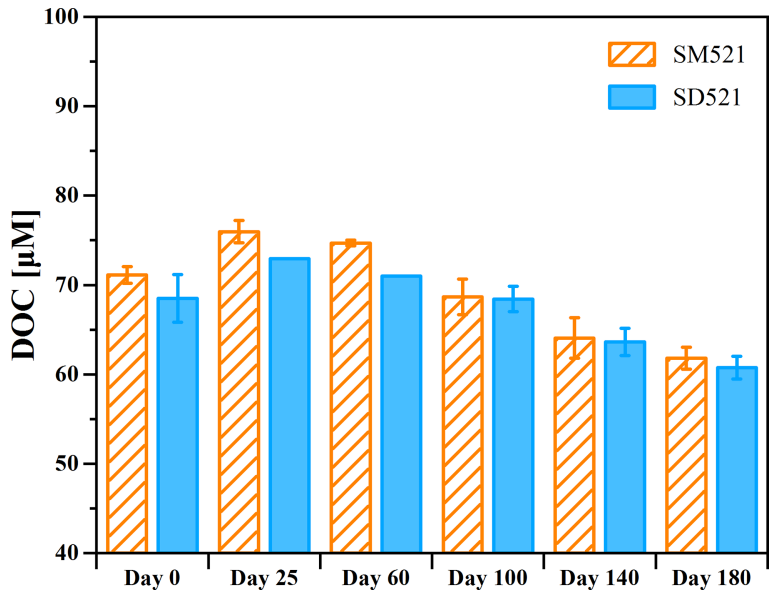

FIGURE 4
Measured DOC concentration changes with time during the two incubation experiments (SM521 and SD521). The error bars denote the means with standard errors from the duplicate analysis.

salinity (S=32.56) water was measured at this station but not at other stations in the study area (Figures 2B, 3A), implying the limited dilution effect of fresh coastal waters. Combined with the low salinity (S=32.56) and high temperature (T=28.3°C) of the surface water, the high DOC concentration at station 2A1 (Figures 2C, 3B) could be modulated by the cross-shelf transport of coastal water. As plotted in Figure 5, significantly high levels of DOC (93-95 μM) were observed in the surface water (≤15 m) at four other stations (D2, G2, F1 and Y1) located near southwestern Taiwan Island and the western Luzon Strait in spring (Figure 5E). At these stations, the salinity in the upper layer was clearly higher than that in the surrounding waters (Figures 5C, D), indicating the intrusion of the Kuroshio Current, which carries high salinity and high DOC water into the region. However, surface DOC concentrations and salinity were not significantly elevated at other stations in the vicinity of the western Luzon Strait in the summer season (stations S1, S5, C16, C20, C26 and C28 in Figures 5D, F). In this context, the intrusion of the Kuroshio Current and the high primary productivity in spring would increase the surface DOC concentrations in the western region of the Luzon Strait. Compared to that in the spring season, the Kuroshio intrusion was weaker in summer and had a limited impact with distance from the Luzon Strait (Du et al., 2013; Nan et al., 2015; Jiang et al., 2020); thus, high surface concentrations were not observed in summer around the same region and at other stations in the SCS basin.

Several studies have used an isopycnal mixing model proposed by Du et al. (2013) to quantify the impact of Kuroshio intrusion on the DOC and chromophoric dissolved organic matter (CDOM) in the upper 100 m water depth of the northern SCS (Wu et al., 2015; Wang et al., 2017; Li et al., 2021). Using this model, we calculated the mixing ratio of the Kuroshio water and SCS water along the isopycnal layer for the *in situ* observed water parcel shown in the *T-S* diagram (Figure 3A). The relative contributions of SCS and Kuroshio water can be derived based on the conservative mixing of salinity or potential temperature (Equations 1-2).

$$R_S\theta_S + R_K\theta_K = \theta \text{ or } R_S S_S + R_K S_K = S \quad (1)$$

$$R_S + R_K = 1 \quad (2)$$

where R_K and R_S denote the Kuroshio and SCS water proportion in the mixed water; S_S, S_K, θ_S *and* θ_K are the end-member values of salinity and potential temperature for the SCS (station S3) and Kuroshio (station C08) water proper in Figure 3A. The station-integrated Kuroshio water fraction (R_{IKW}) were obtained by integrating the Kuroshio water fraction (R_K) over the upper 100 m water column (Figure 6). It appeared that the R_{IKW} in the region near the southwestern Taiwan Island (approximately 0.6) was higher than that in the central northern SCS (< 0.3) in spring (Figure 6A), and both comparable but little higher than that reported in previous studies in the same season (Du et al., 2013; Wu et al., 2015;

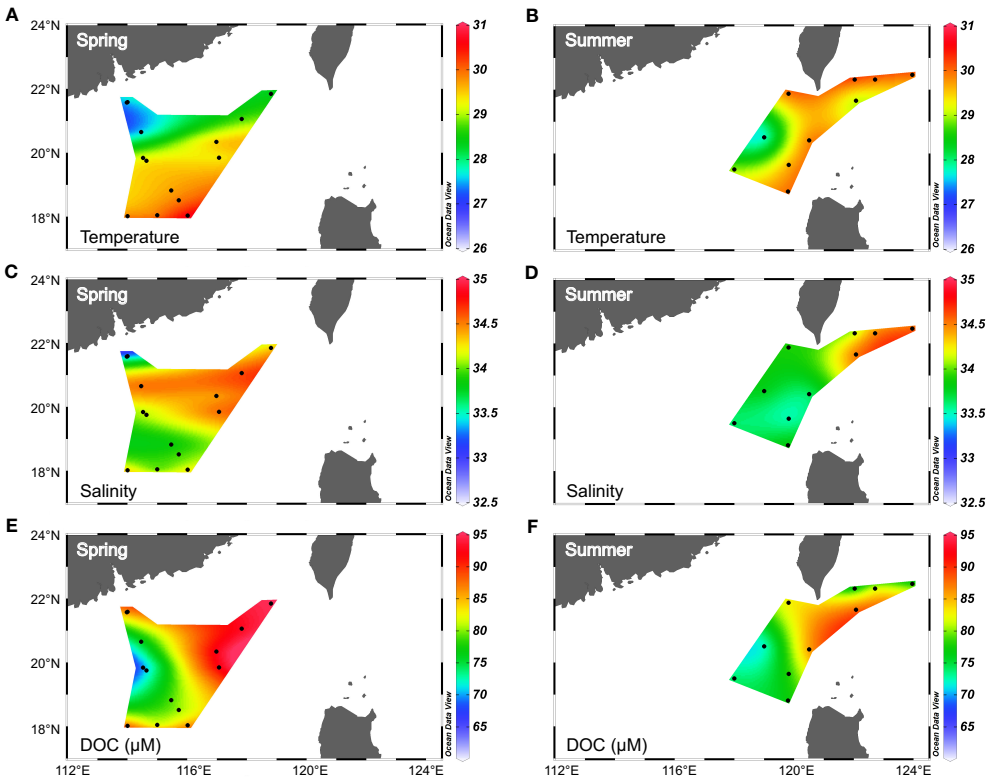

FIGURE 5
Surface distribution (≤15 m water depth) of **(A, B)** temperature (°C), **(C, D)** salinity and **(E, F)** DOC (μM) in the northern SCS and western North Pacific during spring **(A, C, E)** and summer **(B, D, F)** in 2015-2016 and 2019. For comparison, the hydrographic data and DOC concentrations at stations S1, S2, S3, D2, A11, K2, C05 and C08 that were collected during the same three cruises by Ding et al. (2020) are presented. These figures were created using ODV (Schlitzer, 2017).

Wang et al., 2017). During summer, the R_{IKW} was relative lower in the eastern part of the northern SCS with values of approximately 0.2-0.3, excluding the stations C16 and C20 located nearby the Luzon Strait (Figure 6B). The spatial and seasonal distribution of R_{IKW} further support the impact of Kuroshio intrusion on the DOC dynamics in the upper 100 m water depth in the northern SCS.

On the basis of the derived Kuroshio and SCS water fractions (R_K and R_S), DOC concentrations (referred to as DOC_{Model}) along the isopycnal surface due to conservative mixing between

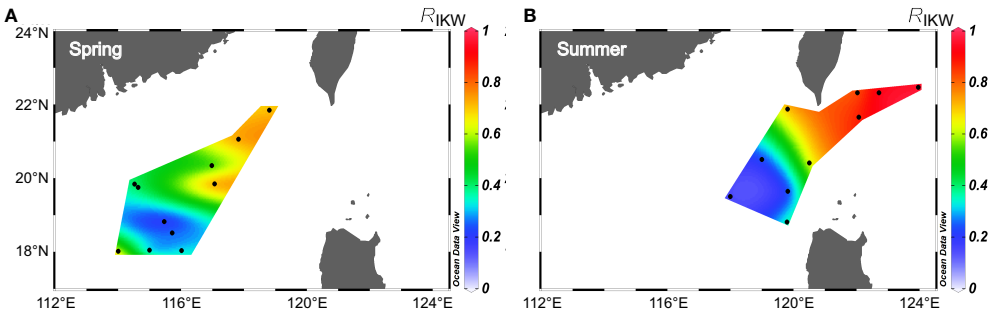

FIGURE 6
Station-integrated Kuroshio water fraction (R_{IKW}) in the upper 100 m of the northern SCS during spring **(A)** and summer **(B)**.

the Kuroshio water proper and SCS water proper can be calculated using Equation 3 (Wu et al., 2015).

$$DOC_{Model} = DOC_S R_S + DOC_K R_K \quad (3)$$

Here, DOC_K and DOC_S are the end-member values of the Kuroshio water (station C08) and SCS water (station S3), respectively. The difference between the field and model calculated DOC concentrations ($\Delta DOC = DOC_{measured} - DOC_{Model}$) could indicate other biologically mediated production (positive ΔDOC value) or degradation (negative ΔDOC value) of DOC in the upper water column. Through this isopycnal mixing model, ΔDOC was estimated in the range of -11 to 10 μM in the upper 100 m of the northern SCS. Therein, the positive ΔDOC values that accounted for approximately 6-14% of the DOC pool at most stations during spring, suggesting a net DOC production. This is consistent with the ~7% increased DOC inventory due to the biological metabolism calculated by Wu et al. (2015) and the fact that the primary production was high in spring (Liu et al., 2002; Liu and Chai, 2009). However, ΔDOC was negative in the upper 50 m at stations S1, S2, S4 and S5 during summer, indicating a net degradation of DOC which accounted for 7-12% of the field DOC pool. The removal of DOC might be attributed to enhanced biodegradation in the mixing zone of SCS and Kuroshio water in summer (Li et al., 2021).

In general, the wide basin of the SCS is oligotrophic year-round and has low primary production due to the low nutrient concentrations and limited influence of Pearl River input (Gong et al., 1992; Lin et al., 2010; Dai et al., 2013). As shown in Figures 2B, 3A, the high salinity signals without freshwater dilution in the slope and basin regions further indicate that the influence of river input was limited in the northern SCS. The DOC depth profiles for the deep stations in the SCS exhibited the same typical vertical patterns as observed in the western NP (stations C05, C06, C08 and C09) and in other open ocean areas with relatively high values (~75 μM) in the surface layer, generally decreased with increasing depth below the euphotic zone by microbial consumption, and then remained low at constant values (~ 40 μM) at greater depths (≥ 1,500 m) and were controlled mainly by hydrodynamic mixing (Carlson et al., 1994; Hansell et al., 2009; Hansell et al., 2012; Druffel and Griffin, 2015; Bercovici and Hansell, 2016). Hung et al. (2007) and Pan and Wong (2015) reported that the distribution of DOC in the northern SCS was largely modulated by physical mixing processes, and the seasonal cycle of surface DOC covaried with temperature rather than primary production, also indicating a physical control on the seasonal variations in DOC. In this respect, we observed a statistically significant negative correlation between DOC and density (σ_t) ($R^2 = 0.82$, $p < 0.001$) at all stations (Figure 7A), suggesting that physical mixing processes played important roles in the distribution and variations in DOC in the northern SCS and western NP. The negative correlation between the DOC and dissolved inorganic carbon (DIC) concentrations (Figure 7B, $R^2 = 0.68$, $p < 0.001$) at the stations also suggested that physical mixing of the water largely influenced the DOC distribution in the northern SCS. However, since DOC is not conservative in the ocean, the observed correlation between DOC and DIC could involve biological and microbial processes (Yang et al., 2016).

Nevertheless, DIC concentrations and Δ^{14}C-DIC could be used as tracers of water mass movement and parcel homogenization as predicted by a solution mixing model and thus supplied evidence of the intensified upwelling and vertical mixing in the water column of the SCS (Ding et al., 2020). To

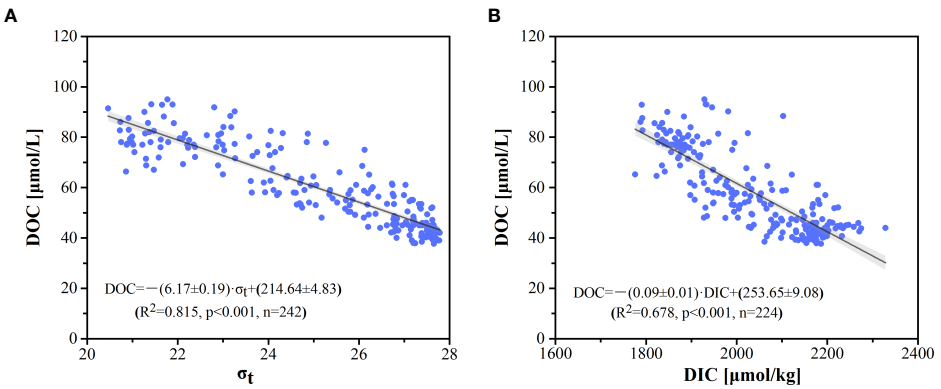

FIGURE 7
Scatterplots of **(A)** DOC concentrations *vs.* density (σ_t) and **(B)** DOC concentrations *vs.* DIC concentrations during the three cruises in the northern SCS and western NP. The solid lines and equations in both plots illustrate the trends of the relationship. The gray areas mark the 95% confidence interval of the linear regression. **(A)** DOC concentrations and the density for all 27 stations were from this study and a previous study; in panel **(B)**, the DIC concentrations were measured at only 25 stations, excluding 2A1 and A10 (Ding et al., 2020 and other unpublished data).

further demonstrate the influence of the physical mixing processes of water on its hydrological and DOC properties, Figure 8 compares the longitudinal distributions of salinity, DOC/DIC concentrations and Δ^{14}C-DIC values for stations across the Luzon Strait. Combined with the *T-S* relationship shown in Figure 3A, the water characteristics in the northern SCS have upwelled and exhibit remarkably weak salinity maximum and minimum values and hence have less curved inverse "*S*" shapes than those in the western NP (Figures 3A, 8A), to which the intensified upwelling and vertical mixing occurring in the SCS might make a significant contribution (Tian et al., 2009; Shu et al., 2014; Wang et al., 2016). In comparison with the chemical parameters at stations C05, C06, C08 and C09 in the western NP, it appeared likely that the deep water in the northern SCS basin, with its low concentrations of DOC and high concentrations and low Δ^{14}C of DIC, upwelled and mixed with the upper water at a depth between 200-500 m, thus diluting the DOC concentrations at stations S1, S5, A11, A10 and K2 (Figures 8B–D). The calculation based on the Δ^{14}C-DIC mass balance revealed that approximately 46-82% of the deep water (≥ 1,500 m) upwelled and mixed with the water in the upper 200-700 m depth (Ding et al., 2020). With the derived deep water fractions, the conservative concentrations of DOC (DOC^0) could be calculated using the same two end-member mixing model. For the end-member values of DOC in the upper 200-500 m depth and deeper waters, we used the average measured DOC concentration of 69 μM in the upper waters and 42 μM in the deep waters in the northern SCS. The DOC^0 could subsequently be calculated within a range of 50-56 μM, which is slightly higher than the measured DOC concentrations (42-53 μM) in the upper 200-500 m depth of the water column at stations S1, S5, A10-A11 and K2 (Figure 8B). The negative ΔDOC values ($DOC_{measured}$ - DOC^0) suggest that net DOC consumption from biological processes could modulate the DOC superimposed on the water physical mixing processes in the northern SCS basin.

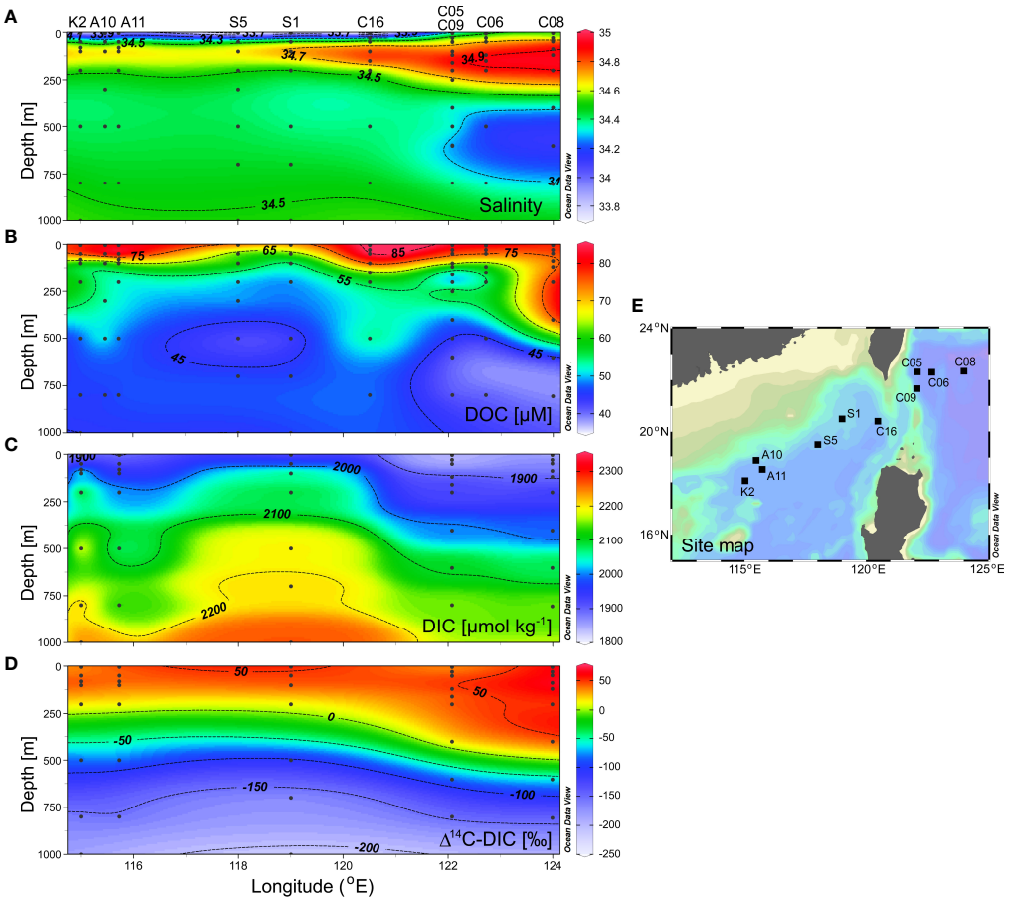

FIGURE 8
Transectional distribution of **(A)** salinity, **(B)** DOC concentrations, **(C)** DIC concentrations and **(D)** Δ^{14}C-DIC values for **(E)** stations sampled from west to the east across the Luzon Strait using ODV (Schlitzer, 2017). Note that DIC concentrations and Δ^{14}C-DIC values are provided for only five stations in panel **(C, D)** due to the lack of data at stations C09, C16, S5 and A10 (Ding et al., 2020).

Given the ΔDOC and the field-measured DOC, we estimated that the bioavailability fraction of DOC in the upper 200-500 m water depth could be in the range of 3-9 μM and account for 6%-20% (average 13 ± 5%) of the total DOC pool at these stations, which was comparable to previous results reported in the slope region of the East China Sea (7%) and the Kuroshio Extension region (8-20%) (Ding et al., 2019).

Below a 1,500 m depth, the DOC concentrations at the stations that were measured during the three cruises were in a narrow range of 42 ± 2 μM, showing no significant difference among stations and seasons, compared to that of 41 ± 2 μM on average at stations in the deep western NP. This deep water DOC appeared to be slightly and unusually enriched (approximately 3-4 μM) in the SCS compared to that found in the NP (39 ± 1 μM) (Feely et al., 2004; Ding et al., 2019; Druffel et al., 2019). The DOC ^{14}C ages in the deep water (≥1,500 m depth) were calculated from Δ^{14}C values at four stations and were plotted against the average deep DOC concentrations of water samples from the northern SCS and other open ocean areas (Figure 9) (Druffel et al., 1992; Druffel and Griffin, 2015; Druffel et al., 2016; Druffel et al., 2019; Ding et al., 2020; Druffel et al., 2021). The ^{14}C ages of the deep DOC in the northern SCS were observed to be close to the ages of the ^{14}C-DOC reported for the deep NP, with values of ~6,000 years (Druffel et al., 2019; Ding et al., 2020; Druffel et al., 2021) (Wang, unpublished data). However, the SCS values departed from the statistical relationship (black line) in the plot shown in Figure 9, also indicating enhanced DOC concentrations at water depths below 1,500 m. The excess DOC in the deep SCS (~ 3-4 μM) we observed was similar to that previously reported by Dai et al. (2009) and Wu et al. (2015). Strong fronts due to the Kuroshio intrusion and interactions with SCS water are associated with enhanced water diapycnal mixing, which could promote distinct lateral transport (Tian et al., 2009; Guo et al., 2017). In addition, a recent study revealed that particles (including sinking and suspended particles) could be laterally transported into the deep SCS and directly provide organic carbon to the dark part of the ocean (Shen et al., 2020). Considering that the residence time of the SCS deep water is less than 30 years (Qu et al., 2006), it is possible that this excess DOC in the deep SCS water results from the breakdown or dissolution of laterally transported particles. Analogously, Lopez and Hansell (2021) also reported deep DOC enrichment within the transitional zone in the NP and suggested that hydrographic fronts could stimulate more carbon export to great depths *via* deep-sinking particles and therefore transfer additional DOC into the deep ocean.

Microbial degradation of DOC

The observed rapid decrease in the DOC concentrations below the euphotic zone in the northern SCS and western NP

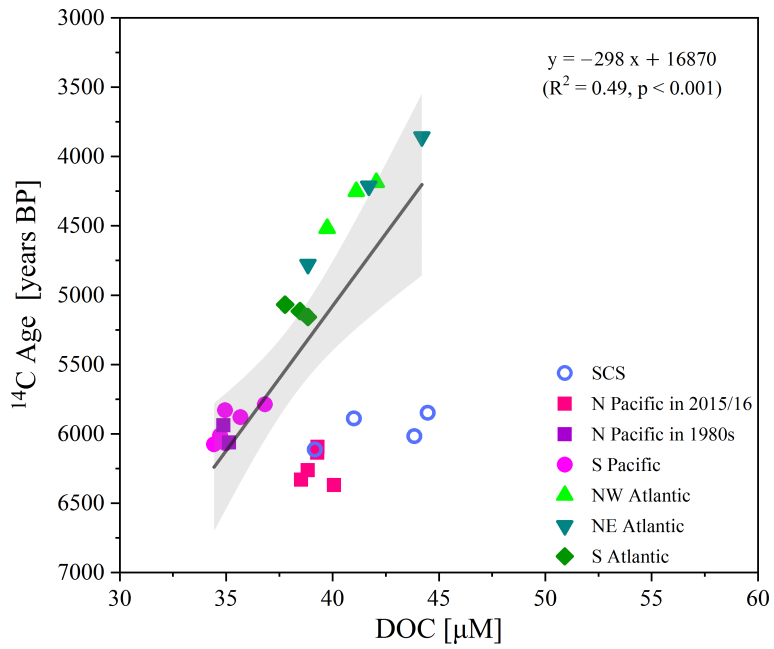

FIGURE 9
Average ^{14}C-DOC ages versus average DOC concentrations at four stations in the northern SCS and in other open ocean sites in the Pacific and Atlantic. Data derived from the SCS (Ding et al., 2020), NP (Druffel et al., 1992; Druffel et al., 2019; Druffel et al., 2021), South Pacific (Druffel and Griffin, 2015; Druffel et al., 2021), and Atlantic (Druffel et al., 2016). The solid line is the Model II geometric mean regression of all points excluding the SCS, and the gray area marks the 95% confidence interval of the linear regression. The equation is also shown in the figure, with a slope of -298 ± 48 and a y-intercept of 16,870 ± 1,832.

clearly indicated that most microbial utilization of DOC took place in the upper water column. For instance, using the changed DOC concentrations in the upper 200 m and the average DOC concentrations (42 μM) below 1,500 m as the background level of refractory DOC in the deep SCS, we calculated the depth distribution of the fractions of labile DOC, semilabile DOC and refractory DOC based on the concentration gradient with depth in the northern SCS. A portion of the surface DOC (approximately 31 ± 5%) was consumed in the upper 200 m depth, which is comparable to the published bioavailable DOC data in the coastal ocean that concluded that bioavailable DOC accounts for 22 ± 12% of the total DOC and the labile DOC fractions (20-40%) of the surface bulk DOC in western North Pacific (Lønborg and Álvarez-Salgado, 2012; Ge et al., 2022). However, most of the DOC, representing 48 to 68% of the surface bulk DOC with a mean value of 54 ± 5%, appeared to be biologically resistant and remained in deep waters in the SCS and western NP.

DOC degradation experiments have been conducted to assess the availability of naturally producing substrates to bacterial assemblages and the corresponding changes in bacterial community structure (Carlson et al., 2004; Nelson and Carlson, 2012; Shen and Benner, 2018; Li et al., 2021). Considering that the labile DOC is largely limited to the euphotic zone (Hansell and Carlson, 2001; Carlson et al., 2010) and based on the depth distribution of the DOC fractions in the northern SCS, the refractory DOC fraction dominated (> 90%) the DOC pool in the 700 m and deeper water layers, indicating that the labile and semilabile DOC only constitutes a small fraction (< 10%, approximately ≤ 5 μM) of the bulk DOC in 700 m and deeper water depth layers. The introduce of labile and semilabile DOC from the mesopelagic and deep seawater could be ignored at a volume/volume ratio of 2:1. The results from our incubation experiments demonstrated that DOC produced in the surface water provided a preferential energy source for deep water bacteria. The bioavailable DOC accounted for a relatively small proportion (approximately 10-13%) and was consumed by microbes over 180 days in the incubation experiments (Figure 4). Most of the DOC (≥87%) persisted until the end of the experiments, confirming the current view that most of the DOC is resistant to microbial degradation in the deep ocean (Hansell et al., 2012; Hansell, 2013; Follett et al., 2014; Carlson and Hansell, 2015). However, in a recent study, the bioavailable DOC observed in the treatment of SCS surface filtered seawater inoculated with unfiltered SCS surface seawater was approximately 3 μM and only accounted for a proportion of 5% (Li et al., 2021). In both the two studies, bioavailable DOC is the concentration difference between the initial DOC and the residual DOC at the end of the experiments. The relatively higher bioavailable DOC, therefore, indicated enhanced biodegradations of DOC by the mesopelagic and deep microbes in our experiments, which agrees with the currently accepted assumption that the accumulated DOC at one water depth can become utilized at another depth, although the reasons remain unknown (Carlson et al., 2004; Carlson et al., 2010; Shen and Benner, 2018; Liu et al., 2022). It is interesting to note that the observed increase in DOC concentrations within 25 days was not detected in previous DOC utilization studies (Carlson et al., 2004; Liu et al., 2020). A notable difference among these studies was the incubation temperature, which was room temperature in the present study, while Carlson et al. (2004) and Liu et al. (2020) used the *in situ* temperatures of mesopelagic and deep waters. When the temperature increased from *in situ* to room temperature, little change in the bacterial community could be found (Zhao et al., 2019). In addition, diverse marine microbes have dual roles as producers and consumers of DOC in the ocean (Lechtenfeld et al., 2015; Shen and Benner, 2018). Lechtenfeld et al. (2015) demonstrated that the remaining DOC at the end of their bioassay experiments was directly or indirectly released from bacteria. Considering that factors such as environmental temperature and microbial assemblages impact the ocean carbon cycle, we propose that the DOC released from marine microbes *via* viral lysis, excretion and other processes (Kawasaki and Benner, 2006; Moran et al., 2022) is expected to increase with increasing environmental temperature during the initial 25 days of incubation. This hypothesis, however, needs to be tested in future research. Nevertheless, the increased DOC within 25 days may also contribute to the enhanced biodegradation of DOC, which is analogous to the priming effect observed when the labile substrates added and increased the removal of DOC in previous bioassay experiments (Shen and Benner, 2020).

It can be clearly seen that the isotopic composition of DOC (both ^{13}C and ^{14}C) varied significantly during the incubation experiments. The remaining DOC at the end of the incubations had more depleted ^{14}C values (-329‰ and -391‰) than did the original DOC (-304‰ and -315‰), but these values were approximately 150‰ higher than the $\Delta^{14}C$-DOC values in the deep SCS (average -525 ± 15‰). This indicated that the removal of DOC that was characterized by these enriched ^{14}C values occurred in the water after 180 days of incubation. Our observations agree with previous studies showing that open-ocean bacteria preferentially assimilated modern components of DOC and were enriched in ^{14}C relative to bulk DOC (Cherrier et al., 1999). Additionally, the $\delta^{13}C$-DOC values at the end of the incubation period were slightly lighter (-0.5‰ and -0.7‰, respectively) than the original values, but all were within the range of -20.5‰ to -23.5‰ that was recently reported for DOC in the SCS and in other open ocean areas (Druffel et al., 2019; Ding et al., 2020; Druffel et al., 2021). The variations in $\delta^{13}C$-DOC values after 180 days of incubation in a closed system indicated that part of the enriched ^{13}C constituents of marine autochthonous DOC could be preferentially removed in the microbial degradation processes, leaving behind DOC with depleted ^{13}C constituents, thus resulting in the residual DOC being relatively depleted in $\delta^{13}C$ (-22.8‰ to -23.1‰). This finding on the DOC isotopic composition changes ($\Delta^{14}C$-DOC and $\delta^{13}C$-DOC) supports the variations in the DOC concentrations discussed above, where recently produced and accumulated DOC can become utilized at

deeper water depth, although it was not available for microbial utilization at the upper depth.

Conclusion

The results of our study indicate that the DOC concentrations ranged from 38 to 95 μM in the shelf-slope-basin regions of the northern SCS and western NP in the spring and summer seasons. The large spatial variations in DOC (53 to 95 μM) in the upper 100 m among the shelf-slope-basin regions in the northern SCS were influenced by a combination of factors, including primary production, terrestrial inputs from the Pearl River and the intrusion of the Kuroshio Current. Compared with the DOC concentrations in the western NP, the diluted DOC concentrations at a mesopelagic depth in the northern SCS basin reflect the primary influence of the mixing process of upwelled deep water. Compared with the DOC levels in the deep Pacific and South Atlantic Oceans, a slight excess of DOC concentrations (~ 3-4 μM) was observed in the deep water of the SCS.

The results of these incubation experiments indicated that 10-20% of the surface DOC was consumed by mesopelagic and/or deep water bacteria. A distinct change in the isotopic compositions of DOC (Δ^{14}C-DOC and δ^{13}C-DOC values) was also simultaneously identified along with shifts in DOC concentrations in response to DOC degradation, indicating that modern and enriched $^{14}C/^{13}C$ constituents of DOC are preferentially removed in the ocean.

Data availability statement

The original contributions presented in the study are included in the article/Supplementary Material. Further inquiries can be directed to the corresponding author.

Author contributions

LD and SS collected samples, participated in the sample analysis and data process. CL analyzed the DOC samples. LD wrote the manuscript. XW designed the study and edited the manuscript. All authors provided intellectual input for data interpretation and contributed to the article and approved the submitted version.

Funding

Financial support for this work was provided by the Ocean Program of the National Natural Science Foundation of China (Grant numbers 91858210 and 91428101).

Acknowledgments

We thank Yuanzhi Qi and Hongmei Zhang for assistance with sample analysis in the laboratory. We also express our thanks to the captains and crew members of R/V *Shiyan 3*, R/V *Dongfanghong 2* and R/V *Haida* for their help during the cruises.

Conflict of interest

The authors declare that the research was conducted in the absence of any commercial or financial relationships that could be construed as a potential conflict of interest.

Publisher's note

All claims expressed in this article are solely those of the authors and do not necessarily represent those of their affiliated organizations, or those of the publisher, the editors and the reviewers. Any product that may be evaluated in this article, or claim that may be made by its manufacturer, is not guaranteed or endorsed by the publisher.

Supplementary material

The Supplementary Material for this article can be found online at: https://www.frontiersin.org/articles/10.3389/fmars.2022.973694/full#supplementary-material

References

Azam, F., and Worden, A. Z. (2004). Microbes, molecules, and marine ecosystems. *Science* 303, 1622–1624. doi: 10.1126/science.1093892

Benner, R., and Amon, R. M. W. (2015). The size-reactivity continuum of major bioelements in the ocean. *Annu. Rev. Mar. Sci.* 7, 185–205. doi: 10.1146/annurev-marine-010213-135126

Bercovici, S. K., and Hansell, D. A. (2016). Dissolved organic carbon in the deep southern ocean: Local versus distant controls. *Global Biogeochem. Cycles* 30, 350–360. doi: 10.1002/2015GB005252

Carlson, C. A., and Ducklow, H. W. (1996). Growth of bacterioplankton and consumption of dissolved organic carbon in the Sargasso Sea. *Aquat. Microb. Ecol.* 10, 69–85. doi: 10.3354/ame010069

Carlson, C. A., Ducklow, H. W., Hansell, D. A., and Smith, W. O. (1998). Organic carbon partitioning during spring phytoplankton blooms in the Ross Sea polynya and the Sargasso Sea. *Limnol. Oceanogr.* 43, 375–386. doi: 10.4319/lo.1998.43.3.0375

Carlson, C. A., Ducklow, H. W., and Michaels, A. F. (1994). Annual flux of dissolved organic carbon from the euphotic zone in the northwestern Sargasso Sea. *Nature* 371, 405–408. doi: 10.1038/371405a0

Carlson, C. A., Ducklow, H. W., and Sleeter, T. D. (1996). Stocks and dynamics of bacterioplankton in the northwestern Sargasso Sea. *Deep. Sea. Res. Part II Top. Stud. Oceanogr.* 43, 491–515. doi: 10.1016/0967-0645(95)00101-8

Carlson, C. A., Giovannoni, S. J., Hansell, D. A., Goldberg, S. J., Parsons, R., and Vergin, K. (2004). Interactions among dissolved organic carbon, microbial processes, and community structure in the mesopelagic zone of the northwestern Sargasso Sea. *Limnol. Oceanogr.* 49, 1073–1083. doi: 10.4319/lo.2004.49.4.1073

Carlson, C. A., and Hansell, D. A. (2015). "DOM sources, sinks, reactivity, and budgets," in *Biogeochemistry of marine dissolved organic matter, 2nd ed.* Eds. D. A. Hansell and C. A. Carlson (San Diego: Academic Press), 65–126.

Carlson, C. A., Hansell, D. A., Nelson, N. B., Siegel, D. A., Smethie, W. M., Khatiwala, S., et al. (2010). Dissolved organic carbon export and subsequent remineralization in the mesopelagic and bathypelagic realms of the north Atlantic basin. *Deep. Sea. Res. Part II* 57, 1433–1445. doi: 10.1016/j.dsr2.2010.02.013

Chen, C. T. A., Wang, S. L., Wang, B. J., and Pai, S. C. (2001). Nutrient budgets for the south China Sea basin. *Mar. Chem.* 75, 281–300. doi: 10.1016/S0304-4203(01)00041-X

Cherrier, J., Bauer, J. E., and Druffel, E. R. M. (1996). Utilization and turnover of labile dissolved organic matter by bacterial heterotrophs in eastern north pacific surface waters. *Mar. Ecol. Prog. Ser.* 139, 267–279. doi: 10.3354/meps139267

Cherrier, J., Bauer, J. E., Druffel, E. R. M., Coffin, R. B., and Chanton, J. P. (1999). Radiocarbon in marine bacteria: Evidence for the ages of assimilated carbon. *Limnol. Oceanogr.* 44, 730–736. doi: 10.4319/lo.1999.44.3.0730

Dai, M., Cao, Z., Guo, X., Zhai, W., Liu, Z., Yin, Z., et al. (2013). Why are some marginal seas sources of atmospheric CO_2? *Geophys. Res. Lett.* 40, 2154–2158. doi: 10.1002/grl.50390

Dai, M. H., Gan, J., Han, A., Kung, H. S., and Yin, Z. (2014). "Physical dynamics and biogeochemistry of the pearl river plume," in *Biogeochemical dynamics at major river-coastal interfaces. linkages with global change.* Eds. T. S. Bianchi, M. Allison and W.-J. Cai (New York: Cambridge University Press), 321–352.

Dai, M., Meng, F., Tang, T., Kao, S.-J., Lin, J., Chen, J., et al. (2009). Excess total organic carbon in the intermediate water of the south China Sea and its export to the north pacific. *Geochem. Geophys. Geosyst.* 10, Q12002. doi: 10.1029/2009GC002752

Ding, L., Ge, T., and Wang, X. (2019). Dissolved organic carbon dynamics in the East China Sea and the northwest pacific ocean. *Ocean. Sci.* 15, 1177–1190. doi: 10.5194/os-15-1177-2019

Ding, L., Qi, Y., Shan, S., Ge, T., Luo, C., and Wang, X. (2020). Radiocarbon in dissolved organic and inorganic carbon of the south China Sea. *J. Geophys. Res. Ocean.* 125, e2020JC016073. doi: 10.1029/2020JC016073

Druffel, E. R. M., and Griffin, S. (2015). Radiocarbon in dissolved organic carbon of the south pacific ocean. *Geophys. Res. Lett.* 42, 4096–4101. doi: 10.1002/2015GL063764

Druffel, E. R. M., Griffin, S., Coppola, A. I., and Walker, B. D. (2016). Radiocarbon in dissolved organic carbon of the Atlantic ocean. *Geophys. Res. Lett.* 43, 5279–5286. doi: 10.1002/2016GL068746

Druffel, E. R. M., Griffin, S., Lewis, C. B., Rudresh, M., Garcia, N. G., Key, R. M., et al. (2021). Dissolved organic radiocarbon in the eastern pacific and southern oceans. *Geophys. Res. Lett.* 48, e2021GL092904. doi: 10.1029/2021GL092904

Druffel, E. R. M., Griffin, S., Wang, N., Garcia, N. G., McNichol, A. P., Key, R. M., et al. (2019). Dissolved organic radiocarbon in the central pacific ocean. *Geophys. Res. Lett.* 46, 5396–5403. doi: 10.1029/2019GL083149

Druffel, E. R. M., Williams, P. M., Bauer, J. E., and Ertel, J. R. (1992). Cycling of dissolved and particulate organic matter in the open ocean. *J. Geophys. Res.* 97, 15639–15659. doi: 10.1029/92JC01511

Ducklow, H. W. (1999). The bacterial component of the oceanic euphotic zone. *FEMS Microbiol. Ecol.* 30, 1–10. doi: 10.1016/S0168-6496(99)00031-8

Du, C., Liu, Z., Dai, M., Kao, S. J., Cao, Z., Zhang, Y., et al. (2013). Impact of the kuroshio intrusion on the nutrient inventory in the upper northern south China Sea: insights from an isopycnal mixing model. *Biogeosciences* 10, 6419–6432. doi: 10.5194/bg-10-6419-2013

Feely, R. A., Dichson, D., Hansell, D. A., and Carlson, C. A. (2004) *Carbon dioxide, hydrographic, and chemical data obtained during the R/V Melville cruise in the pacific ocean on CLIVAR repeat hydrography sections P02_2004 (15 June - 27 august, 2004).* Available at: http://cdiac.ornl.gov/ftp/oceans/CLIVAR/P02_2004.data/.

Fenchel, T. (2008). The microbial loop-25 years later. *J. Exp. Mar. Bio. Ecol.* 366, 99–103. doi: 10.1016/j.jembe.2008.07.013

Follett, C. L., Repeta, D. J., Rothman, D. H., Xu, L., and Santinelli, C. (2014). Hidden cycle of dissolved organic carbon in the deep ocean. *Proc. Natl. Acad. Sci. U.S.A.* 111, 16706–16711. doi: 10.1073/pnas.1407445111

Ge, T., Luo, C., Ren, P., Zhang, H., Chen, H., Chen, Z., et al. (2022). Dissolved organic carbon along a meridional transect in the western north pacific ocean: Distribution, variation and controlling processes. *Front. Mar. Sci.* 9. doi: 10.3389/fmars.2022.909148

Gong, G. C., Liu, K. K., Liu, C. T., and Pai, S. C. (1992). The chemical hydrography of the south China Sea west of Luzon and a comparison with the West Philippine Sea. *Terr. Atmos. Ocean. Sci.* 3, 587–602. doi: 10.3319/TAO.1992.3.4.587(O

Guo, L., Santschi, P. H., Cifuentes, L. A., Trumbore, S. E., and Southon, J. (1996). Cycling of high-molecular-weight dissolved organic matter in the middle Atlantic bight as revealed by carbon isotopic (^{13}C and ^{14}C) signatures. *Limnol. Oceanogr.* 41, 1242–1252. doi: 10.4319/lo.1996.41.6.1242

Guo, L., Xiu, P., Chai, F., Xue, H., Wang, D., and Sun, J. (2017). Enhanced chlorophyll concentrations induced by kuroshio intrusion fronts in the northern south China Sea. *Geophys. Res. Lett.* 44, 11565–11572. doi: 10.1002/2017GL075336

Hansell, D. A. (2013). Recalcitrant dissolved organic carbon fractions. *Annu. Rev. Mar. Sci.* 5, 421–445. doi: 10.1146/annurev-marine-120710-100757

Hansell, D. A., and Carlson, C. A. (1998). Net community production of dissolved organic carbon. *Global Biogeochem. Cycles* 12, 443–453. doi: 10.1029/98gb01928

Hansell, D. A., and Carlson, C. A. (2001). Marine dissolved organic matter and the carbon cycle. *Oceanography* 14, 41–49. doi: 10.5670/oceanog.2001.05

Hansell, D. A., Carlson, C. A., Repeta, D. J., and Schlitzer, R. (2009). Dissolved organic matter in the ocean: A controversy stimulates new insights. *Oceanography* 22, 202–211. doi: 10.5670/oceanog.2009.109

Hansell, D. A., Carlson, C. A., and Schlitzer, R. (2012). Net removal of major marine dissolved organic carbon fractions in the subsurface ocean. *Global Biogeochem. Cycles* 26, GB1016. doi: 10.1029/2011gb004069

Hansell, D. A., Carlson, C. A., and Suzuki, Y. (2002). Dissolved organic carbon export with north pacific intermediate water formation. *Global Biogeochem. Cycles* 16, 1007. doi: 10.1029/2000GB001361

Hung, J. J., Wang, S. M., and Chen, Y. L. (2007). Biogeochemical controls on distributions and fluxes of dissolved and particulate organic carbon in the northern south China Sea. *Deep. Sea. Res. Part II Top. Stud. Oceanogr.* 54, 1486–1503. doi: 10.1016/j.dsr2.2007.05.006

Jiang, Y., Zhang, S., Tian, J., Zhang, Z., Gan, J., and Wu, C.-R. (2020). An examination of circulation characteristics in the Luzon strait and the south China Sea using high-resolution regional atmosphere-ocean coupled models. *J. Geophys. Res. Ocean.* 125, e2020JC016253. doi: 10.1029/2020JC016253

Kawasaki, N., and Benner, R. (2006). Bacterial release of dissolved organic matter during cell growth and decline: Molecular origin and composition. *Limnol. Oceanogr.* 51, 2170–2180. doi: 10.4319/lo.2006.51.5.2170

Kirchman, D. L., Suzuki, Y., Garside, C., and Ducklow, H. W. (1991). High turnover rates of dissolved organic carbon during a spring phytoplankton bloom. *Nature* 352, 612–614. doi: 10.1038/352612a0

Lønborg, C., and Álvarez-Salgado, X. A. (2012). Recycling versus export of bioavailable dissolved organic matter in the coastal ocean and efficiency of the continental shelf pump. *Global Biogeochem. Cycles* 26, GB3018. doi: 10.1029/2012gb004353

Lechtenfeld, O. J., Hertkorn, N., Shen, Y., Witt, M., and Benner, R. (2015). Marine sequestration of carbon in bacterial metabolites. *Nat. Commun.* 6, 6711. doi: 10.1038/ncomms7711

Li, X., Wu, K., Gu, S., Jiang, P., Li, H., Liu, Z., et al. (2021). Enhanced biodegradation of dissolved organic carbon in the western boundary kuroshio current when intruded to the marginal south China Sea. *J. Geophys. Res. Ocean.* 126, e2021JC017585. doi: 10.1029/2021JC017585

Lin, I.-I., Lien, C.-C., Wu, C.-R., Wong, G. T. F., Huang, C.-W., and Chiang, T.-L. (2010). Enhanced primary production in the oligotrophic south China Sea by eddy injection in spring. *Geophys. Res. Lett.* 37, L16602. doi: 10.1029/2010gl043872

Liu, G., and Chai, F. (2009). Seasonal and interannual variability of primary and export production in the south China Sea: a three-dimensional physical-biogeochemical model study. *ICES. J. Mar. Sci.* 66, 420–431. doi: 10.1093/icesjms/fsn219

Liu, K. K., Chao, S. Y., Shaw, P. T., Gong, G. C., Chen, C. C., and Tang, T. Y. (2002). Monsoon-forced chlorophyll distribution and primary production in the south China Sea: observations and a numerical study. *Deep. Sea. Res. Part I* 49, 1387–1412. doi: 10.1016/S0967-0637(02)00035-3

Liu, S., Longnecker, K., Kujawinski, E. B., Vergin, K., Bolaños, L. M., Giovannoni, S. J., et al. (2022). Linkages among dissolved organic matter export, dissolved metabolites, and associated microbial community structure response in the northwestern Sargasso Sea on a seasonal scale. *Front. Microbiol.* 13. doi: 10.3389/fmicb.2022.833252

Liu, S., Parsons, R., Opalk, K., Baetge, N., Giovannoni, S., Bolaños, L. M., et al. (2020). Different carboxyl-rich alicyclic molecules proxy compounds select distinct bacterioplankton for oxidation of dissolved organic matter in the mesopelagic Sargasso Sea. *Limnol. Oceanogr.* 65, 1532–1553. doi: 10.1002/lno.11405

Loh, A. N., Bauer, J. E., and Druffel, E. R. (2004). Variable ageing and storage of dissolved organic components in the open ocean. *Nature* 430, 877–881. doi: 10.1038/nature02780

Lopez, C. N., and Hansell, D. A. (2021). Evidence of deep DOC enrichment *via* particle export beneath subarctic and northern subtropical fronts in the north pacific. *Front. Mar. Sci.* 8. doi: 10.3389/fmars.2021.659034

Ma, W., Xiu, P., Yu, Y., Zheng, Y., and Chai, F. (2022). Production of dissolved organic carbon in the south China Sea: A modeling study. *Sci. China Earth Sci.* 65, 351–364. doi: 10.1007/s11430-021-9817-2

McNichol, A. P., Jones, G. A., Hutton, D. L., Gagnon, A. R., and Key, R. M. (1994). The rapid preparation of seawater ΣCO_2 for radiocarbon analysis at the national ocean sciences AMS facility. *Radiocarbon* 36, 237–246. doi: 10.1017/S0033822200040522

Meng, F., Dai, M., Cao, Z., Wu, K., Zhao, X., Li, X., et al. (2017). Seasonal dynamics of dissolved organic carbon under complex circulation schemes on a large continental shelf: The northern south China Sea. *J. Geophys. Res. Ocean.* 122, 9415–9428. doi: 10.1002/2017jc013325

Moran, M. A., Kujawinski, E. B., Schroer, W. F., Amin, S. A., Bates, N. R., Bertrand, E. M., et al. (2022). Microbial metabolites in the marine carbon cycle. *Nat. Microbiol.* 7, 508–523. doi: 10.1038/s41564-022-01090-3

Nan, F., Xue, H., and Yu, F. (2015). Kuroshio intrusion into the south China Sea: A review. *Prog. Oceanogr.* 137 (Part A), 314–333. doi: 10.1016/j.pocean.2014.05.012

Nelson, C. E., and Carlson, C. A. (2012). Tracking differential incorporation of dissolved organic carbon types among diverse lineages of Sargasso Sea bacterioplankton. *Environ. Microbiol.* 14, 1500–1516. doi: 10.1111/j.1462-2920.2012.02738.x

Pan, X., and Wong, G. T. F. (2015). An improved algorithm for remotely sensing marine dissolved organic carbon: Climatology in the northern south China Sea shelf-sea and adjacent waters. *Deep. Sea. Res. Part II* 117, 131–142. doi: 10.1016/j.dsr2.2015.02.025

Qu, T., Girton, J. B., and Whitehead, J. A. (2006). Deepwater overflow through Luzon strait. *J. Geophys. Res. Ocean.* 111, C01002. doi: 10.1029/2005jc003139

Repeta, D. J. (2015). "Chemical characterization and cycling of dissolved organic matter," in *Biogeochemistry of marine dissolved organic matter, 2nd ed*. Eds. D. A. Hansell and C. A. Carlson (San Diego: Academic Press), 21–63.

Repeta, D. J., and Aluwihare, L. I. (2006). Radiocarbon analysis of neutral sugars in high-molecular-weight dissolved organic carbon: Implications for organic carbon cycling. *Limnol. Oceanogr.* 51, 1045–1053. doi: 10.4319/lo.2006.51.2.1045

Riedel, T., and Dittmar, T. (2014). A method detection limit for the analysis of natural organic matter *via* Fourier transform ion cyclotron resonance mass spectrometry. *Anal. Chem.* 86, 8376–8382. doi: 10.1021/ac501946m

Schlitzer, R. (2017) *Ocean data view*. Available at: http://odv.awi.de.

Sharp, J. H., Benner, R., Bennett, L., Carlson, C. A., Fitzwater, S. E., Peltzer, E. T., et al. (1995). Analyses of dissolved organic carbon in seawater: The JGOFS EqPac methods comparison. *Mar. Chem.* 48, 91–108. doi: 10.1016/0304-4203(94)00040-K

Shen, Y., and Benner, R. (2018). Mixing it up in the ocean carbon cycle and the removal of refractory dissolved organic carbon. *Sci. Rep.* 8, 2542. doi: 10.1038/s41598-018-20857-5

Shen, Y., and Benner, R. (2020). Molecular properties are a primary control on the microbial utilization of dissolved organic matter in the ocean. *Limnol. Oceanogr.* 65, 1061–1071. doi: 10.1002/lno.11369

Shen, J., Jiao, N., Dai, M., Wang, H., Qiu, G., Chen, J., et al. (2020). Laterally transported particles from margins serve as a major carbon and energy source for dark ocean ecosystems. *Geophys. Res. Lett.* 47, e2020GL088971. doi: 10.1029/2020GL088971

Shu, Y., Xue, H., Wang, D., Chai, F., Xie, Q., Yao, J., et al. (2014). Meridional overturning circulation in the south China Sea envisioned from the high-resolution global reanalysis data GLBa0.08. *J. Geophys. Res. Ocean.* 119, 3012–3028. doi: 10.1002/2013JC009583

Tian, J. W., Yang, Q. X., and Zhao, W. (2009). Enhanced diapycnal mixing in the south China Sea. *J. Phys. Oceanogr.* 39, 3191–3203. doi: 10.1175/2009JPO3899.1

Varela, M., Rodríguez-Ramos, T., Guerrero-Feijóo, E., and Nieto-Cid, M. (2020). Changes in activity and community composition shape bacterial responses to size-fractionated marine DOM. *Front. Microbiol.* 11. doi: 10.3389/fmicb.2020.586148

Walker, B. D., Beaupré, S. R., Guilderson, T. P., Druffel, E. R. M., and McCarthy, M. D. (2011). Large-Volume ultrafiltration for the study of radiocarbon signatures and size vs. age relationships in marine dissolved organic matter. *Geochim. Cosmochim. Acta* 75, 5187–5202. doi: 10.1016/j.gca.2011.06.015

Walker, B. D., Primeau, F. W., Beaupré, S. R., Guilderson, T. P., Druffel, E. R. M., and McCarthy, M. D. (2016). Linked changes in marine dissolved organic carbon molecular size and radiocarbon age. *Geophys. Res. Lett.* 43, 10385–10393. doi: 10.1002/2016GL070359

Wang, C., Guo, W., Li, Y., Stubbins, A., Li, Y., Song, G., et al. (2017). Hydrological and biogeochemical bontrols on absorption and fluorescence of dissolved organic matter in the northern south China Sea. *J. Geophys. Res. Biogeosci.* 122, 3405–3418. doi: 10.1002/2017JG004100

Wang, P., and Li, Q. (2009). "Oceanographical and geological background," in *The south China Sea: Paleoceanography and sedimentology*. Eds. P. Wang and Q. Li (Netherlands: Springer), 25–73.

Wang, D., Xiao, J., Shu, Y., Xie, Q., Chen, J., and Wang, Q. (2016). Progress on deep circulation and meridional overturning circulation in the south China Sea. *Sci. China Earth Sci.* 59, 1827–1833. doi: 10.1007/s11430-016-5324-6

Wu, K., Dai, M., Chen, J., Meng, F., Li, X., Liu, Z., et al. (2015). Dissolved organic carbon in the south China Sea and its exchange with the Western pacific ocean. *Deep. Sea. Res. Part II Top. Stud. Oceanogr.* 122, 41–51. doi: 10.1016/j.dsr2.2015.06.013

Wu, K., Dai, M., Li, X., Meng, F., Chen, J., and Lin, J. (2017). Dynamics and production of dissolved organic carbon in a large continental shelf system under the influence of both river plume and coastal upwelling. *Limnol. Oceanogr.* 62, 973–988. doi: 10.1002/lno.10479

Xue, Y., Ge, T., and Wang, X. (2015). An effective method of UV-oxidation of dissolved organic carbon in natural waters for radiocarbon analysis by accelerator mass spectrometry. *J. Ocean. Univ. China* 14, 989–993. doi: 10.1007/s11802-015-2935-z

Yang, L., Chen, C.-T. A., Lui, H.-K., Zhuang, W.-E., and Wang, B.-J. (2016). Effects of microbial transformation on dissolved organic matter in the east Taiwan strait and implications for carbon and nutrient cycling. *Estuar. Coast. Shelf. Sci.* 180, 59–68. doi: 10.1016/j.ecss.2016.06.021

Zhang, M., Wu, Y., Wang, F., Xu, D., Liu, S., and Zhou, M. (2020). Hotspot of organic carbon export driven by mesoscale eddies in the slope region of the northern south China Sea. *Front. Mar. Sci.* 7. doi: 10.3389/fmars.2020.00444

Zhao, Z., Gonsior, M., Schmitt-Kopplin, P., Zhan, Y., Zhang, R., Jiao, N., et al. (2019). Microbial transformation of virus-induced dissolved organic matter from picocyanobacteria: coupling of bacterial diversity and DOM chemodiversity. *ISME. J.* 13, 2551–2565. doi: 10.1038/s41396-019-0449-1

Ziolkowski, L. A., and Druffel, E. R. M. (2010). Aged black carbon identified in marine dissolved organic carbon. *Geophys. Res. Lett.* 37, L16601. doi: 10.1029/2010GL043963

Zweifel, U. L., Norrman, B., and Hagström, Å. (1993). Consumption of dissolved organic carbon by marine bacteria and demand for inorganic nutrients. *Mar. Ecol. Prog. Ser.* 101, 23–32. doi: 10.3354/MEPS101023

frontiers | Frontiers in Marine Science

TYPE Original Research
PUBLISHED 08 September 2022
DOI 10.3389/fmars.2022.934391

OPEN ACCESS

EDITED BY
Fajin Chen,
Guangdong Ocean University, China

REVIEWED BY
Tarron Lamont,
Department of Environment, Forestry and Fisheries (DEFF), South Africa
Haibin Lü,
Jiangsu Ocean University, China

*CORRESPONDENCE
Yuyuan Xie
xieyuyuan@hotmail.com
Bangqin Huang
bqhuang@xmu.edu.cn

SPECIALTY SECTION
This article was submitted to Marine Biogeochemistry, a section of the journal Frontiers in Marine Science

RECEIVED 02 May 2022
ACCEPTED 16 August 2022
PUBLISHED 08 September 2022

CITATION
Liu H, Xie Y, Browning TJ, Xu F and Huang B (2022) Phytoplankton photophysiology across tropical eddies: Deconvolving nutrient, light, and community signals. *Front. Mar. Sci.* 9:934391. doi: 10.3389/fmars.2022.934391

Phytoplankton photophysiology across tropical eddies: Deconvolving nutrient, light, and community signals

Haoran Liu[1,2], Yuyuan Xie[1,3]*, Thomas J. Browning[2], Feipeng Xu[1] and Bangqin Huang[1]*

[1]State Key Laboratory of Marine Environmental Science, Fujian Provincial Key Laboratory of Coastal Ecology and Environmental Studies, Xiamen University, Xiamen, China, [2]Marine Biogeochemistry Division, GEOMAR Helmholtz Centre for Ocean Research Kiel, Kiel, Germany, [3]College of Marine Science, University of South Florida, St. Petersburg, FL, United States

Fast repetition rate fluorometry (FRRf) based on active chlorophyll fluorescence is a powerful, noninvasive tool for studying phytoplankton physiological status at high spatial and temporal resolution. The South China Sea (SCS) is one of the largest tropical–subtropical marginal seas in the world, which plays an important role in modulating regional carbon budget and climate. In this study, underway *in situ* FRRf measurements were carried out throughout the outer continental shelf of the northern SCS, the basin of the northern SCS, the cyclonic eddy influenced domain in the western SCS, and the basin of the southeastern SCS. Pronounced diurnal variability of FRRf-derived parameters were observed, characterized by a large midday depression and slight nocturnal depression of the maximum quantum yield of photosystem II (F_v/F_m) and a slight increase in the functional absorption cross-section of photosystem II photochemistry (σ_{PSII}) at noon. F_v/F_m at the surface was typically as low as 0.1–0.3 and exhibited higher values (~0.4) where internal waves occurred. The cyclonic eddy increased F_v/F_m slightly, implying that it had a limited impact on surface phytoplankton photophysiology. With proper interpretation, FRRf has been a powerful tool to assess the physiological status of phytoplankton in the sea and to correlate that to ocean dynamics in an unprecedented fine scale.

KEYWORDS

diel variation, fast repetition rate fluorometry, photoinhibition, nutrient limitation, South China Sea, eddy

1 Introduction

Phytoplankton account for around half of global primary production (PP) and play an important role in regulating carbon cycling and climate (Longhurst et al., 1995; Falkowski et al., 1998; Field et al., 1998). In contrast to conventional methods requiring water sampling and incubation (e.g., incubation with ^{14}C tracer), fast repetition rate fluorometry (FRRf) (Kolber et al., 1998) is an active chlorophyll-*a* (Chl*a*) fluorescence technique rapidly probing phytoplankton physiological and bio-optical parameters *in situ* (Kolber and Falkowski, 1993; Behrenfeld and Kolber, 1999; Behrenfeld et al., 2006; Suggett et al., 2009; Schuback and Tortell, 2019; Zhu et al., 2022). There is significant potential to use FRRf signals to extend observations to much finer spatial and temporal scales than achievable with conventional techniques (Hughes et al., 2018). However, FRRf-derived signals are the result of the interacting influence of both the phytoplankton communities present and their physiological status, which in turn is impacted by environmental forcing (Suggett et al., 2009; Behrenfeld and Milligan, 2013). Their interpretation is therefore not always straightforward, and there is a need for more studies measuring ancillary biological and environmental parameters alongside FRRf in order to deconvolve these signals (Suggett et al., 2009; Behrenfeld and Milligan, 2013).

Phytoplankton growth in the ocean is frequently limited by nutrient availability, particularly in the sunlit surface waters of the low latitude oceans (Moore et al., 2013). Chlorophyll fluorescence measured by FRRf appears to be highly sensitive to nutrient limitation status, with limitation by either iron (Fe) and/or nitrogen (N)—the main limiting nutrients in the current ocean (Moore et al., 2013)—strongly regulating FRRf-derived parameters (Behrenfeld and Milligan, 2013). Specifically, at dawn and dusk when non-photochemical quenching (NPQ) processes are relaxed, values of the maximum quantum yield of photosystem II (PSII), F_v/F_m, are typically elevated under low N conditions and depressed under elevated N, low Fe conditions (Behrenfeld et al., 2006; Moore et al., 2008; Browning et al., 2014). Furthermore, in the tropical oceans under conditions of low Fe in combination with either low or elevated N, F_v/F_m values have been observed to show night time decreases from dusk to dawn (Behrenfeld and Kolber, 1999). This has been suggested to be due to cyanobacteria using their photosynthetic apparatus for respiratory electron transfer at night (Campbell et al., 1998), which, under low Fe conditions, leads to a strongly reduced plastoquinone (PQ) pool due to the restricted availability of Fe-rich photosystem I and cytochrome b6f proteins relative to the lower Fe PSII (Behrenfeld et al., 2006; Schrader et al., 2011). Night time reductions of σ_{PSII} also reflect increased night time reduction in the PQ pool under low Fe conditions (Behrenfeld and Kolber, 1999). Conversely, under Fe replete, N-limited conditions, nocturnal reductions in F_v/F_m and functional absorption cross-section of PSII photochemistry (σ_{PSII}) are much smaller or absent (Behrenfeld et al., 2006). Therefore, in addition to discrete measurements of F_v/F_m and σ_{PSII} made at any given time point, diurnal patterns in continuous active chlorophyll fluorescence could provide rich information for mapping nutrient stress status, specifically *via* distinguishing Fe, N, or N–Fe (co-)limitations (Behrenfeld and Milligan, 2013).

Independent of nutrient limitation, changes in F_v/F_m can also be related to phytoplankton community structure, with smaller values of F_v/F_m linked to increased antenna size of PSII, which has been found to be the case for small eukaryotic phytoplankton relative to large species in laboratory cultures (Suggett et al., 2009). Furthermore, strong decreases in F_v/F_m are associated with elevated light levels (reflecting light intensity that exceeds photosynthetic demand) (Wei et al., 2020). The suit of mechanisms downregulating F_v/F_m at elevated light levels are collectively termed non-photochemical quenching (NPQ), which can be reversed over timescales of seconds to hours upon exposure of phytoplankton to darkness (Falkowski and Raven, 2007).

The South China Sea (SCS) is the largest marginal sea of the North Pacific. Mesoscale physical processes, such as eddies, occur frequently in different parts of the SCS, significantly impacting nutrient distributions and carbon cycling (Xiu et al., 2010; Xiu and Chai, 2011; Jiao et al., 2014; Li et al., 2017; Zhang et al., 2020). These physical processes result in distinct patterns of phytoplankton community structure (Huang et al., 2010; Wang et al., 2016; Wang et al., 2018), PP (Ning et al., 2004; Liao et al., 2021) and supposedly physiology (Liao et al., 2021). Cyclonic eddies (CEs) occur frequently during summer in the western SCS, driving a shoaling of the nitracline depth to as shallow as 20 m relative to ~70 m in the background state (Jiao et al., 2014). Chl*a* biomass of diatoms and *Synechococcus* alongside overall rates of PP have been observed to rise significantly inside CE as a consequence of enhanced nutrient supply (Wang et al., 2016; Liao et al., 2021). In contrast, the effects of anticyclonic eddies (ACEs) on phytoplankton community structure are more diverse, with ACE leading to convergence of low nutrient surface waters leading to the community structure inside ACE being similar to that of surrounding waters (Huang et al., 2010). In addition, sub-mesoscale upwelling at the edge of ACE has been shown to drive a modest effect of increasing the Chl*a* biomass of diatoms and haptophytes (Wang et al., 2018).

So far, studies of eddies in the SCS accompanying measurements of photophysiology have not been made. However, other studies have indicated that nutrient availability impacts photophysiology in this region (Jin et al., 2016; Xie et al., 2018). Using diel FRRf measurements, Jin et al. (2016) investigated phytoplankton physiology at local noon in the northern SCS, showing decreasing F_v/F_m values from the coast

to central basin and increasing values from the surface to deep. Furthermore, Xie et al. (2018) measured the diel cycle of F_v/F_m for a natural assemblage of *Prochlorococcus*, the most abundant phytoplankton class in the SCS, and related the observed diel variability to nutrient stress. Here, we undertook an FRRf survey over a much larger area of the SCS than in these previous studies, ranging from the outer continental shelf to the entire basin and crossing CE and ACE features, and complementing these measurements with diagnostic pigment analyses to aid with deconvolving nutrient, community, and light effects on F_v/F_m and σ_{PSII}.

2 Materials and methods

2.1 Underway FRRf measurements

Observations were made during cruise KK1808 onboard the R/V *Tan Kah Kee* (18 September–14 October 2018). Underway FRRf measurements were conducted with a FastOcean coupled with an Act2 Laboratory System (Chelsea Technologies, UK). The ship's underway system collected seawater continuously from a depth of ~5 m, which then transitioned through a ~50-m dark pipe before flowing into the Act2 System. The dark acclimation period from water entering the vessel to FRRf measurement was estimated to last approximately 5 min, which is similar to that of Behrenfeld and Kolber (1999). The FRRf was set to perform acquisitions using 100 blue excitation (450 nm) flashlets with 2-ms intervals. Fluorescence transients were fit within the manufacturers' software (ActRun) to yield the initial fluorescence yield (F_o), maximum fluorescence yield (F_m), and σ_{PSII}. Blank fluorescence of deionized water (Milli-Q) samples was subtracted from raw F_o and F_m values and F_v/F_m recalculated.

2.2 Continuous shipboard measurements and satellite data products

Time and geographic coordinates were recorded by the shipboard geographical positioning system (GPS). The time was converted to local time, allowing alignment of light–dark periods. Sea-surface temperature (SST) and salinity were continuously measured by an SBE21 CTD (Sea-Bird Electronics, USA). The FastOcean plus Act2 Laboratory System measured fluorescence-based chlorophyll *a* concentrations ($Chla^{FRRf}$), which was then calibrated against high-performance liquid chromatography (HPLC)-determined concentrations of chlorophyll *a* pigments. To characterize the mesoscale eddies in the study area, daily, 1/4° gridded sea level anomaly (SLA) data between 8 September and 14 October 2018 were downloaded from the Copernicus Marine and Environment Monitoring Service (CMEMS) (available from: http://marine.copernicus.eu/). In addition, a 10-min resolution instantaneous photosynthetically available radiation (iPAR, µmol quanta m^{-2} s^{-1}) was extracted from Himawari-8 level 2 products (available from: https://www.eorc.jaxa.jp/ptree/), and daily integrated surface PAR data (mol quanta m^{-2} day^{-1}) were extracted from the standard MODIS-Aqua Level-3 products at 4-km pixel resolution (available from: http://oceancolor.gsfc.nasa.gov/). Each *in situ* underway measurement was matched with a daily SLA, iPAR, and PAR dataset using the closest pixel of the respective satellite products. Himawari-8-derived iPAR values were consistent with *in situ* measurement derived from PAR sensor mounted in the CTD with p <0.01 and r =0.87 (Supplementary Figure S1).

2.3 Pigments and chemotaxonomic analysis

Seawater samples were collected with Niskin bottles from discrete depths at the stations (Figure 1). Seawater (4–6 L) at

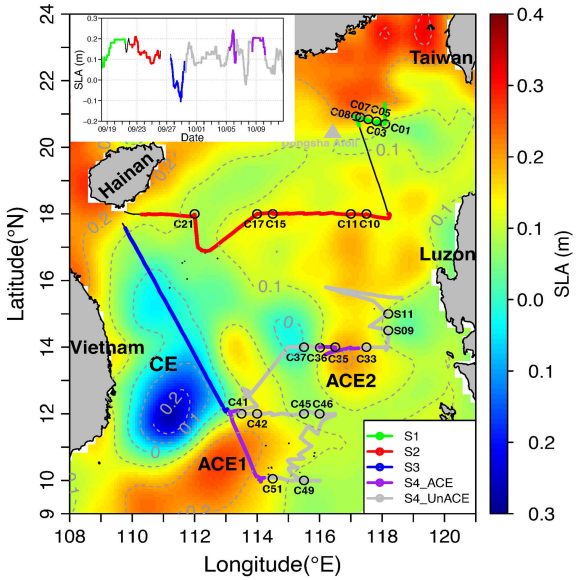

FIGURE 1
Map of sampling stations based on the average sea level anomaly (SLA) from 18/09/2018 to 14/10/2018. The top left box indicates the matched daily sea level anomaly (SLA) of the cruise track. The black dots were stations with phytoplankton pigment survey during the cruise. The color lines were the cruise track, which can be divided into four transects: S1 was selected as the continental shelf of northern SCS; S2 referred to the basin of northern SCS; S3 located in the western SCS where cyclonic eddies occurred; S4 distributed in the basin of southeastern SCS. CE, cyclonic eddy; ACE, anticyclonic eddy. S1, S2, S3, S4_ACE (through ACE1 and ACE2), and S4_UnACE (outside ACE1 and ACE2) were in green, red, blue, purple, and gray, respectively.

each depth was filtered onto a 25-mm diameter GF/F glass fiber filter under gentle vacuum (<75 mmHg) and stored in liquid nitrogen until analysis. In the laboratory, filters were immersed in N, N-dimethylformamide for pigment extraction. Extracts were analyzed with an UltiMate 3000 HPLC system (Thermo Fisher Scientific, USA) calibrated with pigment standards (DHI Water & Environment, Denmark) following the procedure of Furuya et al. (2003).

Thirteen pigments detected included chlorophyll *c*2, chlorophyll *c*3, peridinin, 19'-butanoyloxyfucoxanthin, fucoxanthin, neoxanthin, prasinoxanthin, 19'-hexanoyloxyfucoxanthin, violaxanthin, diadinoxanthin, alloxanthin, diatoxanthin, zeaxanthin, lutein, chlorophyll *a*, chlorophyll *b*, divinyl chlorophyll *a*, α-carotene, and β-carotene. CHEMTAX software was then used to estimate the contribution of different phytoplankton groups to total chlorophyll *a* (the sum of chlorophyll *a* and divinyl chlorophyll *a*) (Mackey et al., 1996). The initial input matrix of ratios of diagnostic pigments to total chlorophyll *a* was identical to the input matrix used in previous studies in the South China Sea (Wang et al., 2015; Xiao et al., 2018). Successive runs were done for each group to gain convergence between input and output ratios according to the CHEMTAX protocols described by Latasa (2007). Nine phytoplankton groups were computed, including Dinoflagellates (Dino), Diatoms (Diat), Type-8 Haptophytes (Hapt_8), Type-6 Haptophytes (Hapt_6), Cryptophytes (Cryp), Chlorophytes (Chlo), Prasinophytes (Pras), *Synechococcus* (*Syne*), and *Prochlorococcus* (*Proc*), and we used only surface phytoplankton information in this study. In addition, the carotenoids were separated into photosynthetic carotenoids (PSCs) and photo-protective carotenoids (PPCs). The former includes peridinin, 19'-butanoyloxyfucoxanth, fucoxanthin, and 19'-hexanoyloxyfucoxanthin. The latter includes violaxanthin, diadinoxanthin, alloxanthin, diatoxanthin, zeaxanthin, ββ- + βε-carotene, and lutein (Barlow et al., 2007).

2.4 Statistical analysis

A one-way ANOVA was used for statistical analysis to compare the difference between environmental and FRRf-derived parameters among sections, Tukey's HSD test was performed for post-hoc test for multi-comparisons. In order to deconvolve light signal and other factors for F_v/F_m, a simple model was constructed. In the model, F_v/F_m is a linear function of iPAR, and the constant of the linear function represents influence of other factors together, but different regions have different constants for their own nutrient conditions; in addition, a two-way ANOVA was conducted in the beginning and determined that both light and region were significant factors and the slope of the linear function is invariant for different regions (because of no interaction effect between light and region, Supplementary Table S1). All statistical analyses were performed using open source statistical software R version 3.6.0 (R Development Core Team, 2016). Figures were plotted using Ocean Data View 5 (Schlitzer, 2019) and R software.

3 Results

Clear variations in hydrographic properties and SLA during the cruise were observed (Figures 1, 2). Chlorophyll fluorescence was relatively elevated in the northern SCS continental shelf transect selected as S1. Relatively lower SST and higher salinity were observed around 18° SCS and was named S2. SLA images identified the positions of one cyclonic eddy (CE) and two anticyclonic eddies (ACEs, ACE1, and ACE2) that our cruise passed through. Accordingly, we then classified S3, S4_ACE, and S4_UnACE (regions outside of the eddies in S4) into different water masses in the western and southeastern SCS (Figure 1). A principal component analysis (PCA) was performed to segment the underway dataset based on biological and environment factors (Figure 3). The first two principal components

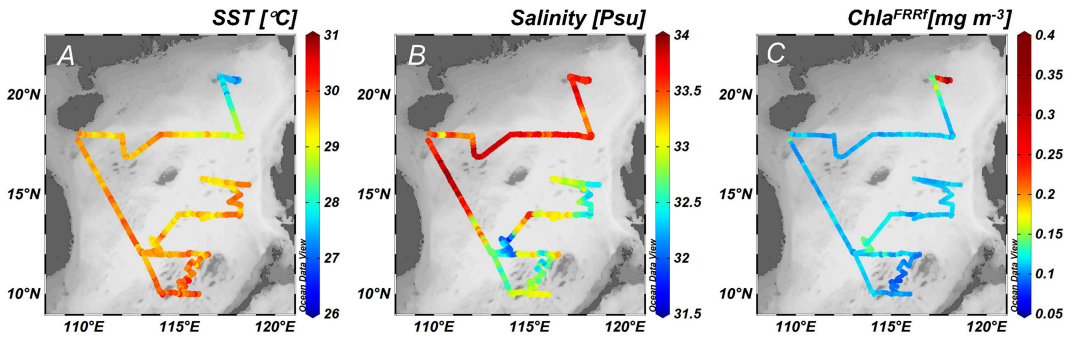

FIGURE 2
Underway surface sea temperature (SST) **(A)**, surface salinity **(B)**, and surface fluorescence ($Chla^{FRRf}$) **(C)** during the cruise.

accounted for more than 60% of the total variation, with the first principal component driven by variations in temperature and chlorophyll fluorescence and the second by SLA (Figure 3). The groups distinguished based on chlorophyll fluorescence, SST, and SLA accordingly separated within PC1–PC2 space.

3.1 The shelf edge of the northern SCS (Section S1)

Section S1 was located at the edge of the northern continental SCS shelf close to the Dongsha Atoll (Figure 1). Section S1 had the lowest SST and highest Chla^{FRRf} of the survey (Figure 2; Table 1). Ranges of SST and Chla^{FRRf} along this section varied from 26.7°C to 28.0°C and from 0.12 to 0.51 mg m^{-3}, respectively, but salinity showed small variability (33.4–33.76 psu; Figures 2, 5). Phytoplankton compositions in this region were also distinct, with higher proportions of Prasinophytes (6%–15%) ($p < 0.01$), Type-8 Haptophytes (9%–19%) ($p < 0.01$), and Diatoms (0%–15%) ($p < 0.05$) and lower proportions of *Prochlorococcus* (18%–30%) ($p < 0.05$) than the other sections (t-test for significantly different means; Figure 4). Between stations C01 and C03, SST declined by ~0.8°C, and Chla^{FRRf} showed a synchronous peak (Figure 5C). Although C03 was not at the center of SST minimum, Chla^{HPLC} was the highest observed (0.4 mg m^{-3}), and the diatom percentage contribution to total chlorophyll-a was also the highest for the cruise (15%). Following C03, Chla^{HPLC} gradually decreased landwards, while the proportions of Prasinophytes and Diatoms decreased but *Synechococcus* and *Prochlorococcus* increased (Figure 4).

A peak of F_v/F_m up to 0.40 matched the SST minimum, closely corresponding with Chla^{FRRf} (Figure 5C). Besides this peak, F_v/F_m values were relatively low (<0.3). The PSII functional absorption cross-section (σ_{PSII}) remained relatively constant (mean of 701 Å^2; Figure 5C). Generally, F_v/F_m exhibited maxima at sunrise (~0.30) and sunset (~0.24) with depressions at midday (~0.20) and at about 22:00 (~0.27). By contrast, diel variability in σ_{PSII} (615–870 Å^2) was relatively minor although demonstrated an afternoon increase (Figure 5E).

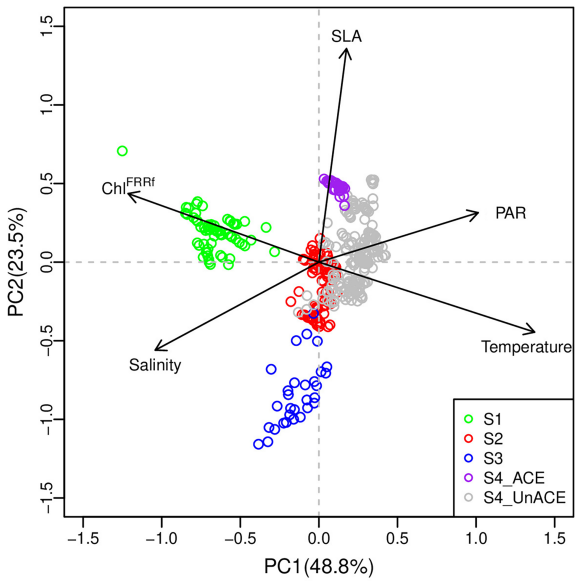

FIGURE 3
Principle component analysis (PCA) of matched underway biological and environment factors during the cruise. S1, S2, S3, S4_ACE (through ACE1 and ACE2), and S4_UnACE (outside ACE1 and ACE2) were dots in green, red, blue, purple, and gray, respectively.

3.2 The northern basin (Section S2)

Section S2 defined the 18°N transect from 118°E to 110°E (Figure 1). SLA showed higher values in the eastern part of the transect, contrasting with lower values around C21 (Figure 1). SST between 28.7°C and 30°C was observed and increased gradually during the daytime in the area until reaching 114°E (Figure 6). Salinity increased generally from 33.5 to 33.9 psu until a sharp drop to 33.3 psu before the station C21 and then a further reduction to 33.0 near Hainan Island (Figures 2, 6B). Both Chla^{FRRf} (0.10–0.12 mg m^{-3}) and Chla^{HPLC} (~0.08 mg m^{-3}) were lower than S1 (Figure 6C, Table 1), and phytoplankton compositions were *Synechococcus* (37%–57%) and *Prochlorococcus* (32%–51%) dominated (Figure 4).

Compared with Section S1, F_v/F_m (0.10–0.30) and σ_{PSII} (416–799 Å^2) values in S2 were significantly lower ($p < 0.01$) (Table 1). However, the fluctuation of diel patterns of F_v/F_m in S2 were more pronounced, showing lower peaks at sunrise (~0.27) and sunset (~0.23) and pronounced midday (~0.14) and more modest night time (~0.20) reductions (Figure 6D). Furthermore, σ_{PSII} showed a clear diel pattern, with a pronounced midday maximum that was approximately 1.4-fold higher than night time values (Figure 6E).

3.3 The eddy domain of the western SCS (Section S3)

Section S3 started from Hainan Island heading southeast, intersecting the edge of a cyclonic eddy to the east of Vietnam (Figure 1). Along this section, SLA were depressed (−0.07–0.13 m), and within the vicinity of the cyclonic eddy, SST ranged 29.3°C–30°C (Table 1; Figure 7B). Chla^{FRRf} remained relatively constant (~0.10 mg m^{-3}) (Figure 7C; HPLC samples not collected).

Values of F_v/F_m were significantly higher than S2 and S4 ($p < 0.01$), varying between 0.14 and 0.32 in the cyclonic eddy (Table 1). F_v/F_m showed a clear diel pattern, with higher

TABLE 1 Mean ± SD of surface environment conditions and FRRf-derived parameters performance in the SCS along the cruise.

Location	Northern SCS		Western SCS	South Eastern SCS	
N	Shelf (S1) 95	Basin (S2) 130	CE (S3) 57	ACE1 and ACE2 (S4) 84	Outside ACE1 and ACE2 (S4) 318
Temperature (°C)	27.38 ± 0.28^{a}	29.32 ± 0.28^{b}	29.68 ± 0.17^{c}	29.53 ± 0.26^{d}	29.66 ± 0.28^{c}
Salinity (psu)	33.64 ± 0.08^{a}	33.61 ± 0.21^{a}	33.38 ± 0.46^{b}	32.98 ± 0.21^{c}	32.72 ± 0.37^{d}
Chla^{FRRf} (mg m^{-3})	0.24 ± 0.10^{a}	0.11 ± 0.01^{b}	0.11 ± 0.01^{b}	0.11 ± 0.01^{b}	0.11 ± 0.01^{b}
SLA (m)	0.12 ± 0.04^{a}	0.13 ± 0.03^{a}	0.01 ± 0.05^{b}	0.21 ± 0.04^{c}	0.13 ± 0.04^{a}
PAR (mol quanta m^{-2} day^{-1})	41.70 ± 6.91^{a}	52.45 ± 3.07^{b}	44.29 ± 7.02^{a}	52.92 ± 0.58^{b}	52.65 ± 4.46^{b}
F_v/F_m	0.23 ± 0.06^{a}	0.20 ± 0.04^{b}	0.24 ± 0.04^{a}	0.15 ± 0.05^{c}	0.17 ± 0.05^{d}
F_v/F_m *(T=dawn)*	0.29 ± 0.07^{a}	0.26 ± 0.03^{a}	0.27 ± 0.03^{a}	0.18 ± 0.04^{b}	0.21 ± 0.05^{b}
F_v/F_m *(T=midnight)*	0.27 ± 0.05^{a}	0.21 ± 0.02^{b}	0.23 ± 0.02^{ab}	0.16 ± 0.04^{c}	0.17 ± 0.04^{c}
F_v/F_m *(T=noon)*	0.17 ± 0.05^{a}	0.14 ± 0.02^{ab}	0.18 ± 0.02^{a}	0.09 ± 0.01^{c}	0.13 ± 0.04^{b}
σ_{PSII} (Å^2)	714 ± 70^{a}	547 ± 77^{b}	508 ± 41^{c}	437 ± 101^{d}	484 ± 77^{c}

The superscript labels a–d implied significant difference at the level of $p < 0.05$ using one-way ANOVA (SLA, sea level anomaly; PAR, daily integrated photosynthetically available radiation at the surface).

sunrise (~0.29), sunset (~0.29), and lower midday (~0.17) and night (~0.23) values (Figure 7D; Table 1). Values of σ_{PSII} remained relatively constant (421–587 Å^2) in the cyclonic eddy, with a small increase around midday (Figure 7E).

3.4 The southeastern basin (Section S4)

This section intersected anticyclonic eddies ACE1 and ACE2 (S4_ACE) with regions outside of the eddies defined as S4_UnACE (Figure 1). Salinity varied between 32.0 and 33.3 psu and SST between 29.2°C and 30.6°C. The map showed that this section, particularly outside the ACEs, was characterized by the lowest salinity among all sections (Figure 2B). Chla^{FRRf} remained relatively constant (0.11–0.12 mg m^{-3}) but increased (~0.14 mg m^{-3}) on the outside of ACE1 associated with a salinity decrease (~32.0 psu). Two abrupt changes in Chla^{FRRf} were observed at the edge of ACEs, with Chla^{FRRf} increasing by ~0.03 mg m^{-3}. Across ACE2, SST and salinity were relatively constant (29.3°C–29.7°C; salinity, ~33.1 psu), while Chla^{FRRf} gradually declined from 0.14 to 0.10 mg m^{-3} (Figure 8). *Synechococcus* and *Prochlorococcus* together were the largest contributor to Chl*a* throughout (Figure 4).

Ranges of F_v/F_m inside and outside the ACEs were 0.07–0.26 and 0.07–0.32, respectively. Smoothed F_v/F_m curves showed that the sunrise (~0.19) and sunset values (~0.17) inside the ACEs were similar with those outside (~0.21 and ~0.19), but those curves overlooked spatial variations. For example, the ACE1 had apparent higher sunrise and sunset F_v/F_m than the ACE2. Nevertheless, the smoothed curves did capture the midday minimum (0.09 ± 0.01) inside the ACEs, which was lower than those outside (0.13 ± 0.04) (Figure 8D; Table 1). The values of σ_{PSII} were the lowest of the cruise and varied between 64 and 663 Å^2 (Table 1), and the diel patterns showed a small increase in σ_{PSII} in the afternoon both inside and outside ACEs (Figure 8E).

3.5 Comparisons between and within sections

Section S1 was distinct to other sections and characterized by lower SST of 27.4 ± 0.3°C and higher Chla^{FRRf} of 0.24 ± 0.10 mg m^{-3} (Table 1). Section S1 was heterogeneous with the abrupt bump of F_v/F_m at the first night (Figure 5). Sections S2 and S3 were relatively homogeneous; F_v/F_m were consistently higher in Section S3 than those in Section S2, although the differences were quantitatively small (Table 1). Moreover, σ_{PSII} in Section S2 had a significant increase in the afternoon, which was not apparent in Section S3 (Figure 6). The average dawn F_v/F_m of sections S1–S3 were all smaller than 0.3 (0.26–0.29) but still higher than that in Section S4 (0.18 and 0.21 inside and outside ACEs, respectively). Corresponding to similar iPAR at noon, ACEs revealed significantly lower noon F_v/F_m (0.09 ± 0.01) than that of S4_UnACE. In general, F_v/F_m experienced <20% reduction at midnight but up to 50% at noon, by using the dawn value as the reference.

4 Discussion

Our results of the active fluorescence measurements in the SCS may reflect diurnal variations in FRRF-derived parameters and spatial changes in photophysiology of phytoplankton assemblages and their taxonomic compositions related to environmental forcing (Behrenfeld et al., 2006; Suggett et al., 2009). Therefore, it was

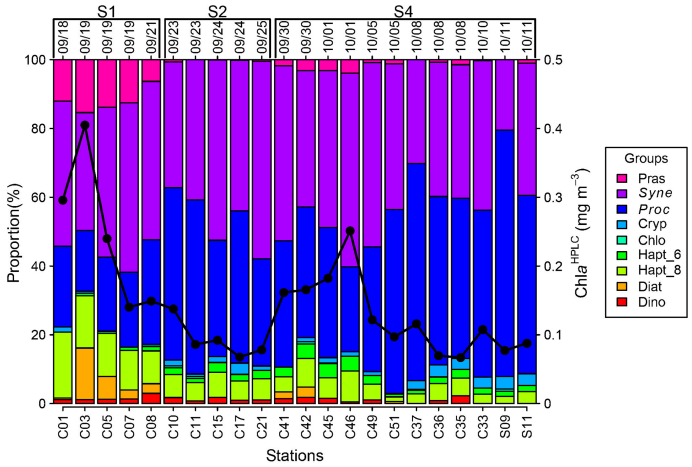

FIGURE 4
The concentration of total Chl *a* ($Chla^{HPLC}$) and contributions of different phytoplankton groups during the cruise. Dino, Diat, Hap_8, Hap_6, Chlo, Cryp, *Proc*, *Syne*, and Pras are the abbreviations for Dinoflagellates, Diatoms, Haptophytes (type 8), Haptophytes (type 6), Chlorophytes, Cryptophytes, *Synechococcus*, *Prochlorococcus*, and Prasinophytes.

challenging to compare any instantaneous F_v/F_m measurement between regions (Supplementary Figure S2). We first discuss the influence of phytoplankton composition on FRRF-derived parameters and typical diurnal patterns over the entire SCS, followed by a discussion on effects of mesoscale eddy structure on phytoplankton photophysiology within the SCS.

4.1 Challenge 1: Understudied photophysiology of prokaryotic phytoplankton

Suggett et al. (2009) showed from active fluorescence data for phytoplankton cultures in previous studies that there was a negative relationship between (optimal) F_v/F_m and σ_{PSII} across

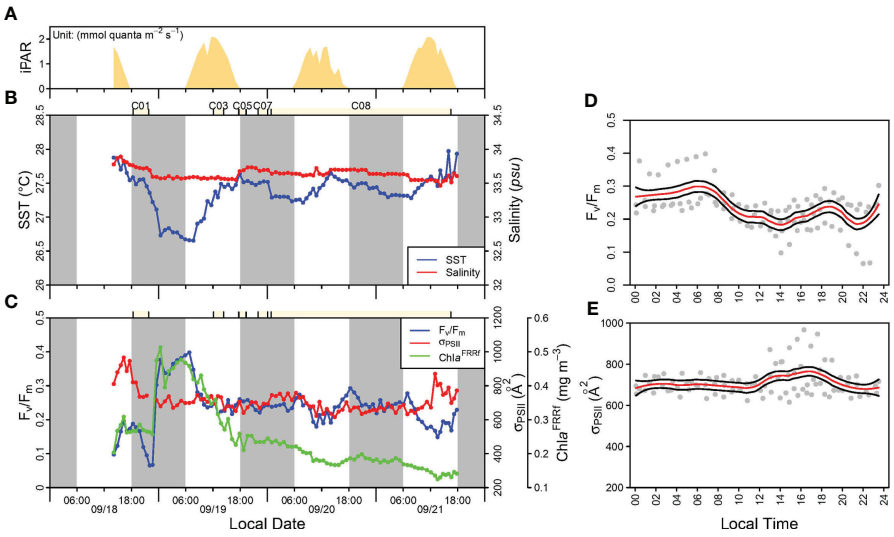

FIGURE 5
The incident irradiance **(A)**; environment conditions including SST and salinity **(B)**; F_v/F_m, σ_{PSII}, and $Chla^{FRRf}$ **(C)**; diel pattern of F_v/F_m **(D)**; and diel pattern of σ_{PSII} **(E)** for the continental shelf of the northern SCS (Section S1). Light yellow, white, and gray-shaded area indicate the HPLC sample station and local daytime and nighttime, respectively. The red lines in panels **(D)** and **(E)** are smoothed using the loess method (span = 0.3), while the black lines represent the regression values ± SE.

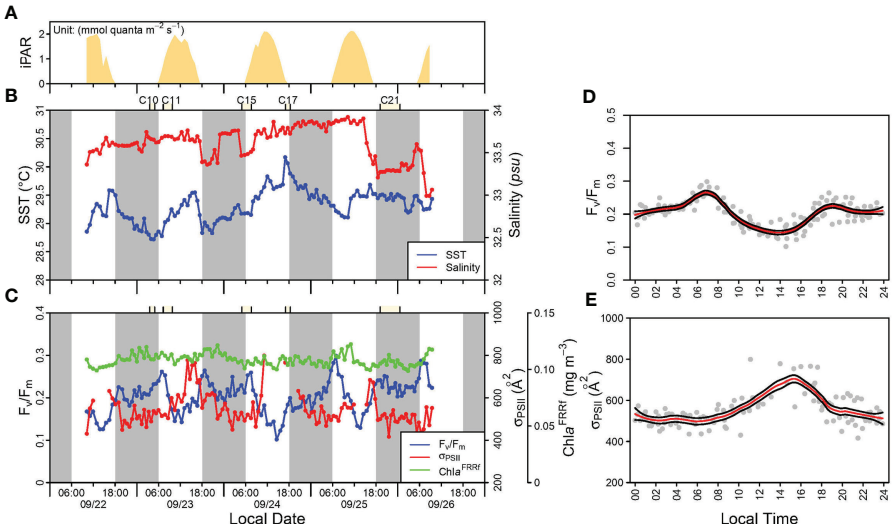

FIGURE 6
Same as Figure 5 but for basin of the northern SCS (Section S2).

eukaryotic taxa. The relationship was explained by the distinct light absorption and excitation energy transfer for each taxon and their energetic interpretation, which were likely related to selective pressure during phytoplankton evolution. However, in this study, no relationship was found between the two measurements (Figure 9A) despite that bulk σ_{PSII} actually reflected the relative amount of light-harvesting pigments (which was governed by phytoplankton composition) (Figures 9B, C). Assuming that F_v/F_m of eukaryotic phytoplankton in the SCS was also taxonomic dependent, perhaps the lack of a negative relationship was due to the contribution by both FRRF parameters from *Synechococcus* predominated in the SCS surface waters. This is because *Synechococcus* have relatively low σ_{PSII} (at blue excitation waveband) and F_v/F_m, attributed to their light absorption maxima being more shifted to "green" and the fluorescence from their relatively abundant PSI and phycocyanin, which disturbs PSII fluorescence signal (Raateoja et al., 2004). On the

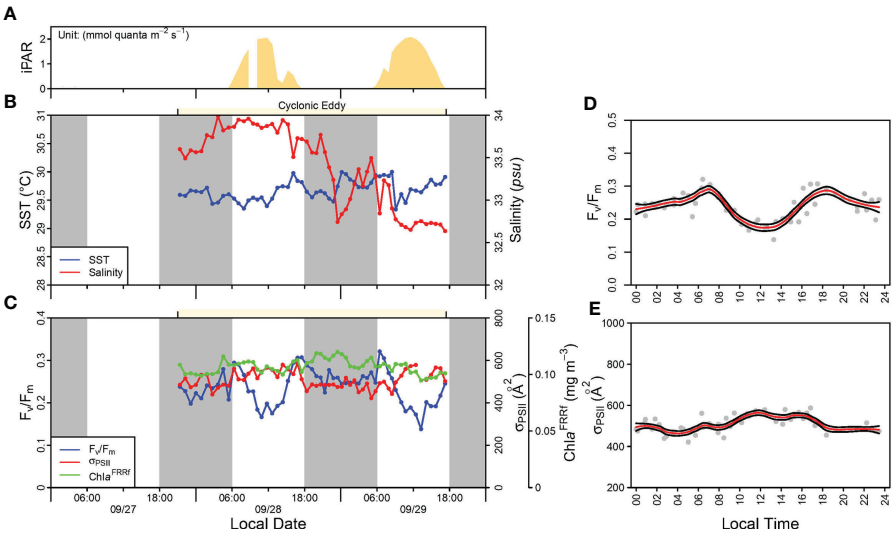

FIGURE 7
Same as Figure 5 but for eddy domains in the Western SCS (Section S3).

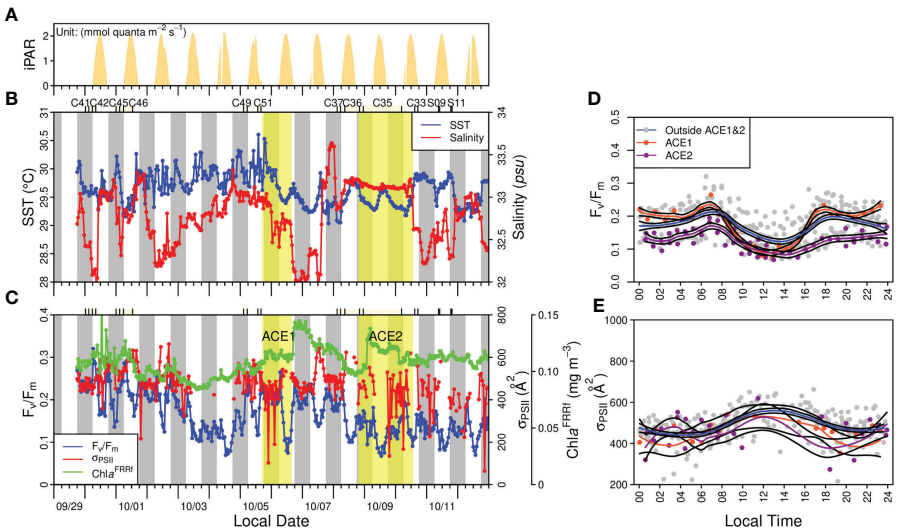

FIGURE 8
Same as Figure 5 but for the basin of the southeast SCS (Section S4).

other hand, *Prochlorococcus*, another dominant species of SCS, has been reported to have different F_v/F_m and σ_{PSII} than *Synechococcus* (Raateoja et al., 2004; Six et al., 2007; Suggett et al., 2009), probably due to distinct pigment compositions with predominantly divinyl chlorophyll (Ting et al., 2002). In any case, the lack of a negative F_v/F_m versus σ_{PSII} relationship as expected from taxonomic changes for eukaryotic phytoplankton was partly due to the dominance of *Synechococcus*, whose parameters do not follow it.

Meanwhile, the low drawn F_v/F_m below 0.3 may be related to the dominance of *Synechococcus*. This is because *Synechococcus* are known to overexpress iron-stress-induced chlorophyll binding protein IsiA under Fe-limited conditions, whereby the extra fluorescence from the IsiA supercomplexes detached to reaction centers would reduce apparent F_v/F_m (Schrader et al., 2011). Antenna proteins similar with IsiA are also found in low-light ecotypes of *Prochorococcus* (Bibby et al., 2003). However, this hypothesis of Fe deficiency in surface waters of the SCS basin appears unlikely, as the measured nitrate concentrations were 0.002–0.2 μM and previously reported Fe concentrations for this region were 0.2–0.3 nM (Wu et al., 2003; Wen et al., 2022), by assuming a threshold of 10:1 N:Fe ratio (μM:nm) for Fe limitation (Browning et al., 2017). Perhaps more likely is that absolute values of F_v/F_m are influenced by the active fluorescence measurement protocol and the instrument used and as such should be evaluated with caution (as discussed in ***Section 4.2***).

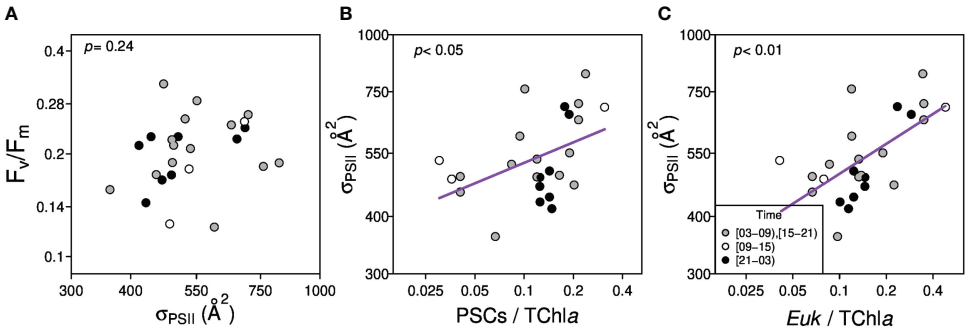

FIGURE 9
The relationship between F_v/F_m and σ_{PSII} **(A)**; σ_{PSII} and photosynthetic carotenoids (PSCs)/TChl *a* **(B)**; σ_{PSII} and *Euk*/TChl a **(C)**. The color represents the time period with the legend in panel (**C**). *Euk* was short for eukaryotic phytoplankton.

4.2 Challenge 2: Widespread diel pattern of F_v/F_m throughout the SCS

Diel variability of F_v/F_m was observed throughout the SCS, with midday minima, maxima at dawn and dusk, and a slight nocturnal decrease (Figures 5–8). This pattern has been observed previously in the central SCS (Xie et al., 2018) and the coastal SCS (Xu et al., 2020; Mai et al., 2021) and several other studies elsewhere in the tropical ocean (Behrenfeld et al., 2006; Mackey et al., 2008; Doblin et al., 2011; Browning et al., 2017). The magnitude of midday minima can vary with incident PAR at noon and the duration of dark acclimation. In this study, the 5-min dark acclimation did not provide sufficient time for phytoplankton to relax the slow NPQ components, which could last for tens of minutes to hours. Furthermore, any repair of damaged PSII reaction centers also requires longer timescales. The sustained quenching to chlorophyll fluorescence led to a lower dark-acclimated F_m and F_v/F_m than it would be with a longer dark acclimation timescale (Supplementary Figure S3). The decline in F_v/F_m relative to its dawn value was positively correlated with the incident PAR (Supplementary Figure S4), suggesting the photoprotective nature of NPQ.

In general, it is expected that the nocturnal reduction in F_v/F_m is due to PQ pool reduction by "chloro-respiration" in the dark and is thought to depend on the degree of Fe stress that would deplete photosynthetic components [such as cytochrome b6f and photosystem I (PSI)] on the accepter side of the electron transfer chain (Behrenfeld and Milligan, 2013). The nocturnal reduction in the SCS was up to ~20% (in Section S4), which is smaller than the nocturnal reduction of >25% seen in Fe-limited surface waters in the equatorial Pacific reported by Behrenfeld et al. (2006). This may suggest that phytoplankton growth in the SCS was not severely Fe limited. Behrenfeld et al. (2006) also used dawn F_v/F_m maxima in combination with nocturnal reduction to delineate three ecophysiological regimes in the tropical Pacific (iron sufficient with low macronutrients, iron limited with low macronutrients, and iron limited with elevated macronutrients). Following their diagnostic diagram [Figure 4 in Behrenfeld et al. (2006)], our SCS data did not belong to any of those three since dawn F_v/F_m was <0.45. While this could imply a substantial difference between the tropical Pacific and the SCS with respect to nutrient availability, such comparisons should be made with caution. This is because absolute values of F_v/F_m are highly dependent on active fluorescence measurement protocols and employed instrumentation. For example, our correction using blank fluorescence from deionized water instead of filtered seawater might have underestimated F_v/F_m measurements (Cullen and Davis, 2003). If the underestimation of F_v/F_m in this study was true, the categorization of the SCS should possibly be the regime "iron-sufficient with low macronutrients," consistent with the reported Fe and nitrate data in the SCS waters in literatures (Wu et al., 2003; Wen et al., 2022). Such speculation should be examined in future nutrient addition experiments.

4.3 Nutrient effects on phytoplankton physiology by cyclonic eddies

Nutrients are usually considered as the most important factor for the growth of phytoplankton in the SCS (Ho et al., 2015) and always depleted in the upper mixed layer in the oligotrophic water along with strong stratification during summer. In this study, as described above, F_v/F_m at the surface was typically as low as 0.1–0.3, and phytoplankton communities were dominated by *Synechococcus* and *Prochlorococcus* at the surface, indicating the oligotrophic condition in most of our study area during this cruise. Within the study area, it is expected that Section S3 region crossing the cyclonic eddy was pumped with some nutrients from the nutrient-rich deeper layer (McGillicuddy, 2016), and therefore, phytoplankton physiological status may have been more favorable. The F_v/F_m exhibited consistently higher values in Section S3 where CE occurred than in the preceding Section S2 ($p < 0.01$) (Figure 7; Table 1), but the increases (about 0.04) were small, and the diel variation remained the same (Figures 6, 7). The high SST of 29.5°C–30°C likely rejected the assumption of large amount of nutrient-rich water injected into the surface. At the same time, the Chla^{FRRf} values in Section S3 were about 0.11 mg m^{-3}, as similar as that in Section S2. Previous studies in the SCS showed both elevated nutrient inventory and Chl*a* in CE, but cold and nutrient-rich water was injected mainly into the lower part of euphotic zone. Chl*a* at the deep chlorophyll maximum layer could be increased to larger than 1 mg m^{-3}, which was more than double of the background concentration, but Chl*a* at the surface was rarely increased; the reported surface Chl*a* within cold eddies (normally 0.1–0.2 mg m^{-3}) was consistent with our observation (Jiao et al., 2014; Wang et al., 2016; Liao et al., 2021). Taken together, these results implied that the CE had limited impacts on the surface phytoplankton communities. On the contrary, small scale but large increases in F_v/F_m were observed in the shelf area. Section S1 adjoined the Dongsha Atoll, where internal waves were frequently detected (Hsu et al., 2000; Zhao et al., 2004; Liu et al., 2006; Pan et al., 2012) (Figure 1). The sudden drop of SST value, corresponding the higher Chla^{FRRf} than those in nearby subregion in this area, is consistent with previous studies and indicated the occurrence of the internal waves between the station C01 and C03 along this transect (Figures 2, 5). The dawn F_v/F_m of as high as 0.4 was accompanied by a Chl*a* concentration of about 0.4 mg m^{-3} and 15% contribution by diatoms at station C03. The results suggested that the F_v/F_m pattern observed in Section S1 was significantly affected by physical processes that can effectively supply nutrients to fuel phytoplankton growth. It also suggests that

this level of nutrient supply cannot be reproduced by physical processes associated with the mesoscale cyclonic eddy structure seen in Section S3. However, it should be noted that the change in F_v/F_m is usually disproportional to the change in carbon fixation; a study in the CE area of the western SCS but half month before this study found a twofold increase in the average Chl*a*-specific carbon fixation rate inside the CE than outside (Liao et al., 2021), with the implication being that FRRf could not probe any altered photosynthetic efficiency that does not occur at the intracellular site of PSII.

4.4 Effects of anticyclonic eddies on phytoplankton physiology

The lowest values of F_v/F_m were found in the southeast basin associated with ACE2 (Figure 8); these may be explained in the case of anticyclonic eddy based on the doming of its isopycnals and nutricline, therefore causing lower sustained phytoplankton biomass in this area (McGillicuddy, 2016). ACE1 was adjacent to the Mekong River plume area characterized by lower salinity of <32.5 psu, while ACE2 was located in the remote and more oligotrophic southeast basin. The river input provides nutrients to promote phytoplankton growth, and the dawn F_v/F_m in ACE1 was 0.24 (Figure 8D). Meanwhile, the ACE2 showed the lowest Chl*a* of 0.07 mg m^{-3} corresponding to a dawn F_v/F_m of 0.17. Huang et al. (2010) reported two ACEs in the northern SCS during wintertime with much more abundant eukaryotic phytoplankton in the ACE with entrainment of coastal water. These phenomena highlighted the effects of source water mass on phytoplankton in ACEs. However, the midday minimums of F_v/F_m were the same (~0.09) between the two ACEs (Figure 8D), with the phytoplankton in the ACE1 exhibiting higher light sensitivity than those in surrounding waters.

5 Conclusions

In this study, underway FRRf measurements were used to record high-resolution diel changes in F_v/F_m and σ_{PSII} throughout the SCS. Pronounced diurnal variability of both F_v/F_m and σ_{PSII} were observed, characterized by large midday depressions and slight nocturnal depressions of F_v/F_m, and slight increases in σ_{PSII} at noon, which was especially pronounced under expected elevated nutrient stress conditions. Slightly but consistently higher F_v/F_m throughout the day in the western SCS compared to the northern SCS basin suggested the potential role of cyclonic eddies in partially relieving nutrient stress. Apparent increase in F_v/F_m occurred only in a shelf area influenced by internal waves, where we hypothesized that nutrients were injected into surface waters. The two ACEs exhibited different dawn, dusk, and night time values of F_v/F_m, indicating effects of source water mass on phytoplankton photophysiology. We recommend that future studies investigating phytoplankton photophysiology in the SCS should focus on more detailed mechanisms (e.g., vertical structure of mesoscale eddies, any other mesoscale process, and typhoon) possibly *via* nutrient addition experiments conducted over different timescales to directly test the impact of nutrient supply on phytoplankton photophysiology.

Data availability statement

The raw data supporting the conclusions of this article will be made available by the authors, without undue reservation.

Author contributions

HL, YX, and BH conceived this study. HL and FX conducted the sample collection and analysis. HL drafted the original manuscript. YX and TJB critically reviewed and edited the manuscript. All authors contributed to the article and approved the submitted version.

Funding

This work was supported by the National Natural Science Foundation of China through grants 42130401 and 42141002.

Acknowledgments

We thank Yin-Ning Zhang who is very gentle to lend us FastOcean plus FastAct, and Gai-Lian Li for her support on cruise preparation. We also thank NSFC Shiptime SharingProject (41749906) for supporting the cruises by R/V *Tan Kah Kee* (No. NORC2018-06). We also thank the captain and crew of R/V *Tan Kah Kee* for their tremendous helps during the cruise. We also thank the reviewers (including one anonymous reviewer) for their thoughtful, and constructive feedback.

Conflict of interest

The authors declare that the research was conducted in the absence of any commercial or financial relationships that could be construed as a potential conflict of interest.

Publisher's note

All claims expressed in this article are solely those of the authors and do not necessarily represent those of their

affiliated organizations, or those of the publisher, the editors and the reviewers. Any product that may be evaluated in this article, or claim that may be made by its manufacturer, is not guaranteed or endorsed by the publisher.

Supplementary material

The Supplementary Material for this article can be found online at: https://www.frontiersin.org/articles/10.3389/fmars.2022.934391/full#supplementary-material

References

Barlow, R., Stuart, V., Lutz, V., Sessions, H., Sathyendranath, S., Platt, T., et al. (2007). Seasonal pigment patterns of surface phytoplankton in the subtropical southern hemisphere. *Deep Sea Res. Part I* 54 (10), 1687–1703. doi: 10.1016/j.dsr.2007.06.010

Behrenfeld, M. J., and Kolber, Z. S. (1999). Widespread iron limitation of phytoplankton in the south pacific ocean. *Science* 283 (5403), 840–843. doi: 10.1126/science.283.5403.840

Behrenfeld, M. J., and Milligan, A. J. (2013). Photophysiological expressions of iron stress in phytoplankton. *Annu. Rev. Mar. Sci.* 5, 217–246. doi: 10.1146/annurev-marine-121211-172356

Behrenfeld, M. J., Worthington, K., Sherrell, R. M., Chavez, F. P., Strutton, P., McPhaden, M., et al. (2006). Controls on tropical pacific ocean productivity revealed through nutrient stress diagnostics. *Nature* 442 (7106), 1025–1028. doi: 10.1038/nature05083

Bibby, T. S., Mary, I., Nield, J., Partensky, F., and Barber, J. (2003). Low-light-adapted prochlorococcus species possess specific antennae for each photosystem. *Nature* 424, 1051–1054. doi: 10.1038/nature01933

Browning, T. J., Achterberg, E. P., Rapp, I., Engel, A., Bertrand, E. M., Tagliabue, A., and Moore, C. M. (2017). Nutrient co-limitation at the boundary of an oceanic gyre. *Nature* 551 (7679), 242–246. doi: 10.1038/nature24063

Browning, T. J., Bouman, H. A., Moore, C. M., Schlosser, C., Tarran, G. A., Woodward, E. M. S., et al. (2014). Nutrient regimes control phytoplankton ecophysiology in the south Atlantic. *Biogeosciences* 11, 463–479. doi: 10.5194/bg-11-463-2014

Campbell, D., Hurry, V., Clarke, A. K., Gustafsson, P., and Öquist, G. (1998). Chlorophyll fluorescence analysis of cyanobacterial photosynthesis and acclimation. *Microbiol. Mol. Biol. Rev.* 62 (3), 667–683. doi: 10.1128/MMBR.62.3.667-683.1998

Cullen, J. J., and Davis, R. F. (2003). The blank can make a big difference in oceanographic measurements. *Limnology Oceanography Bull.* 12, 29–35. doi: 10.1002/lob.200312229

Doblin, M. A., Petrou, K. L., Shelly, K., Westwood, K., van den Enden, R., Wright, S., et al. (2011). Diel variation of chlorophyll-a fluorescence, phytoplankton pigments and productivity in the Sub-Antarctic and polar front zones south of Tasmania, Australia. *Deep Sea Res. Part II* 58, 2189–2199. doi: 10.1016/j.dsr2.2011.05.021

Falkowski, P. G., Barber, R. T., and Smetacek, V. V. (1998). Biogeochemical controls and feedbacks on ocean primary production. *Science* 281 (5374), 200–207. doi: 10.1126/science.281.5374.200

Falkowski, P. G., and Raven, J. A. (2007). Aquatic photosynthesis. 2nd edn. Princeton: Princeton University Press

Field, C. B., Behrenfeld, M. J., Randerson, J. T., and Falkowski, P. (1998). Primary production of the biosphere: Integrating terrestrial and oceanic components. *Science* 281 (5374), 237–240. doi: 10.1126/science.281.5374.237

Furuya, K., Hayashi, M., Yabushita, Y., and Ishikawa, A. (2003). Phytoplankton dynamics in the East China Sea in spring and summer as revealed by HPLC-derived pigment signatures. *Deep Sea Res. Part II* 50 (2), 367–387. doi: 10.1016/S0967-0645(02)00460-5

Ho, T. Y., Pan, X., Yang, H. H., George., T. F. W., and Shiah, F. K. (2015). Controls on temporal and spatial variations of phytoplankton pigment distribution in the northern south China Sea. *Deep Sea Res. Part II* 117, 65–85. doi: 10.1016/j.dsr2.2015.05.015

Hsu, M. K., Liu, A. K., and Liu, C. (2000). A study of internal waves in the China seas and yellow Sea using SAR. *Cont. Shelf Res.* 20 (4-5), 389–410. doi: 10.1016/S0278-4343(99)00078-3

Huang, B. Q., Hu, J., Xu, H. Z., Cao, Z. R., and Wang, D. X. (2010). Phytoplankton community at warm eddies in the northern south China Sea in winter 2003/2004. *Deep Sea Res. Part II* 57, 1792–1798. doi: 10.1016/j.dsr2.2010.04.005

Hughes, D. J., Campbell, D. A., Doblin, M. A., Kromkamp, J. C., Lawrenz, E., Moore, C. M., et al. (2018). Roadmaps and detours: Active chlorophyll-a assessments of primary productivity across marine and freshwater systems. *Environ. Sci. Technol.* 52 (21), 12039–12054. doi: 10.1021/acs.est.8b03488

Jiao, N., Zhang, Y., Zhou, K., Li, Q., Dai, M., Liu, J., et al. (2014). Revisiting the CO2 "sourcce" problem in upwelling areas – a comparative study on eddy upwellings in the south China Sea. *Biogeosciences* 11 (9), 2465–2475. doi: 10.5194/bg-11-2465-2014

Jin, P., Gao, G., Liu, X., Li, F., Tong, S., Ding, J., et al. (2016). Contrasting photophysiological characteristics of phytoplankton assemblages in the northern south China Sea. *PloS One* 11 (5), e0153555. doi: 10.1371/journal.pone.0153555

Kolber, Z. S., and Falkowski, P. G. (1993). Use of active fluorescence to estimate phytoplankton photosynthesis *in-situ*. *Limnol. Oceanogr.* 38 (8), 1646–1665. doi: 10.4319/lo.1993.38.8.1646

Kolber, Z. S., Prasil, O., and Falkowski, P. G. (1998). Measurements of variable chlorophyll fluorescence using fast repetition rate techniques: Defining methodology and experimental protocols. *Biochim. Biophys. Acta Bioenerget.* 1367, 88–106. doi: 10.1016/s0005-2728(98)00135-2

Latasa, M. (2007). Improving estimations of phytoplankton class abundances using CHEMTAX. *Mar. Ecol. Prog. Ser.* 329, 13–21. doi: 10.3354/meps329013

Liao, J., Xu, J., Li, R., and Shi, Z. (2021). Photosynthesis-irradiance response in the eddy dipole in the Western south China Sea. *J. Geophys. Res. Oceans* 126 (5), e2020JC016986. doi: 10.1029/2020jc016986

Liu, C. T., Pinkel, R., Klymak, J., Hsu, M. K., Chen, H. W., and Villanoy, C. (2006). Nonlinear internal waves from the Luzon strait. *Eos* 87 (42), 449–451. doi: 10.1029/2006eo420002

Li, H., Wiesner, M. G., Chen, J., Ling, Z., Zhang, J., and Ran, L. (2017). Long-term variation of mesopelagic biogenic flux in the central south China Sea: Impact of monsoonal seasonality and mesoscale eddy. *Deep Sea Res. Part I* 126, 62–72. doi: 10.1016/j.dsr.2017.05.012

Longhurst, A., Sathyendranath, S., Platt, T., and Caverhill, C. (1995). An estimate of global primary production in the ocean from satellite radiometer data. *J. Plankton Res.* 17 (6), 1245–1271. doi: 10.1093/plankt/17.6.1245

Mackey, M. D., Mackey, D. J., Higgins, H. W., and Wright, S. W. (1996). CHEMTAX – a program for estimating class abundances from chemical markers: Application to HPLC measurements of phytoplankton. *Mar. Ecol. Prog. Ser.* 144 (1-3), 265–283. doi: 10.3354/meps144265

Mackey, K. R. M., Paytan, A., Grossman, A. R., and Bailey, S. (2008). A photosynthetic strategy for coping in a high-light, low-nutrient environment. *Limnol. Oceanogr.* 53 (3), 900–913. doi: 10.4319/lo.2008.53.3.0900

Mai, G., Song, X., Xia, X., Ma, Z., Tan, Y., and Li, G. (2021). Photosynthetic characteristics of smaller and larger cell size-fractioned phytoplankton assemblies in the daya bay, northern south China Sea. *Microorganisms* 10(1), 16. doi: 10.3390/microorganisms10010016

McGillicuddy, D. J. (2016). Mechanisms of physical-Biological-Biogeochemical interaction at the oceanic mesoscale. *Annu. Rev. Mar. Sci.* 8 (1), 125–159. doi: 10.1146/annurev-marine-010814-015606

Moore, C. M., Mills, M. M., Arrigo, K. R., Berman-Frank, I., Bopp, L., Boyd, P. W., et al. (2013). Processes and patterns of oceanic nutrient limitation. *Nat. Geosci.* 6, 701–710. doi: 10.1038/ngeo1765

Moore, C. M., Mills, M. M., Langlois, R., Milne, A., Achterberg, E. P., and La Roche, J. (2008). Relative influence of nitrogen and phosphorous availability on phytoplankton physiology and productivity in the oligotrophic sub-tropical north Atlantic ocean. *Limnol. Oceanogr.* 53, 291–305. doi: 10.4319/lo.2008.53.1.0291

Ning, X., Chai, F., Xue, H., Cai, Y., Liu, C., and Shi, J. (2004). Physical-biological oceanographic coupling influencing phytoplankton and primary production in the south China Sea. *J. Geophys. Res. Oceans* 109, C10005. doi: 10.1029/2004jc002365

Pan, X. J., Wong, G. T. F., Shiah, F. K., and Ho, T. Y. (2012). Enhancement of biological productivity by internal waves: observations in the summertime in the northern south China Sea. *J. Oceanogr.* 68 (3), 427–437. doi: 10.1007/s10872-012-0107-y

Raateoja, M., Seppälä, J., and Ylöstalo, P. (2004). Fast repetition rate fluorometry is not applicable to studies of filamentous cyanobacteria from the Baltic Sea. *Limnology Oceanography* 4(4), 1006–1012. doi: 10.4319/lo.2004.49.4.1006

R Development Core Team (2016). *R: a language and environment for statistical computing* (Vienna, Austria: R Foundation for Statistical Computing). Available at: http://cran.R-project.Org.

Schlitzer, R. (2019) *Data analysis and visualization with ocean data view*. Available at: https://odv.awi.de.

Schrader, P. S., Milligan, A. J., and Behrenfeld, M. J. (2011). Surplus photosynthetic antennae complexes underlie diagnostics of iron limitation in a cyanobacterium. *PloS One* 6 (4), e18753. doi: 10.1371/journal.pone.0018753

Schuback, N., and Tortell, P. D. (2019). Diurnal regulation of photosynthetic light absorption, electron transport and carbon fixation in two contrasting oceanic environments. *Biogeosciences* 16 (7), 1381–1399. doi: 10.5194/bg-16-1381-2019

Six, C., Finkel, Z. V., Irwin, A. J., and Campbell, D. A. (2007). Light variability illuminates niche-partitioning among marine picocyanobacteria. *PloS One* 2, e1341. doi: 10.1371/journal.pone.0001341

Suggett, D. J., Moore, C. M., Hickman, A. E., and Geider, R. J. (2009). Interpretation of fast repetition rate (FRR) fluorescence: Signatures of phytoplankton community structure versus physiological state. *Mar. Ecol. Prog. Ser.* 376, 1–19. doi: 10.3354/meps07830

Ting, C. S., Rocap, G., King, J., and Chisholm, S. W. (2002). Cyanobacterial photosynthesis in the oceans: The origins and significance of divergent light-harvesting strategies. *Trends Microbiol.* 10, 134–142. doi: 10.1016/S0966-842X(02)02319-3

Wang, L., Huang, B. Q., Chiang, K. P., Liu, X., Chen, B. Z., Xie, Y. Y., et al. (2016). Physical-biological coupling in the Western south China Sea: The response of phytoplankton community to a mesoscale cyclonic eddy. *PloS One* 11 (4), e0153735. doi: 10.1371/journal.pone.0153735

Wang, L., Huang, B. Q., Laws, E. A., Zhou, K. B., Liu, X., Xie, Y. Y., et al. (2018). Anticyclonic eddy edge effects on phytoplankton communities and particle export in the northern south China Sea. *J. Geophys. Res. Oceans* 123, 7632–7650. doi: 10.1029/2017jc013623

Wang, L., Huang, B., Liu, X., and Xiao, W. (2015). The modification and optimizing of the CHEMTAX running in the south China Sea. *Acta Oceanol. Sin.* 34, 124–131. doi: 10.1007/s13131-015-0621-z

Wei, Y., Chen, Z., Guo, C., Zhong, Q., Wu, C., and Sun, J. (2020). Physiological and ecological responses of photosynthetic processes to oceanic properties and phytoplankton communities in the oligotrophic Western pacific ocean. *Front. Microbiol.* 11, 1774. doi: 10.3389/fmicb.2020.01774

Wen, Z., Browning, T. J., Cai, Y., Dai, R., Zhang, R., Du, C., et al. (2022). Nutrient regulation of biological nitrogen fixation across the tropical western north pacific. *Sci. Adv.* 8, eabl7564. doi: 10.1126/sciadv.abl7564

Wu, J., Chung, S.-W., Wen, L.-S., Liu, K.-K., Chen, Y.-L. L., Chen, H.-Y., et al. (2003). Dissolved inorganic phosphorus, dissolved iron, and *Trichodesmiumin* the oligotrophic south China Sea. *Global Biogeochem. Cycles* 17, 8-1–8-10. doi: 10.1029/2002gb001924

Xiao, W., Wang, L., Laws, E., Xie, Y., Chen, J., Liu, X., et al. (2018). Realized niches explain spatial gradients in seasonal abundance of phytoplankton groups in the south China Sea. *Prog. Oceanogr.* 162, 223–239. doi: 10.1016/j.pocean.2018.03.008

Xie, Y., Laws, E. A., Yang, L., and Huang, B. (2018). Diel patterns of variable fluorescence and carbon fixation of picocyanobacteria prochlorococcus-dominated phytoplankton in the south China Sea basin. *Front. Microbiol.* 9. doi: 10.3389/fmicb.2018.01589

Xiu, P., and Chai, F. (2011). Modeled biogeochemical responses to mesoscale eddies in the south China Sea. *J. Geophys. Res.* 116 (C10). doi: 10.1029/2010JC006800

Xiu, P., Chai, F., Shi, L., Xue, H., and Chao, Y. (2010). A census of eddy activities in the south China Sea during 1993–2007. *J. Geophys. Res.* 115, C03012. doi: 10.1029/2009jc005657

Xu, G., Liu, J., Song, X., Tan, M., Ren, H., Li, D., et al. (2020). Diel rhythm in photosynthetic performance of phytoplankton assemblages is predicted to be light-dependent from *in situ* and mesocosm chlorophyll fluorescence. *J. Coast. Res.* 104 (SI), 445–454. doi: 10.2112/JCR-SI104-080.1

Zhang, M., Wu, Y., Wang, F., Xu, D., Liu, S., and Zhou, M. (2020). Hotspot of organic carbon export driven by mesoscale eddies in the slope region of the northern south China Sea. *Front. Mar. Sci.* 7. doi: 10.3389/fmars.2020.00444

Zhao, Z. X., Klemas, V., Zheng, Q. N., and Yan, X. H. (2004). Remote sensing evidence for baroclinic tide origin of internal solitary waves in the northeastern south China Sea. *Geophys. Res. Lett.* 31 (6), L06302. doi: 10.1029/2003gl019077

Zhu, Y., Feng, Y., Browning, T. J., Wen, Z., Hughes, D. J., Hao, Q., et al. (2022). Exploring variability of trichodesmium photophysiology using multi-excitation wavelength fast repetition rate fluorometry. *Front. Microbiol.* 13, 813573. doi: 10.3389/fmicb.2022.813573

frontiers | Frontiers in Marine Science

TYPE Original Research
PUBLISHED 19 October 2022
DOI 10.3389/fmars.2022.1023953

OPEN ACCESS

EDITED BY
Guangzhe Jin,
Guangdong Ocean University, China

REVIEWED BY
Xilin Xiao,
Xiamen University, China
Liyin Qu,
Wenzhou University, China

*CORRESPONDENCE
Yao Guan
guanyao@4io.org.cn

SPECIALTY SECTION
This article was submitted to Marine Biogeochemistry, a section of the journal Frontiers in Marine Science

RECEIVED 20 August 2022
ACCEPTED 26 September 2022
PUBLISHED 19 October 2022

CITATION
Zhu Z, Wei H, Guan Y, Zhang L, Jia R, Sun P, Yang Y, Zhang Z and Zhang Q (2022) Distribution, spectral characteristics, and seasonal variation of dissolved organic matter in the northern Beibu Gulf, South China Sea. *Front. Mar. Sci.* 9:1023953. doi: 10.3389/fmars.2022.1023953

Distribution, spectral characteristics, and seasonal variation of dissolved organic matter in the northern Beibu Gulf, South China Sea

Zuhao Zhu[1,2], Huihua Wei[1], Yao Guan[1,2]*, Li Zhang[1,2], Renming Jia[1,2], Pengfei Sun[1,2], Yang Yang[1,2], Zhen Zhang[1,2] and Qiufeng Zhang[2]

[1]Guangxi Key Laboratory of Beibu Gulf Marine Resources, Environment and Sustainable Development, Fourth Institute of Oceanography, Ministry of Natural Resources, Beihai, China, [2]Key Laboratory of Tropical Marine Ecosystem and Bioresource, Fourth Institute of Oceanography, Ministry of Natural Resources, Beihai, China

Dissolved organic matter (DOM) in the land–ocean interface plays a critical role in the global carbon cycle, yet its dynamic is not well understood. Dissolved organic carbon (DOC) in the northern Beibu Gulf was measured seasonally from April 2020 to January 2021. Chromophoric and fluorescent DOM (CDOM and FDOM) were synchronously characterized by absorption and fluorescence spectroscopy. Three fluorescent components were identified from 597 samples using parallel factor analysis, including two humic-like and one protein-like component. DOC displays a significant seasonality with the average level being highest in summer (177 μmol/L) and lowest in winter (107 μmol/L). CDOM and FDOM levels in summer are also higher than those in winter. Although the variation ranges of DOC, CDOM, and FDOM in surface water are generally greater than in bottom water, the difference between the two layers is statistically insignificant. River discharge and anthropogenic input are important external sources of DOM in the low-salinity nearshore waters (i.e., estuaries and coast), whereas DOM in offshore waters is mainly produced by *in situ* biological activity. The mixing behavior of DOM in the northern Beibu Gulf varies spatially but minimally on a seasonal scale. Two distinct conservative mixing behaviors of DOC, CDOM, and humic-like FDOM occur in the nearshore waters from Tieshangang Bay and excluding Tieshangang Bay, respectively. The removal of protein-like FDOM along the salinity gradient and the negative correlation between protein-like FDOM intensity and apparent oxygen utilization are pronounced in the nearshore waters excluding Tieshangang Bay, jointly indicating that oxygen is consumed by microbial communities. In contrast, a net addition of DOC occurs in the high-salinity offshore waters, whereas the CDOM and humic-like FDOM undergoes quasi-conservative mixing. Overall, this study reveals notable spatial and seasonal variations in the concentration, source, and mixing of DOM at the

land–ocean interface and highlights the importance of sources and processes in shaping the amount and composition of DOM exported to the ocean margin.

KEYWORDS

northern Beibu Gulf, dissolved organic carbon, chromophoric dissolved organic matter, fluorescent dissolved organic matter, parafac, seasonality

Introduction

Marine dissolved organic matter (DOM) at 662 ± 32 petagrams of carbon (Pg C) is one of Earth's major, reduced, and exchangeable carbon reservoirs, comparable to atmospheric CO_2 storage (Hedges et al., 1997; Hansell et al., 2009). DOM consists of a heterogeneous mixture of organic molecules originating from a wide variety of sources, such as autochthonous biological production and allochthonous input (Hansell, 2013). The export of riverine DOM from land to the ocean is a crucial pathway of reduced carbon to coastal environments (Raymond and Spencer, 2015). The allochthonous DOM can undergo a variety of biogeochemical reactions in estuaries and coastal sea that ultimately determines both the concentration of dissolved organic carbon (DOC) and the composition of DOM reaching the ocean (Raymond and Spencer, 2015). Unsurprisingly, the behavior of terrestrial DOM during estuarine and coastal mixing varies significantly. The nonconservative mixing of DOM occurs in numerous estuaries and coastal regions because of additions, such as anthropogenic pollution, phytoplankton production, and desorption from sediments (Chen and Gardner, 2004; Spencer et al., 2007; Guo et al., 2014), and removals including flocculation, adsorption onto suspended sediments, and microbial and photochemical degradation (Shank et al., 2005; Yang et al., 2013a). Moreover, the export flux, composition, and fate of riverine DOM are dramatically affected by intensified human activities (Guo et al., 2014), the discharge of organic by-products (Levshina, 2008), dam construction (Zhang et al., 2014), and global climate change (Tian et al., 2013), which significantly impact coastal carbon cycling (Liu et al., 2020).

In addition to bulk DOC, measurements of chromophoric DOM (CDOM) and fluorescent DOM (FDOM) are widely reported from inland watersheds to the deep ocean (Massicotte et al., 2017; Wang et al., 2021a; Wang et al., 2021b; Qu et al., 2022). CDOM absorption coefficients at different wavelengths (e.g., 254, 280, 325, 350, 355, and 443 nm), and fluorescence intensities at specific excitation/emission wavelength pairs are commonly used as good indicators of DOM level (Coble, 1996; Guo et al., 2007; Yang et al., 2013b; Wang et al., 2017; Wang et al., 2021a; Wang et al., 2021b). The qualitative parameters, such as the spectral slope (e.g., $S_{275-295}$), carbon-normalized absorbance (e.g., $SUVA_{254}$), fluorescence index (FI), humification index (HIX), and biological index (BIX), are good proxies for the molecular weight, humification degree, DOM freshness in natural aquatic environments, and its associated photochemical and biological processes (Zsolnay et al., 1999; Weishaar et al., 2003; Cory and Mcknight, 2005; Helms et al., 2008; Huguet et al., 2009). Specifically, FDOM excitation-emission matrices (EEMs) coupled with parallel factor (PARAFAC) analysis are used to characterize the natural DOM in numerous estuaries and coastal gulfs around the world, such as the Yangtze River estuary (Guo et al., 2014), Pearl River estuary (Li et al., 2019), Jiulong River estuary (Guo et al., 2011), Taiwan estuaries (Yang et al., 2013b), Gulf of Mexico (Yamashita et al., 2015), and Gulf of Alaska (Dainard and Guéguen, 2013). The humic-like components tend to be resistant to microbial use but are sensitive to solar radiation (Rochelle-Newall and Fisher, 2002; Helms et al., 2013), whereas the protein-like components are rapidly consumed by microorganisms (Xiao et al., 2021). Thus, bulk DOC combined with its specific optical properties can provide valuable information regarding the quantity, quality, and biogeochemical reactivity of DOM in natural aquatic environments.

Estuaries and coastal gulf waters comprise some of the most biologically productive yet anthropogenically stressed ecosystems from inland watersheds to the global ocean continuum. Besides the *in situ* production of DOM, terrestrial inputs of nutrients and organic carbon are important components driving estuarine and coastal biogeochemical cycling and have implications ranging from degraded ecosystem health to food web perturbations (Beusen et al., 2016). The Beibu Gulf, in the northwestern South China Sea, is located near the rapidly urbanizing and industrializing Beibu Gulf urban cluster. It is a tropical gulf and receives large freshwater discharge with marked seasonal fluctuation and a huge amount of industrial and domestic sewage (See *Study area*). Biogeochemical studies of the Beibu Gulf have thus far mainly focused on nutrient distribution (Kaiser et al., 2014; Lai et al., 2014; Lao et al., 2021a), heavy metals, and organic pollutants (Meng et al., 2013; Zhu and Zheng, 2013; Yang et al., 2015a; Lao et al., 2019; Lao et al., 2021b; Lao et al., 2022; Zhu et al., 2022a, b) and the associated ecological responses (Xu et al., 2019; Li et al., 2020). The results show that these materials are concentrated in

the coastal areas of the Beibu Gulf, suggesting a significant impact of river runoff discharge and human activity on the Beibu Gulf. Nevertheless, the distribution of DOC, CDOM, and FDOM and their seasonality in the Beibu Gulf has not been studied. It greatly limits our understanding of the carbon cycling and ecological effect of a human-influenced coastal gulf in a changing climate background.

For this study, water samples were collected at a high spatial resolution over the four seasons from April 2020 to January 2021 in the northern Beibu Gulf. Our major goals were to (1) provide the first baseline data set on DOC concentrations, CDOM, and EEMs-PARAFAC-derived FDOM parameters in the northern Beibu Gulf; (2) evaluate the sources and mixing behaviors of DOC, CDOM, and FDOM in the northern Beibu Gulf; and (3) reveal the seasonal variabilities of DOM dynamics in the northern Beibu Gulf. The results of this study further increase our understanding of DOM cycling in human-impacted estuarine and coastal waters.

Materials and methods

Study area

The Beibu Gulf is a shallow, semi-enclosed gulf located in the northwestern South China Sea and has an average depth of about 40 m and a total area of about 128,000 km^2. Southwesterly winds prevail in summer, and northeasterly winds in winter are influenced by the East Asian monsoon (Chen et al., 2011). The circulation pattern of the Beibu Gulf is mainly controlled by the East Asian monsoon with cyclonical circulation in winter, causing water accumulation near the western coast of the gulf. The westward water transport from the Qiongzhou Strait could influence the most northern part of the gulf in winter. In contrast, water from the coastal area tends to move offshore and undergoes strong mixing in the center of the gulf in summer (Wang et al., 2018). Several rivers flow into the northern coastal area of the Beibu Gulf, including the Nanliu, Dafeng, Qin, Maoling, and Fangcheng Rivers. The total river runoff discharge is up to 3.3 $\times 10^{11}$ m^3 yr^{-1}, and more than 80% of the water discharge occurs in the wet season (April to October) (Lai et al., 2014). Consequently, the water in the northern Beibu Gulf falls into two categories: diluted and mixed water. The diluted water is found along the northern coast of the Beibu Gulf, and the mixed water mainly occupies the northern Beibu Gulf (Chen et al., 2011). The Beibu Gulf is also an important fishing ground and aquaculture base in China because of its year-round warm temperatures and rich nutrients. Additionally, the northern coastal area hosts numerous developing ports and cities (Beihai, Qinzhou, Fangcheng; see Figure 1). The intensive human activity in this area has led to a high loading of nutrients (Lao et al., 2020), metals (Lao et al., 2019), and organic pollutants (Lao et al., 2021a) in the Beibu Gulf, which has a dramatical impact on the biogeochemistry and ecology of the gulf.

Sample collection and pretreatment

The sampling area covered the northern Beibu Gulf, stretching from the upper estuaries and bays to near the center of the gulf with a total of 127 stations (Figure 1). The labels and coordinates of the stations alongside other sampling information are given in the Supplementary Material. Water temperature and salinity were recorded by using a calibrated SBE 911 plus conductivity–temperature–depth profiler. Water samples were collected from the surface (approximately 1 m deep) and near the bottom (approximately 1 m above the seabed) using a 5 L Niskin sampler in April–May 2020 (spring), July–August 2020 (summer), October–November 2020 (autumn), and December 2020–January 2021 (winter). The samples were analyzed for dissolved oxygen (DO), DOC, CDOM, and FDOM. At 10% of the sampling stations, samples were collected in duplicate to ensure sampling and data reliability. The relative deviations of oxygen, DOC, CDOM, and FDOM for all duplicate samples were <2%. Samples for DO analysis were preferentially collected and measured on board by using the Winkler titration method (Carpenter, 1965). Apparent oxygen utilization (AOU) was calculated as the difference between the oxygen saturation concentration and measured DO concentration using algorithms from Ocean Data View (version 5.2.0). Samples for DOC, CDOM, and FDOM analyses were filtered immediately through precombusted (500°C, 5 h) GF/F filters (nominal pore size ≈0.7 μm) into precombusted amber glass vials with Teflon-lined screw caps under a gentle vacuum of <150 mm Hg (Wang et al., 2017). DOC samples were acidified to pH ≈ 2 with H_3PO_4 (85%, Merck) and stored frozen until analysis. CDOM and FDOM samples were stored in the dark at 4°C until analysis, which was done within 1 week of collection.

Analysis of DOC concentrations

DOC concentration for each sample was determined in triplicate by using an Elementar Vario TOC cube (Germany) in high-temperature catalytic oxidation mode with coefficients of variance of <2% (Wang et al., 2021b). A five-point standard curve was generated by using potassium hydrogen phthalate standards daily. The running blank was determined as the average of the peak area of the Milli-Q water acidified with H_3PO_4. DOC concentrations were obtained by subtracting the running blank from the average peak area of the samples and dividing by the slope of the standard curve. The analytical precision of the DOC analysis was <3% based on DOC consensus reference material provided by the Hansell Lab from the University of Miami, USA.

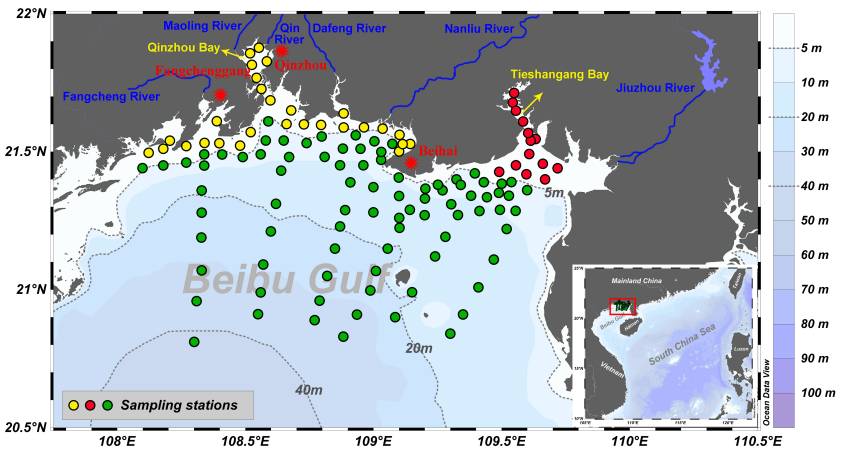

FIGURE 1
Map of the northern Beibu Gulf showing its topography (color background) and the locations of the sampling stations (green dots) in spring (April–May 2020), summer (July–August 2020), autumn (October–November 2020), and winter (December 2020 to January 2021). The blue lines and labels represent major rivers that flow into the northern Beibu Gulf, and the red stars represent cities. Sampling stations were divided into three regions: Region I (nearshore stations with a bottom depth of < 5 m excluding Tieshangang Bay, yellow circles), Region II (Tieshangang Bay, red circles), and Region III (offshore stations with a bottom depth of > 5 m, green circles).

Measurements of CDOM and FDOM and data processing

The CDOM absorbance spectra were measured by using a Shimadzu UV-1780 dual-beam spectrophotometer and 10 cm quartz cuvettes at room temperature. Absorbance A_λ was obtained from 240 and 800 nm at 0.5 nm intervals. The Milli-Q water was used for baseline correction and all absorbance spectra were corrected for baseline offsets by subtracting the average absorbance between 690 and 700 nm (Guo et al., 2007). A Napierian absorption coefficient a_λ (m^{-1}) was calculated as 2.303 times the absorbance A_λ divided by the light path length L of the cell in meters (0.1 m) to quantify CDOM concentration. Absorption coefficients at the wavelengths 254, 280, 300, 325, 350, 355, and 412 nm are widely reported from watershed to the open ocean continuum (Massicotte et al., 2017). The spectral slope between 275 and 295 nm ($S_{275-295}$, nm^{-1}) was calculated based on a linear fit of the log-transformed absorption coefficient, which is a good proxy of the relative molecular weight of the DOM (Helms et al., 2008). Specific ultraviolet absorbance at 254 nm ($SUVA_{254}$, mg C L^{-1}) was calculated to indicate the aromaticity of the DOM by dividing the decadal absorption coefficient [i.e., $A(\lambda)/L$] by the concentration of DOC (Weishaar et al., 2003).

Fluorescence EEMs were acquired by using a Hitachi F-7100 spectrofluorometer with a 1-cm quartz cuvette at room temperature. The excitation (Ex) wavelengths spanned from 240 to 450 nm in 5-nm increments, and the emission (Em) wavelengths spanned from 280 to 600 nm in 2-nm increments. Excitation and emission slit widths were set to 10 and 5 nm, respectively. Raman scattering was compensated for by subtracting Milli-Q water EEMs that were scanned on the same day as the samples. The spectral fluorescence intensities presented in arbitrary units were then normalized to Raman units (RU) following the procedure of Lawaetz and Stedmon (2009). The normalized EEMs were calibrated for potential inner filter effects by using an absorbance-based approach (Kothawala et al., 2013). The HIX and BIX were calculated from the EEMs (Zsolnay et al., 1999; Huguet et al., 2009). The HIX, which is the ratio of fluorescence signals over the emission range 435–480 nm to those over the range of 300–345 nm with excitation at 254 nm, is an indicator of the extent of humification (Zsolnay et al., 1999). The BIX is a surrogate for the autochthonous FDOM and is the ratio of emission intensity at 380 nm to that at 430 nm upon excitation at 310 nm (Huguet et al., 2009).

A PARAFAC analysis was conducted on a total of 597 normalized and calibrated EEMs using the DOMFluor toolbox in MathWorks® MATLAB (R2020b) (Stedmon and Bro, 2008; Murphy et al., 2013; Wang et al., 2017). The models were constrained to nonnegative values. The number of PARAFAC components was determined based on split-half validation. The fluorescence intensity of each component was expressed as F_{max} in RU (Stedmon and Bro, 2008). Based on the analysis of duplicate samples, the uncertainty of F_{max} for each modeled component was <2%. The PARAFAC result was compared with known PARAFAC components taken from the online OpenFluor data set (https://openfluor.lablicate.com/, last access: August 8, 2022) to enhance the robustness of and confidence in the PARAFAC model (Murphy et al., 2014).

Statistical analyses

The significance of DOM comparisons between surface- and bottom-water samples was tested by using Student's *t*-test (two-tailed, $\alpha = 0.05$) in IBM SPSS Statistics 23. A one-way analysis of variance test was conducted to determine the differences in the mean values of the respective parameters at the sampling stations in the different seasons. Correlations between DOM variables were assessed based on Pearson's correlation coefficient *r*, and the significant level *p* was determined by applying a two-sided test.

Results

Hydrological and environmental backgrounds

As shown by the potential temperature-salinity (θ-*S*) diagram in Figure 2 and by the spatial distributions of θ (Figures 3A–H) and salinity (Figures 3I–P), the hydrographic properties of waters differ distinctively over the four seasons. The θ in the northern Beibu Gulf varies from 20.8 to 31.6, 25.9 to 33.7, 17.2 to 25.5, and 12.7 to 22.2°C in spring, summer, autumn, and winter, respectively (Figure 2). The θ of surface waters is almost homogeneous in summer but develops greater spatial differences over the other three seasons (Figures 3A–D). In spring and winter, surface water in the northern Tieshangang Bay, Naliu estuary, and Qinzhou Bay has low θ, which also occurs near the Fangchenggang and eastern coasts of the sampling area. The θ of bottom waters varies over smaller spatial scales but otherwise follows a spatial pattern similar to that of the surface water (Figures 3E–H). The salinity varies over the minimal range of 21.0–32.1 in winter, 10.0–31.8 in autumn, 4.1–34.2 in spring, and 2.2–32.4 in summer (Figure 2). Qinzhou Bay has the lowest salinity surface water over the four seasons, followed by the Nanliu–Dafeng estuary and then Tieshan Bay. High surface salinity is measured in the southwest of the study area in spring and autumn and in the southeast in summer (Figures 3I–L). The low-salinity river plumes are much weaker in bottom water but the spatial distribution of salinity in the bottom water is similar to that of the surface water (Figures 3M–P).

DO concentrations range from 3.5 to 8.7, 5.0 to 7.3, 4.0 to 7.7, and 6.5 to 10.3 mg/L in surface water in spring, summer, autumn, and winter, respectively (Figures 3Q–T). In spring, DO concentrations of surface waters are lower in Tieshangang Bay, Qinzhou Bay, and offshore regions but are higher in the coastal stations near Tieshangang Bay and the cities of Beihai and Fangchenggang (Figure 3Q). However, the distribution characteristics of the DO concentration in surface water in summer are generally opposite those in spring (Figure 3R). In autumn, low surface DO concentrations occur in Tieshangang Bay, Naliu estuary, and Qinzhou Bay, whereas surface water at other sampling stations has either high or comparable DO concentrations (Figure 3S). The DO concentration of surface water generally decreases in going from nearshore to offshore in winter (Figure 3T). The variation ranges and spatial patterns of DO concentrations in bottom waters are very similar to those in spring, autumn, and winter, whereas DO concentrations of bottom water in summer are much less (3.4–6.7 mg/L) and follow completely different spatial distribution patterns than surface-water DO concentrations (Figures 3R,V). AOU in this study is greater than zero (18.5 ± 22.4 μmol/kg), suggesting that oxygen consumption occurs both in the surface and bottom waters over the four seasons. The AOU is greater in bottom water (22.5 ± 22.2 μmol/kg) than in surface water (15.0 ± 23.7 μmol/kg) and follows a pattern that is roughly opposite that of the DO. Notably, AOU reaches up to about 90 μmol/kg in some bottom waters in spring and summer (southwest of the study region) and in the surface water in autumn (Tieshangang Bay).

Distributions of DOC and CDOM

Figure 4 depicts the spatial (surface vs. bottom) and seasonal distributions of DOC concentration and CDOM variables. The DOC concentration of surface water over four seasons varies largely within the range 59.1–509 μmol/L (spring), 95.6–616 μmol/L (summer), 73.2–512 μmol/L (autumn), and 70.8–292 μmol/L (winter) (Figures 4A–D). In comparison, the bottom DOC concentration varies over a smaller range of 69.7–300 μmol/L in spring, 83.3–347.6 μmol/L in summer, 72–540 μmol/L in autumn, and 60.2–414 μmol/L in winter (Figures 4E–H). In terms of spatial distribution, the DOC concentration in spring, autumn, and winter generally follows a similar pattern in both the surface and bottom layers, that is, high DOC concentrations in estuaries and coastal water and low DOC concentrations in offshore water (Figures 4A, B, D–F, H). The horizontal distribution of DOC concentrations in autumn differs slightly with the highest concentrations in coastal water near Beihai and Fangchenggang but moderate concentrations in the Nanliu–Dafeng estuary, Qinzhou Bay, and Tieshan Bay in the surface layers (Figure 4C) and speckled features in the bottom layers (Figure 4G).

Strong positive correlations ($p < .001$, $n = 590$, $r = 0.83–0.99$) occur among CDOM absorption coefficients at the seven selected wavelengths (254, 280, 300, 325, 350, 355, and 412 nm). Thus, for simplicity, we choose the absorption coefficient a_{350} at 350 nm as the indicator of CDOM abundance, and the CDOM absorption coefficients at the other six wavelengths are presented in the Supplementary Material. The coefficient a_{350} is maximal in estuaries and coastal waters and generally decreases with increasing offshore distance over the four seasons

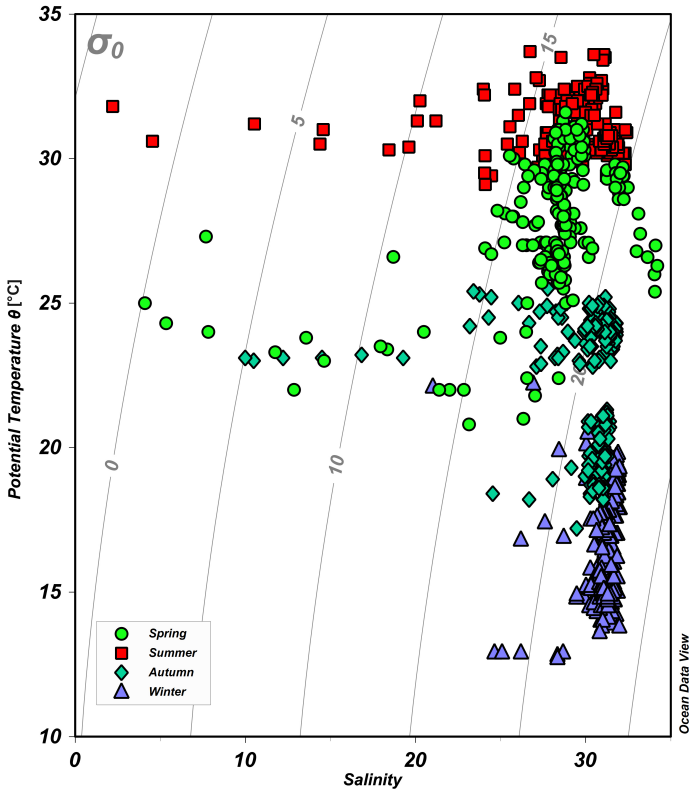

FIGURE 2
Potential temperature versus salinity plot (θ-S diagram) for the sampling stations on the northern Beibu Gulf. Green circles, red squares, cyan diamonds, and purple triangles denote spring, summer, autumn, and winter, respectively. The gray lines indicate the isopycnals (σ_0). The plot was created by using Ocean Data View (https://odv.awi.de).

(Figures 4I–P). For summer and winter, when CDOM data are available at almost all stations, a_{350} in surface waters varies from 0.28 to 4.0 m^{-1} in summer and from 0.33 to 1.6 m^{-1} in winter (Figures 4J, L), and a_{350} in bottom water varies over a smaller range of 0.31–1.5 m^{-1} in summer and 0.34–1.1 m^{-1} in winter (Figures 4N, P). The coefficient a_{350} varies over the range 0.31–4.6 m^{-1} in all water (excluding the offshore water without data in spring) and over the range 0.29–0.85 m^{-1} [excluding the estuarine and coastal waters without data in autumn; see Figures 4I, K.

The spatial pattern of the spectral slope $S_{275-295}$ contrasts with that of a_{350} (Figures 4Q–X), with a range of variation of 0.0161–0.0253 nm^{-1} in surface water (Figures 4Q–T). The spectral slope $S_{275-295}$ in bottom water varies over a range of 0.0170–0.0247 nm^{-1}, which is comparable to that in surface water (Figures 4U–X). The specific ultraviolet absorbance $SUVA_{254}$, with surface and bottom combined, varies over a large range of 0.26–3.87 m^2/g C. High $SUVA_{254}$ values occur in estuarine and coastal water for spring and summer and in almost the entire study area except for the coastal water near Beihai and Tieshangang Bay in winter (Figures 4Y–AF).

PARAFAC results and distribution of FDOM

Three distinct FDOM components are identified by using the EEM-PARAFAC approach (Figure 5) and are compared with FDOM components from the online OpenFluor data set based on the Tucker congruence coefficient (TCC) between different PARAFAC models (Murphy et al., 2014). Component 1 (C1) has two Ex maxima at ≤250 and 280 nm and one Em maximum at 390 nm. It resembles the humic-like C2 component of Murphy et al. (2011); Gueguen et al. (2015), and Yang et al. (2019) (TCC > 0.97). Its EEM contour covers Peak M areas (290–310/370–410 nm) and part of Peak A areas (260/400–460 nm) defined in Coble et al. (1998), which were previously recognized as a traditionally marine-derived humic-like fluorophore. Component 2 (C2, Ex/Em = 250, 345/440 nm) is highly similar to humic-like C1 in Jorgensen et al. (2011); Chen et al. (2017), and Amaral et al. (2021) (TCC > 0.98) and is close to the traditional terrestrial Peak A and Peak C (320–360/420–460 nm). Recently, two humic-like components have been found to be widely distributed in natural aquatic systems from inland

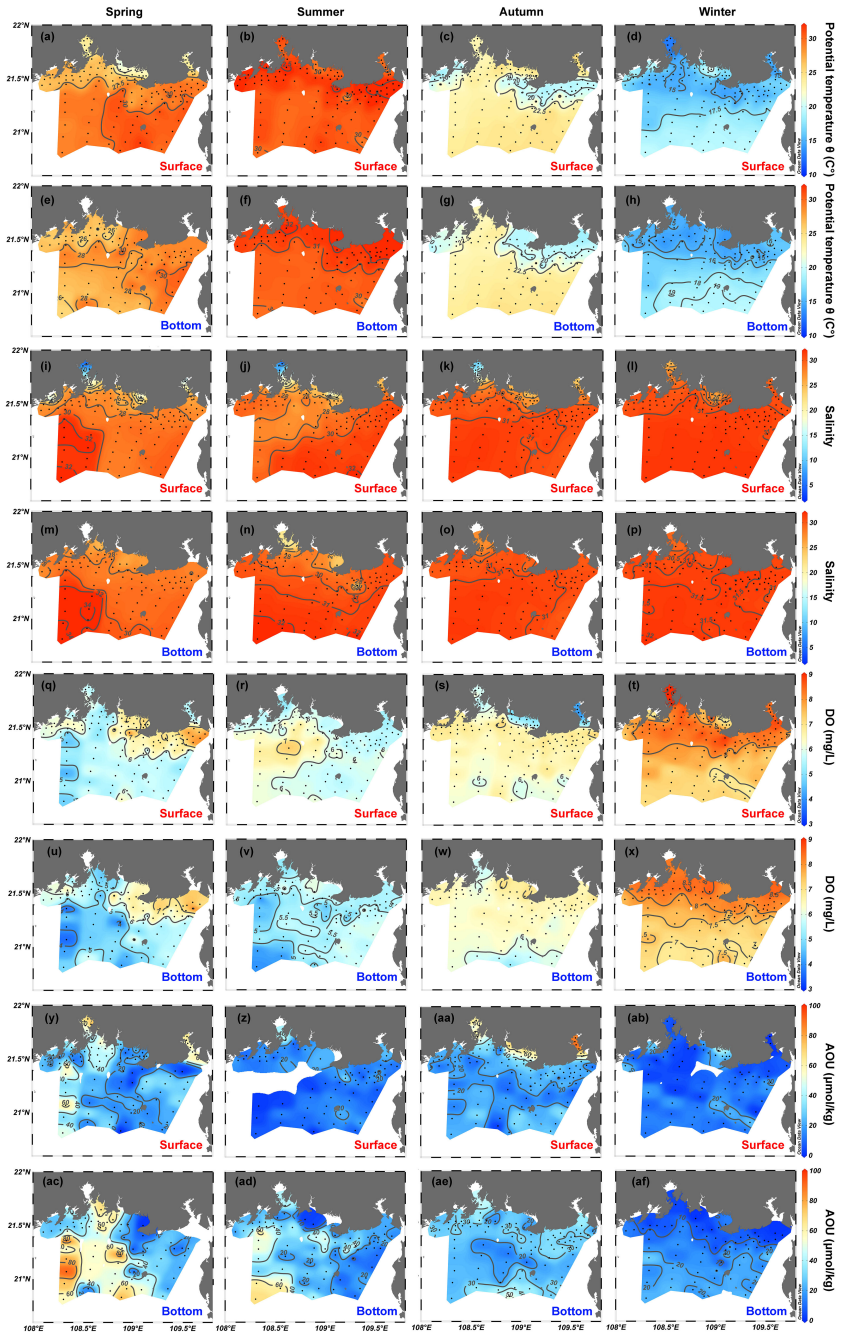

FIGURE 3
Spatial distributions of **(A–H)** potential temperature θ, **(I–P)** salinity, **(Q–X)** dissolved oxygen (DO) and **(Y–AF)** apparent oxygen utilization (AOU) in the surface and bottom layers of the northern Beibu Gulf in spring, summer, autumn, and winter. Surface layer is 1 m deep and is labeled by red text. Bottom layer extends about 1 m above the seafloor and is labeled by blue text. The plot was created by using Ocean Data View (https://odv.awi.de).

watersheds to open oceans and correlate strongly with microbial activities (Qu et al., 2022; Catalá et al., 2015). C3 has Ex/Em maxima at 275/318 nm and is attributed to a combination of the autochthonous tyrosine-like peak B (275/305 nm) and the tryptophan-like peak T (275/340 nm) (Coble, 2007). C3 is highly similar to C4 (TCC > 0.95) in Gao and Guéguen (2018), to C3 in Gueguen et al. (2015), and to C4 in Dainard et al. (2015).

The fluorescence intensities of two humic-like components (C1 and C2) correlate significantly ($r = 0.94$, $p < 0.001$, $n = 539$)

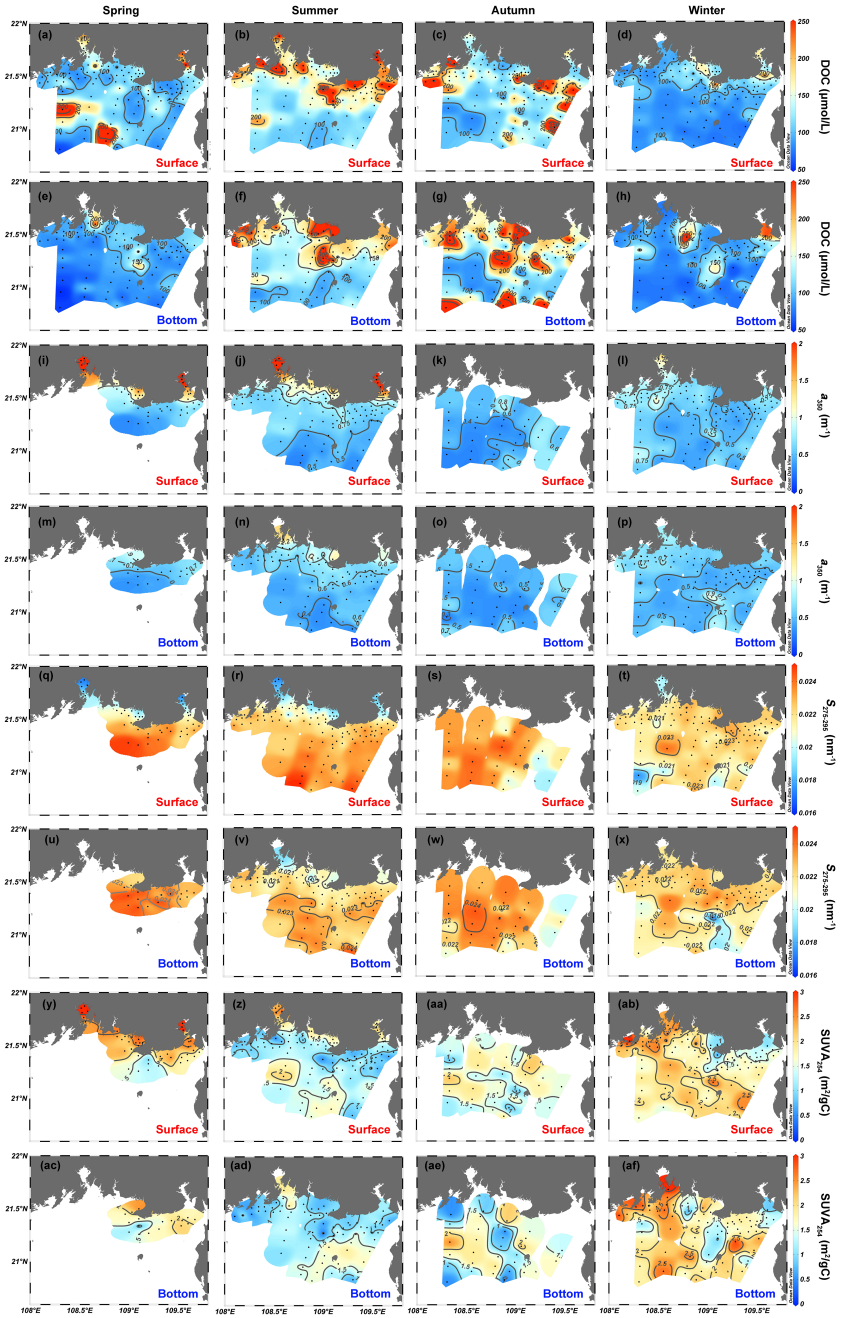

FIGURE 4
Spatial distributions of **(A–H)** DOC, **(I–P)** a_{350}, **(Q–X)** $S_{275-295}$, and **(Y–AF)** $SUVA_{254}$ in the northern Beibu Gulf in spring, summer, autumn, and winter. Surface layer is 1 m deep and labeled by red text. Bottom layer extends about 1 m above the seafloor and is labeled by blue text. The plot was created by using Ocean Data View (https://odv.awi.de).

and follow spatial distribution characteristics very similar to those of a_{350} (Figures 4I–P). The range of variation of C1 and C2 in surface waters over the four seasons is 0.023–0.32 and 0.009–0.18 RU, respectively, whereas C1 and C2 for bottom waters vary over smaller ranges of 0.03–0.19 RU (C1) and 0.008–0.10 RU (C2) (Figures 6A–H). The intensity of protein-like C3 ranges from 0.024 to 0.17 RU in surface waters and from 0.014 to 0.17 RU in bottom waters (Figures 6Q–X). Although weak correlations exist between the intensity of C3 and the two humic-like components (r = 0.25 for C3 vs. C1 and r = 0.33 for C3 vs. C2, p <.001, n = 539), the coefficients generally have spatial features like those of humic-like C1 and C2 both in

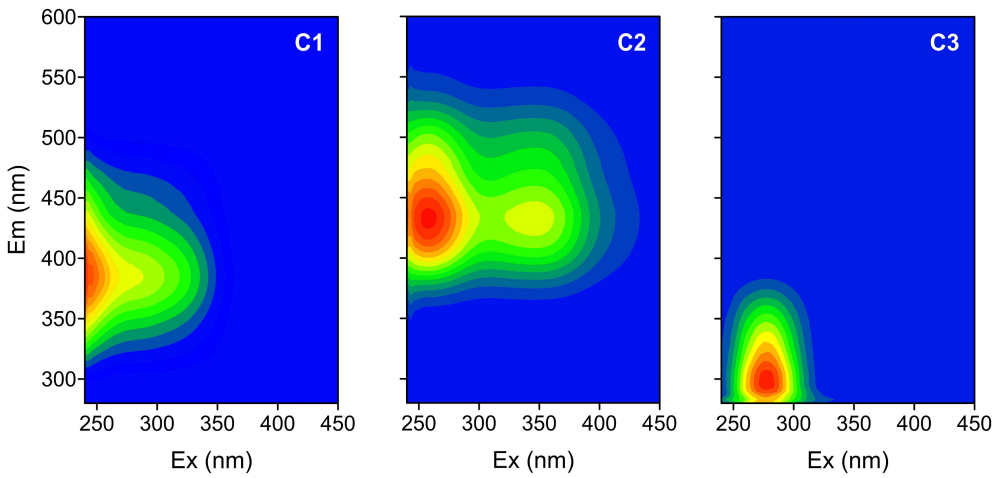

FIGURE 5
Excitation-emission contours of three components identified by PARAFAC model.

surface and bottom water (Figure 6). In all four seasons, high values of C3 have been measured in estuarine and coastal water near cities [e.g., Nanliu–Dafeng estuary, Beihai, Tieshangang Bay, and Qinzhou Bay; Figures 6Q–X).

Compared with the quantitative variables of FDOM, the EEM-derived qualitative metrics (i.e., the HIX and BIX) also reveal clear variations in the horizontal gradient from estuaries and coastal water to offshore water both at the surface and at the bottom (Figures 7A–P). The HIX ranges from 0.4 to 4.3 and from 0.3 to 3.1 in surface and bottom water, respectively. The HIX correlates positively with the intensities of C1 (r = 0.74, p <.001, n = 539) and C2 (r = 0.85, p <.001, n = 539) and shares similar spatial distribution patterns (Figures 7A–H). The BIX varies from 0.88 to 1.54 and 1.04 to 4.33 in surface and bottom water, respectively, and shows a moderate negative correlation with the HIX (r = −0.39, p <.001, n = 560). Except for extremely high values in Qinzhou Bay in winter, the BIX generally increases in going from estuaries and coastal waters to offshore water (Figures 7I–P). The FI is everywhere greater than 1.9 and varies over a small range in surface waters (2.17–2.79) and bottom waters (2.18–2.74). The FI does not correlate with other FDOM-derived variables (p >.05) and does not exhibit clear spatial gradients for any of the four seasons (Figures 7Q–X).

Relationships between DOC, CDOM, and FDOM

DOC linearly correlates with a_{350} in spring (r = 0.66, p <.001, n = 62), summer (r = 0.30, p <.001, n = 204), and autumn (r = 0.32, p <.001, n = 79) but does not correlate with a_{350} in winter (p >.05). The DOC has a moderate linear correlation with two humic-like components (C1 and C2) in spring (r = 0.63 and 0.68, p <.001, n = 59), very weak correlations with C1 and C2 in summer (r = 0.17 and 0.20, p <.001, n = 195) and winter (r = 0.21 and 0.26, p <.001, n = 59), and no correlation with C1 and C2 in autumn (p >.05). DOC correlates weakly with protein-like C3 in summer (r = 0.16, p <.001, n = 195) and winter (r = 0.29, p <.001, n = 206) but does not correlate with C3 in spring and autumn (p >.05). Separately, a_{350} correlates strongly with the intensities of humic-like C1 and C2 over the four seasons (p <.001) with high Pearson r values in spring (0.77 and 0.86), summer (0.94 and 0.95), and winter (0.74 and 0.74) and low r values in autumn (0.30 and 0.38). However, the significant correlations between a_{350} and C3 occur only in summer (r = 0.48, p <.001, n = 195) and winter (r = 0.31, p <.001, n = 206).

Discussion

Sources of DOM in northern Beibu Gulf

The θ-S plots and their spatial distribution patterns confirm that multiple water endmembers (≥3) coexist in the northern Beibu Gulf, and their seasonal differences are evident (Figures 2, 3A–Q). The levels of DOC, CDOM, and FDOM in the northern Beibu Gulf vary by more than one order of magnitude from the estuaries and coastal waters to offshore waters (Figures 4, 6), which further indicates the various sources and processes in shaping the distribution and composition of DOM. The weak or nonexistent correlations between DOC, CDOM, and FDOM suggest that these components are subjected to different sources and processes in the northern Beibu Gulf. For example, anthropogenic input could supply many labile compounds,

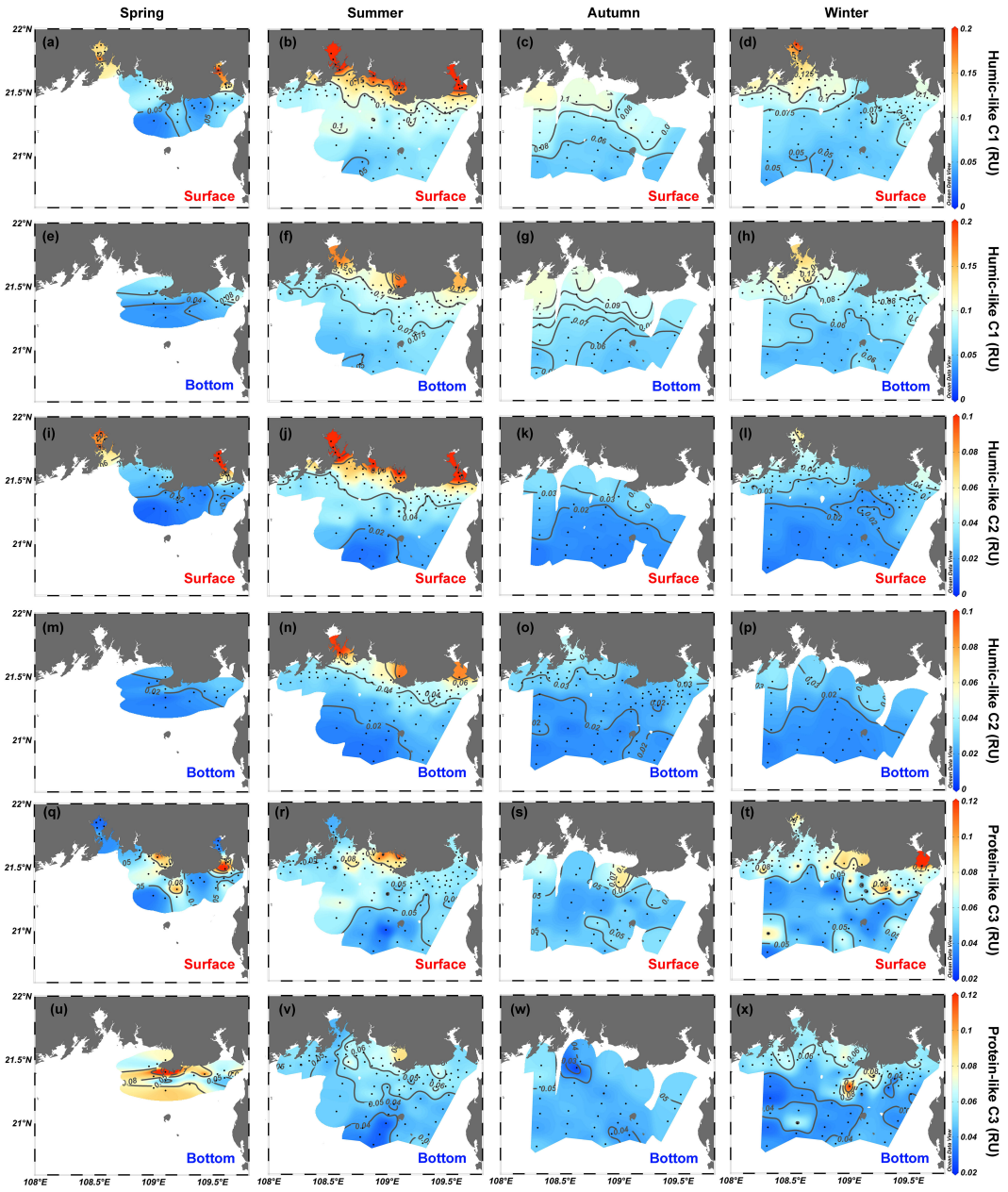

FIGURE 6
Spatial distributions of **(A–H)** humic-like C1 intensity, **(I–P)** humic-like C2 intensity, and **(Q–X)** protein-like C3 intensity in the northern Beibu Gulf in spring, summer, autumn, and winter. Surface layer is 1 m deep and is labeled by red text. Bottom layer extends about 1 m above the seafloor and is labeled by blue text. The plot was created using Ocean Data View (https://odv.awi.de).

such as DOC and protein-like FDOM but less refractory humic-like components (Guo et al., 2014). The *in situ* primary production and microbial activity cooperatively drive the transformation of DOM from a labile to refractory nature, resulting in the decoupling of relationships between DOC, CDOM, and FDOM (Wang et al., 2021a; Wang et al., 2021b).

Clearly, low-salinity waters (<20) are entrenched in Qinzhou Bay, the Nanliu–Dafeng estuary, and upper Tieshangang Bay and are most prominent in summer and spring, likely because of major river discharge in the wet season (April–October) (Lai et al., 2014). Correspondingly, the levels of DOC, CDOM, and humic-like FDOM are almost maximal in these three regions

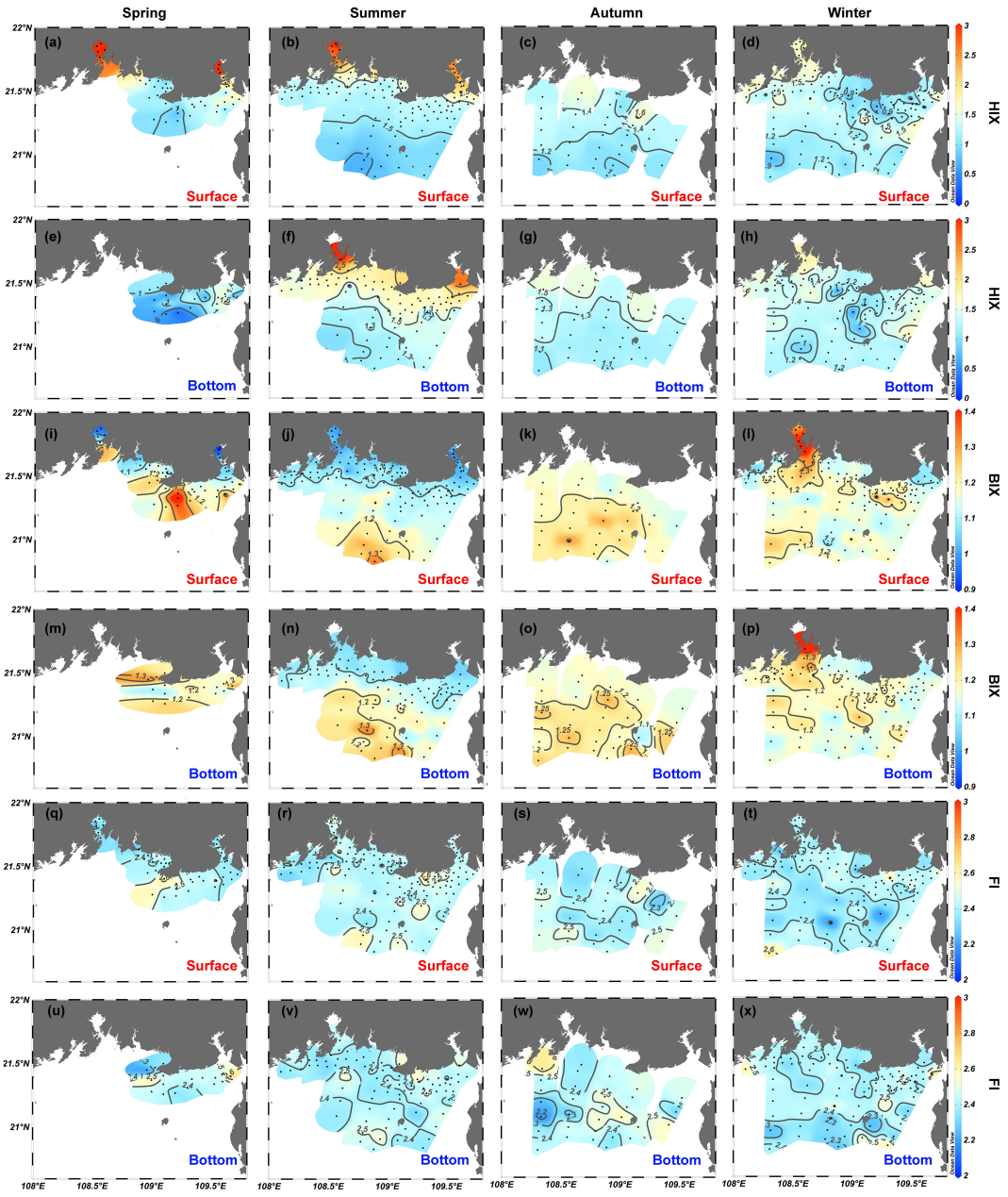

FIGURE 7
Spatial distributions of **(A–H)** humification index (HIX), **(I–P)** biological index (BIX), and **(Q–X)** fluorescence index (FI) in the northern Beibu Gulf in spring, summer, autumn, and winter. Surface layer is 1 m deep and is labeled by red text. Bottom layer extends about 1 m above the seafloor and is labeled by blue text. The plot was created by using Ocean Data View (https://odv.awi.de).

over two seasons (i.e., summer and spring), concurrent with low $S_{275–295}$ and BIX but high HIX and $SUVA_{254}$ (Figures 4, 7). This suggests that the terrigenous molecules with high molecular weight, humification degree, and aromaticity are very popular in DOM pools of the low-salinity regions over two seasons. By comparison with the reported DOC and CDOM data along the global aquatic continuum summarized by Massicotte et al. (2017), both DOC and a_{350} in the low-salinity estuarine and coastal water of the northern Beibu Gulf fall within the range of river–estuary–coastal ecosystems but are lower than those in the inland wetlands and lakes with high productivity. In addition, the riverine terrigenous CDOM and humic-like FDOM signals are limited to a smaller region near the upper estuaries during autumn and winter (Figures 4, 6), which is consistent with the

low water discharges of several rivers to the northern Beibu Gulf in the dry season (Lai et al., 2014). Annually, it differs from other coastal areas with large river runoff, such as that the Yangtze River (Guo et al., 2014), Pearl River (Li et al., 2019), and Amazon River (Nelson et al., 2010), where river discharge makes a remarkable contribution to coastal DOM pools. Even so, considering the characteristics that river-borne organic material degrades easily in the sea by photochemical transformation and biomineralization (Fichot and Benner, 2014), the turnover of riverine DOM might significantly impact the budget of the nutrients and carbon in the estuaries and coast of the northern Beibu Gulf, especially in spring and summer.

Except for the low-salinity Qinzhou Bay, Tieshanggang Bay, and Nanliu–Dafeng estuary, high salinity (>25) was measured at other sampling stations of the northern Beibu Gulf over the four seasons (Figures 3I–P). Although the levels of DOC, CDOM, and FDOM are much lower than those in the low-salinity estuarine and coastal water (Figures 4, 6), they are also significantly greater than those in the adjacent ocean-dominated surface of the South China Sea (Wu et al., 2015; Wang et al., 2017). $S_{275-295}$ in particular is a reliable proxy tracing terrestrial input and photochemical degradation of DOM in the marine environment (Stedmon and Markager, 2003; Helms et al., 2013). Here, $S_{275-295}$ values are less than 0.025 nm^{-1} at all high-salinity stations, which were comparable to the levels in rivers and estuaries dominated by terrestrial organic molecules (Stedmon et al., 2010) and the levels in the deep ocean where the DOM was fully reworked by microbial activities (Wang et al., 2017). However, they were far less than the value of > 0.04 nm^{-1} in photodegraded surface oceanic water (Catala et al., 2016; Wang et al., 2021b). Thus, we conclude that DOM in the high-salinity water of the northern Beibu Gulf is dominated by terrestrial input and microbial reworking. Cultural experiments confirm that both terrestrial and microbial-derived DOM with low $S_{275-295}$ can be easily degraded by light radiation (Helms et al., 2013; Yang et al., 2020). It can be expected that DOM in the high-salinity water of the northern Beibu Gulf also has a large potential for photodegradation, when it was transported into the upper stratified layer of the adjacent South China Sea (Chen et al., 2011). (Figures 4Q–X). Although no direct evidence links DOM and primary productivity, the relatively high chlorophyll concentration (average of 3.0 μg/L in the wet season and 1.5 μg/L in the dry season) measured in the same region (Lao et al., 2021b) supports the hypothesis that the *in situ* primary production and subsequent microbial transformation might be an important source of DOM (Wang et al., 2021b). The high FI (>1.9), high BIX, and low HIX over four seasons further confirm that humic-like FDOM in high-salinity waters of the northern Beibu Gulf is mainly sourced from recent microbial activities (Figure 7). A strong correlation between humic-like FDOM and a_{350} demonstrates that CDOM is subjected to sources and processes similar to those of humic-like FDOM in the northern Beibu Gulf. In contrast, weak or zero correlation between DOC, CDOM, and humic-like FDOM in this study also occurs in coastal and oceanic environments (Massicotte et al., 2017). The most likely explanation is that the kinetic processes (e.g., physical mixing, photochemical transformation, and microbial degradation) operate at different rates on DOC and optical fractions of the DOM pool, which as a result may cause the mentioned decoupling or nonlinear relationship between these pools (Stedmon and Nelson, 2015).

Notably, the high levels of protein-like C3 but low levels of humic-like components were apparent in the outer Tieshangang Bay during spring and winter and on the Beihai coast over four seasons (Figure 6), suggesting the obvious contribution of anthropogenic input and/or enhanced primary production (Guo et al., 2014). The sediment release may also have a considerable contribution to DOM pools in the northern Beibu Gulf as indicated by the elevated levels of DOC, CDOM, and FDOM in the bottom layer (Figures 4, 6) and high concentration of organic carbon in the surface sediment (Liao et al., 2018). The impact of submarine groundwater discharge and atmospheric deposition on the DOM pool in the northern Beibu Gulf has large variability owing to the lack of supporting data. In addition, water intrusions by currents from the adjacent South China Sea considerably affect the water volume of the reservoir and nutrients in the northern Beibu Gulf (Lao et al., 2022) as well as the DOM pool. Thus, these sources and processes should be considered in future research on the DOM budget in the Beibu Gulf.

Mixing of DOM in the northern Beibu Gulf

The mixing behavior based on the relationships between DOM variables and salinity has been used for decades to estimate the apparent removal or addition of DOM in land–ocean interfaces (Noureddin and Courtot, 1989; Guo et al., 2007; Yang et al., 2015b; Li et al., 2019). The hydrological cycle of the northern Beibu Gulf is complex (Figures 2, 3) and is influenced by multiple riverine and low-salinity water sources mixing with water from the adjacent South China Sea with the help of variable wind and circulation patterns (Chen et al., 2011; Wang et al., 2018; Lao et al., 2022). As a result, simple two-end-member mixing of constituents may be unsuitable to describe the mixing behaviors of DOC, CDOM, and FDOM in the northern Beibu Gulf. Over four seasons, DOM at all sampling stations appears remarkably nonconservative with net additions of DOC over four seasons, net additions of CDOM and humic-like FDOM during spring and summer, and net removal of protein-like C3 in spring and summer (Figure 8). However, upon dividing sample stations into the

three categories (Figure 1), the convincing mixing of DOM appears clearly in the northern Beibu Gulf.

In region I, the conservative mixing behavior of bulk DOC, CDOM, and humic-like FDOM occurs over four seasons (Figures 8A–P), which may reflect the fewer changes in these variables along the estuaries. Similar behavior during estuarine mixing was reported in other estuarine and coastal systems (Jaffe et al., 2004; Guo et al., 2007; Guo et al., 2011; Li et al., 2019; Yang et al., 2019; Amaral et al., 2020). Such mixing patterns indicate that the physical mixing of fresh river water and coastal water dominates the distributions of DOC, CDOM, and humic-like FDOM in estuaries and coastal ecosystems. In contrast, the protein-like C3 points in region I in spring and summer fall below the theoretical mixing line, which indicates the removal of C3 during the estuarial mixing process (Figures 8Q, R). The protein-like FDOM components have been recognized as the labile fraction of DOM as indicated by the gradual decrease of its level during the microbial dark incubation (Yamashita and

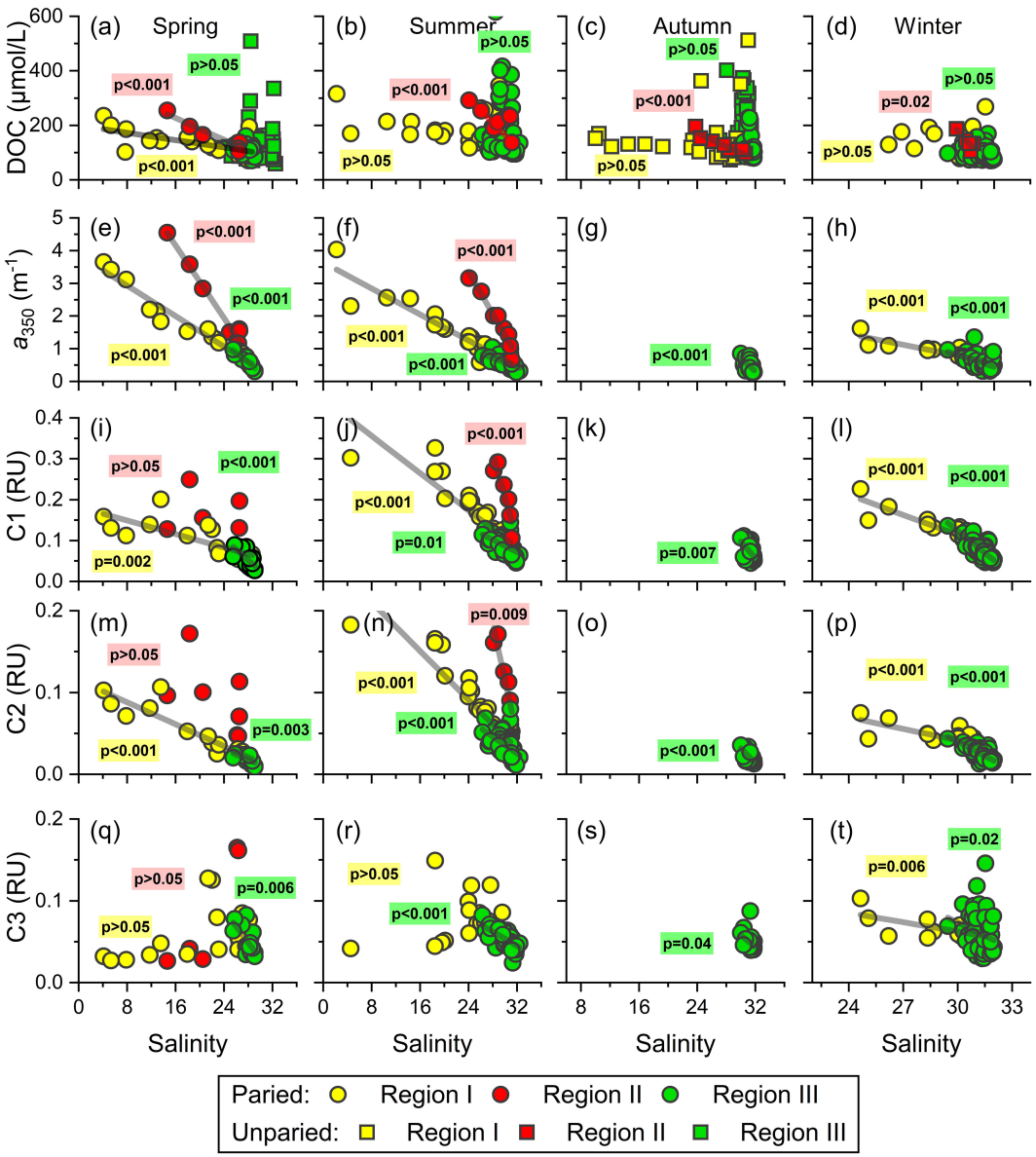

FIGURE 8
Relationships between DOM parameters and salinity in three regions of the northern Beibu Gulf over four seasons. **(A–D)** DOC vs. salinity, **(E–H)** a350 vs. salinity, **(I–L)** humic-like C1 vs. salinity, **(M–P)** humic-like C2 vs. salinity, **(Q–T)** protein-like C3 vs. salinity. The paired data including DOC, CDOM, and FDOM and unpaired data (only DOC) are denoted by circles and squares, respectively.

Tanoue, 2003; Xiao et al., 2021). Coupled with the negative relationships between C3 intensity and AOU in this region in spring and summer (r = −0.65, p <.001), we conclude that protein-like C3 is degraded by bacteria in estuaries.

In region II (i.e., Tieshangang Bay), no CDOM and FDOM data were measured in autumn and winter (Figures 4, 6). The quasi-conservative mixing behavior was determined for DOC over the four seasons and for CDOM and humic-like FDOM in spring and summer (Figures 8A–P). However, the protein-like FDOM does not correlate with salinity in spring (Figures 8Q, R), which might be attributed to the abovementioned anthropogenic input during the sampling period (Figure 6Q). Similar nonconservative addition from human activities has been found in other estuaries and coasts, such as the Yangtze estuary (Guo et al., 2014), thereby potentially impacting the local coastal ecosystem when consumed by microbes. Notably, the conservative mixing lines between DOM and salinity are separated into two regions (Figure 8). The slopes of DOC, CDOM, and humic-like FDOM with respect to salinity in region I are less than those in region II, suggesting that the northern Beibu Gulf receives lower levels of DOM from rivers near the region (Qin River, Maowei River, Dafeng River, and Nanliu River) relative to those from the upper Tieshangang Bay (Figures 8A–N). Conversely, the different slopes for DOC versus salinity in the two regions is lower than slopes for its optical fractions versus salinity, which implies that the two major terrigenous DOM pools delivered into the northern Beibu Gulf differ in their nature and composition. DOM from rivers surrounding region I have higher DOC-normalized CDOM and humic-like FDOM values compared with region II, and, presumably, a high potential for photochemical degradation in the coastal shelf (Helms et al., 2013).

In region III, which contains high-salinity mixing waters from the coast and the adjacent South China Sea, the additions of DOC are highlighted over the four seasons (Figures 8A–D). This result reinforces the hypothesis that DOC in the offshore water of northern Beibu Gulf comes mainly from *in situ* biological activities. However, the CDOM and humic-like FDOM maintain quasi-conservative behavior like those in low-salinity estuarine and coastal waters. Except for the measured low spectral slopes $S_{275-295}$ (<0.025 nm^{-1}), the lack of correlation between CDOM, humic-like FDOM, and AOU is also a noticeable feature in this region. Thus, the biogeochemical processes, such as photochemical bleaching and microbial transformation, should make a minor impact on the distribution patterns of CDOM and humic-like FDOM in the northern Beibu Gulf.

Conclusions

This study demonstrates seasonal and spatial variations of DOC and DOM optical fractions in the northern Beibu Gulf, South China Sea. The DOC and CDOM absorption coefficients and the FDOM intensities range over more than one order of magnitude. Except for spring, DOC correlates weakly with CDOM and FDOM components, indicating that different sources and processes shape their distributions in the northern Beibu Gulf. River discharges are major sources of DOM in several estuaries and coastal waters, especially in spring and summer. Anthropogenic input makes a remarkable contribution to protein-like FDOM in some specific coastal waters near cities, whereas *in situ* biological activity acts as a major source of DOM in offshore waters. The mixing of DOM in the northern Beibu Gulf separates spatially into three regions but does not separate seasonally. The conservative mixing dominates the distributions of DOC, CDOM, and humic-like FDOM in the nearshore waters, excluding Tieshangang Bay (region I) and Tieshangang Bay (region II). This implies that two terrestrial DOM pools with distinct optical properties are transferred into the northern Beibu Gulf. However, the protein-like FDOM in region I is nonconservative and is removed by microbes coupled with the net consumption of oxygen. In the high-salinity offshore waters (region III), the net addition of DOC suggests that it comes from *in situ* biological sources, whereas the CDOM and humic-like FDOM forms a quasi-conservative mixing pattern. The multiple sources and complexity of mixing for various DOM components demonstrate the dynamics of DOM in the estuarine and coastal ecosystem, which make a considerable and varied impact on the carbon cycle in ocean margins.

Data availability statement

The raw data supporting the conclusions of this article will be made available by the authors, without undue reservation.

Author contributions

ZhZ: Conceptualization, Sampling, Sample analysis, Writing. HW: Sampling, Sample analysis, Draft preparation. YG: Data management, Editing. LZ, RJ, PS, YY, ZZ, and QZ: Conceptualization. All authors contributed to the article and approved the submitted version.

Funding

This work was supported by the National Natural Science Foundation of China (U20A20103), an open grant from Guangxi Key Laboratory of Beibu Gulf Marine Resources, Environment and Sustainable Development (MRESD-2022-B01), the Guangxi Funding Project (304024XM20N0006, 2019GXNSFBA185036,

2018AD19280, 2018AD19321), and the Beihai Science & Technology Project (201995037, 202082022, 202082042).

Acknowledgments

We thank all the crews on the R/V Yueke 1, R/V Yuexiayuzhi 20028, and R/V Haike 68 for their assistance with the sampling during the cruises in 2020 and 2021.

Conflict of interest

The authors declare that the research was conducted in the absence of any commercial or financial relationships that could be construed as a potential conflict of interest.

Publisher's note

Supplementary material

The Supplementary Material for this article can be found online at: https://www.frontiersin.org/articles/10.3389/fmars.2022.1023953/full#supplementary-material

References

Amaral, V., Romera-Castillo, C., and Forja, J. (2021). Submarine mud volcanoes as a source of chromophoric dissolved organic matter to the deep waters of the gulf of cadiz. *Sci. Rep.* 11, 3200. doi: 10.1038/s41598-021-82632-3

Amaral, V., Romera-Castillo, C., Garcia-Delgado, M., Gomez-Parra, A., and Forja, J. (2020). Distribution of dissolved organic matter in estuaries of the southern Iberian Atlantic basin: Sources, behavior and export to the coastal zone. *Mar. Chem.* 226, 103857. doi: 10.1016/j.marchem.2020.103857

Beusen, A. H. W., Bouwman, A. F., Van Beek, L. P. H., Mogollon, J. M., and Middelburg, J. J. (2016). Global riverine n and p transport to ocean increased during the 20th century despite increased retention along the aquatic continuum. *Biogeosciences* 13, 2441–2451. doi: 10.5194/bg-13-2441-2016

Carpenter, J. H. J. L. (1965). The Chesapeake bay institute technique for the winkler dissolved oxygen method. *Limnol. Oceanogr.* 10, 141–143. doi: 10.4319/lo.1965.10.1.0141

Catala, T. S., Reche, I., Ramon, C. L., Lopez-Sanz, A., Alvarez, M., Calvo, E., et al. (2016). Chromophoric signatures of microbial by-products in the dark ocean. *Geophys. Res. Lett.* 43, 7639–7648. doi: 10.1002/2016GL069878

Catalá, T. S., Reche, I., Fuentes-Lema, A., Romera-Castillo, C., Nieto-Cid, M., Ortega-Retuerta, E., et al (2015). Turnover time of fluorescent dissolved organic matter in the dark global ocean. *Nature Communications* 6. doi: 10.1038/ncomms6986.

Chen, R. F., and Gardner, G. B. (2004). High-resolution measurements of chromophoric dissolved organic matter in the Mississippi and atchafalaya river plume regions. *Mar. Chem.* 89, 103–125. doi: 10.1016/j.marchem.2004.02.026

Chen, M., Kim, S.-H., Jung, H.-J., Hyun, J.-H., Choi, J. H., Lee, H.-J., et al. (2017). Dynamics of dissolved organic matter in riverine sediments affected by weir impoundments: Production, benthic flux, and environmental implications. *Water Res.* 121, 150–161. doi: 10.1016/j.watres.2017.05.022

Chen, S. L., Li, Y., Hu, J. Y., Zheng, A. R., Huang, L. F., and Lin, Y. S. (2011). Multiparameter cluster analysis of seasonal variation of water masses in the eastern beibu gulf. *J. Oceanogr.* 67, 709–718. doi: 10.1007/s10872-011-0071-y

Coble, P. G. (1996). Characterization of marine and terrestrial DOM in seawater using excitation emission matrix spectroscopy. *Mar. Chem.* 51, 325–346. doi: 10.1016/0304-4203(95)00062-3

Coble, P. G. (2007). Marine optical biogeochemistry: The chemistry of ocean color. *Chem. Rev.* 107, 402–418. doi: 10.1021/cr050350+

Coble, P. G., Del Castillo, C. E., and Avril, B. (1998). Distribution and optical properties of CDOM in the Arabian Sea during the 1995 southwest monsoon. *Deep-Sea. Res. Part Ii-Topical. Stud. Oceanogr.* 45, 2195–2223. doi: 10.1016/S0967-0645(98)00068-X

Cory, R. M., and Mcknight, D. M. (2005). Fluorescence spectroscopy reveals ubiquitous presence of oxidized and reduced quinones in dissolved organic matter. *Environ. Sci. Technol.* 39, 8142–8149. doi: 10.1021/es0506962

Dainard, P. G., and Guéguen, C. (2013). Distribution of PARAFAC modeled CDOM components in the north pacific ocean, Bering, chukchi and Beaufort seas. *Mar. Chem.* 157, 216–223. doi: 10.1016/j.marchem.2013.10.007

Dainard, P. G., Guéguen, C., Mcdonald, N., and Williams, W. J. (2015). Photobleaching of fluorescent dissolved organic matter in Beaufort Sea and north Atlantic subtropical gyre. *Mar. Chem.* 177, 630–637. doi: 10.1016/j.marchem.2015.10.004

Fichot, C. G., and Benner, R. (2014). The fate of terrigenous dissolved organic carbon in a river-influenced ocean margin. *Global Biogeochem. Cycles.* 28, 300–318. doi: 10.1002/2013GB004670

Gao, Z., and Guéguen, C. (2018). Distribution of thiol, humic substances and colored dissolved organic matter during the 2015 Canadian Arctic GEOTRACES cruises. *Mar. Chem.* 203, 1–9. doi: 10.1016/j.marchem.2018.04.001

Gueguen, C., Itoh, M., Kikuchi, T., Eert, J., and Williams, W. J. (2015). Variability in dissolved organic matter optical properties in surface waters in the amerasian basin. *Front. Mar. Sci.* 2, 78. doi: 10.3389/fmars.2015.00078

Guo, W., Stedmon, C. A., Han, Y., Wu, F., Yu, X., and Hu, M. (2007). The conservative and non-conservative behavior of chromophoric dissolved organic matter in Chinese estuarine waters. *Mar. Chem.* 107, 357–366. doi: 10.1016/j.marchem.2007.03.006

Guo, W., Yang, L., Hong, H., Stedmon, C. A., Wang, F., Xu, J., et al. (2011). Assessing the dynamics of chromophoric dissolved organic matter in a subtropical estuary using parallel factor analysis. *Mar. Chem.* 124, 125–133. doi: 10.1016/j.marchem.2011.01.003

Guo, W., Yang, L., Zhai, W., Chen, W., Osburn, C. L., Huang, X., et al. (2014). Runoff-mediated seasonal oscillation in the dynamics of dissolved organic matter in different branches of a large bifurcated estuaryThe changjiang estuary. *J. Geophys. Research-Biogeosci.* 119, 776–793. doi: 10.1002/2013JG002540

Hansell, D. A. (2013). Recalcitrant dissolved organic carbon fractions. *Rev. Marine Sci.*. 5, 421–445. doi: 10.1146/annurev-marine-120710-100757

Hansell, D. A., Carlson, C. A., Repeta, D. J., and Schlitzer, R. (2009). Dissolved organic matter in the ocean a controversy stimulates new insights. *Oceanography* 22, 202–211. doi: 10.5670/oceanog.2009.109

Hedges, J. I., Keil, R. G., and Benner, R. (1997). What happens to terrestrial organic matter in the ocean? *Organic. Geochem.* 27, 195–212. doi: 10.1016/S0146-6380(97)00066-1

Helms, J. R., Stubbins, A., Perdue, E. M., Green, N. W., Chen, H., and Mopper, K. (2013). Photochemical bleaching of oceanic dissolved organic matter and its effect on absorption spectral slope and fluorescence. *Mar. Chem.* 155, 81–91. doi: 10.1016/j.marchem.2013.05.015

Helms, J. R., Stubbins, A., Ritchie, J. D., Minor, E. C., Kieber, D. J., and Mopper, K. (2008). Absorption spectral slopes and slope ratios as indicators of molecular weight, source, and photobleaching of chromophoric dissolved organic matter. *Limnol. Oceanogr.* 53, 955–969. doi: 10.4319/lo.2008.53.3.0955

Huguet, A., Vacher, L., Relexans, S., Saubusse, S., Froidefond, J. M., and Parlanti, E. (2009). Properties of fluorescent dissolved organic matter in the gironde estuary. *Organic. Geochem.* 40, 706–719. doi: 10.1016/j.orggeochem.2009.03.002

Jaffe, R., Boyer, J. N., Lu, X., Maie, N., Yang, C., Scully, N. M., et al. (2004). Source characterization of dissolved organic matter in a subtropical mangrove-dominated estuary by fluorescence analysis. *Mar. Chem.* 84, 195–210. doi: 10.1016/j.marchem.2003.08.001

Jorgensen, L., Stedmon, C. A., Kragh, T., Markager, S., Middelboe, M., and Sondergaard, M. (2011). Global trends in the fluorescence characteristics and distribution of marine dissolved organic matter. *Mar. Chem.* 126, 139–148. doi: 10.1016/j.marchem.2011.05.002

Kaiser, D., Unger, D., and Qiu, G. (2014). Particulate organic matter dynamics in coastal systems of the northern beibu gulf. *Continental. Shelf. Res.* 82, 99–118. doi: 10.1016/j.csr.2014.04.006

Kothawala, D. N., Murphy, K. R., Stedmon, C. A., Weyhenmeyer, G. A., and Tranvik, L. J. (2013). Inner filter correction of dissolved organic matter fluorescence. *Limnol. Oceanogr.: Methods* 11, 616–630. doi: 10.4319/lom.2013.11.616

Lai, J., Jiang, F., Ke, K., Xu, M., Lei, F., and Chen, B. (2014). Nutrients distribution and trophic status assessment in the northern beibu gulf, China. *Chin. J. Oceanol. Limnol.* 32, 1128–1144. doi: 10.1007/s00343-014-3199-y

Lao, Q., Liu, G., Shen, Y., Su, Q., Gao, J., and Chen, F. (2020). Distribution characteristics and fluxes of nutrients in the rivers of the beibu gulf. *Acta Oceanol. Sin.* 42, 93–100. doi: 10.3969/j.issn.0253–4193.2020.12.010

Lao, Q., Liu, G., Shen, Y., Su, Q., and Lei, X. (2021a). Biogeochemical processes and eutrophication status of nutrients in the northern beibu gulf, south China. *J. Earth Syst. Sci.* 130, 199. doi: 10.1007/s12040-021-01706-y

Lao, Q., Liu, G., Zhou, X., Chen, F., and Zhang, S. (2021b). Sources of polychlorinated biphenyls (PCBs) and dichlorodiphenyltrichloroethanes (DDTs) found in surface sediment from coastal areas of beibu gulf: A reflection on shipping activities and coastal industries. *Mar. Pollut. Bull.* 167, 112318. doi: 10.1016/j.marpolbul.2021.112318

Lao, Q., Su, Q., Liu, G., Shen, Y., Chen, F., Lei, X., et al. (2019). Spatial distribution of and historical changes in heavy metals in the surface seawater and sediments of the beibu gulf, China. *Mar. Pollut. Bull.* 146, 427–434. doi: 10.1016/j.marpolbul.2019.06.080

Lao, Q., Zhang, S., Li, Z., Chen, F., Zhou, X., Jin, G., et al. (2022). Quantification of the seasonal intrusion of water masses and their impact on nutrients in the beibu gulf using dual water isotopes. *J. Geophys. Research-Oceans.* 127, e2021JC018065. doi: 10.1029/2021JC018065

Lawaetz, A. J., and Stedmon, C. A. (2009). Fluorescence Intensity Calibration Using the Raman Scatter Peak of Water. *Applied Spectroscopy* 63, 936–40. doi: 10.1366/000370209788964548

Levshina, S. I. (2008). Dissolved and suspended organic matter in the amur and songhua river water. *Water Resour.* 35, 716–724. doi: 10.1134/s0097807808060110

Liao, W., Hu, J., Zhou, H., Hu, J., Peng, P. A., and Deng, W. (2018). Sources and distribution of sedimentary organic matter in the beibu gulf, China: Application of multiple proxies. *Mar. Chem.* 206, 74–83. doi: 10.1016/j.marchem.2018.09.006

Li, N., Chen, X., Zhao, H., Tang, J., Jiang, G., Li, Z., et al. (2020). Spatial distribution and functional profile of the bacterial community in response to eutrophication in the subtropical beibu gulf, China. *Mar. Pollut. Bull.* 161, 111742. doi: 10.1016/j.marpolbul.2020.111742

Li, Y., Song, G., Massicotte, P., Yang, F., Li, R., and Xie, H. (2019). Distribution, seasonality, and fluxes of dissolved organic matter in the pearl river (Zhujiang) estuary, China. *Biogeosciences* 16, 2751–2770. doi: 10.5194/bg-16-2751-2019

Liu, D., Bai, Y., He, X. Q., Chen, C. T. A., Huang, T. H., Pan, D. L., et al. (2020). Changes in riverine organic carbon input to the ocean from mainland China over the past 60 years. *Environ. Int.* 134, 105258. doi: 10.1016/j.envint.2019.105258

Massicotte, P., Asmala, E., Stedmon, C., and Markager, S. (2017). Global distribution of dissolved organic matter along the aquatic continuum: Across rivers, lakes and oceans. *Sci. Total. Environ.* 609, 180–191. doi: 10.1016/j.scitotenv.2017.07.076

Meng, F., Wang, Z., Cheng, F., Du, X., Fu, W., Wang, Q., et al. (2013). The assessment of environmental pollution along the coast of beibu gulf, northern south China Sea: An integrated biomarker approach in the clam meretrix meretrix. *Mar. Environ. Res.* 85, 64–75. doi: 10.1016/j.marenvres.2013.01.003

Murphy, K. R., Hambly, A., Singh, S., Henderson, R. K., Baker, A., Stuetz, R., et al. (2011). Organic matter fluorescence in municipal water recycling schemes: Toward a unified PARAFAC model. *Environ. Sci. Technol.* 45, 2909–2916. doi: 10.1021/es103015e

Murphy, K. R., Stedmon, C. A., Graeber, D., and Bro, R. (2013). Fluorescence spectroscopy and multi-way techniques. PARAFAC. *Anal. Methods* 5, 6557–6566. doi: 10.1039/c3ay41160e

Murphy, K. R., Stedmon, C. A., Wenig, P., and Bro, R. (2014). OpenFluor–an online spectral library of auto-fluorescence by organic compounds in the environment. *Anal. Methods* 6, 658–661. doi: 10.1039/C3AY41935E

Nelson, N. B., Siegel, D. A., Carlson, C. A., and Swan, C. M. (2010). Tracing global biogeochemical cycles and meridional overturning circulation using chromophoric dissolved organic matter. *Geophys. Res. Lett.* 37, L03610. doi: 10.1029/2009GL042325

Noureddin, S., and Courtot, P. (1989). Conservative behavior of humic substances in a macrotidal estuary–composition of particulate and dissolved phases. *Oceanol. Acta* 12, 381–391.

Qu, L., He, C., Wu, Z., Dahlgren, R. A., Ren, M., Li, P., et al. (2022). Hypolimnetic deoxygenation enhanced production and export of recalcitrant dissolved organic matter in a large stratified reservoir. *Water Res.* 219, 118537. doi: 10.1016/j.watres.2022.118537

Raymond, P. A., and Spencer, R. G. M. (2015). "Chapter 11 - riverine DOM," in *Biogeochemistry of marine dissolved organic matter (Second edition)*. Eds. D. A. Hansell and C. A. Carlson (Cambridge: Academic Press), 509–533. doi: 10.1016/B978-0-12-405940-5.00011-X.

Rochelle-Newall, E. J., and Fisher, T. R. (2002). Production of chromophoric dissolved organic matter fluorescence in marine and estuarine environments: An investigation into the role of phytoplankton. *Mar. Chem.* 77, 7–21. doi: 10.1016/S0304-4203(01)00072-X

Shank, G. C., Zepp, R. G., Whitehead, R. F., and Moran, M. A. (2005). Variations in the spectral properties of freshwater and estuarine CDOM caused by partitioning onto river and estuarine sediments. *Estuar. Coast. Shelf. Sci.* 65, 289–301. doi: 10.1016/j.ecss.2005.06.009

Spencer, R. G. M., Baker, A., Ahad, J. M. E., Cowie, G. L., Ganeshram, R., Upstill-Goddard, R. C., et al. (2007). Discriminatory classification of natural and anthropogenic waters in two UK estuaries. *Sci. Total. Environ.* 373, 305–323. doi: 10.1016/j.scitotenv.2006.10.052

Stedmon, C. A., and Bro, R. (2008). Characterizing dissolved organic matter fluorescence with parallel factor analysis: a tutorial. *Limnol. Oceanography-Methods.* 6, 572–579. doi: 10.4319/lom.2008.6.572

Stedmon, C. A., and Markager, S. (2003). Behaviour of the optical properties of coloured dissolved organic matter under conservative mixing. *Estuar. Coast. Shelf. Sci.* 57, 973–979. doi: 10.1016/S0272-7714(03)00003-9

Stedmon, C. A., and Nelson, N. B. (2015). "Chapter 10 - the optical properties of DOM in the ocean," in *Biogeochemistry of marine dissolved organic matter (Second edition)*. Eds. D. A. Hansell and C. A. Carlson (Cambridge: Academic Press), 481–508. doi: 10.1016/B978-0-12-405940-5.00010-8

Stedmon, C. A., Osburn, C. L., and Kragh, T. (2010). Tracing water mass mixing in the Baltic-north Sea transition zone using the optical properties of coloured dissolved organic matter. *Estuar. Coast. Shelf. Sci.* 87, 156–162. doi: 10.1016/j.ecss.2009.12.022

Tian, Y. Q., Yu, Q., Feig, A. D., Ye, C., and Blunden, A. (2013). Effects of climate and land-surface processes on terrestrial dissolved organic carbon export to major U.S. coastal rivers. *Ecol. Eng.* 54, 192–201. doi: 10.1016/j.ecoleng.2013.01.028

Wang, C., Guo, W., Li, Y., Dahlgren, R. A., Guo, X., Qu, L., et al. (2021a). Temperature-regulated turnover of chromophoric dissolved organic matter in global dark marginal basins *Geophysical Research Letters* 48, e2021GL094035. doi: 10.1029/2021GL094035.

Wang, C., Guo, W. D., Li, Y., Stubbins, A., Li, Y. Z., Song, G. D., et al. (2017). Hydrological and biogeochemical controls on absorption and fluorescence of dissolved organic matter in the northern south China Sea. *J. Geophys. Research-Biogeosci.* 122, 3405–3418. doi: 10.1002/2017JG004100

Wang, C., Li, Y., Li, Y., Zhou, H., Stubbins, A., Dahlgren, R. A., et al. (2021b). Dissolved organic matter dynamics in the epipelagic northwest Pacific low-latitude western boundary current system: Insights from optical analyses. *J. Geophys. Res.: Oceans.* 126, e2021JC017458. doi: 10.1029/2021JC017458

Wang, L., Pan, W., Zhuang, W., Yan, X.-H., and Klemas, V. V. (2018). Analysis of seasonal characteristics of water exchange in beibu gulf based on a particle tracking model. *Regional. Stud. Mar. Sci.* 18, 35–43. doi: 10.1016/j.rsma.2017.12.009

Weishaar, J. L., Aiken, G. R., Bergamaschi, B. A., Fram, M. S., Fujii, R., and Mopper, K. (2003). Evaluation of specific ultraviolet absorbance as an indicator of the chemical composition and reactivity of dissolved organic carbon. *Environ. Sci. Technol.* 37, 4702–4708. doi: 10.1021/es030360x

Wu, K., Dai, M. H., Chen, J. H., Meng, F. F., Li, X. L., Liu, Z. Y., et al. (2015). Dissolved organic carbon in the south China Sea and its exchange with the Western pacific ocean. *Deep-Sea. Res. Part Ii-Topical. Stud. Oceanogr.* 122, 41–51. doi: 10.1016/j.dsr2.2015.06.013

Xiao, X., Guo, W., Li, X., Wang, C., Chen, X., Lin, X., et al. (2021). Viral lysis alters the optical properties and biological availability of dissolved organic matter derived from *Prochlorococcus* picocyanobacteria. *Appl. Environ. Microbiol.* 87, e02271–e02220. doi: 10.1128/AEM.02271-20

Xu, Y., Zhang, T., and Zhou, J. (2019). Historical occurrence of algal blooms in the northern beibu gulf of China and implications for future trends. *Front. Microbiol.* 10, 451. doi: 10.3389/fmicb.2019.00451

Yamashita, Y., Fichot, C. G., Shen, Y., Jaffe, R., and Benner, R. (2015). Linkages among fluorescent dissolved organic matter, dissolved amino acids and lignin-derived phenols in a river-influenced ocean margin. *Front. Mar. Sci.* 2, 92. doi: 10.3389/fmars.2015.00092

Yamashita, Y., and Tanoue, E. (2003). Distribution and alteration of amino acids in bulk DOM along a transect from bay to oceanic waters. *Mar. Chem.* 82, 145–160. doi: 10.1016/S0304-4203(03)00049-5

Yang, L., Cheng, Q., Zhuang, W.-E., Wang, H., and Chen, W. (2019). Seasonal changes in the chemical composition and reactivity of dissolved organic matter at the land-ocean interface of a subtropical river. *Environ. Sci. Pollut. Res.* 26, 24595–24608. doi: 10.1007/s11356-019-05700-2

Yang, L., Chen, C.-T. A., Hong, H., Chang, Y.-C., and Lui, H.-K. (2015b). Mixing behavior and bioavailability of dissolved organic matter in two contrasting subterranean estuaries as revealed by fluorescence spectroscopy and parallel factor analysis. *Estuar. Coast. Shelf. Sci.* 166, 161–169. doi: 10.1016/j.ecss.2014.10.018

Yang, L., Guo, W., Hong, H., and Wang, G. (2013a). Non-conservative behaviors of chromophoric dissolved organic matter in a turbid estuary: Roles of multiple biogeochemical processes. *Estuar. Coast. Shelf. Sci.* 133, 285–292. doi: 10.1016/j.ecss.2013.09.007

Yang, L., Hong, H., Chen, C.-T. A., Guo, W., and Huang, T.-H. (2013b). Chromophoric dissolved organic matter in the estuaries of populated and mountainous Taiwan. *Mar. Chem.* 157, 12–23. doi: 10.1016/j.marchem.2013.07.002

Yang, F., Song, G., Massicotte, P., Wei, H., and Xie, H. (2020). Depth-resolved photochemical lability of dissolved organic matter in the Western tropical pacific ocean. *J. Geophys. Res.: Biogeosci.* 125, e2019JG005425. doi: 10.1029/2019JG005425

Yang, J., Wang, W., Zhao, M., Chen, B., Dada, O. A., and Chu, Z. (2015a). Spatial distribution and historical trends of heavy metals in the sediments of petroleum producing regions of the beibu gulf, China. *Mar. pollut. Bull.* 91, 87–95. doi: 10.1016/j.marpolbul.2014.12.023

Zhang, L., Xue, M., Wang, M., Cai, W.-J., Wang, L., and Yu, Z. (2014). The spatiotemporal distribution of dissolved inorganic and organic carbon in the main stem of the changjiang (Yangtze) river and the effect of the three gorges reservoir. *J. Geophys. Research-Biogeosci.* 119, 741–757. doi: 10.1002/2012JG002230

Zhu, Z., Wei, H., Guan, Y., Zhang, L., Sun, P., and Zhang, Q. (2022a). Spatial and seasonal characteristics of dissolved heavy metals in the seawater of beibu gulf, the northern south China Sea. 9. doi: 10.3389/fmars.2022.996202

Zhu, Z., Wei, H., Huang, W., Wu, X., Guan, Y., and Zhang, Q. (2022b). Occurrence of microplastic pollution in the beibu gulf, the northern of south China Sea. *Front. Mar. Sci.* 8 . doi: 10.3389/fmars.2021.821008

Zhu, Z., and Zheng, A. (2013). Distributions and sources of heavy metals in seawater of the northern beibu gulf. *Adv. Mater. Res.* 807-809, 7–13. doi: 10.4028/www.scientific.net/AMR.807-809.7

Zsolnay, A., Baigar, E., Jimenez, M., Steinweg, B., and Saccomandi, F. (1999). Differentiating with fluorescence spectroscopy the sources of dissolved organic matter in soils subjected to drying. *Chemosphere* 38, 45–50. doi: 10.1016/S0045-6535(98)00166-0

frontiers | Frontiers in Marine Science

TYPE Original Research
PUBLISHED 03 November 2022
DOI 10.3389/fmars.2022.1030841

OPEN ACCESS

EDITED BY
Fajin Chen,
Guangdong Ocean University, China

REVIEWED BY
Jianghu Lan,
Institute of Earth Environment (CAS), China
Guoqiang Li,
Lanzhou University, China

*CORRESPONDENCE
Zhongping Lai
zhongping_lai@stu.edu.cn

SPECIALTY SECTION
This article was submitted to Marine Biogeochemistry, a section of the journal Frontiers in Marine Science

RECEIVED 29 August 2022
ACCEPTED 17 October 2022
PUBLISHED 03 November 2022

CITATION
Zhong J, Ling K, Yang M, Shen Q, Abbas M and Lai Z (2022) Radiocarbon and OSL dating on cores from the Chaoshan delta in the coastal South China Sea.
Front. Mar. Sci. 9:1030841.
doi: 10.3389/fmars.2022.1030841

Radiocarbon and OSL dating on cores from the Chaoshan delta in the coastal South China Sea

Jiemei Zhong[1], Ken Ling[2], Meifei Yang[3], Qinjing Shen[1], Mahmoud Abbas[1] and Zhongping Lai[1,4]*

[1]Institute of Marine Sciences, Guangdong Provincial Key Laboratory of Marine Disaster Prediction and Prevention, Shantou University, Shantou, China, [2]Guangdong Geological Survey Institute, Guangzhou, China, [3]School of Earth Sciences, China University of Geosciences, Wuhan, China, [4]Southern Marine Science and Engineering Guangdong Laboratory (Zhuhai), Zhuhai, China

Accurate chronology plays a crucial role in reconstructing delta evolution. Radiocarbon (^{14}C) and optically stimulated luminescence (OSL) dating are widely used to establish a stratigraphic chronology of the late Quaternary sediments. The Chaoshan plain is located on the southern coast of China and borders the South China Sea. The thickness of Quaternary sediments in this area extends to a depth of 140 m and is considered a valuable archive for studying the evolution of the delta in response to climate and sea-level changes. However, reliable chronological data are still very limited. In this paper, eighteen accelerator mass spectrometry (AMS) ^{14}C and thirteen quartz OSL ages were obtained from two cores from the Rongjiang plain, the middle part of the Chaoshan plain: ZK001 (90.85 m in depth) and ZK002 (100 m in depth). The present study aims to provide a reliable chronology of the Chaoshan plain based on OSL and ^{14}C dating methods and examine the upper limit of the ^{14}C dating on plant remains. Our results show that (1) OSL ages of cores ZK001 and ZK002 range from 56 to 1.7 ka and from 177 to 15 ka, respectively; (2) ^{14}C ages of core ZK002 range from 8.8 to 41 cal ka BP, showing that all ^{14}C ages below ca. 30 m depth are younger than OSL ages and that the upper limit of plant remains is around 35 cal ka BP. OSL ages are consistent with stratigraphic order within uncertainties. The oldest OSL age obtained from core ZK002 is 177 $\pm$ 20 ka at a depth of 93 m, and is considered a minimum age. This indicates that the Quaternary deposition in the Rongjiang plain can trace back to at least the marine isotope stage (MIS) 6 during sea-level lowstand, during which the plain is mainly influenced by the fluvial process. The comparison between ^{14}C and OSL ages in the Chaoshan plain suggests that ^{14}C ages older than 35 cal ka BP need to be re-evaluated. However, the OSL dating method proves reliable for establishing a comprehensive chronological framework for the late Quaternary sediments in this area.

KEYWORDS

^{14}C ages of plant remains, OSL dating, estuary sediments, Chaoshan plain, South China Sea

Introduction

Robust chronology is essential for reconstructing the late Quaternary evolution in the delta environment. The radiocarbon dating method is regarded as a reliable dating method with an age limit, theoretically, up to approximately 55,000 years (Hajdas et al., 2021). However, a growing number of geochronologic studies corroborated that the reliability of radiocarbon dating for late Pleistocene sediments is problematic due to the age limit cluster around 35–40 ka BP (Yim et al., 1990; Pigati et al., 2007; Yi et al., 2013; Wang et al., 2018a; Miller and Andrews, 2019; Agatova et al., 2020; Al-Saqarat et al., 2021), or approximately 25 ka BP in practice (Lai et al., 2014; Wang et al., 2014; Song et al., 2015; Li et al., 2020c; Cheng et al., 2022; Long et al., 2022). The optically stimulated luminescence (OSL) dating method has become widely accepted in recent decades, with its merits of a long time-scale range (even up to 200 ka) and abundance of dating materials (e.g., quartz or feldspar) (Murray and Olley, 2002; Rhodes, 2011; Murray et al., 2021). The applicability of OSL dating to coastal and marine sediments allowed the reconstruction of the paleoenvironment of the delta (Chen et al., 2010; Guo et al., 2013; Yi et al., 2013; Wang et al., 2016; Xu et al., 2020; Gao et al., 2021; Long et al., 2022; Xu et al., 2022).

The Chaoshan plain is located on the eastern coast of Guangdong province (Figure 1). The Quaternary sediments in this area reach a depth of up to approximately 140 m, providing valuable archives for understanding the evolution of the delta in response to climate and sea level changes (Li et al., 1987; Wang et al., 1997; Song et al., 2012). Due to the actual detection age limit of the ^{14}C dating method, most of the late Pleistocene chronology of the Chaoshan plain is disputed (Li et al., 1987; Zong, 1987; Li et al., 1988; Sun et al., 2007). Some studies have demonstrated that the oldest Quaternary deposits (fluvial sediments, named the Nanshe Formation) do not exceed 55 ka BP, based on radiocarbon, thermoluminescence (TL) dating, and stratigraphic relationships (Chen, 1984a; Li et al., 1987; Zong, 1987; Li et al., 1988; Sun et al., 2007; Zhou, 2008). Nevertheless, results from other dating methods, including electron spin resonance (ESR) and OSL, have shown that the oldest Quaternary sediments in the Lianjiang plain, the southeastern part of the Chaoshan plain, date back to more than 260 ka (Song et al., 2012; Tang et al., 2018). Yet, our understanding of the formation and evolution of the Chaoshan plain delta is still debated, owing to different dating methods that require further evaluation. A direct comparison between different dating techniques applied to the basal Quaternary deposits would help to answer this question.

In this study, Quaternary estuarine sediments from two cores, ZK001 with a depth of 90.85 m and ZK002 with a depth of 100 m, in the Chaoshan plain were dated using ^{14}C and OSL dating methods. We aim to understand the delta evolution and address the following issues: (1) examining the reliability of ^{14}C and OSL dating by mutual verification; (2) exploring the practical detection limit of ^{14}C dating using plant remains; and (3) determining the age of onset of Quaternary deposition in the area.

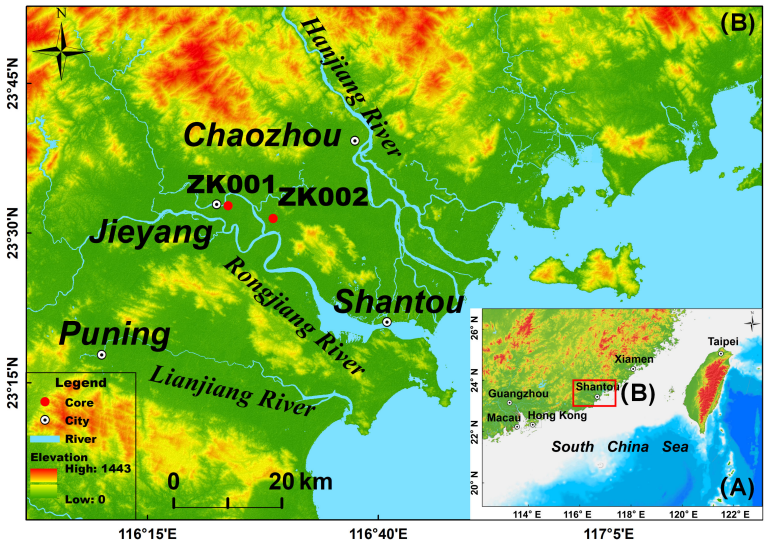

FIGURE 1
Location of the Chaoshan plain and sites of cores ZK001 and ZK002. **(A)** General map around the Chaoshan plain; red square box encompasses the major area of the Chaoshan plain. **(B)** The major area of the Chaoshan plain consists of the Hanjiang Delta, the Rongjiang alluvial plain, and the Lianjiang alluvial plain; two boreholes including cores ZK001 and ZK002 were obtained from the Rongjiang alluvial plain. Base maps are from http://www.gscloud.cn/ and https://www.ngdc.noaa.gov/mgg/global/global.html.

Geological setting and samples

The Chaoshan plain is located on the southeastern coast of China and borders the South China Sea. It consists of the Hanjiang Delta, the Rongjiang alluvial plain, and the Lianjiang alluvial plain and covers an area of 2,600 km² (Figure 1) (Li et al., 1987; Wang et al., 1997). The plain was developed during the Mesozoic Yanshan epoch and is mainly dissected by NE and NW direction fault zones (Li et al., 1987; Liu, 1995). Different uplift and subsidence movements during the Neogene to the early Quaternary transformed the Chaoshan plain into a down-faulted basin (Wang et al., 1997). This resulted in the creation of large accommodation spaces, with an average depth of up to 76.5 m, for the deposition of Quaternary sediments (Wang et al., 1997). The highest thickness of sedimentary sequences has been found in the Hanjiang Delta, the Rongjiang plain, and the Lianjiang plain at 168 m, 90 m, and 141.2 m, respectively (Chen, 1984a; Liu, 1995; Zhou, 2008).

Two terrestrial cores (ZK001 and ZK002) were obtained from Jieyang, the northwestern part of the Rongjiang plain by rotary drilling. Core ZK001 is located in Rongcheng District (116°23′36″ E, 23°32′51″ N; 8 m above sea level (asl)), with a depth of 90.85 m. Core ZK002 lies in Paotai Town (116°28′30″E, 23°31′36″N; 2 m asl), with a depth of 100 m. Both cores ZK001 and ZK002 are dominated by dark gray clay, gray silty clay, and yellowish or grayish-white coarse sands with gravel (Figure 4). Seven OSL samples dating samples were collected from core ZK001and six from core ZK002. Four plant remains were obtained for ^{14}C dating from core ZK001, and eleven plant remains and three rotten leaves from core ZK002.

Methods

Radiocarbon dating

Eighteen samples from cores ZK001 and ZK002 were treated and analyzed at the accelerator mass spectrometry (AMS) laboratory of Peking University for ^{14}C dating. The half-life of ^{14}C used for age calculation in this study was Libby's half-life (5,568 ± 30 a). The ^{14}C ages were calibrated to calendar years (cal a BP or cal ka BP) using IntCal20 atmospheric calibration curves (Reimer et al., 2020) using the OxCal v4.4.4 program with a 95.4% calibrated range (Ramsey and Lee, 2013). The calibrated ^{14}C ages were converted to ka for comparison with OSL ages.

OSL dating

A total of thirteen samples from cores ZK001 and ZK002 were collected for OSL dating. The laboratory work, including sample preparation and measurement, was carried out under subdued red light according to the luminescence dating procedures (Lai and Wintle, 2006; Lai, 2010). The light-exposed outer samples were used to measure dose rate and water content, while the remaining samples were treated sequentially with 10% HCl and 30% H_2O_2 to remove carbonates and organic materials. Wet sieving was used to obtain 38 - 63 μm and 90 - 125 μm fractions based on fraction availability in the sediments. Mid-grained fractions (38–63 μm) were etched by 35% H_2SiF_6 for 2 weeks, while coarse-grained fractions (90–125 μm) were treated with 40% HF for ~30 min to obtain pure quartz and then washed with 10% HCl for about 30 min to remove acid-soluble fluoride. The purity of quartz was checked by infrared-stimulated luminescence (IRSL) signals. Mid-grained fractions (38–63 μm) were pretreated with H_2SiF_6 again because of obvious IRSL signals (beyond 10%) (Lai and Brueckner, 2008). However, the IRSL results still show obvious signals even after retreatment with H_2SiF_6 twice. Therefore, quartz signals of all treated mid-grains (38–63 μm) were stimulated by involving post-IR OSL signal (Roberts and Wintle, 2003). The treated grains were then mounted on the center (7 mm diameter) of 9.7-mm-diameter stainless-steel discs using silicone oil for D_e measurements.

OSL measurements were conducted on a Risø TL/OSL-DA-20 reader equipped with a $^{90}Sr/^{90}Y$ beta source and blue LEDs (λ = 470 ± 20 nm) (Bøtter-Jensen et al., 1999). All optical stimulation (IR and blue-light) measurements for mid-grains (38–63 μm) and coarse-grained quartz (90–125 μm) were stimulated at 130°C for 40 s and recorded by an EMI 9235QA photomultiplier tube fitted with a 7.5-mm Hoya U-340 filter. The equivalent dose (D_e) in this study was measured by the SAR-SGC method (Lai and Ou, 2013), a combination of the single-aliquot regenerative dose (SAR) protocol (Murray and Wintle, 2000) and standard growth curve (SGC) (Roberts and Duller, 2004; Lai, 2006; Lai et al., 2007). The preheat temperature for natural and regenerative dose signals was 260°C for 10 s, and the preheating temperature for test dose response was 220°C for 10 s (Wintle and Murray, 2006). For each sample, 5–6 aliquots were measured by SAR protocol to establish an SGC curve, and 6–12 aliquots were measured by SGC protocol. The final D_e value for a sample age calculation was the average of all D_e values measured by both SAR and SGC protocols.

Inductively coupled plasma mass spectrometry (ICP-MS) was used to measure uranium (U), and thorium (Th), and inductively coupled plasma/optical emission spectrometry (ICP/OES) was used to determine potassium (K). The cosmic ray dose was calculated depending on the depth, altitude, and geomagnetic latitude of each sample (Prescott and Hutton, 1994). The shielding effect of water must be considered when calculating the water content because a 1% increase/decrease in the average water content during the lifetime will usually lead to a 1% increase/decrease in the dose rate (Wallinga and Cunningham, 2015; Murray et al., 2021). Variations in water

content over geologic time can have a significant effect on the dose rate in sediments, and uncertainties in dose rate are large because of the poorly understood history of water content (Lai and Ou, 2013; Wallinga and Cunningham, 2015). The measured water content for cores ZK001 and ZK002 range between 7.4% and 40.5% and between 8% and 18.2%, respectively. Yet, the measured water content cannot accurately reflect the real water content of the sediments at the time of burial. Therefore, based on the variation of water content within the burial period in the study region, we estimated the water content to be 25% ± 5% for all OSL samples in this study instead of using the measured water content.

Results

Radiocarbon ages

^{14}C results of cores ZK001 and ZK002 are listed in Table 1 and can be shown in Figure 4. The plant remains ages of core ZK001 are infinite (>40 ka BP) because these ages are out of the calibration range. The age of the rotten leaves obtained from sample ZK002-C14-01 (3.8 m depth) at 19.34 ± 0.17 cal ka BP is considered overestimated. Plant remains from sample ZK002-C14-04 (18.05 m depth) are dated to 8.81 ± 0.17 cal ka BP, and rotten leaves from sample ZK002-C14-05 (18.95 m depth) are dated to 9.15 ± 0.13 cal ka BP; both are consistent with the stratigraphic order. At depths below 31 m, one sample of rotten leaves and three plant remains have ^{14}C ages that are infinite (>40 ka BP), and the other seven plant remains have finite ages showing age reversals. Potential reasons for age reversals will be discussed below.

OSL ages

OSL ages are listed in Table 2 and can be shown in Figure 4. In core ZK001, the age range is from 1.7 ± 0.1 ka to 56 ± 4.8 ka, and in core ZK002, the age range is from 15 ± 1.1 ka to 177 ± 20 ka. OSL ages of eight samples, namely, ZK001-G12, ZK001-G13, ZK001-G14, ZK002-G02, ZK002-G03, ZK002-G04, ZK002-G05, and ZK002-G06, are considered as minimum ages because of the OSL signal saturation (D_e exceeds 150 Gy) (Wintle and Murray, 2006; Murray et al., 2021). In general, OSL ages of cores ZK001 and ZK002 are in stratigraphic order. Recycling ratio and recuperation are key factors for evaluating the SAR protocol for D_e determination (Wintle and Murray, 2006). The accepted D_e aliquots for each sample in this study matched the criteria of recycling ratios between 0.9 and 1.1 and recuperation ratios of <5%. Representative OSL decay and growth curves of samples ZK001-G04 and ZK002-G01 are shown in Figure 2. The decay curves show that the OSL intensity decreased rapidly to background levels within 2 s, indicating the dominance of the fast components (Wintle and Murray, 2006). The representative growth curves of samples ZK001-G04 and ZK002-G01 are well-fitted, indicating the applicability of a combined SAR-SGC method in this study (Figure 2). Furthermore, the D_e determined by the SGC is consistent with the D_e determined by the SAR protocol.

TABLE 1 ^{14}C ages for samples from cores ZK001 and ZK002, the Chaoshan plain.

Sample ID	Depth (m)	Dating material	^{14}C age (a BP)	Calibrated age (95.4% calibrated range, cal ka BP)
ZK001-C14-10	37.62	Plant remains	>40,820	–
ZK001-C14-11	41.46	Plant remains	>40,820	–
ZK001-C14-13	54.80	Plant remains	>40,820	–
ZK001-C14-14	56.58	Plant remains	>40,820	–
ZK002-C14-01	3.8	Rotten leaves	16,030 ± 60	19.34 ± 0.17
ZK002-C14-04	18.05	Plant remains	7,935 ± 35	8.81 ± 0.17
ZK002-C14-05	18.95	Rotten leaves	8,195 ± 30	9.15 ± 0.13
ZK002-C14-06	30.95	Plant remains	>40,820	–
ZK002-C14-07	33.3	Plant remains	>40,820	–
ZK002-C14-08	40	Rotten leaves	>40,820	–
ZK002-C14-10	57.76	Plant remains	35,450 ± 220	40.57 ± 0.51
ZK002-C14-11	59.32	Plant remains	34,130 ± 240	39.22 ± 0.66
ZK002-C14-12	64.81	Plant remains	>40,820	–
ZK002-C14-14	74.54	Plant remains	28,970 ± 230	33.27 ± 0.92
ZK002-C14-15	87.15	Plant remains	36,440 ± 250	41.47 ± 0.42
ZK002-C14-16	91.6	Plant remains	30,900 ± 190	35.21 ± 0.51
ZK002-C14-17	94.16	Plant remains	30,980 ± 170	35.31 ± 0.52
ZK002-C14-18	96.43	Plant remains	32,850 ± 240	37.43 ± 0.90

10.3389/fmars.2022.1030841

TABLE 2 OSL dating results for samples from cores ZK001 and ZK002, the Chaoshan plain.

Sample ID	Depth (m)	Dating material	Grain size (μm)	Aliquot number	U (ppm)	Th (ppm)	K (%)	Water content (%)	Dose rate (Gy/ka)	D_e (Gy)	OSL age (ka)
ZK001-G01	0.9	Polymineral	38–63	6[a] + 11[b]	4.9 ± 0.24	28.1 ± 2.81	2.44 ± 0.29	25 ± 5	5.11 ± 0.29	8.7 ± 0.4	1.7 ± 0.1
ZK001-G03	8.9	Polymineral	38–63	6[a] + 10[b]	4.77 ± 0.24	24 ± 2.4	2.24 ± 0.27	25 ± 5	4.81 ± 0.27	17.2 ± 0.5	3.6 ± 0.2
ZK001-G04	10.5	Polymineral	38–63	5[a] + 12[b]	4.36 ± 0.22	22.4 ± 2.24	1.96 ± 0.24	25 ± 5	4.59 ± 0.26	23.8 ± 0.4	5.2 ± 0.3
ZK001-G08	14.5	Polymineral	38–63	5[a] + 12[b]	8.02 ± 0.4	27.63 ± 2.76	4.28 ± 0.51	25 ± 5	5.94 ± 0.33	135 ± 1.7	23 ± 1.3
ZK001-G12	21.2	Quartz	90–125	4[a] + 10[b]	11.1 ± 0.55	33.76 ± 3.38	2.87 ± 0.34	25 ± 5	6.09 ± 0.33	>231 ± 18[c]	>38 ± 3.7[d]
ZK001-G13	21.5	Quartz	90–125	5[a] + 12[b]	5.78 ± 0.29	23.64 ± 2.36	2.33 ± 0.28	25 ± 5	4.16 ± 0.24	>235 ± 14[c]	>56 ± 4.8[d]
ZK001-G14	23.4	Polymineral	38–63	12[b]	3.22 ± 0.16	10.23 ± 1.02	2.89 ± 0.35	25 ± 5	3.86 ± 0.22	>211 ± 4.2[c]	>55 ± 3.3[d]
ZK002-G01	19.9	Quartz	90–125	6[a] + 12[b]	2.03 ± 0.1	9.58 ± 0.96	0.66 ± 0.08	25 ± 5	1.43 ± 0.08	22 ± 0.9	15 ± 1.1
ZK002-G02	26.5	Quartz	90–125	5[a] + 12[b]	10.14 ± 0.51	28.97 ± 2.9	2.84 ± 0.34	25 ± 5	5.63 ± 0.31	>153 ± 7.3[c]	>27 ± 2.0[d]
ZK002-G03	41.1	Quartz	90–125	4[a] + 12[b]	5.53 ± 0.28	30.73 ± 3.07	1.43 ± 0.17	25 ± 5	3.78 ± 0.21	>204 ± 7.9[c]	>54 ± 3.6[d]
ZK002-G04	49.8	Quartz	90–125	11[b]	1.28 ± 0.06	4.86 ± 0.49	1.11 ± 0.13	25 ± 5	1.37 ± 0.1	>191 ± 10[c]	>140 ± 12[d]
ZK002-G05	83.6	Quartz	90–125	10[b]	5.74 ± 0.29	8.29 ± 0.83	1.4 ± 0.17	25 ± 5	2.58 ± 0.15	>280 ± 15[c]	>109 ± 8.5[d]
ZK002-G06	93	Quartz	90–125	10[b]	2.88 ± 0.14	5.16 ± 0.52	0.28 ± 0.03	25 ± 5	1.02 ± 0.05	>180 ± 18[c]	>177 ± 20 [d]

[a]Numbers of aliquots measured using the standard SAR method.
[b]Numbers of aliquots measured using the standard SGC method.[c]Minimum De. [d]Minimum age.

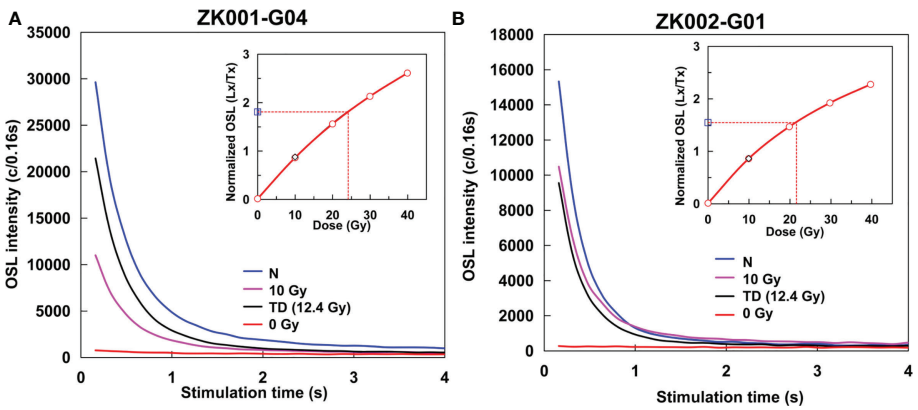

FIGURE 2
OSL decay and growth curves of samples ZK001-G04 **(A)** and ZK002-G01 **(B)**. The growth curves show the dose–response Lx/Tx (where Lx is the ratio of the luminescence signal and Tx is the fixed dose). The decay curves of the natural dose (N), regeneration dose (R), and test dose (TD = 12.4 Gy) show the OSL signals decreasing rapidly during the first second of stimulation, indicating that the OSL signal is dominated by the fast component in these samples.

Discussion

Reliability and upper limit of plant remains ^{14}C dating by comparison with quartz OSL dating Cores

ZK001 and ZK002 were used to reconstruct paleoenvironmental changes by combining the Holocene diatom records, chronology, and sedimentology analysis (Zhang et al., 2020). In addition, the basal Quaternary deposits from core ZK002 were used to establish a new lithostratigraphic unit named the Paotai Formation in the Chaoshan plain (Ling et al., 2021). While the main objectives of this study are to explore the practical detection limit of ^{14}C dating using plant remains and to determine the age of onset of Quaternary deposition in the area.

Eighteen ^{14}C samples of plant remains and rotten leaves from the Rongjiang alluvial plain were dated in this study to obtain a detailed chronological framework. The results show that eight samples are infinite (>40.82 ka BP) and others show age reversals. One rotten leaves ^{14}C age (ZK002-C14-01; 19.34 ± 0.17 cal ka BP) was collected from core ZK002 at a depth of 3.8 m. Plant remains ^{14}C age (ZK002-C14-04; 8.81 ± 0.17 cal ka BP) at a depth of 18.05 m and rotten leaves ^{14}C age (ZK002-C14-05, 9.15 ± 0.13 cal ka BP) at a depth of 18.95 m from a peat layer are consistent with stratigraphic order. Compared with the dates below, rotten leaves ^{14}C age at the top (ZK002-C14-01) is reversed. Potential reasons for age reversals could be (1) sedimentary environment disturbances, (2) the erosion and re-deposition of older sediments, and (3) reworking along the dispersal path from the catchment area to the coast (Goodfriend and Stipp, 1983; Stanley and Chen, 2000; Nian et al., 2018). The layer at the top (3.8 m in depth) of core ZK002 is characterized by a tidal flat phase composed of dark gray silt and silty clay with insets of rotten wood, plants, and shell fragments. Disturbances in the sedimentary environment of the tidal flats might be the ultimate cause of age reversal at the top of the core.

^{14}C age reversals are also common in core ZK002 at depths below 31 m. All reversed ^{14}C ages are significantly underestimated and are not in agreement with quartz OSL ages. Quartz OSL ages of core ZK002 are stratigraphically consistent with general depths, ranging from 15 ka to 177 ka. The comparison between ^{14}C and OSL ages from cores ZK001 and ZK002 is shown in Figure 3. OSL and ^{14}C from core ZK002 at depths greater than ca. 30 m yielded consistent ages up to ca. 35 cal ka BP, while the difference becomes greater beyond 35 cal ka BP. All ^{14}C ages of core ZK002 below ca. 30 m depth are not in agreement with stratigraphic order and clustered around 35–41 cal ka BP. However, OSL ages of core ZK002 successively increase at depths below ca. 30 m, with ages ranging from 54 ka to 177 ka (Figure 4; Table 2). In particular, three ^{14}C ages of plant remains (35–37 cal ka BP) below ca. 91 m depth were underestimated compared with quartz OSL age (ZK002-G06, >177 ± 20 ka).

The potential reasons for the discrepancy between ^{14}C and OSL ages in this study need to be investigated. Because of groundwater-level fluctuations and wet–dry seasonal variations in hydrochemistry in coastal plains and swamps, contamination of humus could occur at different times (Zhang and Shi, 1989). In addition, microbial or plant activities can lead to contamination. For instance, when the organisms (e.g., photosynthetic algae) in sediments are exposed to the atmosphere, they metabolize and produce new organic matters. This process can introduce modern carbon into the sediments, leading to an underestimation of the true age (Cheng et al., 2020). Plant activity such as tree roots could also alter the organic composition of sediments, which could be identified as secondary organic material prior to ^{14}C dating (Palstra et al., 2021). Modern carbon contamination in peat and carbonaceous material cannot be completely eliminated even if some effective pretreatment techniques are used [e.g., acid–base–acid (ABA) and acid–base oxidation (ABOX) pretreatment]. Consequently, the dated samples represent a mixture of old and young carbon that cannot yet be separated at the present time (Bird et al., 1999; Hatté et al., 2001; Agatova et al., 2019).

The amount of original ^{14}C used for age determination in an old sample is scarce due to the half-life (5,730 ± 40 a) of ^{14}C, implying that it is susceptible to modern carbon contamination. The effect of contamination increases with age; even a small amount of secondary carbon can lead to significant errors (Pigati et al., 2007). Sediments at depths of ca. 91–97 m in core ZK002 are terrestrial swamp facies, composed of dark gray silt and clay with fine sands. Contaminant carbon such as humus probably causes an underestimation of the ^{14}C ages of plant remains underestimation at a depth of ca. 91–96 m in terrestrial swamp facies. Finite ^{14}C ages within these layers do not determine depositional dates because they may be intrusive or residual from bioturbation and post-depositional processes. Zheng and Li (2000) have also suggested that radiocarbon dates from terrestrial weathered samples in the Chaoshan plain may have been contaminated by young carbon during periods of low sea level. Contamination with modern carbon is probably the main factor that resulted in the underestimation of the ^{14}C age in this study.

The significant age discrepancy between ^{14}C and OSL from the Chaoshan plain is not particular. Several studies demonstrated that the radiocarbon ages are inconsistent with OSL ages for pre-Holocene samples (Liu and Lai, 2012; Sun et al., 2012; Zhao et al., 2013; Madsen et al., 2014). Regardless of the materials, ^{14}C ages are much younger than luminescence ages. Inconsistencies between ^{14}C and OSL dating have been reported in arid regions in China. Lai et al. (2014) compared previous ^{14}C ages with new OSL ages on lacustrine sediments from Qaidam Basin, northeastern Qinghai-Tibetan Plateau (QTP), and found that the radiocarbon ages of 25–40 ka BP (MIS3) are older by up to approximately 100 ka (MIS 5) using OSL. They suggested that ^{14}C ages older than approximately 25 ka BP are severely

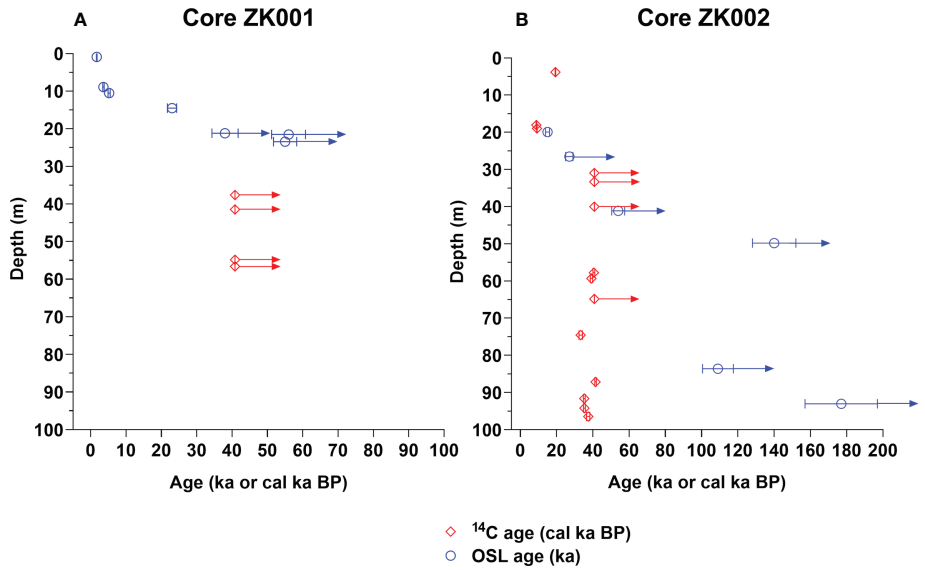

FIGURE 3
Comparison between ^{14}C ages and OSL ages obtained from **(A)** core ZK001 and **(B)** core ZK002. Red open rhomb represents ^{14}C age, red open rhomb with an arrow represents infinite ^{14}C age, blue open rotundity represents OSL age, and blue open rotundity with an arrow represents minimum OSL age. Calibrated ^{14}C ages are reported in cal ka BP and OSL ages are reported in ka.

underestimated, especially for samples from arid regions. The following study from the Ili Basin in Central Asia has confirmed that ^{14}C ages older than 25 cal ka BP are greatly underestimated in other terrestrial deposits in Central Asia (Song et al., 2015). Song et al. (2015) concluded that the ^{14}C ages of >30 cal ka BP from the Ili Basin are scattered between the 2% and 3%–4% modern carbon contamination lines. The problem of underestimation of radiocarbon ages also exists in humid regions. The contrast between ^{14}C ages using plant remains and quartz OSL ages is reported from the Dongjiang plain, southwest of the Chaoshan plain, with an age difference of more than 30 ka when dating sediments beyond ca. 33 ka BP (Guo et al., 2013). Similarly, using plant macrofossil to date Devensian fluvial sediments in lowland Britain, Briant and Bateman (2009) found that radiocarbon ages beyond 40 cal ka BP were remarkably younger than OSL ages. All conventionally pretreated ABA radiocarbon ages fall in the range of ca. 40–45 cal ka BP, while OSL dates fall between ca. 69 and 110 ka (Briant and Bateman, 2009). Likewise, results from Weichselian alluvial in the Netherlands also showed that all ^{14}C ages of Eerbeek-I below 2 m depth were infinite ages (>45.4 cal ka BP), while the OSL dates fall in ca. 49–102 ka at the same depth (Palstra et al., 2021).

It is suggested that plant remains are the ideal material for ^{14}C dating (Nilsson et al., 2001; Reimer, 2012; Väliranta et al., 2014), but ^{14}C ages in this study along with research from fluvial sediments (lowland Britain) (Briant and Bateman, 2009) and Weichselian alluvial (the Netherlands) (Palstra et al., 2021) demonstrated that it is challenging for ^{14}C dating when samples are >35 cal ka BP in practice. Extreme caution is needed to interpret the reliability of published ^{14}C ages beyond 40 ka BP. It is necessary to select plant materials that were most likely part of the original deposit (such as leaves or seeds) when feasible (Briant and Bateman, 2009). The influence of different geological environments on the ^{14}C dating source material should be considered when using ^{14}C ages to establish an age model (Zhang and Shi, 1989; Cheng et al., 2022). Combining radiocarbon dating with different dating techniques is suggested to obtain reliable results.

Luminescence dating has proven useful in addressing the upper age limit (beyond 35 cal ka BP) of radiocarbon dating. Quartz OSL has the advantages of rapid bleaching and signal stability. However, quartz encounters a problem of underestimating the true age at larger doses (150–250 Gy) (Lai, 2006; Wintle and Murray, 2006; Lai, 2010; Lai and Fan, 2014; Ou et al., 2014; Wang et al., 2018b; Li et al., 2020a; Li et al., 2020b; Murray et al., 2021; Xu et al., 2021). Underestimation of quartz OSL age due to saturation was found in estuarine and marine regions. D_e values of quartz OSL samples > 200 Gy from borehole TJC-1 in the western Bohai Sea, China, showed saturated ages beyond 80 ka (Long et al., 2022). Quartz OSL samples from core HPQK01 in Pearl River Delta have also shown that quartz OSL ages ranging from 125 ± 18 ka to 58 ± 6 ka are considered minimum ages due to the OSL saturation >150 Gy (Xu et al., 2022). D_e results (Table 2) show that seven quartz OSL and one polymineral sample have D_es up to 150 Gy,

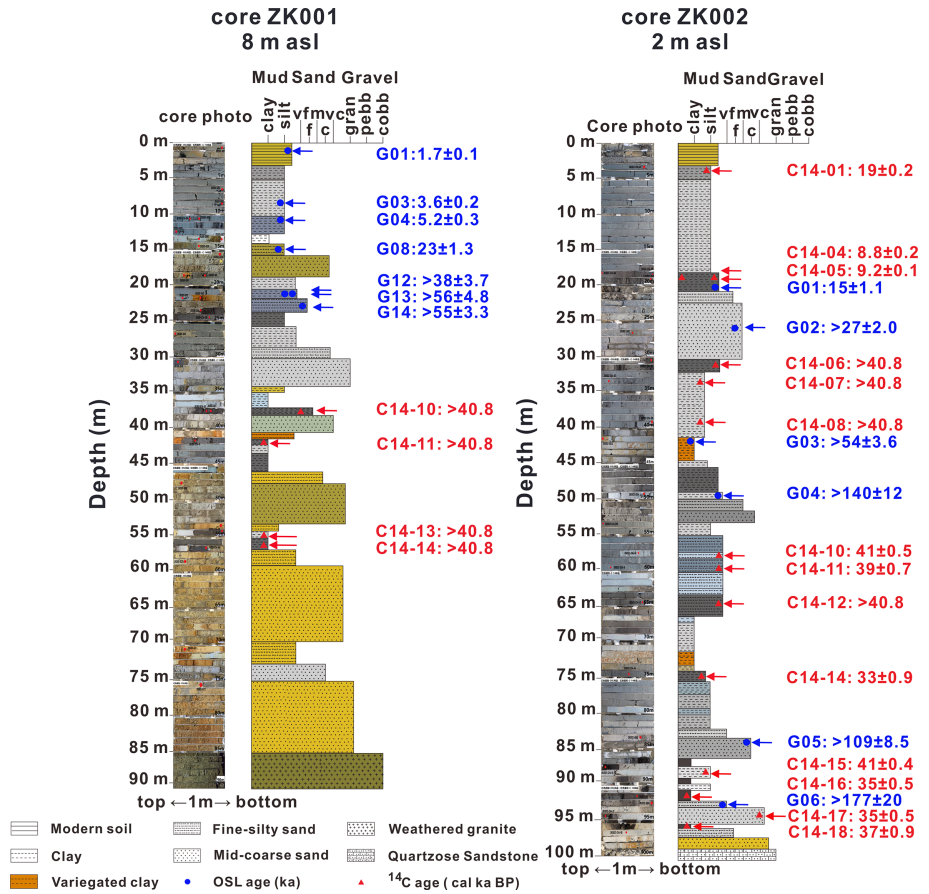

FIGURE 4
Profiles and ages of cores ZK001and ZK002. The red triangle represents the ^{14}C age; blue circle represents the OSL age.

including ZK001-G12 (>231 Gy, 21.2 m in depth), ZK001-G13 (>235 Gy, 21.5 m in depth), ZK001-G14 (>211Gy, 23.4 m in depth), ZK002-G02 (>153 Gy, 26.5 m in depth), ZK002-G03 (>204 Gy, 41.1 m in depth), ZK002-G04 (>191 Gy, 49.8 m in depth), ZK002-G05 (>280 Gy, 83.6 m in depth), and ZK002-G06 (>180 Gy, 93 m in depth). Usually, OSL growth curves can be fitted with a single saturating exponential function of the form $I(D)/I_s = (1 - (\exp - D/D_0))$, where I is the OSL signal intensity, I_s is the saturation intensity, D is the absorbed radiation dose, and D_0 is indicative of the onset of saturation (Singarayer and Bailey, 2003; Wintle and Murray, 2006; Wallinga and Cunningham, 2015). Wintle and Murray (2006) suggested that the reliable D_e should be less than 2^*D_0 when the OSL signal is about 15% below the saturation level based on the assumption of exponential growth. A representative growth curve of five aliquots up to 280 Gy for sample ZK002-G02 (Figure 5) was constructed to investigate the degree of saturation. When fitting a single exponential [$Y = 9.62^*(1 - \exp(-X/156.1))$] (Figure 5), the maximum reliable D_e of sample ZK002-G02 is 312 Gy (2^*D_0). The values of D_0 and 2^*D_0 for eight saturated samples are given in Table 3. The D_e values of samples ZK001-G12, ZK001-G13, and ZK001-G14 are greater than 2^*D_0 (Tables 2 and 3), indicating OSL saturation. As discussed previously, the saturation dose of estuarine samples is approximately 150–200 Gy (Long et al., 2022; Xu et al., 2022). Therefore, the D_es of five samples from core ZK002 are more likely to reach the saturation level, even if these values are lower than 2^*D_0 (Tables 2, 3). The obtained ages of these samples should be considered as minimum ages for paleoenvironmental reconstruction.

Late Quaternary chronological framework of cores ZK001 and ZK002 based on ^{14}C and OSL dating

The chronology of Quaternary deposits in the Chaoshan plain is lacking reliability since most previous work has relied essentially on a radiocarbon dating method confined to ca. 40 ka

TABLE 3 Values of D_0 and 2*D_0 for samples from core ZK001 and ZK002.

Sample ID	D_0 (Gy)	2*D_0 (Gy)
ZK001-G12	101	202
ZK001-G13	116	232
ZK001-G14	116	232
ZK002-G02	156	312
ZK002-G03	183	366
ZK002-G04	183	367
ZK002-G05	185	369
ZK002-G06	181	363

* represents a multiplication sign.

BP (Li et al., 1987; Li et al., 1988). Fossils of rhinoceros, giant pandas, and saber-toothed elephants from an alluvial layer in Jieyang County show that the deposition of the Quaternary sediments in the Chaoshan plain began as early as the middle Pleistocene (Chen, 1984b). On the contrary, some studies argue that the basal part of the Quaternary sediments (fluvial sediments, named the Nanshe Formation) in the Chaoshan plain was deposited no more than 55 ka BP based on ^{14}C, TL ages, and stratigraphic relationships (Chen, 1984a; Li et al., 1987; Li et al., 1988). According to the chronologies published so far, the Nanshe Formation is overlain by a lower marine unit (M2, also named the Jiali Formation) dated at MIS 3 based on ^{14}C (Li et al., 1987; Li et al., 1988). Zong et al. (2015) suggested that the global sea level during MIS 5e (ca. 130–120 ka) (Rohling et al., 2008) was possibly 3–5 m higher than the present sea level but dropped to 60–80 m below the present sea level (BSL) during MIS 3 (ca. 58–24 ka) (Bard et al., 1990; Yokoyama et al., 2001). The depositional surface was very close to the present sea level during the deposition of the lower marine sequence in the Chaoshan plain, as the sea level during MIS 5e was several meters higher than the present (Zong et al., 2015). Accordingly, Zong et al. (2015) demonstrated that the lower marine unit (M2) was deposited at a depth of around 45 to 80 m BSL; therefore, the actual age is likely to be older than MIS 5, rather than MIS 3. Subsequent studies from the Lianjiang plain, the southeastern part of the Chaoshan plain, have confirmed these findings using ESR and OSL (Song et al., 2012; Tang et al., 2018). The combination of ^{14}C, OSL, and ESR dating, of the lower marine unit (M2) from the Lianjiang plain, shows that the results are also at MIS 5 rather than MIS 3 (Song et al., 2012; Tang et al., 2018). ESR ages of the basal terrestrial layer from the core WYZK-06 (at a depth of ca.100–130 m) in the Lianjiang plain fall approximately within MIS 7 (ca. 243–190 ka) to MIS 6 (ca. 190–130 ka) (Song et al., 2012). Quartz OSL dates (>216 ka) from core CN-01 (23.57 m depth) in the Lianjiang plain also indicate that the basal terrestrial sediments were deposited mainly during a substage of MIS7 (Tang et al., 2018). In this study, the oldest quartz OSL age from core ZK002 in the Rongjiang plain (middle part of the Chaoshan plain) is >177 ± 20 ka (ZK002-G06, 93 m depth), which is much older than the results of previous studies (Chen, 1984a; Li et al., 1987; Li et al., 1988). The onset of deposition (consisting of coarse sand with

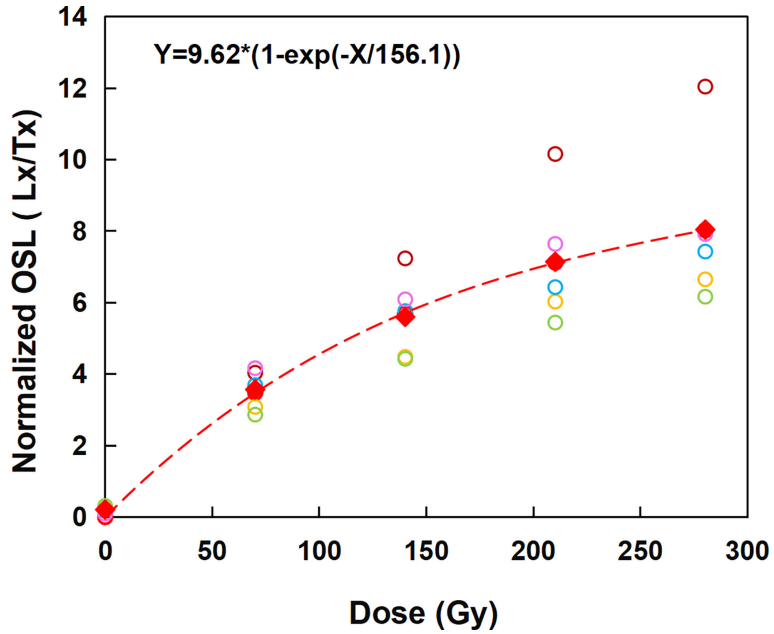

FIGURE 5
Growth curves of five aliquots up to 280 Gy for sample ZK002-G02. The dotted line denotes the average growth curve of the five aliquots.

gray-white color) in the Rongjiang plain is probably attributed to MIS 6 during the sea level lowstand, which was mainly influenced by fluvial processes.

The variegated clay is a weathered clay of fluvial deposits formed in a low-stand fluvial environment and is considered an important cycle boundary with hiatus in the coastal areas of the South China Sea. The results from the Pearl River Delta show that the first and second variegated clay layers were formed during the last glacial maximum (LGM) (ca. 30–20 ka) and MIS 4 (ca.74–60 ka), respectively (Xie et al., 2014). Variegated clay layers are also found in this study in cores ZK001 and ZK002. The hiatus (from ca. 23 ± 1.3 ka to 5.2 ± 0.3 ka) of core ZK001 occurred at a depth of ca. 10.5–14.5 m, with sediments composed of clay and variegated clay. Quartz OSL age (ZK001-G08, 23 ± 1.3 ka, 14.5 m depth) confirmed that variegated clay in this layer was deposited during the LGM in a low-stand fluvial environment (Figure 4). Hiatus (from ca.15 ka to 9.2 cal ka BP) was also observed in core ZK002 at ca. 19–20 m depth (Figure 4). The sediments in this layer are composed of fluvial sediments of gray-white fine sands without variegated clay deposited mainly during the LGM. Unlike core ZK001, two variegated clay layers are recorded in core ZK002. The first variegated clay layer (ca. 41–45 m in depth) was likely to be deposited during MIS 4 based on the quartz OSL age (ZK002-G03, >54 ± 3.6 ka) at a depth of 41.1 m. The second variegated clay layer (ca. 69–74 m in depth) has not been dated in this study due to suitable sample insufficiency. However, we speculate that this layer is likely deposited by a fluvial channel in a sea-level lowstand environment. An obvious lithologic change from fine-grained clay with gray-white color at the bottom to silt with deep gray color on the top can be seen across the hiatus in core ZK001 at a depth of ca.11–15 m. This variation in lithology is also recorded around the hiatus in core ZK002, from coarse sand with gravel in steel gray color at the bottom to middle-fine grain sand with gray color within a depth of ca. 19–30 m across the hiatus. The change in lithology around the depositional hiatus in both cores ZK001 and ZK002 reflects a change in the paleoenvironment from a fluvial to a coastal environment in response to sea-level change.

Conclusions

In this study, we applied ^{14}C and OSL methods to date the late Quaternary sediments from two cores, ZK001 and ZK002, from the Rongjiang plain. Chronological data based on ^{14}C and OSL dating methods from both cores show discrepancies in dates older than 35 cal ka BP. ^{14}C ages were significantly younger than their corresponding OSL ages, suggesting that ^{14}C dating is underestimated. Instead, OSL dating is well applicable to provide a reliable chronology older than 35 ka. In addition, the oldest OSL age (ZK002-G06, >177 ± 20 ka, 93 m depth) from core ZK002 indicates that the onset of sediment accumulation in the Rongjiang plain could be traced back to at least MIS 6.

Data availability statement

The original contributions presented in the study are included in the article/supplementary material. Further inquiries can be directed to the corresponding author.

Author contributions

JZ: Data curation, Visualization, Writing-Original draft. LK: Data curation, Investigation. MY: Data curation, Investigation. QS: Data curation, Investigation. MA: Writing- Reviewing and Editing. ZL: Conceptualization, Methodology, Supervision, Funding acquisition, Reviewing and Editing. All authors contributed to the article and approved the submitted version.

Funding

This research was supported by the China Geological Survey Project (Grants No. DD20160032-14), National Natural Science Foundation of China (Grants No. 41877438), STU Scientific Research Start-Up Foundation for Talents (NTF19003, NTF20006), and Innovation and Entrepreneurship Project of Shantou (2021112176541391).

Acknowledgments

We thank Xianmei Huang for the helpful discussions and Junxiang Miao for sample collection

Conflict of interest

The authors declare that the research was conducted in the absence of any commercial or financial relationships that could be construed as a potential conflict of interest.

Publisher's note

References

Agatova, A. R., Nepop, R. K., Bronnikova, M. A., Zhdanova, A. N., Moska, P., Zazovskaya, E. P., et al. (2020). Problems of 14C dating in fossil soils within tectonically active highlands of Russian Altai in the chronological context of the late pleistocene megafloods. *Catena* 195, 104764. doi: 10.1016/j.catena.2020.104764

Agatova, A., Nepop, R., Zazovskaya, E., Ovchinnikov, I., and Moska, P. (2019). Problems of developing the pleistocene radiocarbon chronology within high mountain terranes by the example of Russian Altai. *Radiocarbon* 61 (6), 2019–2028. doi: 10.1017/RDC.2019.83

Al-Saqarat, B. S., Abbas, M., Lai, Z., Gong, S., Alkuisi, M. M., Hamad, A. M. A., et al. (2021). A wetland oasis at wadi gharandal spanning 125–70 ka on the human migration trail in southern Jordan. *Quaternary Res.* 100, 154–169. doi: 10.1017/qua.2020.82

Bøtter-Jensen, L., Duller, G., Murray, A., and Banerjee, D. (1999). Blue light emitting diodes for optical stimulation of quartz in retrospective dosimetry and dating. *Radiat. Prot. Dosimetry* 84 (1-4), 335–340. doi: 10.1093/oxfordjournals.rpd.a032750

Bard, E., Hamelin, B., and Fairbanks, R. G. (1990). U-Th Ages obtained by mass spectrometry in corals from Barbados: sea level during the past 130,000 years. *Nature* 346 (6283), 456–458. doi: 10.1038/346456a0

Bird, M. I., Ayliffe, L. K., Fifield, L., Turney, C. S. M., Cresswell, R. G., Barrows, T. T., et al. (1999). Radiocarbon dating of "old" charcoal using wet oxidation stepped-combustion procedure. *Radiocarbon* 41 (2), 127–140. doi: 10.1017/S0033822200019482

Briant, R. M., and Bateman, M. D. (2009). Luminescence dating indicates radiocarbon age underestimation in late pleistocene fluvial deposits from eastern England. *J. Quaternary Sci.* 24 (8), 916–927. doi: 10.1002/jqs.1258

Chen, G. (1984a). Quaternary fault block movement in chao-shan plain. *South China J. Of Seismology* 4 (4), 001–018. doi: 10.13512/j.hndz.1984.04.001

Chen, W. (1984b). Several features for the development of sedimentary basin in chaoshan area, guangdong province. *South China J. Seismology* 4 (2), 20–30. doi: 10.13512/j.hndz.1984.02.004

Cheng, P., Burr, G. S., Zhou, W., Chen, N., Hou, Y., Du, H., et al. (2020). The deficiency of organic matter 14C dating in Chinese loess-paleosol sample. *Quaternary Geochronology* 56, 101051. doi: 10.1016/j.quageo.2019.101051

Cheng, P., Dong, J., Zhou, W., Song, Y., Zhou, J., Fan, Y., et al. (2022). Paleoclimatic implications of 14C age deviations in loess organic matter from xinjiang, Northwest China. *CATENA* 212, 106096. doi: 10.1016/j.catena.2022.106096

Chen, H. W., Lee, T. Y., and Wu, L. C. (2010). High-resolution sequence stratigraphic analysis of late quaternary deposits of the changhua coastal plain in the frontal arc-continent collision belt of central Taiwan. *J. OF Asian Earth Sci.* 39 (3), 192–213. doi: 10.1016/j.jseaes.2010.02.009

Gao, L., Long, H., Tamura, T., Hou, Y., and Shen, J. (2021). A~ 130 ka terrestrial-marine interaction sedimentary history of the northern jiangsu coastal plain in China. *Mar. Geology* 435, 106455. doi: 10.1016/j.margeo.2021.106455

Goodfriend, G. A., and Stipp, J. J. (1983). Limestone and the problem of radiocarbon dating of land-snail shell carbonate. *Geology* 11 (10), 575–577. doi: 10.1130/0091-7613(1983)11<575:LATPOR>2.0.CO;2

Guo, L., Wang, P., Zhang, K., Sheng, Q., Zhao, H., and Wang, C. (2013). OSL and ^{14}C ages of the late quaternary sediments in the east pearl river delta. *Geology China* 40 (6), 1842–1849.

Hajdas, I., Ascough, P., Garnett, M. H., Fallon, S. J., Pearson, C. L., Quarta, G., et al. (2021). Radiocarbon dating. *Nat. Rev. Methods Primers* 1 (1), 62. doi: 10.1038/s43586-021-00058-7

Hatté, C., Morvan, J., Noury, C., and Paterne, M. (2001). Is classical acid-alkali-acid treatment responsible for contamination? an alternative proposition. *Radiocarbon* 43 (2A), 177–182. doi: 10.1017/S003382220003798X

Lai, Z. (2006). Testing the use of an OSL standardised growth curve (SGC) for de determination on quartz from the Chinese loess plateau. *Radiat. Measurements* 41 (1), 9–16. doi: 10.1016/j.radmeas.2005.06.031

Lai, Z. (2010). Chronology and the upper dating limit for loess samples from luochuan section in the Chinese loess plateau using quartz OSL SAR protocol. *J. Asian Earth Sci.* 37 (2), 176–185. doi: 10.1016/j.jseaes.2009.08.003

Lai, Z., and Brueckner, H. (2008). Effects of feldspar contamination on equivalent dose and the shape of growth curve for OSL of silt-sized quartz extracted from Chinese loess. *Geochronometria* 30 (1), 49–53. doi: 10.2478/v10003-008-0010-0

Lai, Z., and Fan, A. (2014). Examining quartz OSL age underestimation for loess samples from luochuan in the Chinese loess plateau. *Geochronometria* 41 (1), 57–64. doi: 10.2478/s13386-013-0138-1

Lai, Z., Mischke, S., and Madsen, D. (2014). Paleoenvironmental implications of new OSL dates on the formation of the "Shell bar" in the qaidam basin, northeastern qinghai-Tibetan plateau. *J. Paleolimnology* 51 (2), 197–210. doi: 10.1007/s10933-013-9710-1

Lai, Z., and Ou, X. (2013). Basic procedures of optically stimulated luminescence (OSL) dating. *Prog. Geogr.* 32 (5), 683–693.

Lai, Z.-P., and Wintle, A. G. (2006). Locating the boundary between the pleistocene and the Holocene in Chinese loess using luminescence. *Holocene* 16 (6), 893–899. doi: 10.1191/0959683606hol980rr

Lai, Z., Wintle, A. G., and Thomas, D. S. (2007). Rates of dust deposition between 50 ka and 20 ka revealed by OSL dating at yuanbao on the Chinese loess plateau. *Palaeogeography Palaeoclimatology Palaeoecol.* 248 (3-4), 431–439. doi: 10.1016/j.palaeo.2006.12.013

Li, P. R., Huang, Z. G., and Zong, Y. Q. (1988). New views on geomorphological development of the hanjiang river delta. *Acta Geographica Sin.* 55 (1), 19–34. doi: 10.11821/xb198801003

Li, P., Huang, Z., Zong, Y., and Zhang, Z. (1987). *Hanjiang delta* (Beijing: Ocean Press).

Ling, K., Zhu, S., Li, R., Lai, Z., and Wang, J. (2021). A new lithostratigraphic unit of Quaternary in Chaoshan plain——Paotai Formation. *J. Stratigraphy* 46 (01), 1–8. doi: 10.19839/j.cnki.dcxzz.2021.0042

Li, Y., Song, Y., Orozbaev, R., Dong, J., Li, X., and Zhou, J. (2020c). Moisture evolution in central Asia since 26 ka: Insights from a kyrgyz loess section, Western tian shan. *Quaternary Sci. Rev.* 249, 106604. doi: 10.1016/j.quascirev.2020.106604

Liu, S. R. (1995). The divisions of guangdong province on new structure motion-also disussing the effect of new structure motion on coastline development. *Acta Scientiarum Naturalium Universitatis Sunyatseni* 34 (4), 93–99.

Liu, K., and Lai, Z. P. (2012). Chronology of Holocene sediments from the archaeological salawusu site in the mu us desert in China and its palaeoenvironmental implications. *J. Asian Earth Sci.* 45, 247–255. doi: 10.1016/j.jseaes.2011.11.002

Li, G., Wang, Z., Zhao, W., Jin, M., Wang, X., Tao, S., et al. (2020a). Quantitative precipitation reconstructions from chagan nur revealed lag response of East Asian summer monsoon precipitation to summer insolation during the Holocene in arid northern China. *Quaternary Sci. Rev.* 239, 106365. doi: 10.1016/j.quascirev.2020.106365

Li, G., Yang, H., Stevens, T., Zhang, X., Zhang, H., Wei, H., et al. (2020b). Differential ice volume and orbital modulation of quaternary moisture patterns between central and East Asia. *Earth Planetary Sci. Lett.* 530, 115901. doi: 10.1016/j.epsl.2019.115901

Long, Z., Wang, Z., Tu, H., Li, R., Wen, Z., Wang, Y., et al. (2022). OSL and radiocarbon dating of a core from the bohai Sea in China and implication for late quaternary transgression pattern. *Quaternary Geochronol.* 70, 101308. doi: 10.1016/j.quageo.2022.101308

Madsen, D. B., Lai, Z., Sun, Y., Rhode, D., Liu, X., and Jeffrey Brantingham, P. (2014). Late quaternary qaidam lake histories and implications for an MIS 3 "Greatest lakes" period in northwest China. *J. Paleolimnology* 51 (2), 161–177. doi: 10.1007/s10933-012-9662-x

Miller, G. H., and Andrews, J. T. (2019). Hudson Bay was not deglaciated during MIS-3. *Quaternary Sci. Rev.* 225, 105944. doi: 10.1016/j.quascirev.2019.105944

Murray, A., Arnold, L. J., Buylaert, J.-P., Guérin, G., Qin, J., Singhvi, A. K., et al. (2021). Optically stimulated luminescence dating using quartz. *Nat. Rev. Methods Primers* 1 (1), 72. doi: 10.1038/s43586-021-00068-5

Murray, A. S., and Olley, J. M. (2002). Precision and accuracy in the optically stimulated luminescence dating of sedimentary quartz: A status review. *Geochronometria* 21 (1), 1–16.

Murray, A. S., and Wintle, A. G. (2000). Luminescence dating of quartz using an improved single-aliquot regenerative-dose protocol. *Radiat. measurements* 32 (1), 57–73. doi: 10.1016/S1350-4487(99)00253-X

Nian, X., Zhang, W., Wang, Z., Sun, Q., Chen, J., Chen, Z., et al. (2018). The chronology of a sediment core from incised valley of the Yangtze river delta: Comparative OSL and AMS 14 c dating. *Mar. Geology* 395, 320. doi: 10.1016/j.margeo.2017.11.008

Nilsson, M., Klarqvist, M., Bohlin, E., and Possnert, G. (2001). Variation in 14C age of macrofossils and different fractions of minute peat samples dated by AMS. *Holocene* 11 (5), 579–586. doi: 10.1191/095968301680223521

Ou, X., Lai, Z., Zhou, S., and Zeng, L. (2014). Timing of glacier fluctuations and trigger mechanisms in eastern qinghai–Tibetan plateau during the late quaternary. *Quaternary Res.* 81 (3), 464–475. doi: 10.1016/j.yqres.2013.09.007

Palstra, S. W. L., Wallinga, J., Viveen, W., Schoorl, J. M., van den Berg, M., and van der Plicht, J. (2021). Cross-comparison of last glacial radiocarbon and OSL ages using periglacial fan deposits. *Quaternary Geochronology* 61, 101128. doi: 10.1016/j.quageo.2020.101128

Pigati, J. S., Quade, J., Wilson, J., Jull, A. J. T., and Lifton, N. A. (2007). Development of low-background vacuum extraction and graphitization systems for 14C dating of old (40–60ka) samples. *Quaternary Int.* 166 (1), 4–14. doi: 10.1016/j.quaint.2006.12.006

Prescott, J. R., and Hutton, J. T. (1994). Cosmic ray contributions to dose rates for luminescence and ESR dating: large depths and long-term time variations. *Radiat. measurements* 23 (2-3), 497–500. doi: 10.1016/1350-4487(94)90086-8

Ramsey, C. B., and Lee, S. (2013). Recent and planned developments of the program OxCal. *Radiocarbon* 55 (2), 720–730. doi: 10.1017/S0033822200057878

Reimer, P. J. (2012). Refining the radiocarbon time scale. *Science* 338 (6105), 337–338. doi: 10.1126/science.1228653

Reimer, P. J., Austin, W. E. N., Bard, E., Bayliss, A., Blackwell, P. G., Bronk Ramsey, C., et al. (2020). The IntCal20 northern hemisphere radiocarbon age calibration curve (0–55 cal kBP). *Radiocarbon* 62 (4), 725–757. doi: 10.1017/rdc.2020.41

Rhodes, E. J. (2011). Optically stimulated luminescence dating of sediments over the past 200,000 years. *Annu. Rev. Earth Planetary Sci.* 39, 461–488. doi: 10.1146/annurev-earth-040610-133425

Roberts, H., and Duller, G. A. (2004). Standardised growth curves for optical dating of sediment using multiple-grain aliquots. *Radiat. Measurements* 38 (2), 241–252. doi: 10.1016/j.radmeas.2003.10.001

Roberts, H., and Wintle, A. (2003). Luminescence sensitivity changes of polymineral fine grains during IRSL and [post-IR] OSL measurements. *Radiat. Measurements* 37 (6), 661–671. doi: 10.1016/S1350-4487(03)00245-2

Rohling, E. J., Grant, K., Hemleben, C., Siddall, M., Hoogakker, B., Bolshaw, M., et al. (2008). High rates of sea-level rise during the last interglacial period. *Nat. Geosci.* 1 (1), 38–42. doi: 10.1038/ngeo.2007.28

Singarayer, J., and Bailey, R. (2003). Further investigations of the quartz optically stimulated luminescence components using linear modulation. *Radiat. Measurements* 37 (4-5), 451–458. doi: 10.1016/S1350-4487(03)00062-3

Song, Y., Chen, W., Pan, H., Zhang, Z., He, Z., Chen, X., et al. (2012). Geological age of quaternary series in lianjiang plain. *J. Jilin Univ.(Earth Sci. Ed.)* 42, 154–161. doi: 10.13278/j.cnki.jjuese.2012.s1.040

Song, Y., Lai, Z., Li, Y., Chen, T., and Wang, Y. (2015). Comparison between luminescence and radiocarbon dating of late quaternary loess from the ili basin in central Asia. *Quaternary Geochronology* 30, 405–410. doi: 10.1016/j.quageo.2015.01.012

Stanley, D. J., and Chen, Z. (2000). Radiocarbon dates in china's Holocene Yangtze delta: record of sediment storage and reworking, not timing of deposition. *J. Coast. Res.* 16 (4), 1126–1132. Available at: http://www.jstor.org/stable/4300129

Sun, Y., Lai, Z., Madsen, D., and Hou, G. (2012). Luminescence dating of a hearth from the archaeological site of jiangxigou in the qinghai lake area of the northeastern qinghai-Tibetan plateau. *Quaternary Geochronology* 12, 107–110. doi: 10.1016/j.quageo.2012.01.010

Sun, J.-l., Xu, H. L., Wu, P., Wu, Y.-B., Qiu, X.-L., and Zhan, W.-H. (2007). Late quaternary sedimentological characteristics and sedimentary environment evolution in sea area between nan'ao and chenghai, eastern guangdong. *J. Trop. Oceanogr* 26, 30–36.

Tang, Y., Zheng, Z., Chen, C., Wang, M., and Chen, B. (2018). Evolution of the lian river coastal basin in response to quaternary marine transgressions in southeast China. *Sedimentary Geology* 366, 1–13. doi: 10.1016/j.sedgeo.2018.01.003

Väliranta, M., Oinonen, M., Seppä, H., Korkonen, S., Juutinen, S., and Tuittila, E.-S. (2014). Unexpected problems in AMS 14C dating of fen peat. *Radiocarbon* 56 (1), 95–108. doi: 10.2458/56.16917

Wallinga, J., and Cunningham, A. C. (2015). "Luminescence dating, uncertainties and age range," in *Encyclopedia of scientific dating methods* (Netherlands: Springer), 440–445.

Wang, Y., Chen, T. E. C., An, F., Lai, Z., Zhao, L., et al. (2018b). Quartz OSL and K-feldspar post-IR IRSL dating of loess in the huangshui river valley, northeastern Tibetan plateau. *Aeolian Res.* 33, 23–32. doi: 10.1016/j.aeolia.2018.04.002

Wang, Z., Zhao, H., Dong, G., Zhou, A., Liu, J., and Zhang, D. (2014). Reliability of radiocarbon dating on various fractions of loess-soil sequence for dadiwan section in the western Chinese loess plateau. *Front. Earth Sci.* 8 (4), 540–546. doi: 10.1007/s11707-014-0431-1

Wang, M., Zheng, Z., Gao, Q., Zong, Y., Huang, K., and Shi, S. (2018a). The environmental conditions of MIS5 in the northern south China Sea, revealed by n-alkanes indices and alkenones from a 39 m-long sediment sequence. *Quaternary Int.* 479, 70–78. doi: 10.1016/j.quaint.2017.08.026

Wang, M. Y., Zheng, Z., Huang, K. Y., Zong, Y. Q., Liu, Z. H., Peng, Z. L., et al. (2016). U-37(K ') temperature estimates from eemian marine sediments in the southern coast of hainan island, tropical China. *J. OF Asian Earth Sci.* 127, 91–99. doi: 10.1016/j.jseaes.2016.06.021

Wang, J. H., Zheng, Z., and Wu, C. Y. (1997). Sedimentary facies and paleoenvironmental evolution of the late quaternary in the chaoshan plain, East guangdong. *Acta Scientiarum Naturalium Universitatis Sunyatseni* 36 (1), 95–100.

Wintle, A. G., and Murray, A. S. (2006). A review of quartz optically stimulated luminescence characteristics and their relevance in single-aliquot regeneration dating protocols. *Radiat. Measurements* 41 (4), 369–391. doi: 10.1016/j.radmeas.2005.11.001

Xie, Y., Wang, Q., Long, G., Zhou, Y., Zheng, Z., and Huang, X. (2014). Transgressive sequence since the late pleistocene in xiaolan town–wanqingsha area, zhujiang river estuary. *J. Palaeogeogr.* 16, 835–852. doi: 10.7605/gdlxb.2014.06.067

Xu, X., Li, H., Tang, L., Lai, Z., Xu, G., Zhang, X., et al. (2020). Chronology of a Holocene core from the pearl river delta in southern China. *Front. Earth Sci.* 8 (262). doi: 10.3389/feart.2020.00262

Xu, Y., Tian, T., Shen, Q., Luo, L., and Lai, Z. (2021). Late quaternary aggradation of the datong basin in northern China revealed by OSL dating of core sediments and implications for groundwater arsenic pollution. *Catena* 207, 105650. doi: 10.1016/j.catena.2021.105650

Xu, X., Zhong, J., Huang, X., Li, H., Ding, Z., and Lai, Z. (2022). Age comparison by luminescence using quartz and feldspar on core HPQK01 from the pearl river delta in China. *Quaternary Geochronol.* 71, 101320. doi: 10.1016/j.quageo.2022.101320

Yi, L., Lai, Z., Yu, H., Xu, X., Su, Q., Yao, J., et al. (2013). Chronologies of sedimentary changes in the south b ohai s ea, c hina: constraints from luminescence and radiocarbon dating. *Boreas* 42 (2), 267–284. doi: 10.1111/j.1502-3885.2012.00271.x

Yim, W.-S., Ivanovich, M., and Yu, K.-F. (1990). Young age bias of radiocarbon dates in pre-Holocene marine deposits of Hong Kong and implications for pleistocene stratigraphy. *Geo-Marine Lett.* 10 (3), 165–172. doi: 10.1007/BF02085932

Yokoyama, Y., Esat, T. M., and Lambeck, K. (2001). Coupled climate and sea-level changes deduced from huon peninsula coral terraces of the last ice age. *Earth Planetary Sci. Lett.* 193 (3-4), 579–587. doi: 10.1016/S0012-821X(01)00515-5

Zhang, K., Ling, K., Liu, C., Yin, J., and Wu, Y. (2020). Holocene Diatom records in the rongjiang plain and implications for palaeoenvironmental changes. *Acta Scientiarum Naturalium Universitatis Sunyatseni* 59 (03), 32–42. doi: 10.13471/j.cnki.acta.snus.2020.03.004

Zhang, Y., and Shi, Y. (1989). Problems in Carbon-14 dating of Marine Sediments. *Mar. Sci.* (2), 28–32.

Zhao, J., Yin, X., Harbor, J. M., Lai, Z., Liu, S., and Li, Z. (2013). Quaternary glacial chronology of the kanas river valley, Altai mountains, China. *Quaternary Int.* 311, 44–53. doi: 10.1016/j.quaint.2013.07.047

Zheng, Z., and Li, Q. (2000). Vegetation, climate, and sea level in the past 55,000 years, hanjiang delta, southeastern China. *Quaternary Res.* 53 (3), 330–340. doi: 10.1006/qres.1999.2126

Zhou, Y. (2008). Primary geological hazards to the continental coast in shantou. *Trop. Geogr.* 28 (4), 331–337. doi: 10.13284/j.cnki.rddl.001168

Zong, Y. Q. (1987). Depositional cycles of the Quaternary in the Hanjiang delta. *Trop. Geogr.* 7 (2), 117–126.

Zong, Y., Huang, G., Li, X. Y., and Sun, Y. Y. (2015). Late Quaternary tectonics, sea-level change and lithostratigraphy along the northern coast of the South China Sea. *Geological Soc. London Special Publications* SP429, 421. doi: 10.1144/SP429.1

frontiers | Frontiers in Marine Science

TYPE Original Research
PUBLISHED 16 November 2022
DOI 10.3389/fmars.2022.1031456

OPEN ACCESS

EDITED BY
Fajin Chen,
Guangdong Ocean University, China

REVIEWED BY
Xiaozhong Huang,
Lanzhou University, China
Liang Zhou,
Jiangsu Normal University, China

*CORRESPONDENCE
Zhongping Lai
zhongping_lai@stu.edu.cn
Xiaolin Xu
xiaolinxu_geo@163.com

SPECIALTY SECTION
This article was submitted to Marine Biogeochemistry, a section of the journal Frontiers in Marine Science

RECEIVED 30 August 2022
ACCEPTED 20 October 2022
PUBLISHED 16 November 2022

CITATION
Lin P, Xu X, Yan C, Luo L, Abbas M and Lai Z (2022) Holocene sedimentary of the Pearl River Delta in South China: OSL and radiocarbon dating of cores from Zhuhai. *Front. Mar. Sci.* 9:1031456. doi: 10.3389/fmars.2022.1031456

Holocene sedimentary of the Pearl River Delta in South China: OSL and radiocarbon dating of cores from Zhuhai

Penghui Lin[1], Xiaolin Xu[1]*, Chaoyang Yan[2], Lan Luo[3], Mahmoud Abbas[1] and Zhongping Lai[1,4]*

[1]Institute of Marine Sciences, Guangdong Provincial Key Laboratory of Marine Disaster Prediction and Prevention, Shantou University, Shantou, China, [2]School of Earth Sciences, China University of Geosciences, Wuhan, China, [3]Department of Physics, Purdue Rare Isotope Measurement Laboratory, Purdue University, West Lafayette, IN, United States, [4]Southern Marine Science and Engineering Guangdong Laboratory (Zhuhai), Zhuhai, China

Deltaic sediments provide a window for investigating delta development processes and the effects of human activities. Despite the fact that numerous studies have been conducted in the Pearl River Delta (PRD), the chronological data are still very limited, which hinder the detailed interpretation of the sedimentary records. The current study aims to establish high-resolution chronology on two cores from Zhuhai using quartz optically stimulated luminescence (OSL) and radiocarbon (^{14}C) dating and, further, to reconstruct the Holocene sedimentary history of the PRD. Core P1-1 has a depth of 79 m and core P3-2 a depth of 60 m. Thirteen quartz OSL samples from P1-1 produced ages between 10.4 and 0.16 ka. Eight OSL and eight ^{14}C ages from P3-2 span from 10.7 to 0.3 ka. The OSL and ^{14}C dates show a good agreement above the depth of 26 m (1.4–0.3 ka), but with discrepancies at depths of 26–54 m. ^{14}C ages (10.7–8.1 ka) are generally older (up to c. 2 ka) than quartz OSL ages, and the discrepancy decreases with depth. The age model shows three phases of the sedimentation process: (1) rapid accumulation rates of 7.48 (P1-1) and 7.52 (P3-2) m/ka between c. 10.7 and 7.5 ka in response to high sea level, (2) followed by a significantly reduced rate of 2.24 m/ka (P1-1) and a depositional hiatus (P3-2) from 7.5 to 2.5 ka as a result of reduced sediment supply and strong scouring by tidal processes, and (3) high sedimentation rates of 8.86 (P1-1) and 9.07 (P3-2) m/ka since 2.5 ka associated with intensive human activities and weakening tidal hydrodynamics. This sedimentary pattern is also evident in many other Asian deltas.

KEYWORDS

Pearl River Delta, optically stimulated luminescence dating, radiocarbon dating, sedimentation rate, global change

1 Introduction

Coastal deltas are important sedimentary records for understanding palaeo-environmental changes in land–sea interaction areas in response to sea level variations (Saito et al., 1998; McLean and Tsyban, 2001; Woodroffe et al., 2006; Bianchi and Allison, 2009). Rapid sea level rise is considered as the main driver worldwide for the formation of deltas during the early Holocene (Stanley and Warne, 1994). The rising seawater penetrated into the incised valleys that formed during the last glacial maximum (LGM) (Hori and Saito, 2007; Tamura et al., 2009) and created an accommodation space for deltaic development (Zong et al., 2012; Xu et al., 2019; Wang et al., 2022). Subsequently, as the sea level forcing was almost eliminated by 7 cal ka BP, fluvial runoff and tidal currents controlled the delta progradation (Woodroffe, 2000; Saito et al., 2001; Hori et al., 2002; Zong et al., 2009a).

The Pearl River Delta (PRD) is one of the largest coastal deltas in the world. Boreholes and high-resolution seismic profiles demonstrated that a major marine sequence was deposited in the PRD during the Holocene (Fyfe et al., 1997; Owen et al., 1998; Zong et al., 2009a; Xu et al., 2020). Over the past two decades, several studies have attempted to reconstruct the Holocene evolutionary history of the PRD and elucidated the driving mechanisms by investigating the Holocene strata at different time scales and regional settings (Zong et al., 2009a; Zong et al., 2012; Wu et al., 2017; Xiong et al., 2018a; Fu et al., 2020; Xiong et al., 2020; Xu et al., 2020). For instance six stratigraphic transects from the head area through the central basin to northern estuaries were used to investigate the interactions between sea level rise, monsoon runoff, and the palaeo-landscape in the early Holocene (Zong et al., 2012). Middle Holocene studies have focused on the factors that led to low sedimentation rates and slow progradation in central deltaic plain (Zong et al., 2009a; Fu et al., 2020). For the late Holocene, Xiong et al. (2020) found a rise in land growth rate from 0.36–0.38 to 2.69–10.56 km^2/a, *i.e.*, accelerated coastline advances after c. 2.2 ka using historical archives, genealogical books, and modern survey data. It has been hypothesized to be triggered by agricultural activities and land reclamation with strong human influence, as shown by organic and inorganic geochemical indicators (Zong et al., 2010; Hu et al., 2013) and bathymetric data (Wu et al., 2016).

Despite the fact that a relatively clear understanding of Holocene landform development has been established based on numerous records mentioned above, studies on the sedimentation processes of the southern estuary are limited. The Modaomen estuary, for example, is the largest mouth of the Peal River (Huang et al., 1982; He et al., 2022), but relevant sedimentation research is scarce (Zong et al., 2009b; Lu et al., 2020). Earlier research suggested that sedimentary records from estuary sites could provide information about the palaeo-environment evolution in response to natural and human impacts during the Holocene (Wu et al., 2017; Xiong et al., 2018b; Chen et al., 2019). Therefore, a better knowledge of the deltaic–estuarine sedimentation process is of great importance and may shed light on the interpretation of the evolutionary history of the PRD.

An accurate chronology of delta sediments is pivotal to understanding palaeo-environmental changes. The published ages of the PRD sediments have mainly been based on radiocarbon dating (Huang et al., 1982; Li et al., 1991; Zong et al., 2006; Hu et al., 2013; Wu et al., 2017). However, the carbon reservoir effect of the carbonate-rich PRD region can yield abnormal ^{14}C ages by releasing negative particulate organic carbon to depositional process (Liu et al., 2017). For instance the ^{14}C ages are generally older than OSL ages at similar depths in core DA from the southern PRD, and this discrepancy might be caused by the carbon reservoir effect (Xu et al., 2020). In addition, reworking of carbon materials in deltas with complex hydrodynamics usually causes overestimation of radiocarbon ages, which can be abnormally old by up to 2 ka for surface samples (Yim et al., 2006; Kong et al., 2014). Recently, optically stimulated luminescence (OSL) dating has been recognized as an invaluable method for dating coastal sediments (Yi et al., 2012; Wang et al., 2013; Yi et al., 2014; Gao et al., 2016; Wang et al., 2018; Wang et al., 2019; Xu et al., 2020; Nian et al., 2021; Xu et al., 2022; Long et al., 2022; Wang et al., 2022). In addition, multi-dating technique, such as OSL and ^{14}C dating, has been applied in Holocene deltaic sediments, *e.g.*, from the Yangtze River delta (Nian et al., 2021) and the PRD (Xu et al., 2020), and found to be appropriate for establishing comprehensive chronostratigraphic sequences.

In this study, cores P1-1 and P3-2, drilled from the estuary of the southern PRD, were dated by OSL and accelerator mass spectrometry (AMS) ^{14}C techniques to build a high-resolution chronological framework. Together with the analyses of sedimentological characteristics and sedimentation rates, the Holocene sedimentary history of the PRD was reconstructed.

2 Study area and samples

2.1 Study area

The Pearl River delta is located in the south-central part of Guangdong Province and faces the South China Sea (Figure 1A). The palaeo-Pearl River had evolved to a configuration similar to the present in the early Miocene (He et al., 2020). During the late Quaternary, active faulting and differential uplifting processes resulted in an expansion of accommodation for receiving sediments from drainage basins and marine transgressions (Huang et al., 1982; Yu et al., 2016). Since the Holocene, the fault activity in the PRD became weaker, and the river system basically inherited the pattern before the last marine transgression (Yao et al., 2013). Limited by the altitude of

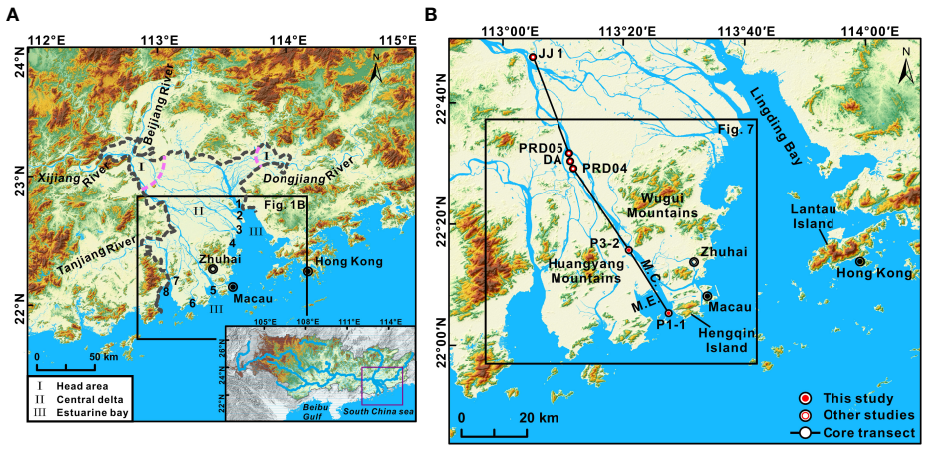

FIGURE 1
(A) Topographic characteristics of the Pearl River Delta (PRD). The PRD is divided into head area (zone I), central basin (zone II), and estuarine bay (zone III). Numbers 1–8 represent the eight estuaries of the PRD, namely, Humen, Jiaomen, Hongqimen, Hengmen, Modaomen, Jitimen, Hutiaomen, and Yamen, respectively. The inset figure shows the drainage system of the Pear River. **(B)** Topographic characteristics of the southern PRD, together with the locations of cores P1-1 and P3-2 (this study) and others reported: core JJ1 (Zong et al., 2009a), core PRD05 (Liu et al., 2008), core DA (Xu et al., 2020), and core PRD04 (Wei and Wu, 2011). M.E. and M.C. indicate the Modaomen Estuary and Modaomen Channel, respectively.

basement bedrock, the thickness of Quaternary sediments in the PRD varies between 10 to 40 m on average and reaches up to 60 m in incised valleys from Xijiang River and Beijiang River deltas (Huang et al., 1982).

The PRD can be divided into the head area, central delta, and estuarine bay according to the distance toward the sea (Figure 1A; Zong et al., 2009a). The water and sediments enter the dense distributary networks and flow out into the ocean through eight main outlets of the PRD (Wei and Wu, 2011). The outlets are morphologically separated by Wugui Mountains into two parts, *i.e.*, Humen, Jiaomen, Hongqimen, and Hengmen in the east and Modaomen, Jitimen, Hutiaomen, and Yamen in the west (Figure 1A). Among these outlets, the Modaomen estuary features the highest flood discharge and sand transport rates (He et al., 2022). The vast palaeo-Modaomen estuary contained a series of bi-directional jet systems which played an important role to the formation of sandbars and the major seaward channel of Xijiang River (Wu et al., 2007). The modern Modaomen estuary is under a stage of weakened estuarine jet (Wu et al., 2010). Due to the artificial deposition-promoting activities and land reclamations, the coastlines of the Modaomen estuary expanded seaward at a rate of 24 m/a during 1976–2006 AD (Zhang et al., 2015).

2.2 Sediment cores and sampling

Cores P1-1 [22°5′34.08″ N, 113°27′24.48″ E, 6 m below the present sea level (bpsl)] and P3-2 (22°15′42.99″ N, 113°20′59.87″ E, 0 m bpsl) are drilled from the southern PRD in Zhuhai, southeast China (Figure 1B). The submarine core P1-1 (79-m-long) was drilled in the Modaomen estuary, and core P3-2 (60-m-long) was drilled in the Zhupai sandbar in the Modaomen Channel. Core P1-1 is composed mainly of a sandy stratum (79.0–58.2 m) and a layer of clay and silt (58.2–0 m). Core P3-2 comprises a basement of dark gray cataclasite and breccia and its overlined sediments. The sediments are characterized by a sand layer (53.8–45.8 m) and a succession of clay and silt with sandy laminations (45.8–3.5 m). The top layer of light-yellow silt with plant roots is treated as modern soil (3.5–0 m).

Thirteen OSL samples were collected from cores P1-1 and eight from P3-2. Eight ^{14}C samples were collected from core P3-2. Part of the OSL and AMS ^{14}C data of core P3-2 were reported by Lu et al. (2020) (see Tables 1, 2 for details) to explore regional fault activity.

3 Methods

3.1 OSL dating

3.1.1 Sample preparation and equipment

The outer layer of OSL samples that might have been light-exposed was removed, and the remaining samples were successively treated to remove carbonate and organic matter with 10% HCl and 30% H_2O_2, respectively. The samples were then wet-sieved to obtain 38–63 or 90–125 μm fractions according to availability. In order to obtain pure quartz OSL grains, the 38–63-μm grains were treated with 35% H_2SiF_6 for

TABLE 1 Optically stimulated luminescence (OSL) dating results from cores P1-1 and P3-2.

Num.	Sample ID	Depth (m)	Grain size (μm)	Aliquot number	K (%)	Th (ppm)	U (ppm)	Moisture (%)	Dose rate (Gy/ka)	D_e (Gy)	Over-dispersion (%)	OSL age (ka)	References
1	P1-1-1	0.35	90–125	6[a]+10[b]	1.58	17.6	3.49	27.1 ± 5	2.97 ± 0.10	0.42 ± 0.04	39.97 ± 7.20	0.14 ± 0.02	This study
2	P1-1-2	4.95	90–125	6[a]+10[b]	1.67	14.4	3.57	28.4 ± 5	2.76 ± 0.10	0.92 ± 0.05	23.38 ± 3.79	0.33 ± 0.03	This study
3	P1-1-9	12.75	90–125	6[a]+12[b]	2.06	17	3.31	30.6 ± 5	3.01 ± 0.10	1.04 ± 0.02	6.81 ± 1.42	0.35 ± 0.01	This study
4	P1-1-17	27.95	90–125	6[a]+10[b]	1.85	18.1	3.21	36.9 ± 5	2.72 ± 0.09	9.33 ± 0.59	27.09 ± 4.85	3.43 ± 0.25	This study
5	P1-1-23	42.05	90–125	4[a]+10[b]	1.79	16.80	3.40	33.7 ± 5	2.70 ± 0.15[c]	24.71 ± 1.15	16.34 ± 3.19	9.15 ± 0.67	This study
6	P1-1-25	47.05	38–63	6[a]+12[b]	1.79	16.80	3.40	32.0 ± 5	2.80 ± 0.16[c]	24.54 ± 0.37	5.38 ± 1.14	8.78 ± 0.51	This study
7	P1-1-27	52.05	90–125	6[a]+12[b]	1.79	16.80	3.40	27.2 ± 5	2.87 ± 0.16[c]	29.45 ± 0.91	11.86 ± 2.10	10.26 ± 0.67	This study
8	P1-1-28	54.05	38–63	6[a]+12[b]	1.79	16.80	3.40	32.0 ± 5	2.74 ± 0.16[c]	28.57 ± 0.33	3.82 ± 1.00	10.41 ± 0.60	This study
9	P1-1-29	56.05	90–125	6[a]+12[b]	1.79	16.80	3.40	28.4 ± 5	2.89 ± 0.17[c]	27.24 ± 0.56	7.87 ± 1.48	9.42 ± 0.57	This study
10	P1-1-30	57.15	90–125	6[a]+12[b]	1.79	16.80	3.40	27.8 ± 5	2.84 ± 0.16[c]	28.03 ± 0.94	13.35 ± 2.33	9.86 ± 0.65	This study
11	P1-1-31	58.15	90–125	6[a]+10[b]	1.79	16.80	3.40	26.2 ± 5	2.89 ± 0.17[c]	29.48 ± 1.10	15.31 ± 2.80	10.19 ± 0.79	This study
12	P1-1-32	61.2	90–125	6[a]+12[b]	1.79	16.80	3.40	30.0 ± 5	2.79 ± 0.16[c]	25.24 ± 1.03	15.79 ± 2.81	9.04 ± 0.63	This study
13	P1-1-34	78.9	90–125	6[a]+12[b]	1.79	16.80	3.40	30.0 ± 5	2.79 ± 0.16[c]	22.7 ± 1.01	19.17 ± 3.40	8.14 ± 0.59	This study
14	P3-2-1	4.68	90–125	6[a]+12[b]	1.48	11.40	2.32	27.3 ± 5	2.25 ± 0.08	0.66 ± 0.04	24.03 ± 3.90	0.29 ± 0.02	Lu et al. (2020)
15	P3-2-2	8.05	90–125	6[a]+12[b]	1.15	10.90	2.10	20.6 ± 5	2.02 ± 0.08	0.79 ± 0.04	19.20 ± 3.01	0.39 ± 0.02	This study
16	P3-2-3	16.7	90–125	5[a]+11[b]	1.40	10.50	2.31	27.9 ± 5	2.06 ± 0.08	0.83 ± 0.04	19.39 ± 3.45	0.41 ± 0.02	Lu et al. (2020)
17	P3-2-4	25.3	90–125	6[a]+12[b]	1.98	16.50	2.97	32.6 ± 5	2.80 ± 0.10	3.93 ± 0.16	18.11 ± 2.83	1.41 ± 0.07	Lu et al. (2020)
18	P3-2-5	32.1	90–125	6[a]+12[b]	2.03	16.90	2.82	36.9 ± 5	2.72 ± 0.09	17.08 ± 0.54	12.83 ± 2.14	6.28 ± 0.29	Lu et al. (2020)
19	P3-2-6	39.7	90–125	6[a]+12[b]	1.93	14.40	2.28	31.8 ± 5	2.54 ± 0.09	24.43 ± 0.80	14.86 ± 2.33	9.61 ± 0.46	Lu et al. (2020)
20	P3-2-7	46.6	90–125	6[a]+11[b]	1.61	13.24	2.50	25.4 ± 5	2.42 ± 0.14[c]	23.93 ± 0.49	7.57 ± 1.48	9.90 ± 0.62	Lu et al. (2020)
21	P3-2-8	53.8	90–125	6[a]+11[b]	1.54	12.93	2.46	28.4 ± 5	2.28 ± 0.13[c]	16.46 ± 0.65	15.27 ± 2.72	7.23 ± 0.51	This study

The superscript "a" means aliquot numbers for single-aliquot regenerative-dose protocol, and the superscript "b" means aliquot numbers for standard growth curve protocol. The superscript "c" represents the dose rates based on the averaged content of U, Th, and K of existing samples.

about 2 weeks, and 90–125-μm grains were etched with 40% HF for 40 min. Both extracted quartz grains were washed with 10% HCl to eliminate fluoride precipitates. The purity of the quartz fractions was tested by OSL IR depletion ratio (Duller, 2003).

OSL measurements were performed on a Risø TL/OSL-DA-20 reader equipped with a $^{90}Sr/^{90}Y$ beta source. The quartz OSL signals were stimulated by a blue light (λ = 470 ± 20 nm) for 40 s at 130°C and recorded by 9235QA photomultiplier through a 7.5-mm Hoya U-340 filter.

3.1.2 D_e measurements

The equivalent dose (D_e) was determined by a combination of single-aliquot regenerative-dose (SAR) protocol (Murray and Wintle, 2000) and standard growth curve (SGC) protocol (Roberts and Duller, 2004; Lai, 2006; Lai et al., 2007). Yu

TABLE 2 Accelerator mass spectrometry 14C dating results from core P3-2.

Sample ID	Depth (m)	Dating material	^{14}C age (ka BP)	Cal date (2σ) (cal ka BP)	Median cal age(cal ka BP)	References
C-P3-2-1	3.2	Bulk organic	0.59 ± 0.03	0.65–0.58	0.6 ± 0.04	This study
C-P3-2-2	5.2	Plant fragment	0.19 ± 0.03	0.30–0.26	0.3 ± 0.02	Lu et al. (2020)
C-P3-2-3	12.5	Plant fragment	0.21 ± 0.03	0.30–0.27	0.3 ± 0.02	Lu et al. (2020)
C-P3-2-4	21.0	Plant fragment	1.10 ± 0.03	1.06–0.94	1.0 ± 0.07	Lu et al. (2020)
C-P3-2-5	28.0	Plant fragment	7.29 ± 0.03	8.20–8.02	8.1 ± 0.08	Lu et al. (2020)
C-P3-2-6	43.8	Bulk organic	9.21 ± 0.03	10.50–10.46	10.5 ± 0.02	Lu et al. (2020)
C-P3-2-7	45.6	Bulk organic	9.36 ± 0.03	10.66–10.51	10.6 ± 0.08	Lu et al. (2020)
C-P3-2-8	53.6	Plant fragment	9.43 ± 0.04	10.75–10.57	10.7 ± 0.09	Lu et al. (2020)

(2017) and Xu et al. (2020) suggested that it is feasible to choose the preheat temperature of 260°C with a duration of 10 s during the SAR–SGC protocol for dating deltaic samples from the PRD. In this study, a preheat at 260°C for 10 s, and a cut heat at 220°C for 10 s were chosen for regeneration doses and test doses, respectively. For each OSL sample, four to six aliquots were measured by SAR procedures to obtain SAR D_es and an SGC curve. The other 10–12 aliquots measured for nature signals (L_N/T_N) were fitted in SGC to get the SGC D_es. The final D_e was calculated using the arithmetic mean.

3.1.3 Dose rate measurements

The U, Th, and K content was determined using neutron activation analysis. The cosmic ray dose was calculated based on altitude, geographical location, and depth of the samples (Prescott and Hutton, 1994). An alpha efficiency factor (a-value) of 0.035 ± 0.003 was used for the 38–63-μm quartz grains (Lai et al., 2008). The water content was measured in the laboratory with an uncertainty of ±5% by considering the seasonal variation of precipitation and the palaeo-climate change in the study area. The D_rs and final ages were calculated on the website program of Dose Rate and Age Calculator (Durcan et al., 2015). Unfortunately, some samples lack measured dose rates due to samples loss. Based on the average value of the available sample data, we calculated the estimated dose rate of these lost samples. The estimated dose rates are generally consistent with the measured dose rates of an upstream core DA (Figure 1B), ranging from 2.09 to 2.92 (Table 1; Xu et al., 2020).

3.2 Radiocarbon dating

Four organic-rich sediments and five plant fragments from core P3-2 were collected for AMS ^{14}C dating. All these AMS ^{14}C samples were analyzed by the Beta Analytic Radiocarbon Dating Laboratory (Florida, USA). All conventional ages were calibrated using Intcal 09 curve (Reimer et al., 2009).

4 Results

4.1 Luminescence characteristics and OSL ages

Figure 2 shows the representative decay and dose–response curves of samples P1-1-17, P1-1-28, P3-2-4, and P3-2-6. The OSL signals of these samples decay rapidly within ~2 s, indicating the dominance of the fast component. The SGC can be fitted by a single exponential function with six regenerative dose aliquots, indicating that the SAR–SGC protocol is suitable to determine the D_e values of the PRD sediments.

Thirteen and eight quartz OSL ages are obtained from core P1-1 and P3-2, respectively. The OSL results are listed in Table 1 and shown in Figure 3. The OSL ages range from 10.41 ± 0.60 to 0.16 ± 0.03 ka within depths of 78.90–0.35 m for core P1-1 and from 9.90 ± 0.62 to 0.30 ± 0.02 ka within depths of 4.68–53.80 m for core P3-2 [the dating results were partly from Lu et al. (2020)]. Except for the outlier (the age of 7.05 ± 0.53 ka from the sample P3-2-8), the OSL results are generally consistent with stratigraphic order within errors.

4.2 Radiocarbon ages

The AMS ^{14}C ages of core P3-2 are summarized in Table 2 and Figure 3. The radiocarbon ages of the five plant fragment samples ranged between 10.7 ± 0.09 and 0.3 ± 0.02 cal ka BP within depths of 53.6–5.2 m. The three bulk organic samples yielded ages of 10.60 ± 0.08 cal ka BP (45.6 m), 10.50 ± 0.03 cal ka BP (43.8 m), and 0.06 ± 0.04 cal ka BP (3.2 m) [the dating results are partly from Lu et al. (2020)]. The ^{14}C sample C-P3-2-1 (3.2 m) yielded a slightly older age (0.6 ± 0.04 cal ka BP), which is considered as reworking material because of human re-filling and will not be considered in the sedimentation rate analyses. Except for this sample, the radiocarbon ages of core P3-2 are in agreement with stratigraphic order with depth.

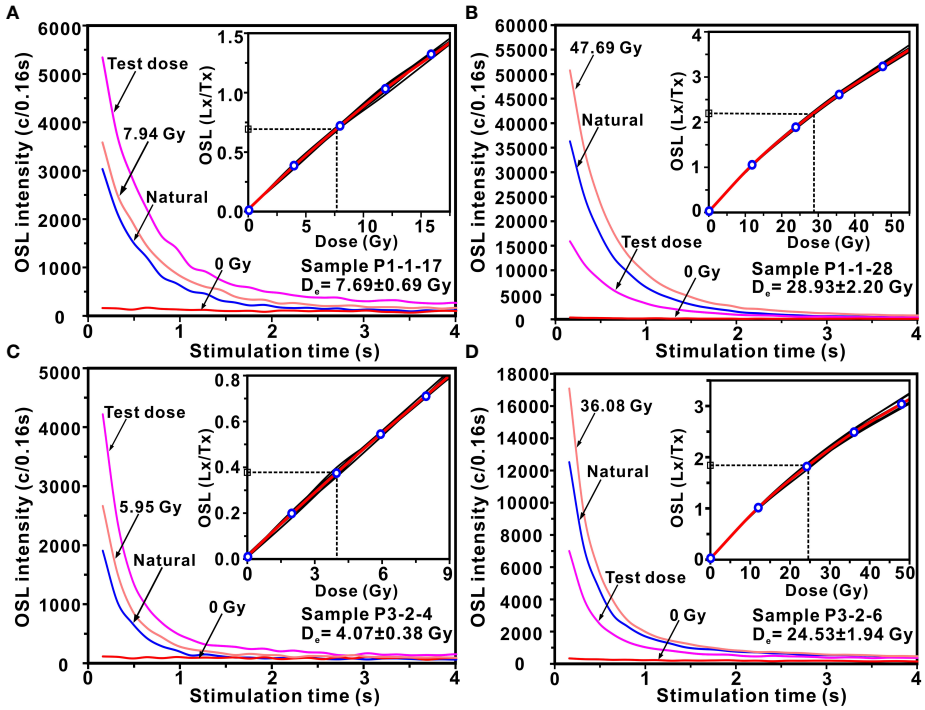

FIGURE 2
Luminescence properties of samples P1-1-17 **(A)**, P1-1-28 **(B)**, P3-2-4 **(C)**, and P3-2-6 **(D)**. The outset figure shows the decay curves of natural signal and the signals of regenerative dose, test dose, and 0 Gy, respectively. The inset figures show the dose–response curves (black lines) of each single-aliquot regenerative-dose aliquot and their standard growth curve (red line). The blue hollow cycles are the regenerative doses.

5 Discussions

5.1 Comparison of OSL and AMS ^{14}C ages

In this study, four quartz OSL ages and three AMS ^{14}C ages of plant fragments show a good agreement above 26 m depth (Figure 4). With increasing depth, the OSL sample P3-2-1 and the ^{14}C sample C-P3-2-2 yielded ages of around 0.3 ka at similar depths (within 0.5 m). The OSL samples P3-2-2, P3-2-3, and P3-2-4 show good constraints for ^{14}C samples C-P3-2-3 and C-P3-2-4 within a range of 0.3 to 1.4 ka. However, the fitting curve show age differences appearing below 26 m in depth, *i.e.*, before 1.4 ka (Figure 4). For instance a c. 2 ka age difference appears between ^{14}C sample C-P3-2-5 (28 m) with an age of 8.1 ± 0.1 cal ka BP and an OSL sample P3-2-5 (32.1 m) with an age of 6.3 ± 0.3 ka. About 30 km north of the study area, core DA revealed a similar age difference by fitting analysis, showing that ^{14}C ages are older (c. 0.5–1 ka) than OSL ages before c. 1.8 ka (Xu et al., 2020). As the depth increases, the age discrepancy of core P3-2 becomes less apparent (Figure 4). For instance at 45.6-m depth, the organic sample C-P3-2-7 (10.6 ± 0.08 cal ka BP) is consistent with the lower OSL sample P-3-2-7 (9.9 ± 0.6 ka) considering age errors.

Comparisons between OSL dating and ^{14}C dating results for Holocene deltaic sediments have been reported in many studies, but their results vary. Research in the eastern PRD showed a good consistency between the Holocene ^{14}C and quartz OSL ages, with only one obviously younger ^{14}C age (Guo et al., 2013). However, as indicated by core DA from the southern PRD, AMS ^{14}C ages are, in general, older than quartz OSL ages for Holocene sediments at similar depths (Xu et al., 2020). The radiocarbon results from the incised valley of the Yangtze River delta likewise showed a good agreement with those in core NT but were mostly older than their corresponding OSL ages in the adjacent core TZ (Nian et al., 2018). Two cores from the Thu Bo River delta in Vietnam revealed a general consistency of quartz OSL and feldspar IR_{50} ages with ^{14}C ages, except two reversal ^{14}C ages from shell samples in core VG-2 (Qiaola et al., 2022). The causes of these abnormal ^{14}C ages were generally considered as influenced by carbon reservoir effect or the reworking of dating materials (Nian et al., 2018; Xu et al., 2020; Qiaola et al., 2022).

Knowledge of the local surface ocean ^{14}C age offset relative to that of atmospheric CO_2, the so-called marine reservoir effect (ΔR), is essential for reliable radiocarbon dating of coastal sediments (Stuiver et al., 1986; Stuiver et al., 1998; Southon et al., 2002). During the Holocene, ΔR variations for the South

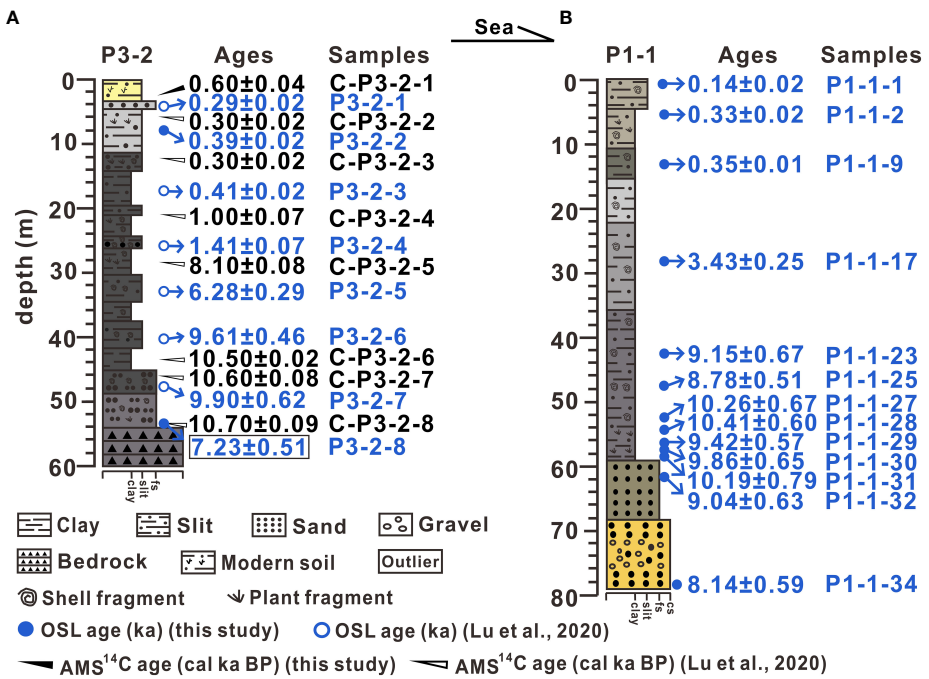

FIGURE 3
Lithology and chronology of cores P3-2 **(A)** and P1-1 **(B)**. Ages were obtained by optically stimulated luminescence (blue) and accelerator mass spectrometry ^{14}C (black) dating methods.

China Sea was c. 410 years for c. 8.1–5.5 ka and c. 200 years for c. 3.5–2 ka (Hua et al., 2020). Over the past 500 years, the mean ΔR values for the south/central South China Sea was determined as −25 ± 20 years, while the ΔR values for the South China coast are even lower, between −25 ± 20 and −149 ± 7 years (Southon et al., 2002). In addition to local marine reservoir, calibration of ^{14}C dating requires analysis of the "dead carbon" effect. For plant samples from drainage systems, the reservoir correction might be higher than that for marine samples due to additional carbonate input from bedrock and soil (Nakanishi et al., 2013). Especially in the carbonated-rich PRD where river flows likely carry old carbon from deeper sediments and sedimentary rocks, the "dead carbon" effect could be more obvious (Liu et al., 2017). For organic matter from the shallow water of the PRD, the high hydrodynamics will produce old carbon and result in abnormally old, by up to 2 ka, ^{14}C ages (Yim et al., 2006; Kong et al., 2014).

As discussed above, the abnormally older ^{14}C ages in this study are likely due to the combined effects of regional carbon reservoir and carbon reworking. The mechanisms of the temporal differences in reservoir effects in the PRD, as observed in core P3-2, require further investigation. Considering that deltas are dynamic and actively evolving complex systems, it remains prudent to date Holocene sediments by radiocarbon dating alone.

5.2 Sedimentary units and depositional setting

According to the sedimentary characteristics, the stratigraphic sequences are identified in ascending order of each core (Figure 5). In core P3-2, a 53.8-m-thick Holocene layer consisting of four sedimentary units unconformably overlies the bedrock (dark gray cataclasite and breccia) (Figure 5A). The lowermost unit P3-U1 (53.8–45.8 m) consists of gray-to-dark gray and medium-to-fine sand with few fragments of plant and shell. Such lithology is likely an indication of a tidal channel deposition environment during c. 10.7–9.9 ka. A similar unit was also recorded at around 10.8–10.5 cal ka BP in core ZK19 (31.4–34.8 m in depth) from Lingding Bay (Chen et al., 2019). Unit P3-U2 (45.8–26.1 m) overlies P3-U1 with a mutation in grain size of dark gray muddy clay intercalated with silty-sand laminations and more shell fragments. The lithological transition implies that the depositional setting might have changed from fluvial channel to an estuary/prodelta environment at nearly 10 ka due to sea level rise. Along the Modaomen Channel, a similar sedimentary environmental change was also recorded in upstream cores PRD05, PRD04 (Wei and Wu, 2011), and DA (Xu et al., 2020) during nearly the same time gap (Figure 6). Unit P3-U3 (26.1–11.4 m) shows dark gray muddy silt and sand containing

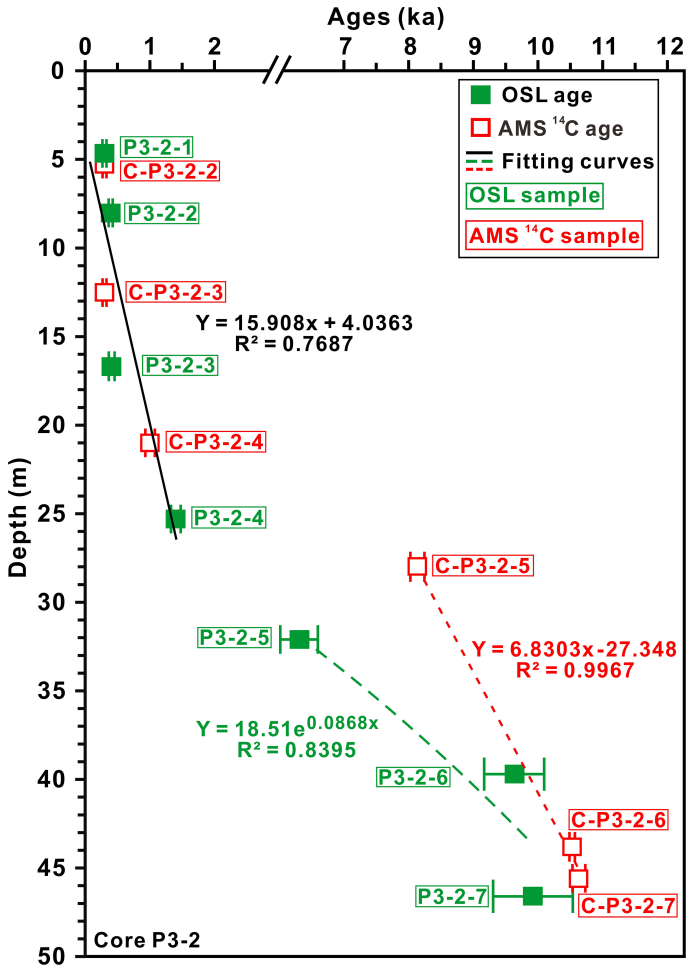

FIGURE 4
Comparison of optically stimulated luminescence (OSL) ages and accelerator mass spectrometry (AMS) ^{14}C ages of core P3-2 and the fitting curves for these ages. Circles and diamonds represent OSL and AMS ^{14}C ages, respectively. Ages above 26 m in depth are well fitted by a linear function (black). Below 26 m in depth, OSL and AMS ^{14}C were fitted by an exponential (green) and a linear function (red), respectively.

abundant shell fragments and coarse sand laminations at the bottom and fine sand laminations at depths of 14.0–11.4 m. The uppermost P3-U4 (11.4–3.5 m) is mainly composed of light gray silt with sporadic fine sandier lenses and a thin sandy layer (5.0–3.5 m). The upward fining-to-coarsening successions and sandier lenses indicate that this site might be deposited in a delta front (P3-U3) to a delta plain (P3-U4) setting (Figure 5A).

Core P1-1 is divided into four units (Figure 5B). The basal unit P1-U1 consists of two subunits. The lower unit P1-U1a (79–68 m) is an 11-m-thick layer of brownish-yellow coarse sand with well-rounded and poorly sorted grave sediments, and the upper unit P1-U1b (68.0–58.2 m) is grayish-yellow medium-to-fine sand. Unit P1-U1 is interpreted as indicating a fluvial channel environment. Unit P1-U2 (58.2–36.0 m) is unconformably in contact with the underlying strata with mutation in color and grain size, consisting of the dark gray color of silty clay, including abundant fragments of oyster shells and plant. The lithologic characteristics of this unit shows a similarity to P3-U2 and is considered as estuarine/bay deposits (Figure 5). This unit was also documented at depths of c. 51–32 m in the adjacent core ZK2, which has been interpreted as retrogradational estuary since c. 7.5 ka (Wei and Wu, 2011). Unit P1-U3 (36.0–22.0 m) appears as a continuous depositional succession of unit P1-U2 with gradual contact, composed of gray silty clay sediments with fewer shell fragments. Unit P1-U4 (22–0 m) occupies the uppermost part of core P1-1 with two subunits. The lower unit P1-U4a (22–16 m) is light gray clay sediments. The upper unit P1-U4b (16–0 m) consists of grayish-brown to brownish-gray clay and sandy silt with organic muddy sediments and a few plant fragments. The upward-coarsening trend and fewer shell fragments compared with P1-U2 probably represent a

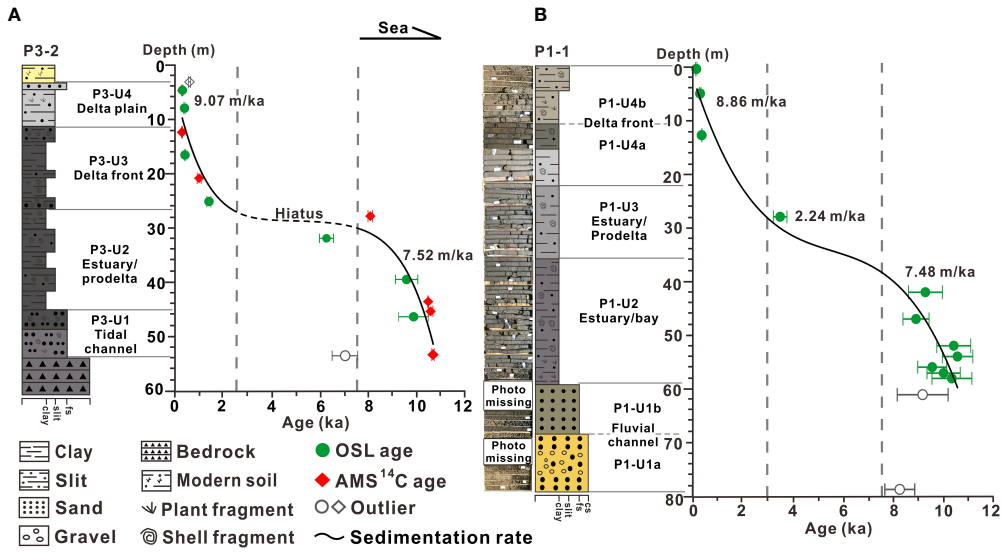

FIGURE 5
Stratigraphic divisions and age–depth model of cores P3-2 **(A)** and P1-1 **(B)**. Solid circles and diamonds represent optically stimulated luminescence (OSL) and accelerator mass spectrometry (AMS) ^{14}C ages, respectively. Hollow circles and diamonds represent the outlier ages of OSL and AMS ^{14}C, respectively. Mass accumulation rates were determined using the polynomial fit method.

transition from estuarine/prodelta (P1-U3) to delta front (P1-U4) environment.

In the present study, unit P1-U1 was subjected to a different depositional system (fluvial system) compared to other units in core P1-1 (Figure 5B) and is excluded from the sedimentation rate analysis. In both cores P3-2 and P1-1, three phases of depositional rate changes are identified based on the obtained ages (Figure 5). During 10.7–7.5 ka, cores P3-2 and P1-1 deposited at a rate of 7.52 and 7.48 m/ka, respectively. Between 7.5 and 2.5 ka, core P3-2 appeared as a sedimentary hiatus, whereas core P1-1 recorded a slow accumulation of 2.24 m/ka from 7.5 to 3.0 ka. The highest accumulation rate is recorded since 3 ka as c. 9.07 m/ka in core P3-2 and 8.86 m/ka in core P1-1.

5.3 Variation of sedimentation rates and its evolutional implication for the Pearl River Delta

5.3.1 Rapid sea level rise and accommodation space infilling

Theoretically, one (or more) sequence(s) of marine sediments can be found within a tectonically subsiding delta basin and its incision valley systems due to sea level changes during glacial-interglacial cycles (Dalrymple et al., 1992; Zaitlin et al., 1994; Nichol et al., 1996). Previous studies have shown that at least two marine sequences have been consistently recorded along the northern coast of the South China Sea during the Quaternary period (Huang et al., 1982; Yim et al., 2008; Zong et al., 2009b; Xu et al., 2022). As indicated by the Quaternary sedimentary record from the PRD, the catchment area was filled with older marine sediments that may have been deposited during MIS 5 (Yim et al., 1990; Zong et al., 2009b; Yu, 2017) as well as fluvial sands and gravels. This older sedimentary succession is generally overlined bedrock or gravel beds in the coastal areas of southern China (Zong et al., 2015). Since the LGM, when the sea level dropped to about 120 m bpsl (Chappell et al., 1996), the Pearl River cut through the older succession and created incised channels (Figure 7A; Zong et al., 2009b). Along with sea level that reached to about 40 m bpsl at c. 10 cal ka BP (Siddall et al., 2003; Xiong et al., 2018b), available space was created at many locations along the coast that would be filled during the Holocene (*e.g.*, Zong et al., 2012).

When the relative sea level in the study area rose from about 40 to 0 m bpsl between c. 10 and 7.5 ka (*e.g.*, Xiong et al., 2018b), seawater inundated the study area and transformed it into a broad estuary (Figure 7B). At the same time, units P1-U2 and P3-U1 deposited in an estuary environment at high accumulation rates of 7.47 m/ka in core P1-1 and 7.39 m/ka in core P3-2 (Figure 5). This rapid sedimentation during the early Holocene has been widely reported from the head (*e.g.*, Zong et al., 2009a; Fu et al., 2020), central deltaic plain (Zhao et al., 2014; Fu et al., 2020), and estuarine areas (Chen et al., 2019) in the context of rising sea level. Previous studies showed that the rate of relative sea level rise increased from about 16.4 m/ka by

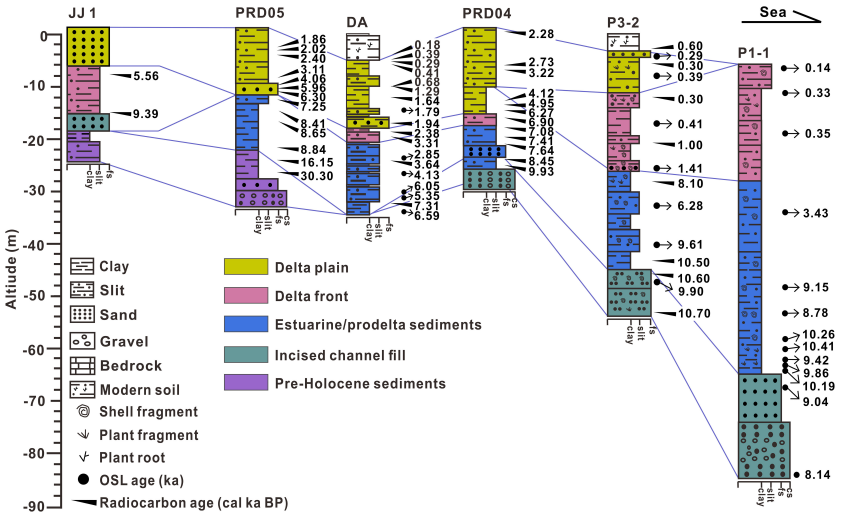

FIGURE 6
Stratigraphic transect along the palaeo-valley from central deltaic plain to the Modaomen estuary showing the distribution of major sediment facies and the seaward-thickening Holocene stratum. The stratigraphic analyses of cores were cited from previous studies, *i.e.*, JJ1 by Zong et al. (2009a), PRD05 by Liu et al. (2008), DA by Xu et al. (2020), and PRD04 by Wei and Wu (2011).

10.5 cal ka BP to a peak of c. 33.0 m/ka by 9.5 cal ka BP (Xiong et al., 2018b). As the seaward part of the delta, an estuarine area would respond immediately to rapid sea level rise, opening a narrow accommodation space for fast infilling of incision channels (Chen et al., 2019).

5.3.2 Slow sedimentation in the middle Holocene

As the relative sea level approximately ceased rising around 7.5 cal ka BP at a reduced rate of 1.7 m/ka (Xiong et al., 2018b), core P1-1 experienced a markedly slow deposition at 2.24 m/ka between 7.5 and 3.0 ka (Figure 5B). This slow sedimentation rate during the middle Holocene has been recorded in many boreholes from the PRD (Zong et al., 2009a; Hu et al., 2013; Liu et al., 2016; Fu et al., 2020). The reasons for this phenomenon are argued as follows: (1) low sediment supply as sedimentation was concentrated in the head area (Fu et al., 2020), (2) less sediment generation under the influence of the weakening summer monsoon (Zong et al., 2006), and (3) strong tidal currents that transported parts of suspended sediments into the South China Sea (Wu et al., 2007). Consequently, limited sediments entered the estuary and were frequently reworked by tidal currents. However, small and large former/present rocky islands across the estuary of the PRD may have contributed to the trapping of sediments to its adjacent areas (Huang et al., 1982; Wu et al., 2007; Fu et al., 2020). For example, in the bay area, core HKUV11 near Lantau Island (Hong Kong) recorded continuous sedimentation (1.8 m/ka) over the last 8 ka (Xiong et al., 2018b). Therefore, despite the low sediment supply from the PRD, Hengqin Island, adjacent to core P1-1 (Figure 1B), may have supplied some sediment flux and contributed to the formation of unit P1-U3 (36.0–23.0 m) during 7.5–3.0 ka (Figure 5).

However, core P3-2, located about 20 km upstream of core P1-1, underwent an exceptionally low depositional rate of 0.7 m/ka from 7.5 to 2.5 ka. This rate is much lower than that of downstream core P1-1 (2.24 m/ka) during 7.5–3.0 ka (Figure 5) and also those (1.27–5.66 m/ka) in modern PRD estuaries (Liu et al., 2014). Here the slow sedimentation process is interpreted as a depositional hiatus during the middle Holocene (Figure 5A). In Lingding Bay, sedimentary hiatuses from 8.1 to 2.2 cal ka BP and from 7.6 to 2.9 cal ka BP were also reported for cores ZK19 and ZK13, respectively (Chen et al., 2019). In these cores, the palaeo-morphology of the PRD is suggested as a key factor of the hiatuses (Chen et al., 2019). Core P3-2 is located in the Modaomen Channel and is surrounded by mountains (*e.g.*, Wugui Mountains) and rocky islands (Figures 1B, 7B), where a special hydrology called tidal bi-directional jet flows (TBJFs) likely developed as the extensive transgression passed through (Wu et al., 2010). However, core P1-1 is located in the mouth of the Modaomen estuary, where tidal currents are more complex and exhibit significant dissipation of tidal energy. Such a turbulent environment is unfavorable for the existence of TBJFs (Wei et al., 2011). Recent studies reported that the TBJFs enhanced seafloor erosion in the tidal channel with strong influx and convergence of palaeo-tidal energy (Wu et al., 2010; Wei and Wu, 2014). A long-term morphodynamic model simulated the tidal current velocity in the PRD, showing that the highest

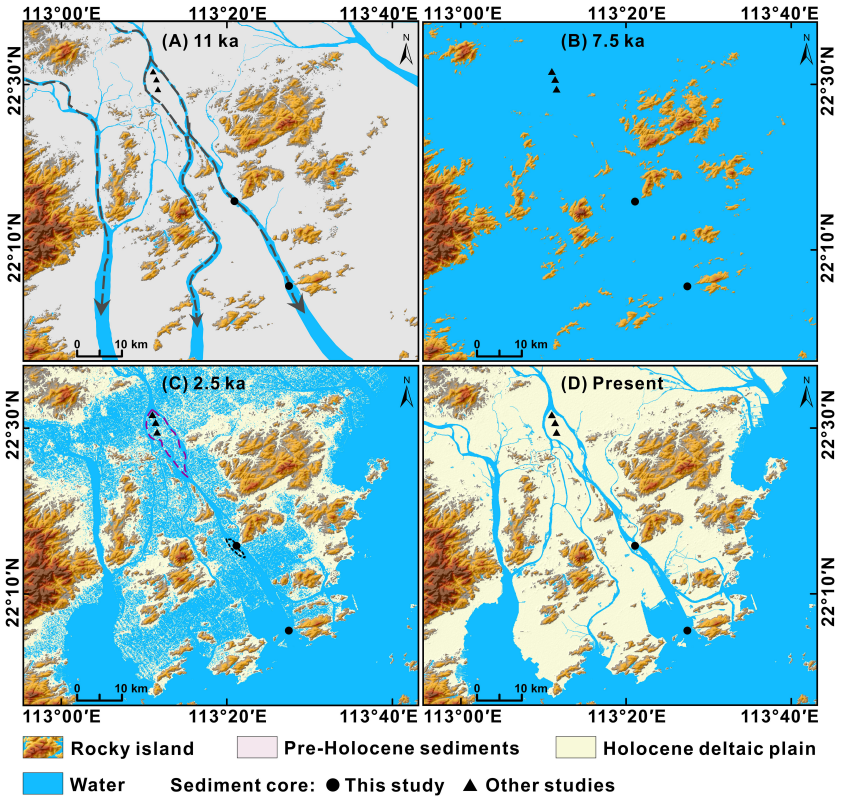

FIGURE 7
Changes of landscapes of the southern Pearl River Delta estuary during the Holocene. **(A)** Prior to the Holocene marine transgression, the fluvial forces (gray dotted arrows) created incised valleys and cut through pre-Holocene sediments. **(B)** Stage I occurred at the maximum transgressive invasion at c. 7.5 ka when seawater flooded the study area and turned it into estuarine condition, with only rocky islands emerging. **(C)** Stage II took place during marine regression when progradation of deltaic plain started since c. 2.5 ka, with sporadic wetlands. The dotted lines represent the developing formation of Daao sandbar (in purple) and Zhupai sandbar (in black). **(D)** In stage III of the past 2.5 ka, the Daao sandbar and Zhupai sandbar had already formed under rapid sedimentation rates. The black dots show the locations of the sediment cores by this study, with black triangles as those proposed by Liu et al. (2008); Xu et al. (2020), and Wei et al. (2011) from north to south, respectively.

velocity is distributed in the southwest side of Wugui Mountains from 6.0 to 2.5 ka (Wu et al., 2010). In core P3-2, such a strong hydrodynamic condition is characterized as plenty of coarse sand and shell fragments at depths of 26.1–26.3 m (Figure 3A). Together with the low sediment supply, core P3-2 has closely ceased deposition since 7.5 ka.

5.3.3 Accelerated sedimentation and formation of the deltaic plain

The slow sedimentation rate transitioned to rapid deposition (c. 9 m/ka) as observed in both cores in 2.5 ka (Figure 5). Extremely rapid deposition became a major feature of the PRD in a period of relative sea level stability during the late Holocene (Zong et al., 2010). As the central basin was gradually filled between c. 4 and 2 ka (Fu et al., 2020), the deltaic progradation shifted to the estuary area since c. 2.5 ka (Figure 7C), and the sedimentation rate was up to 5.33 m/ka, on average, for the Modaomen estuary (Wei et al., 2011). Human activities, such as catchment land clearance, diking, and reclamation, have been intensified since c. 2.2 ka (Cheng et al., 2018; Xiong et al., 2020; Chen et al., 2022), causing increased soil erosion (Yu et al., 2010; Hu et al., 2013; Zong et al., 2013; Zheng et al., 2021) and more sediment trapping (Figure 7C; Zong et al., 2009a; Xiong et al., 2020). In the estuary, cores B1/2 and HKUV1 showed that the progressively higher kaolinite contents since 2.5 ka were due to older weathered soils caused by widespread agriculture (Hu et al., 2013); core ZK19 showed a strengthening of anthropogenic influence, as evidenced by gradually positive $\delta^{13}C$ values at depths of 9.8–0 m (gray to brown and gray clayey silt) since c. 1.7 ka (Chen et al., 2019). A similar lithology was also recorded in unit P1-U4b (grayish brown to brownish gray, clay and silty sand) at the same time (Figure 5B). Therefore, the fast deposition in core P1-1 could be associated with intense human activities.

After c. 2.5 ka, the TBJFs has switched into a unidirectional jet flow with weakened tidal energy (Wu et al., 2010; Wu and

Wei, 2021), and thus sedimentation of core P3-2 in the Modaomen Channel is likely reactivated. Based on the records of cores PRD04 and PRD05, the tidal sand bodies of the Modaomen Channel were aerial in origin and formed sandbars (*e.g.*, Daao sandbar; Figure 7C) at c. 2.2 ka (He et al., 2007; Wei and Wu, 2011). About 34 km downstream from core PRD05, units P3-U3 and P3-U4 consist of coarsing upward sediments near the land surface, implying that core P3-2 had gradually switched from the underwater sand body to the modern deltaic floodplain (Zhupai sandbar; Figures 5A, 7C, D). Xu et al. (2020) suggested that the Modaomen estuary changed from a relatively open estuarine bay to a relatively closed one at 2 ka, which caused the reduction in outward sediment flux and trapping of a large amount of sediment. Hence, the rapid sedimentation in core P3-2 is more likely to be controlled by the weakening tidal process.

5.4 Comparison with other Asian megadeltas

The three-stage sedimentation model proposed in this study has also been recorded in many Asian deltas. For instance the high sediment accumulation rates in the Yangtze River delta vary between c. 4.2 and 10.0 m/ka during the early Holocene (c. 10–7 ka) (Nian et al., 2018; Wang et al., 2018; Jiang et al., 2020). In addition, in the Mekong River delta, a c. 20-m-thick layer of marine and brackish-water sediments were deposited in a short time period of 11.6–9.1 cal ka BP (Tamura et al., 2012). A similar sequence has also been recorded in the southern Ganges–Brahmaputra delta (Goodbred and Kuehl, 2000) and the Song Hong delta (Tanabe et al., 2006). Subsequently during c. 7–2 ka, the sedimentation rate was less than 5 m/ka, on average, in the Yangtze River delta, possibly because of the migration of the depo-center (Nian et al., 2018; Wang et al., 2018; Jiang et al., 2020). In the Mekong River delta, the accumulation rate significantly slowed down to 0.3–0.7 m/ka, which was associated with the lateral switching of distributary channels (Tamura et al., 2009; Tamura et al., 2012). The delta front progradation rate at 10 m bpsl also decelerated from 22 to 4 m/a in the Song Hong delta at c. 6 cal ka BP (Tanabe et al., 2006). In the last 2 ka, accelerated sedimentation and rapid coastline advances occurred in the Yangtze River and Mekong River deltas due to the gradual seaward shift of sandy shoals and bars (Tamura et al., 2012; Wang et al., 2018; Jiang et al., 2020).

Though under common monsoon climate and sea level histories, differences still exist in Asian megadeltas on their sedimentary characteristics. In contrast to the broad channel of the Yangtze River delta (60–70-km-wide in the estuary; Li et al., 2002), the palaeo-incised valley of the PRD is tight [30–60-km-wide for the central basin and estuarine bay; from Zong et al. (2012)]. In addition, the Holocene strata of the PRD show a trend of gradual thickening from the central deltaic plain to the estuary (Figure 6), with an average of about 20 m and more than 25 m in palaeo-incised valleys (Huang et al., 1982; Zong et al., 2009a). Nevertheless, cores P1-1 and P3-2 show remarkably thicker Holocene sediments (c. 79 and 54 m, respectively), which might be related to differences in palaeo-topography. The narrower and seaward deepening estuarine channel may have amplified the effects of monsoonal fluvial processes on the evolution of the estuarine-deltaic landscape during the early Holocene (Zong et al., 2012). Strong fluvial forcing was recorded at c. 10.6–9.6 ka in cores HKUV12 and HKUV10 along a palaeo-incised channel of Lantau Island, supported by a low abundance of brackish diatoms and high TOC content from terrigenous materials (Xiong et al., 2018a). Compared with tidal-dominated silt and clay deposited contemporaneously in other Asian deltas (Goodbred and Kuehl, 2000; Tamura et al., 2012; Wang et al., 2018), unit 1 (early-Holocene sequence) of cores P1-1 and P3-2 is dominated by sands (Figure 5), also implying a possible link to the strong fluvial influence.

Conclusions

In this study, cores P1-1 and P3-2 were drilled in the Southern PRD for OSL and AMS ^{14}C dating. The chronology of core P1-1 ranging from 10.4 to 0.16 ka is obtained from 13 quartz OSL ages. Core P3-2 spans from 10.7 to 0.3 ka, including eight OSL ages and eight AMS ^{14}C ages. The OSL and ^{14}C data shows a good consistency above 26 m (1.4–0.3 ka), but with differences at depths of 26–54 m where AMS ^{14}C ages (8.1–10.7 ka) are, in general, older (up to c. 2 ka) than quartz OSL ages. This discrepancy decreases with depths. Therefore, one should remain cautious when dating Holocene sediments by only radiocarbon dating.

The obtained chronostratigraphy reveals three stages of sedimentation: (1) high accumulation rates of 7.48 (P1-1) and 7.52 (P3-2) m/ka between c. 10.7 and 7.5 ka as a result of rapid marine transgression, (2) followed by an exceptionally decreasing rate 2.24 m/ka (P1-1) and a sedimentary hiatus (P3-2) during c. 7.5–2.5 ka as most sediments were trapped in the head area and due to strong scouring by tidal forces in the estuary, and (3) rapid sedimentation at a rate of c. 9 m/ka since c. 2.5 ka, which was related to intensive human activities and weakening tidal hydrodynamics.

This sedimentary model is also evident in other Asian deltas. However, differences still exist due to the unique palaeo-morphology of the PRD. The narrower and seaward deepening estuarine channel may have led to the stronger fluvial influence during the early Holocene.

Data availability statement

The original contributions presented in the study are included in the article/supplementary material. Further inquiries can be directed to the corresponding authors.

Author contributions

ZL organized the work. PL, XX, and ZL wrote the original draft. YC and PL measured the optically stimulated luminescence samples in the laboratory. MA revised and helped to improve the manuscript. PL, YC, XX, and ZL analyzed the data. ZL and LL collected the samples during drilling. All authors contributed to the article and approved the submitted version.

Funding

This research was supported by STU Scientific Research Start-Up Foundation for Talents (NTF19003 and NTF20006), and Innovation and Entrepreneurship Project of Shantou (2021112176541391).

Acknowledgments

We thank Chang Huang of Hong Kong University and Ping Wang of China Earthquake Administration for help in the field work.

Conflict of interest

The authors declare that the research was conducted in the absence of any commercial or financial relationships that could be construed as a potential conflict of interest.

Publisher's note

All claims expressed in this article are solely those of the authors and do not necessarily represent those of their affiliated organizations, or those of the publisher, the editors and the reviewers. Any product that may be evaluated in this article, or claim that may be made by its manufacturer, is not guaranteed or endorsed by the publisher.

References

Bianchi, T. S., and Allison, M. A. (2009). Large-River delta-front estuaries as natural "recorders" of global environmental change. *Proc. Natl. Acad. Sci. U.S.A.* 106 (20), 8085–8092. doi: 10.1073/pnas.0812878106

Chappell, J., Omura, A., Esat, T., McCulloch, M., Pandolfi, J., Yoko, O., et al. (1996). Reconciliation of late quaternary Sea levels derived from coral terraces at huon peninsula with deep Sea oxygen records. *Earth Planet1 Sci. Lett.* 144 (1), 227–236.

Cheng, Z., Weng, C., Steinke, S., and Mohtadi, M. (2018). Anthropogenic modification of vegetated landscapes in southern China from 6,000 years ago. *Nat. Geosci.* 11 (12), 939–943. doi: 10.1038/s41561-018-0250-1

Chen, X., Huang, X., Wu, D., Chen, J., Zhang, J., Zhou, A., et al. (2022). Late Holocene land use evolution and vegetation response to climate change in the watershed of xingyun lake, SW China. *Catena* 211. doi: 10.1016/j.catena.2021.105973

Chen, H. X., Wang, J. H., Khan, N. S., Waxi, L. L., Wu, J. X., Zhai, Y. H., et al. (2019). Early and late Holocene paleoenvironmental reconstruction of the pearl river estuary, south China Sea using foraminiferal assemblages and stable carbon isotopes. *Estua. Coast. Shelf. Sci.* 222, 112–125. doi: 10.1016/j.ecss.2019.04.002

Dalrymple, R. W., Zaitlin, B. A., and Boyd, R. (1992). Estuarine facies models; conceptual basis and stratigraphic implications. *J. Sediment. Res.* 62 (6), 1130–1146. doi: 10.1306/d4267a69-2b26-11d7-8648000102c1865d

Duller, G. A. T. (2003). Distinguishing quartz and feldspar in single grain luminescence measurements. *Radiat. Measure.* 37 (2), 161–165. doi: 10.1016/s1350-4487(02)00170-1

Durcan, J. A., King, G. E., and Duller, G. A. T. (2015). DRAC: Dose rate and age calculator for trapped charge dating. *Quatern. Geochronol.* 28, 54–61. doi: 10.1016/j.quageo.2015.03.012

Fu, S. Q., Xiong, H. X., Zong, Y. Q., and Huang, G. Q. (2020). Reasons for the low sedimentation and slow progradation in the pearl river delta, southern China, during the middle Holocene. *Mar. Geol.* 423. doi: 10.1016/j.margeo.2020.106133

Fyfe, J. A., Selby, I. C., Shaw, R., James, J. W. C., and Evans, C. D. R. (1997). Quaternary sea-level change on the continental shelf of Hong Kong. *J. Geolog. Soc.* 154 (6), 1031–1038. doi: 10.1144/gsjgs.154.6.1031

Gao, L., Long, H., Shen, J., Yu, G., and Yin, Y. (2016). High-resolution OSL dating of a coastal sediment sequence from the south yellow Sea. *Geochronometria* 43 (1), 143–154. doi: 10.1515/geochr-2015-0044

Goodbred, S. L., and Kuehl, S. A. (2000). The significance of large sediment supply, active tectonism, and eustasy on margin sequence development: Late quaternary stratigraphy and evolution of the Ganges–Brahmaputra delta. *Sediment. Geol.* 133 (3-4), 227–248. doi: 10.1016/s0037-0738(00)00041-5

Guo, L. T., Wang, P., Zhang, K., Sheng, Q., Zhao, H., and Wang, C. M. (2013). OSL and 14C ages of the late quaternary sediments in the east pearl river delta (in Chinese with English abstract). *Geol. China* 40 (6), 1842–1849.

He, J., Garzanti, E., Cao, L. C., and Wang, H. (2020). The zircon story of the pearl river (China) from Cretaceous to present. *Earth-Sci. Rev.* 201. doi: 10.1016/j.earscirev.2019.103078

He, Y., Liu, X. J., Duan, Z. H., Liu, C., Hou, P., Lu, C., et al. (2022). Long-term morphodynamic evolution in the modaomen estuary of the pearl river delta, south China. *Geomorphology* 398. doi: 10.1016/j.geomorph.2021.108057

He, Z., Mo, W., Liu, C., and Wu, ,. C. (2007). Formation of xijiang daao sha in pearl river delta during the postglacial period from a perspective of sedimentation rates and sediment grain size (in Chinese with English abstract). *J. Palaeogeogr.* 9 (3), 331–336. doi: 10.3969/j.issn.1671-1505.2007.03.011

Hori, K., and Saito, Y. (2007). An early Holocene sea-level jump and delta initiation. *Geophys. Res. Lett.* 34 (18). doi: 10.1029/2007gl031029

Hori, K., Saito, Y., Zhao, Q. H., and Wang, P. X. (2002). Architecture and evolution of the tide-dominated changjiang (Yangtze) river delta, China. *Sediment. Geol.* 146 (3-4), 249–264. doi: 10.1016/s0037-0738(01)00122-1

Hua, Q., Ulm, S., Yu, L., Clark, T. R., Nothdurft, L. D., Leonard, N. D., et al (2020). Temporal variability in the Holocene marine radiocarbon reservoir effect for the Tropical and South Pacific. *Quaternary Sci. Rev.* 249. doi: 10.1016/j.quascirev.2020.106613

Huang, Z. G., Li, P. R., Zhang, Z. Y., Li, K. H., and Qiao, P. N. (1982). *The formation and evolution of pearl river delta* (Guangzhou: Science Populariazaiton Press).

Hu, D. K., Clift, P. D., Böning, P., Hannigan, R., Hillier, S., Blusztajn, J., et al. (2013). Holocene Evolution in weathering and erosion patterns in the pearl river delta. *Geochem. Geophys. Geosyst.* 14 (7), 2349–2368. doi: 10.1002/ggge.20166

Jiang, F., Zhao, X. S., Chen, J., Liu, Y., Sun, Q. L., Chen, J., et al. (2020). Depocenter shift and en-echelon shoal development in the pre-Holocene incised valley of the Yangtze delta, China. *Mar. Geol.* 426. doi: 10.1016/j.margeo.2020.106212

Kong, D. M., Zong, Y. Q., Jia, G. D., Wei, G. J., Chen, M. T., and Liu, Z. H. (2014). The development of late Holocene coastal cooling in the northern south China Sea. *Quatern. Int.* 349, 300–307. doi: 10.1016/j.quaint.2013.08.055

Lai, Z. P. (2006). Testing the use of an OSL standardised growth curve (SGC) for determination on quartz from the Chinese loess plateau. *Radiat. Measure.* 41 (1), 9–16. doi: 10.1016/j.radmeas.2005.06.031

Lai, Z. P., Wintle, A. G., and Thomas, D. S. G. (2007). Rates of dust deposition between 50 ka and 20 ka revealed by OSL dating at yuanbao on the Chinese loess plateau. *Palaeogeogr. Palaeoclimatol. Palaeoecol.* 248 (3-4), 431–439. doi: 10.1016/j.palaeo.2006.12.013

Lai, Z. P., Zöller, L., Fuchs, M., and Brückner, H. (2008). Alpha efficiency determination for OSL of quartz extracted from Chinese loess. *Radiat. Measure.* 43 (2-6), 767–770. doi: 10.1016/j.radmeas.2008.01.022

Li, P. R., Lin, X. D., and Huang, G. Q. (1991). Geomorphological characteristics and development in East river delta (in Chinese with English abstract). *Geo. Res.* 10 (2).

Li, C., Wang, P., Sun, H., Zhang, J., Fan, D., and Deng, B. (2002). Late Quaternary incised-valley fill of the Yangtze delta (China): its stratigraphic framework and evolution. *Sedimentary Geology* 152 (1–2), 133–158. doi: 10.1016/s0037-0738(02)00066-0

Liu, Y. L., Gao, S., Wang, Y. P., Yang, Y., Long, J. P., Zhang, Y. Z., et al. (2014). Distal mud deposits associated with the pearl river over the northwestern continental shelf of the south China Sea. *Mar. Geol.* 347, 43–57. doi: 10.1016/j.margeo.2013.10.012

Liu, C. L., TFursich, F., Dong, Y. X., Che, X. G., Chen, L., and Zhuang, C. (2008). High resolution ostracod records of borehole PRD05 and the late quaternary palaeoenvironment in the pearl river delta (in Chinese with English abstract). *J. Palaeogeogr.* 10 (3), 313–322.

Liu, C. Y., Yin, J., Liu, C. L., Huang, Y., and Wu, Y. Q. (2016). Holocene Mollusc records and palaeoenvironmental changes in the pearl river delta (in Chinese with English abstract). *Trop. Geogr.* 36 (3), 355–363. doi: 10.13284/j.cnki.rddl.002830

Liu, Z. H., Zhao, M., Sun, H. L., Yang, R., Chen, B., Yang, M. X., et al. (2017). "Old" carbon entering the south China Sea from the carbonate-rich pearl river basin: Coupled action of carbonate weathering and aquatic photosynthesis. *Appl. Geochem.* 78, 96–104. doi: 10.1016/j.apgeochem.2016.12.014

Long, Z. R., Wang, Z. B., Tu, H., Li, R. H., Wen, Z. H., Wang, Y. X., et al. (2022). OSL and radiocarbon dating of a core from the bohai Sea in China and implication for late quaternary transgression pattern. *Quatern. Geochronol.* 70. doi: 10.1016/j.quageo.2022.101308

Lu, B. H., Wang, P., Wang, H. Y., Lai, Z. P., Deng, Z. H., Bi, L. S., et al. (2020). Latest progress on activity of heshan-modaomen segment, xijiang fault. *Seismol. Geol.* 42 (6), 1370–1384. doi: 10.3969/j.issn.0253-4967.2020.06.007

McLean, R. F., and Tsyban, A. (2001). "Coastal zones and marine ecosystems," in *Climate change 2001: impacts, adaptation, and vulnerability*. Eds. J. J. Carthy, O. F. Canziani, N. A. Leary, D. J. Dokken and K. S. White (London: Cambridge University Press), 343–379.

Murray, A. S., and Wintle, A. G. (2000). Luminescence dating of quartz using an improved single-aliquot regenerative-dose protocol. *Radiat. Measure.* 32 (1), 57–73. doi: 10.1016/s1350-4487(99)00253-x

Nakanishi, T., Hong, W., Sung, K. S., and Lim, J. (2013). Radiocarbon reservoir effect from shell and plant pairs in Holocene sediments around the yeongsan river in Korea. *Nucl. Instruments Methods Phys. Res. Section B: Beam Interact. Materials Atoms* 294, 444–451. doi: 10.1016/j.nimb.2012.09.025

Nian, X., Zhang, W., Wang, Z., Sun, Q., and Chen, Z. (2021). Inter-comparison of optically stimulated luminescence (OSL) ages between different fractions of Holocene deposits from the Yangtze delta and its environmental implications. *Mar. Geol.* 432. doi: 10.1016/j.margeo.2020.106401

Nian, X. M., Zhang, W. G., Wang, Z. H., Sun, Q. L., Chen, J., and Chen, Z. Y. (2018). Optical dating of Holocene sediments from the Yangtze river (Changjiang) delta, China. *Quatern. Int.* 467, 251–263. doi: 10.1016/j.quaint.2018.01.011

Nichol, S. L., Boyd, R., and Penland, S. (1996). Sequence stratigraphy of a coastal-plain incised valley estuary: Lake calcasieu, Louisiana. *J. Sediment. Res.* 66. doi: 10.1306/d426841e-2b26-11d7-8648000102c1865d

Owen, R. B., Neller, R. J., Shaw, R., and Cheung, P. C. T. (1998). Late quaternary environmental changes in Hong Kong. *Palaeogeogr. Palaeoclimatol. Palaeoecol.* 138 (1-4), 151–173. doi: 10.1016/s0031-0182(97)00129-6

Prescott, J. R., and Hutton, J. T. (1994). Cosmic ray contributions to dose rates for luminescence and ESR dating: Large depths and long-term time variations. *Radiat. Measure.* 23 (2-3), 497–500. doi: 10.1016/1350-4487(94)90086-8

Qiaola, S., Nguyen, T. M. L., Ta, T. K. O., Nguyen, V. L., Gugliotta, M., Saito, Y., et al. (2022). Luminescence dating of Holocene sediment cores from a wave-dominated and mountainous river delta in central Vietnam. *Quatern. Geochronol.* 70. doi: 10.1016/j.quageo.2022.101277

Reimer, P. J., Baillie, M. G. L., Bard, E., and Bayliss, A. (2009). INTCAL09 and Marine09 radiocarbon age calibration curves, 0-50000years. *Radiocarbon* 51 (4), 1111–1150. doi: 10.1017/S0033822200048864

Roberts, H. M., and Duller, G. A. T. (2004). Standardised growth curves for optical dating of sediment using multiple-grain aliquots. *Radiat. Measure.* 38 (2), 241–252. doi: 10.1016/j.radmeas.2003.10.001

Saito, Y., Katayama, H., Ikehara, K., Kato, Y., Matsumoto, E., Oguri, K., et al. (1998). Transgressive and highstand systems tracts and post-glacial transgression, the East China Sea. *Sediment. Geol.* 122 (1-4), 217–232. doi: 10.1016/s0037-0738(98)00107-9

Saito, Y., Yang, Z. S., and Hori, K. (2001). The huanghe (Yellow river) and changjiang (Yangtze river) deltas: a review on their characteristics, evolution and sediment discharge during the Holocene. *Geomorphology* 41 (2-3), 219–231. doi: 10.1016/s0169-555x(01)00118-0

Siddall, M., Rohling, E. J, Almogi-Labin, A., Hemleben, C., Meischner, D., Schmelzer, I., et al (2003). Sea-level fluctuations during the last glacial cycle. *Nature* 423 (6942), 853–858. doi: 10.1038/nature01690

Southon, J., Kashgarian, M., Fontugne, M., Metivier, B., and W-S Yim, W. (2002). Marine reservoir corrections for the Indian ocean and southeast Asia. *Radiocarbon* 44 (1), 167–180. doi: 10.1017/s0033822200064778

Stanley, D. J., and Warne, A. G. (1994). Worldwide initiation of holocene marine deltas by deceleration of sea-level rise. *Science* 265 (5169), 228–231. doi: 10.1126/science.265.5169.228

Stuiver, M., Pearson, G. W., and Braziunas, T. (1986). Radiocarbon age calibration of marine samples back to 9000 Cal yr BP. *Radiocarbon* 28 (2B), 980–1021. doi: 10.1017/s0033822200060264

Stuiver, M., Reimer, P. J., and Braziunas, T. F. (1998). High-precision radiocarbon age calibration for terrestrial and marine samples. *Radiocarbon* 40 (3), 1127–1151. doi: 10.1017/s0033822200019172

Tamura, T., Saito, Y., Nguyen, V. L., Ta, T. K. O., Bateman, M. D., Matsumoto, D., et al. (2012). Origin and evolution of interdistributary delta plains; insights from Mekong river delta. *Geology* 40 (4), 303–306. doi: 10.1130/g32717.1

Tamura, T., Saito, Y., Sieng, S., Ben, B., Kong, M., Sim, I., et al. (2009). Initiation of the Mekong river delta at 8 ka: evidence from the sedimentary succession in the Cambodian lowland. *Quatern. Sci. Rev.* 28 (3-4), 327–344. doi: 10.1016/j.quascirev.2008.10.010

Tanabe, S., Saito, Y., Lan Vu, Q., Hanebuth, T. J. J., Lan Ngo, Q., and Kitamura, A. (2006). Holocene Evolution of the song Hong (Red river) delta system, northern Vietnam. *Sediment. Geol.* 187 (1-2), 29–61. doi: 10.1016/j.sedgeo.2005.12.004

Wang, Z. H., Jones, B. G., Chen, T., Zhao, B. C., and Zhan, Q. (2013). A raised OIS 3 sea level recorded in coastal sediments, southern changjiang delta plain, China. *Quatern. Res.* 79 (3), 424–438. doi: 10.1016/j.yqres.2013.03.002

Wang, Z. H., Saito, Y., Zhan, Q., Nian, X. M., Pan, D. D., Wang, L., et al. (2018). Three-dimensional evolution of the Yangtze river mouth, China during the Holocene: impacts of sea level, climate and human activity. *Earth-Sci. Rev.* 185, 938–955. doi: 10.1016/j.earscirev.2018.08.012

Wang, Z. B., Yang, S. Y., Tang, H. Y., Zheng, Y. L., Wang, H. Y., Zhang, Z. X., et al. (2022). Revisit the sedimentary stratigraphic evolution and environmental changes on the outer shelf of the East China Sea since MIS 5. *Front. Mar. Sci.* 9. doi: 10.3389/fmars.2022.863245

Wang, F., Zhang, W. G., Nian, X. M., Ge, C., Zhao, X. Q., Cheng, Q. Z., et al. (2019). Refining the late-Holocene coastline and delta development of the northern Yangtze river delta: Combining historical archives and OSL dating. *Holocene* 29 (9), 1439–1449. doi: 10.1177/0959683619854522

Wei, X., Mo, W. Y., and Wu, C. Y. (2011). Analysis on the sedimentation rates and depositional environment of the pearl river delta area since Holocene. *Acta Sedimentol. Sin.* 29 (2), 328–335. doi: 10.14027/j.cnki.cjxb.2011.02.017

Wei, X., and Wu, C. (2011). Holocene Delta evolution and sequence stratigraphy of the pearl river delta in south China. *Sci. China Earth Sci.* 54 (10), 1523–1541. doi: 10.1007/s11430-011-4238-6

Wei, X., and Wu, C. Y. (2014). Long-term process-based morphodynamic modeling of the pearl river delta. *Ocean. Dynamics* 64 (12), 1753–1765. doi: 10.1007/s10236-014-0785-7

Woodroffe, ,. C. D., Nicholls, R. J., Saito, Y., Chen, Z., and Goodbred, S. L. (2006). "Landscape variability and the response of Asian megadeltas to environmental change," in *Global change and integrated coastal management* (Berlin: Springer), 277–314. doi: 10.1007/1-4020-3628-0_10

Woodroffe, C. D. (2000). Deltaic and estuarine environments and their late quaternary dynamics on the sunda and sahul shelves. *J. Asian Earth Sci.* 18 (4), 393–413. doi: 10.1016/s1367-9120(99)00074-7

Wu, C. Y., Ren, J., Bao, Y., Lei, Y. P., and Shi, H. Y. (2007). "A long-term morphological modeling study on the evolution of the pearl river delta, network system, and estuarine bays since 6000 yr B.P," in *Coastline changes: Interrelation of*

climate and geological processes (Colorado: Geological Society of America), 426, 199–210.

Wu, Z. Y., Saito, Y., Zhao, D. N., Zhou, J. Q., Cao, Z. Y., Li, S. J., et al. (2016). Impact of human activities on subaqueous topographic change in lingding bay of the pearl river estuary, China, during 1955-2013. *Sci. Rep.* 6, 37742. doi: 10.1038/srep37742

Wu, C. Y., and Wei, X. (2021). From drowned valley to delta: Discrimination and analysis on issues of the formation and evolution of the zhujiang river delta (in Chinese with English abstract). *Acta Oceanol. Sin.* 43 (1), 1–26. doi: 10.12284/hyxb2021019

Wu, C. Y., Xing, W., Jie, R., Yun, B., Zhigang, H., Yiaping, L., et al. (2010). Morphodynamics of the rock-bound outlets of the pearl river estuary, south China — a preliminary study. *J. Mar. Syst.* 82, S17–S27. doi: 10.1016/j.jmarsys.2010.02.002

Wu, M. S., Zong, Y. Q., Mok, K. M., Cheung, K. M., Xiong, H. X., and Huang, G. Q. (2017). Holocene Hydrological and sea surface temperature changes in the northern coast of the south China Sea. *J. Asian Earth Sci.* 135, 268–280. doi: 10.1016/j.jseaes.2017.01.004

Xiong, H. X., Zong, Y. Q., Huang, G. Q., and Fu, S. Q. (2018a). Sedimentary responses to Holocene sea-level change in a shallow marine environment of southern China. *J. Asian Earth Sci.* 166, 95–106. doi: 10.1016/j.jseaes.2018.07.033

Xiong, H. X., Zong, Y. Q., Huang, G. Q., and Fu, S. Q. (2020). Human drivers accelerated the advance of pearl river deltaic shoreline in the past 7500 years. *Quatern. Sci. Rev.* 246. doi: 10.1016/j.quascirev.2020.106545

Xiong, H. X., Zong, Y. Q., Qian, P., Huang, G. Q., and Fu, S. Q. (2018b). Holocene Sea-level history of the northern coast of south China Sea. *Quatern. Sci. Rev.* 194, 12–26. doi: 10.1016/j.quascirev.2018.06.022

Xu, Y. T., Lai, Z. P., and Li, C. A. (2019). Sea-Level change as the driver for lake formation in the Yangtze plain – a review. *Global Planet1 Change* 181. doi: 10.1016/j.gloplacha.2019.102980

Xu, X. L., Li, H. W., Tang, L. J., Lai, Z. P., Xu, G. J., Zhang, X. H., et al. (2020). Chronology of a Holocene core from the pearl river delta in southern China. *Front. Earth Sci.* 8. doi: 10.3389/feart.2020.00262

Xu, X. L., Zhong, J. M., Huang, X. M., Li, H. W., Ding, Z. J., and Lai, Z. P. (2022). Age comparison by luminescence using quartz and feldspar on core HPQK01 from the pearl river delta in China. *Quatern. Geochronol.* 71. doi: 10.1016/j.quageo.2022.101320

Yao, Y., Zhan, W., Liu, Z., Zhang, Z., Zhan, M., and Sun, J. (2013). Neotectonics and its relations to the evolution of the pearl river delta, guangdong, China. *J. Coast. Res.* 66, 1–11. doi: 10.2112/si_66_1

Yi, L., Lai, Z. P., Yu, H. J., Xu, X. Y., Su, Q., Yao, J., et al. (2012). Chronologies of sedimentary changes in the south bohai Sea, China: constraints from luminescence and radiocarbon dating. *Boreas* 42 (2), 267–284. doi: 10.1111/j.1502-3885.2012.00271.x

Yim, W. W. S., Hilgers, A., Huang, G. Q., and Radtke, U. (2008). Stratigraphy and optically stimulated luminescence dating of subaerially exposed quaternary deposits from two shallow bays in Hong Kong, China. *Quatern. Int.* 183 (1), 23–39. doi: 10.1016/j.quaint.2007.07.004

Yim, W. W. S., Huang, G. Q., Fontugne, M. R., Hale, R. E., Paterne, M., Pirazzoli, P. A., et al. (2006). Postglacial sea-level changes in the northern south China Sea continental shelf: Evidence for a post-8200 calendar yr BP meltwater pulse. *Quatern. Int.* 145-146, 55–67. doi: 10.1016/j.quaint.2005.07.005

Yim, W. W. S., Ivanovich, M., and Yu, K. F. (1990). Young age bias of radiocarbon dates in pre-holocene marine deposits of Hong Kong and implications for pleistocene stratigraphy. *Geo-Mar. Lett.* 10 (3), 165–172. doi: 10.1007/bf02085932

Yi, L., Ye, X. Y., Chen, J. B., Li, Y., Long, H., Wang, X. L., et al. (2014). Magnetostratigraphy and luminescence dating on a sedimentary sequence from northern East China Sea: Constraints on evolutionary history of eastern marginal seas of China since the early pleistocene. *Quatern. Int.* 349, 316–326. doi: 10.1016/j.quaint.2014.07.038

Yu, Z. X. (2017). *The age of the lower transgression cycle in the pearl river delta and its implication of Sea-level changes and neotectonic movements*. Ph. D. thesis Sun Yat-sen University Guangzhou.

Yu, Z. X., Zhang, K., Liang, H., and Li, Z. Y. (2016). Late quaternary tectonic movements in the pearl river delta, china, revealed from stratigraphic profiles (in Chinese with English abstract). *Trop. Geogr.* 36, 334–342. doi: 10.13284/j.cnki.rddl.002850

Yu, F. L., Zong, Y. Q., Lloyd, J. M., Huang, G. Q., Leng, M. J., Kendrick, C., et al. (2010). Bulk organic δ13C and C/N as indicators for sediment sources in the pearl river delta and estuary, southern China. *Estua. Coast. Shelf. Sci.* 87 (4), 618–630. doi: 10.1016/j.ecss.2010.02.018

Zaitlin, B. A., Dalrymple, R. W., and Boyd, R. (1994). "The stratigraphic organization of incised-valley systems associated with relative Sea-level change," in *Incised-valley systems: Origin and sedimentary sequences*. Eds. R. W. Dalrymple, B. A. Zaitlin and A. Peter, (Virginia: Society for Sedimentary Geology), 51, 45–60. doi: 10.2110/pec.94.12.0045

Zhang, W., Xu, Y., Hoitink, A. J. F., Sassi, M. G., Zheng, J. H., Chen, X. W., et al. (2015). Morphological change in the pearl river delta, China. *Mar. Geol.* 363, 202–219. doi: 10.1016/j.margeo.2015.02.012

Zhao, X., Chen, S., Huang, C., Zeng, M., Chen, W., Dong, H., et al. (2014). Facies architecture and depositional model of a macrotidal incised valley succession (Qiantang River estuary, eastern China), and differences from other macrotidal systems (in Chinese with English abstract). *Geol. Bulletin China* 33 (10) 1635–1641. doi: 10.3969/j.issn.1671-2552.2014.10.023

Zheng, Z., Ma, T., Roberts, P., Li, Z., Yue, Y., Peng, H., et al. (2021). Anthropogenic impacts on late Holocene land-cover change and floristic biodiversity loss in tropical southeastern Asia. *Proc. Natl. Acad. Sci. U.S.A.* 118 (40). doi: 10.1073/pnas.2022210118

Zong, Y. Q., Huang, G. Q., Switzer, A. D., Yu, F. L., and Yim, W. W. S. (2009a). An evolutionary model for the Holocene formation of the pearl river delta, China. *Holocene* 19 (1), 129–142. doi: 10.1177/0959683608098957

Zong, Y. Q., Huang, K. Y., Yu, F. L., Zheng, Z., Switzer, A., Huang, G. Q., et al. (2012). The role of sea-level rise, monsoonal discharge and the palaeo-landscape in the early Holocene evolution of the pearl river delta, southern China. *Quatern. Sci. Rev.* 54, 77–88. doi: 10.1016/j.quascirev.2012.01.002

Zong, Y. Q., Lloyd, J. M., Leng, M. J., Yim, W. W. S., and Huang, G. Q. (2006). Reconstruction of Holocene monsoon history from the pearl river estuary, southern China, using diatoms and carbon isotope ratios. *Holocene* 16 (2), 251–263. doi: 10.1191/0959683606hl911rp

Zong, Y. Q., Yim, W. W. S., Yu, F. L., and Huang, G. Q. (2009b). Late quaternary environmental changes in the pearl river mouth region, China. *Quatern. Int.* 206 (1-2), 35–45. doi: 10.1016/j.quaint.2008.10.012

Zong, Y. Q., Yu, F. L., Huang, G. Q., Lloyd, J. M., and Yim, W. W. S. (2010). Sedimentary evidence of late Holocene human activity in the pearl river delta, China. *Earth Surface Processes Landforms* 35 (9), 1095–1102. doi: 10.1002/esp.1970

Zong, Y., Huang, G., Li, X. Y., and Sun, Y. Y. (2015). Late Quaternary tectonics, sea-level change and lithostratigraphy along the northern coast of the South China Sea. *Geol. Soc. Lond. Spec. Publ.* 429(1), 123–136. doi: 10.1144/sp429.1

Zong, Y. Q., Zheng, Z., Huang, K. Y., Sun, Y. Y., Wang, N., Tang, M., et al. (2013). Changes in sea level, water salinity and wetland habitat linked to the late agricultural development in the pearl river delta plain of China. *Quatern. Sci. Rev.* 70, 145–157. doi: 10.1016/j.quascirev.2013.03.020

frontiers | Frontiers in Marine Science

TYPE Original Research
PUBLISHED 20 December 2022
DOI 10.3389/fmars.2022.1079301

OPEN ACCESS

EDITED BY
Fajin Chen,
Guangdong Ocean University, China

REVIEWED BY
Rui Wang,
Guangxi University, China
Zhongping Lai,
Shantou University, China
Jiantao Cao,
Tongji University, China

*CORRESPONDENCE
Jingyao Zhao
zjy1230@xjtu.edu.cn
Tiegang Li
tgli@fio.org.cn

†PRESENT ADDRESS
Xiaoxiao Yu,
State Key Laboratory of Isotope Geochemistry and CAS Center for Excellence in Deep Earth Science, Guangzhou Institute of Geochemistry, Chinese Academy of Sciences, Guangzhou, China

SPECIALTY SECTION
This article was submitted to Marine Biogeochemistry, a section of the journal Frontiers in Marine Science

RECEIVED 25 October 2022
ACCEPTED 28 November 2022
PUBLISHED 20 December 2022

CITATION
Yu X, Duan B, Zhao J, Gu D, Feng A, Liu Y and Li T (2022) Deep submerged speleothems in the Sansha Yongle Blue Hole (South China Sea) as determination of low sea levels during the Last Glacial Maximum. *Front. Mar. Sci.* 9:1079301. doi: 10.3389/fmars.2022.1079301

Deep submerged speleothems in the Sansha Yongle Blue Hole (South China Sea) as determination of low sea levels during the Last Glacial Maximum

Xiaoxiao Yu[1†], Baichuan Duan[1], Jingyao Zhao[2*], Dongqi Gu[1], Aiping Feng[1], Yanxiong Liu[1] and Tiegang Li[1*]

[1]First Institute of Oceanography, Ministry of Natural Resources, Qingdao, China, [2]Institute of Global Environmental Change, Xi'an Jiaotong University, Xi'an, China

Although Last Glacial Maximum (LGM) sea levels have been the focus of much attention in climate and marine sciences, the timing, duration, and magnitude need further research. Here we present observations and analyses of the deepest speleothems (-116 m) collected from the deepest known blue hole on a global scale, the Sansha Yongle Blue Hole, Xisha Islands, South China Sea. The field investigations illustrate that submerged speleothems are irregular cauliflower-like coatings on the downward cave ceiling from water depths of ~90 to 120 m. The downward growth direction and negative stable carbon and oxygen stable isotopes of submerged speleothems suggest that they may deposit in an air-filled condition through gravity drip, indicating the maximum LGM sea level. The deep submerged speleothems were dated, indicating two U–Th ages of 29.16 ± 0.17 and 26.04 ± 0.18 ka BP and one radiocarbon age of 18.64 ± 0.12 ka BP, respectively. The investigated deep submerged speleothems therefore clearly determine the minimum onset and maximum termination times for LGM terms of sea level. The results show that LGM began at ~29 ka BP and ended at ~18.5 ka BP. This study therefore provides initial evidence for the use of deep speleothems to determine LGM sea levels and emphasizes the importance of deep submerged speleothems in the reconstruction of Pleistocene low sea levels.

KEYWORDS

sea level, U–Th dating, ^{14}C dating, speleothem, LGM, coastal cave

Introduction

When global sea levels declined during past glacial epochs, speleothems might have deposited in air-filled coastal karst caves that were probably flooded by subsequent transgressions (*e.g.*, Richards et al., 1994; Melim et al., 2001; Bard et al., 2002; Dorale et al., 2010; Moseley et al., 2015; De Waele et al., 2018; Dumitru et al., 2021; Steidle et al., 2021). Because elevations and absolute ages of speleothems can be accurately determined, they have significant potential for the determination of past maximum sea levels (Gascoyne et al., 1979; Richards et al., 1994; Bard et al., 2002; Dumitru et al., 2019). Though previous studies over four decades have thoroughly illustrated variable maximum sea levels using U–Th and U–Pb dating of speleothems in coastal caves (Harmon et al., 1978; Gascoyne et al., 1979; Bard et al., 2002; Dorale et al., 2010; Moseley et al., 2015; Dumitru et al., 2019), the deepest speleothems collected so far were from -54.9 m of a blue hole in South Andros Island (Richards et al., 1994). These speleothems are therefore unable to determine Pleistocene low sea levels, which were often over 100 m lower than they are at present (Richards et al., 1994; Lambeck and Chappell, 2001; Spratt and Lisiecki, 2016; Huybers et al., 2022). Therefore, deep submerged speleothems (-116 m) collected from the Sansha Yongle Blue Hole (SYBH) with reliable ages are useful for determining Last Glacial Maximum (LGM) low sea levels.

One of the most highlighted features of the LGM is its low sea level, which was ~120–130 m lower than it is today (Hanebuth et al., 2000; Yokoyama et al., 2001; Clark and Mix, 2002; Clark et al., 2009; Hanebuth et al., 2009; Lambeck et al., 2014; Yokoyama et al., 2018). The onset and termination of the LGM is of particular importance but poorly identified by field data. Mix et al. (2001) considered the LGM spanned 24–18 ka BP, whereas a slightly earlier epoch from 26 to 21 ka BP, depending on global sea level minima, was proposed as the LGM duration by another study (Peltier and Fairbanks, 2006). A 10-m sea level rise that started around 19.6 ka BP was thought to have terminated the LGM (Hanebuth et al., 2000; Yokoyama et al., 2001; Hanebuth et al., 2009). Clark et al. (2009) compiled 5,704 reliable global ice-sheet extent data and demonstrated that the LGM extended from 26.5 to 19.0 ka BP. Recently, however, two studies concluded that the LGM ended around 19.0 ka BP and began around 31–29 ka BP with a rapid ~40-m sea level falling over 2,000 years (Lambeck et al., 2014; Yokoyama et al., 2018). These discrepancies about LGM onset and termination suggest that it is imperative to find more evidence, especially from remote areas such as the South China Sea (SCS). In addition to the discrepancies, previous LGM low sea level proxies, such as corals and tidal flat sediments, usually exhibit large errors of up to 5–10 m, which could cause large uncertainties of LGM low sea levels (Dumitru et al., 2021). Speleothems and their phreatic overgrowths, deposited under air-filled conditions indicating maximum sea level, potentially provide more accurate sea level determination (van Hengstum et al., 2019).

In this study, we reported timing results from the deepest submerged speleothems so far collected from the Sansha Yongle Blue Hole (SYBH), Xisha Islands, SCS (Figure 1). SCS is far removed from the glacial isostatic effect (Peltier, 2004), and the Xisha Islands have been a tectonic stable marginal setting since the Last Interglacial (Ma et al., 2021; Yu et al., 2022); hence, this area is suitable for determining past sea levels. Our speleothems were dated using radiocarbon and ^{230}Th–^{234}U–^{238}U methods. Based on the obtained ages, we determined the onset and termination of the LGM. This novel evidence suggests that deep submerged speleothems may be a promising fingerprint for Pleistocene low sea levels.

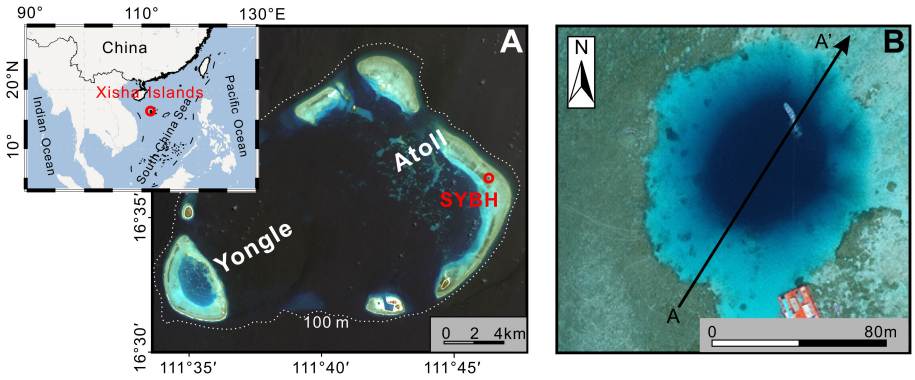

FIGURE 1
Location map **(A)** and aerial photography of Sansha Yongle Blue Hole **(B)** in Yongle Atoll, Xisha Islands, South China Sea. The A–A′ cross-section line in the right panel represents vertical profiles of Figure 2.

Regional setting

SYBH (latitude: 16°31′29″ N; longitude: 111°46′04″ E) is the deepest (-301.19 m) known coastal carbonate cave globally. This ocean blue hole is located in the eastern end of the Yongle Atoll (Figure 1A), which consists of highly porous carbonate corals and coralline algae bindstones that initially developed in the early Miocene (19.6 Ma) with a volcanic base belonging to the Xisha uplift (Jiang et al., 2019). Based on a lithological study of a CK-2 borehole from nearby Chenhang Island, the bottom of SYBH approximately matches with an interface of ~4.0 Ma (Fan et al., 2019). SYBH has a planform at the surface which is shaped like a comma, with a maximum width of 162.3 m (Figure 1B).

As shown in Figure 2, SYBH displays a fracture-guide hole pattern which is differentiated from other complex karst caves with branch-work caves (Mylroie et al., 1995; Li et al., 2018). SYBH exhibits four distinct and successive sections from top to bottom as caves I to IV, respectively (Figure 2B; Yu et al., 2022). Corals grow at the uppermost entrance of SYBH, whereas massive sediments and fallen rocks cover the lower hole (Figure 2A). For our study, fortunately, a ceiling (cave III) was observed at water depths between ~90 and 160 m on the northeastern inner wall. Irregular and popcorn-like cave coatings extensively cover the seaward ceiling between water depths of ~90 and 120 m (Figure 2A).

Materials and methods

Sampling and site description

In total, 13 short rock cores (5 cm in diameter) with length < 30 cm were drilled from the SYBH during May and June 2017 using a miniature underwater drilling rig carried by the FCV2000D remotely operated vehicle (ROV; Yu et al., 2022). Three-dimensional morphology was reconstructed using an unmanned sea-robot ship equipped with a multibeam system above 15 m and a professional-grade ROV equipped with a multibeam system below 15 m (Li et al., 2018). In addition to morphology, a high-resolution underwater camera was carried by the ROV to gather more detailed knowledge. This study focuses on a short core (length: 26 cm; latitude: 16.52°; longitude: 111.77°) consisting of speleothems and substrates from the depth of 116-m (Bh116; Figure 3). In Bh116, the speleothems broke into small pieces during the drilling processes due to their weak cements. Therefore, the relative positions for these broken pieces could not be accurately reconstructed though we carefully protected them during the collection, transportation, and rinsing.

Petrography

We rinsed the subsamples one by one to remove covered slurries contaminated during the drilling process and put them back to their original positions. Substrates and the largest speleothem subsample (Figure 3A) were sliced for petrographic investigation under polarization microscopy. Unfortunately, the largest speleothem subsample of Bh116 was broken and lost after thin section grinding. In order to remove possible contaminants, we rinsed the subsamples by ultrasonic cleaning in deionized water for 12 hours and repeated three times before subsequent geochemical analyses. Generally, no debris was observed after the third rinsing. For the high-resolution surface structure analysis of calcite, samples of freshly broken pieces were studied with Hitachi-SU8010

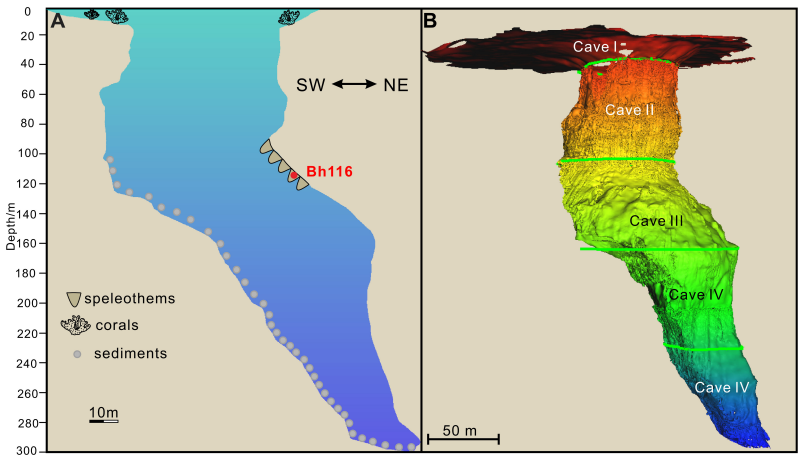

FIGURE 2
Cross-section **(A)** and 3-D topography **(B)** of Sansha Yongle Blue Hole.

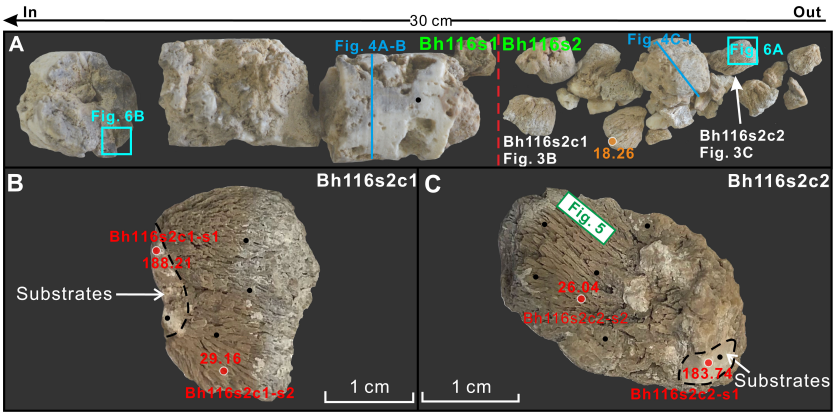

FIGURE 3
Photographs of sample Bh116 **(A)** and two subsamples **(B, C)** showing locations for thin section (blue lines;Figure 4), scanning electron microscopy (green rectangles; Figure 5), XRD (cyan rectangles; Figure 6), carbon and oxygen isotopes (black circles; Figure 7), U–Th dating (red circles; Table 1), and radiocarbon dating (orange circles; Table 1). The dotted red lines in **(A)** divide the core samples into substrates and speleothems, *i.e.*, Bh116s1 and Bh116s2.

(Japan) at Guangzhou Institute of Geochemistry, Chinese Academy of Sciences (Guangzhou, China). Calcium, carbon, oxygen, and magnesium concentrations of microporous calcite were determined by SAPPHIRE EDAX detector and Apollo X-SDD detector, respectively.

Mineralogy and elemental analyses

The carbonate mineralogy was determined by X-ray diffraction measurements. Two subsamples (~2 g) were milled from cleaned carbonates (Figure 3A) using a stage-mounted dental drill fitted with silicon carbide dental blade and measured using a Rigaku D/max-rB Theta-theta X-ray powder diffractometer at the First Institute of Oceanology, Ministry of Natural Resources. Copper K_α radiation (40 kV, 100 mA) was used as an X-ray source. Samples were packed into a rectangle cavity in an aluminum holder and scanned in a step-scan mode (0.02°/step) over the angular range of 3° to 70° (2θ). The mineralogical compositions of samples were constructed using the 104 reflection of calcite with 2θ from 29.25° to 29.80°, the 111 reflection of aragonite with 2θ between 25.5° and 26.5°, and the 104 reflection of dolomite with 2θ from 30.58° to 31.28°. Usually, the calcite 104 reflection branches into two asymmetric peaks, of which both high-magnesium calcite and low-magnesium calcite co-exist (Kontoyannis and Vagenas, 2000; Csoma et al., 2006; Zhai et al., 2015).

For elemental analyses, four samples (~50 mg) were milled after having been repeatedly rinsed with carbonates using a stage-mounted dental drill fitted with tungsten carbide dental burs (Figure 3). Major elements, including Ca and Mg, were analyzed using an inductively coupled plasma optical emission spectrometer (ICP-OES), and minor elements were performed by inductively coupled plasma mass spectrometry (ICP-MS) at the First Institute of Oceanology, Ministry of Natural Resources. First, 50.00 mg carbonate powder was dissolved in 1.50 ml high-purity HNO_3 and 1.50 ml high-purity HF in a digestion bottle with Teflon liner at 190°C for 48 h. Solutions in the Teflon liners were evaporated to dryness on a heating plate. Next, the samples were added with 3 ml of 7 N HNO_3 and 0.5 ml Rh internal standard solution and heated at 150°C for 8 h. Finally, the samples were diluted to 50.00 g to be measured by ICP-OES (Icap6300, Thermo Fisher, USA). Exactly 10.00 g solutions were extracted from the 50.00 g solutions and diluted to 20.00 g to analyze by ICP-MS (X Series II, Thermo Fisher, USA). These four carbonate samples were measured together with 34 further carbonate samples from the SYBH. Up to three standard solutions and a laboratory blank were used to calculate the calibration curves for each element.

Stable carbon and oxygen isotopes

Stable carbon and oxygen isotopes were analyzed to discriminate the origins of deep submerged speleothems between seawater and air-filled conditions. Approximately ~10 mg carbonate powder was collected from 11 positions (Figure 3) and measured on a Thermo Scientific MAT-253 Plus mass spectrometer coupled with an online carbonate preparation device (Kiel-IV) in the Isotope Laboratory of the Xi'an Jiaotong University. Carbonates were reacted with anhydrous phosphoric acid at 75°C. Results are reported relative to the Vienna Pee Dee Belemnite standard. The analytical errors (1 σ) are ±0.06‰ and ±0.03‰ for $\delta^{18}O$ and $\delta^{13}C$ (Zhao et al., 2021), respectively.

U–Th and radiocarbon dating

As relative positions for speleothems could not be accurately determined, we chose three subsamples with substrates to determine the possible onset and termination time of speleothems (Figure 3). Approximately 100 mg of carbonate powder was collected from the speleothems (Figures 3B, C) using a stage-mounted dental drill fitted with tungsten carbide dental bur. The U and Th isotopes of these samples were determined by a plasma-sourced multi-collector mass spectrometer (MC-ICP-MS; Neptune-*plus*, Thermo-Finnigan) at the Isotope Laboratory of the Xi'an Jiaotong University. Chemistry procedures to separate U and Th followed Edwards et al. (1987). ^{229}Th–^{233}U–^{236}U isotope dilution method was applied to correct for instrumental fractionation and to determine Th/U isotopic ratios and concentrations. U and Th isotopes were measured on a Mas-Com multiplier behind the retarding potential quadrupole in a peak-jumping mode. The instrumentation, standardization, and ^{230}Th–^{234}U half-lives were reported in Cheng et al. (2000); Cheng et al. (2013). Uncertainties in U/Th isotopic data, including corrections for blanks, multiplier dark noise, abundance sensitivity, and contents of the same nuclides in spike solution, were calculated offline at 2σ level (Cheng et al., 2013).

In addition to U–Th ages, one radiocarbon dating (Figure 3A) was determined by accelerator mass spectrometry at Beta Analytic, Inc. (Miami, USA) to provide additional geochronological identification. This radiocarbon date (Table 1) was subsequently calibrated to the calendar age using the recently published IntCal20 curve (Reimer et al., 2020).

Results

Morphology and distribution of speleothems in SYBH

The morphologic features of SYBH, interpreted from 3-D topography data (Figure 2B) and underwater photographs (Figure 8), provide meso-to-micro scale surface evidence to trace the deep submerged speleothems. The 3-D topography reveals a downward ceiling from -90 to -160 m along seaside walls (Figure 2). Irregular and popcorn-like cave coatings extensively cover the ceiling between -90 and -120 m (Figure 8). These coating-like speleothems presented in SYBH are small with centimeter dimensions. They prefer to cluster as a cauliflower-like shapes with downward growth direction from their substrates (Figures 8B, C). Most coatings, if not all, display a gravity-fed downward direction (Figure 8), which probably suggests that these speleothems were formed through slow water dripping in air-filled conditions (Bian et al., 2019).

Petrology and geochemistry

Petrographic investigations show the textures and fabrics of Bh116 including substrates and speleothems (Figures 3, 4). The inside substrates and outside speleothems can be identified by the naked eye depending on their distinct structures (Figure 3A). The obtained substrates (Bh116s1) are composed of gray and gray-white broken limestone characterized by loose, yellow, fine sediments. The speleothems (Bh116s2), however, consist of popcorn-like precipitates characterized by column fibers

TABLE 1 U-series and radiocarbon ages of sample Bh116 from Sansha Yongle Blue Hole.

Sample number	^{238}U (ppb)	^{232}Th (ppt)	^{230}Th/^{232}Th (×10^{-6})	δ^{234}U (0) (‰)	(^{230}Th/^{238}U)	Raw ^{230}Th age (kyr)	δ^{234}U (T)$_{corr}$ (‰)	Age$_{corr}$ (kyr B.P.)
Bh116s2c1-s1	1,731.4 ± 3.9	499.09 ± 10.03	54 ± 1	112.7 ± 2.3	0.9494 ± 0.029	195.54 ± 2.04	192 ± 5	188.21 ± 5.49
Bh116s2c1-s2a	6,570.5 ± 15.5	0.18 ± 0.01	15,425 ± 60,911	108.2 ± 1.8	0.2616 ± 0.0012	29.23 ± 0.17	117 ± 2	29.16 ± 0.17
Bh116s2c2-s1	1,530.7 ± 1.5	225.87 ± 4.52	104 ± 2	110.5 ± 1.2	0.9319 ± 0.0015	187.48 ± 1.00	186 ± 3	183.74 ± 2.78
Bh116s2c2-s2a	675.9 ± 1.1	4.55 ± 0.09	555 ± 11	55.3 ± 1.7	0.2265 ± 0.0009	26.30 ± 0.13	59 ± 2	26.04 ± 0.18
Bh116s2c3[a]	–	–	–	–	–	15.36 ± 0.04	–	18.64 ± 0.12

$\delta^{234}U = ([^{234}U/^{238}U]_{activity} - 1) \times 1{,}000$. δ^{234}U (0) was calculated based on ^{230}Th age (T), i.e., $\delta^{234}U(0) = \delta^{234}U_{measured} \times e^{(\lambda 234)\times T}$. $\delta^{234}U(T)_{corr} = ([^{234}U/^{238}U]_{activity} - 1) \times 1{,}000$. Corrected ^{230}Th ages assume the initial ^{230}Th/^{232}Th atomic ratio of 4.4 ± 2.2 × 10^{-6}. Those are the values for material at secular equilibrium, with the bulk earth ^{232}Th/^{238}U value of 3.8. The errors are arbitrarily assumed to be 50%.

[a]Beta-511711: radiocarbon age.

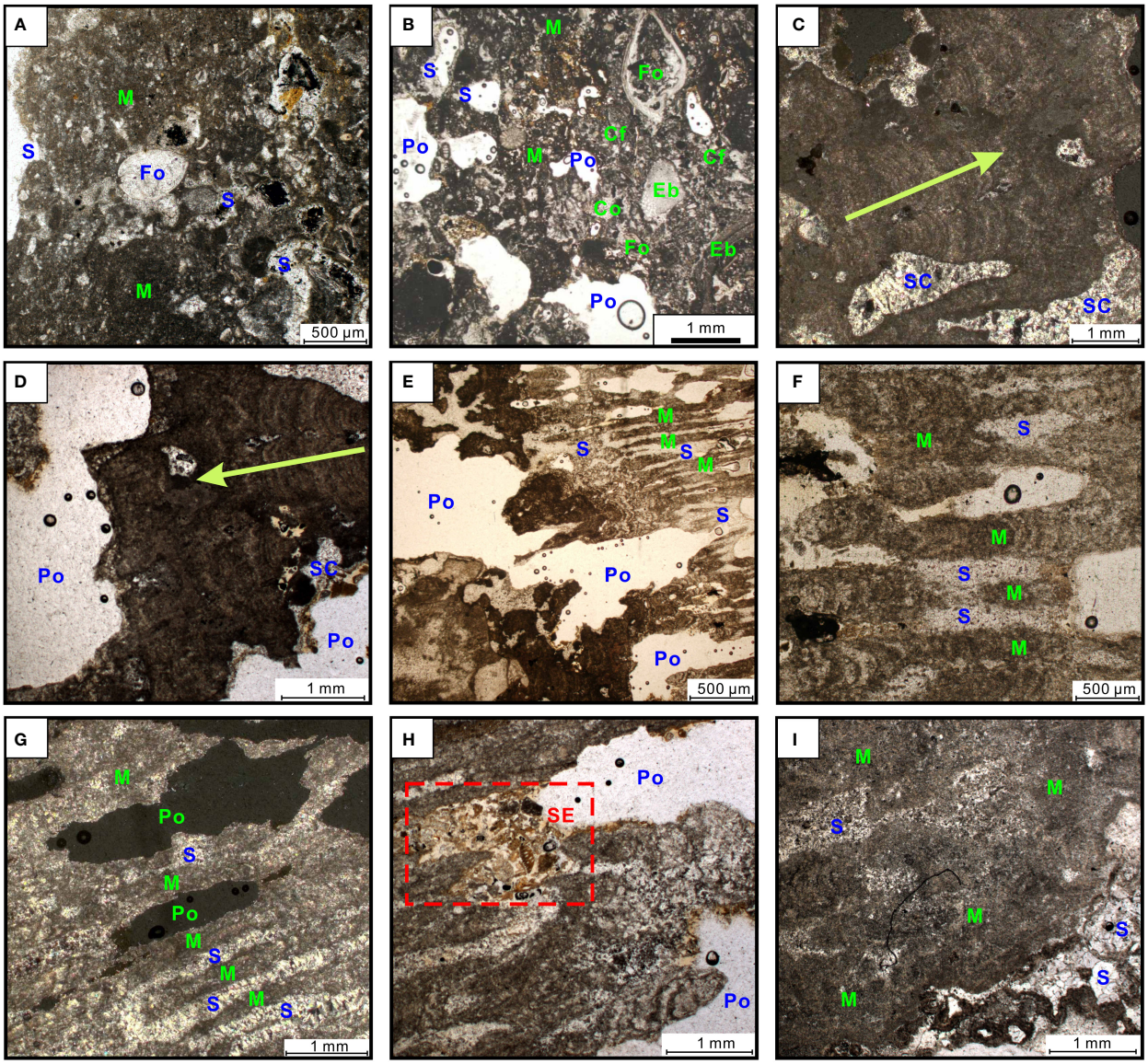

FIGURE 4
Thin-section micrographs of sample Bh116. **(A, B)** Micritic areas with sparite, foraminifera, echinoderm brachiopods, coral fragments, and pore structure in Bh116s1. **(C, D)** Laminated microcrystalline fabric structure with secondary cement and pores. The arrows show the growth direction. **(E–G)** Microcrystalline and sparite crystals alternating with fabric microporous calcite. **(H, I)** Sediments and sparite in the margin of the pores (see Figure 3 for the locations of the thin sections).

(Figures 3B, C). A thin section of the substrates shows that Bh116s1 consists of lagoonal sand with biologic debris consisting of coral fragments, foraminifers, echinoderms, and brachiopods (Figures 4A, B), reflecting a lagoon slope depositional environment, which corresponds to that found by Fan et al. (2019). While the speleothems are characterized by more complex textures (Figures 4C–I), they contain two recognizable fabrics: laminated microcrystalline fabric (Figures 4B–D) and microcrystalline and sparite crystals alternating with fabric microporous calcite (Figures 4E–H). Both of these two structures are highly porous, some of which have been cemented by sparite crystal precipitates (Figure 4C). Moreover, the laminated microcrystalline fabric calcites are surrounded by sparite crystal precipitates with dark terminations (Figures 4C, D) (Csoma et al., 2006; Bontognali et al., 2016; De Waele et al., 2018). In addition, brownish fine sediments and broken marine shells are observed at the margin of pores (Figure 4H). The SEM images show secondary calcite crystals (Figures 5A–C), dissolution points, and edges of calcites (Figures 5D–F). The secondary calcite crystals show an inner-

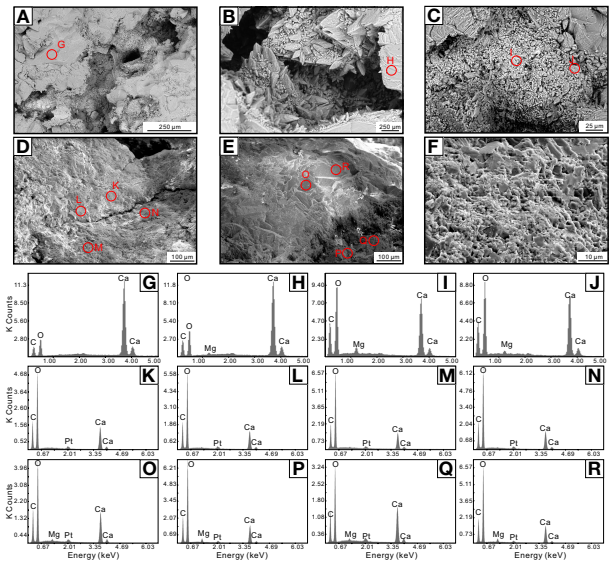

FIGURE 5
SEM images of calcareous speleothem samples **(A–F)** and geochemical composition **(G–R)**. **(A–C)** Secondary cemented pores. **(D, E)** Calcite crystals are dissolved.

core growth direction (Figures 5B, C), probably indicating the cements re-precipitated from the surrounding dissolved calcites (Tuccimei et al., 2010; Bontognali et al., 2016; De Waele et al., 2018). The geochemical compositions of surrounding calcites and cements are relatively homogeneous, in which $MgCO_3$ varied between 5% and 20% (Figures 5G–R). The presence of Mg in the deep submerged speleothems is also confirmed by the existence of high-magnesium calcite from bulk sample analysis (Figure 6). Based on XRD, the substrates of Bh116 consist entirely of low-magnesium calcite (Figure 6A), while ~85% low-magnesium calcite and ~15% high-magnesium calcite constitute the speleothems in Bh116 (Figure 6B).

Both carbon and oxygen isotope values of speleothems and substrates are negative in the Bh116 (Figure 7). The speleothems exhibit isotopically depleted values with respect to the substrates in both ^{18}O and ^{13}C. In addition, the oxygen and carbon isotope ratios of the speleothems from different subsamples are variable, and the outer one (Bh116s2c2) is more depleted in ^{13}C and slightly enriched in ^{18}O with respect to those of the internal subsample (Bh116s2c1).

Dating

The ^{232}Th concentrations of substrates in two subsamples are 499.09 and 225.87 ppt (Table 1). In contrast, the ^{232}Th concentrations of speleothems are 0.18 and 4.55 ppt, which are much lower than the substrates. The ^{238}U concentrations of speleothems are variable with concentrations of 6570.5 and 675.9 ppb. The U–Th ages of substrates are 188.21 ± 5.49 and 183.74 ± 2.78 ka BP, suggesting that they may have experienced deposition and secondary alterations and are not suitable for U–Th dating. The substrates are expected to have been deposited at about 1.4 Ma based on the depth of nearby borehole CK-2 (Fan et al., 2019). The U–Th ages of the speleothems, Bh116s2c1 and Bh116s2c2, are 29.16 ± 0.17 and 26.04 ± 0.18 ka BP, respectively (Figure 3 and Table 1). The radiocarbon age of a subsample of speleothems (Bh116s2c3) is 18.64 ± 0.12 ka BP.

Discussion

Aerial growth of speleothems

It is evident that deep submerged calcite coatings in SYBH are speleothems that precipitated under air-filled conditions during sea level lowstands. Substances of marine origin, including marine overgrowth on speleothems and marine substrates, are excluded for their negative carbon and oxygen isotopes with values as low as -6.7‰ to -5.3‰ and -5.0‰ to -2.8‰ (Figure 7), respectively. These isotopic features differ from the marine overgrowth on speleothem, marine corals, and substrates but are close to subaerial speleothems collected from other coastal caves (Surić et al., 2005; Tuccimei et al., 2010; Gischler et al., 2017). This suggests that the deep submerged calcite coatings developed in SYBH grew under aerial conditions and can be used to determine maximum sea levels (Richards et al., 1994). The calcareous coatings resemble mushroom-shaped speleothems and phreatic overgrowths on speleothems and are porous (Tuccimei et al.,

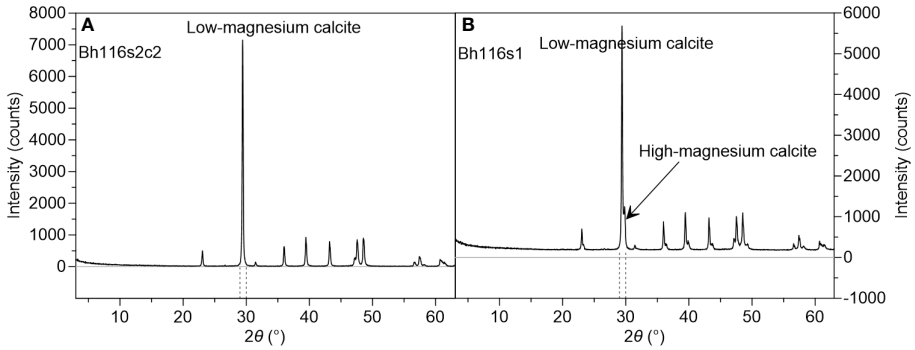

FIGURE 6
Characteristic spectrum of minerals low-Mg calcite **(A)** and high-Mg calcite **(B)** in Bh116.

2010; Bontognali et al., 2016; De Waele et al., 2018), probably suggesting that they exhibit the same aerial origin.

Determination of LGM low sea levels

As our deep submerged speleothems initially grew at ~29 ka under the air-filled vadose environment through calcite precipitation in coastal karst cave (Fairchild et al., 2006; Tuccimei et al., 2010; De Waele et al., 2018), the maximum sea level at ~29 ka BP should be lower than -116 m relative to the present. Our results agree well with previous data (Figure 9A) from Barbados (Bard et al., 1990; Peltier and Fairbanks, 2006) and Bonaparte (Yokoyama et al., 2000), as well as the reconstructed global ice volume equivalent (Figure 9B) and mean sea levels (Figure 9C) (Lambeck et al., 2014; Yokoyama et al., 2018). Lambeck et al. (2014) documented a ~40-m sea level falling around ~31–29 ka BP according to compiled data. Our results confirm that this rapid fall in sea level reached as low as -116 m at ~29 ka BP, and LGM was initiated at ~29 ka BP. It is noted that the sea level data from Bonaparte, indicating the onset of LGM (Yokoyama et al., 2000), have large uncertainties of up to 7.8 m. Our data also refined large sea level errors.

The LGM was thought to have been terminated by a rise in sea level (Hanebuth et al., 2000; Yokoyama et al., 2000). It began at ~19 ka BP, and the sea level rose 10–15 m within 500 years based on the interpretation of mangrove muds from the Sunda Shelf and Bonaparte Gulf in which tectonics are stable (Figure 9A). Recently,

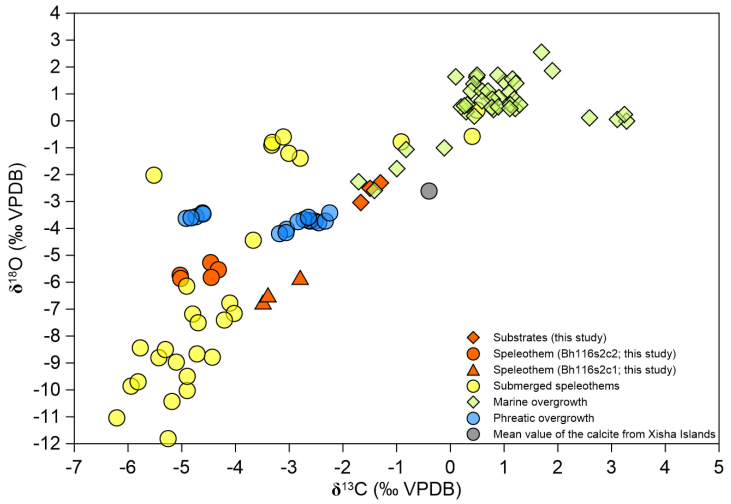

FIGURE 7
Stable carbon and oxygen isotopic composition of subsamples from coastal caves. Data of submerged speleothems, marine overgrowth, and phreatic overgrowth are from coastal caves of Belize, Eastern Adriatic Coast, and Mallorca (Surić et al., 2005; Tuccimei et al., 2010; Gischler et al., 2017). The mean values of the calcite from Xisha Islands are adopted from Bi et al. (2018).

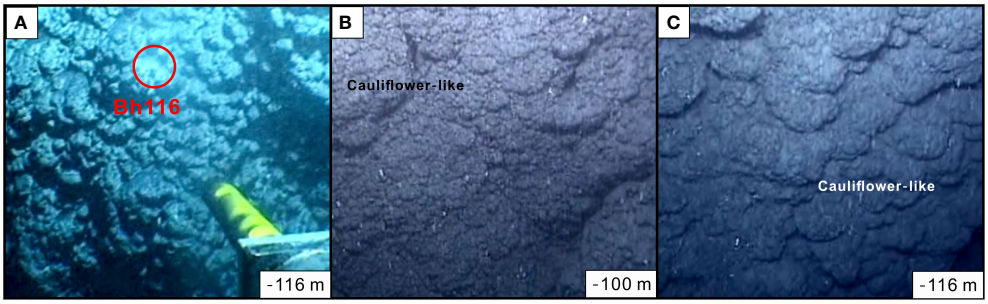

FIGURE 8
Underwater photographs of deep submerged speleothems from Sansha Yongle Blue Hole with water depths of ~116 **(A)**, ~100 **(B)**, and ~116 m **(C)**. The red circle in the left panel indicates the location of Bh116. Speleothems cluster as cauliflower-like coatings **(B, C)**.

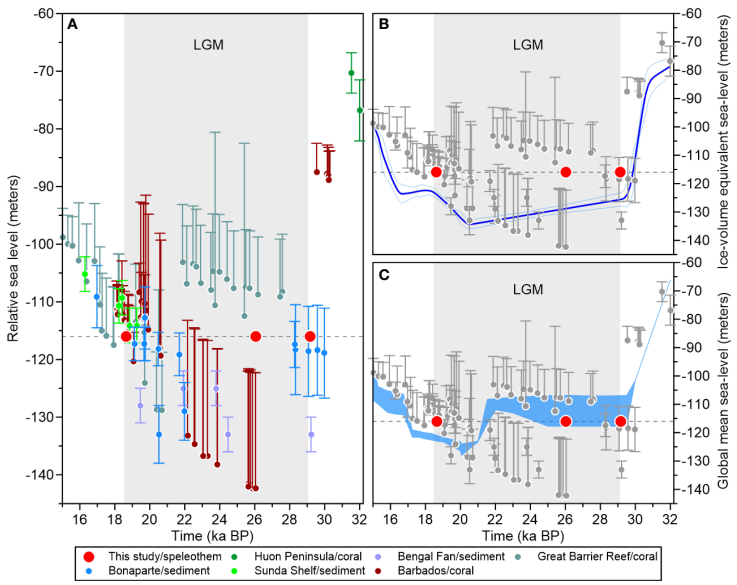

FIGURE 9
Last Glacial Maximum (LGM) sea levels with observational data and ice volume equivalent and global mean sea levels. **(A)** Previously documented LGM sea level data from Bonaparte Gulf (Yokoyama et al., 2000; De Deckker and Yokoyama, 2009), Huon Peninsula (Yokoyama et al., 2001), Sunda Shelf (Hanebuth et al., 2000; Hanebuth et al., 2009), Bengal Fan (Wiedicke et al., 1999), Barbados (Bard et al., 1990; Peltier and Fairbanks, 2006), and Great Barrier Reef (Yokoyama et al., 2018). **(B, C)** Previously constructed ice volume equivalent (Lambeck et al., 2014) and global mean sea levels (Yokoyama et al., 2018).

however, both Lambeck et al. (2014) and Yokoyama et al. (2018) demonstrated that this 10–15-m sea level rise was slower and lasted for ~3,000 years from 21 to 18 ka BP (Figures 9B, C). The possible termination of the speleothems from the SYBH with a radiocarbon age of 18.64 ± 0.12 ka BP suggests that the sea level was lower than -116 m at ~18.5 ka BP. Our results agree well with those sea levels reconstructed from Sunda Shelf and Bonaparte Gulf within errors and suggest that the termination of LGM is slightly later than the previous estimation (Figure 9A). However, our obtained results are inconsistent with the data reported from Barbados and the Great Barrier Reef, which experienced a rapid tectonic uplift of up to 0.34 mm/year (Fairbanks, 1989). The divergence in the conclusions regarding the termination of the LGM based on by sea level data from the SYBH, Bonaparte Gulf (Yokoyama et al., 2000; De Deckker and Yokoyama, 2009), and Sunda Shelf (Hanebuth et al., 2000; Hanebuth et al., 2009), as well as those determined from Barbados (Bard et al., 1990; Peltier and Fairbanks, 2006) and the Great Barrier Reef (Yokoyama et al., 2018), could be due to diverse and aged carbon, local carbon reservoir effects, and contaminated cement (Nakada et al., 2016), as they were determined from different materials (Hanebuth et al., 2000; Yokoyama et al., 2000). In addition, we confirm that the

presence of old carbon was not significant in our samples and would not affect our results. Conversely, subsequent cement observed in thin sections from our obtained submerged speleothems may cause the measured radiocarbon age to be less than its actual value. In addition, our results coincide with the constructed ice volume equivalent and global mean sea level, suggesting that the deep submerged speleothems may be a promising way to determine Pleistocene low sea levels.

Conclusions

This study used U–Th and radiocarbon ages of deep submerged speleothems (-116 m) from SYBH to determine low LGM sea levels. Our results show that the deep speleothems grew at 29.16 ± 0.17 ka BP and were submerged at <18.64 ± 0.12 ka BP under air-filled conditions above sea level. The initial age of the speleothems indicates onset of the LGM at ~29 ka BP, and the obtained radiocarbon age indicates the termination of LGM at ~18.5 ka BP. As elevations and ages can be accurately identified, deep submerged speleothems may be a promising way to determine Pleistocene low sea levels.

Data availability statement

The datasets presented in this study can be found in online repositories. The names of the repository/repositories and accession number(s) can be found below: https://doi.org/10.6084/m9.figshare.13379504.v1.

Author contributions

TL conceived this study. TL, AF, YL, and DG designed this study. XY, BD, and JZ carried out the laboratory measurements. XY wrote the original manuscript. TL, BD, and JZ reviewed and edited the manuscript. All authors contributed to the article and approved the submitted version.

Funding

This study was funded jointly by the National Natural Science Foundation of China (grant nos. T2192951 and U1906211) and the Taishan Scholars Project Funding (grant no. ts20190963).

Acknowledgments

We would like to thank Prof. David Richards from the University of Bristol for his constructive comments to improve this manuscript.

Conflict of interest

The authors declare that the research was conducted in the absence of any commercial or financial relationships that could be construed as a potential conflict of interest.

Publisher's note

References

Bard, E., Antonioli, F., and Silenzi, S. (2002). Sea-Level during the penultimate interglacial period based on a submerged stalagmite from argentarola cave (Italy). *Earth Planet. Sci. Lett.* 196, 135–146. doi: 10.1016/S0012-821X(01)00600-8

Bard, E., Hamelin, B., and Fairbanks, R. (1990). U-Th Ages obtained by mass spectrometry in corals from Barbados: Sea level during the past 130,000 years. *Nature* 346, 456–458. doi: 10.1038/346456a0

Bian, F., Coleborn, K., Flemons, I., Baker, A., Treble, P. C., Hughes, C. E., et al. (2019). Hydrological and geochemical responses of fire in a shallow cave system. *Sci. Total Environ.* 662, 180–191. doi: 10.1016/j.scitotenv.2019.01.102

Bi, D., Zhai, S., Zhang, D., Liu, X., Liu, X., Jiang, L., et al. (2018). Constraints of Fluid Inclusions and CO Isotopic compositions on the origin of the dolomites in the Xisha Islands, south China Sea. *Chem. Geol.* 493, 504–517. doi: 10.1016/j.chemgeo.2018.07.005

Bontognali, T. R. R., D'angeli, I. M., Tisato, N., Vasconcelos, C., Bernasconi, S. M., Gonzales, E. R. G., et al. (2016). Mushroom speleothems: Stromatolites that formed in the absence of phototrophs. *Front. Earth Sci.* 4 (49), 1–8. doi: 10.3389/feart.2016.00049

Cheng, H., Edwards, R. L., Hoff, J., Gallup, C. D., Richards, D. A., and Asmerom, Y. (2000). The half-lives of uranium-234 and thorium-230. *Chem. Geol.* 169, 17–33. doi: 10.1016/S0009-2541(99)00157-6

Cheng, H., Edwards, R. L., Shen, C. C., Polyak, V. J., Asmerom, Y., Woodhead, J., et al. (2013). Improvements in ^{230}Th dating, ^{230}Th and ^{234}U half-life values, and U–Th isotopic measurements by multi-collector inductively coupled plasma mass spectrometry. *Earth Planet. Sci. Lett.* 371-372, 82–91. doi: 10.1016/j.epsl.2013.04.006

Clark, P. U., Dyke, A. S., Shakun, J. D., Carlson, A. E., Clark, J., Wohlfarth, B., et al. (2009). The last glacial maximum. *Science* 325, 710–714. doi: 10.1126/science.1172873

Clark, P. U., and Mix, A. C. (2002). Ice sheets and Sea level of the last glacial maximum. *Quat. Sci. Rev.* 21, 1–7. doi: 10.1016/S0277-3791(01)00118-4

Csoma, A. E., Goldstein, R. H., and Pomar, L. (2006). Pleistocene speleothems of mallorca: Implications for palaeoclimate and carbonate diagenesis in mixing zones. *Sedimentology* 53, 213–236. doi: 10.1111/j.1365-3091.2005.00759.x

De Deckker, P., and Yokoyama, Y. (2009). Micropalaeontological evidence for late quaternary Sea-level changes in Bonaparte gulf, Australia. *Glob. Planet Change* 66, 85–92. doi: 10.1016/j.gloplacha.2008.03.012

De Waele, J., D'angeli, I. M., Bontognali, T., Tuccimei, P., Scholz, D., Jochum, K. P., et al. (2018). Speleothems in a north Cuban cave register Sea-level changes and pleistocene uplift rates. *Earth Surf Proc. Land* 43, 2313–2326. doi: 10.1002/esp.4393

Dorale, J. A., Onac, B. P., Fornós, J. J., Ginés, J., Ginés, A., Tuccimei, P., et al. (2010). Sea-Level highstand 81,000 years ago in mallorca. *Science* 327, 860. doi: 10.1126/science.1181725

Dumitru, O. A., Austermann, J., Polyak, V. J., Fornós, J. J., Asmerom, Y., Ginés, J., et al. (2019). Constraints on global mean Sea level during pliocene warmth. *Nature* 574, 233–236. doi: 10.1038/s41586-019-1543-2

Dumitru, O. A., Polyak, V. J., Asmerom, Y., and Onac, B. P. (2021). Last interglacial Sea-level history from speleothems: A global standardized database. *Earth Syst. Sci. Data* 13, 2077–2094. doi: 10.5194/essd-13-2077-2021

Edwards, R. L., Chen, J. H., and Wasserburg, G. J. (1987). ^{238}U-^{234}U-^{230}Th-^{232}Th systematics and the precise measurement of time over the past 500,000 years. *Earth Planet. Sci. Lett.* 81, 175–192. doi: 10.1016/0012-821X(87)90154-3

Fairbanks, R. G. (1989). A 17,000-year glacio-eustatic Sea level record: Influence of glacial melting rates on the younger dryas event and deep-ocean circulation. *Nature* 324, 637–642. doi: 10.1038/342637a0

Fairchild, I. J., Smith, C. L., Baker, A., Fuller, L., Spötl, C., Mattey, D., et al. (2006). Modification and preservation of environmental signals in speleothems. *Earth Sci. Rev.* 75, 105–153. doi: 10.1016/j.earscirev.2005.08.003

Fan, T., Yu, K., Zhao, J., Jiang, W., Xu, S., Zhang, Y., et al. (2019). Strontium isotope stratigraphy and paleomagnetic age constraints on the evolution history of coral reef islands, northern south China Sea. *Geol. Soc Am. Bull.* 132 (3-4), 803–816. doi: 10.1130/B35088.1

Gascoyne, M., Benjamin, G., Schwarcz, H., and Ford, D. (1979). Sea-Level lowering during the illinoian glaciation: Evidence from a bahama" blue hole". *Science* 205, 806–808. doi: 10.1126/science.205.4408.806

Gischler, E., Birgel, D., Brunner, B., Eisenhauer, A., Meyer, G., Buhre, S., et al. (2017). A giant underwater, encrusted stalactite from the blue hole, lighthouse reef, Belize, revisited: A complex history of biologically induced carbonate accretion under changing meteoric and marine conditions. *J. Sediment. Res.* 87, 1260–1284. doi: 10.2110/jsr.2017.72

Hanebuth, T. J. J., Stattegger, K., and Bojanowski, A. (2009). Termination of the last glacial maximum Sea-level lowstand: The sunda-shelf data revisited. *Global Planet. Change* 66, 76–84. doi: 10.1016/j.gloplacha.2008.03.011

Hanebuth, T., Stattegger, K., and Grootes, P. M. (2000). Rapid flooding of the sunda shelf: a late-glacial sea-level record. *Science* 288, 1033–1035. doi: 10.1126/science.288.5468.1033

Harmon, R. S., Schwarcz, H. P., and Ford, D. C. (1978). Late pleistocene Sea level history of Bermuda. *Quat. Res.* 9, 205–218. doi: 10.1016/0033-5894(78)90068-6

Huybers, P., Liautaud, P., Proistosescu, C., Boulahanis, B., Carbotte, S. M., Katz, R. F., et al. (2022). Influence of late pleistocene Sea-level variations on midocean ridge spacing in faulting simulations and a global analysis of bathymetry. *Proc. Nati. Acad.Sci.* 119, e2204761119. doi: 10.1073/pnas.2204761119

Jiang, W., Yu, K., Fan, T., Xu, S., Wang, R., Zhang, Y., et al. (2019). Coral reef carbonate record of the pliocene-pleistocene climate transition from an atoll in the south China Sea. *Mar. Geol.* 411, 88–97. doi: 10.1016/j.margeo.2019.02.006

Kontoyannis, C. G., and Vagenas, N. V. (2000). Calcium carbonate phase analysis using XRD and FT-raman spectroscopy. *Analyst* 125, 251–255. doi: 10.1039/a908609i

Lambeck, K., and Chappell, J. (2001). Sea Level change through the last glacial cycle. *Science* 292, 679–686. doi: 10.1126/science.1059549

Lambeck, K., Rouby, H., Purcell, A., Sun, Y., and Sambridge, M. (2014). Sea Level and global ice volumes from the last glacial maximum to the Holocene. *Proc. Nati. Acad.Sci.* 111, 15296–15303. doi: 10.1073/pnas.1411762111

Li, T., Feng, A., Liu, Y., Li, Z., Guo, K., Jiang, W., et al. (2018). Three-dimensional (3D) morphology of sansha yongle blue hole in the south China Sea revealed by underwater remotely operated vehicle. *Sci. Rep.* 8, 17122. doi: 10.1038/s41598-018-35220-x

Ma, Y., Qin, Y., Yu, K., Li, Y., Long, Y., Wang, R., et al. (2021). Holocene Coral reef development in chenhang island, northern south China Sea, and its record of Sea level changes. *Mar. Geol.* 440, 106593. doi: 10.1016/j.margeo.2021.106593

Melim, A., Shinglman, M., Boston, J., Northup, E., Spilde, N., and Queen, J. M. (2001). Evidence for microbial involvement in pool finger precipitation, hidden cave, new Mexico. *Geomicrobiol. J.* 18, 311–329. doi: 10.1080/01490450152467813

Mix, A. C., Bard, E., and Schneider, R. (2001). Environmental processes of the ice age: Land, oceans, glaciers (EPILOG). *Quat. Sci. Rev.* 20, 627–657. doi: 10.1016/S0277-3791(00)00145-1

Moseley, G. E., Richards, D. A., Smart, P. L., Standish, C. D., Hoffmann, D. L., Ten Hove, H., et al. (2015). Early–middle Holocene relative Sea-level oscillation events recorded in a submerged speleothem from the Yucatán Peninsula, Mexico. *Holocene* 25, 1511–1521. doi: 10.1177/0959683615585832

Mylroie, J. E., Carew, J. L., and Moore, A. I. (1995). Bahamian Blue holes: Description and definition. *Carbonate Evaporite* 10, 225–233. doi: 10.1007/BF03175407

Nakada, M., Okuno, J. I., and Yokoyama, Y. (2016). Total meltwater volume since the last glacial maximum and viscosity structure of earth's mantle inferred from relative Sea level changes at Barbados and Bonaparte gulf and GIA-induced J̇2. *Geophys. J. Int.* 204, 1237–1253. doi: 10.1093/gji/ggv520

Peltier, W. R. (2004). Global glacial isostasy and the surface of the ice-age earth: the ICE-5G (VM2) model and grace. *Annu. Rev. Earth Planet. Sci.* 32, 111–149. doi: 10.1146/annurev.earth.32.082503.144359

Peltier, W. R., and Fairbanks, R. G. (2006). Global glacial ice volume and last glacial maximum duration from an extended Barbados Sea level record. *Quat. Sci. Rev.* 25, 3322–3337. doi: 10.1016/j.quascirev.2006.04.010

Reimer, P. J., Austin, W. E. N., Bard, E., Bayliss, A., Blackwell, P. G., Bronk Ramsey, C., et al. (2020). The IntCal20 northern hemisphere radiocarbon age calibration curve (0–55 cal kBP). *Radiocarbon* 62, 725–757. doi: 10.1017/RDC.2020.41

Richards, D. A., Smart, P. L., and Lawrence, E. R. (1994). Maximum Sea levels for the last glacial period from U-series ages of submerged speleothems. *Nature* 367, 357–360. doi: 10.1038/367357a0

Spratt, R. M., and Lisiecki, L. (2016). A late pleistocene Sea level stack. *Clim. Past* 12, 1079–1092. doi: 10.5194/cp-12-1079-2016

Steidle, S. D., Warken, S. F., Schorndorf, N., Förstel, J., Schröder-Ritzrau, A., Moseley, G. E., et al. (2021). Reconstruction of middle to late quaternary Sea level using submerged speleothems from the northeastern yucatán peninsula. *J. Quat. Sci.* 36, 1190–1200. doi: 10.1002/jqs.3365

Surić, M., Juračić, M., Horvatinčić, N., and Krajcar Bronić, I. (2005). Late pleistocene–Holocene Sea-level rise and the pattern of coastal karst inundation: Records from submerged speleothems along the Eastern Adriatic coast (Croatia). *Mar. Geol.* 214, 163–175. doi: 10.1016/j.margeo.2004.10.030

Tuccimei, P., Soligo, M., Ginés, J., Ginés, A., Fornós, J., Kramers, J., et al. (2010). Constraining Holocene Sea levels using U-Th ages of phreatic overgrowths on speleothems from coastal caves in mallorca (Western Mediterranean). *Earth Surf. Proc. Land.* 35, 782–790. doi: 10.1002/esp.1955

van Hengstum, P. J., Cresswell, J. N., Milne, G. A., and Lliffe, T. M. (2019). Development of anchialine cave habitats and karst subterranean estuaries since the last ice age. *Sci. Rep.* 9, 1–10. doi: 10.1038/s41598-019-48058-8

Wiedicke, M., Kudrass, H.-R., and Hübscher, C. (1999). Oolitic beach barriers of the last glacial Sea-level lowstand at the outer Bengal shelf. *Mar. Geol.* 157, 7–18. doi: 10.1016/S0025-3227(98)00162-5

Yokoyama, Y., Esat, T. M., and Lambeck, K. (2001). Coupled climate and Sea-level changes deduced from huon peninsula coral terraces of the last ice age. *Earth Planet Sci. Lett.* 193, 579–587. doi: 10.1016/S0012-821X(01)00515-5

Yokoyama, Y., Esat, T. M., Thompson, W. G., Thomas, A. L., Webster, J. M., Miyairi, Y., et al. (2018). Rapid glaciation and a two-step Sea level plunge into the last glacial maximum. *Nature* 559, 603–607. doi: 10.1038/s41586-018-0335-4

Yokoyama, Y., Lambeck, K., De Deckker, P., Johnston, P., and Fifield, L. K. (2000). Timing of the last glacial maximum from observed Sea-level minima. *Nature* 406, 713–716. doi: 10.1038/35021035

Yu, X., Duan, B., Guo, K., Li, T., Feng, A., Du, J., et al. (2022). Mapping and U-Th dating of the world's deepest blue hole (South China sea): Implications for its timing, possible volcanogenic origin, and pleistocene eolianites in the xisha islands. *Mar. Geol.* 447, 106776. doi: 10.1016/j.margeo.2022.106776

Zhai, S., Mi, L., Shen, X., Liu, X., Xiu, C., Sun, Z., et al. (2015). Mineral compositions and their environmental implications in reef of shidao island, xisha. *Earth Sci. J. China Univ. Geosci.* 40, 597–605. doi: 10.3799/dqkx.2015.047

Zhao, J., Tan, L., Yang, Y., Pérez-Mejías, C., Brahim, Y. A., Lan, J., et al. (2021). New insights towards an integrated understanding of NE Asian monsoon during mid to late Holocene. *Quat. Sci. Rev.* 254, 106793. doi: 10.1016/j.quascirev.2020.106793

frontiers | Frontiers in Marine Science

TYPE Original Research
PUBLISHED 28 December 2022
DOI 10.3389/fmars.2022.1003749

OPEN ACCESS

EDITED BY
Ed Hathorne,
GEOMAR Helmholtz Center for Ocean Research Kiel (HZ), Germany

REVIEWED BY
Howie Daniel Scher,
University of South Carolina, United States
Hajime Obata,
The University of Tokyo, Japan

*CORRESPONDENCE
Qiong Wu
qiongwu@hhu.edu.cn

SPECIALTY SECTION
This article was submitted to Marine Biogeochemistry, a section of the journal Frontiers in Marine Science

RECEIVED 26 July 2022
ACCEPTED 13 December 2022
PUBLISHED 28 December 2022

CITATION
Wu Q, Liu Z, Colin C, Douville E, Zhao Y, Wu J, Dapoigny A, Bordier L, Ma P and Huang Y (2022) Dissolved rare earth element and neodymium isotope distributions in the South China Sea: Water mass source versus particle dissolution.
Front. Mar. Sci. 9:1003749.
doi: 10.3389/fmars.2022.1003749

Dissolved rare earth element and neodymium isotope distributions in the South China Sea: Water mass source versus particle dissolution

Qiong Wu[1]*, Zhifei Liu[2], Christophe Colin[3], Eric Douville[4], Yulong Zhao[2], Jiawang Wu[5], Arnaud Dapoigny[4], Louise Bordier[4], Pengfei Ma[2] and Yi Huang[3]

[1]College of Oceanography, Hohai University, Nanjing, China, [2]State Key Laboratory of Marine Geology, Tongji University, Shanghai, China, [3]Université Paris-Saclay, CNRS, GEOPS, Orsay, France, [4]Laboratoire des Sciences du Climat et de l'Environnement, LSCE/IPSL, CEA-CNRS-UVSQ, Université Paris-Saclay, Gif-sur-Yvette, France, [5]School of Marine Sciences, Sun Yat-Sen University, Zhuhai, Guangdong, China

Dissolved rare earth elements (REEs) and neodymium isotopes (εNd) have been jointly used to evaluate water mass mixing and lithogenic inputs in the ocean. As the largest marginal sea of the West Pacific, the South China Sea (SCS) is an ideal region for reconstructing past hydrological changes. However, its REE and εNd distributions and underlying controlling mechanisms remain poorly understood. On the basis of four seawater profiles spread across the SCS, this study presents dissolved REE concentrations and εNd data under summer condition to better understand the processes that potentially influence changes in these parameters and their marine cycling. The results show high concentrations of REEs and large variations in εNd (−6.7 to −2.8) in surface water, likely caused by the dissolution of riverine and marine particles. Comparison with published data from samples taken during the winter of different years in this and previous studies suggests a possible seasonal variability of middle REE enrichment. The SCS deep water shows a narrow εNd range from −4.3 to −3.4, confirming the dominant presence of the North Pacific Deep Water in the deep SCS. The intermediate water in the central SCS is characterized by a more negative εNd signal (−4.2 to −3.4) than that found in its counterpart in the West Pacific (−3.5 to −2.8), indicating alterations by deep water through three-dimensional overturning circulation from the northern to southern SCS below ~500 m. The contributions of external sources could be quantitatively estimated for the SCS in terms of Nd. The dissolution of particles

from the SCS surrounding rivers (0.26–1.3 tons/yr in summer; 5.6–29 tons/yr in winter) and continental margins (2–12 tons/yr in summer; 23–44 tons/yr in winter) may play an important role in providing additional Nd to the SCS surface water.

KEYWORDS

rare earth elements, neodymium isotopes, South China Sea, West Pacific, particle dissolution

1 Introduction

The rare earth elements (REEs) are a chemically coherent group of fourteen elements. Dissolved REE concentrations in the ocean are typically higher in deep water than in the upper layers because of vertical processes (e.g., reversible scavenging) (Elderfield, 1988; Nozaki and Alibo, 2003; Akagi, 2013; Garcia-Solsona et al., 2014; de Baar et al., 2018; Pham et al., 2019). Dissolved REEs in seawater are potentially influenced by the mixing of water masses (Osborne et al., 2015; Zheng et al., 2016; Behrens et al., 2020). In addition, river discharge, dust, hydrothermal inputs, and the dissolution of marine particles can also influence dissolved REE concentrations and patterns in the ocean (e.g., Chen et al., 2013; Grenier et al., 2013; Rousseau et al., 2015; Stichel et al., 2015; Yu et al., 2017; Grenier et al., 2018; Che et al., 2022). These external inputs have been shown to possibly cause relative enrichments of middle REEs (MREEs: Sm, Eu, Gd, Tb, and Dy) and less depletion of Ce in surface water (Greaves et al., 1994; Grenier et al., 2013; Grasse et al., 2017; Yu et al., 2017; Grenier et al., 2018; Hathorne et al., 2020). Submarine groundwater discharge could also be a significant contributor to the REE budget of coastal seawater (Johannesson and Burdige, 2007; Kim and Kim, 2014). In addition, the diffusive benthic flux of REEs from pore fluid to bottom water may account for the "missing" flux of REEs in the ocean, as predicted by modeling (Abbott et al., 2015; Haley et al., 2017).

The neodymium (Nd) isotopic composition ($^{143}Nd/^{144}Nd$) is expressed as εNd and defined as:

$$\varepsilon Nd = \left(\frac{(143_{Nd}/144_{Nd})_{sample}}{(143_{Nd}/144_{Nd})_{CHUR}} - 1\right) \times 10^4$$

where CHUR (Chondritic Uniform Reservoir, $^{143}Nd/^{144}Nd$ = 0.512638) represents the average $^{143}Nd/^{144}Nd$ ratio of present-day Earth. Over the last decade, the accumulation of present-day Nd concentration and isotopic data – especially *via* the GEOTRACES Programme – has significantly improved our understanding of REE cycle in the ocean (van de Flierdt et al., 2016 and references therein; Tachikawa et al., 2017). On the basis of knowledge gained from the present-day ocean, εNd has been recognized as a quasi-conservative property of water masses, and widely used to track past changes in ocean circulation at different time scales (Piotrowski et al., 2012; Scher et al., 2015; Dubois-Dauphin et al., 2016; Hu et al., 2016; Le Houedec et al., 2016; Molina-Kescher et al., 2016; Tachikawa et al., 2017; Colin et al., 2019; Wu et al., 2019; Du et al., 2020; Colin et al., 2021). Nevertheless, the seawater-derived εNd signal extracted from authigenic phases is not always reliable for reconstructing ocean circulation (Osborne et al., 2014; Abbott et al., 2015; Tachikawa et al., 2017; Blaser et al., 2019; Patton et al., 2021). The main debate centers on whether the record of temporal seawater εNd can faithfully reflect the mixing of water masses, especially when εNd values of seawater endmembers have changed (Wilson et al., 2014; Tachikawa et al., 2017; Zhao et al., 2019; Du et al., 2020).

Continental inputs of REEs are able to modify seawater εNd, especially in surface water, where continental Nd signatures are distinct from those of upstream seawater (Singh et al., 2012; Fröllje et al., 2016). These inputs are part of a process referred as "boundary exchange", which also integrates scavenging processes, and can alter the dissolved εNd without necessarily affecting Nd concentration (Lacan and Jeandel, 2005; Zieringer et al., 2019). Enhanced lithogenic inputs during interglacial periods could have markedly impacted seawater εNd, with εNd values offset by as much as 1- to 2-ε units (Noble et al., 2013; Yu et al., 2018; Zhao et al., 2019). Seasonal changes in seawater REE concentrations and εNd have been reported; these changes are generally attributed to the influence of biogeochemical cycling or seasonally variable terrigenous inputs (Crocket et al., 2018; Grenier et al., 2018; Hathorne et al., 2020). The Nd released from pore fluid can also act as a benthic source to bottom water, leading to the alteration of primary seawater εNd value (Abbott et al., 2016; Du et al., 2016; Haley et al., 2017). Therefore, evaluating the applicability of seawater-derived Nd isotopes in paleoceanographic studies is crucial, especially in various marginal seas that are significantly affected by terrigenous inputs.

The South China Sea (SCS) is the largest marginal sea of the West Pacific and receives substantial sediment discharges from numerous large Asian rivers, which are characterized by a larger range εNd (river sediments: –13.5 to +7) than the dissolved εNd of SCS water masses (–8.5 to –1.9) (Milliman and Farnsworth, 2011; Wei et al., 2012 and references therein; Figure 1).

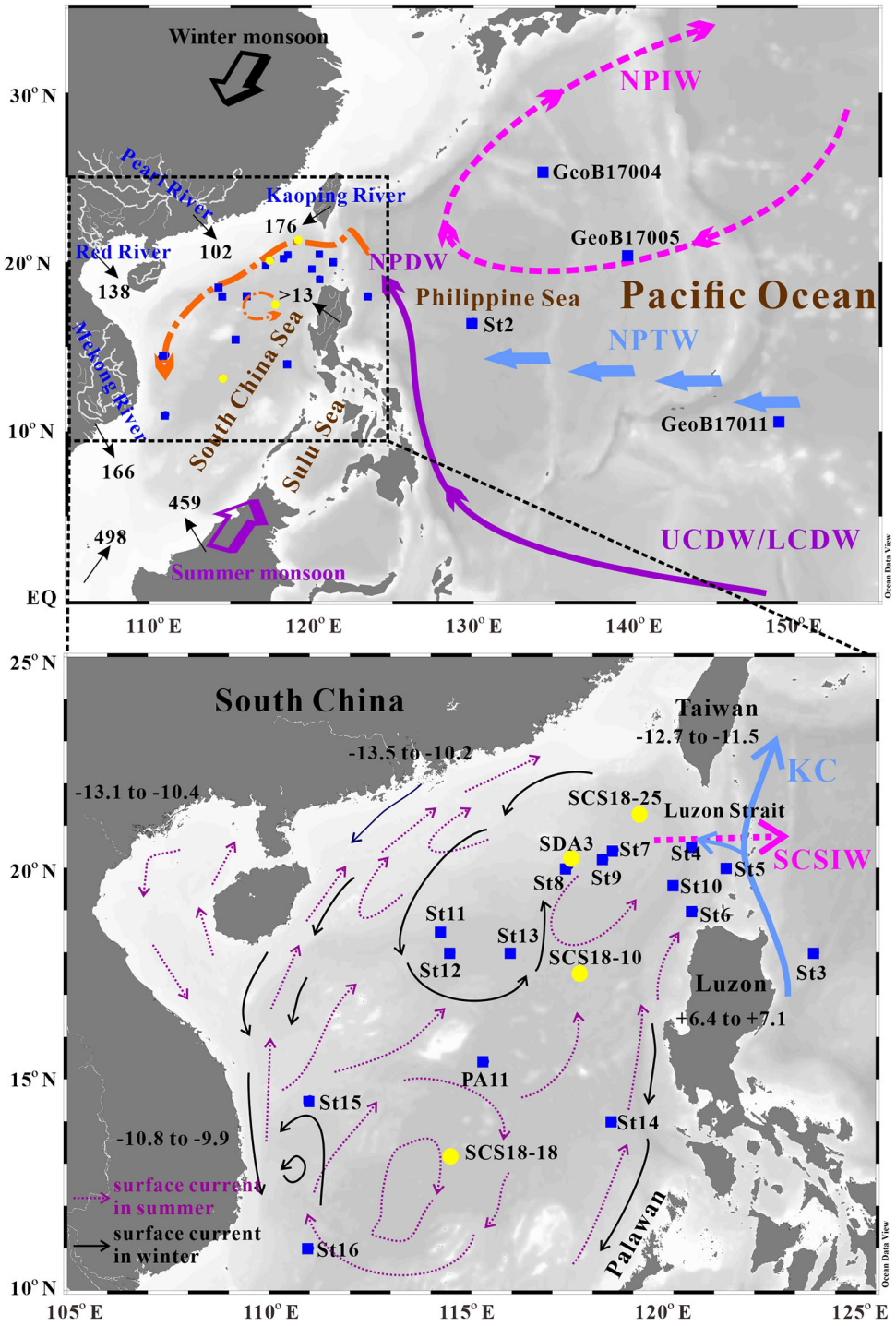

FIGURE 1
Sampling maps showing seawater stations mentioned in text and regional oceanic currents. Black arrows with numbers indicate fluvial sediment discharges from the surrounding continents (x 10^6 tons/yr; Milliman and Farnsworth, 2011; Liu et al., 2016, and references therein). Yellow dots represent the sampling stations in this study, while blue squares show the stations of published data (Alibo and Nozaki, 2000; Wu et al., 2015; Behrens et al., 2018a). The purple line denotes schematic pathway of the Upper/Lower Circumpolar Deep Water (UCDW/LCDW) in the western Pacific Ocean (modified after Kawabe and Fujio, 2010). The flow path of North Pacific Intermediate Water (NPIW) is indicated by the pink dashed line (after You, 2003). The North Pacific Tropical water (NPTW) is shown by the light blue arrows. The flow direction of North Pacific Deep Water (NPDW) in the South China Sea is shown by orange dashed lines. The local seasonal reversed monsoon directions are indicated by black and purple arrows. The black line and purple dashed line represent surface circulation in winter and summer, respectively. The map was produced using Ocean Data View (Schlitzer, 2014).

Therefore, the SCS is an ideal area to study the processes that control the marine REE cycle. Recent studies have shown that there is a decreasing trend in surface-water εNd from the northern to southern SCS, whereas the maximum of Nd concentration occurs in the central gyre (Alibo and Nozaki, 2000; Amakawa et al., 2000; Wu et al., 2015). This indicates that besides lateral water mass mixing, there might be inputs of REEs from local sources to the SCS (Amakawa et al., 2000). However, existing vertical profiles of dissolved εNd are mainly confined to the northern SCS, and seawater REE data have mostly been reported from the samples collected in winter (Alibo and Nozaki, 2000; Amakawa et al., 2000; Wu et al., 2015). To date, little is known about the geochemical cycling of seawater REEs and εNd in the central and southern SCS, in particular the potential seasonal changes in REE distribution.

In this study, we present dissolved REE and εNd data from 56 samples, collected in April-May 2018 at four seawater stations spread across the SCS. The objectives of this work are (1) to better understand the sources and geochemical cycling of dissolved REEs, in particular Nd, from the northern to central SCS; and (2) to evaluate the relative importance of water-mass mixing and external inputs (riverine water/particles, atmospheric dust, and marine particles from continental margins) on the dissolved εNd distribution. Overall, this study examines the evolution of seawater εNd as it is transported from the West Pacific to the central SCS basin.

2 Regional oceanography

The SCS is a semi-enclosed marginal sea connecting the Pacific and Indian oceans. The Luzon Strait is the single deep channel between the SCS and Pacific Ocean (Figure 1). Previous studies have revealed a vertical sandwich-like structure of the Luzon Strait, with three layers of net SCS inflow-outflow-inflow in the upper, intermediate, and deep layers, respectively (Yuan, 2002; Tian et al., 2006; Shu et al., 2014; Gan et al., 2016; Zhu et al., 2016; Zhu et al., 2019; Wang et al., 2019).

The upper layer includes the South China Sea Tropical Water (SCSTW), characterized by a salinity maximum at a depth of ~150 m. The salinity maximum of the SCSTW is relatively low compared with its counterpart North Pacific Tropical Water (NPTW) in the Philippine Sea (Figure 2). The surface circulation of the SCS is mainly driven by a complex system including the seasonally reversed monsoon activity and tidal processes (Fang et al., 1998; Li and Qu, 2006; Wang et al., 2019). In general, in the southern SCS, surface circulation is essentially driven by the seasonal reversal of monsoon winds that induces a cyclonic gyre during the winter and anti-cyclonic gyre during the summer (Fang et al., 1998). In the northern SCS, forcing induced by reversal of monsoon winds and the intrusion of the Kuroshio branch generates more complex surface currents (Fang et al., 1998; Wang et al., 2013). In addition to the wind-driven gyres, mesoscale anti-cyclonic eddies and coastal currents also affect areas along the northern continental slope of the SCS (Hu et al., 2000; Yuan et al., 2007; Han et al., 2021; Wang et al., 2021).

The South China Sea Intermediate Water (SCSIW), characterized by relatively low salinity with minimum value of ~ 34.38 between 300 and 500 m, plays an important role in the formation of meridional overturning circulation in the SCS (Tian et al., 2006; Yang et al., 2010; Gan et al., 2016; Zhu et al., 2016; Wang et al., 2019; Figure 2). The net transport of intermediate water is from the SCS to the West Pacific, balanced by a net inflow of both upper and deep water from the West Pacific (Tian et al., 2006; Tian et al., 2009). In addition, the outflow of intermediate water occurs in the northern part of the Luzon Strait in winter and the southern part in summer; while the westward flow of intermediate water into the SCS occurs in the southern part of the Luzon Strait in winter, and the northern part in summer (Tian et al., 2006; Yang et al., 2010; Xie et al., 2011; Zhu et al., 2016).

The deep water of the SCS is mainly fed by the North Pacific Deep Water (NPDW), which is derived from the Upper/Lower Circumpolar Water. With the deepest sill at ~2400 m in the Luzon Strait, the physical properties of the SCS deep water are relatively homogenous and similar to the NPDW in the Philippine Sea at ~2000 m (Broecker et al., 1986; Qu et al., 2006; Zhu et al., 2019). A basin-scale cyclonic deep current driven by the Luzon deep water overflow was observed based on density and oxygen distribution, and further supported by model results (Qu et al., 2006; Gan et al., 2016; Zhu et al., 2017). A deep western boundary current along the northern slope and a sub-basin-scale recirculation current have also been identified through modeling and mooring observations (Wang et al., 2011; Zhou et al., 2017; Zhou et al., 2020; Figure 1). In addition to these large scale currents, mesoscale eddy dissipation has been suggested to force the horizontal circulation and vertical diffusion in mid-deep layers, resulting in enhanced mid-deep overturning circulation (Tian et al., 2009; Chen et al., 2015; Wang et al., 2019).

3 Materials and methods

A total of 56 seawater samples were collected from four stations in the SCS during the KK1803 cruise carried out by R/V Jiageng from April to May, 2018 (Figure 1). The northernmost water station, SCS18-25, is located in the deep-water pathway close to the Luzon Strait. To our knowledge, station SCS18-18 is the southernmost station documenting the vertical profile of dissolved REE data in the SCS. Station SCS18-10 is located in the northeastern SCS between stations SCS18-25 and SCS18-18. Four seawater samples were collected at station SDA3, close to Dongsha Island, where a series of large drift sediments have been identified (Lüdmann et al., 2005).

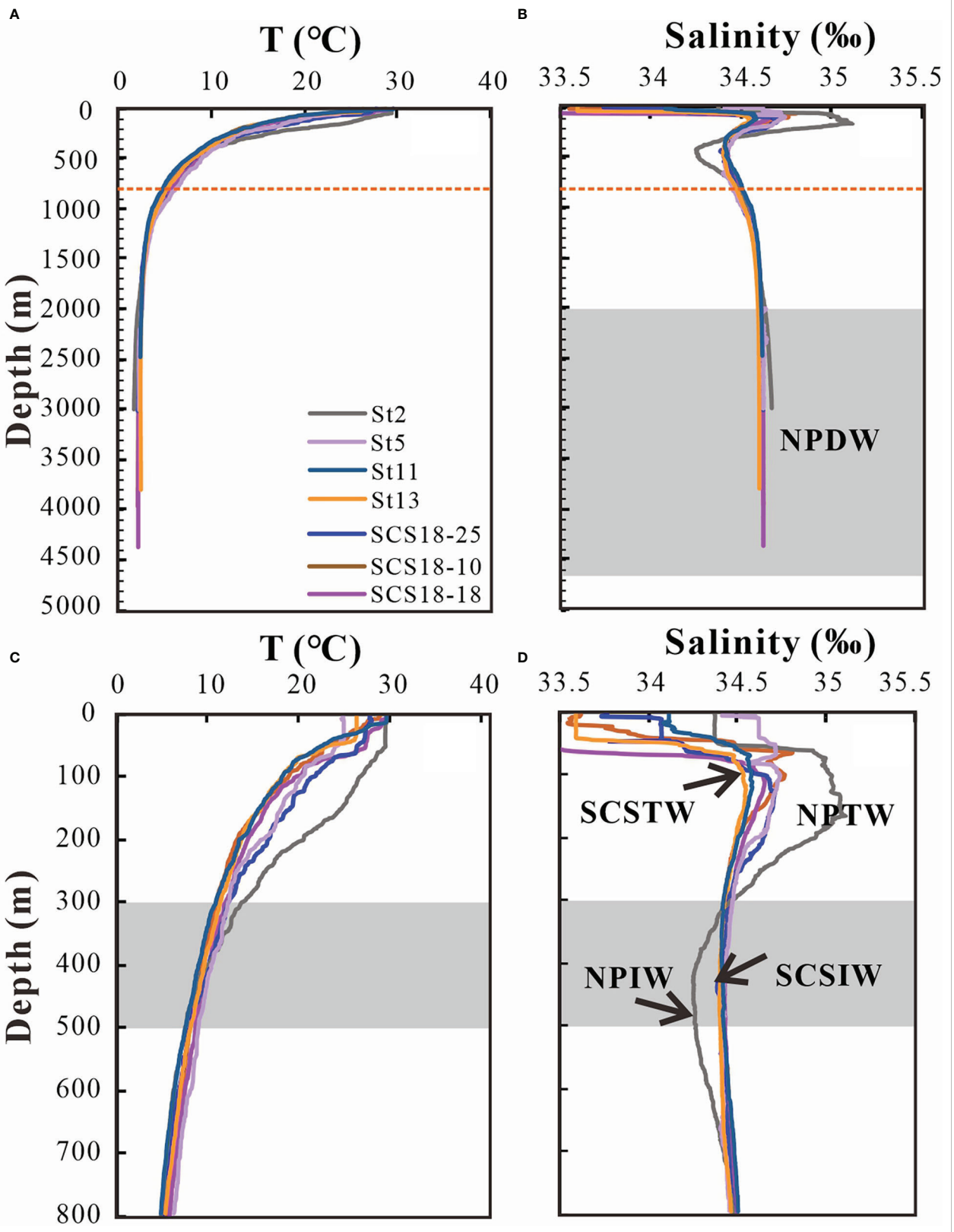

FIGURE 2
Physical water properties **(A–D)** at our sampling stations over the northern and central SCS. Data of St2, St5, St11, and St13 stations (Wu et al., 2015) are combined with our data and shown.

For the SCS18-25, SCS18-10, and SCS18-18 stations, 10 L of seawater was collected per sample using Niskin bottles mounted on a 24-position Sea-Bird's 911plus CTD-rosette. The sensor of the WetLabs C-Star transmissometer was also mounted on the CTD to measure the seawater transmissivity. Four additional intermediate-bottom water samples were collected at station SDA3 using 6 L Niskin bottles mounted on a ROV (ROPOS). Approximately 500 mL of seawater was subsampled for REE concentration measurements. All seawater samples were immediately filtered onboard using a 0.45 µm pore size filter (AcroPak^{TM} 500 Capsules, Pall Laboratory) and acidified to pH ≤ 2 with ultraclean 6 N HCl.

At the land-based laboratory, seawater Nd was purified following the protocol described by Jeandel et al. (2013). In brief, the seawater was first preconcentrated on a C18 SepPak cartridge previously loaded with a REE complexant. REEs were separated from the matrix using Bio-Rad AG50W-X8 resin (200–400 µm mesh size); Nd was then purified using Eichrom Ln-Spec resin (100–150 µm mesh size). The Nd isotopes of the purified fractions were measured using a ThermoScientific Neptune^{plus} Multi-Collector Inductively Coupled Plasma Mass Spectrometer (MC-ICP-MS) at the Laboratoire des Sciences du Climat et de l'Environnement (LSCE) in Gif-sur-Yvette (France). The Neptune^{plus} was operated using a static mode with radio frequency ranging from 1200 to 1350 W. The sample and skimmer cones were Jet and X-shape cones, respectively. We used the Apex Omega system and ESI Apex-ST PFA 100 µL/min as the desolvating system and nebulizer, respectively. During the analytical sessions, every group of two samples was bracketed with analyses of the Nd standard solution JNdi-1 (^{143}Nd/^{144}Nd of 0.512115 ± 0.000006; Tanaka et al., 2000). Sample and standard concentrations were matched at 10 ppb. The ^{143}Nd/^{144}Nd ratios were corrected for mass-dependent fractionation using ^{146}Nd/^{144}Nd = 0.7219 and an exponential law. The offset value between the results and the certified value of JNdi-1 was 0.3 epsilon units for all the analyses presented in this study. The analytical errors reported herein correspond to the external two-sigma standard deviation (based on repeat analyses of the JNdi-1 during different analytical sessions). The analytical errors obtained ranged from 0.3 to 0.4 epsilon units. Procedural blanks corresponding to all analytical procedures, including the preconcentration of Nd from the seawater matrix, were less than 200 pg. This represents< 1.6% of the lowest Nd concentration of surface water in this study. As a result, no blank correction was applied.

Dissolved REE concentrations were measured in 250 mL seawater samples using the ThermoScientific XseriesII Inductively Coupled Plasma-Mass Spectrometer (ICP-MS) at the LSCE. Each sample was spiked with a Pr and Tm solution to correct for the recovery of REEs after the chemical extraction procedures. Rare earth elements were co-precipitated with ultra-pure iron hydroxide and then extracted by successive ion exchange procedures (AG1W-X8 resin) (Jeandel et al., 2013). The BCR-2 standard solution was diluted by 47,200 times. It was not put through the column chemistry and no spike was added. The diluted BCR-2 standard solution was analyzed (n = 6) together with the seawater samples and yielded uncertainties (%; RSD: internal error of relative standard deviation was derived from a measurement repeated 10 times) of ~2% for LREEs (La, Ce, Pr, and Nd), ~3% for MREEs (Sm, Eu, Gd, Tb, and Dy), and ~5% for HREEs (Ho, Er, Tm, Yb, and Lu). REE concentrations were corrected for sensitivity drift (if any) of the machine using In and Re as internal standards. Owing to the systematic impact of the Pr spike on Tb concentrations of seawater samples, the Tb data have high uncertainties. The analytical uncertainties (RSD) of our measurements ranged from ~5% for the lightest REE to ~10% for the heaviest REE, except for a few samples with analytical uncertainties of ~20% for Sm and Eu (Table S1). The total blank of REEs averaged ~15%, except for the HREEs Yb and Lu (which averaged ~36% and ~40%, respectively), and was subtracted for all seawater samples.

4 Results

4.1 Seawater Nd isotopes

Dissolved εNd values are reported in Table 1 and Figure 3A. There are significant variations in the εNd values of surface/subsurface

TABLE 1 Location, water depts, salinity, potential temperature, ^{143}Nd/^{144}Nd ratio, εNd value and Nd concentration of the seawater samples analyzed in this study.

Depth(m)	Salinity	Pot.Temp (°C)	^{143}Nd/^{144}Nd (± 2SD)	εNd (± 2σ*)	Nd (pmol/kg)
1. Site SCS18-25 (21.307° N, 119.198° E; 3005 m; May 2018)					
5	33.935	27.511	0.512494 ± 0.000016	−2.8 ± 0.4	9.75
50	34.052	26.623	0.512517 ± 0.000014	−2.4 ± 0.3	11.09
150	34.671	18.518	0.512496 ± 0.000016	−2.8 ± 0.4	6.63
300	34.427	11.864	0.512490 ± 0.000014	−2.9 ± 0.3	7.92

(Continued)

10.3389/fmars.2022.1003749

TABLE 1 Continued

Depth(m)	Salinity	Pot.Temp (°C)	$^{143}Nd/^{144}Nd$ (± 2SD)	εNd (± 2σ*)	Nd (pmol/kg)
450	34.398	8.462	0.512461 ± 0.000011	−3.5 ± 0.3	11.24
600	34.427	6.661	0.512463 ± 0.000010	−3.4 ± 0.3	
750	34.472	5.251	0.512462 ± 0.000009	−3.4 ± 0.3	15.85
900	34.502	4.515	0.512446 ± 0.000008	−3.8 ± 0.3	16.88
1050	34.536	3.738	0.512450 ± 0.000008	−3.7 ± 0.3	17.18
1200	34.569	3.134	0.512443 ± 0.000008	−3.8 ± 0.3	20.06
1350	34.584	2.821	0.512438 ± 0.000007	−3.9 ± 0.3	20.36
1500	34.593	2.628	0.512443 ± 0.000009	−3.8 ± 0.3	23.12
1650	34.601	2.473	0.512427 ± 0.000009	−4.1 ± 0.3	24.75
1800	34.606	2.378	0.512440 ± 0.000008	−3.9 ± 0.3	24.90
1950	34.611	2.286	0.512433 ± 0.000011	−4.0 ± 0.3	25.74
2100	34.613	2.237	0.512427 ± 0.000009	−4.1 ± 0.3	25.41
2250	34.615	2.199	0.512428 ± 0.000008	−4.1 ± 0.3	25.22
2400	34.617	2.159	0.512434 ± 0.000008	−4.0 ± 0.3	25.32
2550	34.619	2.129	0.512424 ± 0.000008	−4.2 ± 0.3	25.64
2700	34.621	2.100	0.512424 ± 0.000007	−4.2 ± 0.3	25.02
2850	34.622	2.086	0.512444 ± 0.000008	−3.8 ± 0.3	25.97
2990	34.622	2.076	0.512439 ± 0.000009	−3.9 ± 0.3	23.10
2. Site SCS18-10 (17.519° N, 117.744° E; 3960 m; April 2018)					
20	33.638	26.905	0.512343 ± 0.000013	−5.8 ± 0.3	8.46
200	34.486	13.075	0.512425 ± 0.000016	−4.2 ± 0.4	9.07
500	34.414	8.176	0.512441 ± 0.000010	−3.8 ± 0.3	11.32
800	34.489	5.365	0.512452 ± 0.000018	−3.6 ± 0.5	15.15
1100	34.553	3.658	0.512383 ± 0.000008	−5.0 ± 0.3	17.68
1400	34.605	2.498	0.512451 ± 0.000008	−3.7 ± 0.3	20.57
1700	34.613	2.315	0.512448 ± 0.000007	−3.7 ± 0.3	23.39
2000	34.614	2.311	0.512444 ± 0.000008	−3.8 ± 0.3	24.26
2300	34.618	2.214	0.512443 ± 0.000008	−3.8 ± 0.3	25.62
2600	34.621	2.154	0.512455 ± 0.000009	−3.6 ± 0.3	26.78
2900	34.622	2.123	0.512459 ± 0.000008	−3.5 ± 0.3	26.50
3200	34.623	2.098	0.512457 ± 0.000008	−3.5 ± 0.3	26.47
3500	34.624	2.079	0.512449 ± 0.000010	−3.7 ± 0.3	25.18
3800	34.625	2.061	0.512440 ± 0.000009	−3.9 ± 0.3	24.30
3950	34.626	2.049	0.512449 ± 0.000009	−3.7 ± 0.3	25.26
3. Site SCS18-18 (13.167° N, 114.498° E; 4250 m; May 2018)					
5	33.416	26.668	0.512296 ± 0.000013	−6.7 ± 0.3	9.93
50	34.507	13.896	0.512376 ± 0.000010	−5.1 ± 0.3	7.39

(Continued)

TABLE 1 Continued

Depth(m)	Salinity	Pot.Temp (°C)	$^{143}Nd/^{144}Nd$ (± 2SD)	εNd (± 2σ*)	Nd (pmol/kg)
100	34.425	8.420	0.512424 ± 0.000013	−4.2 ± 0.3	10.83
300	34.488	5.509	0.512437 ± 0.000011	−3.9 ± 0.3	12.91
800	34.556	3.763	0.512423 ± 0.000010	−4.2 ± 0.3	15.99
1400	34.589	2.932	0.512424 ± 0.000010	−4.2 ± 0.3	20.02
1700	34.606	2.522	0.512438 ± 0.000008	−3.9 ± 0.3	23.14
2000	34.614	2.317	0.512451 ± 0.000009	−3.7 ± 0.3	24.07
2300	34.618	2.228	0.512444 ± 0.000008	−3.8 ± 0.3	25.32
2600	34.620	2.169	0.512464 ± 0.000009	−3.4 ± 0.3	
2900	34.622	2.129	0.512453 ± 0.000008	−3.6 ± 0.3	
3200	34.623	2.114	0.512450 ± 0.000007	−3.7 ± 0.3	
3500	34.623	2.106	0.512460 ± 0.000008	−3.5 ± 0.3	27.51
3800	34.624	2.101	0.512446 ± 0.000007	−3.8 ± 0.3	
4200	34.624	2.095	0.512459 ± 0.000008	−3.5 ± 0.3	
4. Site SDA3 (20.132°N, 117.473°E, May 2018)					
1100			0.512450 ± 0.000013	−3.7 ± 0.3	
1400			0.512420 ± 0.000013	−4.3 ± 0.3	
1700			0.512442 ± 0.000012	−3.8 ± 0.3	
1850			0.512417 ± 0.000009	−4.3 ± 0.3	

*A combined error of $\sqrt{(\text{internal error}^2 + \text{external error}^2)}$ was used when the internal error was larger than the external error.

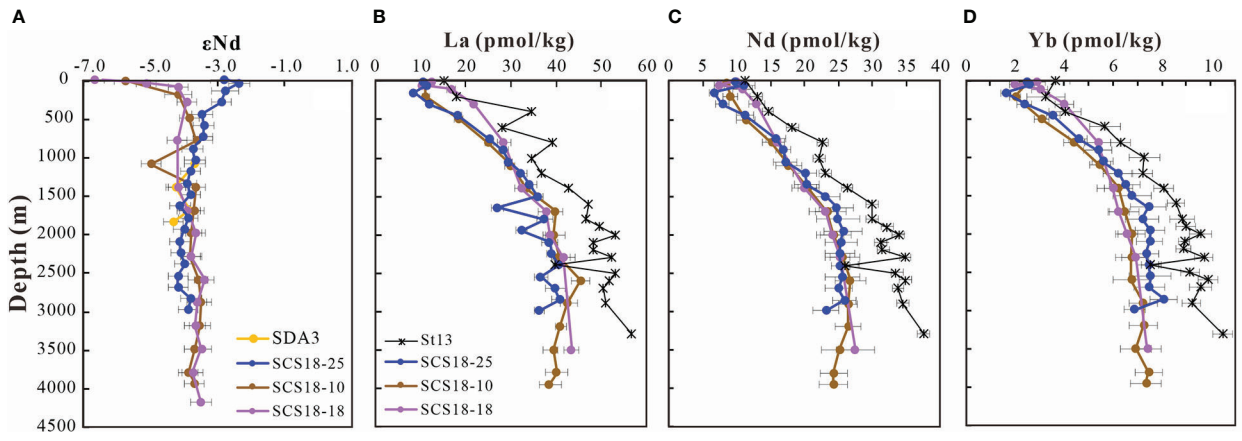

FIGURE 3
Vertical profiles of dissolved εNd **(A)** and dissolved concentrations of La **(B)**, Nd **(C)**, and Yb **(D)** reported in this study and by Wu et al. (2015; St13).

water between the investigated stations. The most unradiogenic εNd value of −6.7 ± 0.3 was observed at the southernmost station (SCS18-18) at the surface (5 m), while the most radiogenic εNd value of −2.4 ± 0.3 was found at the northernmost station (SCS18-25) at 50 m. For station SCS18-10, εNd values were −5.8 ± 0.3 and −4.2 ± 0.4 at depths of 20 and 200 m, respectively.

The εNd values of intermediate water ranged from −3.9 (1350 m) to −2.9 (300 m) at station SCS18-25. Intermediate-

water εNd at station SCS18-18 was slightly lower (−4.2) than at stations SCS18-25 and SCS18-10 (−3.7), except for a more negative value of −5.0 ± 0.3 obtained at 1100 m at station SCS18-10. For deep water, εNd values exhibited a narrow range from −4.2 to −3.4 for the aforementioned stations. The four seawater samples from station SDA3 displayed εNd values (from −4.3 to −3.7) similar to those found at corresponding depths at other stations in the SCS (from −4.2 to −3.5) and slightly lower than those in the West Pacific (from −4.1 to −2.6) (Wu et al., 2015; Behrens et al., 2018b; Figure 3A).

4.2 Seawater REE concentrations and patterns

Rare earth element concentrations are reported in Table S1. The vertical distributions of La, Nd, and Yb concentrations are plotted in Figure 3. The ranges of La, Nd, and Yb concentrations were 8.48–45.55, 8.46–27.51, and 1.63–8.08 pmol/kg, respectively. Figure 3 shows that REE concentrations decreased from surface to subsurface water, except for a minimum Nd concentration at 5 m at station SCS18-10. The lowest concentrations of other REEs were observed at 150 m at SCS18-25, 200 m at SCS18-10, and 50 m at SCS18-18. Below these water depths, REE concentrations at stations SCS18-10 and SCS18-25 gradually increased with depth, except for several deep-bottom samples below ~2500 m, from where they generally decreased.

The REE concentrations of the upper ~300 m in our study (La: 8.5–21.9 pmol/kg; Nd: 6.6–12.9 pmol/kg; Yb: 1.6–4.0 pmol/kg) are similar to those of station St13 (La: 15.2–18.0 pmol/kg; Nd: 11.2–13.4 pmol/kg; Yb: 3.3–3.6 pmol/kg; Wu et al., 2015; Figure 3). However, below this depth, the REE concentrations of this study are generally lower compared to station St13 (Wu et al., 2015; Figure 3).

Post-Archean Australian Shale (PAAS)-normalized (Taylor and McLennan, 1985) REE patterns are shown in Supplementary Figure S1. Typical seawater REE patterns with a negative Ce anomaly and an enrichment in HREEs were observed for all seawater samples, which are similar to the findings of previous studies on the SCS and open West Pacific (Wu et al., 2015; Behrens et al., 2020). In most cases, the levels of HREE enrichment were more pronounced in deep-water samples than in surface-water samples.

5 Discussion

5.1 Continental sources supplying surface water of the SCS

Figure 4 presents the PAAS-normalized REE patterns of the SCS surface water (5–20 m), together with previous results obtained from the SCS, West Pacific and northeast Indian Ocean (Alibo and Nozaki, 2000; Nozaki and Alibo, 2003; Wu et al., 2015; Yu et al., 2017; Behrens et al., 2018a). The surface Nd concentrations in the SCS (8–15 pmol/kg) are considerably higher than those in the West Pacific (2–8 pmol/kg), but lower than those in the northeast Indian Ocean (18–51 pmol/kg) (Table 1; Alibo and Nozaki, 2000; Nozaki and Alibo, 2003; Wu et al., 2015; Yu et al., 2017; Behrens et al., 2018a). The higher Nd concentrations of surface water reported in the northeast Indian Ocean have been attributed to the immense sediment discharge (~2000 × 10^6 tons/yr) from large Asian rivers, such as the Ganges–Brahmaputra, Irrawaddy and Salween (Nozaki and Alibo, 2003; Yu et al., 2017; Hathorne et al., 2020). Similarly, the SCS also receives substantial sediment discharge from several large rivers owing to frequent tectonic activity and heavy monsoon rainfall (~300 × 10^6 tons/yr in the north and ~1200 × 10^6 tons/yr in the south; Milliman and Farnsworth, 2011; Liu et al., 2016, and references therein). The relatively high Nd concentrations in surface water in the SCS compared with the West Pacific are thus likely associated with REE inputs from external sources.

In order to assess which external sources could significantly contribute to the REE distributions in the SCS, we compiled REE data of filtered water, Asian dust (loess), marine particles, river sediments, and rock from the SCS and its surrounding continents (Ding et al., 2001; Chung et al., 2009; Bayon et al., 2015; Padrones et al., 2017; Liu et al., 2018; Ma et al., 2019; Figure 5). The REE pattern of the dissolved fraction of the Kaoping River exhibit negative Ce anomaly and relative MREE enrichment, similar to those of the SCS surface water (Figure 5). However, riverine dissolved REEs could be effectively removed in estuarine areas as a result of the salt-induced coagulation of riverine colloids (Goldstein and Jacobsen, 1987; Sholkovitz and Szymczak, 2000; Lawrence and Kamber, 2006; Rousseau et al., 2015; Adebayo et al., 2018). The average Nd concentrations in the Kaoping and Pearl rivers are ~ 12 and ~370 pmol/kg, respectively (Chung et al., 2009; Ma et al., 2019). If we assume that 50–90% of river-borne REEs would be removed in low salinity areas (S< ~5‰) (Rousseau et al., 2015; Adebayo et al., 2018; Grenier et al., 2022), the remaining Nd concentrations supplied by the Kaoping and Pearl rivers would range from 1.2 to 6, and from 37 to 185 pmol/kg, respectively. The total dissolved Nd inputs from these rivers to the SCS were calculated. The runoff in the regions of Taiwan Island and South China are ~16.5 × 10^6 and ~355 × 10^6 tons/yr, respectively (Milliman and Farnsworth, 2011; Liu et al., 2016, and references therein). The result shows that the contributions of Nd from rivers after removal in estuarine areas range from 0.003 to 9 tons/yr, which are lower than the required Nd addition (53 ± 9 tons/yr) as estimated in section 5.3.1 (Table 2). In addition, the dissolved REE pattern of the Pearl River, characterized by significantly higher Nd concentration compared to the Kaoping River, does not show MREE

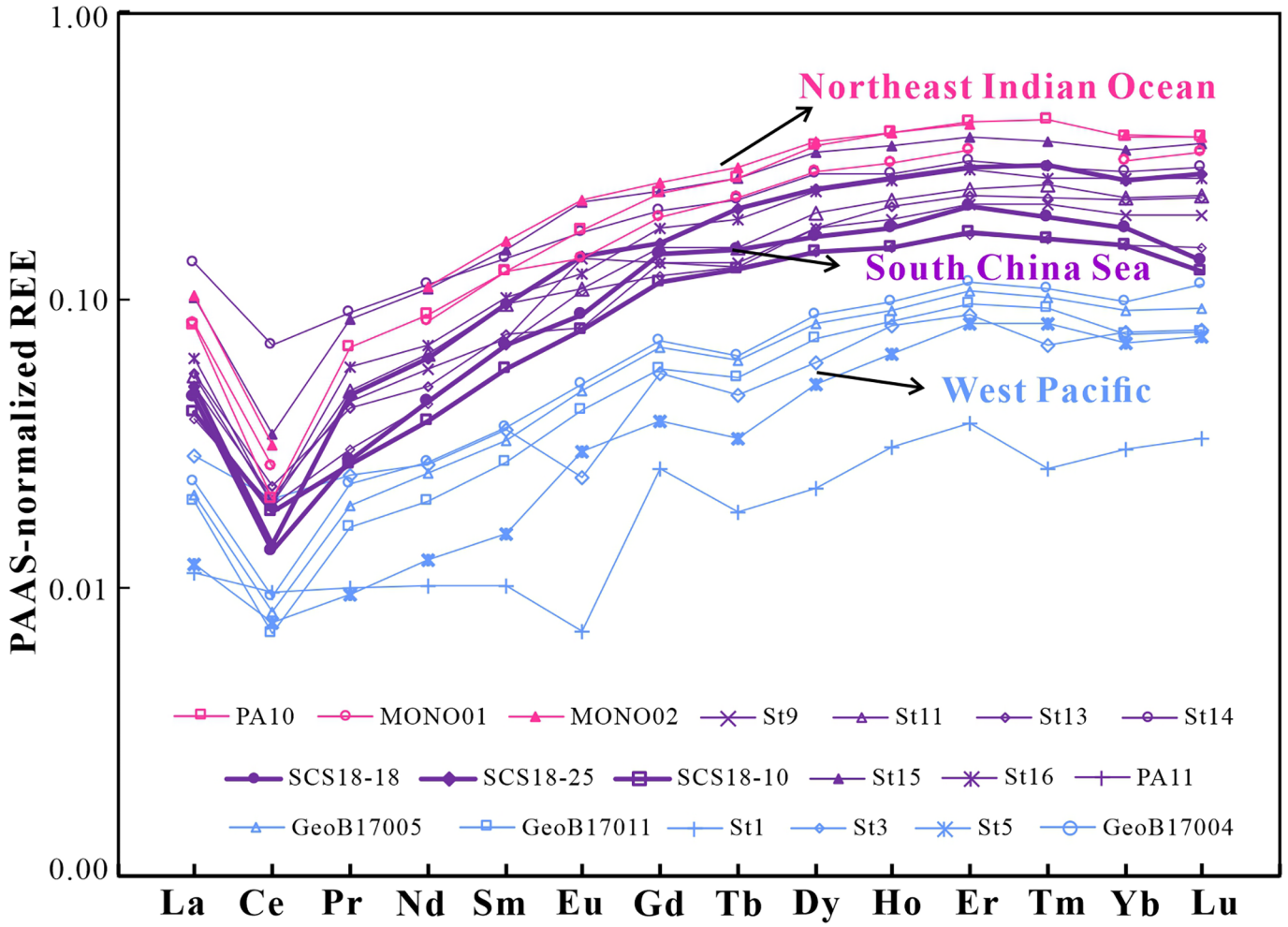

FIGURE 4
PAAS-normalized REE patterns of surface water in the SCS (this study; Alibo and Nozaki, 2000; Wu et al., 2015), the West Pacific (Wu et al., 2015; Behrens et al., 2018a), and the northeast Indian Ocean (Nozaki and Alibo, 2003; Yu et al., 2017). The locations of stations studied by Alibo and Nozaki (2000); Wu et al. (2015) and Behrens et al. (2018a) are shown in Figure 1. Stations PA10, MONO01, and MONO02 from the northeast Indian Ocean are located at 8° N, 89° E; 8° N, 89.4° E; and 11.8° N, 88.7° E, respectively (Nozaki and Alibo, 2003; Yu et al., 2017).

10.3389/fmars.2022.1003749

TABLE 2 Estimated Nd inputs from surrounding rivers.

	Initial		Flow magnitude	Final		ϵNd of	$F^{Addition}$	$F^{Removal}$
	ϵNd (± 2δ)	[Nd] (± 2δ)	(10^6 m^3/s)	ϵNd (± 2δ)	[Nd] (± 2δ)	source	(tons Nd/yr)	(tons Nd/yr)
< 50 m (summer)[a]	−6.7 ± 0.3 (SCS18-25)	9.93 ± 0.32 (SCS18-25)	0.3	−2.8 ± 0.4 (SCS18-18)	9.75 ± 0.45 (SCS18-18)	0.6	15 ± 3	16 ± 3
						7.1	5 ± 1	5 ± 1
< 50 m (winter)[b]	−2.9 ± 0.5 (St5)	2.84 ± 1.1 (St5)	1	−7 ± 0.3 (St13)	11.24 ± 0.66 (St13)	−8	53 ± 9	15 ± 9
> 1500 m[c]	−3.6 ± 0.4 (St3)	27.19 ± 0.33 (St3)	1.6	−3.8 ± 0.3 (St13)	32.84 ± 0.29 (St13)	−4.3	81 ± 13	41 ± 14

[a]Initial and final ϵNd and Nd concentration data are from this study. Flow magnitude of surface water from the Luzon Strait is from Gan et al. (2016). ϵNd values of river sediment sources are from Wei et al. (2012).
[b]Initial and final ϵNd and Nd concentration data are from Wu et al. (2015). Flow magnitude of surface water from the Luzon Strait is from Gan et al. (2016). ϵNd values of river sediment sources are from Wei et al. (2012).
[c]Initial and final ϵNd and Nd concentration data are from Wu et al. (2015). Flow magnitude of deep water from the Luzon Strait is from Zhao et al. (2014). ϵNd values of river sediment sources are from Wei et al. (2012).

enrichment as observed in the SCS surface water (Figure 5). This indicates that the effect of riverine dissolved Nd inputs on the SCS is possibly limited.

Another potential factor that could influence the REE pattern of SCS surface water is the dissolution of deposited Asian dust. It has been suggested that the dust deposition flux decreases rapidly from the coastal area to open ocean in the North Pacific region (Uematsu et al., 2003). The estimated dry and wet depositions of dust to the SCS are ~1.3×10^6 and ~0.6×10^6 tons/yr, respectively (Uematsu et al., 2003). If the dissolution efficiency of the atmospheric particles (Nd concentration: ~29.5 μg/g; Ding et al., 2001) is similar to basaltic particulate materials (~0.4%; Pearce et al., 2013), the net Nd contributions of the total atmospheric deposits to the SCS surface water are from 0.02 to 0.1 tons/yr, which are negligible compared to the required Nd inputs (53 ± 9 tons/yr; Table 2).

Furthermore, a plot of MREE/MREE* versus ϵNd (Figure 6) was used to assess the extent to which these external sources could influence the surface-water REEs, particularly ϵNd, from the northern to southern SCS. The SCS surface data in this and previous studies were compared with those of surface water in the West Pacific, sediments offshore from southern Luzon, and sinking particles collected by sediment traps in the northern SCS

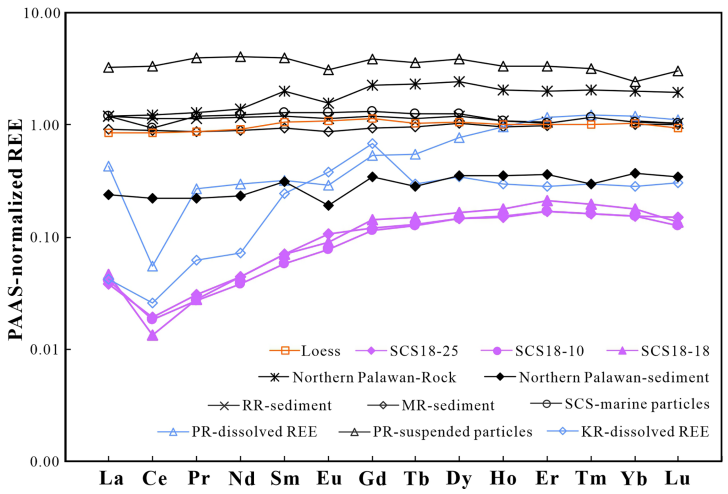

FIGURE 5
PAAS-normalized REE patterns of surface water in the SCS (× 10^6), Pearl River (PR) water (× 1; NA: 22.53° N, 113.49° E) and PR suspended particles (× 10^{-3}; L7: 22.06° N, 113.50° E) (Ma et al., 2019), Kaoping River (KP) water (× 10^2; KP3) (Chung et al., 2009), Red River sediment (RR, × 10^{-3}; 20: 20.26° N, 106.52° E) (Bayon et al., 2015), loess (× 10–3; Ding et al., 2001), northern Palawan rock (× 10–3) and sediment (× 10–3) (Padrones et al., 2017), Mekong River sediment (MR, × 10^{-3}; 12: 10.96° N, 105.06° E) (Bayon et al., 2015), and northern SCS sinking particles (× 10^{-3}; SCS-NW-1: 17.43° N, 110.67° E) (Liu et al., 2018).

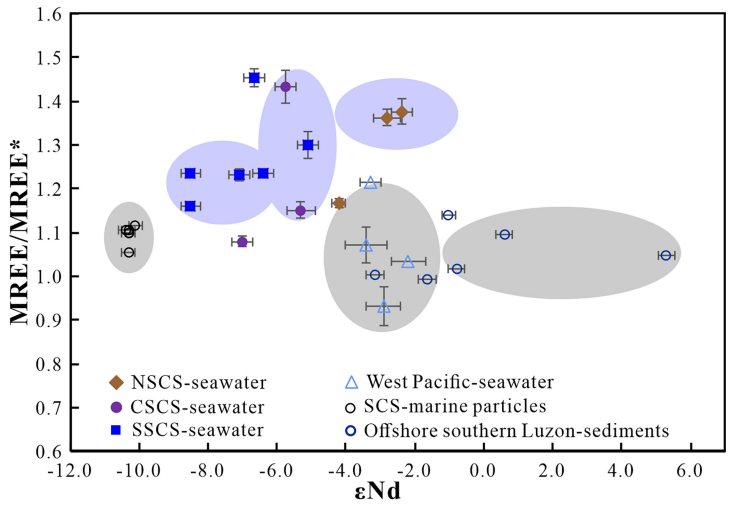

FIGURE 6
Plot of MREE/MREE* vs. εNd values for West Pacific seawater, SCS seawater, offshore southern Luzon sediments, and the SCS sinking particles (Amakawa et al., 2000; Wei et al., 2012; Wu et al., 2015; Behrens et al., 2018b; Liu et al., 2018). MREE/MREE* = 2 × (Gd + Tb + Dy)/(La + Pr + Nd + Tm + Yb + Lu) (All REEs are PAAS-normalized; Martin et al., 2010).

(Amakawa et al., 2000; Wei et al., 2012; Wu et al., 2015; Behrens et al., 2018b; Liu et al., 2018). Clearly, the MREE/MREE* values of the SCS surface water are higher than those of the West Pacific surface water (Figure 6). MREE enrichment of seawater has been documented and linked to the chemical weathering of phosphate minerals and interaction with sediment and/or suspended particles (Sholkovitz et al., 1999; Pearce et al., 2013; Crocket et al., 2018; Molina-Kescher et al., 2018). The higher MREE/MREE* values in the SCS surface water compared with those in the West Pacific indicate that the addition of MREEs may be associated with lithogenic inputs, which could preferentially release MREEs into seawater. However, most MREE/MREE* values of the SCS are also higher than those of offshore Luzon sediments and the northern SCS sinking particles (Figure 6), the contributions from these external sources are possibly not sufficient to explain this difference. There might be other fractionation processes involved to generate MREE enrichments in the SCS surface water.

In terms of εNd, the SCS surface water are generally characterized by less radiogenic Nd than West Pacific surface water. In the West Pacific, the surface-water εNd values range from −3.5 to 1.6 owing to the influence of volcanic materials (Grenier et al., 2013; Behrens et al., 2018b). The SCS surface water is characterized by large variations in εNd (−7 to −3; Figure 6). Strongly negative εNd values of surface water (< −5) are mainly found in the central and southern SCS, and these are more negative than those in the northern SCS and West Pacific (> −3.5; Wu et al., 2015; Behrens et al., 2018b). As there is no dissolved εNd data reported for riverine inputs, we cannot assess the Nd contribution of river water to SCS surface water. However, river sediments surrounding the SCS have εNd values of −13.5 to −9.9, except for those of Luzon Island (εNd: 6.4–7.1; Goldstein and Jacobsen, 1988; Wei et al., 2012, and references therein). The sinking particles obtained from the northern SCS sediment trap are also characterized by negative εNd values of −10 (Liu et al., 2018). We suspect that there is a modification of the εNd of West Pacific surface inflow caused by terrigenous inputs, which are characterized by more positive εNd values of ~7 in Luzon Island and more negative εNd values of ~−10 in the northern SCS (Goldstein and Jacobsen, 1988; Wei et al., 2012, and references therein). This might also explain the observed southward decrease in surface-water εNd from the northern to southern SCS (Figure 7).

This spatial pattern agrees with previous studies showing the most negative εNd in the southern SCS and the most positive εNd in the vicinity of Luzon Island in the north (Amakawa et al., 2000; Wu et al., 2015; Figure 7). The less negative εNd in the northern SCS compared with the southern SCS possibly results from the influence of advection of the NPTW, which is characterized by εNd signatures of −3.1 to −1.7 (Behrens et al., 2018b). Meanwhile, the contribution of lithogenic inputs from Luzon Island, characterized by radiogenic Nd isotopic composition (εNd > 6) and relatively enriched MREEs, could also modify the εNd of surface water in the northern SCS (Goldstein and Jacobsen, 1988; Padrones et al., 2017; Figure 6). For the southern SCS, the negative εNd values are probably related to the dissolution of particles from the Pearl River, which mainly supplies sediments to the southwest of the northern SCS (Shao et al., 2009). Overall, the εNd values of SCS surface water become more negative with increased distance

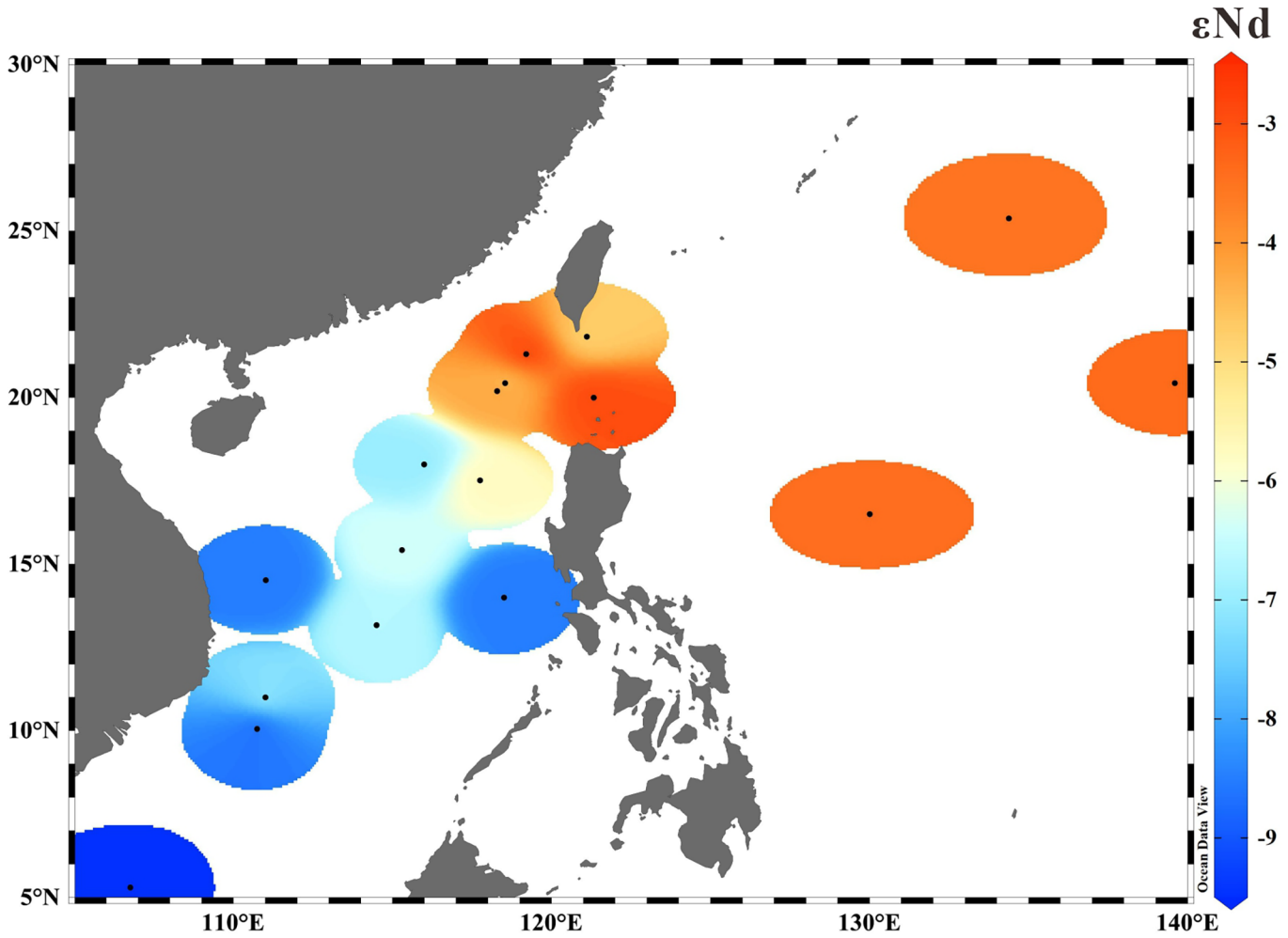

FIGURE 7
Distribution of surface water εNd in the SCS and West Pacific. Data sources: this study, Amakawa et al. (2000); Wu et al. (2015), and Behrens et al. (2018b). The figure was created using Ocean Data View (Schlitzer, 2014).

10.3389/fmars.2022.1003749

from the Luzon Strait (Figure 7). The northeast-southwest decreasing contribution of particle dissolution from Luzon Island (εNd: ~7) and the increasing contribution of the northern SCS river sediments (εNd: ~−10) might result in such persistent changes in SCS surface-water εNd.

Combining basin-wide surface-water MREE/MREE* values with our newly obtained SCS seawater εNd data, our results suggest an important role of terrigenous inputs in controlling surface-water εNd and emphasize the need for the investigation of whether such MREE enrichments can result from the dissolution of these particulate sources. Other possible explanations of MREE enrichments are explored below.

5.2 Seasonal variation in REEs in the SCS

We compiled published REE data from the SCS and West Pacific to better understand the exchange of REEs between the marginal sea and open ocean (Alibo and Nozaki, 2000; Wu et al., 2015; Behrens et al., 2018a). High-resolution vertical profiles of PAAS-normalized seawater MREE/MREE*, MREE/HREE, and Nd/Yb ratios for the SCS and West Pacific are shown in Figure 8. All seawater samples investigated in this study were collected in late April and May, 2018, when the southwest summer monsoon starts to prevail in the SCS, whereas seawater samples at stations St5, St13, and PA11 were collected during the period in which the northeast winter monsoon intensifies (Alibo and Nozaki, 2000; Wu et al., 2015). Accordingly, our data compilation allows potential seasonal variability to be assessed.

Overall, the vertical profiles of MREE/MREE*, MREE/HREE, and Nd/Yb ratios show a decrease from a maximum at the surface to a minimum at approximately 1000 m depth, followed by an increase, reaching another maximum at approximately 2000–3000 m depth.

Of particular interest is a clear seasonal variability in the vertical distribution of MREE/MREE* and MREE/HREE ratios within the SCS (Figure 8), with higher values for the samples collected in summer (MREE/MREE*: 1.0 to 1.4) and lower values for those collected in winter (MREE/MREE*: 0.8 to 1.2) (Alibo and Nozaki, 2000; Wu et al., 2015). Notably, the SCS samples collected in winter show similar ratios of MREE/MREE* and MREE/HREE to those of the West Pacific. However, there is no discernable seasonal variation in Nd/Yb ratios, suggesting that LREEs vary similarly to HREEs between summer and winter (Figure 8). In the following, we attempt to explain the observed vertical distributions of MREE/MREE*, MREE/HREE, and Nd/Yb ratios in the SCS.

First, the seasonal variations may be associated with the enhanced inflow from the West Pacific to the SCS in winter, which is characterized by relatively low MREE/MREE* and MREE/HREE ratios compared with those found in the SCS in summer. Specifically, the upper layer of the SCS is strongly fed (3.5–10 Sv) by West Pacific water through the Luzon Strait when the northeast monsoon prevails over the SCS (i.e., in winter); while in summer, the upper layer water in the SCS outflows to the West Pacific (~5 Sv) (Tian et al., 2006; Yang et al., 2010; Gan et al., 2016). In this case, the seasonal variabilities in MREE/MREE* and MREE/HREE ratios might reflect the variations of the water-mass mixing between the West Pacific and SCS. However, Nd/Yb ratios in the SCS do not show significant changes between summer and winter, but are higher than those in the West Pacific, suggesting that the mixing of West Pacific and SCS water masses cannot be fully responsible for the seasonal MREE/MREE* variations in the SCS.

Second, the observed seasonal variations in MREE/MREE* and MREE/HREE ratios could be related to lithogenic inputs and the associated preferential removal of LREEs and MREEs by particles. Sediment trap data from the northwest SCS have shown three peaks of lithogenic flux during August 2012, October 2012, and February 2013, while the flux is relatively low in May (Zhang et al., 2018). A potential release of LREEs and MREEs from sediment to the water column has been suggested (Crocket et al., 2018; Molina-Kescher et al., 2018). If the higher lithogenic inputs in winter are sources of MREEs in the SCS, the results would be contrary to those observed for MREE/MREE* and MREE/HREE (i.e., lower values in winter compared with summer). In contrast, lithogenic inputs could also be a sink for LREEs and MREEs because these elements are more easily adsorbed to particles and surface coatings (i.e., iron-oxide) compared with HREEs (Elderfield, 1988; Sholkovitz et al., 1994). Various inorganic and biogenic phases can remove LREEs and MREEs in the Kerguelen Plateau area (Grenier et al., 2018). However, a preferential scavenging of LREEs and MREEs by lithogenic inputs is not supported by the similar distribution patterns of Nd/Yb ratios between summer and winter in the SCS.

A third possible explanation is the release of MREEs from surface coatings (i.e., iron-oxide) affiliated to particles caused by seasonal changes in dissolved oxygen content. Surface coatings, such as iron-oxides, can preferentially scavenge LREEs and MREEs in the surface ocean and preferentially release them in deep water layers (Sholkovitz et al., 1994). Meanwhile, the desorption of MREEs from iron-oxides is likely sensitive to environmental oxygen content (Haley et al., 2004). In the SCS, the water oxygen content in summer is lower than that in winter owing to the reduced inflow of deep water with a relatively high oxygen content from the West Pacific (Lin and Han, 1997; Li and Qu, 2006; Wang et al., 2018; Figure S2). Such an oxygen-depleted environment might favor the release of MREEs adsorbed to preformed iron-oxide into the water column, leading to higher MREE/MREE* and MREE/HREE ratios in summer compared with winter (Figure 8).

The inferred seasonal pattern in oxygen content may be strengthened by an enhanced primary productivity in summer compared with winter, as higher productivity would consume more dissolved oxygen for the degradation of organic matters

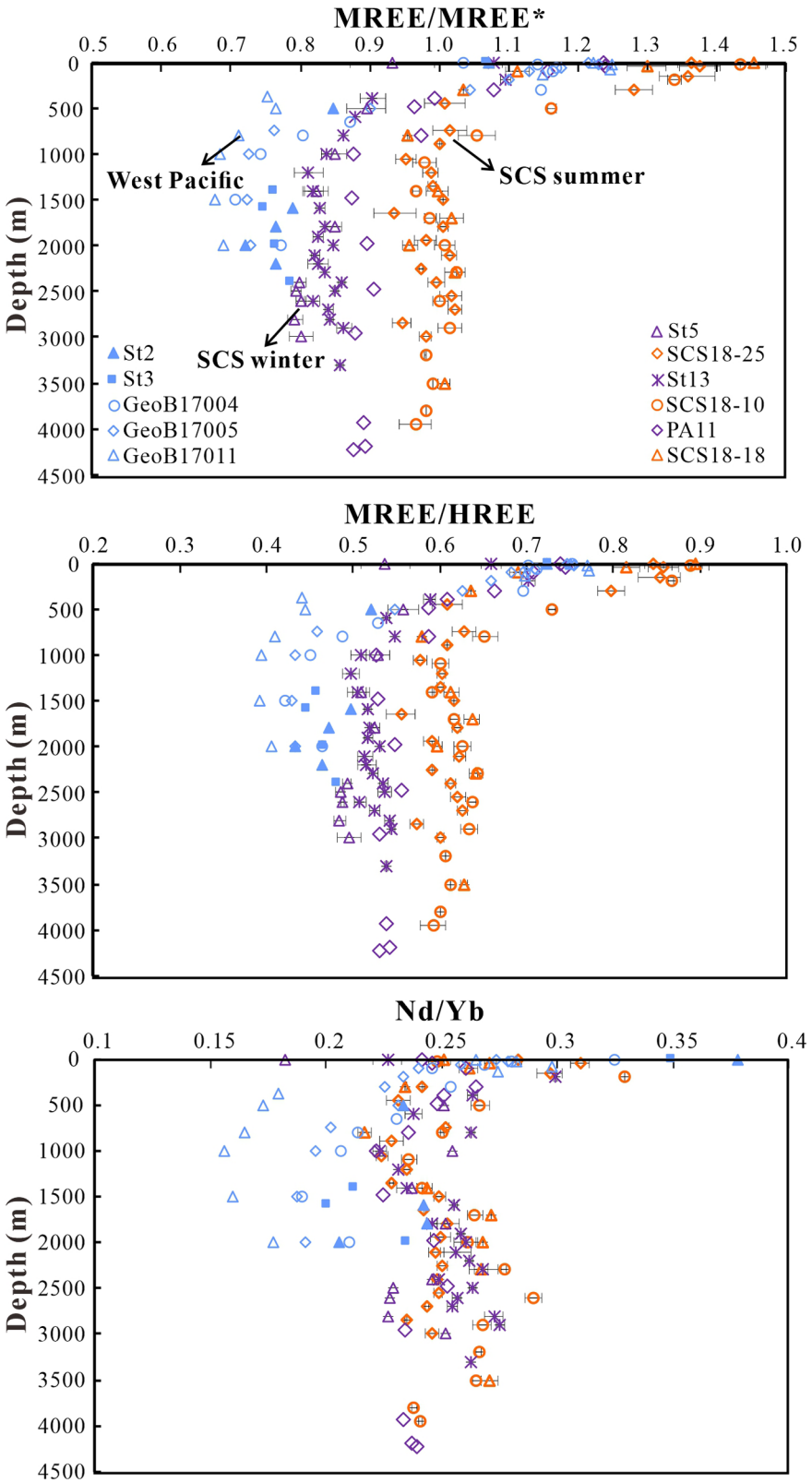

FIGURE 8
Vertical distribution of MREE/MREE*, MREE/HREE, and Nd/Yb ratios in the SCS (this study; Wu et al., 2015) and West Pacific (Behrens et al., 2018a). MREE/HREE is calculated using: MREE/HREE = (Gd + Tb + Dy)/(Tm + Yb + Lu).

settling down through the water column. However, the seasonal change in primary productivity remains a matter of debate. A higher productivity in summer has been attributed to increased river discharge and coastal upwelling related to the Asian summer monsoon (Song et al., 2012; Xie et al., 2020). In contrast, evidence from particulate organic carbon fluxes suggests a higher productivity in the central SCS in winter, rather than summer, owing to stronger vertical mixing induced by the northeast monsoon (Chen et al., 1998; Li et al., 2017). Besides, the seasonal changes in oxygen concentrations in the SCS are not significant (Figure S2), with respect to seasonality, further studies on the relationship between changes in dissolved MREEs and oxygen content are required.

Fourth, microbial activity may also affect the distribution of MREEs in the SCS. It was implied that microbes (e.g., microbial siderophores) can complex REEs and may affect the fractionation of REEs through iron cycling in the ocean (Haley et al., 2014). In the Gulf of Alaska, the "bio-reactive" REE group shows different REE patterns from those of "passive" REE group. The MREE/MREE* of "bio-reactive" group is ~1.2, which is higher than the latter group (~1.0) (Haley et al., 2014). The preferentially adsorption of HREEs by organically bound Fe, *via* microbial mediation, may result in the relative MREE enrichments in seawater.

Indeed, it has been suggested that relatively high temperature (~25 °C) and moderate pH (~7.5) would favor bacterial growth; when the pH is ~8.5, the bacterial growth decreased quickly (Sinha and Parli, 2020). A recent study on the Canadian Arctic Archipelago indicated that the pH and dissolved organic carbon concentration could partly influence the dissolved REE concentrations in rivers (Grenier et al., 2022).

In the SCS, bacterial production grew fast due to the increases in bacterial abundance and dissolved organic carbon inputs in summer (Xu et al., 2018). The surface water pH in summer (~7.6) is generally lower than in winter (~8.1) (Liu et al., 2014). The low pH in summer might also enhance bacterial growth including the siderophores production. It is likely that both lower pH and more dissolved organic carbon inputs in summer may result in the MREE enrichments of surface water as observed in this study. But note that, the available data are very scarce and mostly limited to the upper layer of the water column (Chen et al., 2021). The association between the MREE enrichment and microbial activity in the SCS requires to be better constrained.

As discussed above, although the seasonal variations in MREE/MREE* and MREE/HREE ratios in the SCS is clear, it could not be explained by a single factor alone. It seems that MREE/MREE* vary distinctly from LREEs and HREEs. However, as seawater samples in this and previous studies were collected in different years and the locations are slightly different (Alibo and Nozaki, 2000; Wu et al., 2015; Behrens et al., 2018b), it is uncertain that if the physical properties of seawater were changed in different years. Further investigations are highly required to unravel and better understand the underlying processes leading to the MREE enrichments observed for the SCS.

5.3 Processes influencing the εNd distribution in the SCS

5.3.1 Factors influencing the ϵNd of the SCS upper 200 m

Figure 9 presents the comparison of the ϵNd between the SCS and Northwest Pacific (Wu et al., 2015; Behrens et al., 2018b). For the upper 200 m, the ϵNd values of the central SCS (−6.7 to −4.2) are more negative than those in the Northwest Pacific (−3.5 to −2.2) and northern SCS (−2.8 to −2.4; Figures 9B, D). The subsurface-water ϵNd values in the central SCS are more negative compared to those of the northern SCS (Figures 9B, D).

Modifications of seawater Nd isotopic signatures through continental inputs have been observed in several oceanic regions, especially near basaltic continental margins (Grasse et al., 2012; Grenier et al., 2013; Yu et al., 2017; Behrens et al., 2018b). In the northern SCS, sedimentary ϵNd values of the surrounding rivers range from −13.5 to −10.2, except for the more positive values obtained from the Luzon Island (0.6–7.1; Goldstein and Jacobsen, 1988; Wei et al., 2012 and references therein). Assuming that the shift in ϵNd from the northern to southern SCS surface/subsurface water are associated with the Nd released from suspended and sinking particles supplied by continental margins and river discharge, we attempted to calculate the Nd fluxes in the SCS. The calculation was performed using the following equations (1) and (2), defined by Lacan and Jeandel (2005). F_w and F_{Nd} refer to the flow magnitude of current (Sv, 10^6 m^3/s) and Nd flux, respectively. *Initial* and *Final* refer to measured parameters of upstream and downstream, respectively. *Addition* and *Removal* refer to fluxes from the external sources to the water mass and leaving the water mass, respectively.

$$F_{Nd}^{Addition} = F_W \times [Nd]^{Initial} \times \frac{\epsilon_{Nd}^{Final} - \epsilon_{Nd}^{Initial}}{\epsilon_{Nd}^{Addition} - \epsilon_{Nd}^{Final}} \quad (1)$$

$$F_{Nd}^{Removal} = F_W \times \frac{[Nd]^{Final} \times \left(\epsilon_{Nd}^{Final} - \epsilon_{Nd}^{Addition}\right) - [Nd]^{Initial} \times \left(\epsilon_{Nd}^{Initial} - \epsilon_{Nd}^{Addition}\right)}{\epsilon_{Nd}^{Addition} - \epsilon_{Nd}^{Final}} \quad (2)$$

The parameters were setup as follows: for the upper 50 m, the flow magnitude from the Luzon Strait to the SCS is approximately 0.3 Sv in summer and 1 Sv in winter. This setup is based on the simulated net transport and volume flux through the Luzon Strait (Gan et al., 2016). The flow magnitude of deep water across the Luzon Strait is ~1.6 Sv (Zhao et al., 2014).

Because there is no surface-water ϵNd data reported for the West Pacific in summer and the surface water outflow from the

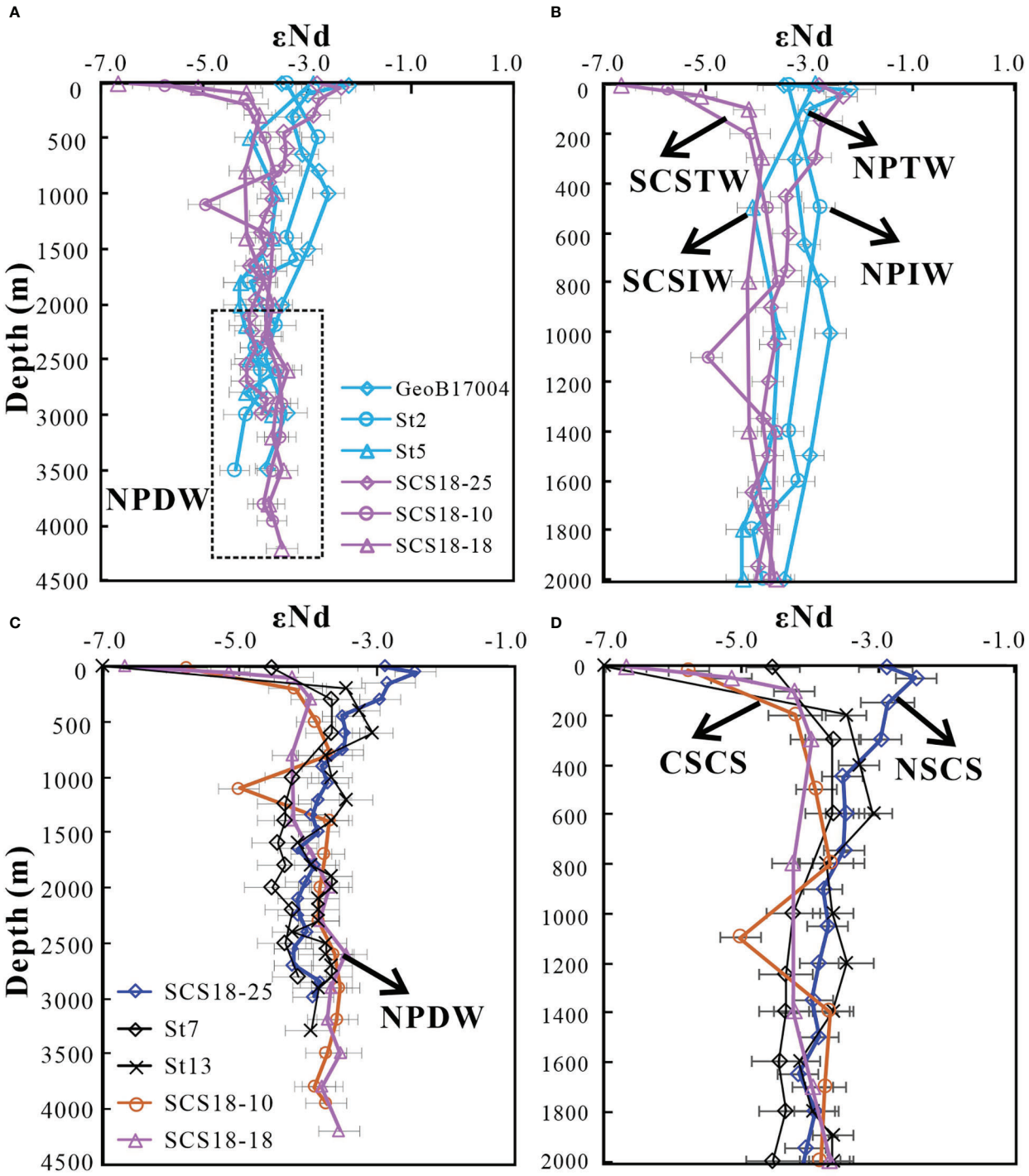

FIGURE 9
Comparisons of εNd vertical profiles between the SCS and the North Pacific **(A, B)**, and within the SCS **(C, D)**. εNd values of the North Pacific are from Wu et al. (2015); Behrens et al. (2018b).

SCS to the West Pacific, we took the surface-water εNd and Nd concentrations from the southernmost (SCS18-18) and northernmost (SCS18-25) stations as the initial and final values, respectively (Table 2). The Nd from the Luzon Island (εNd: 0.6–7.1) is the only external source that could provide radiogenic Nd to the SCS (Goldstein and Jacobsen, 1988; Wei et al., 2012 and references therein). In the winter season, surface-water εNd and Nd concentrations from the Luzon Strait (St5, initial station) and central SCS (St13, final station) were used for calculation. To obtain the valid Nd addition and Nd removal (> 0) in the SCS, the εNd of external sources should range from –8.5 to –7.3 (average ~–8). This external εNd source is the result of mixing of ~75% of less radiogenic εNd (average εNd in Taiwanese and Pearl rivers sediments: ~–12) and ~25% of more radiogenic εNd (average εNd in Luzon Island sediments: +4) (Goldstein and Jacobsen, 1988; Wei et al., 2012 and references therein).

In summer, the Nd flux of the surface water from SCS18-25 to SCS18-18 was estimated as 5 to 15 tons/yr for Nd addition, and 5 to 16 tons/yr for Nd removal (Table 2). In winter, the estimated Nd flux from the stations St5 to St13 in the SCS suggests a Nd addition/removal of ~53/~15 tons/yr. To evaluate the relative Nd contributions of external sources to the SCS surface water, we further assessed the Nd inputs from the river-borne Nd and the dissolution of riverine and marine particles. The efficiency of particle dissolution (~0.4%) and Nd removal (50–90%) in low salinity areas were taken into account when calculating the Nd inputs from particle dissolution (Pearce et al., 2013; Rousseau et al., 2015; Adebayo et al., 2018; Grenier et al., 2022).

Sedimentary Nd concentrations and the river discharge from the Luzon Island are ~50 μg/g and ~13 tons/yr, respectively (Milliman and Farnsworth, 2011; Padrones et al., 2017), the calculated Nd inputs from the dissolution of riverine particles range from ~0.26 to ~1.3 tons/yr. These values are smaller than the required Nd addition in summer (5 to 15 tons/yr), suggesting more contributions from other external sources. The runoff from the Luzon Island are 72 × 10^6 tons/yr, assuming that the Nd concentrations of river water from Luzon Island could be as high as those of Pearl River water (~370 pmol/kg), the contributions of dissolved Nd from Luzon Island rivers to the SCS surface water could be no more than ~1.8 tons/yr (Milliman and Farnsworth, 2011). The total Nd inputs (< 3.1 tons/yr) from the Luzon Island are still not sufficient to explain the required Nd inputs. The "missing" Nd inputs range from 2 to 12 tons/yr. We suspect that this "missing" Nd inputs might be from the dissolution of re-suspended particles from continental margins of the Luzon Island.

In winter, the required Nd addition is ~53 tons/yr (Table 2). The estimated Nd addition from the unradiogenic (e.g., Taiwanese and Pearl rivers) and radiogenic Nd (e.g., Luzon Island) are ~39.75 and ~13.25 tons/yr, respectively. Nd concentrations of sediments from the Taiwanese (176 × 10^6 tons/yr) and Pearl (102 × 10^6 tons/yr) rivers are ~40 and ~70 μg/g, respectively (Chung et al., 2009; Bayon et al., 2015; Ma et al., 2019). Thus, the Nd inputs to the SCS surface water through particle dissolution range from 5.6 to 28 tons/yr. The contributions of the remaining river-borne Nd (0.003 to 9 tons/yr) were also integrated, the total Nd inputs from these two external sources could be 6–37 tons/yr, which are smaller than the expected Nd addition from unradiogenic Nd (~39.75 tons/yr), especially when the strong Nd removal (~90%) take place. There is also a gap of ~10 tons/yr between the total Nd inputs (< 3.1 tons/yr) and the expected Nd addition (~13.25 tons/yr) from the Luzon Island. Such results indicate that the Nd inputs from the dissolution of re-suspended particles from continental margins (23–44 tons/yr) are required.

Overall, the Nd fluxes to the SCS surface water in both summer and winter imply that the dissolution of lithogenic inputs, including particles supplied by river and continental margins, may play an important role in modifying the surface εNd within the SCS.

5.3.2 Factors influencing the εNd of the intermediate and deep water in the SCS

For the intermediate water (300–1500 m), the εNd values in the central SCS are generally lower (−4.2 to −3.9) than those in the northern SCS (−3.8 to −2.9) and Northwest Pacific (−3.3 to −2.6; Wu et al., 2015; Behrens et al., 2018b; Figures 9A, C). We observed a negative excursion of seawater εNd at station SCS18-10 (−5.0 ± 0.3; Figures 3A, C) that was not accompanied by any change in the Nd concentration (Table 1). This is probably related to particle–seawater exchanges that mainly impact seawater Nd isotopic composition without altering seawater Nd concentration. This interpretation is supported by the transmissivity data showing a rapid decrease at ~1000 m depth at station SCS18-10, which indicates the existence of a nepheloid layer that contains a large volume of suspended particles (Figure S3).

Nevertheless, the εNd values of intermediate water in the central SCS are generally similar to those obtained from deep water in the northern SCS (−4.2 to −3.8; Figures 9A, C). Diapycnal mixing in the mid–deep SCS can reach up to 10^{-3} m^2/s, which is sufficient to maintain a three-dimensional circulation in the mid–deep layer of the SCS (Wang et al., 2019, and references therein). The generally low εNd values in the central SCS compared with the northern SCS appear to be related to the three-dimensional overturning circulation (below ~500 m) of the SCS (Wang et al., 2016; Wang et al., 2019, and references therein), permitting the Nd isotopic composition of deep water in the northern SCS to be mixed with intermediate water in the central SCS.

Below 2000 m in the SCS, the εNd values generally range from −4.2 to −3.4, similarly to those at ~2000 m in the North Pacific (−3.9 to −3.5). This result is consistent with physical oceanographic studies, showing the predominance of NPDW in the SCS (Tian et al., 2006; Tian et al., 2009; Wang et al., 2019).

While the εNd values of deep layer (> 1500 m) are similar between the SCS and West Pacific, the SCS has higher Nd concentrations than the West Pacific. To understand the evolution of the Nd concentration and εNd from the West Pacific to the SCS, we also calculated the Nd flux of deep water in the SCS. Averaged εNd and Nd concentrations from stations St3 (1600–2000 m) and St13 (1600–3300 m) were set as the initial and final values, respectively. The required εNd of external sources ranges from ~–4.7 to ~–3.9 (average εNd: ~–4.3), as a result of the mixing of less radiogenic (εNd: ~–12) and radiogenic Nd (εNd: ~+4) (Goldstein and Jacobsen, 1988; Wei et al., 2012 and references therein). The relative contributions from the unradiogenic and radiogenic Nd are ~52% and ~48%, respectively (Goldstein and Jacobsen, 1988; Wei et al., 2012 and references therein). The estimated Nd addition to the SCS deep water is ~81 tons/yr (Table 2). Thus, the expected Nd inputs from the unradiogenic and radiogenic Nd are ~42 tons/yr and ~39 tons/yr, respectively. These values are larger than the total Nd inputs from the unradiogenic (e.g., Taiwanese and Pearl rivers: 6–37 tons/yr) and radiogenic Nd (e.g., Luzon Island: ~3.1 tons/yr). Such results imply that the Nd input from the SCS surrounding continental margins is required. Meanwhile, the Nd removal from the SCS deep water is ~41 tons/yr (Table 2). The net Nd addition to the SCS deep water is ~ 40 tons/yr, which could be the explanation for increased deep water Nd concentrations from the West Pacific to the SCS.

Our results indicate that the limited modification of deep-water εNd is probably related to the similar εNd between the mixed external sources and the SCS deep water that could contribute to the increased Nd concentration without altering the εNd of deep water.

6 Conclusions

We present seawater REE and Nd isotope data from four stations collected in the South China Sea (SCS). Along with previous results, this study provides a better understanding of the behavior of dissolved REEs and Nd isotopes as they are transported from the West Pacific to SCS. The major conclusions drawn are as follows:

(1) Our data reveal a general increase in REE concentrations with depth, except for surface water and bottom water. The relatively high REE concentrations and low εNd values in surface water compared with subsurface water in the SCS are possibly linked to the dissolution of particles from surrounding rivers and continental margins. The relatively low εNd values in the SCS surface and subsurface water in the areas away from the Luzon Strait, when compared with those in the West Pacific, likely reflect the decreasing influence of the Luzon Island and increasing influence of the Taiwan Island and South China.

(2) Seasonal variations in the vertical distributions of MREE/MREE* and MREE/HREE are clearly observed, while the Nd/Yb ratios are similar between summer and winter. The features suggest that LREEs and HREEs vary similarly while MREEs vary distinctly from LREEs and HREEs. The fractionation processes affecting MREE enrichments in the SCS (e.g., particle dissolution/scavenge, oxygen content variation, and microbial activity) need to be further studied in future.

(3) The differences in intermediate-water εNd values between the northern and central SCS are most likely related to the basin-scale three-dimensional overturning circulation that introduces the deep-water εNd signature from the northern SCS to intermediate water in the central SCS. Our results show a relatively constant value of ~–3.8 for the SCS deep water, confirming the predominance of the NPDW in the deep SCS (Wu et al., 2015; Behrens et al., 2018b).

(4) Based on the present and previous data along with the relevant knowledge, we calculated the Nd contributions from major external sources, and the Nd exchanges between seawater and particles were quantitatively estimated for the SCS basin. We find that in addition to riverine particles, the dissolution of re-suspended particles from continental margins could be an important external source of Nd to the SCS. The limited modification of deep-water εNd by particle–seawater interaction during the propagation of deep water from the West Pacific to the SCS is likely related to the similar εNd between the mixed external sources and the SCS deep water.

Data availability statement

The datasets presented in this study can be found in online repositories. The names of the repository/repositories and accession number(s) can be found below: www.pangaea.de, https://doi.pangaea.de/10.1594/PANGAEA.943241.

Author contributions

QW, ZL, and CC designed the research and wrote the draft of the manuscript with contributions from ED and JW. YZ and PM collected seawater samples. QW, YH, AD, and LB performed Nd isotope and REE concentration analyses. All authors contributed to the data interpretation and writing the manuscript.

Funding

This research was supported by National Natural Science Foundation of China (Nos. 42176058, 42130407, and 41506057), Open Fund of the Key Laboratory of Marine Geology and Environment, Chinese Academy of Sciences (No. MGE2019KG12), and the Labex L-IPSL (No. ANR-10-LABX-0018).

Acknowledgments

We thank the scientific team, captain and crew of R/V Jiageng for their collaboration during sampling. We also thank Xiaodong Zhang for his assistance with seawater pretreatment in the laboratory. We are grateful to two reviewers who provided valuable views during our previous submission. We kindly thank the Editor Dr. Hathorne for his efforts to handle this manuscript and all the reviewers including two ones for their constructive suggestions that helped us to improve our present manuscript.

Conflict of interest

The authors declare that the research was conducted in the absence of any commercial or financial relationships that could be construed as a potential conflict of interest.

Publisher's note

All claims expressed in this article are solely those of the authors and do not necessarily represent those of their affiliated organizations, or those of the publisher, the editors and the reviewers. Any product that may be evaluated in this article, or claim that may be made by its manufacturer, is not guaranteed or endorsed by the publisher.

Supplementary material

The Supplementary Material for this article can be found online at: https://www.frontiersin.org/articles/10.3389/fmars.2022.1003749/full#supplementary-material

References

Abbott, A., Haley, B., and McManus, J. (2016). The impact of sedimentary coatings on the diagenetic Nd flux. *Earth Planet. Sci. Lett.* 449, 217–227. doi: 10.1016/j.epsl.2016.06.001

Abbott, A., Haley, B., McManus, J., and Reimers, C. (2015). The sedimentary source of dissolved rare earth elements to the ocean. geochim. *Cosmochim. Acta* 154, 186–200. doi: 10.1016/j.gca.2015.01.010

Adebayo, S., Cui, M., Hong, T., White, C., Martin, E., and Johannesson, K. (2018). Rare earth elements geochemistry and Nd isotopes in the Mississippi river and gulf of Mexico mixing zone. *Front. Mar. Sci.* 5. doi: 10.3389/fmars.2018.00166

Akagi, T. (2013). Rare earth element (REE)–silicic acid complexes in seawater to explain the incorporation of REEs in opal and the "leftover" REEs in surface water: new interpretation of dissolved REE distribution profiles. *Geochim. Cosmochim. Acta* 113, 174–192. doi: 10.1016/j.gca.2013.03.014

Alibo, D. S., and Nozaki, Y. (2000). Dissolved rare earth elements in the south China Sea: Geochemical characterization of the water masses. *J. Geophys. Res. Oceans* 105, 28771–28783. doi: 10.1029/1999JC000283

Amakawa, H., Alibo, D. S., and Nozaki, Y. (2000). Nd Isotopic composition and REE pattern in the surface waters of the eastern Indian ocean and its adjacent seas. *Geochim. Cosmochim. Acta* 64, 1715–1727. doi: 10.1016/S0016-7037(00)00333-1

Bayon, G., Toucanne, S., Skonieczny, C., André, L., Bermell, S., Cheron, S., et al. (2015). Rare earth elements and neodymium isotopes in world river sediments revisited. *Geochim. Cosmochim. Acta* 170, 17–38. doi: 10.1016/j.gca.2015.08.001

Behrens, M. K., Pahnke, K., Cravatte, S., Marin, F., and Jeandel, C. (2020). Rare earth element input and transport in the near-surface zonal current system of the tropical Western pacific. *Earth Planet. Sci. Lett.* 549, 116496. doi: 10.1016/j.epsl.2020.116496

Behrens, M. K., Pahnke, K., Paffrath, R., Schnetger, B., and Brumsack, H. J. (2018a). Rare earth element distributions in the West pacific: trace element sources and conservative vs. non-conservative behavior. *Earth Planet. Sci. Lett.* 486, 166–177. doi: 10.1016/j.epsl.2018.01.016

Behrens, M. K., Pahnke, K., Schnetger, B., and Brumsack, H.-J. (2018b). Sources and processes affecting the distribution of dissolved Nd isotopes and concentrations in the West pacific. *Geochim. Cosmochim. Acta* 222, 508–534. doi: 10.1016/j.gca.2017.11.008

Blaser, P., Pöppelmeier, F., Schulz, H., Gutjahr, M., Frank, M., Lippold, J., et al. (2019). The resilience and sensitivity of northeast Atlantic deep water ϵNd to overprinting by detrital fluxes over the past 30,000 years. *Geochim. Cosmochim. Acta* 245, 79–97. doi: 10.1016/j.gca.2018.10.018

Broecker, W. S., Patzert, W. C., Toggweiler, J. R., and Stuive, M. (1986). Hydrography, chemistry, and radioisotopes in the southeast Asian basins. *J. Geophys. Res. Oceans* 91, 14345–14354. doi: 10.1029/JC091iC12p14345

Che, H., Zhang, J., Liu, Q., He, H., and Zhao, Z. (2022). Refining the contribution of riverine particulate release to the global marine Nd budget. *Prog. Earth Planet. Sc.* 9:22. doi: 10.1186/s40645-022-00479-2

Chen, T.-Y., Lai, C.-C., Tai, J.-H., Ko, C.-Y., and Shiah, F.-K. (2021). Diel to seasonal variation of picoplankton in the tropical south China Sea. *Front. Mar. Sci.* 8. doi: 10.3389/fmars.2021.732017

Chen, T., Li, G., Frank, M., and Ling, H. (2013). Hafnium isotope fractionation during continental weathering: Implications for the generation of the seawater Nd-hf isotope relationships. *Geophys. Res. Lett.* 40, 916–920. doi: 10.1002/grl.50217

Chen, G., Wang, D., Dong, C., Zu, T., Xue, H., Shu, Y., et al. (2015). Observed deep energetic eddies by seamount wake. *Sci. Rep.* 5, 17416. doi: 10.1038/srep17416

Chen, J., Zheng, L., Wiesner, M., Chen, R., Zheng, Y., and Wong, H. (1998). Estimations of primary production and export production in the south China Sea based on sediment trap experiments. *Sci. China Earth Sci.* 43, 583–586. doi: 10.1007/BF02883645

Chung, C.-H., You, C.-F., and Chu, H.-Y. (2009). Weathering sources in the gaoping (Kaoping) river catchments, southwestern Taiwan: Insights from major elements SR isotopes, and rare earth elements. *J. Mar. Syst.* 76, 433–443. doi: 10.1016/j.jmarsys.2007.09.013

Colin, C., Duhamel, M., Siani, G., Dubois-Dauphin, Q., Ducassou, E., Liu, Z., et al. (2021). Changes in the intermediate water masses of the Mediterranean Sea during the last climatic cycle - new constraints from neodymium isotopes in foraminifera, paleoceanogr. *Paleoclimatol* 36 (4), 1–28. doi: 10.1029/2020PA004153

Colin, C., Tisnérat-Laborde, N., Mienis, F., Collart, T., Pons-Branchu, E., Dubois-Dauphin, Q., et al. (2019). Millennial-scale variations of the Holocene north Atlantic mid-depth gyre inferred from radiocarbon and neodymium isotopes in cold water corals. *Quat. Sci. Rev.* 211, 93–106. doi: 10.1016/j.quascirev.2019.03.011

Crocket, K., Hill, E., Abell, R., Johnson, C., Gary, S., Brand, T., et al. (2018). Rare earth element distribution in the NE Atlantic: Evidence for benthic sources, longevity of the seawater signal, and biogeochemical cycling. *Front. Mar. Sci.* 5. doi: 10.3389/fmars.2018.00147

de Baar, H. J. W., Bruland, K. W., Schijf, J., van Heuven, S. M. A. C., and Behrens, M. K. (2018). Low cerium among the dissolved rare earth elements in the central north pacific ocean, geochim. *Cosmochim. Acta* 236, 5–40. doi: 10.1016/j.gca.2018.03.003

Ding, Z., Sun, J., Yang, S., and Liu, T. (2001). Geochemistry of the pliocene red clay formation in the Chinese loess plateau and implications for its origin, source provenance and paleoclimate change. *Geochim. Cosmochim. Acta* 65, 901–913. doi: 10.1016/S0016-7037(00)00571-8

Dubois-Dauphin, Q., Bonneau, L., Colin, C., Montero-Serrano, J.-C., Montagna, P., Blamart, D., et al. (2016). South Atlantic intermediate water advances into the north-east Atlantic with reduced Atlantic meridional overturning circulation during the last glacial period. *Geochem. Geophys. Geosyst.* 17, 2336–2353. doi: 10.1002/2016GC006281

Du, J., Haley, B. A., and Mix, A. C. (2016). Neodymium isotopes in authigenic phases, bottom waters and detrital sediments in the gulf of Alaska and their

implications for paleocirculation reconstruction. *Geochim. Cosmochim. Acta* 193, 14–35. doi: 10.1016/j.gca.2016.08.005

Du, J., Haley, B. A., and Mix., A. C. (2020). Evolution of the global overturning circulation since the last glacial maximum based on marine authigenic neodymium isotopes. *Quat. Sci. Rev* 193, 14–35. doi: 10.1016/j.quascirev.2020.106396

Elderfield, H. (1988). The oceanic chemistry of the rare-earth elements. *Philos. Trans. R. Soc A* 325, 105–126. doi: 10.1098/rsta.1988.0046

Fang, W., Guo, Z., and Huang, Y. (1998). Observational study of the circulation in the southern south China Sea, chin. *Sci. Bull.* 43, 898–905. doi: 10.1007/BF02884607

Fröllje, H., Pahnke, K., Schnetger, B., Brumsack, H.-J., Dulai, H., and Fitzsimmons, J. N. (2016). Hawaiian Imprint on dissolved Nd and Ra isotopes and rare earth elements in the central north pacific: local survey and seasonal variability. *Geochim. Cosmochim. Acta* 189, 110–131. doi: 10.1016/j.gca.2016.06.001

Gan, J., Liu, Z., and Hui, R. (2016). A three-layer alternating spinning circulation in the south China Sea. *J. Phys. Oceanogr.* 46, 2309–2315. doi: 10.1175/JPO-D-16-0044.1

Garcia-Solsona, E., Jeandel, C., Labatut, M., Lacan, F., Vance, D., Chavagnac, V., et al. (2014). Rare earth elements and Nd isotopes tracing water mass mixing and particle– seawater interactions in the SE Atlantic. *Geochim. Cosmochim. Acta* 125, 351–372. doi: 10.1016/j.gca.2013.10.009

Goldstein, S., and Jacobsen, S. (1987). The Nd and Sr isotopic systematics of river-water dissolved material: implications for the sources of Nd and Sr in seawater. *Chem. Geol.* 66, 245–272. doi: 10.1016/0168-9622(87)90045-5

Goldstein, S. J., and Jacobsen, S. B. (1988). Nd And Sr isotopic systematics of river water suspended material — implications for crustal evolution. *Earth Planet. Sci. Lett.* 87, 249–265. doi: 10.1016/0012-821X(88)90013-1

Grasse, P., Bosse, L., Hathorne, E. C., Böning, P., Pahnke, K., and Frank, M. (2017). Short-term variability of dissolved rare earth elements and neodymium isotopes in the entire water column of the Panama basin. *Earth Planet. Sci. Lett.* 475, 242–253. doi: 10.1016/j.epsl.2017.07.022

Grasse, P., Stichel, T., Stumpf, R., Stramma, L., and Frank, M. (2012). The distribution of neodymium isotopes and concentrations in the Eastern equatorial pacific: water mass advection versus particle exchange. *Earth Planet. Sci. Lett.* 353–354, 198–207. doi: 10.1016/j.epsl.2012.07.044

Greaves, M. J., Statham, P. J., and Elderfield, H. (1994). Rare earth element mobilization from marine atmospheric dust into seawater. *Mar. Chem.* 46, 255–260. doi: 10.1016/0304-4203(94)90081-7

Grenier, M., Brown, K. A., Colombo, M., Belhadj, M., Baconnais, I., Pham, V., et al. (2022). Controlling factors and impacts of river-borne neodymium isotope signatures and rare earth element concentrations supplied to the Canadian Arctic archipelago. *Earth Planet. Sci. Lett.* 578, 117341. doi: 10.1016/j.epsl.2021.117341

Grenier, M., Garcia-Solsona, E., Lemaitre, N., Trull, T. W., Bouvier, V., and Jeandel, C. (2018). Differentiating lithogenic supplies, water mass transport and biological processes on and off the kerguelen plateau using rare earth element concentrations and neodymium isotopic compositions. *Front. Mar. Sci.* 5. doi: 10.3389/fmars.2018.00147

Grenier, M., Jeandel, C., Lacan, F., Vance, D., Venchiarutti, C., Cros, A., et al. (2013). From the subtropics to the central equatorial pacific ocean: neodymium isotopic composition and rare earth element concentration variations. *J. Geophys. Res. Oceans* 118, 592–618. doi: 10.1029/2012jc008239

Haley, B. A., Du, J., Abbott, A. N., and McManus, J. (2017). The impact of benthic processes on rare earth element and neodymium isotope distributions in the oceans. *Front. Mar. Sci.* 4. doi: 10.3389/fmars.2017.00426

Haley, B. A., Frank, M., Hathorne, E., and Pisias, N. (2014). Biogeochemical implications from dissolved rare earth element and Nd isotope distributions in the gulf of Alaska. *Geochim. Cosmochim. Acta* 126, 455–474. doi: 10.1016/j.gca.2013.11.012

Haley, B. A., Klinkhammer, G., and McManus, J. (2004). Rare earth elements in pore waters of marine sediments. *Geochim. Cosmochim. Acta* 68, 1265–1279. doi: 10.1016/j.gca.2003.09.012

Han, A., Gan, J., Dai, M., Lu, Z., Liang, L., and Zhao, X. (2021). Intensification of downslope nutrient transport and associated biological responses over the northeastern south China Sea during wind-driven downwelling: a modeling study. *Front. Mar. Sci.* 8. doi: 10.3389/fmars.2021.772586

Hathorne, E. C., Frank, M., and Mohan, P. M. (2020). Rare earth elements in Andaman island surface seawater: Geochemical tracers for the monsoon? *Front. Mar. Sci.* 6. doi: 10.3389/fmars.2019.00767

Hu, J., Kawamura, H., Hong, H., and Qi, Y. (2000). A review on the currents in the south China Sea: Seasonal circulation, south China Sea warm current and kuroshio intrusion. *J. Oceanogr.* 56, 607–624. doi: 10.1023/A:1011117531252

Hu, R., Noble, T., Piotrowski, A., McCve, N., Bostock, H., and Neil, H. (2016). Neodymium isotopic evidence for linked changes in southeast Atlantic and southwest pacific circulation over the last 200 kyr. *Earth Planet. Sci. Lett.* 455, 106–114. doi: 10.1016/j.epsl.2016.09.027

Jeandel, C., Delattre, H., Grenier, M., Pradoux, C., and Lacan, F. (2013). Rare earth element concentrations and Nd isotopes in the south East pacific ocean. *Geochem. Geophys. Geosyst.* 14, 328–341. doi: 10.1029/2012GC004309

Johannesson, K., and Burdige, D. (2007). Balancing the global oceanic neodymium budget: evaluating the role of groundwater. *Earth Planet. Sci. Lett.* 253 (1–2), 129–142. doi: 10.1016/j.epsl.2006.10.021

Kawabe, M., and Fujio, S. (2010). Pacific ocean circulation based on observation. *J. Oceanogr.* 66, 389–403. doi: 10.1007/s10872-010-0034-8

Kim, I., and Kim, G. (2014). Submarine groundwater discharge as a main source of rare earth elements in coastal waters. *Mar. Chem.* 160, 11–17. doi: 10.1016/j.marchem.2014.01.003

Lacan, F., and Jeandel, C. (2005). Neodymium isotopes as a new tool for quantifying exchange fluxes at the continent-ocean interface. *Earth Planet. Sci. Lett.* 232, 245–257. doi: 10.1016/j.epsl.2005.01.004

Lawrence, M., and Kamber, B. (2006). The behaviour of the rare earth elements during estuarine mixing–revisited. *Mar. Chem.* 100, 147–161. doi: 10.1016/j.marchem.2005.11.007

Le Houedec, S., Meynadier, L., and Allègre, C. J. (2016). Seawater Nd isotope variation in the Western pacific ocean since 80 ma (ODP 807, ontong Java plateau). *Mar. Geol.* 380, 138–147. doi: 10.1016/j.margeo.2016.07.005

Lin, H., and Han, W. (1997). Study on the dissolved oxygen flux in the south China Sea. *Chin. J. Oceanol. Limnol.* 15, 19–24. doi: 10.1007/BF02850577

Li, L., and Qu, T. (2006). Thermohaline circulation in the deep south China Sea basin inferred from oxygen distributions. *J. Geophys. Res. Oceans* 111, C05017. doi: 10.1029/2005JC003164

Liu, Y., Peng, Z., Zhou, R., Song, S., Liu, W., You, C.-F., et al. (2014). Acceleration of modern acidification in the south China Sea driven by anthropogenic CO2. *Sci. Rep.* 5, 5148. doi: 10.1038/srep05148

Liu, X., Wei, G., Zou, J., Guo, Y., Ma, J., Chen, X., et al. (2018). Elemental and Sr-Nd isotope geochemistry of sinking particles in the northern south China Sea: implications for provenance and transportation. *J. Geophys. Res. Oceans* 123, 9137–9155. doi: 10.1029/2018JC014312

Liu, Z., Zhao, Y., Colin, C., Stattegger, K., Wiesner, M. G., Huh, C.-A., et al. (2016). Source-to-sink transport processes of fluvial sediments in the south China Sea. *Earth Sci. Rev.* 153, 238–273. doi: 10.1016/j.earscirev.2015.08.005

Li, H., Wiesner, M., Chen, J., Lin, Z., Zhang, J., and Ran, L. (2017). Long-term variation of mesopelagic biogenic flux in the central south China Sea: Impact of monsoonal seasonality and mesoscale eddy. *Deep-sea Res. I* 126, 62–72. doi: 10.1016/j.dsr.2017.05.012

Lüdmann, T., Wong, H. K., and Berglar, K. (2005). Upward flow of north pacific deep water in the northern south China Sea as deduced from the occurrence of drift sediments. *Geophys. Res. Lett.* 32, L05614. doi: 10.1029/2004GL021967

Ma, L., Dang, D., Wang, W., Evans, R. D., and Wang., W.-X. (2019). Rare earth elements in the pearl river delta of China: Potential impacts of the REE industry on water, suspended particles and oysters. *Environ. pollut.* 244, 190–201. doi: 10.1016/j.envpol.2018.10.015

Martin, E., Blair, W., Kamenov, D., Scher, D., Bourbon, E., Basak, C., et al. (2010). Extraction of Nd isotopes from bulk deep sea sediments for paleoceanographic studies on Cenozoic time scales. *Chem. Geol.* 269, 414–431. doi: 10.1016/j.chemgeo.2009.10.016

Milliman, J. D., and Farnsworth, K. L. (2011). *River discharge to the coastal ocean: A global synthesis* (Cambridge: Cambridge University Press), 384.

Molina-Kescher, M., Frank, M., Tapia, R., Ronge, T. A., Dirk Nürnberg, D., and Tiedemann, R. (2016). Reduced admixture of north Atlantic deep water to the deep central south pacific during the last two glacial periods. *Paleoceanogr. Paleoclimatol.* 31, 651–668. doi: 10.1002/2015PA002863

Molina-Kescher, M., Hathorne, E., Osborne, A., Behrens, M., Kölling, M., Pahnke, K., et al. (2018). The influence of basaltic islands on the oceanic REE distribution: A case study from the tropical south pacific. *Front. Mar. Sci.* 5. doi: 10.3389/fmars.2018.00050

Noble, T. L., Piotrowski, A. M., and McCave, I. N. (2013). Neodymium isotopic composition of intermediate and deep waters in the glacial southwest pacific. *Earth Planet. Sci. Lett.* 384, 27–36. doi: 10.1016/j.epsl.2013.10.010

Nozaki, Y., and Alibo, D. S. (2003). Importance of vertical geochemical processes in controlling the oceanic profiles of dissolved rare earth elements in the northeastern Indian ocean. *Earth Planet. Sci. Lett.* 205, 155–172. doi: 10.1016/S0012-821X(02)01027-0

Osborne, A. H., Haley, B. A., Hathorne, E. C., Flögel, S., and Frank, M. (2014). Neodymium isotopes and concentrations in Caribbean seawater: tracing water mass mixing and continental input in a semi-enclosed ocean basin. *Earth Planet. Sci. Lett.* 406, 174–186. doi: 10.1016/j.epsl.2014.09.011

Osborne, A. H., Haley, B. A., Hathorne, E. C., Plancherel, Y., and Frank, M. (2015). Rare earth element distribution in Caribbean seawater: Continental inputs versus lateral transport of distinct REE compositions in subsurface water masses. *Mar. Chem.* 177, 172–183. doi: 10.1016/j.marchem.2015.03.013

Padrones, J., Iami, A., and Takahashi, R. (2017). Geochemical behavior of rare earth elements in weathered graniticrocks in northern palawan, Philippines. *Resour. Geol.* 67, 231–253. doi: 10.1111/rge.12123

Patton, G., Francois, R., Weis, D., Hathorne, E., Gutjahr, M., Frank, M., et al. (2021). An experimental investigation of the acquisition of Nd by authigenic phases of marine sediments. *Geochim. Cosmochim. Acta* 301, 1–29. doi: 10.1016/j.gca.2021.02.010

Pearce, C., Jones, M., Oelkers, E., Pradoux, C., and Jeandel, C. (2013). The effect of particulate dissolution on the neodymium (Nd) isotope and rare earth element (REE) composition of seawater. *Earth Planet. Sci. Lett.* 369, 138–147. doi: 10.1016/j.epsl.2013.03.023

Pham, V., Grenier, M., Cravatte, S., Michael, S., Jacquet, S., Belhadj, M., et al. (2019). Dissolved rare earth elements distribution in the Solomon Sea. *Chem. Geol.* 524, 11–36. doi: 10.1016/j.chemgeo.2019.05.012

Piotrowski, A. M., Galy, A., Nicholl, J. A. L., Roberts, N., Wilson, D. J., Clegg, J. A., et al. (2012). Reconstructing deglacial north and south Atlantic deep water sourcing using foraminiferal Nd isotopes. *Earth Planet. Sci. Lett.* 357–358, 289–297. doi: 10.1016/j.epsl.2012.09.036

Qu, T., Girton, J. B., and Whitehead, J. A. (2006). Deepwater overflow through Luzon strait. *J. Geophys. Res. Oceans* 111, C01002. doi: 10.1029/2005JC003139

Rousseau, T. C. C., Sonke, J. E., Chmeleff, J., Van Beek, P., Souhaut, M., Boaventura, G., et al. (2015). Rapid neodymium release to marine waters from lithogenic sediments in the Amazon estuary. *Nat. Commun.* 6, 7592. doi: 10.1038/ncomms8592

Scher, H., Whittaker, J., William, S., Latimer, J., Kordesch, W., and Delaney, M. (2015). On-set of Antarctic circumpolar current 30 million years ago as Tasmanian gateway aligned with westerlies. *Nature* 523, 580–583. doi: 10.1038/nature14598

Schlitzer, R. (2014) *Ocean data view*. Available at: http://odv.awi.de.

Shao, L., Qiao, P., Pang, X., Wei, G., Li, Q., Miao, W., et al. (2009). Nd Isotopic variations and its implications in the recent sediments from the northern south China Sea. *Chin. Sci. Bull.* 54, 311–317. doi: 10.1007/s11434-008-0453-8

Sholkovitz, R., Elderfield, H., Szymczak, R., and Casey, K. (1999). Island weathering: river sources of rare earth elements to the Western pacific ocean. *Mar. Chem.* 68, 39–57. doi: 10.1016/S0304-4203(99)00064-X

Sholkovitz, R., Landing, M., and Lewis, L. (1994). Ocean particle chemistry: the fractionation of rare earth elements between suspended particles and seawater. geochim. *Cosmochim. Acta* 58, 1567–1580. doi: 10.1016/0016-7037(94)90559-2

Sholkovitz, E., and Szymczak, R.. (2000). The estuarine chemistry of rare earth elements: comparison of the Amazon, Fly, Sepik and the Gulf of Papua systems. *Earth Planet. Sci. Lett.* 179, 299–309. doi: 10.1016/S0012-821X(00)00112-6

Shu, Y., Xue, H., Wang, D., Chai, F., Xie, Q., Yao, J. L., et al. (2014). Meridional overturning circulation in the south China Sea envisioned from the high-resolution global reanalysis data GLBa0.08. *J. Geophys. Res.* 119, 3012–3028. doi: 10.1002/2013JC009583

Singh, P., Singh, K., Goswami, V., Bhushan, R., and Rai, K. (2012). Spatial distribution of dissolved neodymium and eNd in the bay of Bengal: role of particulate matter and mixing of water masses. *Geochim. Cosmochim. Acta* 94, 38–56. doi: 10.1016/j.gca.2012.07.017

Sinha, A. K., and Parli, B. V. (2020). Siderophore production by bacteria isolated from mangrove sediments: A microcosm study. *J. Exp. Mar. Biol. Ecol.* 524, 151290. doi: 10.1016/j.jembe.2019.151290

Song, X., Lai, Z., Ji, R., Chen, C., Zhang, J., Huang, L., et al. (2012). Summer time primary production in northwest south China Sea: Interaction of coastal eddy, upwelling and biological processes. *Cont Shelf Res.* 48, 110–121. doi: 10.1016/j.csr.2012.07.016

Stichel, T., Hartman, A. E., Duggan, B., Goldstein, S. L., Scher, H., and Pahnke, K. (2015). Separating biogeochemical cycling of neodymium from water mass mixing in the eastern north Atlantic. *Earth Planet. Sci. Lett.* 412, 245–260. doi: 10.1016/j.epsl.2014.12.008

Tachikawa, K., Arsouze, T., Bayon, G., Bory, A., Colin, C., Dutay, J.-C., et al. (2017). The large-scale evolution of neodymium isotopic composition in the global modern and Holocene ocean revealed from seawater and archive data. *Chem. Geol.* 457, 131–148. doi: 10.1016/j.chemgeo.2017.03.018

Tanaka, T., Togashi, S., Kamioka, H., Amakawa, H., Kagami, H., Hamamoto, T., et al. (2000). JNdi-1: A neodymium isotopic reference in consistency with LaJolla neodymium. *Chem. Geol.* 168, 279–281. doi: 10.1016/S0009-2541(00)00198-4

Taylor, S., and McLennan, S. (1985). *The continental crust: Its composition and evolution* (Palo Alto, CA: Blackwell Scientific Publisher).

Tian, J., Yang, Q., Liang, X., Xie, L., Hu, D., Wang, F., et al. (2006). Observation of Luzon strait transport. *Geophys. Res. Lett.* 33, L19607. doi: 10.1029/2006GL026272

Tian, J., Yang, Q., and Zhao, W. (2009). Enhanced diapycnal mixing in the south China Sea. *J. Phys. Oceanogr.* 39, 3191–3203. doi: 10.1175/2009JPO3899.1

Uematsu, M., Wang, Z., and Uno, I. (2003). Atmospheric input of mineral dust to the western north pacific region based on direct measurements and a regional chemical transport model. *Geophys. Res. Lett.* 30 (6), 1342. doi: 10.1029/2002GL016645

van de Flierdt, T., Griffiths, A. M., Lambelet, M., Little, S. H., Stichel, T., and Wilson, D. J. (2016). Neodymium in the oceans: a global database, a regional comparison and implications for palaeoceanographic research. philos. *Trans. R. Soc A* 374, 20150293. doi: 10.1098/rsta.2015.0293

Wang, A., Du, Y., Peng, S., Liu, K., and Huang, R. (2018). Deep water characteristics and circulation in the south China Sea. *Deep Sea Res. Part I* 134, 55–63. doi: 10.1016/j.dsr.2018.02.003

Wang, J., Shu, Y., Wang, D., Xie, Q., Wang, Q., Chen, J., et al. (2021). Observed variability of bottom-trapped topographic rossby waves along the slope of the northern south China Sea. *J. Geophys. Res. Oceans* 126, e2021JC017746. doi: 10.1029/2021JC017746

Wang, D., Wang, Q., Cai, S., Shang, X., Peng, S., Shu, Y., et al. (2019). Advances in research of the mid-deep south China Sea circulation. *Sci. China Earth Sci.* 62. doi: 10.1007/s11430-019-9546-3

Wang, D., Wang, Q., Zhou, W., Cai, S., Li, L., and Hong, B. (2013). An analysis of the current deflection around dongsha islands in the northern south China Sea. *J. Geophys. Res. Oceans* 118, 490–501. doi: 10.1029/2012JC008429

Wang, D., Xiao, J., Shu, Y., Xie, Q., Chen, J., and Wang, Q. (2016). Progress on deep circulation and meridional overturning circulation in the south China Sea. *Sci. China Earth Sci.* 59, 1827–1833. doi: 10.1007/s11430-016-5324-6

Wang, G., Xie, S., Qu, T., and Huang, R. (2011). Deep south China Sea circulation. *Geophys. Res. Lett.* 38, L05601. doi: 10.1029/2010GL046626

Wei, G., Liu, Y., Ma, J., Xie, L., Chen, J., Deng, W., et al. (2012). Nd S.R. isotopes and elemental geochemistry of surface sediments from the south China Sea: implications for provenance tracing. *Mar. Geol.* 319–322, 21–34. doi: 10.1016/j.margeo.2012.05.007

Wilson, D., Crocket, K., van de Flierdt, T., Robinson, L., and Adkins, J. (2014). Dynamic intermediate ocean circulation in the north Atlantic during Heinrich stadial 1: a radiocarbon and neodymium isotope perspective. *Paleoceanography* 29, 1072–1093. doi: 10.1002/2014PA002674

Wu, Q., Colin, C., Liu, Z., Douville, E., Dubois-Dauphin, Q., and Frank, N. (2015). New insights into hydrological exchange between the south China Sea and the Western pacific ocean based on the Nd isotopic composition of seawater. *Deep Sea Res. Part II* 122, 25–40. doi: 10.1016/j.dsr2.2015.11.005

Wu, J., Pahnke, K., Böning, P., Wu, L., Michard, A., and de Lange, G. J. (2019). Divergent Mediterranean seawater circulation during Holocene sapropel formation – reconstructed using Nd isotopes in fish debris and foraminifera. *Earth Planet. Sci. Lett.* 511, 141–153. doi: 10.1016/j.epsl.2019.01.036

Xie, Y., Lin, L., Xiao, W., Yu, W., Lan, X., and Huang, B. (2020). Striking seasonal pattern of primary production in the river-dominated ocean margin of the northern south China Sea (NSCS-RiOMar) revealed by new field and remotely sensed data. *Prog. Oceanogr.* 1021, 2470. doi: 10.1016/j.pocean.2020.102470

Xie, L., Tian, J., Zhang, S., Zhang, Y., and Yang., Q. (2011). An anticyclonic eddy in the intermediate layer of the Luzon strait in Autumn2002, 005. *J. Oceanogr.* 67, 37–46. doi: 10.1007/s10872-011-0004-9

Xu, J., Li, X., Shi, Z., Li, R., and Li, Q. (2018). Bacterial carbon cycling in the river plume in the northern south China Sea during summer. *J. Geophys. Res. Oceans* 123, 8106–8121. doi: 10.1029/2018JC014277

Yang, Q., Tian, J., and Zhao, W. (2010). Observation of Luzon strait transport in summer2002, 007. *Deep Sea Res. Part I* 57, 670–676. doi: 10.1016/j.dsr.2010.02.004

You, Y. (2003). The pathway and circulation of north pacific intermediate water. *Geophys. Res. Lett.* 30, 2291. doi: 10.1029/2003GL018561

Yuan, D. (2002). A numerical study of the south China Sea deep circulation and its relation to the Luzon strait transport. *Acta Oceanol. Sin.* 21, 187–202.

Yuan, D., Han, W., and Hu, D. (2007). Anti-cyclonic eddies northwest of Luzon in summer-fall observed by satellite altimeters. *Geophys. Res. Lett.* 34, L13610. doi: 10.1029/2007GL029401

Yu, Z., Colin, C., Douville, E., Meynadier, L., Duchamp-Alphonse, S., Sepulcre, S., et al. (2017). Yttrium and rare earth element partitioning in seawaters from the bay of Bengal. *Geochem. Geophys. Geosyst.* 18, 1388–1403. doi: 10.1002/2016GC006749

Yu, Z., Colin, C., Ma, R., Meynadier, L., Wan, S., Wu, Q., et al. (2018). Northward invasion of Antarctic intermediate water in the northern Indian ocean during the last deglaciation. *Earth Planet. Sci. Lett.* 500, 67–75. doi: 10.1016/j.epsl.2018.08.006

Zhang, J., Li, H., Xuan, J., Wu, Z., Yang, Z., Wiesner, M., et al. (2018). Enhancement of mesopelagic sinking particle fluxes due to upwelling, aerosol

deposition, and monsoonal influences in the northwestern south China Sea. *J. Geophys. Res. Oceans* 124, 99–112. doi: 10.1029/2018JC014704

Zhao, N., Oppo, D., Huang, K., Howe, J., Blusztajn, J., and Keigwin, L. (2019). Glacial–interglacial Nd isotope variability of north Atlantic deep water modulated by north American ice sheet. *Nat. Commun.* 10, 5773. doi: 10.1038/s41467-01913707-z

Zhao, W., Zhou, C., Tian, J., Yang, Q., Wang, B., Xie, L., et al. (2014). Deep water circulation in the Luzon strait. *J. Geophys. Res. Oceans* 119, 790–804. doi: 10.1002/2013JC009587

Zheng, X., Plancherel, Y., Saito, M. A., Scott, P. M., and Henderson, G. M. (2016). Rare earth elements (REEs) in the tropical south Atlantic and quantitative deconvolution of their non-conservative behavior. *Geochim. Cosmochim. Acta* 177, 217–237. doi: 10.1016/j.gca.2016.01.018

Zhou, M., Wang, G., Liu, W., and Chen, C. (2020). Variability of the observed deep western boundary current in the south China Sea. *J. Geophys. Res. Oceans* 50, 2953–2963. doi: 10.1175/JPO-D-20-0013.1

Zhou, C., Zhao, W., Tian, J., Zhao, X., Zhu, Y., Yang, Q., et al. (2017). Deep western boundary current in the south china sea. *Sci. Rep.* 7, 9303. doi: 10.1038/s41598-017-09436-2

Zhu, Y., Fang, G., Wei, Z., Wang, Y., Teng, F., and Qu, T. (2016). Seasonal variability of the meridional overturning circulation in the south China Sea and its connection with inter-ocean transport based on SODA2.2.4. *J. Geophys. Res. Oceans* 121, 3090–3105. doi: 10.1002/2015JC011443

Zhu, Y., Sun, J., Wang, Y., Li, S., Xu, T., Wei, Z., et al. (2019). Overview of the multi-layer circulation in the south China Sea. *Prog. Oceanogr.* 175, 171–182. doi: 10.1016/j.pocean.2019.04.001

Zhu, Y., Sun, J., Wang, Y., Wei, Z., Yang, D., and Qu, T. (2017). Effect of potential vorticity flux on the circulation in the south China Sea. *J. Geophys. Res. Oceans* 122, 6454–6469. doi: 10.1002/2016JC012375

Zieringer, M., Frank, M., Stumpf, R., and Hathorne, E. C. (2019). The distribution of neodymium isotopes and concentrations in the eastern tropical north Atlantic. *Chem. Geol.* 511, 265–278. doi: 10.1016/j.chemgeo.2018.11.024

frontiers | Frontiers in Marine Science

TYPE Original Research
PUBLISHED 26 January 2023
DOI 10.3389/fmars.2023.1076991

OPEN ACCESS

EDITED BY
Tim Jennerjahn,
Leibniz Centre for Tropical Marine Research (LG), Germany

REVIEWED BY
Dirk Jacob Koopmans,
University of Virginia, United States
Dipnarayan Ganguly,
National Centre for Sustainable Coastal Management, India
Zhijian Jiang,
South China Sea Institute of Oceanology (CAS), China

*CORRESPONDENCE
Wen-Chen Chou
wcchou@mail.ntou.edu.tw

SPECIALTY SECTION
This article was submitted to Marine Biogeochemistry, a section of the journal Frontiers in Marine Science

RECEIVED 22 October 2022
ACCEPTED 05 January 2023
PUBLISHED 26 January 2023

CITATION
Chou W-C, Fan L-F, Hung C-C, Shih Y-Y, Huang W-J, Lui H-K and Chen T-Y (2023) Dynamics of O_2 and pCO_2 in a Southeast Asia seagrass meadow: Metabolic rates and carbon sink capacity. *Front. Mar. Sci.* 10:1076991. doi: 10.3389/fmars.2023.1076991

Dynamics of O_2 and pCO_2 in a Southeast Asia seagrass meadow: Metabolic rates and carbon sink capacity

Wen-Chen Chou[1,2,3]*, Lan-Feng Fan[1], Chin-Chang Hung[4], Yung-Yen Shih[4,5], Wei-Jen Huang[4], Hon-Kit Lui[4] and Tzong-Yueh Chen[1]

[1]Institute of Marine Environment and Ecology, National Taiwan Ocean University, Keelung, Taiwan, [2]Center of Excellence for the Oceans, National Taiwan Ocean University, Keelung, Taiwan, [3]Graduate Institute of Marine Biology, National Dong Hwa University, Pingtung, Taiwan, [4]Department of Oceanography, National Sun Yat-sen University, Kaohsiung, Taiwan, [5]Department of Applied Science, Republic of China (R.O.C.) Naval Academy, Kaohsiung, Taiwan

Dissolved oxygen (DO) and partial pressure of CO_2 (pCO_2) were measured at half-hourly intervals from June 29 to September 9, 2019, in a seagrass meadow in the Southeast Asia archipelagos region. The open water mass balance of the O_2 approach was used to calculate metabolic rates (i.e., gross primary production (GPP), community respiration (CR), and net community production (NCP). The calculations show that GPP and CR rates in the seagrass meadow of Dongsha Island were approximately 2.5 times higher than the global means (GPP, 507 ± 173 *vs.* 225 ± 11 mmol O_2 m^{-2} d^{-1}; CR, 497 ± 171 *vs.* 188 ± 10 mmol O_2 m^{-2} d^{-1}), while NCP was similar to the global mean (8 ± 61 *vs.* 27 ± 6 mmol O_2 m^{-2} d^{-1}), suggesting that seagrass meadows with high GPP may not necessarily hold high potential for carbon sequestration. The current data set also reveal that NCP tended to increase with GPP only at lower GPP levels, while NCP did not increase with GPP anymore at higher GPP levels. Moreover, the autotrophic/heterotrophic status did not correspond well to the sink/source behavior of CO_2, suggesting that organic carbon metabolism could not be the only dominant factor in determining the sink/source status in a typical seagrass meadow underlain by carbonate sediments, which was further supported by the observed decrease in the trend of pCO_2 with a relatively stable NCP level over the study period. These results demonstrate that the metabolism and the relationship between NCP and pCO_2 in the seagrass meadows of Dongsha Island may deviate greatly from the global mean condition. To obtain a better assessment of the global potential of seagrass meadows as a nature-based solution for carbon sequestration, more regional-specific studies are still needed in the key regions, such as Indonesia and the Pacific archipelagos, that support extensive seagrass meadows but have not been charted.

KEYWORDS

seagrass, Dongsha Island, blue carbon, Southeast Asia, dissolved oxygen, carbon dioxide

1 Introduction

Seagrass meadows are highly productive habitats in shallow coastal waters and rank among the most productive ecosystems (Duarte and Chiscano, 1999). Recently, they have received substantial attention as a 'blue carbon' sink due to their high rates of primary production and carbon burial in sediments (Duarte et al., 2010; Fourqurean et al., 2012). As such, seagrass conservation and restoration are considered potential climate change mitigation and adaptation strategies (Nellemann et al., 2009; McLeod et al., 2011; Duarte et al., 2013). Yet, the high production and carbon input also render the seagrass meadow as sites of elevated abundance and activity of heterotrophs, which support high community respiration rates (Middelburg et al., 2005). As a result, the status of seagrass meadows as a source or a sink of carbon may largely depend on the metabolic balance of the primary producers (including seagrass itself, epiphytic algae, and microphytobenthos) and the associated heterotrophs (including the pelagic and benthic compartments) in the community.

The community metabolic status in seagrass meadows can be described by net community production (NCP), referring to the difference between gross primary production (GPP) and community respiration (CR). Autotrophic meadows (NCP > 0) fix organic carbon in excess to local demand (GPP > CR) and may, therefore, either store or export organic carbon to adjacent communities, while heterotrophic meadows (NCP< 0) require additional organic carbon and that the community may be sustained by allochthonous organic carbon (Duarte et al., 2010). Determining the metabolic status of seagrass meadows is therefore crucial for a better understanding of their potential in "blue carbon" sink and thus in climate change mitigation (Champenois and Borges, 2021).

Seagrass meadows support a large range of metabolic rates from autotrophy (Barrón et al., 2006) to heterotrophy (Van Dam et al., 2019), which vary significantly among different community types and species along with seasonal variations (Duarte et al., 2010). In fact, earlier efforts at assessing seagrass metabolism existed a large imbalance in the geographic distributions of the data available. In particular, there is a considerable gap in reports of seagrass community metabolism in the Indo-Pacific, Africa, and South America (Duarte et al., 2013). To gain a better sink potential of seagrass meadows on a global scale, observations are required from the key regions where supporting extensive seagrass meadows have not been reported.

Despite being a hot spot for the diversity of seagrass species and habitat types, the seagrass meadows in Southeast Asia archipelagos have been poorly studied (Fortes et al., 2018), and to our knowledge, metabolic rates in this region have not yet been reported. Lee et al. (2017) have reported the community-scale metabolism of seagrass meadows in East Asia (Korea) for the first time as autotrophic state, but their study site was located in temperate area. In the present study, we report a data set of O_2, partial pressure of CO_2 (pCO_2), and pH measurements at half-hourly intervals, which have been recorded continuously from June 29 to September 9, 2019, in a seagrass meadow on the northern shore of Dongsha Island, located in the largest tropical marginal sea in Southeast Asia (i.e., the South China Sea). Community metabolic rates (GPP, CR, and NCP) were estimated on a daily basis from this data set using the open water mass balance of the O_2 approach (Odum, 1956; Champenois and Borges, 2021). We also investigated the relationship between metabolism and concurrent concentrations of pCO_2 in the water column. Overall, the objectives of this study are (i) to document the metabolism rates and the relationships between them for the first time in the seagrass meadows in the Southeast Asia archipelagos region, (ii) to compare the present result with previously global synthesis, and (iii) to provide new insight into the relationship between metabolism and pCO_2 dynamics for tropical seagrass meadows.

2 Materials and methods

2.1 The study site

Dongsha Island (also known as Pratas Island) is a coral island located on the western side of Dongsha Atoll, a ring-shaped coral reef ecosystem in the northern South China Sea (Figure 1). The island is quite small around 2.80 km long and 0.87 km wide with an area of approximately 1.74 km^2, and it is made up of coral atolls and reef flats. Vines and bushes cover some of the island, and the rest is surrounded by white coral sand (Dai, 2006). The East Asia Monsoon prevails over Dongsha Island with distinct seasonality: the southwesterly monsoon starts in June and lasts until August in the summer, while the northeasterly monsoon starts in October and predominates over the winter and early spring. The transition periods are April-May for the southwesterly monsoon and September for the northeasterly monsoon (Chai et al., 2009). As a military control zone, there is no permanent inhabitants on the island, and it is visited only by military personnel, researchers and fishermen. Furthermore, there is no freshwater flow into the sea from the island, and most of freshwater on the island is produced by seawater desalination and recycled. Therefore, the inflow from the artifact at Dongsha Island nearly could be negligible.

Despite the small area of Dongsha Island, massive seagrass meadows extend from the intertidal to the subtidal zones with a total coverage area of 11.85 km^2 around the entire island (Huang et al., 2015). A total of seven seagrass species from six genera and two families have been identified at Dongsha Island, including *Thalassia hemprichii*, *Halophila ovalis*, *Cymodocea rotundata*, *C. serrulata*, *Halodule uninervis*, *Syringodium isoetifolium*, and *Thalassodentron ciliatum* (Lin et al., 2005), and the coverage of seagrass meadows was generally >75% around the island (Lee et al., 2021). Among them, the most abundant species around Dongsha Island are *T. hemprichii*, *H. uninervis*, *C. rotundata*, and *C. serrulata* (Huang et al., 2015), and which are also popular species in Indo-Pacific (Short et al., 2007). Besides, *T. hemprichii* and *H. uninervis* are widely appeared in Hengchun Peninsula and surrounding islands of Taiwan, but *C. rotundata, and C. serrulata* are only recorded in Dongsha and Penghu Islands (Lin et al., 2005).This study was conducted in the seagrass meadow on the northern shore (NS, Figure 1) of Dongsha Island, which is a multispecies seagrass meadow with three dominant species of *T. hemprichii*, *C. rotundata*, and *C. serrulata*. The average total seagrass biomass, total seagrass production, seagrass cover, and shoot density were previously reported to be 949.4 ± 62.1 (g DW m^{-2}), 8.47 ± 2.92 (g DW m^{-2}), 81.91 ± 2.13 (%), and 2677 ± 485

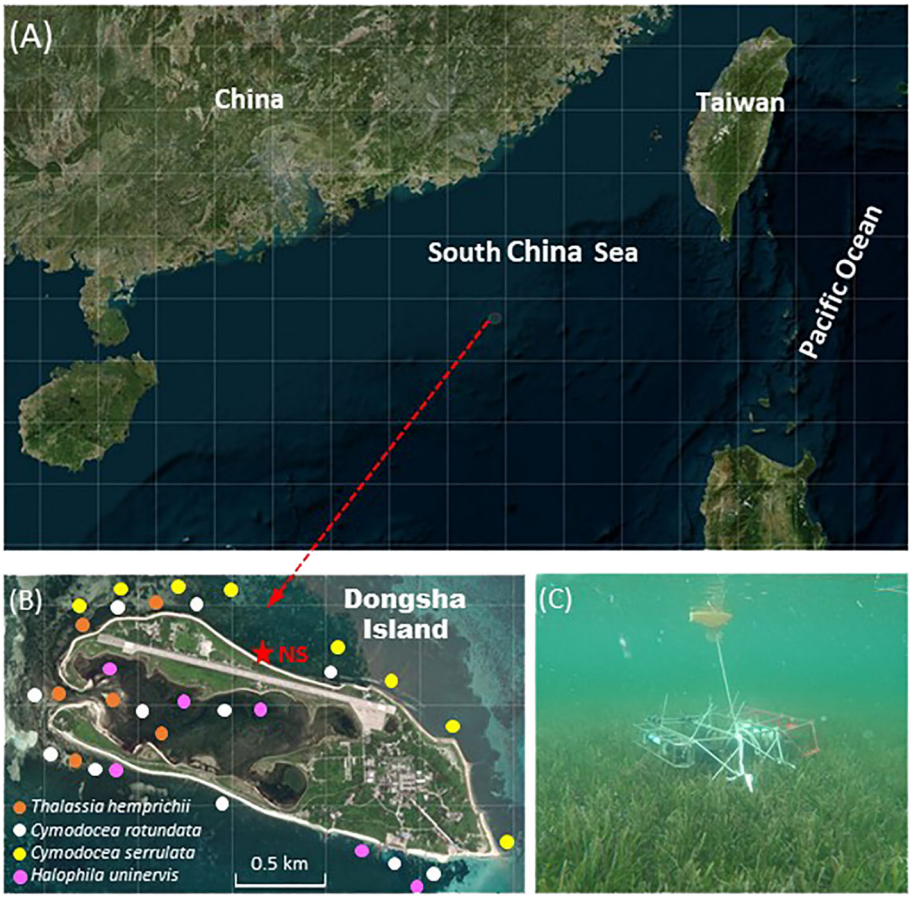

FIGURE 1
Map showing **(A)** the location of Dongsha Atoll, **(B)** the distribution of dominant seagrass (studies by Lin et al., 2005) and the study site on the northern shore of Dongsha Island (NS, asterisk), and **(C)** a photo of the sensors deployed within the seagrass canopy.

(shoots m^{-2}), respectively, based on four seasonal surveys in April, August, October 2010, and February 2011 (Lee et al., 2015). The large area of the seagrass meadow, the high shoot density and coverage of seagrasses indicate that the seagrass on Dongsha Island is in a good heath condition (Lin et al., 2005). The epiphytic algae cover on seagrass leaves was previously reported to be approximately 4%, 5%, 9%, and 5% in April, June, August, and October 2010, respectively (Chang, 2012). The seasonal variations in salinity and chlorophyll *a* concentration in water column around the Dongsha Island were relatively minor, which were 33.8 ± 0.4, 33.8 ± 0.5, 33.8 ± 0.5, 34.6 ± 0.3 for salinity (Chou et al., 2021), and 0.81 ± 0.37, 0.70 ± 0.20, 0.60 ± 0.25, 0.41 ± 0.13 mg m^{-3} for Chlorophyll *a* (Liang, 2012) in spring, summer, autumn, and winter, respectively. Furthermore, only 4 rainy days were recorded during the entire study period with tiny precipitation less than 2 mm d^{-1}, suggesting that salinity could remain within a relatively stable level in the study site during the study period.

2.2 Dissolved oxygen, pCO_2, pH, and light intensity measurements

High-resolution dissolved O_2 (DO), pCO_2, and pH were measured simultaneously at intervals of 30 min, 1 h, and 30 min using HOBO U26 Dissolved Oxygen Data Logger (Onset, MA, USA) and Submersible Autonomous Moored Instrument sensors (SAMI-CO_2 and SAMI-pH; Sunburst Sensors, LLC, MT, USA), respectively. To avoid biofouling, SAMI-CO_2 and SAMI-pH are designed to isolate the sensor in an enclosed cell that is periodically flushed with sample that has been exposed to a biocide such as tributyl tin or copper, which has been proven to be useful in keeping biofouling to a minimum (Lai et al., 2018). Furthermore, the sensors using in this study were covered by copper mesh to protect from fish bites and other sources of damages (Lai et al., 2018). Before deploying, the DO logger was first calibrated to 100% saturation by placing it in water-saturated air and then to 0% saturation by placing it in sodium sulfite solution. The accuracy and resolution of DO measurement were 6 and 0.6 µM, respectively. SAMI-CO_2 and SAMI-pH sensors were returned to Sunburst Sensors LLC for re-calibration and refurbishment just before their deployments. The accuracy and resolution of pCO_2 and pH measurements were ±3 µatm and<1 µatm and ±0.003 and<0.001 pH units, respectively. The long-term drift of SAMI-CO_2 and SAMI-pH sensors was<1 µatm and<0.001, respectively, over six months. Light intensity was recorded by a HOBO UA-002-64 Data Logger (Onset, MA, USA) at an interval of 30 min, and the measured lux was converted to photosynthetically active radiation (PAR, µmol/m^2/s) by dividing lux by 52.63 (Langhans and Tibbitts, 1997). These sensors were deployed within the seagrass canopy 0.1 m above the bottom

(Figure 1C), for a period of 73 days, from 6/29 to 9/9 2019. The water column depth is approximately 1 m at the study site. Furthermore, the wind, wave and tide data during the study period were collected by Central Weather Bureau of Taiwan (Buoy Observation Data Annual Report 2019 and Tide Tables 2019).

2.3 Gross primary production, community respiration, and net community production calculations

The metabolic rates (i.e., gross primary production, GPP; community respiration, CR; net community production, NCP) were computed using the open water mass balance of O_2 (Odum, 1956). First, the hourly respiration was calculated as the temporal excursion in DO during the nighttime hours (18:00–06:00) with corrections for air-water gas exchange using the following equation:

$$\mathrm{CR} = \frac{\Delta \mathrm{DO}}{\Delta \mathrm{t}} \times h - (\text{air} - \text{water } O_2 \text{ flux})$$

where $\frac{\Delta DO}{\Delta t}$ is the rate of change in DO between two consecutive measurements (0.5 h); h is the water depth (m); and air-water O_2 flux is the air-water exchange flux of O_2, calculated with a bulk transfer approach using the formula of Wanninkhof (1992):

$$\text{Air} - \text{water } O_2 \text{ flux} = k_{600} \times S_c \times \left(O_{2(\text{water})} - O_{2(\text{air})}\right)$$

where k_{600} was the gas transfer velocity estimated using the parametrization of Ho et al. (2006), in which wind data was obtained from the meteorology station on Dongsha Island; S_c was Schmidt numbers calculated from *in situ* salinity and temperature data (Wanninkhof, 1992); $O_{2(\text{water})}$ and $O_{2(\text{air})}$ were measured and saturated DO concentrations, respectively. Time-series variations in k_{600} were shown in Figure S1, and an error analysis on the calculations of CR, GPP and NCP resulted from the uncertainty in k_{600} were given in Figure S2. Likewise, the change in the rate of DO between two consecutive measurements corrected for the exchange of O_2 with the atmosphere during daytime (06:00–18:00) corresponds to the hourly rate of NCP. Assuming a constant hourly rate of CR through the diel cycle, the hourly rate of GPP was calculated as NCP-CR (Champenois and Borges, 2012). Daily integrated GPP was computed by multiplying the average hourly rate by 12 (i.e., the daytime hours); daily integrated CR was calculated by multiplying the average hourly rate by 24 (i.e., the daytime + nighttime hours); and daily integrated NCP was computed as the sum of daily integrated GPP and daily integrated CR.

3 Results

3.1 Site characteristics: Wind, wave, and tide

The daily wind, wave and tide variations are showed in Figure 2. Daily mean wind speed ranged from 1.6 to 11 m s^{-1} with an average speed of 6.0 m s^{-1} during the study periods. Southwesterly wind direction was dominant before Julian day 232 and wind direction was variated after that day. These results reflect that southwesterly monsoon was prevailed during the summer (July and August) but ceased in the early autumn (September), which is consistent with the general pattern of the East Asia Monsoon. Daily mean wave was within a range of 0.56 – 3.37 m with an average level of 1.9 m, and most of daily wave were southwesterly direction. Tidal range was from 0.04 m of neap tide to 1.42 m of spring tide with an average level of 0.73 m.

3.2 *In-situ* monitoring of temperature, light intensity, dissolved oxygen, pCO_2, and pH

The diel patterns of temperature, light intensity, DO, pCO_2, and pH are shown in Figure 3. Over the study period, water temperature varied between 27.5 and 35.0 °C and averaged 30.4 ± 1.4 °C with a regular diurnal trend (i.e., increasing during daytime and decreasing during nighttime). The lowest temperature period occurred on Julian days 213–214 and 232–233, which corresponded well with the lowest PAR intensity period, suggesting light intensity may exert a strong control over water temperature variation. The variation ranges and the means (± SD) of DO, pCO_2, and pH were 16–529 µM and 195 ± 102 µM, 39–1565 µatm and 438 ± 252 µatm, and 7.55–8.38 and 7.97 ± 0.16 pH units, respectively. Generally, DO, pCO_2, and pH revealed distinct diurnal patterns, with DO and pH increasing but pCO_2 decreasing during the day and DO and pH decreasing but pCO_2 increasing during the night. As shown in Figure S3, both DO saturation and pCO_2 closely followed the diurnal cycle of photosynthesis and respiration, suggesting that organic carbon metabolism could play an important role in regulating the CO_2 dynamics in the seagrass meadows of Dongsha Island (Chou et al., 2018). Furthermore, similar to the temperature variation, the smallest amplitude of diel variation in DO corresponded to the lowest PAR intensity period, implying a possible important role of light intensity in regulating metabolic activities (i.e., photosynthesis and respiration) in seagrass meadows.

Provided that the average atmospheric pCO_2 with 100% humidity was 395 µatm during the study period, seawater pCO_2 was lower and higher than the atmospheric pCO_2 in up to 52% and 48% of the time, respectively, indicating contrasting times when seagrass meadows could either act as a CO_2 sink or source for the atmosphere. Likewise, assuming that the pH value of the source water was 8.0, pH was lower and higher than the source water pH in up to 55% and 45% of the time, respectively, during the entire study period, demonstrating divergent times when seagrass meadows would either enhance or mitigate ocean acidification.

3.3 Daily variability of gross primary production, community respiration, and net community production

The daily variability of GPP, CR, and NCP is presented in Figure 4. Over the study period, GPP was characterized by strong day-to-day variability, ranging between 82 and 832 mmol O_2 m^{-2} d^{-1}

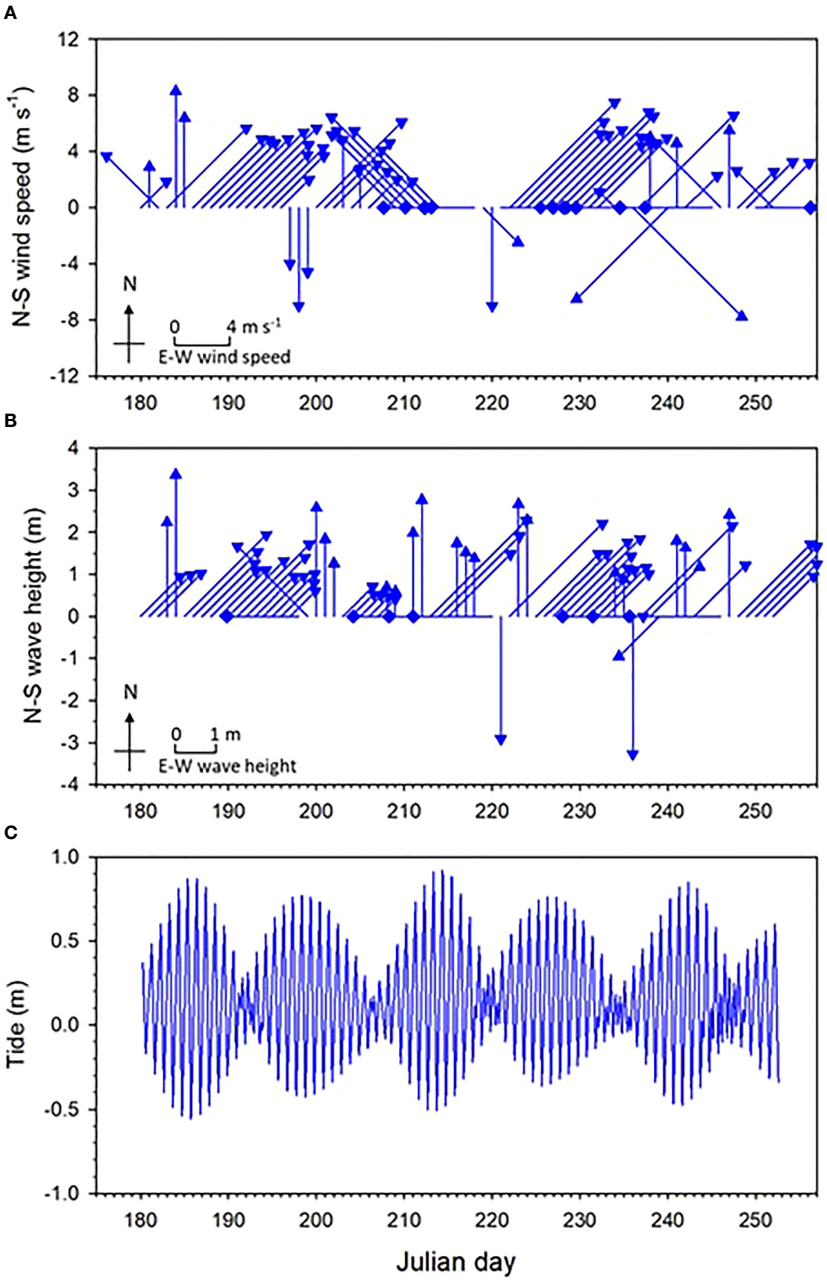

FIGURE 2
Time-series variations in **(A)** wind, **(B)**, wave, and **(C)** tide variation during the study period. Wind and wave are showed in eight directions.

with an average of 507 ± 173 mmol O_2 m^{-2} d^{-1}. The lower GPP corresponded well with the lower PAR intensity, suggesting that GPP variations could be closely related to the daily variability of irradiance. CR ranged between 99 and 900 mmol O_2 m^{-2} d^{-1} with an average of 497 ± 171 mmol O_2 m^{-2} d^{-1}, and its variations closely tracked those of GPP, implying that high GPP could also support high CR. NCP also showed a strong day-to-day variability but did not track those of either GPP or CR. During the study period, NCP ranged between −138 and 197 mmol O_2 m^{-2} d^{-1} and averaged 8 ± 61 mmol O_2 m^{-2} d^{-1}, indicating the range of ecosystem metabolism from a distinctly autotrophic to a clearly heterotrophic status and might be near metabolic balance, in general.

4 Discussion

4.1 Comparison of seagrass community metabolism between the present study and global synthesis

Based on a data set containing 403 individual estimates derived from a total of 155 different sites, Duarte et al. (2010) estimated the global mean of GPP, CR, and NCP (mean ± SE) in seagrass meadows to be 225 ± 11, 188 ± 10, and 27 ± 6 mmol O_2 m^{-2} d^{-1}, respectively, while these metabolic rates were 507 ± 173, 497 ± 171, and 8 ± 61 mmol O_2 m^{-2} d^{-1}, respectively, in the present study (Table 1). This

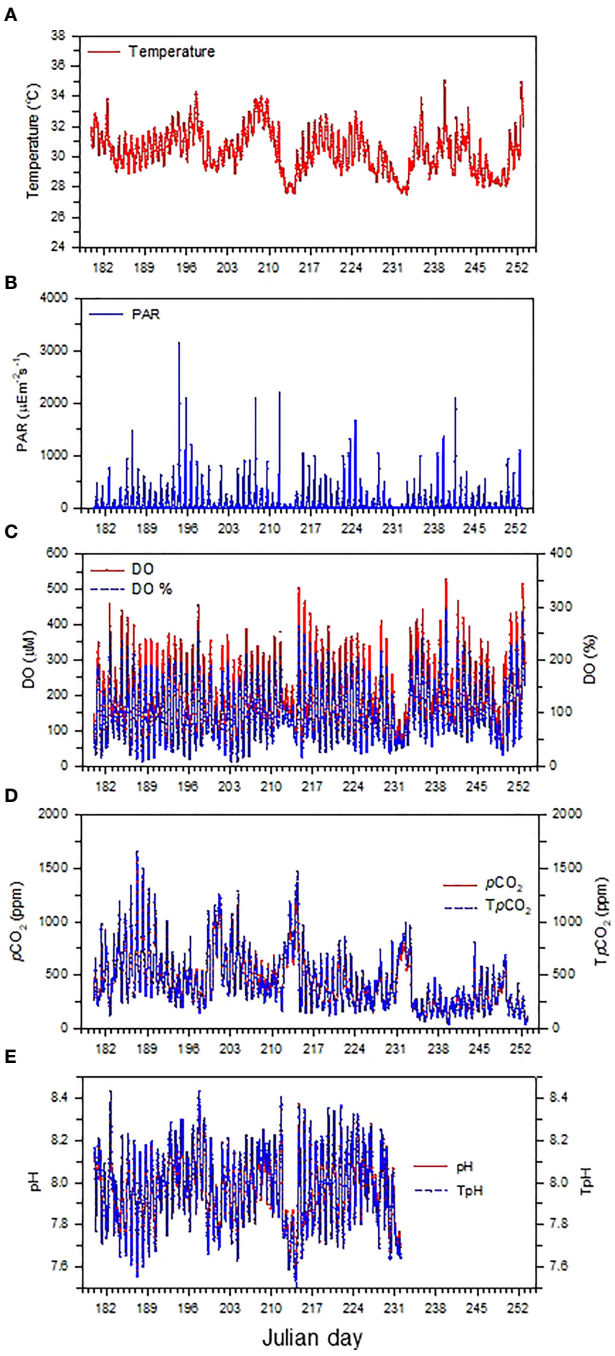

FIGURE 3
Time-series variations in **(A)** temperature, **(B)** PAR, **(C)** DO and DO saturation level (DO%), **(D)** pCO_2 (red solid line) and temperature normalized pCO_2 ($TpCO_2$, blue dashed line), and **(E)** pH (red solid line) and temperature normalized pH (TpH, blue dashed line). $TpCO_2$ and TpH were normalized to a constant temperature of 30.4 °C, the average temperature during the study period.

comparison clearly demonstrates that the averaged GPP and CR in the seagrass meadows on the northern shore of Dongsha Island were nearly 2.5 times higher than the global means, in contrast, the average NCP was similar to the global mean. This finding may not be surprising because the previous syntheses have shown that GPP, CR, and NCP reveal significant differences across different biogeographic locations and that tropical seagrass meadows tended to support higher metabolic rates, with somewhat lower NCP than temperate ones (Duarte et al., 2010). As Dongsha Island is located in the largest tropical marginal sea (the South China Sea) in the northwest Pacific, higher GPP and CR but lower NCP could be expected. Additionally, it is worth noting that the average total biomass of seagrass meadows on Dongsha Island (947-1047 g DW m^{-2}, Huang et al., 2015) is within the high end of the global dataset (716 ± 140 g DW m^{-2}, Fourqurean et al., 2012; Table 1). Furthermore, previous study has found that *Thalassia hemprichii* has the highest specific GPP to seagrass biomass ratio for meadows dominated by different species, including *Cymodocea nodosa, Cymodocea rotundata, Enhalus acoroides, Halodule uninervis, Halodule wrightii, Halophila ovalis, Posidonia oceanica, Ruppia maritime, Syringodium filiforme, Syringodium isoetifolium, Thalassia hemprichii, Thalassia testudinum* and *Zostera marina* (Duarte et al., 2010), and *Thalassia hemprichii* is one of the dominant species in the seagrass meadows on the northern shore of Dongsha Island (Lee et al., 2015). Therefore, the high biomass and high species-specific GPP to biomass ratio may partially explain the observed high GPP in the present study.

With the increasing recognition of their importance for carbon sequestration, seagrass conservation and restoration have been widely proposed as blue carbon strategies to mitigate and adapt to climate change (Nellemann et al., 2009; McLeod et al., 2011; Macreadie et al., 2019). Nevertheless, the present study suggests that seagrass meadows with high GPP in the tropical northwest Pacific do not necessarily hold a high potential for carbon sequestration due to the lower NCP. Accordingly, to obtain a better assessment of the potential of seagrass meadows as a nature-based solution for carbon sequestration, more regional-specific metabolic studies are imperatively needed before implementing any seagrass conservation and restoration plans, particularly in the northwestern Pacific archipelagos, where are hot spots of seagrass meadows but with very few record of community metabolism.

4.2 Relationships between community respiration, net community production, and gross primary production

A strong quadratic relationship was observed between CR and GPP ($CR = 129 + 0.42xGPP + 0.0006xGPP^2$, r=0.94; Figure 5A), indicating that high production rates may support high community respiration rates. In seagrass meadows, CR comprises both autotrophic respiration (AR) and heterotrophic respiration (HR). Generally, AR is linked to GPP at the time scale of minutes to hours, whereas HR is linked to GPP at the time scale of hours to days for bacteria and days to weeks for metazoans (Del Giorgio and Williams, 2005; Champenois and Borges, 2021). We observed a strong coupling between daily CR and GPP (Figure 5A), thus suggesting that HR from metazoans is less likely the dominant contributor to the observed strong coupling of GPP and CR in seagrass meadows of Dongsha Island. In contrast, seagrasses could release a substantial amount of DOC (Barrón and Duarte, 2009), which can support bacterial HR, so enhanced HR in response to DOC release associated with high GPP might contribute to the close coupling of GPP and CR. It is then likely that the tight coupling between CR and GPP is mainly due to a close coupling between AR and GPP and/or HR for bacteria and GPP. Furthermore, the

10.3389/fmars.2023.1076991

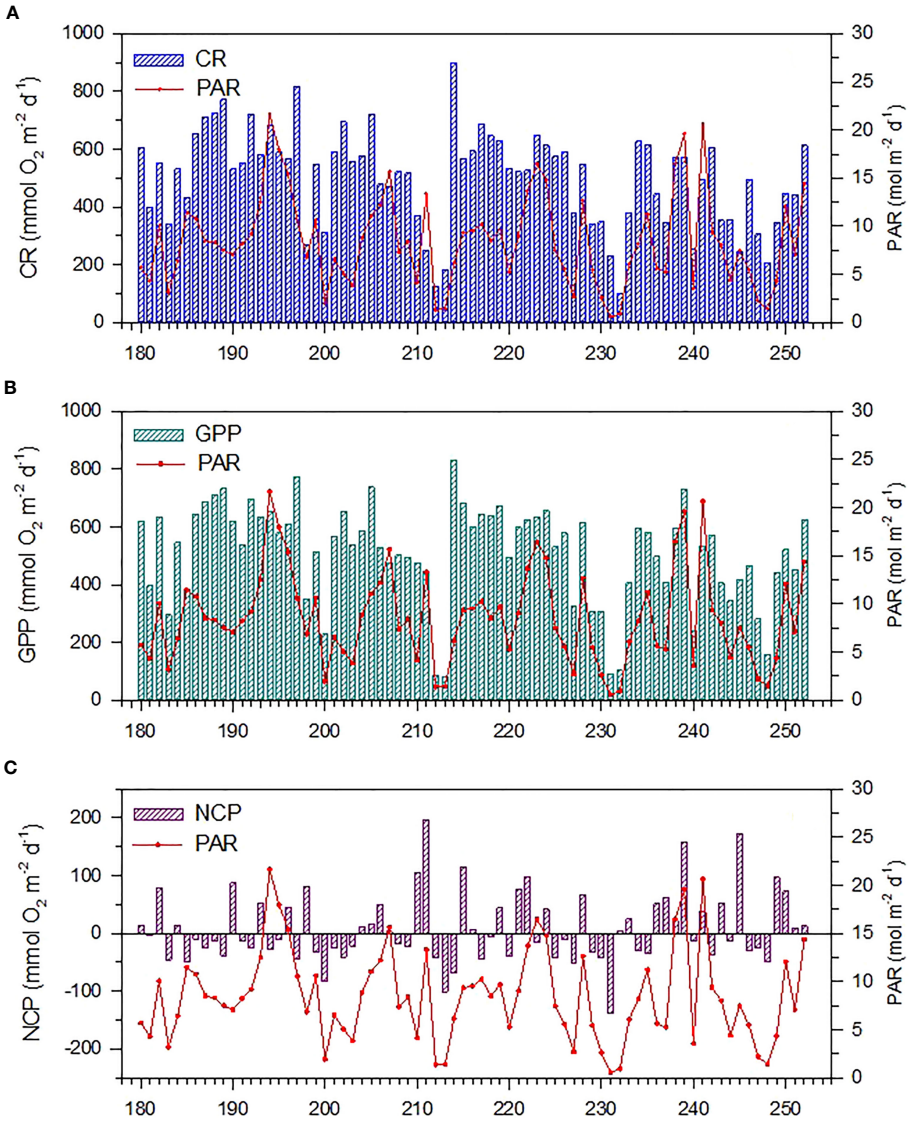

FIGURE 4
Daily **(A)** community respiration (CR), **(B)** gross primary production (GPP), and **(C)** net community production (NCP) from June 29 to September 9, 2019 (Julian day 180–252) over a seagrass meadow on the northern shore of Dongsha Island. The superimposed red line represents the daily photosynthetically active radiation (PAR).

quadratic increasing trend between CR and GPP suggest that the rate of increase in CR with GPP would be lower at lower GPP than that at higher GPP. The different CR increasing rates at various GPP levels implies that the individual contribution of AR and HR to CR could respond differently to the variation in GPP. In fact, the separation of the individual contribution of AR and HR to CR remains a challenge to date in the metabolism studies of seagrass meadows (Champenois and Borges, 2021). The current results further suggest that how the

TABLE 1 Comparison of gross primary production (GPP), community respiration (CR), net community production (NCP), and seagrass biomass in dry weight units of Dongsha Island (this study) with those for global, temperate, and tropical seagrass meadows as studied by Duarte et al. (2010) for GPP,CR and NCP, and Fourqurean et al. (2012) for total biomass.

	GPP	CR	NCP	Seagrass biomass
	(mmol O_2 m^{-2} d^{-1})			(g DW m^{-2})
Global	225±11	188±10	27±6	716 ± 140
Temperate	166 ± 14	130±10	33±8	
Tropical	252±14	217±14	24±8	
This study	507±173	497±171	8±61	947–1047

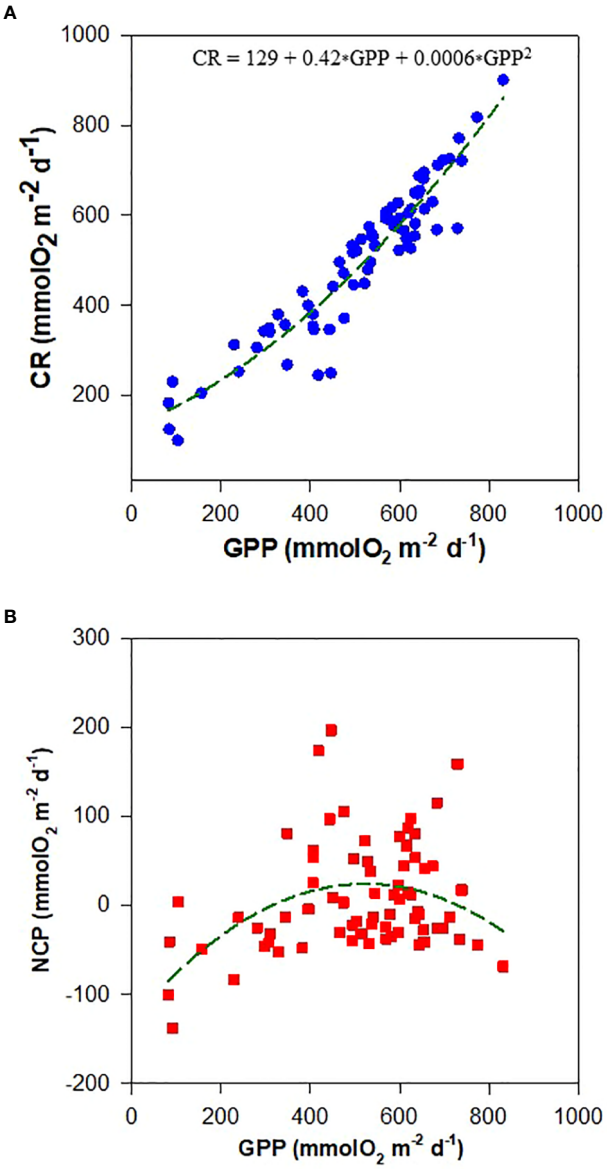

FIGURE 5
The relationship between **(A)** community respiration (CR) and gross community production (GPP) and **(B)** net community production (NCP) and GPP in seagrass meadows of Dongsha Island.

AR and HR may respond differently to GPP variations is also an open question that needs to be carefully examined for a better understanding of the relationship between CR and GPP.

Unlike the strong correlation between CR and GPP, variability was observed in the relationship between NCP and GPP (Figure 5B). Although previous studies have suggested that NCP tends to increase with GPP (Duarte and Agustí, 1998; Champenois and Borges, 2021), the present dataset revealed that the increasing trend of NCP with GPP only held true at lower GPP (GPP<~500 mmol O_2 m^{-2} d^{-1}), and NCP did not increase with GPP anymore at higher GPP (GPP>~500 mmol O_2 m^{-2} d^{-1}; Figure 5B). Interestingly, the lower rate of increase in CR at low GPP but a higher rate of increase in CR at high GPP can reasonably explain the observed divergent relationships between NCP and GPP at different GPP levels.

An average threshold GPP of 186 mmol O_2 m^{-2} d^{-1} on a global scale was proposed by Duarte et al. (2010), above which the seagrass meadows tended to be autotrophic (NCP>0) and shifted to heterotrophy (NCP<0) at lower GPP values. The average GPP in the current study was higher than 186 mmol O_2 m^{-2} d^{-1}, and NCP was positive and thus qualitatively in agreement with the global assessment. In spite of this agreement, the present dataset revealed a quite different GPP threshold from the global average; the present results show that seagrass meadows in the study area tended to be heterotrophic when GPP< 347 and GPP > 620 mmol O_2 m^{-2} d^{-1}, but they tended to be autotropic when GPP between 347 and 620 mmol O_2 m^{-2} d^{-1} (Figure 5B). These results demonstrate again that the metabolic relationship in the seagrass meadows of Dongsha Island may deviate greatly from the global mean condition reported in previous synthesis studies, and thus more regional-specific studies are still needed in the key regions where support extensive seagrass meadows but have not yet been charted, such as Indonesia and Pacific archipelagos.

4.3 Relationship between net community production and pCO_2

Although NCP and daily average pCO_2 showed an expected negative correlation (Champenois and Borges, 2021; Figure 6A), the autotrophic/heterotrophic status did not correspond well to the sink/source behavior of CO_2 in the seagrass meadow of Dongsha Island on a daily scale. As shown in Figure 6A, when NCP<0 (heterotrophic), pCO_2 could fluctuate from a strong sink status (pCO_2< 200 µatm) to a strong source status (pCO_2 > 900 µatm), providing air pCO_2 = 395 µatm. Similarly, when NCP>0 (autotrophic), pCO_2 could also demonstrate either a sink or a source status. These results suggest that the organic carbon metabolism could not be the only dominant factor in determining the sink/source status of seagrass meadows (Macreadie et al., 2017; Saderne et al., 2019). This proposition can be further supported by the observed divergent temporal trends of NCP and pCO_2 in the present dataset. As shown in Figure 6B, NCP did not show either a decrease or an increasing trend over the study period, while pCO_2 revealed a significant decreasing trend with time.

Several recent studies have highlighted that in addition to organic metabolism, inorganic carbon processing (i.e., calcium carbonate precipitation/dissolution; Macreadie et al., 2017; Saderne et al., 2019) and the external sources of land-based pollutants (Banerjee et al., 2018) may also play a pivotal role in regulating the capacity of CO_2 sequestration of seagrass meadows. Since Dongsha Island is a military control zone, there is no permanent inhabitants neither no freshwater flow into the sea from the island, the impact of land-based pollution sources could be negligible. In terms of carbonate precipitation/dissolution, Van Dam et al. (2021) recently reported that calcification-induced CO_2 emissions may exceed organic carbon sequestration in the seagrass-dominated estuary in central Florida Bay, and they argued that net carbon sequestration of seagrasses might be overestimated if calcification-induced CO_2 emissions are not accounted for. On the contrary, our previous studies around Dongsha Island revealed that the enhancement of total alkalinity (TA) coupled with carbonate dissolution may enhance the CO_2 sequestration capacity in seagrass meadows (Chou et al., 2018; Chou et al., 2021). We suggest that the lower pCO_2 in late August and early September (Julian day 230–250) compared with that in late June and early July (Julian day 180–200) could be associated with the favorable condition for TA accumulation in water column deriving from sedimentary carbonate dissolution and/or anaerobic metabolism. During the monsoon

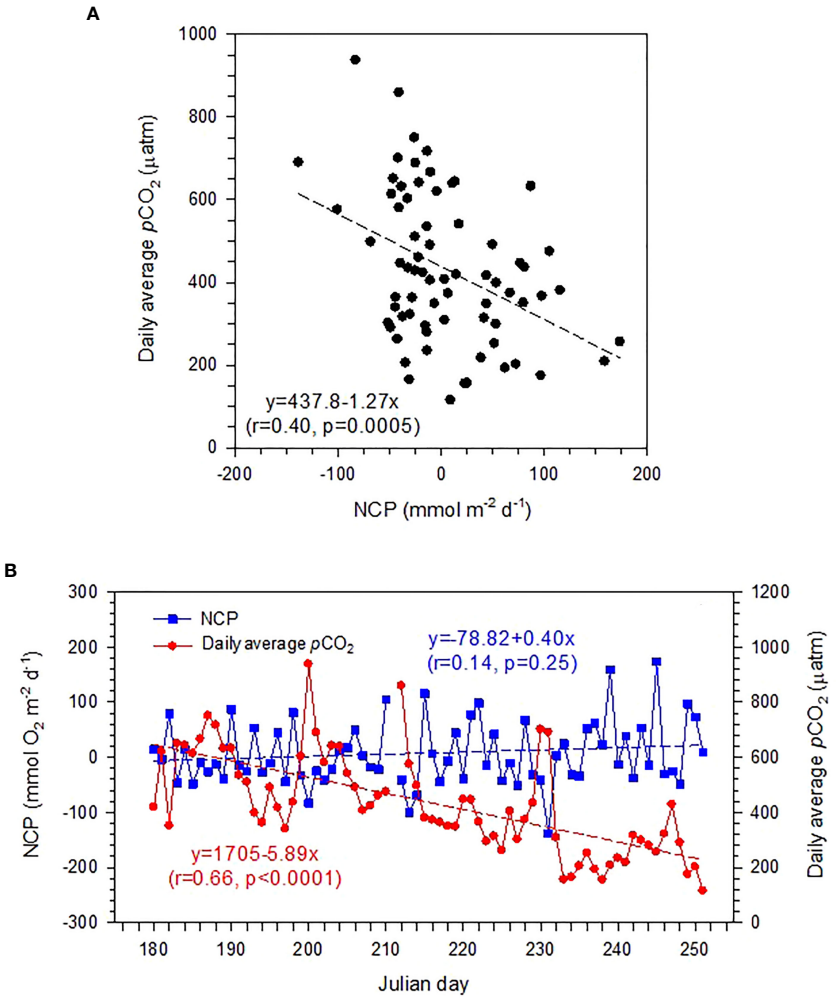

FIGURE 6
(A) The relationship between daily average pCO_2 and net community production (NCP), and **(B)** daily variations in NCP and average pCO_2 during the study period (June 29 to September 9, 2019, Julian day 180–252).

transition period, the weak wind results in less energetic hydrodynamics and longer residence time for the waters around Dongsha Island, making it favorable for the occurrence of sedimentary metabolic carbonate dissolution and/or anaerobic TA generation and the subsequent TA accumulation in the overlying waters (Chou et al., 2018; Chou et al., 2021). The elevated TA may lead to a lower pCO_2 level at a relatively stable NCP level. Unfortunately, TA data were unavailable during the monsoon transition period for northeasterly in September, but Chou et al. (2021) indeed found significantly higher TA during the monsoon transition period for southwesterly in April than in summer. This result implies that the different hydrodynamic regimes may lead to divergent sedimentary organic and inorganic metabolic processes, which may exert an important influence on regulating the carbon sequestration capacity of seagrass meadows. Therefore, the focus on organic carbon metabolism alone may not be enough, and hydrodynamics and calcium carbonate cycling remain key uncertainties that will need to be addressed to more accurately estimate the net carbon sequestration potential of seagrass meadows, especially for seagrass meadows with underlying carbonate sediments.

In summary, the present study is the first to report the metabolic rates of seagrass meadows in the Southeast Asia region. The results show that although daily NCP varied largely from autotrophy to heterotrophy, the average NCP over the entire study period was nearly in balance. Furthermore, the calculated GPP and CR in the present study were significantly higher, but NCP was similar to the global means, suggesting that seagrass meadows with higher GPP may not necessarily hold higher blue carbon potential. We also found that organic carbon metabolism was not the only dominant factor in determining the sink/source status in seagrass meadows of Dongsha Island, and hydrodynamics and calcium carbonate cycling may exert an important influence on regulating the carbon sequestration capacity of carbonate seagrass meadows. Since the present work was done mainly during the southwesterly monsoon period, more studies with better temporal coverage, in particular during the northeasterly monsoon and monsoon transition period are still needed to elucidate the linkage between monsoon-driven change in hydrodynamic and biogeochemical processes controlling CO_2 variation in seagrass meadow on Dongsha Island. Overall, the current results in the Southeast Asia region deviate greatly from the global mean condition, and thus regional-specific studies are imperatively needed before implementing any seagrass conservation and restoration as a nature-based solution for carbon sequestration.

Data availability statement

The raw data supporting the conclusions of this article will be made available by the authors, without undue reservation.

Author contributions

W-CC conceived the study design, performed the field work, and wrote the manuscript. L-FF, C-CH, Y-YS, W-JH, H-KL, and T-YC contributed to the data collection and interpretation. All authors contributed to the article and approved the submitted version.

Funding

Funding was provided by the Ministry of Science and Technology of Taiwan, under grants no. #110-2611-M-019 -012 – and #111-2119-M-019 -002, awarded to W-CC.

Acknowledgments

We are grateful to the Dongsha Atoll Research Station, Dongsha Atoll National Park, and Coast Guard Administration for assistance in field sampling. We would also like to thank Ying-Hsuan Chen, Hui-Chuan Chu, Kuan-Chieh Wu, and Chang-Chang Yang for their help with the field and laboratory work.

Conflict of interest

The authors declare that the research was conducted in the absence of any commercial or financial relationships that could be construed as a potential conflict of interest.

Publisher's note

Supplementary material

The Supplementary Material for this article can be found online at: https://www.frontiersin.org/articles/10.3389/fmars.2023.1076991/full#supplementary-material

References

Banerjee, K., Paneerselvam, A., Ramachandran, P., Ganguly, D., Singh, G., and Ramesh, R. (2018). Seagrass and macrophyte mediated CO_2 and CH_4 dynamics in shallow coastal waters. *PloS One* 13 (10), e0203922. doi: 10.1371/journal.pone.0203922

Barrón, C., and Duarte, C. M. (2009). Dissolved organic matter release in a *Posidonia oceanica* meadow. *Mar. Ecol. Prog. Ser.* 374, 75–84. doi: 10.3354/meps07715

Barrón, C., Duarte, C. M., Frankignoulle, M., and Borges, A. V. (2006). Organic carbon metabolism and carbonate dynamics in a Mediterranean seagrass (*Posidonia oceanica*) meadow. *Estuar. Coast.* 29, 417–426. doi: 10.1007/BF02784990

Chai, F., Liu, G., Xue, H., Shi, L., Chao, Y., Tseng, C. M., et al. (2009). Seasonal and interannual variability of carbon cycle in south China Sea: a three-dimensional

physical-biogeochemical modeling study. *J. Oceanogr.* 65, 703–720. doi: 10.1007/s10872-009-0061-5

Champenois, W., and Borges, A. V. (2012). Seasonal and interannual variations of community metabolism rates of a *Posidonia oceanica* seagrass meadow. *Limnol. Oceanogr.* 57, 347–361. doi: 10.4319/lo.2012.57.1.0347

Champenois, W., and Borges, A. V. (2021). Net community metabolism of a *Posidonia oceanica* meadow. *Limnol. Oceanogr.* 66, 2126–2140. doi: 10.1002/lno.11724

Chang, H.-Y. (2012). *Spatial-temporal variation of epiphytic assemblages on seagrass leaves around dongsha island* (Taichung, Taiwan: National Chung Hsing University). Master thesis (in Chinese with English abstract).

Chou, W.-C., Chu, H.-C., Chen, Y.-H., Syu, R.-W., Hung, C.-C., and Soong, K. (2018). Short-term variability of carbon chemistry in two contrasting seagrass meadows at dongsha island: Implications for pH buffering and CO_2 sequestration. *Estuar. Coast. Shelf Sci.* 210, 36–44. doi: 10.1016/j.ecss.2018.06.006

Chou, W.-C., Fan, L.-F., Yang, C.-C., Chen, Y.-H., Hung, C.-C., Huang, W.-J., et al. (2021). A unique diel pattern in carbonate chemistry in the seagrass meadows of dongsha island: the enhancement of metabolic carbonate dissolution in a semienclosed lagoon. *Front. Mar. Sci.* 8. doi: 10.3389/fmars.2021.717685

Dai, C.-F. (2006). "Dongsha atoll in the South China Sea: Past, present and future," in *Proceeding of 10th International Coral Reef Symposium*, Okinawa, Japan. June 28-July 2, 2004. 1587–1592 pp.

Del Giorgio, P. A., and Williams, P. J. L. B. (2005). *Respiration in aquatic ecosystems* (New York: Oxford Univ. Press), 315. doi: 10.1093/acprof:oso/9780198527084

Duarte, C. M., and Agustí, S. (1998). The CO_2 balance of unproductive aquatic ecosystems. *Science* 281, 234–236. doi: 10.1126/science.281.5374.234

Duarte, C. M., and Chiscano, C. L. (1999). Seagrass biomass and production: a reassessment. *Aquat. Bot.* 65, 159–174. doi: 10.1016/S0304-3770(99)00038-38

Duarte, C. M., Kennedy, H. A., Marbá, N., and Hendriks, I. (2013). Assessing the capacity of seagrass meadows for carbon burial: Current limitations and future strategies. *Ocean Coast. Manage.* 83, 32–38. doi: 10.1016/j.ocecoaman.2011.09.001

Duarte, C. M., Marbà, N., Gacia, E., Fourqurean, J. W., Beggins, J., Barrón, C., et al. (2010). Seagrass community metabolism: Assessing the carbon sink capacity of seagrass meadows. *Global Biogeochem. Cycles* 24, GB4032. doi: 10.1029/2010GB003793

Fortes, M. D., Ooi, J. L. S., Tan, Y. M., Prathep, A., Bujang, J. S., and Yaakub, S. M. (2018). Seagrass in southeast Asia: a review of status and knowledge gaps, and a road map for conservation. *Botanica Marina;* 61, 269–288. doi: 10.1515/bot-2018-0008

Fourqurean, J. W., Duarte, C. M., Kennedy, H., Marbà, N., Holmer, M., Mateo, M. A., et al. (2012). Seagrass ecosystems as a globally significant carbon stock. *Nat. Geosci.* 5, 505–509. doi: 10.1038/ngeo1477

Ho, D. T., Law, C. S., Smith, M. J., Schlosser, P., Harvey, M., and Hill, P. (2006). Measurements of air-sea gas exchange at high wind speeds in the southern ocean: Implications for global parameterizations. *Geophys. Res. Lett.* 33, L16611. doi: 10.1029/2006GL026817

Huang, Y. H., Lee, C. L., Chung, C. Y., Hsiao, S. C., and Lin, H. J. (2015). Carbon budgets of multispecies seagrass beds at dongsha island in the south China sea. *Mar. Environ. Res.* 106, 92–102. doi: 10.1016/j.marenvres.2015.03.004

Lai, C.-Z., DeGrandpre, M. D., and Darlington, R. C. (2018). Autonomous optofluidic chemical analyzers for marine applications: insights from the submersible autonomous moored instruments (SAMI) for pH and pCO_2. *Front. Mar. Sci.* 4. doi: 10.3389/fmars.2017.00438

Langhans, R. W., and Tibbitts, T. W. (1997). *Plant Growth Chamber Handbook. (Iowa Agriculture and Home Economics Experiment Station Special Report No. 99 (SR-99) and North Central Regional Research Publication No. 340.)*. R. W. Langhans and T. W. Tibbitts Eds. (Ames, IA, USA: Iowa State University).

Lee, C.-L., Huang, Y.-H., Chung, C.-Y., Hsiao, S.-C., and Lin, H.-J. (2015). Herbivory in multi-species, tropical seagrass beds. *Mar. Ecol. Prog. Ser.* 525, 65–80. doi: 10.3354/meps11220

Lee, J. S., Kang, D.-J., Hineva, E., Slabakova, V., Todorova, V., Park, J., et al. (2017). Estimation of net ecosystem metabolism of seagrass meadows in the coastal waters of the East Sea and black Sea using the noninvasive eddy covariance technique. *Ocean Sci. J.* 52, 243–256. doi: 10.1007/s12601-017-0032-5

Lee, C.-L., Lin, W.-J., Liu, P.-J., Shao, K.-T., and Lin, H.-J. (2021). Highly productive tropical seagrass beds support diverse consumers and a Large organic carbon pool in the sediments. *Diversity* 13, 544. doi: 10.3390/d13110544

Liang, C.-H. (2012). *Temporal-spatial variation of heterotrophic bacterioplankton production and its growth controlling factor in dong-sha atoll* (Keelung, Taiwan: National Taiwan Ocean University). Master thesis (in traditional Chinese with English abstract).

Lin, H. J., Hsieh, L. Y., and Liu, P. J. (2005). Seagrasses of tongsha island, with descriptions of four new records to Taiwan. *Bot. Bull. Acad.* 46, 163–168.

Macreadie, P. I., Anton, A., Raven, J. A., Beaumont, N., Connolly, R. M., Friess, D. A., et al. (2019). The future of blue carbon science. *Nat. Commun.* 10, 3998. doi: 10.1038/s41467-019-11693-w

Macreadie, P. I., Serrano, O., Maher, D. T., Duarte, C. M., and Beardall, J. (2017). Addressing calcium carbonate cycling in blue carbon accounting. *Limnol. Oceanogr. Lett.* 2, 195–192. doi: 10.1002/lol2.10052

McLeod, E., Chmura, G. L., Bouillon, S., Salm, R., Björk, M., Duarte, C. M., et al. (2011). A blueprint for blue carbon: toward an improved understanding of the role of vegetated coastal habitats in sequestering CO_2. *Front. Ecol. Environ.* 9, 552–560. doi: 10.1890/110004

Middelburg, J. J., Duarte, C. M., and Gattuso., J.-P. (2005). "Respiration in coastal benthic communities," in *Respiration in aquatic ecosystems*. Eds. P. A. del Giorgio and P.J.l. Williams (Oxford, U. K.: Oxford Univ. Press), 206–224.

Nellemann, C., Corcoran, E., Duarte, C. M., Valdes, L., DeYoung, C., Fonseca, L., et al. (2009). *Blue carbon, the role of healthy oceans in binding carbon, a rapid response assessment, united nations environment programme, GRID-arendal.* (Birkeland Trykkeri AS: Norway) 80.

Odum, H. T. (1956). Primary production in flowing waters. *Limnol. Oceanogr.* 1, 102–117. doi: 10.4319/lo.1956.1.2.0102

Saderne, V., Geraldi, N. R., Macreadie, P. I., Maher, D. T., Middelburg, J. J., Serrano, O., et al. (2019). Role of carbonate burial in blue carbon budgets. *Nat. Commun.* 10, 1106. doi: 10.1038/s41467-019-08842-6

Short, F., Carruthers, T., Dennison, W., and Waycott, M. (2007). Global seagrass distribution and diversity: A bioregional model. *J. Exp. Mar. Biol. Ecol.* 350, 3–20. doi: 10.1016/j.jembe.2007.06.012

Van Dam, B. R., Zeller, M. A., Lopes, C., Smyth, A. R., Böttcher, M. E., and Osburn, C. L. (2007). Calcification-driven CO2 emissions exceed "Blue Carbon" sequestration in a carbonate seagrass meadow. *Sci. Adv.* 7, eabj1372. doi: 10.1126/sciadv.abj1372

Van Dam, B. R., Lopes, C., Osburn, C. L., and Fourqurean, J. W. (2019). Net heterotrophy and carbonate dissolution in two subtropical seagrass meadows. *Biogeosciences* 16, 4411–4428. doi: 10.5194/bg-16-4411-2019

Wanninkhof, R. H. (1992). Relationship between wind speed and gas exchange. *J. Geophys. Res.* 97, 7373–7382. doi: 10.1029/92JC00188

Frontiers in Marine Science

Explores ocean-based solutions for emerging global challenges

The third most-cited marine and freshwater biology journal, advancing our understanding of marine systems and addressing global challenges including overfishing, pollution, and climate change.

Discover the latest Research Topics

See more →

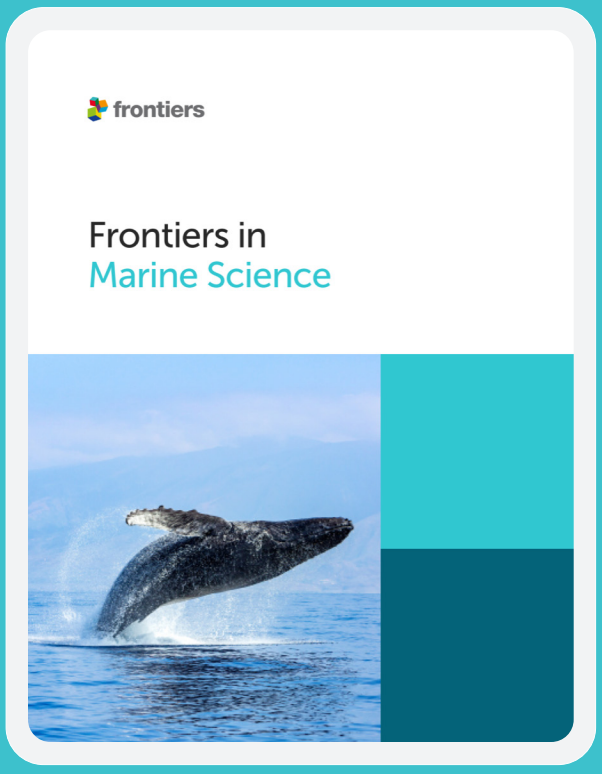

Frontiers

Avenue du Tribunal-Fédéral 34
1005 Lausanne, Switzerland
frontiersin.org

Contact us

+41 (0)21 510 17 00
frontiersin.org/about/contact